Title
Metal-Organic Frameworks for Gas Storage and Separation

Author
Mason, Jarad Adam

Publication Date
2015

Peer reviewed|Thesis/dissertation

Metal-Organic Frameworks for Gas Storage and Separation

by

Jarad Adam Mason

A dissertation submitted in partial satisfaction of the

requirements for the degree of

Doctor of Philosophy

in

Chemistry

in the

Graduate Division

of the

University of California, Berkeley

Committee in charge:

Professor Jeffrey R. Long, Chair
Professor T. Don Tilley
Professor Jeffrey A. Reimer

Summer 2015

Metal-Organic Frameworks for Gas Storage and Separation

by

Jarad Adam Mason

Abstract

Metal-Organic Frameworks for Gas Storage and Separation

By

Jarad Adam Mason

Doctor of Philosophy in Chemistry

University of California, Berkeley

Professor Jeffrey R. Long, Chair

The work presented in this dissertation describes the design, synthesis, and characterization of metal-organic frameworks for applications in gas storage and gas separations, with a specific focus on natural gas and hydrogen storage for mobile applications and on post-combustion carbon dioxide capture from coal- or natural gas-fired power plants. A wide variety of techniques and spectroscopic methods are covered, including gas adsorption, x-ray diffraction, infrared and UV-vis-NIR spectroscopies, and calorimetry.

Chapter One provides a brief introduction to metal-organic frameworks as a new class of porous materials for gas adsorption-related applications. The potential of metal-organic frameworks for use in post-combustion carbon dioxide capture and natural gas storage is discussed, and the unique and promising properties of adsorbents with stepped adsorption isotherms for these applications are highlighted.

In *Chapter Two*, two representative metal-organic frameworks, $Zn_4O(BTB)_2$ (BTB^{3-} = 1,3,5-benzenetribenzoate; MOF-177) and $Mg_2(dobdc)$ ($dobdc^{4-}$ = 1,4-dioxido-2,5-benzenedicarboxylate; Mg-MOF-74, CPO-27-Mg), are evaluated in detail for their potential use in post-combustion CO_2 capture via temperature swing adsorption (TSA). Low-pressure single-component CO_2 and N_2 adsorption isotherms were measured every 10 °C from 20 to 200 °C, allowing the performance of each material to be analyzed precisely. In order to gain a more complete understanding of the separation phenomena and the thermodynamics of CO_2 adsorption, the isotherms were analyzed using a variety of methods. These results show that the presence of strong CO_2 adsorption sites is essential for a metal-organic framework to be of utility in post-combustion CO_2 capture via a TSA process, and present a methodology for the evaluation of new metal-organic frameworks via analysis of single-component gas adsorption isotherms.

Chapter Three briefly discusses high-pressure adsorption measurements and reviews efforts to develop metal-organic frameworks with high methane storage capacities. To illustrate the most important properties for evaluating adsorbents for natural gas storage and for designing a next generation of improved materials, six metal-organic frameworks and an activated carbon, with a range of surface areas, pore structures, and surface chemistries representative of the most promising adsorbents for methane storage, are evaluated in detail. High-pressure methane adsorption isotherms are used to compare gravimetric and volumetric capacities, isosteric heats of adsorption, and usable storage capacities. Additionally, the relative importance of increasing

volumetric capacity, rather than gravimetric capacity, for extending the driving range of natural gas vehicles is highlighted. Other important systems-level factors, such as thermal management, mechanical properties, and the effects of impurities, are also considered, and potential materials synthesis contributions to improving performance in a complete adsorbed natural gas system are discussed.

Chapter Four discusses the design and validation of a high-throughput multicomponent adsorption instrument that can measure equilibrium adsorption isotherms for mixtures of gases at conditions that are representative of an actual flue gas from a power plant. This instrument is used to study 15 different metal-organic frameworks, zeolites, mesoporous silicas, and activated carbons representative of the broad range of solid adsorbents that have received attention for CO_2 capture. While the multicomponent results provide many interesting fundamental insights, only adsorbents functionalized with alkylamines are shown to have any significant CO_2 capacity in the presence of N_2 and H_2O at equilibrium partial pressures similar to those expected in a carbon capture process. Most significantly, the amine-appended metal organic framework mmen-Mg_2(dobpdc) (mmen = *N*,*N*′-dimethylethylenediamine, dobpdc^{4-} = 4,4′-dioxido-3,3′-biphenyldicarboxylate) exhibits a record CO_2 capacity of 4.2±0.2 mmol/g (16 wt %) at 0.1 bar and 40 °C in the presence of a high partial pressure of H_2O.

In *Chapter Five*, the flexible metal-organic frameworks M(bdp) (M = Fe, Co; bdp^{2-} = 1,4-benzene-dipyrazolate) are shown to exhibit methane adsorption isotherms that feature a sharp step, giving rise to unprecedented performance characteristics for ambient temperature methane storage. Adsorption measurements combined with *in situ* powder X-ray diffraction and microcalorimetry experiments performed on Co(bdp) demonstrate a new approach to designing adsorbents for gas storage, wherein a reversible phase transition is used to achieve a high deliverable capacity while providing intrinsic thermal management. Importantly, the energy of the phase transition, together with the adsorption and desorption step pressures, can be controlled through variations in the framework structure, such as replacing Co with Fe, or by application of mechanical pressure. This approach overcomes many of the challenges to developing adsorbents for natural gas storage discussed in Chapter Three and is also relevant to other gas storage applications.

Chapter Six discusses the synthesis and characterization of a new Ti(III) metal-organic framework that is constructed from 1,4-benzenedicarboxylate bridged $Ti_3O(COO)_6$ clusters. While many metal-organic frameworks have been synthesized with exposed divalent metal cations, there are comparatively few examples of metal-organic frameworks with coordinatively unsaturated trivalent metal centers. Among other potential applications, frameworks with exposed trivalent metal cations are of particular interest for ambient temperature H_2 storage. Additionally, there are also very few reported titanium-based metal-organic frameworks and none that contain all titanium(III). Through a combination of adsorption measurements, diffraction analysis, EPR, infrared, and UV-vis-NIR spectroscopies, and magnetic measurements, this framework is shown to contain five-coordinate Ti^{3+} cations that irreversibly bind O_2 to form titanium(IV)-superoxo and -peroxo species.

To my parents,
Eric and Lori Mason

Table of Contents

List of Figures

Chapter 1

Chapter 2

Chapter 3

Chapter 4

Chapter 5

Chapter 6

Appendix A

List of Tables and Schemes

Acknowledgements

The work presented in my thesis would not have been possible without significant contributions from my advisor, fellow group members, and collaborators. Throughout my entire PhD at Berkeley, I have been fortunate enough to have worked with and become friends with many exceptionally talented scientists.

While it was not an easy choice, going to Berkeley to work for Jeff was one of the best decisions I ever made. Jeff has taught me how to be a better presenter, a better writer, a better figure-maker, and a better scientist. I'm thankful for the wide range of opportunities he has given me while in his group and for all of the advice he has given and continues to give me.

Dave Harris was the first one of Jeff's graduate students that I met at Berkeley. Although he had already left the group when I started, he played a big role in convincing me to come to Berkeley and has given me valuable advice on many occasions ever since. I only overlapped with Jeff Rinehart and Hema Karundasa for a short time, but both represented the types of scientists I hoped I could eventually become by the end of my PhD. I have always wanted to be able to give as good of a research talk as those I saw from Jeff and Hema during my first year.

When I first arrived at Berkeley, Kenji Sumida helped me get started in the group. He played a major role in teaching me how to make nice figures, give clear presentations, and write effective papers. Despite pretending to be a grumpy, bitter, and jaded senior grad student, Joe Zadrozny also gave me a lot of helpful advice as I was getting started. He taught be me how to deal with sitting close to Xiaowen, how not to react if you light your trashcan on fire, and how not to flag down an AC Transit bus late at night.

Tom McDonald and I have worked together on countless projects over the course of my PhD, and he has consistently been the first person I go to when trying to understand new concepts and interpret confusing results. My PhD would certainly not have been as successful or as enjoyable if it were not for being able to work so closely with him. Brian Wiers was always an entertaining person to have around, and I have never met anyone who knew so much about such a diverse range of topics. At the end of my first year, Brian synthesized a very interesting new compound that resulted in the first structure I ever solved from powder diffraction. I enjoyed sitting near Zoey Herm during my first several years of grad school. She played a significant role in helping me start thinking about the best ways to fit and analyze adsorption data and to perform accurate high-pressure adsorption measurements. I also had the pleasure of getting to know Curtis Wray during my first year in graduate school. Curtis was a great person to have around lab, and he taught me many things during the short time we overlapped.

Eric Bloch and I worked together for the majority of my PhD. We had a long-running competition to be the first to arrive in lab each morning and were routinely blasting country music (including plenty of Taylor Swift) by 6am. My time in Berkeley would have been far less enjoyable had Eric not been around. Xiaowen Feng sat less than 5 feet away from me in lab for 4 long years. In spite of his constant supply of stupid questions (e.g. uhh…Jarad…uhh…Jarad…uhh…Jarad…how do you spell "reaction"?), weird friskiness, and many other annoying habits, lab would not have been the same without him, and I probably did enjoy at least some of our interactions. In contrast, Katie Meihaus and Dana Levine have always been great people to have around lab, and I've enjoyed talking to and working with both of them.

Jordan Axelson and David Zee joined Jeff's group at the same time as me, and both have been good friends throughout my entire time in Berkeley. During most of my first year, Jordan and I were usually the last ones left at work, blasting music in each of our labs until well past

midnight. I still do not understand why David insists on trying to give me awkwardly long hugs at every opportunity, but I mostly enjoyed having him around. I've always been impressed with David's knowledge of inorganic chemistry, and he has often been able to offer useful questions about and insights into my research.

Dianne "Hulk" Xiao was the first person I tried to recruit to join our group, and, most of the time, I do not regret this. Aside from when she shot hexanes directly into my eye, I've enjoyed nearly all of my many conversations with Dianne. Miguel Gonzales quickly became an expert in single crystal diffraction after joining the group, and he has worked with me on several projects and offered insightful advice on many others. I've always been impressed with his attention to detail, whether in his chemistry, his manuscript reviews, or his bartending. I was equally impressed with how quickly Mike Aubrey became an expert in conductivity, forcing the MOF subgroup to sit through so many rollercoaster plots that he managed to create his own subgroup. I know the group will be in good hands with Mike watching over our lab space.

In my 3rd year, Phil Bunting, Matt Kapelewski, Lucy Darago, and Doug Reed joined the group. Matt is my first friend who actually went to Penn State, and surprisingly, he's not all that bad. Although it hasn't always been easy, we have somehow managed to keep (most) program managers happy while working together on several projects. Phil has also been great to have around, but I'm probably most grateful for all the packages of candy his mom sent to me during my last two years. Lucy rapidly took control of the magnetism subgroup and contributed significantly to the last chapter of my thesis. Doug has also been a great addition to the group and has taken on a lot of responsibility in maintaining our adsorption equipment.

Julia Oktawiec, Mercedes Taylor, Rodi Torres-Gavosto, and Jon Bachman joined the group in my 4th year. Both Julia and Mercedes had particularly significant contributions to what is probably the most important chapter of my thesis, and I will always be grateful for that. I know our group's powder diffraction efforts are in good hands with Julia in control. Even though he is not a mechanical engineer, which would have been far more useful, Jon Bachman has gotten off to a great start as the group's first chemical engineering graduate student. We've had many fruitful discussions about thermodynamics and adsorption that have had a big impact on much of my research during the last two years.

In my final year, Rebecca Siegelman and Kristin Colwell joined the group. Rebecca has already taken on an impressive amount of responsibility around lab, and I am excited to see everything they accomplish over the next few years.

I have had the privilege of getting to know and working with many postdocs from all over the world during my time in Berkeley. Hye-Jin Choi sat next to me for my first year in the Long group. She is by far the nicest person I have encountered during my PhD, and she is an extremely talented scientist who taught me a lot when I was getting started. Hye-Jin and I shared a secret stash of candy in lab, and I always appreciated how careful she was to make sure no one else found out about it. Tae-Hyun Bae started in the group just before me, and we sat through numerous meetings with Wildcat and went on several troubleshooting trips to San Diego together. One of the major chapters of my thesis would most certainly have not been possible without his help.

When Wendy Queen showed up, I was surprised to discover that our purported visiting Australian postdoc was in fact from South Carolina. Nonetheless, many parts of my PhD would not have been possible without her persistence, ideas, and expertise. Wendy taught me how to build anything out of Swagelok parts and how to never give up on an experiment, no matter what the challenges were. Although Michael Nippe looks (and sometimes acts) like an evil villain

straight out of a James Bond movie, he was a really great person to have in the group, and we had many very useful conversations about research over beef egg udon bowls on the Northside. Perhaps just as importantly, Michael taught me how to properly react to lighting your trashcan on fire.

I enjoyed working closely with many other great postdocs during my time in Berkeley, and I am particularly thankful for all the advice I received from Elizabeth Montalvo, Paulina Gomora, Rob Ameloot, Jeff van Humbeck, Selly Demir, and Keith Keitz.

I also was able to work with many talented undergraduates, including Mary Anne Manumpil, Kaitlyn Weeber, David Gygi, Raymond Yu, and Jo Melville. David and Raymond were particularly helpful during many parts of my PhD, and I look forward to watching both have very successful graduate careers of their own.

While in Jeff's group, I have been lucky enough to work with very knowledgeable collaborators from all over the world. Norberto Masciocchi taught me everything I know about powder diffraction during 3 weeks in Italy at the beginning of my PhD, and he has remained an integral part of many of my research projects ever since. I've also enjoyed working with and getting to Craig Brown over the course of my entire PhD, and I hope to continue collaborating with him in the future. Regardless of what Tom and Julia might say, Craig will always be a young, physically fit scientist in my mind.

I never would have gotten to where I am today were it not for the many people who have helped me along the way. My high school chemistry teacher Mr. Rushin introduced me to chemistry and single-handedly put me on the path to a PhD in chemistry. At Penn, Prof. Don Berry gave me a lot of helpful advice and ultimately convinced me to go to graduate school. As an undergraduate, I worked in the groups of Prof. Brad Wayland and Prof. Larry Sneddon, both of whom have had a big impact on my scientific career. In my last year at Penn, Prof. Sneddon is the one who pointed me to Jeff Long's group at UC Berkeley.

Getting to graduate school also would not have been possible without the support of my family. My parents, Eric and Lori, have always encouraged me to do whatever made me happy and have provided me the education, support, and motivation to get where I am today. My brother Andrew and sister Sabrina have always been there for me, and talking to them on the phone while walking up and down the hill to lab always made me feel happy and refreshed. My family continues to be there anytime I need them, and I am grateful for everything they have done and continue to do for me.

Throughout my entire PhD, Ivy has been my best friend and a constant source of support and encouragement. Staying close while being in graduate school over 2,000 miles apart was one of the more challenging parts of my time in Berkeley, but through countless redeye flights, 48-hour weekend trips, and Skype conversations, we have been able to still share and enjoy many things together over the last 5 years. I thank Ivy for always being there for me, and I'm incredibly excited to start our next adventure together.

To all my friends, family, and colleagues, thank you.

Chapter 1: Metal-Organic Frameworks for Gas Storage and Separation

1.1. Introduction

Metal-organic frameworks are a relatively new class of porous solids that are composed of metal ions or clusters bridged by organic ligands to form a three-dimensional coordination network. Owing to their high surface areas, convenient modular synthesis, and tunable surface properties, these materials have received significant attention for a wide range of applications, including gas adsorption, catalysis, conductivity, and drug delivery.[1] Since both the metal and organic components can be judiciously selected, use of the appropriate components can result in a porous material tailored for a specific application. Metal-organic frameworks hold particular promise as a next generation of advanced porous materials for storing and separating gases.[2,3] Performing energy-efficient gas separations and maximizing the amount of gas that can be stored in a given volume are fundamental materials challenges that have become increasingly important to meeting the world's energy demands in a more sustainable way. As will be shown, unique adsorption properties can be realized in appropriately designed metal-organic frameworks, leading unprecedented performance for applications in gas storage and gas separation.

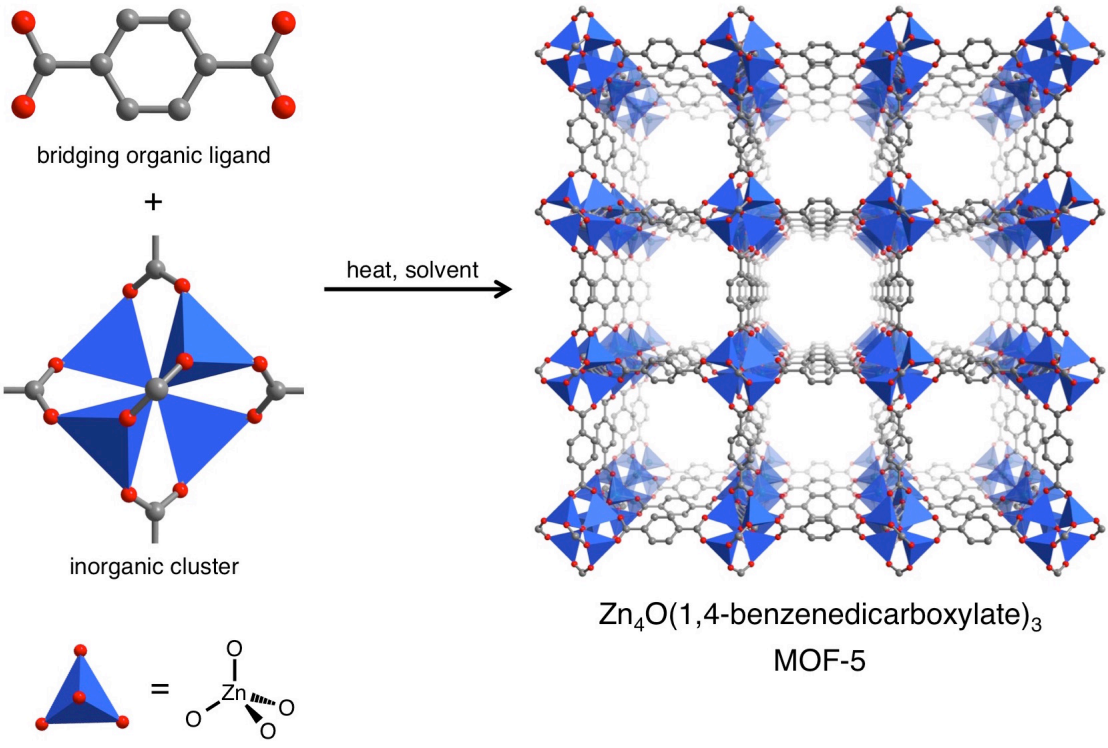

Figure 1.1. Using 1,4-benzenedicarboxylate (bdc^{2-}) to bridge clusters of $[Zn_4O]^{6+}$ results in the formation of the three-dimensional metal-organic framework $Zn_4O(bdc)_3$ (MOF-5). Gray and red spheres represent C and O atoms, respectively; H atoms have been omitted for clarity. Blue tetrahedral represent Zn_4O units.

1.2. Post-Combustion Carbon Dioxide Capture

As the ramifications of rising anthropogenic carbon dioxide emissions become clearer, it is becoming increasingly important to meet the world's growing energy demands in a more sustainable way.[4] With coal-fired power plants contributing more than 40% to annual global CO_2 emissions from fuel combustion, the development of practical and effective methods for CO_2 capture and sequestration is critical to mitigating the impacts of escalating CO_2 levels in the short term.[5] In post-combustion CO_2 capture at a coal-fired power plant, CO_2 is present in the flue gas at a partial pressure of 0.15 bar, while N_2 is the primary component at 0.75 bar.[6] Consequently, the separation of CO_2 from N_2 is the major challenge to capturing pure CO_2 from flue gas so that it can be efficiently compressed, transported, and permanently sequestered.[7] As will be shown in Chapters 2 and 4, materials that reversibly adsorb large amounts of CO_2 in the presence of H_2O and that have a high selectivity for CO_2 over N_2 are critical for practical CO_2 capture applications.

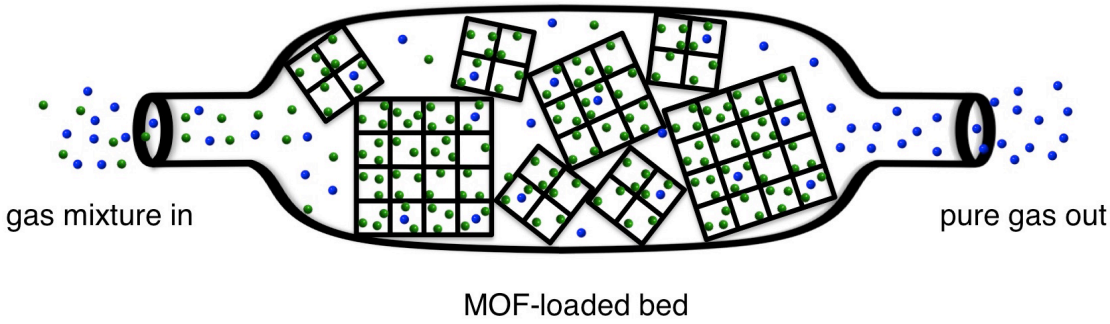

Figure 1.2. Illustration of a MOF-loaded adsorbent bed for the selective capture of CO_2 (green) over N_2 (blue).

In existing capture technologies employing aqueous alkanolamine solutions (amine "scrubbers"), the primary cost of the CO_2/N_2 separation is associated with the high energy requirements of regeneration of the capture material (representing as much as 40% of the energy output of the power plant) owing to the large quantity of water that must be heated in order to evolve CO_2 from the saturated adsorbent.[8,9] Thus, materials that feature a lower energy penalty for regeneration, while maintaining a high selectivity towards CO_2 over the other components of the flue gas, are crucial for improving the efficiency of CO_2 capture.

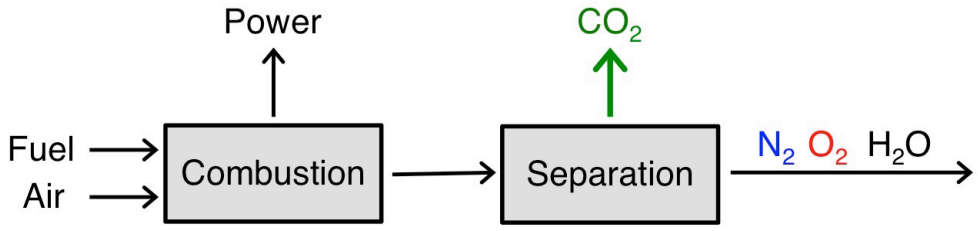

Figure 1.3. In a post-combustion CO_2 capture process, CO_2 is extracted from a flue gas mixture that contains mostly N_2, O_2, and H_2O.

As solid adsorbents, metal-organic frameworks are expected to have lower regeneration costs compared to aqueous alkanolamine solutions since the majority of the energy supplied as heat

will go directly toward desorbing CO_2 and not heating water.[10] Moreover, the strength of the CO_2-adsorbent interaction can be optimally tuned by introducing specific functionalities on the pore surface of the metal-organic framework. Strong adsorption sites are necessary in order for the material to selectively bind CO_2 over N_2, although if the sites bind CO_2 too strongly, the energy required to regenerate the material will result in a CO_2 capture process that is too expensive to be practical.

One of the most promising strategies for tuning the pore surface for various applications in both gas storage and separation is the introduction of exposed metal cation (open metal) sites.[11] Open metal sites are typically introduced by heating the metal-organic framework to remove coordinated solvent molecules from the metal centers. The resulting Lewis acidic sites are highly-polarizing, and serve to increase the binding energy and facilitate a high adsorption capacity and selectivity for certain small molecules. Indeed, open metal sites have been shown to have stronger interactions with CO_2 due to its higher quadrupole moment and greater polarizability than that of N_2.[12] Moreover, open metal sites offer an additional opportunity for tuning the surface chemistry of a metal-organic framework through post-synthetic functionalization. In Chapter 4 and Appendix A, for instance, the attachment of diamine molecules to open metal sites is shown to give materials with unprecedented CO_2 capture performance.

1.3. Natural Gas Storage

Natural gas has the potential to replace petroleum as the world's primary fuel for transportation. Consisting mainly of methane (CH_4), natural gas has the highest H to C ratio of any fossil fuel, resulting in less CO and CO_2 released per unit of energy generated.[13] Lower sulfur and nitrogen contents also lead to lower SO_x and NO_x emissions, making natural gas a significantly cleaner burning fuel than gasoline.[14] Indeed, initial field tests found up to 86% less CO, 26% less CO_2, and 77% less NO_x emissions after converting gasoline cars to run on natural gas.[15] In addition, recent engineering advances in horizontal drilling and hydraulic fracturing have led to a rapid increase in global natural gas reserves, driving the price of natural gas below that of gasoline in many countries.[16]

In spite of this, several challenges have prevented the widespread use of natural gas in vehicles. Most importantly, the volumetric energy density of natural gas at ambient temperature and pressure is only 0.04 MJ/L, compared to 32.4 MJ/L for gasoline.[17] The volumetric energy density can be increased by compression or liquefaction, but both of these solutions are costly and poorly suited for light-duty passenger vehicles. For instance, compressed natural gas (CNG) requires expensive multi-stage compressors that consume energy, as well as heavy, bulky fuel tanks that reduce passenger and cargo space. Even with compression to 250 bar, the energy density of CNG (near 9 MJ/L) is only 26% that of gasoline,[14a] leading to a significant reduction in the driving range of a vehicle. Moreover, CNG refueling stations are not yet common enough for convenient refueling and are costly to build.[18]

As a result of the low critical temperature of CH_4 (190.6 K, Table 1), natural gas cannot be liquefied by compression alone, and cryogenic cooling is necessary to store liquefied natural gas (LNG). While the volumetric energy density of LNG can reach 20.8 MJ/L (64% of gasoline),[17] the overall system energy density is reduced due to the insulation required to maintain a low temperature and prevent boil-off. Additionally, the high cost of cooling systems and complications of handling a cryogenic fuel make LNG unlikely to find much application in the

transportation sector beyond commercial trucking and public transportation.[19]

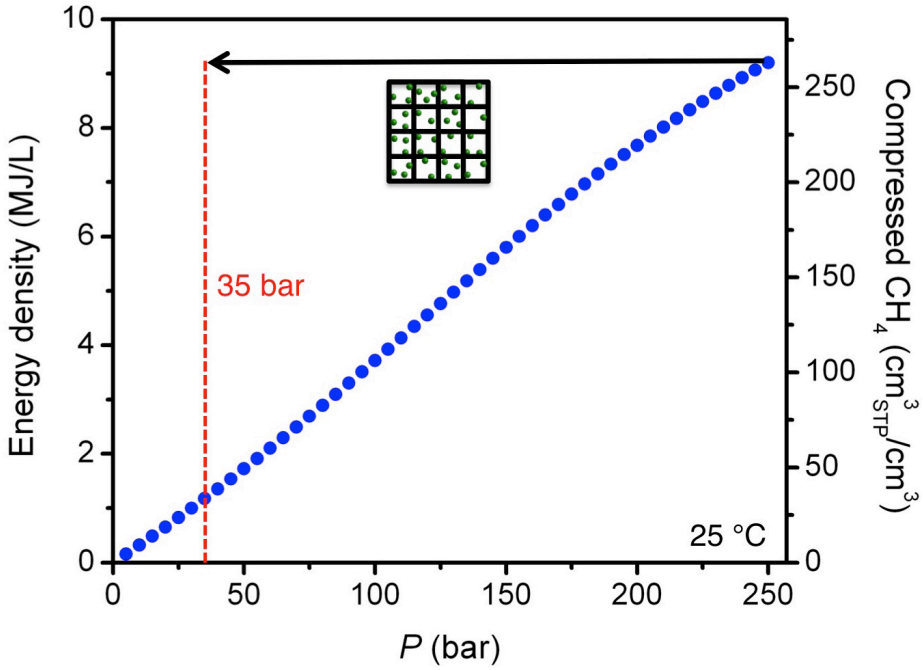

Figure 1.4. In natural gas storage applications, an adsorbent is used to store high densities of a gas at lower pressures than would be required in an empty fuel tank.

As an alternative to CNG and LNG, using adsorbents to store natural gas at higher densities at ambient temperature and moderate pressures has been an active area of research since the early 1970s.[20a] Significantly, adsorbents that operate at relatively low pressures should allow the use of inexpensive on-board fuel tanks and single-stage compressors. Lower storage pressures also facilitate at-home refueling,[19] which would reduce the large investment needed to build a new refueling infrastructure since natural gas distribution networks are already connected to many homes throughout the world.[18] Additionally, adsorbed natural gas (ANG) systems would permit the use of lightweight, conformable fuel tanks that can be more optimally integrated into the limited space available within a small car.[21] Note that in addition to natural gas powered cars, which are the focus of this work, ANG systems have also been evaluated for use in mobile natural gas tankers and for large-scale, stationary storage on natural gas distribution pipelines.[22] Although it is important to evaluate and optimize a similar set of adsorbent properties for each of these applications, the relevant storage conditions can differ significantly.

While early efforts in ANG storage focused primarily on zeolites, their relatively low surfaces areas of less than 1,000 m^2/g resulted in insufficient CH_4 capacities.[19,20] With considerably higher surface areas, activated carbons have been the most studied class of materials for ANG over the last several decades.[23] A large portion of research has involved investigating the effects of surface area, pore size, and pore shape on the CH_4 adsorption properties of different carbons. Indeed, it was demonstrated that slit-shaped pores with a diameter of 7.6 Å, which can accommodate two layers of CH_4, are ideal for maximizing the volumetric density of CH_4 stored at 35 bar and 25 °C.[24,25] Note that 35 bar has been widely used as a standard pressure for evaluating adsorbents for ANG storage, as this has represented the maximum pressure achievable by most inexpensive single-stage compressors.[26] Additionally,

strategies for compacting and shaping activated carbons to optimize packing inside a storage tank have been explored in depth,[13] and prototype activated carbon ANG systems have been demonstrated and tested.[27]

In 2012, the US Department of Energy set new CH_4 storage targets for absorbents at 350 $cm^3_{STP}/cm^3_{adsorbent}$ (v/v)[28] and 0.5 $g_{CH4}/g_{adsorbent}$ (699 cm^3_{STP}/g).[29] Assuming a 25% loss in volumetric capacity due to packing an adsorbent inside a fuel tank, the target of 350 v/v is required for an ANG system to have a volumetric energy density of 263 v/v, equivalent to that of CNG at 250 bar and 25 °C. The highest reported volumetric CH_4 capacities for activated carbons are in the range of 100-170 v/v,[30] well below the energy density of CNG, and computational studies have predicted a theoretical maximum volumetric capacity for carbons of 198 v/v at 34 bar and 25 °C.[24] Accordingly, a next generation of adsorbents is required to meet these storage targets without moving to higher adsorption pressures or lower temperatures, both of which would add significant complexity and cost to an ANG vehicle. Owing to their high porosity and tunable pore surfaces, metal-organic frameworks have received significant attention as a new class of adsorbents for gas storage.[31] While early research on these materials for gas storage applications was mostly related to H_2,[32] a growing number of frameworks have been evaluated for CH_4 storage.[33,34] As will be shown in Chapters 3 and 5, several metal-organic frameworks have CH_4 capacities comparable to and even exceeding those of the best activated carbons.

Table 1.1. The volumetric and gravimetric energy densities of natural gas are compared to petroleum.

	Energy Density	
	(MJ/L)	(MJ/kg)
Diesel	37.3	46.2
Gasoline	34.2	46.4
Natural Gas	0.04	50.0
LNG (111 K)	22.2	50.0
CNG (250 bar)	9.2	50.0

1.4. Metal-Organic Frameworks with Stepped Adsorption Isotherms

The majority of metal-organic frameworks that have been studied for adsorption-related applications exhibit classical Langmuir-type adsorption isotherms, where the amount of gas adsorbed increases continuously and with decreasing steepness as the pressure is increased. As will be shown in Chapters 4 and 5 and Appendix A, metal-organic frameworks that feature adsorption isotherms with sharp steps have significant advantages for many gas storage and gas separation processes. For instance, high usable (working) capacities can be achieved with smaller decreases in pressure or increases in temperature than would be required for classical adsorbents. Stepped adsorption isotherms generally result from a discrete phase transition occurring at a temperature-dependent transition pressure. Such reversible phase transitions in metal-organic frameworks can arise both from structural flexibility (pore expansion and collapse) and from cooperative chemical reactions that occur on the pore surface.[35 - 40] Significantly, the

thermodynamics of the phase transitions can be controlled via chemical modifications and by external stimuli to tune an adsorbent for a specific application.

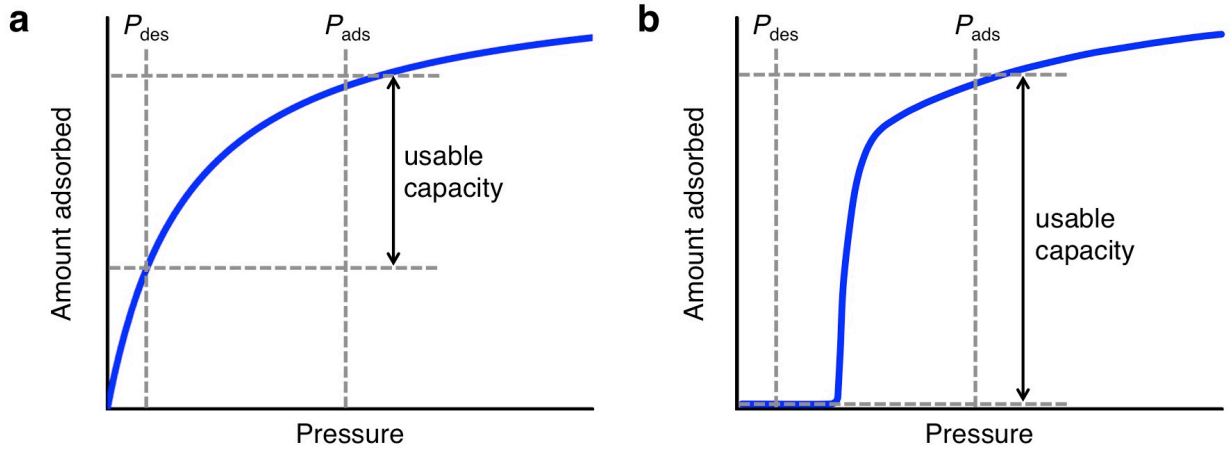

Figure 1.5. The usable capacity is compared for an idealized adsorbent that exhibits a classical Langmuir-type adsorption isotherm (a) and an "S-shaped", or stepped, adsorption isotherm (b).

1.5. References

(1) (a) Kitagawa, S.; Kitaura, R.; Noro, S. *Angew. Chem. Int. Ed.* **2004**, *43*, 2334. (b) Férey, G.; Mellot-Draznieks, C.; Serre, C.; Millange, F. *Acc. Chem. Res.* **2005**, *38*, 217. (c) Kitagawa, S.; Matsuda, R. *Coord. Chem. Rev.* **2007**, *251*, 2490. (d) Férey, G. *Chem. Soc. Rev.* **2008**, *37*, 191. (e) Furukawa, H.; Ko, N.; Go, Y. B.; Aratani, N.; Choi, S. B.; Choi, E.; Yazaydin, A. O.; Snurr, R. Q.; O'Keefe, M.; Kim, J.; Yaghi, O. M. *Science* **2010**, *329*, 424.

(2) (a) Eddaoudi, M.; Rosi, N.; Vodak, D.; Wachter, J.; O'Keeffe, M.; Yaghi, O. M. *Science* **2002**, *295*, 469. (b) Matsuda, R.; Kitaura, R.; Kitagawa, S.; Kubota, Y.; Belosludov, R. V.; Kobayashi, T. C.; Sakamoto, H.; Chiba, T.; Takata, M.; Kawazoe, Y.; Mita, Y. *Nature* **2005**, *436*, 238. (c) Millward, A. R.; Yaghi, O. M. *J. Am. Chem. Soc.* **2005**, *127*, 17998. (d) Furukawa, H.; Miller, M. A.; Yaghi, O. M. *J. Mater. Chem.* **2007**, *17*, 3197. (e) Ma, S.; Sun, D,; Simmons, J. M.; Collier, C. D.; Yuan, D.; Zhou, H.-C. *J. Am. Chem. Soc.* **2008**, *130*, 1012. (f) Morris, R. E.; Wheatley, P. S. *Angew. Chem., Int. Ed.* **2008**, *47*, 4966. (g) Llewellyn, P. L.; Bourrelly, S.; Serre, C.; Vimont, A.; Daturi, M.; Hamon, L.; de Weireld, G.; Chang, J.-S.; Hong, D.-Y.; Hwang, Y. K.; Jhung, S. H.; Férey, G. *Langmuir* **2008**, *24*, 7245. (h) Murray, L. J.; Dincă, M.; Long, J. R. *Chem. Soc. Rev.* **2009**, *38,* 1294-1314. (i) Chen, B.; Xiang, S.; Qian, G. *Acc. Chem. Res.* **2010**, 1115.

(3) (a) Hayashi, H.; Côté, A. P.; Furukawa, H.; O'Keeffe, M.; Yaghi, O. M. *Nat. Mater.* **2007**, *6*, 501. (b) Britt, D,; Tranchemontagne, D. J.; Yaghi, O. M. *Proc. Natl. Acad. Sci.* U.S.A. **2008**, *105*, 11623. (c) Britt, D.; Furukawa, H.; Wang, B.; Glover, T. G.; Yaghi, O. M. *Proc. Natl. Acad. Sci.*, U.S.A. **2009**, *106*, 20637. (d) Li, J.-R.; Kuppler, R. J.; Zhou, H.-C. *Chem. Soc. Rev.* **2009**, *38*, 1477.

(4) Metz, B,; Davidson, O.; de Coninck, H.; Loos, M.; Meyer, L. *Intergovernmental Panel on Climate Change. Special Report on Carbon Dioxide Capture and Storage*, Cambridge Press, Cambridge, **2005**, http://www.ipcc.ch/.
(5) *CO_2 Emissions from Fuel Combustion*, International Energy Agency, Paris, **2010**, http:/www.iea.org.
(6) (a) Granite, E. J.; Pennline, H. W. *Ind. Eng. Chem. Res.* **2002**, *41*, 5470. (b) Lee, K. B.; Sircar, S. *AIChE Journal* **2008**, *54*, 2293.
(7) Haszeldine, R. S. *Science* **2009**, *325*, 1647.
(8) Rochelle, G. T. *Science* **2009**, *325*, 1652.
(9) Figueroa, J. D.; Fout, T.; Plasynski, S.; McIlvried, H.; Srivastava, R. D. *Intl. J. of Green House Gas Control* **2008**, *2*, 9.
(10) (a) Li, G. R.; Kuppler, R. J.; Zhou, H.-C. *Chem. Soc. Rev.* **2009**, *38*, 1477. (b) Yazayydin, A. Ö.; Snurr, R. Q.; Park, T. H.; Koh, K.; Liu, J.; LeVan, M. D.; Benin, A. I.; Jakubczak, P.; Lanuza, M.; Galloway, D. B.; Low, J. J.; Willis, R. R. *J. Am. Chem. Soc.* **2009**, *131*, 18198. (c) D'Alessandro, D. M.; Smit, B.; Long, J. R. *Angew. Chem. Int. Ed.* **2010**, *49*, 6058. (d) Keski, S.; van Heest, T. M.; Sholl, D. S. *ChemSusChem* **2010**, *3*, 879. (e) Férey, G.; Serre, C.; Devic, T.; Maurin, G.; Jobic, H.; Llewellyn, P. L.; de Weireld, G.; Vimont, A.; Daturi, M.; Chang, J. S. *Chem. Soc. Rev.* **2011**, *40*, 550. (f) Simmons, J. M.; Wu, H.; Zhou, W.; Yildirim, T. *Energy Environ. Sci.* **2011**, *4*, 2177.
(11) (a) Dietzel, P. D. C.; Morita, T.; Blom, R.; Fjellvag, H. *Angew. Chem., Int. Ed.* **2005**, *44*, 6354. (b) Dincă, M.; Long, J. R. *J. Am. Chem. Soc.* **2005**, *127*, 9376. (c) Vimont, A.; Goupil, J.-M.; Lavalley, J.-C.; Daturi, M.; Surblé, S.; Serre, C.; Millange, F.; Férey, G.; Audebrand, N. *J. Am. Chem. Soc.* **2006**, *128*, 3218. (d) Moon, H. R.; Kobayashi, N.; Suh, P. M. *Inorg. Chem.* **2006**, *45*, 8672. (e) Dincă, M.; Dailly, A.; Liu, Y.; Brown, C. M.; Neumann, D. A.; Long, J. R. *J. Am. Chem. Soc.* **2006**, *128*, 16876. (f) Dietzel, P. D. C.; Panella, B.; Hirscher, M.; Blom, R.; Fjellvag, H. *Chem. Commun.* **2006**, 959. (g) Dincă, M.; Han, W. S.; Liu, Y.; Dailly, A.; Brown, C. M.; Long, J. R. *Angew. Chem., Int. Ed.* **2007**, *46*, 1419. (h) Dietzel, P. D. C.; Blom, R.; Fjellvag, H. *Eur. J. Inorg. Chem.* **2008**, 3624. (i) Liu, Y.; Kabbour, H.; Brown, C. M.; Neumann, A. D.; Ahn, C. C. *Langmuir* **2008**, *24*, 4772. (j) Dietzel, P. D. C.; Johnsen, R. E.; Fjellvag, H.; Bordiga, S.; Groppo, E.; Chavan, S.; Blom, R. *Chem. Commun.* **2008**, 5125. (k) Zhou, W.; Wu, H.; Yildirim, T. *J. Am. Chem. Soc.* **2008**, *130*, 15268. (l) Dietzel, P. D. C.; Besikiotis, V.; Blom, R. *J. Mater. Chem.* **2009**, *19*, 7362. (m) Sumida, K.; Horike, S.; Kaye, S. S.; Herm, Z. R.; Queen, W. L.; Brown, C. M.; Grandjean, F.; Long, G. J.; Dailly, A.; Long, J. R. *Chem. Sci.* **2010**, *1*, 184.
(12) Chowdhury, P.; Bikkina, C.; Gumma, S. *J. Phys. Chem. C*, **2009**, *113*, 6616.
(13) Celzard, A.; Fierro, V. *Energy Fuels* **2005**, *19*, 573.
(14) (a) Talu, O. *Proc. IVth Int. Conf. on Fundamentals of Adsorption*, Kyoto, **1992**, 655. (b) Lozanao-Castelló, D.; Alcañiz-Monge, J.; de la Casa-Lillo, M. A.; Cazorla-Amorós, D.; Linares-Solano, A. *Fuel* **2002**, *81*, 1777.
(15) Blazek, C. F.; Grimes, J.; Freman, P.; Bailey, B. K.; Colucci, C. *Amer. Chem. Soc. Preprints* (*Div. Fuel Chem.*) **1994**, *39*, 476.
(16) International Energy Agency, "World Energy Outlook 2011: Are We Entering a Golden Age of Gas", <www.worldenergyoutlook.org>.

(17) Alternative Fuels Data Center – Fuel Properties Comparison, **2013**, <http://www.afdc.energy.gov/fuels/fuel_comparison_chart.pdf>.
(18) (a) Yeh, S. *Energy Policy* **2007**, *35*, 5865. (b) Whyatt, G. A. "Issues Affecting Adoption of Natural Gas in Light- and Heavy-Duty Vehicles", **2010**, PNNL-19745.
(19) Menon, V. C.; Komarneni, S. *J. Porous Mater.*, 1998, **5**, 43.
(20) (a) Munson, R. A.; Clifton, R. A. *Natural Gas Storage with Zeolites*, U.S. Dept. of the Interior, **1971**. (b) Cracknell, R. F.; Gordon, P.; Gubbins, K. E. *J. Phys. Chem.* **1993**, *97*, 494.
(21) Wegrzyn, J.; Gurevich, M. *Appl. Energy* **1996**, *55*, 71.
(22) (a) Judd, R. W.; Gladding, D.T. M.; Hodrien, R. C.; Bates, D. R.; Ingram, J. P.; Allen, M. *Amer. Chem. Soc. Preprints* (*Div. Fuel Chem*) **1998**, *43*, 575. (b) Dvorak, K.; Hodrien, R. C. "Development of Adsorbed Natural Gas Technology for Large Scale Diurnal Storage Applications", *Int. Gas Research Conference*, Amsterdam, **2001**. (c) Lau, L. Y.; Judd, R. "New Approach to Natural Gas Storage – Advances in Adsorbed Natural Gas (ANG) Technology", *Int. Gas Research* Conference, Paris, **2008**.
(23) Parkyns, N. D.; Quinn, D. F. *Porosity in Carbons*, ed. Patrick, J. W.; Edward Arnold, London, **1995**, ch. 11.
(24) Matranga, K. R.; Myers, A. L.; Glandt, E. D. *Chem. Eng. Sci.* **1992**, *47*, 569.
(25) Note that 11.4 Å pores, which can accommodate 3 layers of CH_4, are optimal for maximizing the amount of usable CH4 for adsorption near 35 bar and desorption near 1 bar.
(26) Quinn, D. F.; MacDonald, J. A.; Sosin, K. *Amer. Chem. Soc. Preprints* (*Div. Fuel Chem*) **1994**, *39*, 451.
(27) Pfeifer, P.; Aston, L.; Banks, M.; Barker, S.; Burress, J.; Carter, S.; Coleman, J.; Crockett, S.; Faulhaber, C.; Flavin, J.; Gordon, M.; Hardcastle, L.; Kallenborn, Z.; Kemiki, M.; Lapilli, C.; Pobst, J.; Schott, R.; Shah, P.; Spellerberg, S.; Suppes, G.; Taylor, D.; Tekeei, A.; Wexler, C.; Wood, M.; Buckley, P.; Breier, T.; Downing, J.; Eastman, S.; Freeze, P.; Graham, S.; Grinter, S.; Howard, A.; Martinez, J.; Radke, D.; Vassalli, T.; Ilavsky, J. *Chaos*, **2007**, *17*, 041108.
(28) The unit cm^3_{STP} is defined as the volume occupied by an ideal gas at a standard temperature and pressure (STP). Here, STP is defined as 273.15 K and 1 atm, resulting in a volume of 22.414 mL for 1 mmol of ideal gas at STP.
(29) "Methane Opportunities for Vehicular Energy", Advanced Research Project Agency – Energy, U.S. Dept. of Energy, Funding Opportunity No. DE-FOA-0000672, **2012**.
(30) Cook, T. L.; Komodromos, C.; Quinn, D. F.; Ragan, S. *Carbon Materials for Advanced Technologies*, ed. Burchell, T. D. Elsevier, Amsterdam, **1999**, ch. 9.
(31) (a) Li, H.; Eddaoudi, M.; O'Keeffe, M.; Yaghi, O. M. *J. Am. Chem. Soc.* **1999**, *402*, 276. (b) Matsuda, R.; Kitaura, R.; Kitagawa, S.; Kubota, Y.; Belosludov, R. V.; Kobayashi, T. C.; Sakamoto, H.; Chiba, T.; Takata, M.; Kawazoe,Y.; Mita, Y. *Nature* **2005**, *436*, 238. (c) Millward, A. R.; Yaghi, O. M. *J. Am. Chem. Soc.* **2005**, *127*, 17998. (d) Morris, R. E.; Wheatley, P. S. *Angew. Chem., Int. Ed.* **2008**, *47*, 4966. (e) Czaja, A. U.; Trukhan, N.; Müller, U. *Chem. Soc. Rev.* **2009**, *38*, 1284. (f) Chen, B.; Xiang, S.; Qian, G. *Acc. Chem. Res.* **2010**, 1115. (g) Zhou, H.-C.; Long, J. R.; Yaghi, O. M. *Chem. Rev.* **2012**, *112*, 673. (h) Sumida, K.; Rogow, D. L.; Mason, J. A.; McDonald, T. M.; Bloch, E. D.; Herm, Z. R.;

Bae, T.-H.;. Long, J. R. *Chem. Rev.* **2012**, *112*, 724. (i) Li, J.-R.; Sculley, J.; Zhou, H.-C. *Chem. Rev.* **2012**, *112*, 869.
(32) (a) Furukawa, H.; Miller, M. A.; Yaghi, O. M. *J. Mater. Chem.* **2007**, *17*, 3197. (b) Dincă, M.; Long, J. R. *Angew. Chem. Int. Ed.* **2008**, *47*, 6766. (c) Suh, M. P.; Park, H. J.; Prasad, T. K.; Lim, D.-W. *Chem. Rev.* **2012**, *112*, 782.
(33) Kondo, M.; Yoshitomi, T.; Seki, K.; Matsuzaka, H.; Kitagawa, S. *Angew. Chem. Int. Ed. Engl.* **1997**, *36*, 1725.
(34) (a) Eddaoudi, M.; Kim, J.; Rosi, N.; Vodak, D.; Wachter, J.; O'Keeffe, M.; Yaghi, O. M. *Science* **2002**, *295*, 469. (b) Düren, T.; Sarkisov, L.; Yaghi, O. M.; Snurr, R. Q.; *Langmuir* **2004**, *20*, 2683. (c) Zhou, W. *Chem. Rec.* **2010**, *10*, 200. (d) Getman, R. B.; Bae, Y.-S.; Wilmer, C. E.; Snurr, R. Q. *Chem. Rev.* **2012**, *112*, 703. (e) Konstas, K.; Osl, T.; Yang, Y.; Batten, M.; Burke, N.; Hill, A. J.; Hill, M. R. *J. Mater. Chem.* **2012**, *22*, 16698. (f) Makal, T. A.; Li, J.-R.; Lu, W.; Zhou, H.-C. *Chem. Soc. Rev.* **2012**, *41*, 7761. (g) He, Y.; Zhou, W.; Krishna, R.; Chen, B. *Chem. Commun.* **2012**, *48*, 11813. (h) Wilmer, C. E.; Leaf, M.; Yeon Lee, C.; Farha, O. K.; Hauser, B. G.; Hupp, J. T.; Snurr, R. Q. *Nat. Chem.* **2012**, *4*, 83.
(35) Horike, S.; Shimomura, S.; Kitagawa, S. *Nature Chem.* **2009**, *1*, 695-704.
(36) Férey, G.; Serre, C. *Chem. Soc. Rev.* **2009**, *38*, 1380-1399.
(37) Schneemann, A.; Bon, V.; Schwedler, I.; Senkovska, I.; Kaskel, S.; Fischer, R. A. *Chem. Soc. Rev.* **2014**, *43*, 6062-6096.
(38) Li, D.; Kaneko, K. *Chem. Phys. Lett.* **2001**, *335*, 50-56.
(39) Kitaura, R.; Seki, K.; Akiyama, G.; Kitagawa, S. *Angew. Chem. Int. Ed.* **2003**, *42*, 428-431.
(40) McDonald, T. M.; Mason, J. A.; Kong, X.; Bloch, E. D.; Gygi, D.; Dani, A.; Crocellà, V.; Giordanino, F.; Odoh, S. O; Drisdell, W. S.; Vlaisavljevich, B.; Dzubak, A. L.; Poloni, R.; Schnell, S. K.; Planas, N.; Lee, K.; Pascal, T.; Wan, L. F.; Prendergast, D.; Neaton, J. B.; Smit, B.; Kortright, J. B.; Gagliardi, L.; Bordiga, S.; Reimer, J. A.; Long, J. R. *Nature* **2015**, *519*, 303-308.

Chapter 2: Evaluating Metal-Organic Frameworks for Post-Combustion Carbon Dioxide Capture via Temperature Swing Adsorption

2.1. Introduction

As concerns over the environmental impact of rising carbon dioxide emissions from anthropogenic sources continue to mount, it is becoming increasingly evident that the world's energy demands must be met in a more sustainable way.[1] With regard to fuel combustion, coal-fired power plants contribute more than 40% to annual global CO_2 emissions, and this number is projected to increase over the next several decades as a result of economic growth and increased industrialization in developing nations.[2] Although a shift in the global infrastructure toward cleaner energy sources is crucial for the reduction of greenhouse gas emissions, such a transition is expected to proceed gradually owing to the need to modify or replace major components of the existing energy framework. Consequently, efforts to mitigate the rising levels of CO_2 in the short-term via the development of effective methods for CO_2 capture and sequestration are of high priority.[3]

One potential scenario under which CO_2 capture could be rapidly deployed is in the context of post-combustion capture and storage, wherein the CO_2 is selectively removed from a power plant flue gas stream and sequestered through storage in underground geological formations.[4] In existing capture technologies employing aqueous alkanolamine solutions (amine "scrubbers"), the primary cost of the capture process is associated with the high energy requirements needed for regeneration of the capture media.[5] Indeed, as much as 40% of the energy output of the power plant is required to evolve the CO_2 from the solutions, with much of the energy being expended in heating the water itself to the regeneration temperature.[6] Thus, materials that feature a lower energy penalty for regeneration, while maintaining a high selectivity towards CO_2 over the other components of the flue gas, are crucial for improving the efficiency of CO_2 capture.

Metal-organic frameworks present a promising platform for the development of next-generation capture materials as a result of their high capacity for gas adsorption and tunable pore surfaces that can facilitate highly selective binding of CO_2.[7,8] Note that the composition of a typical flue gas dictates the separation to be primarily a CO_2/N_2 separation, although the presence of other lesser components, such as H_2O, O_2, CO, SO_x, and NO_x, must also be considered when assessing the performance of new materials. Nevertheless, the high degree of control over the surface functionalities within the pores of metal-organic frameworks is expected to enable the precise tuning of the optimal affinity towards CO_2, allowing the total energy penalty of the CO_2 capture process to be reduced to levels approaching the predicted minimum of 11%.[9a]

The regeneration of an industrial solid adsorbent is usually accomplished via pressure swing adsorption (PSA), vacuum swing adsorption (VSA), temperature swing adsorption (TSA), or a combination of these processes.[10] Since each of these regeneration methods implies a different set of ideal adsorbent properties, this actually presents the possibility of tailoring the industrial regeneration process to match the properties of a given metal-organic framework. However, among these methods, TSA is particularly promising for post-combustion CO_2 capture, owing to difficulties with compressing or applying a vacuum to such large volumes of a low-pressure gas stream, as well as to the potential availability of low-grade heat in a power plant as a source of energy for regeneration.[9] Thus, the energy requirement for CO_2 capture utilizing TSA may be

significantly reduced over the corresponding PSA or VSA processes. As illustrated in Figure 2.1, a TSA cycle involves heating the saturated adsorbent under ambient pressure to desorb the captured gas and regenerate the capture material.

Despite the promise of metal-organic frameworks for use in a post-combustion CO_2 capture scenario, their performance within a TSA-based capture process has not yet been examined in detail. Indeed, despite the large body of literature investigating CO_2 adsorption within this class of materials, the range of temperatures for which adsorption isotherms have been reported is significantly narrower than the scope of temperatures that may be reasonably considered for a TSA-based process. Indeed, to the best of our knowledge, the highest temperature CO_2 isotherms at the relevant pressures (< 1 bar) reported for metal-organic frameworks are around 70 °C,[11] which is still far lower than the likely range of 100-200 °C to be employed as the desorption temperature within an actual TSA CO_2 capture system.[12] Thus, in order to more fully understand the performance and properties of metal-organic frameworks in this type of process, there is an urgent need for low-pressure CO_2 adsorption experiments to be performed at higher temperatures.

Herein, we report the first detailed study of metal-organic frameworks in a temperature swing setting, and provide a methodology for assessing the likely performance of new materials within a real TSA system. For such an application, metal-organic frameworks fall into two general categories of potential interest: those with an exceptionally high specific surface area presenting only weak physisorptive sites, such as present in an activated carbon, and those that in addition feature strong adsorption sites designed specifically for binding CO_2. With a BET surface area of 4690 m^2/g and a high capacity for CO_2 at high pressure, $Zn_4O(BTB)_2$ (BTB^{3-} = 1,3,5-benzenetribenzoate; MOF-177) was selected as representative of the former class of materials.[7d,13] In contrast, $Mg_2(dobdc)$ ($dobdc^{4-}$ = 1,4-dioxido-2,5-benzenedicarboxylate; Mg-MOF-74, CPO-27-Mg)[14b] possesses a somewhat lower BET surface area of 1800 m^2/g, but features a high density of exposed Mg^{2+} cation sites following activation. The presence of these strong adsorption sites has been demonstrated to afford a significant CO_2 uptake at low pressures, leading to a high selectivity at the pressures relevant for CO_2 capture from a flue gas.[8b,14] Note that, beyond unsaturated metal coordination sites[15] of the type found in $Mg_2(dobdc)$, strong CO_2 binding sites can also be achieved through the use of polar functional groups[16] or functionalities inserted post-synthetically.[17] Importantly, the methodology we present provides a means of assessing the viability of any such material for TSA-based CO_2 capture through the analysis of simple single-component gas adsorption isotherms.

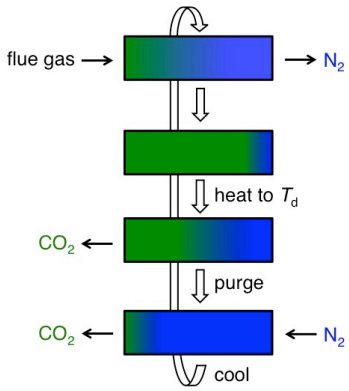

Figure 2.1. Schematic diagram of an idealized temperature swing adsorption (TSA) process for post-combustion CO_2 capture. Flue gas is introduced to the

fixed bed, which selectively adsorbs CO_2 (green) over N_2 (blue) until the bed is saturated with CO_2. The flue gas is then redirected, and the bed is heated to the desorption temperature, T_d. The CO_2 is desorbed from the bed and then pushed out by an N_2 purge until the CO_2 rich stream coming off the bed falls below a desired purity level. The bed is then cooled and readied for the next adsorption cycle.

2.2. Experimental

2.2.1. General Information. Anhydrous dichloromethane was obtained from a Vac anhydrous solvent system. All other reagents were obtained from commercial vendors and used without further purification. UHP-grade (99.999% purity) carbon dioxide, nitrogen, and helium were used for all adsorption measurements. Powder X-ray diffraction patterns were collected on a Bruker D8 Advance diffractometer with a Cu anode (λ = 1.5406 Å). Infrared spectra were obtained on a Perkin-Elmer Spectrum 100 Optica FTIR spectrometer furnished with an attenuated total reflectance accessory.

2.2.2. Synthesis and Activation of MOF-177. The compound MOF-177 was synthesized as previously reported,[18] and was activated using a strategy adopted from a literature procedure.[19] The reaction product was transferred into a nitrogen-filled glove bag, where the solid was soaked in anhydrous DMF (50 mL) for 24 h. The supernatant was decanted and replenished twice over two days. The solid was then soaked in anhydrous dichloromethane (50 mL) for 6 h. The supernatant was decanted and replenished four times over three days. The product was stored in a glovebox under a dinitrogen atmosphere before activation under dynamic vacuum for 24 h. The successful synthesis and activation of the framework was confirmed by comparing the X-ray powder diffraction pattern, infrared spectrum, and Langmuir and BET surface areas to those previously reported (see Figure 2.S1 and S3).

2.2.3. Synthesis and Activation of Mg_2(dobdc). The compound Mg_2(dobdc) was synthesized and activated using a strategy adopted from previous reports.[14b,c] Following the reaction of $Mg(NO_3)_2 \cdot 6H_2O$ and 2,5-dihydroxyterephthalic acid, the resulting yellow microcrystalline material was combined, washed repeatedly with N,N-dimethylformamide (DMF), and then soaked in DMF in a nitrogen-filled glove bag. After 24 h, the DMF was decanted, and freshly distilled methanol was added. The solid was then transferred to a nitrogen-filled glovebox. The methanol was decanted, and the solid was soaked in DMF on a hot-plate set at 100 °C for 18 h. The DMF was decanted and replaced, and the solid was soaked at 100 °C for 4 h. The DMF was decanted and replaced by methanol at room temperature, which was decanted and replenished six times with a minimum of 6 h between washes. The dark yellow powder was isolated and heated under dynamic vacuum at 180 °C for 24 h. The successful synthesis and activation of the framework was confirmed by comparing the X-ray powder diffraction pattern, infrared spectrum, and Langmuir and BET surface areas to those previously reported (see Figure 2.S2-2.S3).

2.2.4. Low-Pressure Gas Sorption Measurements and Surface Area Calculations. Gas adsorption isotherms for pressures in the range 0-1.1 bar were measured using a Micromeritics ASAP 2020 instrument. Samples of MOF-177 and Mg_2(dobdc) were transferred under a

dinitrogen atmosphere to preweighed analysis tubes, which were capped with a Transeal. The samples were evacuated on the ASAP until the outgas rate was less than 2 mTorr/min. The evacuated analysis tubes containing degassed samples were then carefully transferred to an electronic balance and weighed to determine the mass of sample (174 mg for MOF-177 and 91.5 mg for Mg_2(dobdc)). The tube was transferred back to the analysis port of the gas adsorption instrument. The outgas rate was again confirmed to be less than 2 mTorr/min. Langmuir and BET[20] surface areas were determined by measuring N_2 adsorption isotherms in a 77 K liquid nitrogen bath and calculated using the Micromeritics software. Adsorption isotherms between 20 and 80 °C were measured using a recirculating dewar (Micromeritics) connected to a Julabo F32-MC isothermal bath. In order to collect isotherm data above 80 °C, a thermocouple was affixed to the analysis tube using copper wire and connected to a Glas-Col DigiTroll II temperature controller. A furnace was connected to the temperature controller, placed around the analysis tube, and filled with sand. The temperature controller was set to the desired temperature, and the automatic tuning function was used to set the proportional-integral-derivative (PID) parameters and equilibrate the sand bath temperature. The error in sample temperature associated with each measurement using the furnace is estimated at ±0.3 °C. After each isotherm measurement, the sample was evacuated under dynamic vacuum, until the outgas rate was less than 2 mTorr/min, prior to continuing on to the next measurement.

2.2.5. High-Pressure Gas Sorption Measurements. In a typical measurement, at least 200 mg of sample was loaded in a sample holder in a glovebox under a dinitrogen atmosphere. Carbon dioxide excess adsorption measurements were performed on an automated Sieverts' apparatus (PCTPro-2000 from Hy-Energy Scientific Instruments LLC) over a pressure range of 0-50 bar. Pore volumes determined from the high-pressure data were 1.59 cm^3/g for MOF-177 and 0.5727 cm^3/g for Mg_2(dobdc). The absolute adsorbate loadings were obtained using the following procedure. The fluid densities at any given temperature were first determined using the Peng-Robinson equation of state. Subsequently, these values were multiplied by the pore volume of each material to obtain the loadings in the "bulk" of the pore space. Addition of the loadings in the "bulk" to the experimentally determined "excess" loadings yields the "absolute" component loadings. All isotherm fits, and subsequent analyses to determine selectivities and isosteric heats of adsorption, were carried out using the absolute loadings.

2.2.6. Heat Capacity Measurements. All thermal analyses were performed on a TA Instruments Q200 differential scanning calorimeter (DSC) equipped with a refrigerated cooling system RSC90 under a nitrogen or helium flow. Baseline data for the empty heating chamber was collected between temperatures of –90 °C and 400 °C, followed by a temperature calibration using the melting point of an indium sample (m.p. 156.60 °C). The energy axis was calibrated by collecting heat flow data on a sapphire sample (21.8 mg) and fitting this data to the literature values.[21]

A sample of activated MOF-177 (6.5 mg) or Mg_2(dobdc) (9.4 mg) was hermetically sealed within an aluminum pan in a glovebox under a nitrogen atmosphere, and the sample was quickly transferred to the calorimeter. The heat flow data were collected using a temperature ramp rate of 3 °C/min in the temperature range of –50 to 250 °C, using a temperature modulation of ± 1 °C every 60 s. The sample was then cooled back to –50 °C, the heating cycle was repeated a further two times, and the data for the three runs were averaged. The heat capacity was obtained using the following expression:

$$C_{\mathrm{p}}(\mathrm{sample}) = \frac{H_{\mathrm{sample}}}{H_{\mathrm{ref}}} \cdot \frac{m_{\mathrm{ref}}}{m_{\mathrm{sample}}} \cdot C_{\mathrm{p}}(\mathrm{ref}) \tag{2.1}$$

where C_p(sample) and C_p(ref) represent the heat capacities of the sample and reference material (sapphire), H_{sample} and H_{ref} represent the heat flows for the sample and reference material detected by the calorimeter with respect to an empty aluminum pan, and m_{sample} and m_{ref} represent the experimental masses of the sample and reference material, respectively.

2.2.7. Fitting of Isotherms. The measured experimental data on pure component isotherms for CO_2 and N_2, in terms of excess loadings, in MOF-177 and Mg_2(dobdc) at temperatures ranging from 293 K to 473 K were first converted to absolute loading using the Peng-Robinson equation of state for estimation of the fluid densities. For calculation of the absolute component loadings, the pore volume data of Herm et al. was used.[27] For MOF-177 and Mg_2(dobdc), the pore volumes are 1.59 cm^3/g and 0.573 cm^3/g, respectively. The absolute component loadings were fitted with either a single-site Langmuir model or a dual-site Langmuir model.

For CO_2/MOF-177, N_2/MOF-177, and N_2/Mg_2(dobdc) there are no discernible isotherm inflections and therefore the single-site Langmuir model

$$q = \frac{q_{sat} b p}{1 + bp} \tag{2.2}$$

was used for isotherm fitting for these three guest/host combinations. The temperature dependence of the Langmuir constant, b, is expressed as

$$b = b_0 \exp\left(\frac{E}{RT}\right); \quad \ln(b) = \ln(b_0) + \frac{E}{RT} \tag{2.3}$$

Equation 2.2 can be expressed in terms of the fractional occupancy, q, as follows

$$\theta \equiv \frac{q}{q_{sat}} = \frac{bp}{1 + bp} \tag{2.4}$$

Re-arranging Equation 2.4 yields

$$p = \frac{1}{b} \frac{1}{1 - \theta} \tag{2.5}$$

and

$$\ln p = -\ln(b) - \ln(1 - \theta) \tag{2.6}$$

The isosteric heat of adsorption, Q_{st}, is defined as

$$Q_{st} = RT^2 \left(\frac{\partial \ln p}{\partial T} \right)_q \tag{2.7}$$

where the derivative in the right member of Equation 2.7 is determined at constant adsorbate loading, q. Using Equation 2.7 we can write the following expression for the isosteric heat of adsorption in which the derivative with respective to temperature is at constant occupancy q

$$Q_{st} = RT^2 \left(\frac{\partial \ln p}{\partial T} \right)_\theta = -RT^2 \left(\frac{\partial \ln b}{\partial T} \right)_\theta \tag{2.8}$$

Differentiating Equation 2.3 yields

$$Q_{st} = -E \tag{2.9}$$

The situation with CO_2/Mg_2(dobdc) is different and a similar approach to the above using single-site Langmuir model fits is inadequate. This is demonstrated in Figure 2.S9 which shows the parity plot for fitting the experimental data, all of which were measured for pressure up to 100 kPa, to a single-site Langmuir model. The statistical "best" fit yields significant deviations at either ends of the loading range; see the parity plots in Figure 2.S9 comparing the experimental values of absolute loadings for CO_2/Mg_2(dobdc) measured in this work and the values of the loadings calculated using the single-site Langmuir model along with the parameters specified in Table 2.S5 (y-axis). The important conclusion to be drawn here is that even though the experimental loadings are below 8 mol/kg, the single-site Langmuir model provides an inadequate description for the entire range of temperatures.

The inflection characteristics of the CO_2 isotherms of Mg_2(dobdc) necessitate the use of the dual-site Langmuir model

$$q \equiv q_A + q_B = \frac{q_{sat,A} b_A p}{1 + b_A p} + \frac{q_{sat,B} b_B p}{1 + b_B p} \tag{2.10}$$

where we have two distinct adsorption sites A and B. Table 2.S6 provides the fit constants. For all experimental data, the dual-site Langmuir model provides a good description of the inflection characteristics.

For comparing the performance of Mg_2(dobdc) with zeolite NaX in post combustion carbon capture we used the experimental data of Belmabkhout et al. and Cavenati et al. for adsorption of CO_2 and N_2 at a variety of temperatures.[32] The dual-site Langmuir model was used for fitting purposes. The fitted parameters are specified in Tables 2.S7 and 2.S8.

2.3. Results and Discussion

2.3.1. Adsorption Isotherm Data. The low-pressure CO_2 and N_2 adsorption isotherms collected every 10 °C from 20 to 200 °C for MOF-177 and Mg_2(dobdc) are presented in Figure 2.2. As expected, the quantity adsorbed decreases with temperature for both gases as a result of

the greater thermal energy of the molecules at higher temperatures. Additionally, the quantity of CO_2 adsorbed is higher than that for N_2 at all temperatures for both compounds as a result of the greater quadrupole moment and polarizability of CO_2 (13.4×10^{-40} C m^2 and 26.3×10^{-25} cm^3, respectively) compared to N_2 (4.7×10^{-40} C m^2 and 17.7×10^{-25} cm^3, respectively).[22] In the case of Mg_2(dobdc), an initial steep increase in CO_2 uptake at low pressure is observed due to the presence of coordinatively-unsaturated Mg^{2+} sites on the surface of the material (see Figure 2.2c).[14b] Such a behavior is characteristic of any material with high-affinity binding sites for CO_2. Importantly, as the temperature is increased, the initial steep rise in the data becomes less prominent, and the isotherms become nearly linear beyond 120 °C. This is presumably due to the thermal energy of the gas molecules overcoming the heat of adsorption at the exposed Mg^{2+} sites, resulting in an apparently homogenous surface at higher temperatures. In contrast, the lack of high-affinity binding sites within MOF-177 leads to a linear CO_2 adsorption isotherm across all temperatures, similar to what is commonly observed for activated carbons.

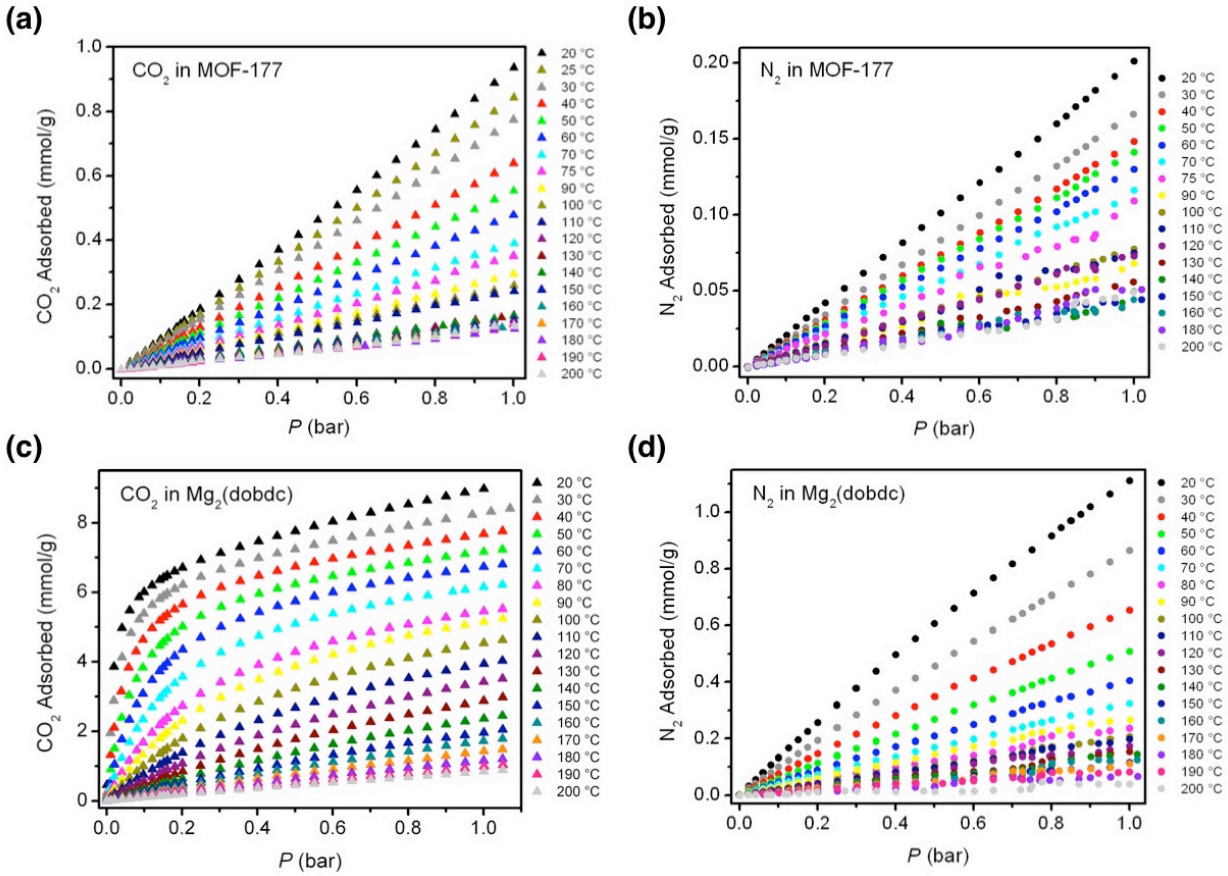

Figure 2.2. Excess CO_2 (triangles) and N_2 (circles) adsorption isotherms for MOF-177 (a and b) and Mg_2(dobdc) (c and d) measured from 20 to 200 °C.

Post-combustion flue gas is released at a temperature in the range of 40 to 60 °C and at a total pressure of approximately 1 bar, wherein CO_2 is present at a relatively low partial pressure of 0.13-0.16 bar.[23] Thus, the adsorption capacity for CO_2 in the low-pressure region is critically important. Indeed, at 40 °C and 0.15 bar, Mg_2(dobdc) adsorbs 5.28 mmol/g CO_2 (18.9 wt %), while the corresponding adsorption capacity for MOF-177 is just 0.097 mmol/g CO_2 (0.43 wt

%).[24] In post-combustion CO_2 capture, the solid adsorbent will likely be packed into a large fixed bed, and, as such, the volumetric uptake is also a vital consideration from the perspective of minimizing the size of the column towers, which may affect the heating efficiency during the regeneration step. In terms of the volumetric capacity, the high gravimetric uptake coupled with the relatively dense structure of Mg_2(dobdc) combine to provide a CO_2 uptake of 4.83 mmol/cm^3 (213 g/L), while the large pores within MOF-177 lead to a volumetric capacity of just 0.041 mmol/cm^3 (1.8 g/L).

The process design of a TSA system for any material requires precise knowledge of the thermodynamics of the adsorption of both CO_2 and N_2. Here, the single-component gas adsorption isotherms have been fit to allow the determination of precise isosteric heats of adsorption and to enable application of ideal adsorbed solution theory (IAST) in simulating the performance of each material under a mixed component gas. Although the N_2 adsorption isotherms for both MOF-177 and Mg_2(dobdc) and the CO_2 adsorption isotherms for MOF-177 can all be modeled adequately using a single-site Langmuir model, the simultaneous fitting of all the CO_2 isotherm data for Mg_2(dobdc) necessitates the use of a dual-site Langmuir model due to the inherent heterogeneity of the pore surface and the much higher affinity of CO_2 for the exposed Mg^{2+} cation sites compared to other adsorption sites within the material. The resulting fit of the adsorption isotherm data for Mg_2(dobdc) at 40 and 50 °C using the dual-site Langmuir model is shown in Figure 2.3 (see Figure 2.S11 for illustrations of the accuracy of the fit at other temperatures). Note that a single-site Langmuir isotherm cannot adequately describe the inflection that occurs for temperatures below 120 °C at loadings corresponding to roughly one CO_2 per Mg^{2+} center (calculated to be 8.24 mmol/ g).[25] Hence, this simpler model is not able to fit the adsorption data at pressures below 1 bar, which is the region of interest for post-combustion CO_2 capture.

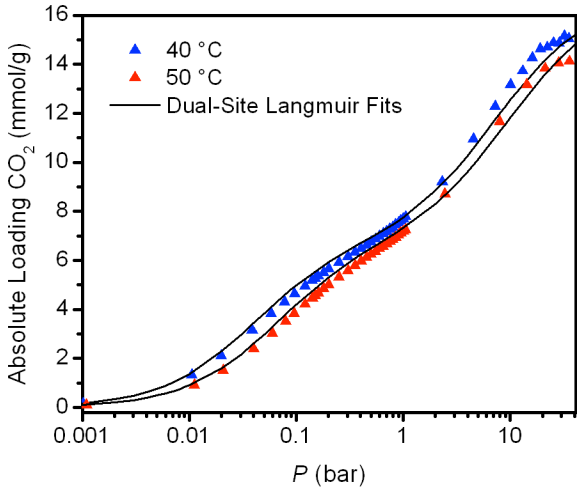

Figure 2.3. Low- and high-pressure CO_2 adsorption isotherms for Mg_2(dobdc) at 40 and 50 °C, along with the corresponding dual-site Langmuir fits (black lines). Loadings have been converted from excess adsorption to absolute adsorption. Note that the fits shown result from simultaneously modeling all of the isotherm data collected between 20 and 200 °C, not just the data at 40 and 50 °C.

Although Mg_2(dobdc) represents an unusual case, in that it has an exceptionally high density of binding sites with a strong affinity for CO_2 in addition to a comparable number of relatively

weak binding sites, similar arguments should hold for other metal-organic frameworks featuring a combination of strong and weak binding sites. Specifically, modeling of the lower-pressure adsorption isotherms using a single-site Langmuir model considering only the Mg^{2+}cation sites (and neglecting the weaker adsorption sites) is not appropriate even at low loadings due to the high-affinity sites becoming close to saturated at pressures well below 1 bar. It is expected that even below the ratio of 1 CO_2:Mg^{2+} site, there will be a distribution of occupied binding sites across all temperatures, resulting in the dual-site Langmuir model being necessary even at the lowest temperatures and pressures. This demonstrates the importance of selecting the most appropriate adsorption model, depending on the material and adsorbed gas, such that the isotherms can be consistently modeled across the entire pressure and temperature range.

2.3.2. Isosteric Heat of Adsorption. The regeneration temperature of a CO_2 capture material in a TSA process largely depends on the thermodynamics of adsorption. This is commonly expressed as the isosteric heat of adsorption, Q_{st}, which represents the average binding energy of an adsorbing gas molecule at a specific surface coverage. Isosteric heats of adsorption are often calculated by fitting isotherms at two or three different temperatures with the virial equation. In this work, however, we have instead fit the entire set of isotherms for all temperatures using the simplest physically-realistic single-site or dual-site Langmuir model.

Based on the single-site Langmuir fit, MOF-177 has a constant isosteric heat of adsorption of 14 kJ/mol (see Figure 2.4), indicative of the relatively weak CO_2-adsorbent interaction observed in the CO_2 isotherms and lack of strong adsorption sites in the framework. Note that in contrast to a single-site Langmuir model, determination of the isosteric heat of adsorption from isotherms modeled using a dual-site Langmuir is complicated by the need to obtain an explicit analytical expression for pressure as a function of the loading for calculating Q_{st} (Equation 2.11).

$$Q_{st} = RT^2 \left(\frac{\partial \ln p}{\partial T} \right)_q \tag{2.11}$$

We have therefore developed an exact analytic procedure for calculating Q_{st} as a function of loading. To the best of our knowledge, this represents the first time that isosteric heats of adsorption have been calculated from a dual-site Langmuir fit.

As a direct result of the inflection in the isotherm for CO_2 adsorption in Mg_2(dobdc), there is a corresponding inflection in the isosteric heat of adsorption curve, coinciding with the saturation of the exposed Mg^{2+} adsorption sites (see Figure 2.4). The isosteric heat of adsorption falls from 42 kJ/mol (corresponding approximately to the heat of adsorption for the strong sites) at loadings below 5 mmol/g to 24 kJ/mol (approximately the heat of adsorption for the weak sites) at loadings above 8 mmol/g. This is in excellent agreement with the calculated loading of 8.24 mmol/g corresponding to one CO_2 molecule per Mg^{2+} cation. Note that the zero-coverage isosteric heat of adsorption is also in good agreement with literature values, which were computed using conventional methods.[14b,d] However, previous reports have found an increase in Q_{st} at high loadings, which was attributed to increasing CO_2-CO_2 interactions.[8f,14d] In contrast, we were able to determine Q_{st} as a function of loading by fitting all of the CO_2 isotherms for Mg_2(dobdc) simultaneously, using the large amount of low-pressure data from 20 to 200 °C and the corresponding high-pressure isotherms (see Figure 2.S12), without needing to invoke CO_2-CO_2 interactions. It is important to note that absolute loadings, which are not experimentally measurable, must be used in the isotherm fits and subsequent determination of Q_{st}.[26] Failure to

use absolute loadings will result in significant differences at high pressures, estimated to be as much as 10-12%, and likely gives rise to the increasing heats of adsorption at high loadings that have been reported previously. Additionally, Q_{st} is only a weak function of temperature, and the isosteric heat of adsorption curves do not change significantly at different temperatures.

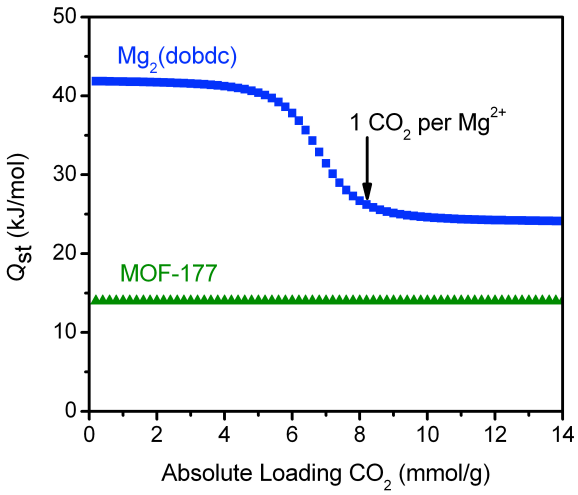

Figure 2.4. Isosteric heat of adsorption, Q_{st}, as a function of absolute loading of CO_2 for MOF-177 and Mg_2(dobdc) calculated at 40 °C using a single site Langmuir and dual-site Langmuir model, respectively. Note that Q_{st} is only weakly dependent upon temperature (see Figure 2.S12).

For post-combustion CO_2 capture, the CO_2 is adsorbed at a partial pressure of 0.15 bar, and the resulting uptake of CO_2 is below 5.5 mmol/g at relevant flue gas temperatures (40-60 °C). Thus, the corresponding Q_{st} value is around 42 kJ/mol. Additionally, the sharp decrease in isosteric heat of adsorption is an important result that has direct consequences for the application of Mg_2(dobdc), or any similar material, in other applications involving CO_2 capture. For instance, Mg_2(dobdc) was recently studied for use as an adsorbent in hydrogen purification and in precombustion CO_2 capture.[27] Both of these applications require separation of CO_2 from H_2 at high pressures, and although Mg_2(dobdc) shows great promise with a high CO_2/H_2 selectivity and high working capacity, concerns were raised over the energy that would be required to regenerate the framework after CO_2 adsorption. The isosteric heat of adsorption calculations demonstrate, however, that the regeneration penalty is not as high as originally anticipated, since at 40 °C and 1 bar, Mg_2(dobdc) has a CO_2 uptake of 7.7 mmol/g, with a relevant Q_{st} value around 24 kJ/mol. Consequently, for a PSA process operating between 1 and 40 bar, the regeneration energy should be significantly less than was originally expected for a 42 kJ/mol heat of adsorption, since most of the stronger binding sites will not need to be regenerated.

2.3.3. Selectivity. We now address the issue of determining the selectivity factor, S_{ads}, for binary mixtures using pure component isotherm data. The use of an adsorption model, such as IAST,[28] is essential in practice, because collection of experimental data for a mixed component gas cannot be conveniently and rapidly performed.[29] The accuracy of the IAST procedure has already been established for adsorption of a wide variety of gas mixtures in different zeolites[30] and for CO_2 capture within metal-organic frameworks.[31] The method is employed here for

estimation of the adsorption selectivity across the entire temperature range for which single-component isotherms were collected for MOF-177 and Mg_2(dobdc).

The IAST estimations of adsorption selectivities for CO_2 over N_2 were calculated for an idealized flue gas mixture composed of 0.15 bar CO_2 and 0.75 bar N_2 based on the fits to the isotherm data for MOF-177 and Mg_2(dobdc) (see Figure 2.5a). As one of the most studied adsorbents for CO_2 separation processes, the selectivities for zeolite NaX were also calculated from previously reported data for comparison.[32] Notably, MOF-177 has a selectivity factor near unity under these conditions, while Mg_2(dobdc) demonstrates a tremendous selectivity, with an IAST selectivity factor of 148.1 at the typical flue gas temperature of 50 °C. Indeed, Mg_2(dobdc) outperforms zeolite NaX, which has an IAST selectivity factor of 87.4 at 50 °C.

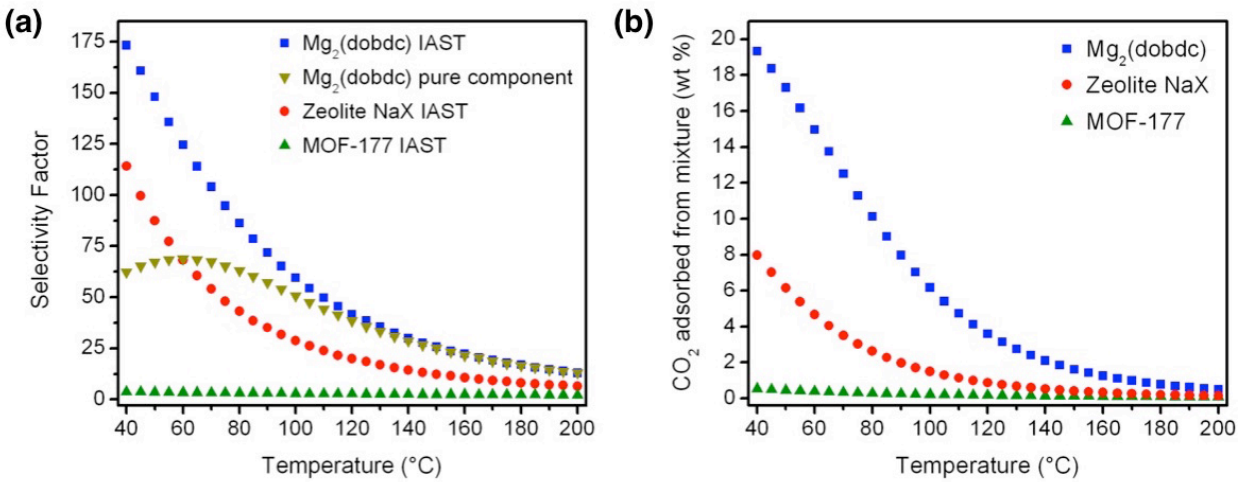

Figure 2.5. (a) Selectivity factors as a function of temperature calculated using IAST for MOF-177, Mg_2(dobdc), and zeolite NaX compared to the selectivity factors calculated from the pure component isotherms for Mg_2(dobdc). (b) IAST calculations of weight percent of CO_2 adsorbed from a mixture of 0.15 bar CO_2 and 0.75 bar N_2 as a function of temperature for MOF-177, Mg_2(dobdc), and zeolite NaX.

Gas adsorption selectivities for metal-organic frameworks are often reported simply as the ratio of number of moles of each component adsorbed at the relevant partial pressures in the individual single-component isotherms. Figure 2.5a demonstrates the importance of using IAST to calculate selectivity values, especially when high-energy binding sites are present. For Mg_2(dobdc), using the simpler selectivity calculation (Equation 2.3 with loadings, q_i, determined only from the single-component isotherms) not only produces very different values, but, significantly, the trend in selectivity as a function of temperature is inconsistent with the more physically accurate IAST model. With its greater polarizability and larger quadrupole moment,[22] CO_2 has stronger interactions with the open metal sites of Mg_2(dobdc) than does N_2.[14b,e] As the thermal energy of the gas molecules increases, the difference in binding energies of CO_2 and N_2, which are reasonably constant with temperature, becomes less significant, and the selectivity should consequently decrease. This result demonstrates that IAST calculations are necessary in order to obtain reasonable selectivity values. It is also important to note that it is not generally appropriate to use the ratio of Henry's constants from each pure component isotherm as a means of calculating selectivities for post-combustion CO_2/N_2 separation, since, for example, the CO_2

uptake in Mg_2(dobdc) is not in the linear Henry regime at the relevant flue gas conditions of 40 to 60 °C and 0.15 bar.

When evaluating any material for a particular application, it is important to determine selectivity factors at conditions relevant to that application. For post-combustion CO_2 capture, selectivity factors should be calculated for a mixture of approximately 0.15 bar CO_2 and 0.75 bar N_2, at around 50 °C.[23] For example, MOF-177 has a reasonably high CO_2/N_2 selectivity at 1 bar CO_2 and 1 bar N_2; however, this does not make MOF-177 a good candidate for any practical CO_2/N_2 separation due to its poor selectivity at the relevant partial pressures. In addition, it is important to clearly define how reported selectivity factors were calculated in order to facilitate the comparison of different materials. Selectivity factors should also be normalized to the composition of the gas mixture as shown in Equation 2.12, where q_i is the uptake and p_i is the partial pressure of component *i*.

$$S_{\text{ads}} = \frac{q_1/q_2}{p_1/p_2} \tag{2.12}$$

2.3.4. Breakthrough Simulations. A TSA process consists of adsorption and desorption cycles that rely on the raising and lowering of the system temperature. In this section, we focus on evaluating the separation performance of a material with a real mixed gas under the adsorption phase of a TSA process. In post-combustion CO_2 capture, the flue gas will likely pass through packed beds containing the solid adsorbent. Breakthrough measurements can provide a good indication of the performance of a material in such a system, but are challenging to perform accurately. Variations in particle size, column packing, and flow rates can lead to difficulties in comparing breakthrough measurement results for different samples. Breakthrough simulations therefore offer a convenient alternative. These were performed for MOF-177, Mg_2(dobdc), and zeolite NaX in the temperature range 40-80 °C using a previously developed adsorber model—which incorporates IAST to describe local thermodynamic equilibrium between the gas phase that is in contact with the adsorbent particle—to evaluate the performance of each material for a mixture of 0.15 bar CO_2 and 0.75 bar N_2.[33]

Figure 2.6a demonstrates the relatively poor performance of MOF-177 with CO_2 breakthrough occurring rapidly at 40 °C. On the other hand, Mg_2(dobdc) has a significantly longer breakthrough time and outperforms zeolite NaX. Figure 2.6c shows the quantity of CO_2 adsorbed at breakthrough, defined as when the outlet gas stream contains 1 mol % of CO_2. Importantly, Mg_2(dobdc) exhibits longer breakthrough times and greater amounts of CO_2 adsorbed over the entire temperature range. Longer breakthrough times are desirable from a practical point of view because this implies a less frequent requirement for regeneration. Figure 2.5b also shows the IAST calculations of wt % of CO_2 adsorbed from the same mixture as a function of temperature. The IAST results presented in Figure 2.5b are slightly higher than the corresponding ones shown in Figure 2.6c for the adsorber breakthrough simulations, because IAST allows the system to reach equilibrium over the entire bed. In the breakthrough calculations, the operation is terminated when the exit gas reaches the selected purity level of 1 mol % CO_2, implying that portions of the bed are not entirely in equilibrium with the inlet gas and are therefore underutilized.

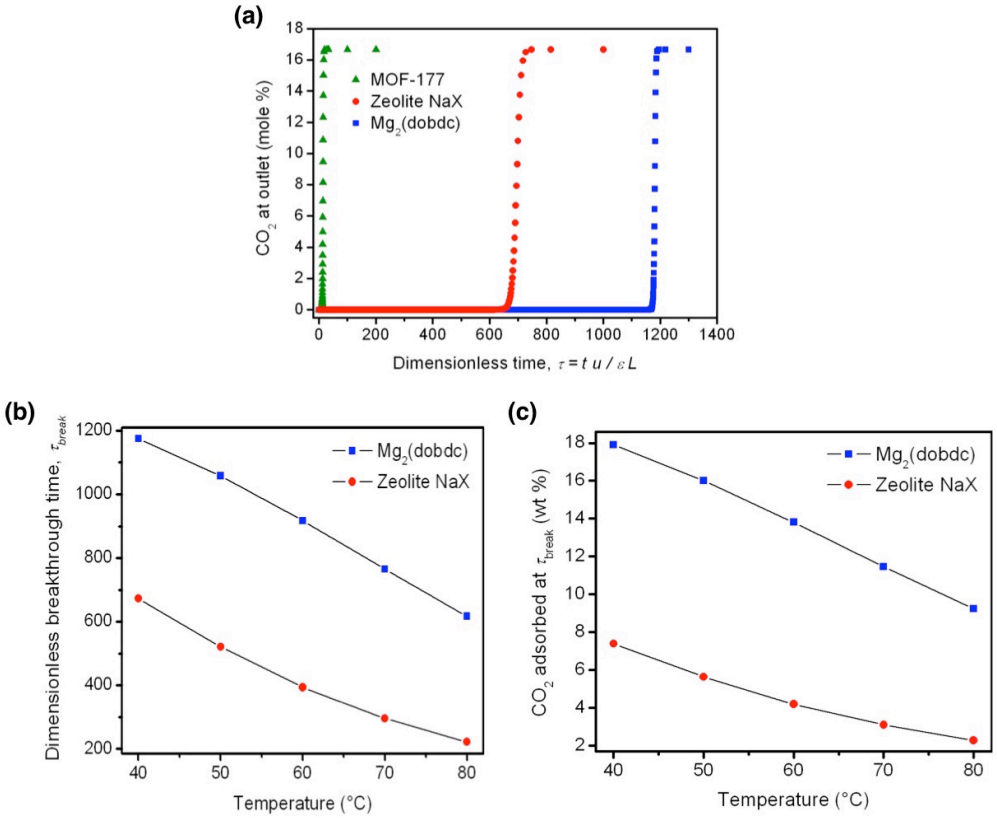

Figure 2.6. (a) Simulated breakthrough curves for MOF-177, Mg_2(dobdc), and zeolite NaX at 40 °C for a gas mixture of 0.15 bar CO_2 and 0.75 bar N_2. The *x*-axis is a *dimensionless* time, *t*, obtained by dividing the actual time, *t*, by the contact time between the gas and the crystallites.[33] For a given adsorbent, under chosen operating conditions, the breakthrough characteristics are uniquely defined by *t*, allowing the results presented here to be equally applicable to laboratory scale equipment as well as to industrial scale adsorbers. (b) Simulated breakthrough time, t_{break}, as a function of temperature for Mg_2(dobdc) and zeolite NaX with a 0.15 bar CO_2 and 0.75 bar N_2 input gas mixture. The breakthrough time is defined as when the outlet gas stream contains 1 mol % CO_2. (c) The weight percent of CO_2 adsorbed at the breakthrough time as a function of temperature.

2.3.5. Working Capacity. The working capacity corresponds to the actual amount of CO_2 that can be captured during a full adsorption/desorption cycle and is thus a critically important parameter in evaluating the potential of any adsorbent in a real process. As such, working capacities were estimated for MOF-177, Mg_2(dobdc), and zeolite NaX based on an idealized temperature swing adsorption system described previously by Berger and Bhown (see Figure 2.1).[12] In this simplified model, flue gas at an initial temperature, T_0, with a composition of 0.15 bar CO_2, 0.75 bar N_2, and 0.1 bar of other minor components, enters a packed bed column containing the adsorbing material. As the flue gas travels through the bed, CO_2 is selectively adsorbed, and an N_2-rich stream exits from the end of the column. Once the percentage of CO_2 coming off of the column rises above a certain threshold value, regeneration is necessary. The incoming flue gas is redirected to another bed, while the saturated bed is heated to the desorption

temperature, T_d. High-purity CO_2 is desorbed from the bed during heating, causing the pressure to increase and a CO_2-rich gas stream to be forced out the open end of the column. Once the bed has equilibrated at T_d, no more CO_2 will elute, and an N_2 purge is used to push the remaining CO_2 out of the column. This is continued until the CO_2 coming off the column falls below a desired purity level, at which point the column is cooled and readied for the next cycle. Such an adsorption cycle has already been validated experimentally using zeolites as a means of extracting high purity CO_2 from a CO_2/N_2 mixture.[34]

Based on this model, a working capacity can be approximated as the difference between the amount of CO_2 adsorbed at 0.15 bar and T_0 and the amount of CO_2 adsorbed at 1 bar and T_d, the latter of which corresponds to the amount of CO_2 that remains on the bed at the desorption temperature.[12] The CO_2 adsorption values used in these calculations were based on the pure component fits of the CO_2 isotherms. If anything, this model will over-estimate the actual working capacity for a material with low CO_2/N_2 selectivity, since the gas desorbed at T_d will be less than 100% CO_2. However, it should be reasonably accurate for any highly selective adsorbent and serves as a useful and easily calculated metric for comparing different materials.

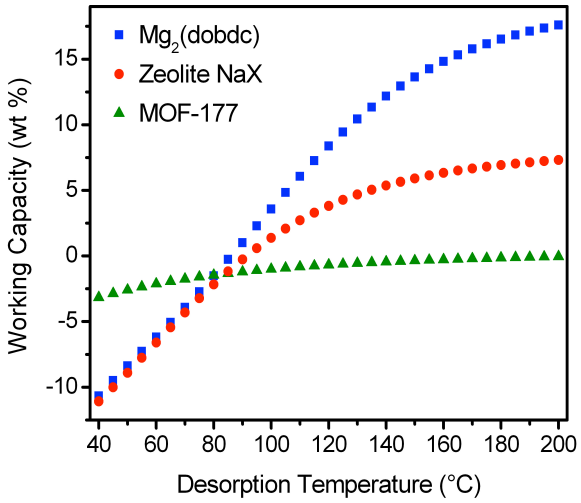

Figure 2.7. Estimated working capacity as a function of desorption temperature, T_d, for MOF-177, Mg_2(dobdc), and zeolite NaX. The working capacity is calculated as the difference between the amount of CO_2 adsorbed at 0.15 bar at a flue gas temperature of 40°C and the amount of CO_2 adsorbed at 1 bar at the desorption temperature. The pure component isotherm fits were used for performing the calculations.

The working capacities calculated for MOF-177, Mg_2(dobdc), and zeolite NaX assuming a flue gas temperature of T_0 = 40 °C are plotted in Figure 2.7. Here, Mg_2(dobdc) reaches a positive working capacity at a regeneration temperature of T_d = 90 °C and attains a value of 4.85 mmol/g (17.6 wt %) at T_d = 200 °C. Furthermore, Mg_2(dobdc) outperforms zeolite NaX at all desorption temperatures, due primarily to its higher surface area and stronger adsorption sites. Significantly, MOF-177 does not exhibit a positive working capacity at any desorption temperature up to 200 °C. By analogy, other metal-organic frameworks possessing only weak physisorptive sites are not expected to be of utility for CO_2 capture via TSA. Note that, in all cases, the working capacity approaches a maximum value at high desorption temperatures, as the amount of CO_2 that remains adsorbed approaches zero. Consequently, there is a tradeoff between energy costs

for heating the bed to higher temperatures and increased working capacities. The optimal desorption temperature for a given material, as well as the optimal CO_2 binding energy for a given set of power plant constraints, is dependent on many variables, and further studies considering the energetic implications and optimization of TSA CO_2 capture processes with strongly adsorbing metal-organic frameworks are currently underway.

While the absolute uptake of CO_2 is often used as a metric for comparing different materials, the working capacity is a far more important indicator of true performance. The working capacity in any TSA process is directly related to the temperature dependence of the CO_2 adsorption isotherms.[12] Determining the working capacity for a solid adsorbent in a process with a temperature swing requires the measurement of high-temperature isotherms, which have been systematically collected for the first time in this work. Furthermore, the results reported here demonstrate that strong adsorption sites are necessary for a metal-organic framework to be useful in a TSA-based CO_2 capture process. Metal-organic frameworks that have high CO_2 uptake at 0.15 bar and flue gas temperatures, coupled with a rapid decrease in CO_2 adsorbed near atmospheric pressure and higher temperatures, will be most promising for CO_2 capture. In particular, high thermal stability of the metal-organic frameworks will be important so that the materials can withstand repeated cycling to the optimal desorption temperature.

2.3.6. Heat Capacity. The regeneration step of a TSA process requires heating of the sorbent up to the desorption temperature, which, depending on the specific configuration of the power plant, may be as high as 200 °C. One parameter that is expected to impact considerably the efficiency of this process is the heat capacity (C_p) of the sorbent itself. The use of a low-heat capacity sorbent would be expected to afford a lower energy penalty for the regeneration step, which would be of significant benefit for reducing the total energy cost of post-combustion CO_2 capture.

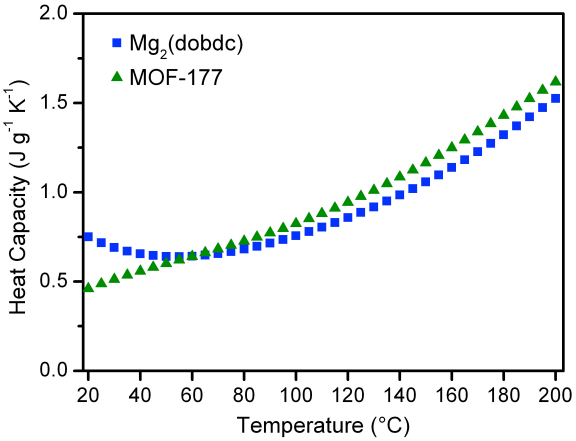

Figure 2.8. Heat capacity of MOF-177 (green triangles) and Mg_2(dobdc) (blue squares) as a function of temperature measured under N_2.

The heat capacities for evacuated samples of MOF-177 and Mg_2(dobdc) recorded under a flow of N_2 are presented in Figure 2.8. Interestingly, Mg_2(dobdc) initially exhibits a slight decrease in its heat capacity curve at temperatures up to 60 °C, presumably due to the desorption of bulk N_2 from the pores of the framework. Such an effect is not observed when the heat capacity measurement is conducted under a continuous He flow, since the adsorption of He is negligible across this temperature range (see Figure 2.S4). In contrast, MOF-177, which adsorbs

only a small quantity of N_2 at these temperatures, exhibits a nearly linear increase in the heat capacity with temperature. At temperatures above 60 °C, the heat capacities of the two materials are similar, reaching ca. 1.6 J g^{-1} K^{-1} at 200 °C. Nevertheless, consideration of the effect of adsorbed species on the heat capacity will be important in evaluating the regeneration energy requirements of any metal-organic framework in a TSA process since the material will contain significant amounts of adsorbed gas molecules (primarily CO_2) during the initial heating.

The heat capacity values reported here are comparable to the corresponding values for non-porous metal-organic frameworks and zeolites.[35] Importantly, the heat capacities are considerably lower than those of aqueous alkanolamine solutions, which carry a significant disadvantage in that the water in which the amine molecules are dissolved must also be heated to the desorption temperature of CO_2 (typically > 100 °C). For example, for a 30 wt % monoethanolamine (MEA) solution, the heat capacity at 25 °C is 3.73 J g^{-1} K^{-1}, which is close to the corresponding value for pure water (4.18 J g^{-1} K^{-1} at 25 °C), and is more than four times larger than the heat capacities of the metal-organic frameworks studied here.[36] Although the heat capacities of the metal-organic frameworks increase with temperature, the values at 200 °C are still less than half of the heat capacity of the MEA solution. This result highlights one of the key advantages of adopting a temperature swing adsorption process employing a metal-organic framework or other porous solid, wherein the contribution to the energy penalty arising from heating the adsorbent would be greatly reduced compared to the conventionally employed aqueous amine solutions.

2.4. Outlook and Conclusions

The forgoing results demonstrate the importance of strong binding sites in metal-organic frameworks for post-combustion CO_2 capture using temperature swing adsorption. Frameworks with homogenous pore surfaces containing only weak adsorption sites are impractical for such a process, due to a poor selectivity and low working capacity. We have demonstrated that studying materials with strong CO_2 binding sites necessitates the use of a dual-site Langmuir adsorption model to adequately describe the adsorption profile, even when only the low-pressure range is to be considered for assessment of the material properties. Promising metal-organic frameworks are not limited to those with open metal sites. Work is currently underway to evaluate frameworks with other pore surface functionalities for TSA CO_2 capture and to study the effect of minor flue gas components on the framework properties. Indeed, materials possessing functionalities such as amino groups, which also give rise to strong CO_2-adsorbent interactions, may be less likely to be poisoned by other flue gas components such as H_2O, NO_x, or SO_x. The synthesis of new materials that exhibit improved chemical robustness towards these impurities will also be a crucial endeavor in the development of next-generation CO_2 capture materials.

2.5. Acknowledgements

This research was funded by the Advanced Research Projects Agency - Energy (ARPA-E), U.S. Department of Energy. We thank Prof. Berend Smit, Dr. Abhoyjit S. Bhown, and Dr. Sergey N. Maximoff for helpful discussions. We acknowledge Dr. Rajamani Krishna for assisting with all isotherm fitting, heat of adsorption, and IAST calculations, Dr. Zoey Herm for performing the high-pressure adsorption measurement for Mg_2(dobdc), and Dr. Kenji Sumida for performing the heat capacity measurements.

2.6. References and Supplementary Figures

(1) Metz, B.; Davidson, O.; Coninck, H. de; Loos, M.; Meyer, L. *Intergovernmental Panel on Climate Change. Special Report on Carbon Dioxide Capture and Storage*, Cambridge University Press, Cambridge, **2005**, http://www.ipcc.ch/.

(2) *CO_2 Emissions from Fuel Combustion*, International Energy Agency, Paris, **2010**, http:/www.iea.org.

(3) Haszeldine, R. S. *Science* **2009**, *325*, 1647.

(4) Klara, S. M.; Srivastava, R. D.; McIlvried, H. G. *Energy Conv. Manage.* **2003**, *44*, 2699.

(5) Rochelle, G. T. *Science* **2009**, *325*, 1652.

(6) Figueroa, J. D.; Fout, T.; Plasynski, S.; McIlvried, H.; Srivastava, R. D. *Intl. J. of Green House Gas Control* **2008**, *2*, 9.

(7) (a) Eddaoudi, M.; Kim, J.; Rosi, N.; Vodak, D.; Wachter, J.; O'Keeffe, M.; Yaghi, O. M. *Scienc*e **2002**, *295*, 469. (b) Kitagawa, S.; Kitaura, R.; Noro, S.-I. *Angew. Chem., Int. Ed.* **2004**, *43*, 2334. (c) Matsuda, R.; Kitaura, R.; Kitagawa, S.; Kubota, Y.; Belosludov, R. V.; Kobayashi, T. C.; Sakamoto, H.; Chiba, T.; Takata, M.; Kawazoe Y.; Mita, Y. *Nature* **2005**, *436*, 238. (d) Millward. A, R.; Yaghi, O. M. *J. Am. Chem. Soc.*, **2005**, *127*, 17998. (e) Furukawa, H.; Miller, M. A.; Yaghi, O. M. *J. Mater. Chem.* **2007**, *17*, 3197. (f) Férey, G. *Chem. Soc. Rev.* **2008**, *37,* 191. (g) Ma, S.; Sun, D.; Simmons, J. M.; Collier, C. D.; Yuan, D.; Zhou, H. C. *J. Am. Chem. Soc.* **2008**, *130*, 1012. (h) Morris R. E.; Wheatley, P. S. *Angew. Chem., Int. Ed.* **2008**, *47*, 4966. (i) Llewellyn, P. L.; Bourrelly, S.; Serre, C.; Vimont, A.; Daturi, M.; Hamon, L.; de Weireld, G.; Chang, J. S.; Hong, D.-Y.; Hwang, Y. K.; Jhung, S. H.; Férey, G. *Langmuir* **2008**, *24*, 7245. (j) Murray, L. J.; Dincă, M.; Long, J. R. *Chem. Soc. Rev.* **2009**, *38,* 1294-1314. (k) Chen, B.; Xiang, S.; Qian, G. *Acc. Chem. Res.*, **2010**, 1115.

(8) (a) Li, G. R.; Kuppler. R. J.; Zhou, H. C. *Chem. Soc. Rev.* **2009**, *38*, 1477. (b) Yazayydin, A. Ö.; Snurr, R. Q.; Park, T. H.; Koh, K.; Liu, J.; LeVan, M. D.; Benin, A. I.; Jakubczak, P.; Lanuza, M.; Galloway, D. B.; Low, J. J.; Willis, R. R. *J. Am. Chem. Soc.* **2009**, *131*, 18198. (c) D'Alessandro, D. M.; Smit. B.; Long, J. R. *Angew. Chem. Int. Ed.* **2010**, *49*, 6058. (d) Keski, S.; van Heestm, T. M.; Sholl, D. S. *ChemSusChem* **2010**, *3*, 879. (e) Férey, G.; Serre, C.; Devic, T.; Maurin, G.; Jobic, H.; Llewellyn, P. L.; de Weireld, G.; Vimont, A.; Daturi, M.; Chang, J. S. *Chem. Soc. Rev.* **2011**, *40*, 550. (f) Simmons, J. M.; Wu, H.; Zhou, W.; Yildirim, T. *Energy Environ. Sci.* **2011**, *4*, 2177.

(9) (a) House, K. Z.; Harvey, C. F.; Aziz, M. J.; Schrag, D. P. *Energy Environ. Sci.* **2009**, *2*, 193. (b) Ishibashi, M.; Ota, H.; Akutsu, N.; Umeda, S.; Motaki, T.; Izumi, J.; Yasutake, A.; Kabata, T.; Kageyama, T. *Energy Convers. Mgmt.* **1996**, *37*, 929.

(10) Mulgundmath, V.; Tezel, H. *Adsorption* **2010**, *16*, 587.

(11) (a) Debatin, F.; Thomas, A.; Kelling, A.; Hedin, N.; Bacsik, Z.; Senkovska, I.; Kaskel, S.; Junginger, M.; Müller, H.; Schilde, U.; Jäger, C.; Friedrich A.; Holdt, H. J. *Angew. Chem. Int. Ed.* **2010**, *49*, 1258. (b) Aprea, P.; Caputo, D.; Gargiulo, N.; Iucolano, F.; Pepe, F. *J. Chem. Eng. Data* **2010**, *55*, 3655.

(12) Berger; A. H.; Bhown, A. S. *Energy Procedia* **2011**, *4*, 562.

(13) (a) Chae, H. K.; Siberio-Pérez, D. Y.; Kim, J.; Go, Y.; Eddaoudi, M.; Matzger, A. J.; O'Keefe, M.; Yaghi, O. M. *Nature* **2004**, *427*, 523. (b) Zheng, C.; Liu, D.; Yang, Q.;

Zhong, C.; Mi, J. *Ind. Eng. Chem. Res.* **2009**, *48*, 10479. (c) Saha, D.; Bao, Z.; Jia, F.; Deng, S. *Environ. Sci. Technol.* **2010**, *44*, 1820.

(14) (a) Rosi, N. L.; Kim, J.; Eddaoudi, M.; Chen, B.; O'Keeffe, M.; Yaghi, O. M. *J. Am. Chem. Soc.* **2005**, *127*, 1504. (b) Caskey, S. R.; Wong-Foy, A. G.; Matzger, A. J. *J. Am. Chem. Soc.* **2008**, *130*, 10870. (c) Britt, D.; Furukawa, H.; Wang, B.; Glover, T. G.; Yaghi, O. M. *Proc. Nat. Acad. Sci.*, *USA* **2009**, *106*, 20637. (d) Dietzel, P. D. C.; Besikiotis, V.; Blom, R. *J. Mater. Chem.* **2009**, *19*, 7362. (e) Wu, H.; Simmons, J. M.; Srinivas, G.; Zhou, W.; Yildirim, T. *J. Phys. Chem. Lett.* **2010**, *1*, 1946. (f) Valenzano, L.; Civalleri, B.; Chavan, S.; Palomino, G. T.; Areán, C. O.; Bordiga, S. *J. Phys. Chem. C* **2010**, *114*, 11185. (g) Sumida, K.; Brown, C. M.; Herm, Z. R.; Chavan, S.; Bordiga, B.; Long, J. R. *Chem. Commun.* **2011**, *47*, 1157. (h) Bao, Z.; Yu, L.; Ren, Q.; Lu, X.; Deng, S. *J. Colloid Interface Sci*, **2011**, *353*, 549.

(15) (a) Dietzel, P. D. C.; Morita, T.; Blom R.; Fjellvag, H. *Angew. Chem., Int. Ed.* **2005**, *44*, 6354. (b) Dincă, M.; Long, J. R. *J. Am. Chem. Soc.* **2005**, *127*, 9376. (c) Vimont, A.; Goupil, J.-M.; Lavalley, J.-C.; Daturi, M.; Surblé, S.; Serre, C.; Millange, F.; Férey, G.; Audebrand, N. *J. Am. Chem. Soc.* **2006**, *128*, 3218. (d) Moon, H. R.; Kobayashi, N.; Suh, P. M. *Inorg. Chem.* **2006**, *45*, 8672. (e) Dincă, M.; Dailly, A.; Liu, Y.; Brown, C. M.; Neumann, D. A.; Long, J. R. *J. Am. Chem. Soc.* **2006**, *128*, 16876. (f) Dietzel, P. D. C.; Panella, B.; Hirscher, M.; Blom, R.; Fjellvag, H. *Chem. Commun.* **2006**, 959. (g) Dincă, M.; Han, W. S.; Liu, Y.; Dailly, A.; Brown, C. M.; Long, J. R. *Angew. Chem., Int. Ed.* **2007**, *46*, 1419. (h) Dietzel, P. D. C.; Blom, R.; Fjellvag, H. *Eur. J. Inorg. Chem.* **2008**, 3624. (i) Liu, Y.; Kabbour, H.; Brown, C. M.; Neumann, A. D.; Ahn, C. C. *Langmuir* **2008**, *24*, 4772. (j) Dietzel, P. D. C.; Johnsen, R. E.; Fjellvag, H.; Bordiga, S.; Groppo, E.; Chavan, S.; Blom, R. *Chem. Commun.* **2008**, 5125. (k) Zhou, W.; Wu, H.; Yildirim, T. *J. Am. Chem. Soc*, **2008**, *130*, 15268. (l) Sumida, K.; Horike, S.; Kaye, S. S.; Herm, Z. R.; Queen, W. L.; Brown, C. M.; Grandjean, F.; Long, G. J.; Dailly, A.; Long, J. R. *Chem. Sci.* **2010**, *1*, 184.

(16) (a) Neofotistou, E.; Malliakas, C. D.; Trikalitis, P. N. *Chem. Eur. J.* **2009**, *15*, 4523. (b) Couck, S.; Denayer, J. F. M.; Baron, G. V.; Remy, T.; Gascon, J.; Kapteijn, F. *J. Am. Chem. Soc.* **2009**, *131*, 6326. (c) Arstad, B.; Fjellvag, H.; Kongshaug, O. K.; Swang, O.; Blom, R. *Adsorption* **2008**, *14*, 755.

(17) (a) Tanabe, K. K.; Wang, Z.; Cohen, S. M. *J. Am. Chem. Soc.* **2008**, *130*, 8508. (b) Bae, Y. S.; Farha, O. K.; Hupp, J. T.; Snurr, R. Q. *J. Mater. Chem.* **2009**, *19*, 2131. (c) Demessence, A.; D'Alessandro, D. M.; Foo, M. L.; Long, J. R. *J. Am. Chem. Soc.* **2009**, *131*, 8784. (d) Doonan, C. J.; Morris, W.; Furukawa, H.; Yaghi, O. M. *J. Am. Chem. Soc.* **2009**, *131*, 9492. (e) Bloch, E. D.; Britt, D.; Doonan, C. J.; Uribe-Romo, F. J.; Furukawa, H.; Long, J. R.; Yaghi, O. M. *J. Am. Chem. Soc.* **2010**, *132*, 14382.

(18) Poirier, E.; Dailly, A. *Nanotechnology* **2009**, *20*, 204006.

(19) Kaye, S. S.; Dailly, A.; Yaghi, O. M.; Long, J. R. *J. Am. Chem. Soc.* **2007**, *129*, 14176.

(20) Walton, K. S.; Snurr, R. Q. *J. Am. Chem. Soc.* **2007**, *129*, 8552.

(21) Archer, D. G. *J. Phys. Chem. Ref. Data* **1992**, *22*, 1441.

(22) Bae, Y.-S.; Lee, C.-H. *Carbon* **2005**, *43*, 95.

(23) (a) Granite, E. J.; Pennline, H. W. *Ind. Eng. Chem. Res*, **2002**, *41*, 5470. (b) Jassim, M. S.; Rochelle, G. T. *Ind. Eng. Chem. Res.* **2006**, *45*, 2465. (c) Lee, K. B.; Sircar, S. *AIChE J.*, **2008**, *54*, 2293.
(24) Note that various definitions of weight percent, wt %, are found in the literature, presenting a challenge when directly comparing the performance of different materials. In this work, wt % is defined as:

$$\text{wt } \% = \frac{\text{mass gas adsorbed}}{\text{mass adsorbent} + \text{mass gas adsorbed}} \times 100\%$$

The other commonly used definition, which neglects the mass of the adsorbed gas in the denominator, is more appropriately referred to as the weight ratio:

$$\text{wt ratio} = \frac{\text{mass gas adsorbed}}{\text{mass adsorbent}}$$

(25) Vlugt, T. J. H.; Krishna, R.; Smit, B *J. Phys. Chem. B.* **1999**, *103*, 1102.
(26) Mertens, O. F. *Surface Science* **2009**, *603*, 1979.
(27) Herm, Z. R.; Swisher, J. A.; Smit, B.; Krishna, R.; Long, J. R. *J. Am. Chem. Soc.* **2011**, *133*, 5664.
(28) Myers, A. L.; Prausnitz, J. M. *A.I.Ch.E. J.* **1965**, *11*, 121.
(29) Talu, O. *Adv. Colloid Interface Sci.* **1998**, *77*, 227.
(30) (a) Krishna, R.; Calero, S.; Smit, B. *Chem. Eng. J.* **2002**, *88*, 81. (b) Krishna, R.; van Baten, J. M. *Chem. Eng. J.* **2007**, *133*, 121.
(31) Krishna, R.; van Baten, J. M. *Phys. Chem. Chem. Phys.* **2011**, *13*, 10593.
(32) (a) Belmabkhout, Y.; Pirngruber, G.; Jolimaitre, E.; Methivier, A. *Adsorption* **2007**, *13*, 341. (b) Cavenati, S.; Grande, C. A.; Rodrigues, A. E. *J. Chem. Eng. Data* **2004**, *49*, 1095.
(33) Krishna, R. Long, J. R. *J. Phys. Chem. C* **2011**, *115*, 12941.
(34) Merel, J.; Clausse, M.; Meunier, F. *Ind. Eng. Chem. Res.* **2008**, *47*, 209.
(35) (a) Chue, K. T.; Kim, J. N.; Yoo, Y. J.; Cho, S. H.; Yang, R. T. *Ind. Eng. Chem. Res.* **1995**, *34*, 591. (b) Qiu, L.; Murashov, V.; White, M. A. *Solid State Sci.* **2000**, *2*, 841. (c) Song, L.-F.; Jiang, C.-H.; Zhang, J.; Sun, L.-X.; Xu, F.; Tian, Y.-Q.; You, W.-S.; Cao, Z.; Zhang, L.; Yang, D.-W. *J. Therm. Anal. Calorim.* **2010**, *101*, 365. (d) Song, L.-F.; Jiang, C.-H.; Zhang, J.; Sun, L.-X.; Xu, F.; You, W.-S.; Zhao, Y.; Zhang, Z.-H.; Wang, M.-H.; Sawada, Y.; Cao, Z.; Zeng, J.-L. *J. Therm. Anal. Calorim.* **2010**, *100*, 679.
(36) Wieland, R. H.; Dingman, J. C.; Cronin, D. B. *J. Chem. Eng. Data* **1997**, 42, 1004.

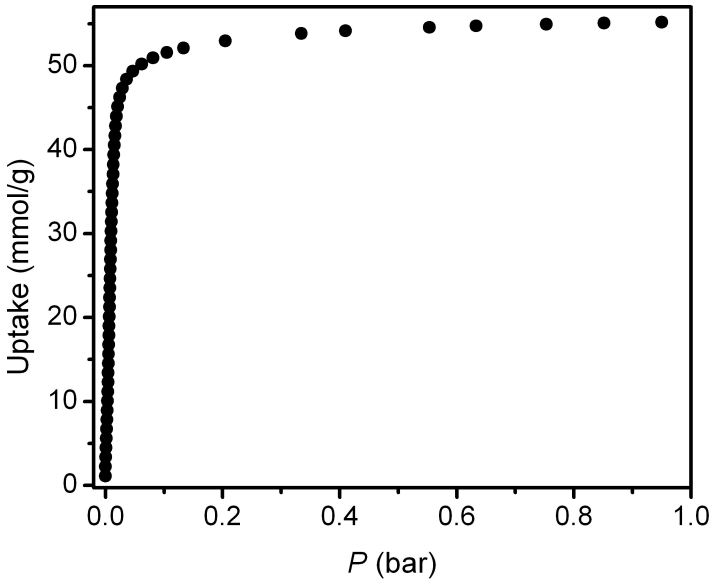

Figure 2.S1. Adsorption isotherm for N_2 in MOF-177 at 77 K, resulting in a calculated Langmuir surface area of 5400 m^2/g and BET surface area of 4690 m^2/g.

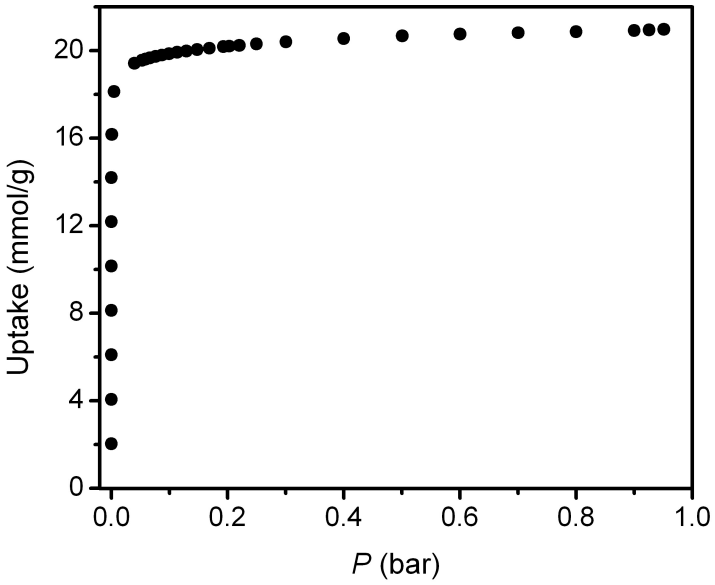

Figure 2.S2. Adsorption isotherm for N_2 in Mg_2(dodbc) at 77 K, resulting in a calculated Langmuir surface area of 2060 m^2/g and BET surface area of 1800 m^2/g.

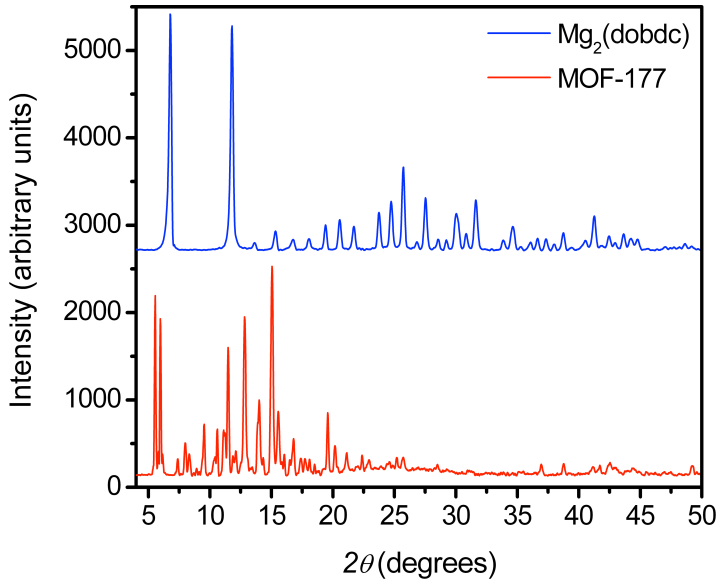

Figure 2.S3. X-ray powder diffraction patterns, with background subtracted, of as synthesized MOF-177 (bottom) and Mg_2(dobdc) (top).

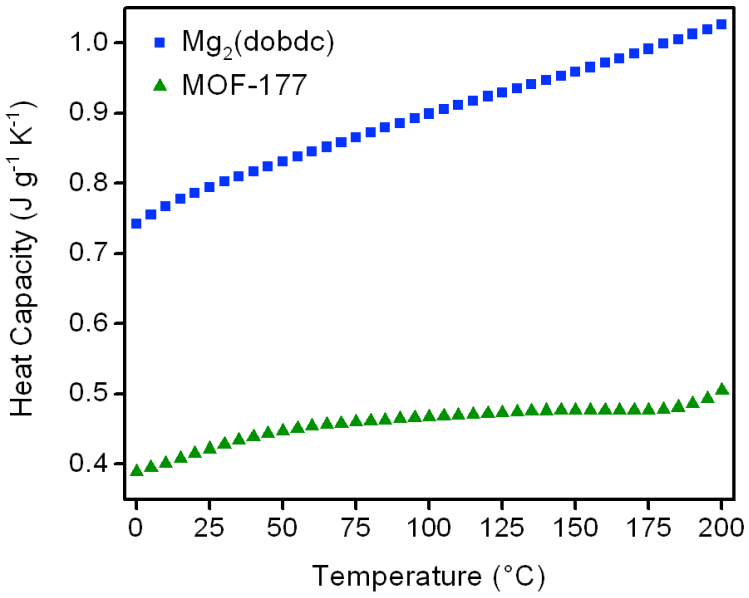

Figure 2.S4. Heat capacity of MOF-177 (green triangles) and Mg_2(dobdc) (blue squares) as a function of temperature measured under He.

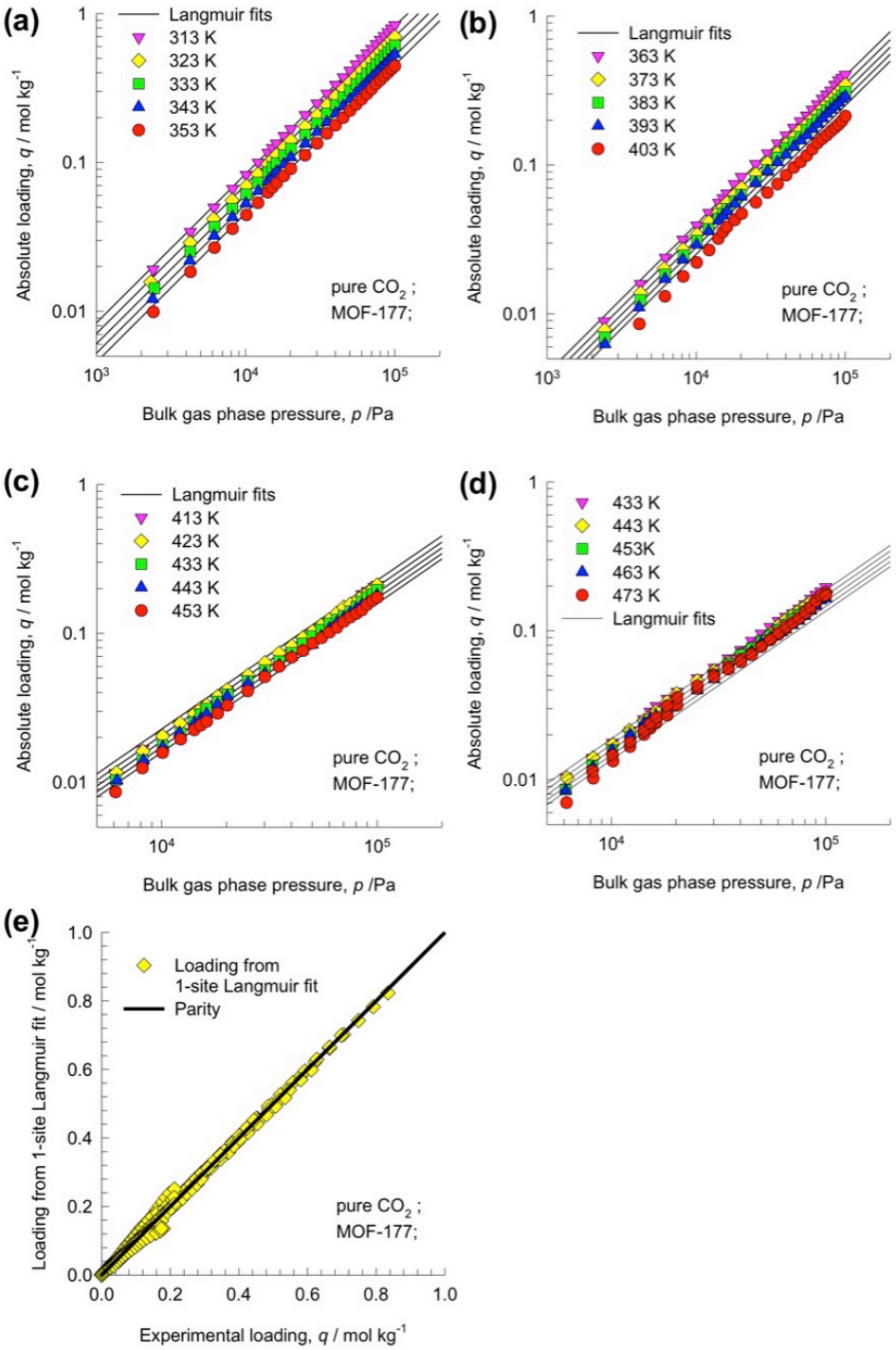

Figure 2.S5. (a, b, c, d) Experimental data for adsorption of CO_2 in MOF-177. The continuous solid lines are the single-site Langmuir fits using the parameters specified in Table 2.S2. (e) Parity plot comparing the experimentally measured absolute loadings for the entire data set (*x*-axis) and the values of the loadings calculated using the single-site Langmuir model along with the parameters specified in Table 2.S2 (*y*-axis).

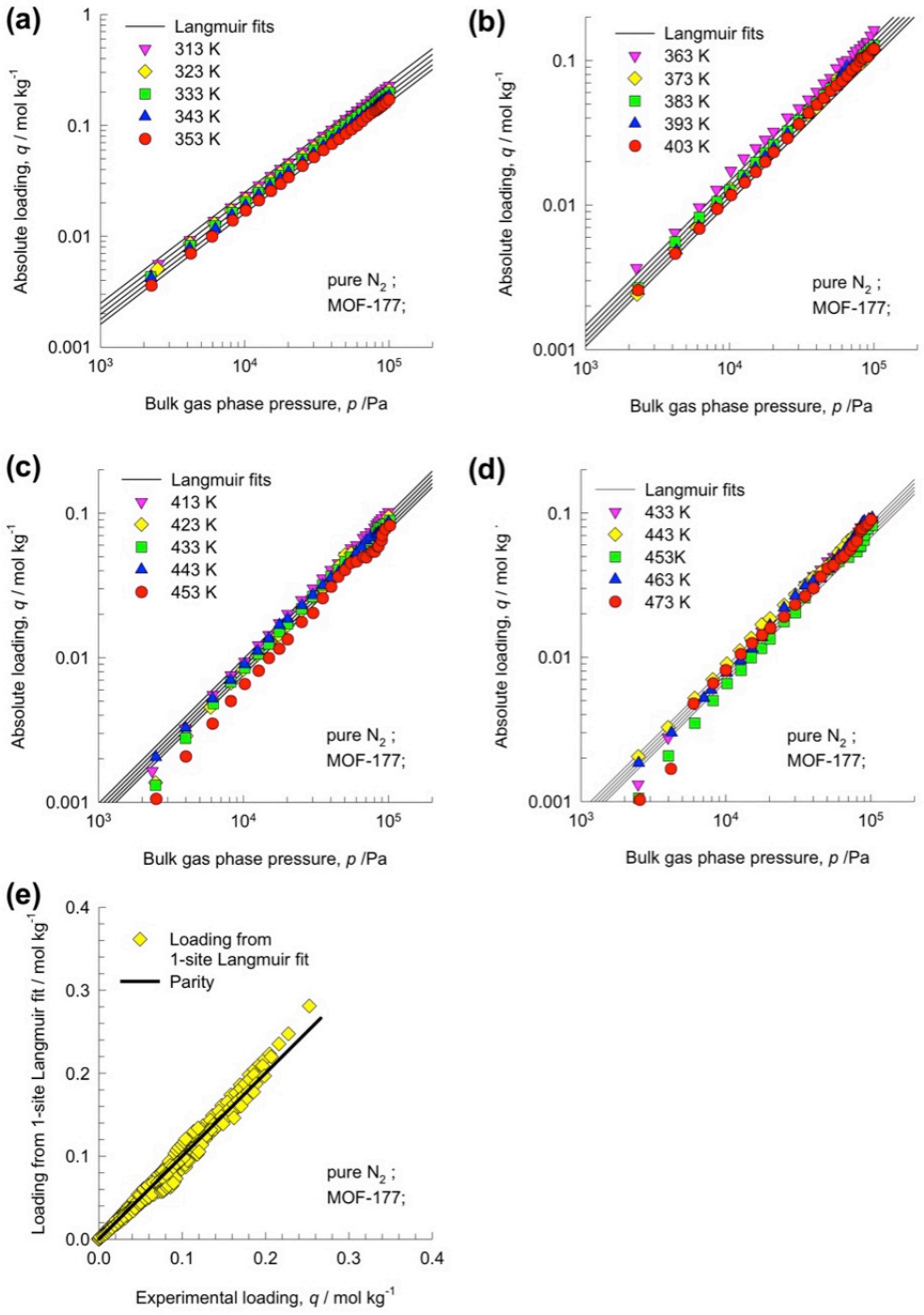

Figure 2.S6. (a, b, c, d) Experimental data for adsorption of N_2 in MOF-177. The continuous solid lines are the single-site Langmuir fits using the parameters specified in Table 2.S3. (e) Parity plot comparing the experimentally measured absolute loadings for the entire dataset (*x*-axis) and the values of the loadings calculated using the single-site Langmuir model along with the parameters specified in Table 2.S3 (*y*-axis).

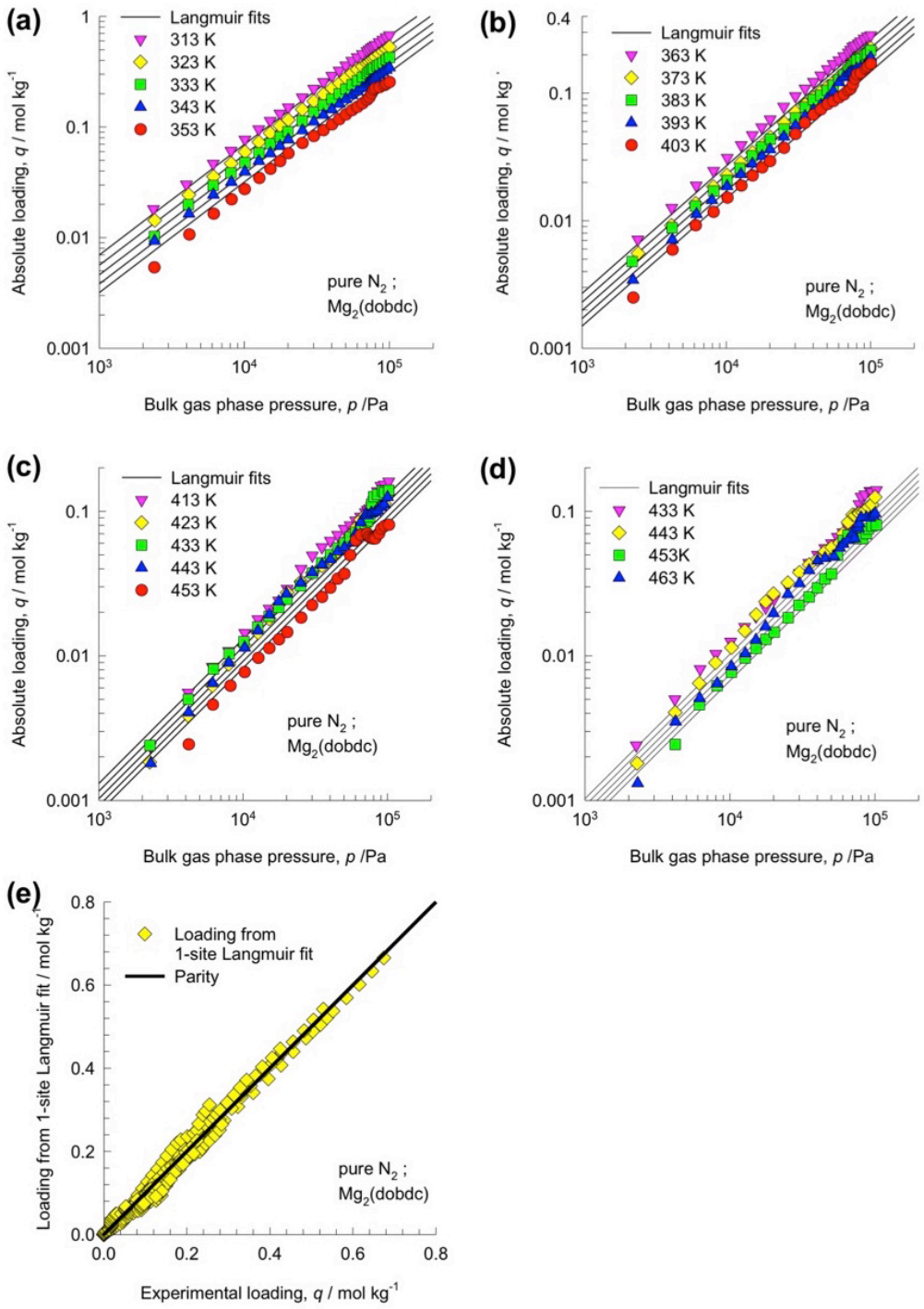

Figure 2.S7. (a, b, c, d) Experimental data for adsorption of N_2 in Mg_2(dobdc). The continuous solid lines are the single-site Langmuir fits using the parameters specified in Table 2.S4. (e) Parity plot comparing the experimentally measured absolute loadings for the entire data set (*x*-axis) and the values of the loadings calculated using the single-site Langmuir model along with the parameters specified in Table 2.S4 (*y*-axis).

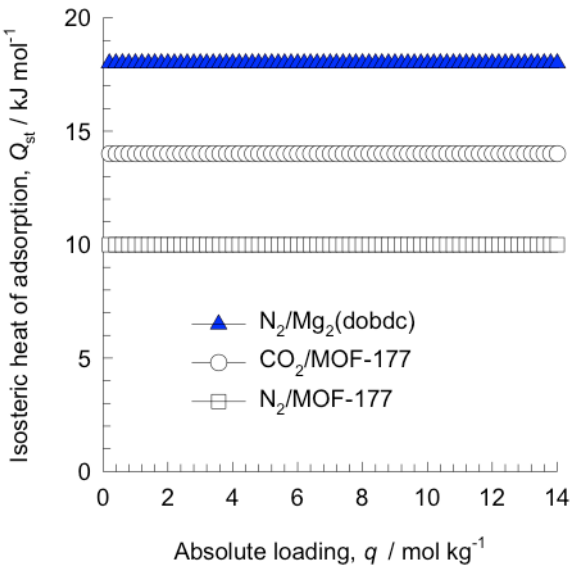

Figure 2.S8. Comparison of the isosteric heats of adsorption, Q_{st}, for CO_2/MOF-177, N_2/MOF-177, and N_2/Mg_2(dobdc).

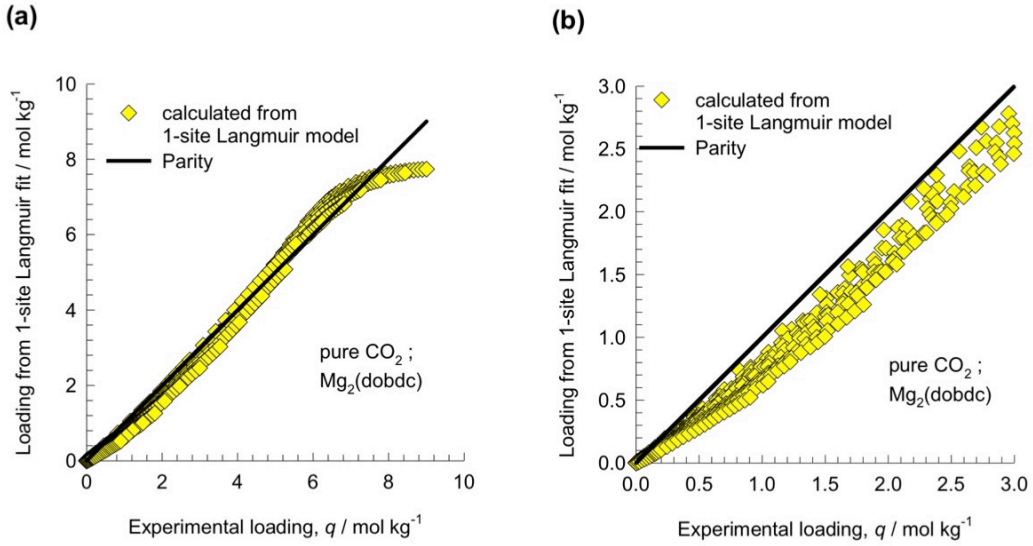

Figure 2.S9. Parity plot comparing the experimental values of absolute loadings for CO_2/Mg_2(dobdc) measured in this work and the values of the loadings calculated using the single-site Langmuir model along with the parameters specified in Table 2.S5 (y-axis).

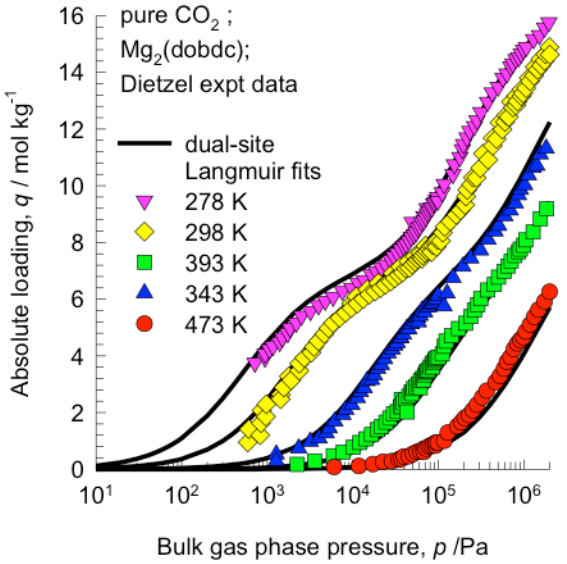

Figure 2.S10. Adsorption isotherms for CO_2 in Mg_2(dobdc) at 278 K, 298 K, 343 K, 393 K, and 473 K measured in the work of Dietzel et al.[14d] Their data for excess loadings have been converted to absolute loadings by estimating the fluid densities within the pores using the Peng-Robinson equation of state. Their experimental value of the pore volume, 0.63 cm^3/g, was used in this conversion. The continuous solid lines are the dual-site Langmuir fits using the parameters specified in Table 2.S6.

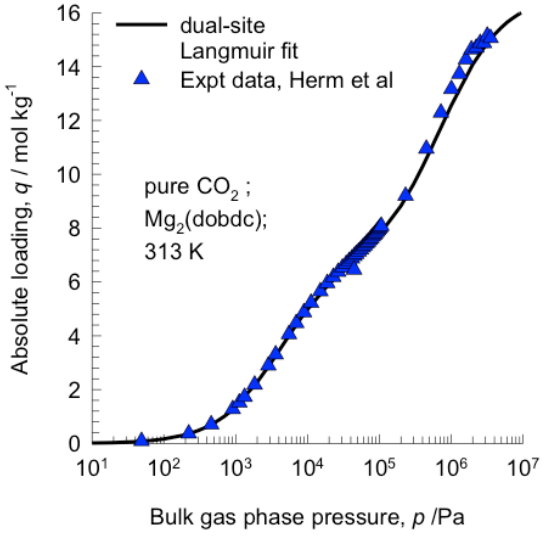

Figure 2.S11. Adsorption isotherms for CO_2 in Mg_2(dobdc) at 313 K. The continuous solid lines are the dual-site Langmuir fits using the parameters specified in Table 2.S6.

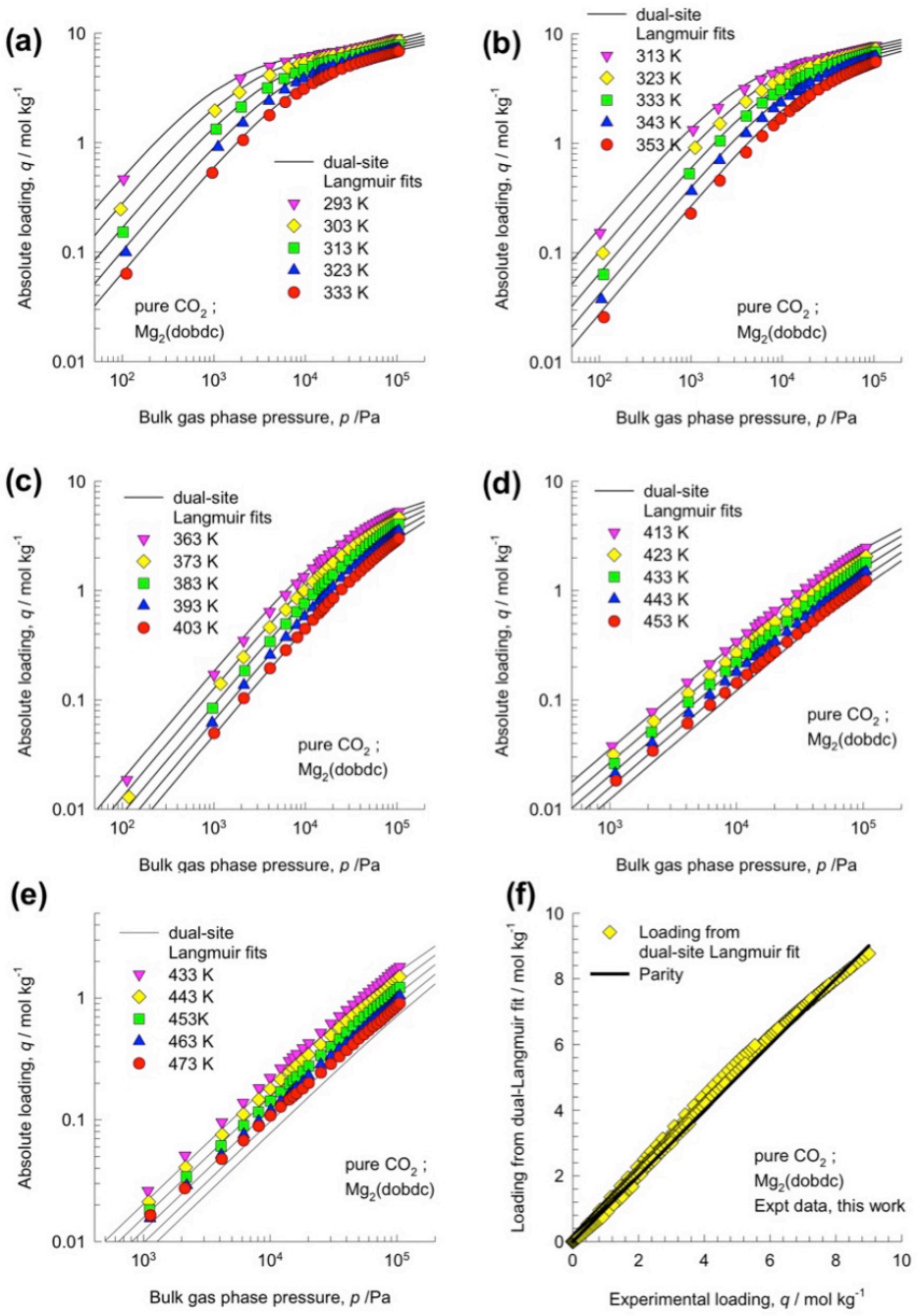

Figure 2.S12. (a, b, c, d, e) Experimental data for adsorption of CO_2 in Mg_2(dobdc) for a variety of temperatures generated in the current work. The continuous solid lines are the dual-site Langmuir fits using the parameters specified in 2. S6. (f) Parity plot comparing the experimentally measured absolute loadings for the entire data set (*x*-axis) and the values of the loadings calculated using the dual-site Langmuir model along with parameters specified in Table 2.S6 (*y*-axis). The parity plot includes only the dataset generated in this work.

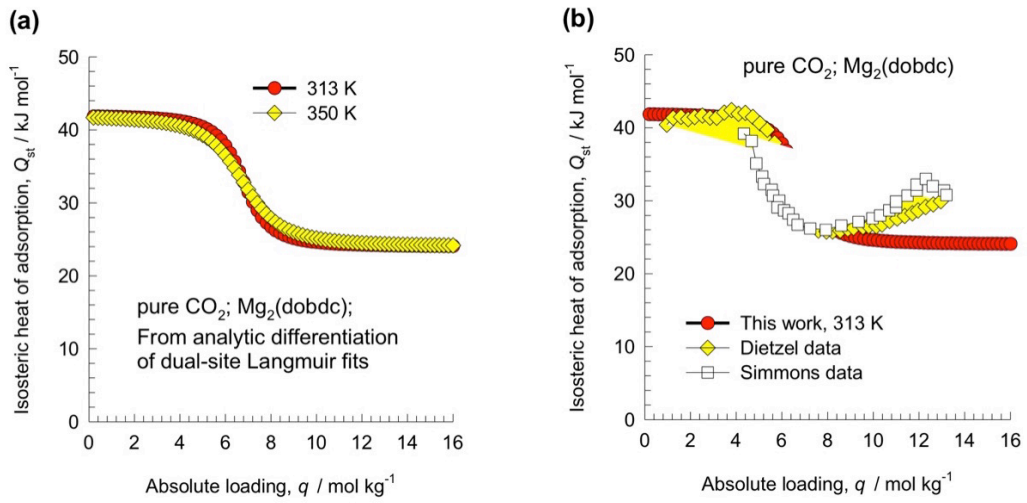

Figure 2.S13. (a) The isosteric heats of adsorption, Q_{st}, for CO_2/Mg_2(dobdc) obtained from analytic differentiation of the dual-site Langmuir fits. The Q_{st} are shown for 313 K and 350 K. We note that the temperature dependence is very weak. (b) Comparison of our Q_{st} with the published data of Dietzel et al.[14d] and Simmons et al.[8f]

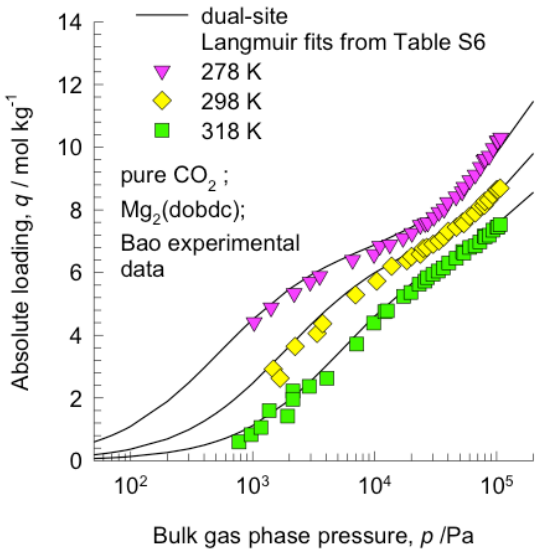

Figure 2.S14. Experimental data of Bao et al.[14h] (denoted by symbols) of CO_2 isotherms in Mg_2(dobdc) at 278 K, 298 K, and 318 K, compared with calculations of the absolute loading using the dual-Langmuir fits with parameters specified in Table 2.S6.

Table 2.S1. High-pressure CO_2 adsorption data for Mg_2(dobdc) at 50 °C. The high-pressure CO_2 adsorption data for MOF-177 and Mg_2(dobdc) at 40 °C was previously reported.[27]

Pressure (bar)	Excess Uptake (mmol/g)	Total Uptake (mmol/g)
2.4585	8.65423	8.708273358
7.967838	11.47412	11.65650558
14.34587	12.83591	13.17339535
21.16477	13.32603	13.84033891
28.33638	13.35482	14.0713281
35.79211	13.1753	14.12419199
43.65606	12.37505	13.59879711
50.21045	10.71721	12.19738362

Table 2.S2. Single-site Langmuir parameter for adsorption of CO_2 in MOF-177. These parameters were determined by fitting adsorption isotherms for temperatures ranging from 293 K to 473 K.

$$q = \frac{q_{sat} bp}{1 + bp}$$

$$q_{sat} = 48 \,\text{mol kg}^{-1}$$

$$b = b_0 \exp\left(\frac{E}{RT}\right);$$

$$b_0 = 8.06 \times 10^{-10} \text{ Pa}^{-1}$$

$$E = 14 \text{ kJ mol}^{-1}$$

Table 2.S3. Single-site Langmuir parameter for adsorption of N_2 in MOF-177. These parameters were determined by fitting adsorption isotherms for temperatures ranging from 293 K to 473 K.

$$q = \frac{q_{sat} bp}{1 + bp}$$

$$q_{sat} = 48 \text{ mol kg}^{-1}$$

$$b = b_0 \exp\left(\frac{E}{RT}\right);$$

$$b_0 = 1.11 \times 10^{-9} \text{ Pa}^{-1}$$

$$E = 10 \text{ kJ mol}^{-1}$$

Table 2.S4. Single-site Langmuir parameter for adsorption of N_2 in Mg_2(dobdc). These parameters were determined by fitting adsorption isotherms for temperatures ranging from 293 K to 473 K.

$$q = \frac{q_{sat} b p}{1 + bp}$$

$$q_{sat} = 14 \text{ mol kg}^{-1}$$

$$b = b_0 \exp\left(\frac{E}{RT}\right);$$

$$b_0 = 4.96 \times 10^{-10} \text{ Pa}^{-1}$$

$$E = 18 \text{ kJ mol}^{-1}$$

Table 2.S5. Single-site Langmuir parameter for adsorption of CO_2 in Mg_2(dobdc). These parameters were determined by fitting adsorption isotherms for temperatures ranging from 293 K to 473 K. The choice of E = 42 kJ/mol is dictated by the fact that the measured data have loadings in the range 0 – 8 mol/kg and in this range the isosteric heat of adsorption is 42 kJ/mol as reported in the work of Dietzel et al.[14d]

$$q = \frac{q_{sat} b p}{1 + bp}$$

$$q_{sat} = 7.9 \text{ mol kg}^{-1}$$

$$b = b_0 \exp\left(\frac{E}{RT}\right);$$

$$b_0 = 1.557 \times 10^{-11} \text{ Pa}^{-1}$$

$$E = 42 \text{ kJ mol}^{-1}$$

Table 2.S6. Dual-site Langmuir parameter for adsorption of CO_2 in Mg_2(dobdc). These parameters were determined by fitting adsorption isotherms for temperatures ranging from 278 K to 473 K.

$$q \equiv q_A + q_B = \frac{q_{sat,A} b_A p}{1 + b_A p} + \frac{q_{sat,B} b_B p}{1 + b_B p}$$

$$q_{sat,A} = 6.8 \text{ mol kg}^{-1}$$

$$q_{sat,B} = 9.9 \text{ mol kg}^{-1}$$

$$b_A = b_{A0} \exp\left(\frac{E_A}{RT}\right);$$

$$b_{A0} = 2.44 \times 10^{-11} \text{ Pa}^{-1}$$

$$E_A = 42 \text{ kJ mol}^{-1}$$

$$b_B = b_{B0}\exp\left(\frac{E_B}{RT}\right);$$
$$b_{B0} = 1.39\times10^{-10}\ \text{Pa}^{-1}$$
$$E_B = 24\ \text{kJ mol}^{-1}$$

Table 2.S7. Dual-site Langmuir parameter for adsorption of CO_2 in NaX zeolite. These parameters were determined by fitting adsorption isotherm data reported in the works of Belmabkhout et al.[32a] and Cavenati et al.[32b]

$$q \equiv q_A + q_B = \frac{q_{sat,A}b_A p}{1+b_A p} + \frac{q_{sat,B}b_B p}{1+b_B p}$$
$$q_{sat,A} = 3.5\,\text{mol kg}^{-1}$$
$$q_{sat,B} = 5.2\,\text{mol kg}^{-1}$$
$$b_A = b_{A0}\exp\left(\frac{E_A}{RT}\right);$$
$$b_{A0} = 3.64\times10^{-13}\ \text{Pa}^{-1}$$
$$E_A = 35\ \text{kJ mol}^{-1}$$
$$b_B = b_{B0}\exp\left(\frac{E_B}{RT}\right);$$
$$b_{B0} = 6.04\times10^{-11}\ \text{Pa}^{-1}$$
$$E_B = 35\ \text{kJ mol}^{-1}$$

Table 2.S8. Dual-site Langmuir parameter for adsorption of N_2 in Zeolite NaX. These parameters were determined by fitting adsorption isotherm data reported in the works of Belmabkhout et al.[32a] and Cavenati et al.[32b]

$$q \equiv q_A + q_B = \frac{q_{sat,A}b_A p}{1+b_A p} + \frac{q_{sat,B}b_B p}{1+b_B p}$$
$$q_{sat,A} = 3\ \text{mol kg}^{-1}$$
$$q_{sat,B} = 6\,\text{mol kg}^{-1}$$
$$b_A = b_{A0}\exp\left(\frac{E_A}{RT}\right);$$
$$b_{A0} = 4.08\times10^{-9}\ \text{Pa}^{-1}$$
$$E_A = 13\ \text{kJ mol}^{-1}$$
$$b_B = b_{B0}\exp\left(\frac{E_B}{RT}\right);$$
$$b_{B0} = 4.68\times10^{-10}\ \text{Pa}^{-1}$$
$$E_B = 13\ \text{kJ mol}^{-1}$$

Chapter 3: Evaluating Metal-Organic Frameworks for Natural Gas Storage

3.1. Introduction

Natural gas has significant environmental and economic advantages over other fossil fuels as a source of energy for the transportation sector.[1,2] Owing to their high porosity and tunable pore surfaces, metal-organic frameworks have received significant attention as a new class of adsorbents for natural gas storage.[3] While early research on these materials for gas storage applications was mostly related to H_2,[4] a growing number of frameworks have been evaluated for CH_4 storage.[5,6] Significantly, several metal-organic frameworks have reported CH_4 capacities comparable to or exceeding those of the best activated carbons; however, inconsistencies in reporting adsorption results and a lack of comparative studies have made it challenging to compare the performance of different materials. Here, we discuss the most important material properties for evaluating both new and existing metal-organic frameworks for natural gas storage and briefly review recent work. In this context, six metal-organic frameworks and an activated carbon, with a range of surface chemistries, pore structures, and surface areas representative of the most promising adsorbents for CH_4 storage, are evaluated in detail.

Table 3.1. Relevant physical properties of pure CH_4.

Critical temperature	190.6 K
Boiling point	111.7 K
Kinetic diameter	3.80 Å
Polarizability	2.6 $Å^3$
Volumetric density (1 bar, 25 °C)	0.9 v/v
Volumetric density (250 bar, 25 °C)	263 v/v
Volumetric density (1 bar, −162 °C)	591 v/v

3.2. Experimental

3.2.1. General Information. Anhydrous dichloromethane and N,N-dimethylformamide were obtained from a Vac anhydrous solvent system. The ligand 5,5´-(9,10-anthracenediyl)-di-isophthalic acid (H_4adip) was synthesized according to a literature procedure.[27a] The AX-21 carbon was purchased from a commercial vendor and activated at 200 ºC under vacuum for 24 h prior to use. All other reagents were obtained from commercial vendors and used without further purification. UHP-grade (99.999% purity) helium, nitrogen, and methane were used for all adsorption measurements. Infrared spectra were obtained on a Perkin-Elmer Spectrum 100 Optica FTIR spectrometer furnished with an attenuated total reflectance accessory. Diffraction data were collected with 0.02° steps using a Bruker AXS D8 Advance diffractometer equipped with Cu-Kα radiation (λ = 1.5418 Å), a Göbel mirror, a Lynxeye linear position-sensitive detector, and mounting the following optics: fixed divergence slit (0.6 mm), receiving slit (3 mm), and secondary beam Soller slits (2.5°). The generator was set at 40 kV and 40 mA.

3.2.2. Low-Pressure Gas Adsorption Measurements. Gas adsorption isotherms for pressures in the range 0-1.1 bar were measured using a Micromeritics ASAP 2020 instrument.

For standard measurements in ASAP low-pressure glass sample holders, activated samples were transferred under a N_2 atmosphere to preweighed analysis tubes, which were capped with a Transeal. The samples were evacuated on the ASAP until the outgas rate was less than 3 μbar/min. The evacuated analysis tubes containing degassed samples were then carefully transferred to an electronic balance and weighed to determine the mass of sample (typically 100-200 mg). The tube was fitted with an isothermal jacket and transferred back to the analysis port of the gas adsorption instrument. The outgas rate was again confirmed to be less than 3 μbar/min. Langmuir surface areas and pore volumes were determined by measuring N_2 adsorption isotherms in a 77 K liquid N_2 bath and calculated using the Micromeritics software, assuming a value of 16.2 $Å^2$ for the molecular cross-sectional area of N_2.

3.2.3. Metal-Organic Framework Synthesis. The compound Ni_2(dobdc) (Ni-MOF-74, CPO-27-Ni; dobdc^{4-} = 2,5-dioxido-1,4-benzenedicarboxylate) was synthesized and activated using a strategy adopted from previous reports.[23b] Specifically, H_4dobdc (1.42 g, 7.2 mmol) and $Ni(NO_3)_2 \cdot 6H_2O$ (5.23 g, 18 mmol) were combined with 350 mL of anhydrous dimethylformamide (DMF) and 42 mL of anhydrous methanol (MeOH) in a 500 mL Schlenk flask under N_2. The solution was heated at 120 ºC under a positive N_2 pressure with stirring for 18 h. After cooling, the resulting yellow-orange precipitate settled to the bottom of the Schlenk flask, and the reaction solvent was removed via cannula, replaced with fresh DMF, and heated to 100 ºC for 5-6 h. The DMF was replaced with fresh DMF two additional times. The DMF was then exchanged with MeOH, and the mixture was heated to 60 ºC for 5-6 h. The MeOH was replaced with fresh MeOH two additional times. The majority of MeOH was then removed via cannula, and the resulting bright orange compound was activated at 180 ºC under vacuum for 24-48 hr to yield 1.5 g of desolvated Ni_2(dobdc). Note that while the solvent exchanges were conducted under N_2, anhydrous solvents were not used. The successful synthesis and activation of the framework was confirmed by comparing the X-ray powder diffraction pattern and Langmuir surface area to those previously reported (see Figures 3.S1, 3.S7).

The compound Co_2(dobdc) (Co-MOF-74, CPO-27-Co) was synthesized and activated using a strategy adopted from a previous report.[23b] Specifically, H_4dobdc (0.964 g, 4.9 mmol) and $Co(NO_3)_2 \cdot 6H_2O$ (4.754 g, 16.3 mmol) were combined with a 1:1:1 (v/v/v) mixture of DMF:ethanol:H_2O (400 mL) in a 1 L jar, sparged with N_2 for 1 h, and heated at 100 ºC for 24 h. Following the reaction, the resulting red-violet crystals were collected by filtration and washed repeatedly with DMF. The compound was then soaked in DMF at 120 °C for 5-6 h. The DMF was decanted, replaced with fresh DMF, and again heated to 120 °C for 5-6 h. This was repeated one additional time. Then, the DMF was decanted and replaced by MeOH, which was heated to 60 ºC for 5-6 h. The MeOH was decanted, replaced with fresh MeOH, and again heated to 60 °C for 5-6 h. This was repeated 2 additional times. The final product was collected by filtration and then activated under vacuum at 180 °C for 24-48 h. The successful synthesis and activation of the framework was confirmed by comparing the X-ray powder diffraction pattern and Langmuir surface areas to those previously reported (see Figures 3.S2, 3.S8).

The compound Mg_2(dobdc) (Mg-MOF-74, CPO-27-Mg) was synthesized and activated using a strategy adopted from previous reports.[23b, 23o] Specifically, H_4dobdc (1.11 g, 5.6 mmol) and $Mg(NO_3)_2 \cdot 6H_2O$ (4.75 g, 18.6 mmol) were dissolved in a 15:1:1 (v/v/v) mixture of DMF:ethanol:H_2O (500 mL) and sparged with N_2 for 1 h. The resulting solution was evenly distributed into thirty-eight 20 mL vials, which were sealed with Teflon-lined caps and heated to 120 ºC for 8 h. Following the reaction, the resulting yellow microcrystalline material was

collected by filtration and washed repeatedly with DMF. The solid was then soaked in DMF at 120 °C for 5-6 h. The DMF was decanted, replaced with fresh DMF, and again heated to 120 °C for 5-6 h. This was repeated one additional time. Then, the DMF was decanted and replaced by MeOH, which was heated to 60 ºC for 5-6 h. The MeOH was decanted, replaced with fresh MeOH, and again heated to 60 °C for 5-6 h. This was repeated 2-3 additional times, until the DMF C=O stretch (~1650 cm^{-1}) was no longer observed in the infrared spectrum. The resulting dark yellow powder was collected by filtration and then activated under vacuum at 180 °C for 24-48 h. The successful synthesis and activation of the framework was confirmed by comparing the X-ray powder diffraction pattern and Langmuir surface areas to those previously reported (see Figures 3.S3, 3.S9).

The compound HKUST-1 (HKUST-1; btc^{3-} = 1,3,5-benzenetricarboxylate) was synthesized and activated using a strategy adopted from a previous report.[25f] Specifically, $Cu(NO_3)_2 \cdot 2.5H_2O$ (2.4 g, 10.3 mmol) was dissolved in 30 mL deionized H_2O, and 1,3,5-benzenetricarboxylic acid (0.68 g, 3.2 mmol) was dissolved in 30 mL ethanol. The two solutions were combined in a 250 mL one-neck round-bottom flask. DMF (2 mL) was added, and the flask was sealed with a rubber septum. The reaction mixture was heated at 80 ºC for 24 h with stirring. The resulting light blue compound was filtered and washed with H_2O and EtOH. The product was further suspended in EtOH at 55 ºC for 12 h. The EtOH was removed, fresh EtOH was added, and the suspension was again heated at 55 ºC for 12 h. The final product was collected by filtration and activated by heating at 150 ºC under vacuum for 24 h. The successful synthesis and activation of the framework was confirmed by comparing the X-ray powder diffraction pattern and Langmuir surface areas to those previously reported (see Figures 3.S4, 3.S10).

The compound PCN-14 (PCN-14; $adip^{4-}$ = 5,5′-(9,10-anthracenediyl)-di-isophthalate) was synthesized and activated using a strategy adopted from a previous report.[27a] Specifically, H_4adip (0.6 g, 1.2 mmol) and $Cu(NO_3)_2 \cdot 2.5H_2O$ (2.4 g, 10.3 mmol) were fully dissolved in DMF (180 mL) with 10 drops of HBF_4. The solution was evenly distributed into twenty-found 20 mL vials, which were sealed with Teflon-lined caps and heated to 75 ºC for 24 h. The resulting green powder was collected by filtration and washed with DMF. The product was further suspended in DMF for 12 h at room temperature, then the DMF was exchanged with MeOH. After 6 h, the MeOH was decanted and replaced with fresh MeOH. This was repeated one further time. The final product was collected by filtration and activated by heating at 120 ºC under vacuum for 24 h. The successful synthesis and activation of the framework was confirmed by comparing the X-ray powder diffraction pattern and Langmuir surface areas to those previously reported (see Figures 3.S5, 3.S11-3.S13).

The compound MOF-5 (MOF-5, IRMOF-1; bdc^{2-} = 1,4-benzenedicarboxylate) was synthesized and activated using a strategy adopted from a previous report.[28e] Specifically, H_2bdc (0.66 g, 4.0 mmol), $Zn(NO_3)_2 \cdot 6H_2O$ (3.6 g, 12.1 mmol), and diethylformamide (100 mL) were combined in a 250 mL Schlenk flask sealed with a rubber septum. The Schlenk flask was heated at 90 ºC for 24 h, then placed under N_2, and the reaction solvent was removed via cannula and replaced with anhydrous DMF at room temperature. The DMF was exchanged with fresh, anhydrous DMF two further times. The DMF was then exchanged with anhydrous dichloromethane (DCM) at room temperature. The DCM was exchanged with fresh, anhydrous DCM two further times, then the majority of the DCM was removed via cannula. The resulting clear, cubic crystals were activated by heating at 150 ºC under vacuum for 24 h. The successful synthesis and activation of the framework was confirmed by comparing the X-ray powder

diffraction pattern and Langmuir surface areas to those previously reported (see Figures 3.S6, 3.S14).

3.2.4. High-Pressure Gas Adsorption Measurements. High-pressure adsorption isotherms in the range of 0-100 bar were measured on a HPVA-II-100 from Particulate Systems, a Micromeritics company. In a typical measurement, 0.3-0.7 g of activated sample was loaded into a tared 2 mL stainless steel sample holder inside a glove box under a N_2 atmosphere. Prior to connecting the sample holder to the VCR fittings of the complete high-pressure assembly inside the glove box, the sample holder was weighed to determine the sample mass.

The fully assembled sample holder was transferred to an ASAP 2020 low-pressure adsorption instrument, fitted with an isothermal jacket, and evacuated at the material's original activation temperature for at least 1 h. Then, a 77 K N_2 adsorption isotherm was measured. This was used to verify that the high-pressure sample mass was correct and the sample was still of high quality by comparing the resulting Langmuir surface area to the expected value (Figures 3.S7-3.S15). Note that a specially designed OCR adapter was used to connect the stainless steel high-pressure adsorption cell directly to the ASAP 2020 analysis port, allowing the measurement of accurate low-pressure isotherms on the exact same samples used for high-pressure measurements in the same sample holders.

The sample holder was then transferred to the HPVA-II-100, connected to the instrument's analysis port via an OCR fitting, and evacuated at room temperature for at least 1 h. The sample holder was placed inside an aluminum recirculating dewar connected to a Julabo FP89-HL isothermal bath filled with Julabo Thermal C2 fluid, for which the temperature stability is ± 0.02 °C. Note that while the majority of the sample holder is placed inside the temperature bath (analysis zone), there is still a significant volume that is exposed to the air (ambient zone) and is affected by fluctuations in room temperature (Figure 3.S16). A small upper volume of the sample holder above the analysis port is inside a temperature controlled heated enclosure, along with the gas dosing manifold (manifold zone). While this setup is typical of most volumetric adsorption instruments, it creates challenges in determining the free space (or empty volume) of the sample holder that is in each temperature zone. Accurately determining these volumes is particularly important because nonideality corrections have a significant temperature dependence that can lead to large errors at higher pressures.

For measurements at room temperature, the ambient and analysis zones will be at the same temperature. Since the dosing manifold volume is known accurately from volume calibrations during manufacturing, He can be used to determine the total free space in the sample holder by using the standard method of expanding from the dosing manifold to the evacuated sample holder and recording the change in pressure, assuming He adsorption is negligible. Note that the HPVA-II-100 is equipped with two pressure transducers: 1) a 100,000 torr GE Sensing UNIK5000 series transducer (accuracy of ± 0.04% full scale), and 2) a 1000 torr transducer (accuracy of ± 0.15% reading). The addition of the low-pressure transducer allows the He free space measurement to be performed at lower pressures (0.7-0.8 bar), where He adsorption is negligible for most materials.

For measurements at non-ambient temperatures, it further becomes necessary to determine both the volume of the sample holder that is at ambient temperature and the volume that is at the analysis temperature. Note that there are several approaches to doing this. By default, the commercial HPVA-II-100 software uses He to measure the total volume in both the ambient and analysis temperature zones, with all volumes set to the ambient temperature. Then, the

temperature of the analysis zone is changed to the desired analysis temperature, and the resulting change in He pressure is used to calculate the volume that is in the analysis temperature zone. Unfortunately, the pressure changes that result from most temperature changes are relatively small (especially for measurements near ambient temperature), and the 1000 torr transducer is not accurate or stable enough to reliably determine the analysis volume using this method. Indeed, small errors in the pressure readings were found to lead to large errors in the calculated analysis volume, and consequently, large errors in the resulting isotherms, especially at the high pressures where the temperature-dependent nonideality corrections are most significant (Figure 3.S17).

An alternative method, which was used here, is to determine the volumes of the ambient and analysis temperatures zones for an empty sample holder. Since the portion of the sample holder containing the sample is always fully immersed in the constant temperature bath and the bath is always placed at the exact same height on the sample holder, the ambient volume will always be constant, regardless of the amount of sample present. On the other hand, the analysis volume will depend on the amount of sample present, but it can be easily determined by subtracting the volume of the sample from the analysis volume of the empty sample holder. Here, the sample volume is determined by subtracting the total free space of the filled sample holder from that of the empty sample holder. The total free spaces of the empty or filled sample holders were determined using ambient temperature He free space measurements, which were repeated 20 times and averaged. The analysis volumes of the empty sample holder were determined by performing He free space measurements at each potential analysis temperature and calculated using the ideal gas law with the measured total empty volume of the sample holder, the ambient temperature, the analysis temperature, the He dose pressure, the He equilibrium pressure, the known dosing manifold volume, and the dosing manifold temperature. It is worth noting that by using this technique, it is only necessary to measure the He free space at ambient temperature for a new sample, and it is not necessary to measure He free space at any other analysis temperatures.

Other approaches to accounting for the different temperature zones are certainly possible, but regardless of the exact method used, it is critical to ensure that background CH_4 adsorption is negligible, or at least properly corrected for, at all relevant pressures and temperatures. To this end, background CH_4 adsorption were measured for a sample holder containing 0.34 mL of glass beads (similar in volume to a typical sample) at −25, 0, 25, 38, 50, 75, 100, and 150 °C. All background measurements were repeated at least 3 times at each temperature. With the exception of at −25 °C, background CH_4 adsorption was less than ± 4 cm^3_{STP} at pressures from 0-100 bar. At 35 bar, the background CH_4 adsorption was less than ± 1 cm^3_{STP}. This relatively low background confirms that all volume and temperature calibrations are accurate, and provides an estimate of the error of a typical measurement, which is inversely proportional to the sample mass used. For instance, the error for a 0.5 g sample can be estimated a ± 2 cm^3_{STP}/g at 35 bar and ± 8 cm^3_{STP}/g at 100 bar.

For the −25 °C background measurements, a significant negative background was observed, which is most likely due to a temperature gradient between the analysis and ambient zones on the sample holder (Figure 3.S19). This would affect the accuracy of nonideality corrections that assume there is a sharp temperature change between the ambient and analysis temperature. However, the background at −25 °C is consistent across several measurements, and as a result, it was fit with a 3rd order polynomial that was used to perform a background correction on all subsequent −25 °C isotherms.

3.2.5. Volumetric Capacity Calculations. Single crystal densities were used to convert experimentally measured gravimetric adsorption uptakes to volumetric uptakes. Note that all crystal structures were chosen to be as representative of the state of each metal-organic framework during ambient temperature CH_4 adsorption as possible. Since the activated carbon AX-21 is not crystalline, its density, ρ_{bulk}, was estimated at 0.487 g/cm^3 based on the measured pore volume, V_p, from 77 K N_2 adsorption (1.64 cm^3/g) and the skeletal density, ρ_{sk}, from a He free space measurement at 25 °C using Eqn 3.1. To the best of our knowledge, this density calculation is the most appropriate for a meaningful comparison with the volumetric uptakes of metal-organic frameworks as it should represent the maximum achievable density of AX-21 in the absence of any packing losses.

$$\rho_{bulk} = \frac{\rho_{sk}}{\rho_{sk} V_p + 1} \tag{3.1}$$

3.2.6. Isotherm Fitting. Prior to fitting the CH_4 adsorption isotherms, experimentally measured excess adsorption (n_{ex}) was converted to total adsorption (n_{tot}) using total pore volumes (V_p; Table S1), as determined from N_2 isotherms at 77 K (P/P_0 = 0.9), and the bulk gas density at each temperature and pressure from the NIST Refprop database (Eqn 3.2).

$$n_{tot} = n_{ex} + V_p \cdot \rho_{bulk}(P,T) \tag{3.2}$$

Total CH_4 adsorption isotherms for each material were then fit with either a single- or dual-site Langmuir equation (Eqn 3.3), where n is the total amount adsorbed in mmol/g, P is the pressure in bar, $n_{sat,i}$ is the saturation capacity in mmol/g, and b_i is the Langmuir parameter in bar^{-1} for up to two sites 1 and 2. The Langmuir parameter can be expressed using Eqn 3.4, where S_i is the site-specific molar entropy of adsorption in J/mol•K, E_i is the site-specific binding energy in kJ/mol, R is the gas constant in J/mol•K, and T is the temperature in K. The fitted parameters for each adsorption isotherm can be found in Table S3. Plots of the total adsorption isotherms with the corresponding single- or dual-site Langmuir fits can be found in Figure 3.S28-S34. Note that isotherm data at all measured temperatures were fit simultaneously with one set of parameters.

$$n = \frac{n_{sat,1} b_1 P}{1 + b_1 P} + \frac{n_{sat,2} b_2 P}{1 + b_2 P} \tag{3.3}$$

$$b_i = e^{-S_i/R} e^{E_i \cdot 1000/RT} \tag{3.4}$$

3.2.7. Isosteric Heats of Adsorption. Using the single- and dual-site Langmuir fits, the isosteric heat of adsorption can be calculated for each material as a function of the total amount of CH_4 adsorbed using the Clausius-Clapeyron relation (Eqn 3.5). The isosteric heat of adsorption for a single-site Langmuir model is constant by definition. For a dual-site Langmuir model, however, it is necessary to derive an expression for the loading dependence of the isosteric heat of adsorption (Eqn 3.6). Note that, as written, Eqn 3.6 gives the isosteric heat of adsorption as a function of pressure, rather than the amount adsorbed. To calculate the isosteric

heat of adsorption for evenly spaced loadings, Mathematica was used to solve each dual-site Langmuir equation at 25 °C for the pressures that correspond to specific loadings, and these calculated pressures were then used in Eqn 3.6 to determine the heat of adsorption as a function of the total amount of CH_4 adsorbed (Figure 3.5).

$$-Q_{\mathrm{st}} = \mathrm{R}T^2\left(\frac{\partial \ln P}{\partial T}\right)_n \tag{3.5}$$

$$-Q_{\mathrm{st}} = \frac{E_1 n_{\mathrm{sat},1} b_1 (1+b_2P)^2 + E_2 n_{\mathrm{sat},2} b_2 (1+b_1P)^2}{n_{\mathrm{sat},1} b_1 (1+b_2P)^2 + n_{\mathrm{sat},2} b_2 (1+b_1P)^2} \tag{3.6}$$

3.2.8. Optimal Binding Enthalpy Calculations. Using a single-site Langmuir model, it is possible to calculate the optimal binding enthalpy for maximizing the usable capacity for a given set of adsorption-desorption conditions.[46] In this simple model, it is assumed that the pore surface contains one type of adsorption site with a maximum capacity of n_{sat}, a binding energy of E, and a molar entropy of adsorption of S. Based on this, the usable capacity can be calculated for different adsorption pressures, P_{ads}, and temperatures, T_{ads}, and desorption pressures, P_{des}, and temperatures, T_{des} (Eqn 3.7). Here, adsorption was assumed to be at 35 bar and 25 °C, while desorption was at 5 bar and temperatures ranging from 25 to 145 °C. The usable capacity can then be calculated at different binding energies, assuming a constant S.

For CH_4, S is often assumed to be near $-9.5R$, however, there is a correlation between adsorption enthalpy and entropy, whereby as the binding energy increases, the entropy also increases.[46] This enthalpy-entropy correlation results in higher optimal binding energies than would otherwise be predicted, but the relationship between desorption temperature and optimal binding enthalpy is unchanged. To illustrate the affects of the enthalpy-entropy correlation, the percentage of the saturation capacity that is usable ($n_{\mathrm{usable}}/n_{\mathrm{sat}}$) is plotted as a function of binding energy and desorption temperature using a molar entropy of adsorption of −9.5R (Figure 3.7) and 10.5R (Figure 3.S48). The optimal binding energy at each desorption temperature occurs at the maximum of each curve. For example, the optimal binding energies for 25 °C desorption are −17.1 kJ/mol and −19.6 kJ/mol for entropies of $-9.5R$ and $-10.5R$, respectively.

$$n_{\mathrm{usable}} = \frac{n_{\mathrm{sat}} e^{-S/R} e^{E\cdot 1000/RT_{\mathrm{ads}}} P_{\mathrm{ads}}}{1 + e^{-S/R} e^{E\cdot 1000/RT_{\mathrm{ads}}} P_{\mathrm{ads}}} - \frac{n_{\mathrm{sat}} e^{-S/\mathrm{R}} e^{E\cdot 1000/RT_{\mathrm{des}}} P_{\mathrm{des}}}{1 + e^{-S/\mathrm{R}} e^{E\cdot 1000/RT_{\mathrm{des}}} P_{\mathrm{des}}} \tag{3.7}$$

3.3. Results and Discussion

3.3.1. High-Pressure Adsorption. All evaluations of adsorbents for natural gas storage rely on the measurement of accurate high-pressure adsorption isotherms. However, high-pressure experiments introduce several complexities, both in terms of collecting isotherm data and interpreting the results, that are not as significant at lower pressures. For instance, there is often inconsistent usage of the terms excess, total, and absolute when describing high-pressure adsorption capacities, which can lead to needless uncertainty when comparing the uptakes of different materials.

3.3.1.1. Excess, Total, and Absolute Adsorption. At a fundamental level, a gas is considered to be adsorbed when attractive forces from a surface result in a greater density of gas molecules than would normally be present at the same temperature, T, and pressure, P. For

adsorption on a two-dimensional surface, the strength of the interaction between the gas and surface will decrease with increasing distance until the attractive forces of the surface become negligible and only bulk or free gas molecules are present. At this distance, an imaginary line, known as the Gibbs dividing surface, can be drawn to divide the total free volume into *adsorbed* and *bulk* regions (Figure 3.1a).[7] The *absolute* amount adsorbed, n_{abs}, is defined simply as the total number of molecules that are in the adsorbed region. Unfortunately, absolute adsorption cannot be directly measured since it is not possible to determine the location of the Gibbs dividing surface or the size of the adsorbed region experimentally.[8] As a result, all adsorption measurements give *excess* adsorption, n_{ex}, which is the difference between the absolute adsorption amount and the amount of bulk gas that would have been present in the adsorbed region, V_a, in the absence of a surface (Eqn 3.8).[8]

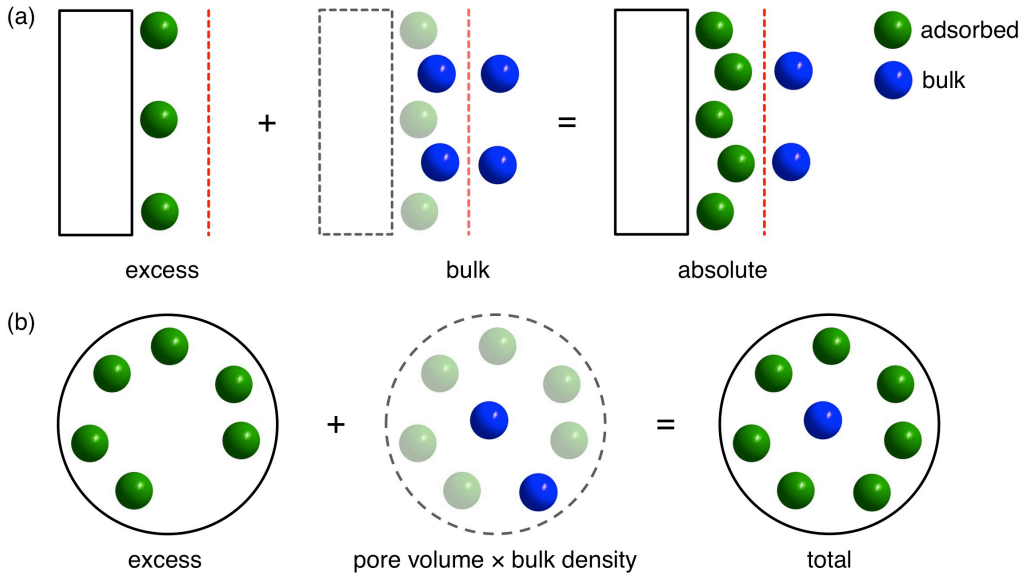

Figure 3.1. (a) For adsorption on a two-dimensional surface (rectangle), the Gibbs dividing surface (red) divides the free volume into two regions where gas molecules are either in an adsorbed (green) or bulk (blue) state.[7] *Absolute* adsorption, which includes all gas molecules in the adsorbed state, is the sum of the experimentally measured *excess* adsorption and the bulk gas molecules that would have been present in the adsorbed region in the absence of a surface. (b) For porous materials, the *total* adsorption includes all gas molecules inside the total pore volume, which corresponds to the sum of the *excess* adsorption and the bulk gas that would have been present in the pore volume in the absence of adsorption. Note that for microporous materials, the total adsorption is often used as an approximation for absolute adsorption, since it is not possible to determine the location of the Gibbs dividing surface experimentally.

Since it is not possible to determine V_a experimentally, there is no straightforward method for calculating absolute adsorption from the measured excess adsorption. Instead, the *total* adsorption,[9,10] which includes all gas molecules within the pores of an adsorbent, is often used as an approximation for absolute adsorption (Figure 3.1b).[11,12] Total adsorption can be calculated from the excess adsorption using Eqn 3.9 and the experimentally measured total pore volume,

V_p. Note that the total pore volume is typically determined from an N_2 adsorption isotherm at 77 K by assuming all pores have been completely filled with condensed N_2 at a sufficiently high P/P_0, where P_0 is the N_2 saturation pressure.[13] Based on the Gurvich rule,[14,15] the total pore volume can be calculated by assuming that the molar volume of liquid N_2 is the same regardless of the size or surface chemistry of the pore it is condensed within. For microporous materials with negligible external surface areas, which have a well-defined plateau in the N_2 adsorption isotherm at 77 K, the exact P/P_0 used is not particularly important. However, a P/P_0 of 0.9-0.95 is typical and will include any pores less than 200-400 Å in the total volume calculation.[16] Other adsorbates, such as CH_4, can be used similarly to determine the total pore volume, but results generally do not vary significantly as long as all pores are equally accessible to the different probe molecules.[17] In most cases, small errors in the total pore volume do not have a significant impact on the calculated total adsorption.[18]

$$n_{ex} = n_{abs} - V_a \cdot \rho_{bulk}(P,T) \tag{3.8}$$

$$n_{tot} = n_{ex} + V_p \cdot \rho_{bulk}(P,T) \tag{3.9}$$

For gas storage applications, the total adsorption is most relevant for comparing the capacities of different adsorbents, as it is an intrinsic property of a material that represents the total amount of gas that can be stored inside its pores.[10] Since the density of gas in the bulk phase, r_{bulk}, is significant at high pressures, there is usually a large difference between the excess and total amount adsorbed at conditions relevant to natural gas storage. As a result, inconsistent usage of the terms excess, absolute, and total makes comparing CH_4 capacities of different materials challenging, and it is always important to specify clearly the type of adsorption capacity that is being reported.

3.3.1.2. High-Pressure Adsorption Measurements. Due primarily to the large pressure range that is covered and the increasing nonideal behavior of gases above ambient pressure, adsorption experiments are inherently more difficult to perform accurately at high pressures than at low pressures. This can lead to large errors that make it challenging to compare the properties of different materials. Most commercial high-pressure adsorption instruments operate using either a gravimetric or volumetric measurement technique. At a basic level, gravimetric instruments measure the amount of CH_4 adsorbed by using a balance to record the change in weight of a sample at different equilibrium pressures of CH_4, while volumetric instruments record the change in pressure when dosing CH_4 from a calibrated volume to a volume containing the sample. In both cases, it is important to be aware of the most common issues that can affect the quality of the experimental data.

For both gravimetric and volumetric adsorption measurements, He is used to determine the precise volume occupied by the adsorbent inside the sample holder, which is needed for buoyancy corrections and free space calculations in gravimetric and volumetric experiments, respectively. Techniques for performing these corrections have been discussed in detail elsewhere,[10,19] but it is worth emphasizing that errors in buoyancy and free space calculations can significantly affect the accuracy of adsorption data (Figure 3.S17). Note that for both corrections, He adsorption by the sample is assumed to be negligible, and as such, it is best to perform He measurements at the low pressures and high temperatures where this is most likely to be true.[8,20]

Regardless of the exact method used to perform buoyancy or freespace corrections, there will always be many other potential sources of error in high-pressure experiments, such as volume calibrations, thermocouple readings, pressure transducer readings, sample mass measurements, nonideality corrections and temperature gradients.[19c] Therefore, it is essential to measure background CH_4 adsorption isotherms with empty sample holders, or with a nonadsorbing material similar in volume to a typical sample, at all potential analysis temperatures and pressures.[10] Ensuring that background adsorption is negligible under the exact same conditions as in an actual experiment confirms that all calibrations, corrections, measurements, and calculations are valid, which is critical for verifying the accuracy of the resulting adsorption data. Note that this is equally important for volumetric, gravimetric, commercial, and custom-built high-pressure instruments.

Additionally, for gravimetric adsorption measurements, it is particularly important to ensure that no impurities are present in the CH_4 used, as even small quantities of more strongly adsorbing impurities, such as heavier hydrocarbons or water, can lead to large errors in the measured uptake. Similarly, large errors in volumetric measurements can often result from the fact that high-pressure sample holders, which are typically constructed from stainless steel, are very heavy compared to a typical sample. As a result, it is usually not practical to weigh an activated adsorbent in a fully assembled sample holder, as is common for low-pressure experiments. Thus, it can be difficult to obtain an accurate sample mass, which can lead to significant errors in measured capacities that have a 1:1 dependence on the amount of sample present. One potential solution is to measure the surface area of a sample directly prior to a high-pressure measurement in a fully assembled high-pressure sample holder. By confirming that the surface area is as expected, uncertainties associated with sample mass can be mostly eliminated.

3.3.2. Evaluating Metal-Organic Frameworks. Although high-pressure CH_4 adsorption isotherms have been measured for almost one hundred metal-organic frameworks, their CH_4 uptakes have been reported in a variety of different units and at a range of pressures and temperatures, which makes evaluating the relative performance of a particular compound difficult. To facilitate comparisons between existing materials for which ambient temperature, high-pressure CH_4 adsorption isotherms have been published, Table 3 lists the total CH_4 uptake of all metal-organic frameworks at conditions as close to 35 bar and 25 °C as possible. To make comparisons between materials more meaningful, all isotherm data that was originally reported in terms of excess adsorption has been converted to total adsorption using each framework's measured pore volume and the bulk gas density from the NIST Refprop database at the appropriate temperature and pressure (Eqn 3.2). Note, however, that in a number of instances there was no indication of whether reported data were given in terms of excess, total, or absolute adsorption, adding significant uncertainty to comparisons of these uptakes to those of other materials.

In almost all standard adsorption measurements, the amount adsorbed is determined per unit mass, not volume, of adsorbent. However, the amount of CH_4 adsorbed per volume, which ultimately determines the amount of natural gas that can be stored in a given fuel tank, has to be calculated using the density of a material. For metal-organic frameworks, the ideal crystallographic density has commonly been used to convert gravimetric adsorption capacities to a volumetric capacity that represents the maximum possible volumetric uptake in the absence of any loss in density from packing actual particles together inside a fuel tank. This method of calculating volumetric capacities certainly over-estimates what is realistically achievable, but it

is still useful for initial comparisons between adsorbents, provided the crystallographic densities used are appropriate. Here, a substantial effort was made to ensure that all crystallographic densities were as representative as possible of the framework during CH_4 adsorption, which mainly involved confirming that both metal-bound and free solvent molecules from solvated crystal structures were not included in density calculations. Based upon these and other observations made while surveying published CH_4 adsorption data for metal-organic frameworks, we make the following recommendations for future evaluations of new frameworks for ANG storage:

1) Report background high-pressure CH_4 adsorption isotherms for an empty sample holder (or sample holder with a nonadsorbing solid) at all measured temperatures and pressures as supporting information.[10,21]
2) Specify whether all isotherms are reported in terms of excess, total, or absolute adsorption. Methods used to convert experimental excess adsorption data to total or absolute adsorption should be detailed, including any assumptions made about the size of the adsorbed volume.[10] If a pore volume was used to calculate total adsorption, it should be reported along with the isotherm used to calculate it.
3) When volumetric uptakes are reported, the density used should be given and the type of density (e.g. crystallographic, bulk, tap, pellet) specified.[22] When crystallographic densities are used, details of their calculation should be provided, including at a minimum: unit cell volume, unit cell content, and any potential differences between the state of the framework when the unit cell was determined and when adsorption isotherms were measured, which may involve desolvation, removal of excess ligand, framework flexibility, and/or different measurement temperatures.
4) If the unit cm^3_{STP} is used to report adsorption data, the standard temperature and pressure should be defined.
5) When isosteric heats of adsorption are reported, the method used to calculate them should be specified. Note that stating that the Clausius-Clapeyron relation was used is not sufficient, as this does not give any indication about how interpolations between measured data points were made.
6) When mathematical models are used to fit experimental adsorption isotherms, all fitted parameters should be given, and the quality of the isotherm fits should be illustrated.

3.3.3. Methane Adsorption Isotherms. In examining Table 3, there are many cases, particularly for the highest capacity frameworks, where CH_4 adsorption isotherms have been reported for the same material in multiple publications with inconsistent results. This makes it challenging to compare different frameworks and to understand the effects of different characteristics of the materials on CH_4 uptake. For example, HKUST-1 has been reported to have total CH_4 uptakes at 35 bar ranging between 184 and 220 v/v. By synthesizing and activating a selection of the most promising compounds in the same laboratory and measuring high-pressure isotherms on the same instrument, evaluating and comparing their CH_4 adsorption properties becomes more straightforward. To this end, the six metal-organic frameworks depicted in Figure 3.2, along with an activated carbon for comparison, were chosen for a detailed evaluation. The seven materials have features that are common to many of the adsorbents that have shown the highest gravimetric and volumetric CH_4 uptakes at 35 bar, including strong adsorption sites, pores shaped by Cu_2-paddlewheel units, and high surface areas.

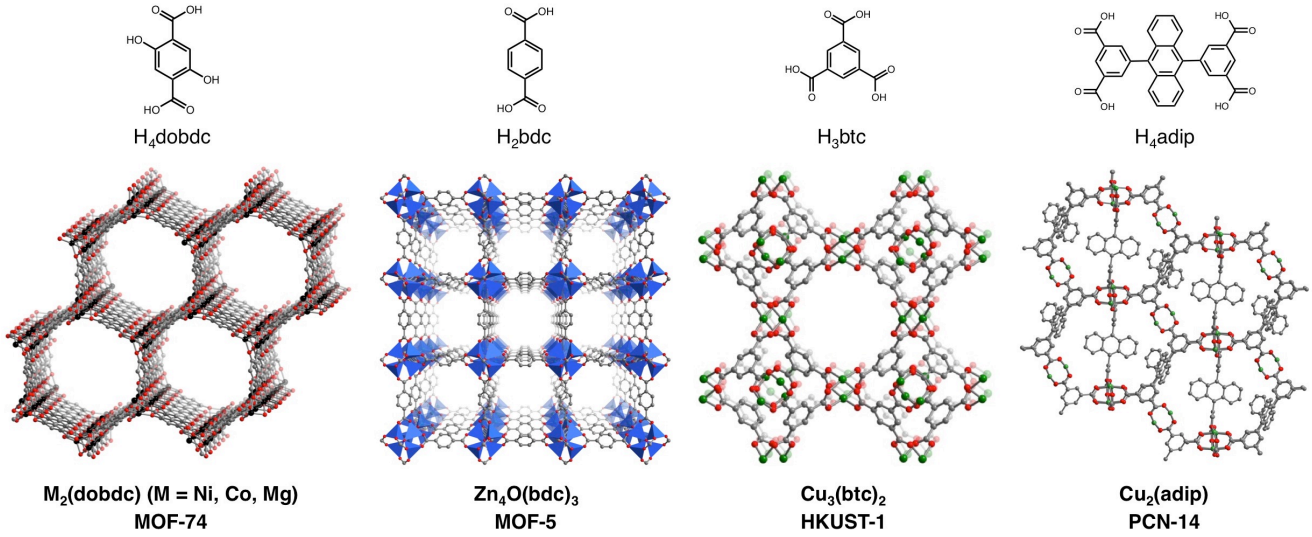

Figure 3.2. Crystal structures and organic bridging ligands for the six metal-organic frameworks evaluated in this work: $M_2(dobdc)$ (M = Ni, Co, Mg; $dobdc^{4-}$ = 2,5-dioxido-1,4-benzenedicarboxylate; M-MOF-74, CPO-27-M), $Zn_4O(bdc)_3$ (bdc^{2-} = 1,4-benzenedicarboxylate; MOF-5, IRMOF-1), $Cu_3(btc)_2$ (btc^{3-} = 1,3,5-benzenetricarboxylate; HKUST-1), and $Cu_2(adip)$ ($adip^{4-}$ = 5,5′-(9,10-anthracenediyl)di-isophthalate; PCN-14). Green, gray, and red spheres represent Cu, C, and O atoms, respectively; H atoms have been omitted for clarity. Black spheres represent Ni, Co, or Mg atoms, and blue tetrahedra represent Zn atoms.

With modest gravimetric surface areas of 1500-2000 m^2/g, the $M_2(dobdc)$ (M = Ni, Co, Mg; $dobdc^{4-}$ = 2,5-dioxido-1,4-benzenedicarboxylate; M-MOF-74, CPO-27-M) compounds have one-dimensional hexagonal channels featuring square pyramidal metal cations that have been shown to act as strong adsorption sites for many small gas molecules.[23,24] The compounds $Cu_3(btc)_2$ (btc^{3-} = 1,3,5-benzenetricarboxylate; HKUST-1)[25,26] and $Cu_2(adip)$ ($adip^{4-}$ = 5,5′-(9,10-anthracenediyl)di-isophthalate; PCN-14)[26c,27] are built from Cu_2-paddlewheels that also contain exposed metal cations upon desolvation; however, their pore structures are significantly more complicated than $M_2(dobdc)$, with several differently sized pores and pore windows. Significantly, PCN-14 has been widely cited as one of the best existing metal-organic frameworks for CH_4 storage, based upon its reported total volumetric uptake of 230 v/v at 17 °C and 35 bar.[27a] The compound $Zn_4O(bdc)_3$ (bdc^{2-} = 1,4-benzene-dicarboxylate; MOF-5, IRMOF-1) has a high Langmuir surface area of 3995 m^2/g, but does not contain any inherently strong adsorption sites for CH_4.[3a,5a,28] Indeed, its pore surface is more similar to that of an activated carbon. For comparison, the activated carbon AX-21, which has an exceptionally high Langmuir surface area of 4880 m^2/g and is one of many activated carbons that have been studied in detail for ANG storage, was also evaluated.[29]

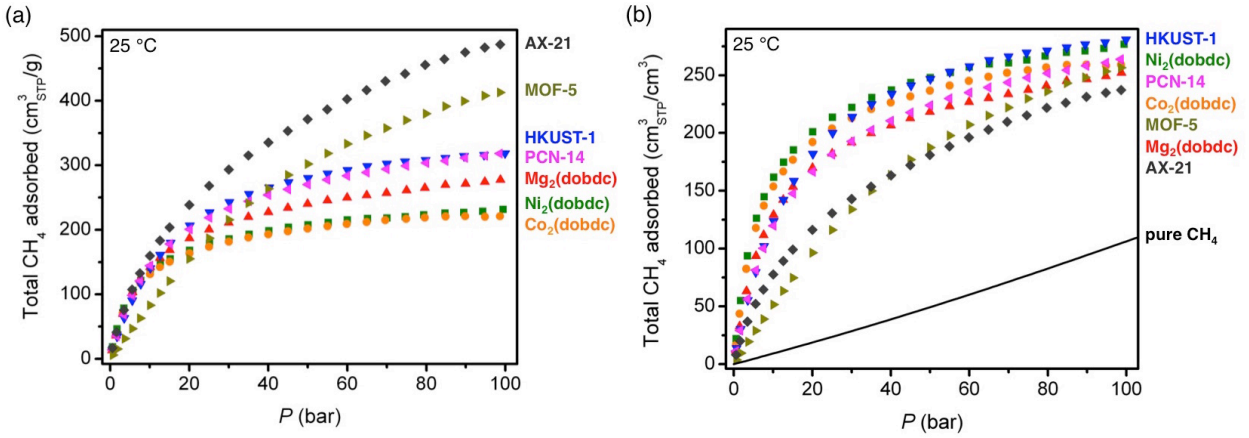

Figure 3.3. Total gravimetric (a) and volumetric (b) CH_4 adsorption isotherms at 25 ºC. Note that crystallographic densities were used to calculate volumetric adsorption. The solid line corresponds to the volumetric density of pure CH_4 at 25 ºC.

After synthesis, surface areas and pore volumes were measured for all seven materials to ensure samples were fully activated and of high quality (Figures 3.S7-3.S15). High-pressure CH_4 adsorption isotherms from 0 to 100 bar were then measured for each material at −25, 25, 38, and 50 °C. Experimentally measured excess adsorption isotherms were converted to total adsorption using total pore volumes, as determined from N_2 isotherms at 77 K ($P/P_0 = 0.9$), and the bulk gas density at each temperature and pressure from the NIST Refprop database (Eqn 3.2). Volumetric adsorption was calculated using the crystallographic densities of desolvated structures at as near ambient temperature as possible (Table S2).

In Figure 3.3, the 25 °C high-pressure CH_4 isotherms of all materials measured in this work are compared in terms of total gravimetric and volumetric adsorption. Of the materials measured, AX-21 has the highest gravimetric uptake at all pressures. For the metal-organic frameworks, HKUST-1 has the highest gravimetric uptake (255 cm^3_{STP}/g = 0.183 g_{CH4}/g) at 35 bar, but the capacity of MOF-5 is highest at pressures greater than 40 bar. At high pressures, the gravimetric capacity is reasonably well correlated with the gravimetric surface area (Figure 3.S38), which is consistent with previous observations for both metal-organic frameworks and activated carbons.[5fh,42] Indeed, the metal-organic frameworks in Table 3 with the three highest reported gravimetric uptakes at 25 °C and 35 bar all have exceptionally high specific surfaces areas: DUT-49 with an uptake of 0.26 g_{CH4}/g and a surface area of 5476 m^2/g, NU-111 with an uptake of 0.24 g_{CH4}/g and a surface area of 4930 m^2/g, and PCN-68 with an uptake of 0.24 g_{CH4}/g and a surface area of 5109 m^2/g.[30,31,32]

In addition to the different CH_4 capacities of the frameworks studied here, there are important differences in the shapes of their adsorption isotherms. Specifically, AX-21 and MOF-5 have shallower isotherms at low pressures and do not begin to approach saturation until much higher pressures than M_2(dobdc), HKUST-1, and PCN-14. This is expected based on the lack of strong adsorption sites in AX-21 and MOF-5, and has important consequences for the amount of CH_4 that can actually be delivered by each material.

Importantly, as will be discussed in detail below, achieving a high volumetric adsorption capacity is much more critical than a high gravimetric capacity for extending the driving range of a vehicle. While the overall shapes of the volumetric isotherms are similar to the gravimetric

ones, the trends in capacity differ significantly. For instance, Ni_2(dobdc) and Co_2(dobdc) have the highest uptakes at lower pressures, and Ni_2(dobdc) and HKUST-1 have the highest total volumetric uptakes at 35 bar: 230 and 225 v/v, respectively. Note that the total volumetric uptake of Ni_2(dobdc) is the highest value yet reported for any metal-organic framework at 25 °C and 35 bar. Although PCN-14 has been widely cited as the best existing metal-organic framework for volumetric CH_4 storage, Ni_2(dobdc) and HKUST-1 have significantly higher volumetric capacities at 35 bar and 25 °C.

It is worth noting that in contrast to gravimetric adsorption, the volumetric uptake at 35, 65, or 100 bar, does not correlate with volumetric surface area (Figure 3.S39). Indeed, MOF-5 has a volumetric surface area 30% greater than Ni_2(dobdc), but a volumetric uptake that is lower at all pressures measured here of less than 100 bar. This highlights the importance of the density and strength of specific CH_4 adsorption sites, rather than just surface area and pore volume, for achieving high volumetric capacities.

3.3.4. Methane Adsorption Sites in Ni_2(dobdc) and HKUST-1. While Ni_2(dobdc) and HKUST-1 have the highest volumetric uptakes of all metal-organic frameworks reported to date (Table 3), they are still well short of the 350 v/v target that is expected to achieve a volumetric energy density similar to that of CNG. In designing a next generation of improved framework materials to meet this target, it is useful to consider the fundamental mechanisms responsible for the high volumetric uptakes of Ni_2(dobdc) and HKUST-1. Detailed powder x-ray and neutron diffraction experiments have previously been used in several studies to identify the strongest CH_4 adsorption sites in both structures.[24,26] Note that the only structural study of CH_4 in M_2(dobdc) was for the Mg analogue,[24] but based on the similar adsorption isotherms and previous structural studies with H_2 and CO_2,[23d-f,i,j,l,m] it is reasonable to expect similar CH_4 binding sites within Ni_2(dobdc).

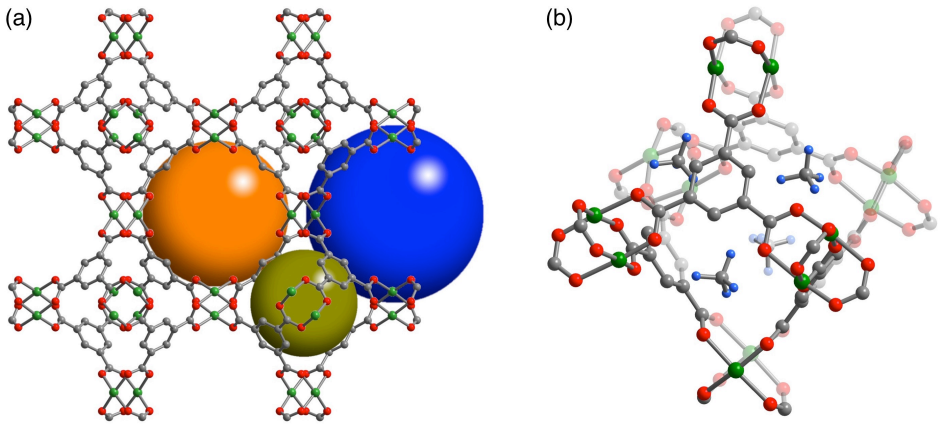

Figure 3.4. (a) Crystal structure of HKUST-1 highlighting the three different types of pores in the structure that have diameters of roughly 5 Å (dark yellow), 11 Å (orange), and 13.5 Å (blue). Note that the open coordination site of the exposed Cu^{2+} cations is only directed into the 13.5 Å (blue) pores. Atomic coordinates are taken from a desolvated crystal structure at 100 K. (b) Location of adsorbed CD_4 molecules at the four windows sites of an octahedral cage. The atomic coordinates are taken from a previously published powder neutron diffraction structure with a loading of 1.1 CD_4 per Cu^{2+} at 4 K. Green, gray, red,

and light blue spheres represent Cu, C, O, and D atoms, respectively; H atoms have been omitted for clarity.

In both HKUST-1 and Ni_2(dobdc), the exposed Cu^{2+} and Ni^{2+} cations act as strong binding sites that can contribute a maximum of 98 v/v and 172 v/v, respectively, to the total volumetric capacity when one CH_4 is bound to each metal. These are the only strong binding sites expected in Ni_2(dobdc), and just weaker secondary adsorption sites should be available for CH_4 after the Ni^{2+} sites are fully occupied.[24] In contrast, HKUST-1 has additional strong adsorption sites, located in the four windows of each octahedral cage, which are populated at the same time as the Cu^{2+} sites,[26] suggesting both adsorption sites have similar CH_4 binding energies (Figure 3.4). These window sites bind CH_4 strongly due to several close interactions, in the range 2.7-3.2 Å, between framework O atoms and an adsorbed CH_4 molecule.

Significantly, the window sites can contribute an additional 65 v/v to the volumetric capacity of HKUST-1, bringing the total contribution of strong adsorption sites to 163 v/v, just below that of Ni_2(dobdc) (172 v/v). On the other hand, there is a more pronounced difference in the contribution of strong adsorption sites to the total gravimetric capacity of each material at 144 cm^3_{STP}/g and 185 cm^3_{STP}/g for Ni_2(dobdc) and HKUST-1, respectively. Further, while both materials have similar volumetric surface areas (Table S1), HKUST-1 has a significantly greater gravimetric surface area that can be expected to lead to a higher gravimetric density of weak CH_4 adsorption sites. Taken together, the similar volumetric and different gravimetric capacities of strong and weak adsorption sites can help explain the experimental CH_4 isotherms, wherein both materials have similar volumetric uptakes at 35 bar, but HKUST-1 has a much higher gravimetric uptake. In order to explain why Ni_2(dobdc) has a steeper isotherm at lower pressures, it is necessary to also consider differences in the binding energies of the strong adsorption sites of each material.

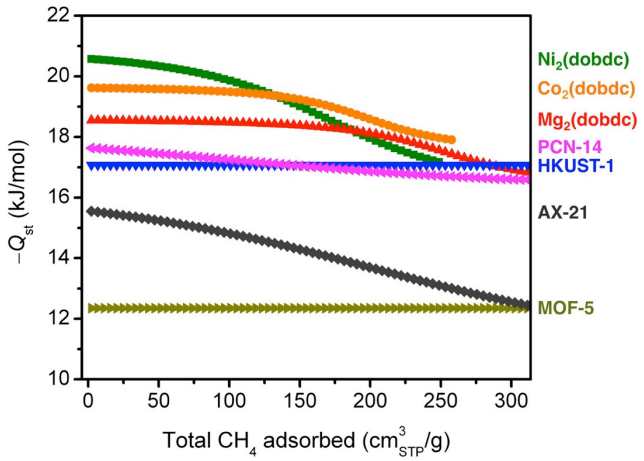

Figure 3.5. Isosteric heats of adsorption, $-Q_{st}$, at 25 °C as a function of the total amount of CH_4 adsorbed.

3.3.5. Isosteric Heats of Adsorption. To gain further insight into differences between the seven materials, isosteric heats of adsorption (Q_{st}), which represent the average binding energy of an adsorbing molecule at a specific surface coverage, were determined as a function of the amount of CH_4 adsorbed, n, by using the Clausius-Clapeyron relation (Eqn 3.5).[33]

In order to employ this relation, it is first necessary to fit the high-pressure isotherm data with

a mathematical model, such that it is possible to interpolate between measured data points to determine the exact pressures that correspond to the same amount adsorbed at different temperatures. Regardless of the mathematical model used, it is important to remember that the Clausius-Clapeyron equation is fundamentally a thermodynamic relation that describes a phase transition of a gas from a bulk to adsorbed state, and as such, it is based on the absolute amount adsorbed, which includes all gas molecules that experience an attractive potential from the adsorbent surface.[8d] For microporous materials, the total adsorption is often used as an approximation for absolute in heat of adsorption calculations, as most gas molecules inside micropores will have some degree of interaction with the pore surface.[4a,11] In contrast to low-pressure experiments, there is a significant difference between excess and total adsorption at high pressures, and *it is critical that the total adsorption is used for all thermodynamic calculations*,[18] unless the relevant thermodynamic relations have been specifically altered for excess quantities.[8d]

Virial-type equations have been routinely used to fit high-pressure adsorption data for metal-organic frameworks,[34] despite the fact that most virial parameters lack any physical meaning.[35] In contrast, equations that are based on physical models of adsorption, such as the Dubinin-Astakhov (DA)[36] and multi-site Langmuir equations,[37] have been more widely used in analyzing CH_4 isotherms of activated carbons.[38] One major advantage of fitting isotherm data with physically relevant parameters is that it makes extrapolation to temperatures and pressures that were not experimentally measured more meaningful, which is important not only for calculating heats of adsorption but also for process modeling and systems design. Additionally, errors in high-pressure isotherm data can be significant, especially when compared to low-pressure experiments, and leveraging at least some physical constraints on the fitting parameters can help ensure that the resulting isosteric heats are reasonable. Here, single- and dual-site Langmuir models were used to fit the adsorption data of each material at all measured temperatures with one set of parameters (see ESI for details). Several recent studies have demonstrated the ability of Langmuir-type equations to successfully model adsorption in metal-organic frameworks, especially those that have well-defined adsorption sites on the pore surface.[18,23n-r,39]

The importance of the method used for calculating Q_{st} can be illustrated by examining the heats of adsorption originally reported for PCN-14, wherein the low-coverage binding enthalpy of –30 kJ/mol is nearly double the value of –18 kJ/mol determined in this work (Figure 3.S37).[27a] It was suggested that this record high heat of adsorption was largely responsible for the high volumetric uptake of PCN-14, but no details of the Q_{st} calculations were reported. While PCN-14 certainly does exhibit high volumetric uptake, the reported values of Q_{st}, which influenced several follow-up computational studies,[5h,26c,27b] can hinder efforts to understand the underlying adsorption mechanisms that are responsible and to design improved materials.

For all seven materials evaluated in this work, the isosteric heats of adsorption as a function of the total CH_4 loading are plotted in Figure 3.5. As expected based upon its steep isotherm and high volumetric uptake, Ni_2(dobdc) has the highest Q_{st} at low coverage, followed by Co_2(dobdc) > Mg_2(dobdc) > PCN-14 ~ HKUST-1 > AX-21 > MOF-5. It is interesting to note differences in the shape of Q_{st} curves as the CH_4 loading is increased. For example, the M_2(dobdc) compounds have relatively constant binding energies at low loadings that begin to decrease as the exposed metal cation sites become populated. On the other hand, PCN-14 and HKUST-1 have heats of adsorption near –17 kJ/mol regardless of the amount of CH_4 adsorbed, confirming that the exposed Cu^{2+} cations and window adsorption sites in both materials have similar CH_4 binding strengths. Likewise, MOF-5 exhibits a constant, but much weaker, binding energy of

−12.3 kJ/mol. These differences are consistent with the shapes of the adsorption isotherms, for which the M_2(dobdc) compounds have the steepest rises at low pressures, while MOF-5 is the most shallow. Note that the gradual decline in the isosteric heat of adsorption of AX-21 from 15.5 to 12.4 kJ/mol is likely due to the wide distribution of pore sizes present in the activated carbon, whereby smaller pores will tend to have stronger interactions with CH_4 than larger pores.

It is important to emphasize that while the single- and dual-site Langmuir models used here describe the experimental adsorption data very well over a wide temperature and pressure range, there may be other models that result in equally good, or in some cases perhaps even better, fits to the data. Some of these models may involve an increase in the isosteric heat of adsorption at high CH_4 loadings due to the contribution of $CH_4 \cdots CH_4$ interactions at high pressures, as has been reported for several frameworks.[40] Unfortunately, the experimental high-pressure adsorption data is typically not accurate enough to determine reliably whether such an increase actually exists in any of the materials studied here. However, it is worth noting that several studies have clearly shown that using excess adsorption isotherms to calculate Q_{st} can lead to large increases in Q_{st} at higher loadings that do not occur when using absolute or total adsorption.[10,18] Moreover, the contribution of $CH_4 \cdots CH_4$ interactions to the overall heat of adsorption has been estimated to be less than 2 kJ/mol, which would be difficult to detect accurately at the high pressures where it would be most influential and the adsorption data is least accurate.[41] Regardless, the differences in isosteric heats of adsorption at pressures most relevant to ANG storage are clear, and these have important consequences for the amount of CH_4 that can actually be delivered by each material inside a vehicle.

3.3.6. Usable CH_4 Capacity. Comparing the 35 bar CH_4 capacities of different adsorbents is useful for initial evaluations, but not all of this capacity will be accessible when delivering natural gas to an engine that requires a minimum inlet pressure to operate. As such, the usable CH_4 capacity is defined as the amount of CH_4 that can be delivered when decreasing from the filling or adsorption pressure to a specific desorption pressure (Figure 3.6a).[10] For ANG storage, the adsorption pressure is usually assumed to be 35 bar, since this is a typical benchmark for the maximum achievable pressure of inexpensive single-stage compressors. While 5 bar is commonly cited as a minimum desorption pressure,[31,42] engines that can operate at lower inlet pressures would allow for a greater usable CH_4 capacity and increased vehicle driving range. Currently, most natural gas vehicles contain gasoline engines that have been retrofitted to run on natural gas. If the demand for natural gas vehicles increases dramatically, the minimum operating pressure may decrease as engines are built and optimized specifically to burn natural gas. It is important to note that the amount of CH_4 retained by the adsorbent during desorption can also be reduced by heating, ideally taking advantage of waste heat from the engine.[43]

The volumetric usable CH_4 capacities of all materials evaluated here are plotted in Figure 3.6b for adsorption at 35 bar and 25 °C and desorption at 5 bar and temperatures from 25 to 145 °C. Despite the fact that Ni_2(dobdc) has a higher total volumetric uptake at 35 bar, HKUST-1 has the highest usable CH_4 capacity for all calculated desorption temperatures. This is a direct result of the weaker interaction of CH_4 with HKUST-1 than with Ni_2(dobdc), which results in significantly less CH_4 retained by HKUST-1 at 5 bar. Indeed, the usable CH_4 capacity of Ni_2(dobdc) is only 115 v/v for desorption at 25 °C, which is just 50% of its 35-bar capacity. In contrast, the usable capacity of HKUST-1 under the same conditions is 149 v/v, which is 66% of its 35 bar capacity.

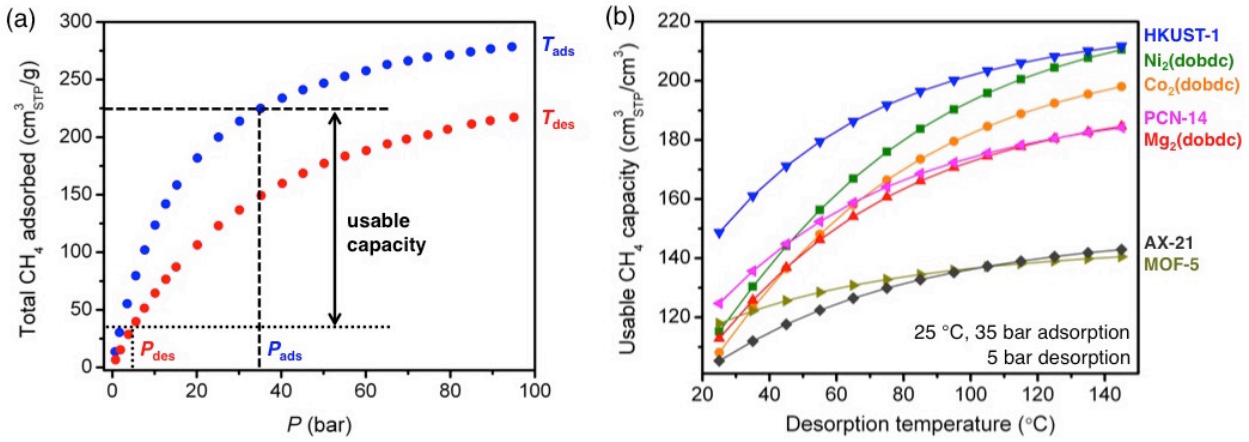

Figure 3.6. (a) The usable capacity represents the amount of CH_4 that can be delivered when discharging from a specific adsorption temperature, T_{ads}, and pressure, P_{ads}, to a desorption temperature, T_{des}, and pressure, P_{des}. (b) The volumetric usable CH_4 capacity as a function of desorption temperature for adsorption at 25 °C and 35 bar and desorption at 5 bar.

The gravimetric usable CH_4 capacity is plotted in Figure 3.S40 for the same adsorption-desorption conditions. In this case, AX-21 has the highest usable capacity at all desorption temperatures, while MOF-5 is the best metal-organic framework for desorption temperatures below 60 °C. Although HKUST-1 exhibits a higher total gravimetric uptake at 35 bar, its usable capacity is below that of MOF-5 unless the desorption temperature is increased. This is due to the weak interaction of MOF-5 with CH_4 (−12 kJ/mol), which results in only a small amount of CH_4 adsorbed at 5 bar. Usable capacity plots as a function of desorption pressure are also given as supplementary figures and show similar trends between materials, as is expected since decreasing the desorption pressure has a similar effect to increasing the desorption temperature (Figures 3.S41-3.S42).

Adsorption at lower temperatures or higher pressures can also be considered as a strategy for increasing the usable capacity (Figures 3.S43-3.S46). Indeed, by decreasing the adsorption temperature to −25 °C, the usable capacity of HKUST-1 reaches 222 v/v for desorption at 5 bar and 25 °C, which is 67% greater than for adsorption at 25 °C. However, a full systems-level analysis is necessary to determine whether the higher costs associated with cooling the fuel and the thermal management of the tank, or with compressing natural gas to higher pressures, would be worth the increase in usable capacity and driving range.

Of all the metal-organic frameworks previously evaluated by others and those studied here, HKUST-1 appears to be the most promising current framework for natural gas storage, as it features one of the highest usable volumetric capacities for CH_4. A similar conclusion was also reached by others while this manuscript was in preparation,[44] and it is perhaps not surprising that HKUST-1 was chosen by BASF for use in a prototype ANG van in 2007.[45]

3.3.7. Optimal Binding Enthalpy. The differences in the usable CH_4 capacities between the materials studied illustrate the importance of both increasing capacity and optimizing binding enthalpy when designing improved adsorbents. If the binding enthalpy is too high, then too much CH_4 will be retained at low pressures, decreasing the usable capacity. On the other hand, if the

binding enthalpy is too low, then too little CH_4 will be adsorbed at higher pressures. Using a single-site Langmuir model, it can be shown that the optimal binding enthalpy for CH_4 adsorption at 35 bar and 25 °C and desorption at 5 bar is –17 kJ/mol,[46] exactly equal to that determined for HKUST-1 over the entire pressure range of 5 to 35 bar.

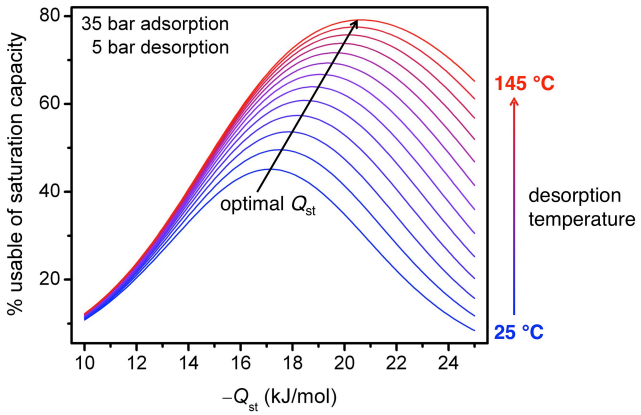

Figure 3.7. Assuming a single-site Langmuir isotherm, the percentage of the saturation capacity that is usable is plotted for isosteric heats of adsorption, Q_{st}, ranging from –10 to –25 kJ/mol and desorption temperatures from 25 to 145 °C, with adsorption at 35 bar, desorption at 5 bar, and a molar entropy of adsorption

Note that the optimal binding enthalpy is dependant on the exact desorption conditions used. Indeed, Figure 3.7 shows the percentage of the saturation capacity that is usable at different binding energies and desorption temperatures. As the desorption temperature is increased, or desorption pressure decreased, the optimal binding enthalpy increases (see ESI for details). Note that the simple analysis presented here ignores correlations between the adsorption enthalpy and entropy, but these correlations would be expected to lead to even larger increases in the optimal Q_{st} as the desorption temperature is increased.[47] Regardless, Figure 3.7 illustrates the importance of optimizing binding enthalpy and the benefits of using higher desorption temperatures to maximize usable capacity. Nevertheless, employing a material with optimal binding enthalpy is useless if the density of adsorption sites having that enthalpy is small, resulting in a low optimized capacity. Since dramatic improvements in both gravimetric and volumetric capacities are needed to meet the Department of Energy targets at 35 bar and ambient temperature, increasing capacity must be the primary focus of materials development efforts, but these efforts will be most beneficial if the binding enthalpy is near optimal.

3.3.8. Relative Importance of Gravimetric and Volumetric Capacity. It is important to recognize that the acceptability and viability of natural gas vehicles are directly linked to their utility and value to the customer. As indicated, the lower volumetric energy density of compressed natural gas significantly reduces the driving range in comparison to conventional gasoline vehicles and therefore reduces the utility of the vehicle. In designing a next generation of adsorbents for natural gas storage, it is essential to consider the relative importance of improvements in gravimetric versus volumetric usable capacity toward increasing the maximum achievable driving range of an ANG vehicle.

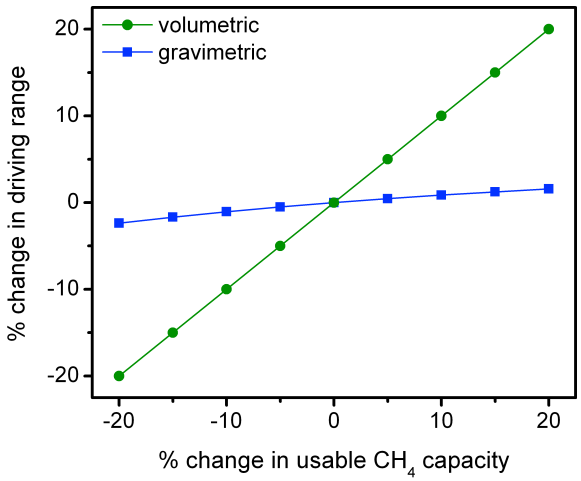

Figure 3.8 Effects of changes in gravimetric and volumetric CH_4 usable capacity on vehicle driving range. To isolate each effect, the gravimetric case assumes a 10 GGE vehicle with a constant volumetric capacity, while the volumetric case assumes a fixed amount of space available for a fuel tank and a constant gravimetric capacity.

In order to make the comparison more informative, the effects of changes in gravimetric and volumetric usable capacity on driving range are considered independently using a few simple assumptions (Figure 3.8). In the gravimetric case, a 10 GGE (gallons gasoline equivalent) vehicle is assumed to have an adsorbent capable of delivering 0.12 g_{CH4}/g, which is equal to the usable capacity of HKUST-1 for 35 bar adsorption and 5 bar desorption at 25 °C. In order to isolate the effects of changing the usable gravimetric capacity, this analysis assumes a fixed volumetric capacity and changes in gravimetric capacity thus lead to an increase or decrease in the weight of adsorbent required to achieve a 10 GGE energy density (2.567 kg CH_4).[48] As a general rule, the fuel economy on conventional light-duty vehicles can be improved or reduced by up to 2% per 100 lbs (45 kg) of weight subtracted or added.[49] Since the total amount of natural gas is fixed, changes in the fuel economy are directly proportional to changes in the driving range for this scenario. For example, a 10% improvement in the usable gravimetric capacity of HKUST-1 results in a 19 kg reduction in weight and a 0.8% improvement in fuel economy and driving range.

To isolate the effects of changing usable volumetric capacity, it is assumed that a light-duty vehicle will have a fixed amount of space available for a fuel tank. As a result, there is a roughly 1:1 correlation between the usable volumetric capacity of an adsorbent and the expected driving range of a vehicle.

As shown in Figure 3.8, improvements in gravimetric capacity have considerably less impact than improvements in volumetric capacity. While increases in gravimetric capacity are still important, similar improvement percentages do not have as significant an impact as volumetric on increasing driving range, since the increased weight of the adsorbent material has a minor effect on the fuel economy of the vehicle. Therefore, increasing the usable volumetric CH_4 capacity is significantly more important than increasing the usable gravimetric capacity for natural gas storage in light-duty vehicles.

These relationships, along with knowledge of the importance of certain vehicle attributes to consumers, such as driving range and cost, are critical for directing adsorbent material improvements and tradeoffs toward the optimal solution for a viable ANG system.

3.3.9. Adsorbed Natural Gas System Requirements. While working to synthesize a next generation of metal-organic frameworks with improved volumetric and gravimetric capacities, it is also important to consider the complete ANG storage system, as there are several factors that can dramatically affect the ultimate performance of a material when delivering natural gas to an engine. It is worth nothing that many of these systems-level issues are not just engineering problems and are fundamentally related to materials properties that can potentially be tuned through synthetic chemistry to improve performance.

3.3.10. Thermal Properties. In an actual ANG system, the heats of adsorption (exothermic) and desorption (endothermic) will likely lead to large temperatures changes that both have a negative impact on the usable CH_4 capacity.[50] Specifically, an adsorbent bed will release heat during refueling and cool during discharge, resulting in less CH_4 stored during adsorption and more retained during desorption. Faster refueling and discharge rates, which are often desirable, lead to even greater temperature changes. Indeed, a prototype activated carbon storage tank cooled by as much as 37 °C at a discharge rate typical for a normal driving speed, resulting in a 20% loss in CH_4 capacity compared to isothermal desorption.[50] Various thermal management strategies have been proposed to minimize the impacts of heat flowing in and out of the adsorbent bed, including incorporating a heat exchanger inside the storage tank, changing how natural gas flows inside the tank, and altering the material and geometry of the tank.[50,51] While some form of thermal management will ultimately be necessary, all of these engineering solutions involve a significant tradeoff between cost, weight, and available space.

More importantly, all efforts to manage heat flow are highly dependent on the heat capacity and thermal conductivity of the adsorbent. High heat capacities decrease the magnitude of temperature changes resulting from the energy released or consumed during adsorption and desorption, while high thermal conductivities allow heat to dissipate more quickly and permit the use of simpler external or internal temperature control systems. With this in mind, it is worth noting that overcoming thermal management challenges is not just an engineering problem, and there can be a significant contribution from a more fundamental materials synthesis perspective.

While heat capacities have been reported for several metal-organic frameworks,[23o,52] to the best of our knowledge, there have been just two thermal conductivity measurements, both of which were for MOF-5.[53] As is typical of many porous materials, the MOF-5 thermal conductivities were very low at less than 0.32 $W \cdot m^{-1} \cdot K^{-1}$ for both a single crystal and packed powder. It is possible to improve the thermal conductivity by incorporating an additive such as graphite, but this will lead to a decrease in both the gravimetric and volumetric CH_4 capacities.[53b] To better understand these tradeoffs, there is a clear need for thermal conductivity and heat capacity measurements on a much wider range of metal-organic frameworks, especially with experiments designed to identify structural and chemical features that are likely to lead to frameworks with higher intrinsic thermal conductivities and heat capacities.

3.3.11. Mechanical Properties. As has been emphasized, the volumetric CH_4 capacity of an adsorbent has a critical impact on the ultimate driving range of an ANG vehicle. Notably, almost all reported volumetric uptakes for metal-organic frameworks, including those in this study, are calculated using the density of a perfect single crystal and represent the maximum possible volumetric capacity. In reality, metal-organic frameworks synthesized on a large enough scale to fill a fuel tank will likely be powders that contain a significant amount of empty space between

particles. This interparticle void space results in a much lower density, and consequently a lower volumetric CH_4 capacity, for a bulk powder than that calculated for a single crystal. Indeed, the bulk powder density of MOF-5 was measured at just 0.13 g/cm^3, 79% less than the single crystal density of 0.621 g/cm^3.[54d] Note that in addition to decreasing volumetric capacity, low packing densities also lead to lower thermal conductivities.

In order to minimize the losses in capacity and thermal conductivity that result from packing adsorbent particles inside a tank, it will be essential to compact the material in some fashion. Compaction reduces the interparticle void space and increases the bulk density of the powder, but it can also cause partial or complete collapse of framework pores. As a result, materials with higher mechanical stability are desirable, as they are more likely to survive compaction to higher densities without significant losses in porosity. While there have been initial studies on the intrinsic mechanical properties of different metal-organic frameworks, the majority of work has been limited to frameworks that can be synthesized as large single crystals.[55]

Additional research efforts have examined changes in surface area, pore volume, and gas uptake when compacting different metal-organic framework powders, including MOF-5, HKUST-1, and Ni_2(dobdc), at increasing mechanical pressures.[25c,54] For instance, tablets of HKUST-1 compacted to 66% of its crystallographic density adsorbed just 94 v/v of CH_4 at 35 bar and 30 °C,[25c] highlighting the importance of packing losses on the actual volumetric capacity of an adsorbent. Similarly, a pellet of Ni_2(dobdc) compacted with 0.1 GPa of pressure adsorbed just 100 v/v of CH_4 at 34 bar and 30 °C,[54c] significantly less than the 230 v/v measured here. These types of compaction studies are certainly useful, but it is difficult to compare the intrinsic mechanical properties of each material based on such measurements, since compaction is affected by particle size and shape in addition to mechanical stability. More importantly, comparisons of the volumetric usable capacity of different materials will be highly dependent on the mechanical stability of the framework and the maximum compaction density that can be achieved. Based on current work, the extent of varying degrees of mechanical stability between different metal-organic frameworks is poorly understood.

With this in mind, efforts to understand fundamental relationships between framework structure and mechanical properties will be extremely valuable in directing synthesis efforts toward robust materials that can be compacted to sufficiently high densities without structural changes that might affect CH_4 adsorption capacities.[56] Equally important will be research toward obtaining finer control over the size and morphology of metal-organic framework particles. In particular, studies on compacting activated carbons have demonstrated that significantly higher packing densities can be achieved when particles of two or more different sizes are mixed and compacted at the same time.[57] To our knowledge, there have not yet been any studies evaluating the effects of the particle size distribution and shape on the achievable packing density for metal-organic frameworks. Note that in addition to evaluating changes in porosity upon compaction, it is also important to consider potential affects on the adsorption and desorption kinetics, as fast kinetics are important for achieving practical refueling and discharge rates in a vehicle.[58]

3.3.12. Natural Gas Impurities. Although CH_4 is the largest component, pipeline-quality natural gas contains many other impurities that can affect the long-term stability and capacity of an adsorbent (Table 2).[59] In an ANG vehicle, a guard bed will likely be placed before the storage tank during refueling to minimize exposure to impurities. Still, the adsorbent will inevitably be exposed to at least some level of each impurity throughout its lifetime. Additionally, most guard beds are unlikely to remove a significant amount of the C2 and C3 hydrocarbons that are present

in natural gas, and it is unclear how this might affect the usable CH_4 capacity of an adsorbent. Smaller levels of other impurities, especially sulfur-containing compounds, H_2O, O_2, and C4 and greater hydrocarbons, may slowly poison CH_4 adsorption sites or degrade the framework over an extended time period. Performing cycling studies in the presence of all expected natural gas impurities will be critical to designing metal-organic frameworks with the long lifetimes necessary for use in a natural gas powered vehicle.

Table 3.2. Example composition of pipeline natural gas (Union Gas).

Component	mol %
CH_4	87−96
C_2H_6	1.5−5.1
C3 or greater hydrocarbons	0.1−2.3
C6 or greater hydrocarbons	< 0.1
N_2	0.7−5.6
CO_2	0.1−1.0
O_2	< 0.1
H_2	< 0.02
H_2O	< 80 mg/m^3
Sulfur (including odorants)	5.5 mg/m^3

3.4. Outlook and Conclusions

With some of the highest volumetric and gravimetric CH_4 capacities ever reported, metal-organic frameworks have shown significant potential as adsorbents for natural gas storage. There are still, however, some formidable challenges to overcome before they are likely to find widespread use in natural gas vehicles. Most importantly, substantial increases in the usable volumetric capacity are needed for improving the driving range to levels closer to that of gasoline vehicles. To go beyond just incremental improvements in capacity, completely new design strategies will likely be necessary. For instance, new types of strong binding sites that occupy a small volume but can each polarize multiple CH_4 molecules should dramatically increase the volumetric density of stored CH_4. Above all, any efforts to minimize the amount of wasted volume inside frameworks that does not contribute to optimally attracting CH_4 molecules, without significant decreases in porosity, should be beneficial. This includes extra empty space inside large pores, as well as adsorption sites on the pore surface that are too weak or too strong for maximizing the usable capacity.

It is important to emphasize that efforts to design a next generation of high-capacity metal-organic frameworks for natural gas storage must address systems-level factors that will heavily influence the actual performance of a material, including compaction, heat capacity, thermal conductivity, and tolerance to impurities. Studies that address these areas are not only important for determining the practically achievable usable capacity and lifetime of different materials, but improving our fundamental understanding of the relationship of framework structure and chemical composition with thermal properties, mechanical properties, and long-term stability will also help guide synthetic efforts toward the most useful materials. Ultimately, the cost of the material will also be an important factor in determining the competitiveness of an ANG vehicle.

While it is difficult to predict the large-scale cost of organic ligands for which there are currently little demand, basic economic analyses of the best current metal-organic frameworks would be useful for identifying strategies to target materials with the greatest potential for scale-up to the levels required to have an impact in natural gas vehicles.

3.5. Acknowledgements

This research was funded by the Advanced Research Projects Agency – Energy (ARPA-E), U.S. Department of Energy. We thank Dr. Mike Veenstra, Dr. Bruce Hardy, Dr. Donald Anton, Michael SantaMaria, Dr. Bill Dolan, Dr. Lena Arnold, Dr. Stefan Marx, and Dr. Dane Boysen for helpful discussions.

Table 3.3. Crystallographic density, pore volume, surface area and total CH_4 adsorption near 35 bar and ambient temperature for metal-organic frameworks (sorted by decreasing volumetric uptake).

chemical formula[a]	common name	ρ_{cryst} (g/cm^3)	V_p (cm^3/g)	surface area (m^2/g)		total CH_4 adsorption[b]				
				BET	Langmuir	cm$^3_{STP}$/cm^3	cm$^3_{STP}$/g	*P* (bar)	*T* (°C)	ref
Ni_2(dobdc)	Ni-MOF-74, CPO-27-Ni	1.195	0.56		1593	230	193	35	25	this work
			0.47	1218		214	179	35	25	23h
			0.44	1027		206	172	35	25	24
Cu_3(btc)$_2$	HKUST-1	0.881	0.77		2203	225	255	35	25	this work
			0.75	1663		220	250	35	22	25e
			0.67	1850		217	246	35	30	25g
			0.76	1502	2216	198	225	35	30	25b
			0.71	1555		194	221	35	30	25d
			0.72			184	209	35	30	26b
	HKUST-1 tablet (3 × 3 mm)	0.582[c]				94[d]	162[d]	35	30	25c
Co_2(dobdc)	Co-MOF-74, CPO-27-Co	1.173	0.51		1433	221	188	35	25	this work
			0.48	1056		194	165	35	25	24
Cu_2(adip)	PCN-14	0.829	0.83	1984	2360	202	244	35	25	this work
			0.87	1753	2176	235	283	35	17	27a
Mg_2(dobdc)	Mg-MOF-74, CPO-27-Mg	0.909	0.69		1957	200	220	35	25	this work
			0.63	1542		188	207	35	25	23h
			0.61	1332		168	184	35	25	24
Cu_2(bdpp)	NJU-Bai10	0.668	1.11	2883	3108	197	296	35	17	60
Cu_2(1,4-nddi)	NOTT-109	0.790	0.85	2110		197	250	35	27	42
Zn(bdc)(ted)$_{0.5}$		0.893	0.65	1794	2015	197[d]	221[d]	35	25	61
Cu_3(bdb)	UTSA-20	0.91	0.63	1156		197	217	35	27	62
Cu_2(tptc)	NOTT-101	0.684	1.08	2805		196	286	35	27	42
Cu_2(sbtc)	PCN-11	0.749	0.91	1931	2442	194	259	35	25	63
Cu_2(bptc)	NOTT-100, MOF-505	0.927	0.677	1661		194	209	35	27	42
Cu_2(2,6-nddi)	NOTT-103	0.643	1.157	2958		194	301	35	27	42
$[Zn_3(OH)]_4$(tbcppm)(H$_2$tbcppm)$_2$		0.685	1.14	2718	3120	194	283	35	25	64
Cu_2(ebdc)	PCN-16	0.724	1.06	2273	2800	192	265	35	27	65
$Cu_2(C_{26}H_{20}O_8)$	NOTT-107	0.756	0.767	1770		191	252	35	25	5h, 66
Cu_2(pddi)	ZJU-5	0.679	1.074	2823		190	280	35	27	67
Zn_2(dobdc)	Zn-MOF-74	1.231	0.41	885		188	153	35	25	24
Al(OH)(bdc)	MIL-53 (Al)	0.978	0.54	1235	1627	186[d]	190[d]	35	30	68
			0.54	1140	1590	155	159	35	31	69, 70
			0.56			121	124	35	30	71
Cu_3(tdpat)		0.782	0.93	1938	2608	182	232	35	25	32
Cu_2(qptc)	NOTT-102	0.587	1.268	3342		181	308	35	27	42
Cu_2(fddi)	ZJU-25	0.622	1.18	2125	3304	180	289	35	27	72
$Cu_3[(C_6H_3)(C_2N_3H)_3(C_6H_3)_3(COO)_6]$	NU-125	0.578	1.29	3120		179	310	35	25	73
$Zn_4O(C_2H_4$-bdc$)_3$	IRMOF-6	0.65	0.92		2630	177	272	36.5	25	74
Mn_2(dobdc)	Mn-MOF-74	1.084	0.5	1102		176	163	35	25	24
Zn_2(bdc)$_2$(dabco)		0.822	0.75	1448	2104	164	199	35	30	25b
			0.68	1450		159	194	35	23	75
Cu_3(OH-stpdc)	SDU-6	0.611	1.17	2826		172	281	35	25	76
Cu_3(btei)	PCN-61	0.56	1.36	3000	3500	171	306	35	25	77
Cu_2(bdi)	PCN-46	0.619	1.012	2500	2800	171	277	35	25	78
Zn_4O(bdc)$_3$	IRMOF-1, MOF-5	0.621	1.4[e]			168	271	36.5	25	5a
			1.4		3995	150	241	35	25	this work
			1.2			143	230	36	27	21
			1.55	3800	4400	138	223	35	25	28d
$Zr_6O_4(OH)_4(NH_2$-bdc$)_6$	UiO-66-NH_2	1.36	0.4	1080		167	123	35	30	25g
Cr(OH)(bdc)	MIL-53 (Cr)	1.04	0.5		1500	165	159	35	31	69

chemical formula[a]	common name	ρ_{cryst} (g/cm^3)	V_p (cm^3/g)	surface area (m^2/g)		total CH_4 adsorption[b]				
				BET	Langmuir	cm^3_{STP}/cm^3	cm^3_{STP}/g	P (bar)	T (°C)	ref
$Co_2(bdc)_2(dabco)$		0.815	0.82	1600	2300	161	197	35	30	79
$Cu_3(Me\text{-}stpdc)$	SDU-7	0.605	1.1	2713		159	263	35	25	76
$Cu_3(tipb)$	UTSA-34	0.84	0.542	991		159	189	35	17	80
$Cu_2(dceni)$	UTSA-40	0.827	0.65	1630	1661	152	184	35	27	81
$Cu_2(ndc)_2(dabco)$	DUT-8 (Cu)	0.681	1.04	2535		148	217	35	25	82
$Cu_2(bttcd)$	PCN-80	0.575	1.47	3850	4150	147	255	35	23	83
$Zn_4O(tcbpa)_2$	SNU-77	0.586	1.52	3670	4180	147	250	35	25	84
$Cu_3(iBu\text{-}stpdc)$	SDU-8	0.613	1.02	2516		146	238	35	25	85
$Zr_6O_4(OH)_4(bdc)_6$	UiO-66	1.32	0.36	970		146	110	35	30	25g
$Zn_4O(NH_2\text{-}bdc)_3$	IRMOF-3	0.63	1.07			144	228	36.5	25	5a, 86
$Ti_8O_8(OH)_4(bdc)_6$	MIL-125	0.81	0.67	1820		141	174	35	30	25g
$Yb_3O[(C_6H_3)_4(C_6H_4)_6(COO)_6](NO_3)$	UTSA-62	0.59	0.91	2190		139	236	35	25	87
$Cu_3(tcepbb)$	NU-111	0.409	2.09	4930		136	333	35	25	31
$Cu_3(ntei)$	PCN-66	0.44	1.63	4000	4600	134	304	35	25	88
$Co_2(bipy)_3(btb)_4$	DUT-23 (Co)	0.401	2.03	4850		133	331	35	25	89
$Zn(MeIM)_2$	ZIF-8	1.141	0.49			131	115	36	27	21
			0.59	1445		124	109	35	30	90
$Zn_4O(ceb)_3$	SNU-71	0.835	0.709	1770	1923	130	155	35	25	91
$Ni(ndc)(ted)_{0.5}$		0.789	0.84	2307	2647	128[d]	162[d]	35	25	61
$Cu_3(ptei)$	PCN-68	0.38	2.13	5109	6033	126	332	35	25	77
$Zn_4O(btb)_2$	MOF-177	0.427	1.89	4500	5340	126	293	35	25	28d
			1.55			106	249	35	25	92
$Cu(SiF_6)(4,4'\text{-}bpy)_2$		0.86			1337	125	146	36.5	25	93
			0.56	1337		124	144	35	25	94
$Zn_3O(2,7\text{-}ndc)_2$		1.04	0.458	901	1281	125	120	35	25	95
$Cu(GeF_6)(4,4'\text{-}bpy)_2$		0.925				124	134	36.5	25	93
$Cu_2(bdcppi)$	SNU-50	0.65	1.08	2300	2450	123	189	35	25	96
$Al(OH)(ndc)$	DUT-4	0.773	0.68	1308	1996	122	158	35	30	97
$Zn_4O(ndc)_3$	UTSA-38	0.962	0.61	1090	1690	120[d]	124[d]	35	27	98
$Cr_3O(btc)_2F$	MIL-100 (Cr)	0.7	1.1	1900		120	171	35	30	99
$Zn_4O(btb)_{4/3}(ndc)$	MOF-205	0.38	2.16	4460	6170	119	314	35	25	28d
$Zn_4O(ndc)_3$	IRMOF-8	0.448	1.827	4326		114	254	35	25	100
$Zn_4O(btb)_{4/3}(ndc)$	DUT-6	0.39	2.02		6005	106	271	35	25	101
$Fe_3O(btc)_2F$	MIL-100 (Fe)	0.7	0.99	2410		117	167	35	30	25g
$Al(OH)(bpdc)$	DUT-5	0.634	0.81	1613	2335	113	179	35	30	97
$Cu_2(bbcdc)$	DUT-49	0.311	2.91	5476		113	363	35	25	30
$Zn_4O(cvb)_3$	SNU-70	0.408	2.17	5290	6100	111	273	35	25	102
$Zn_6(btb)_4(4,4'\text{-}bpy)_3$	FJI-1	0.405	1.43	4043	4624	111	273	35	25	103
$Zn(Im)_{1.5}(cbIM)_{0.5}$	ZIF-76	0.869	0.57	1340		110	126	35	30	104
$Cu_3(C_{66}H_{36}O_{12})$	NOTT-119	0.361	2.35	4118		106	294	35	25	105
$Cd(bpydb)$		1.21	0.35	346		104	86	35	25	106
$Ni_5O_2(btb)_2$	DUT-9	0.358	2.18		6120	101	283	35	25	107
$Cr_3O(bdc)_3F$	MIL-101 (Cr)	0.44	2.15	4230		101	230	35	30	99
			1.57	3870		87	197	35	30	25g
			1.38	2674		82	186	35	22	25e
			1.303	2693	4492	79	178	35	30	25b
$Zn_4O(BenzTB)_{3/2}$	DUT-13	0.385	1.98		5570	96	250	35	25	108
$Zn_4O(bte)_{4/3}(bpdc)$	MOF-210	0.25	3.6	6240	10400	83	331	35	25	28d
$Co_2(4,4'\text{-}bpy)_3(NO_3)_4$		1.36				73	54	35	25	5
$Zn_4O(bbc)_2$	MOF-200	0.22	3.59	4530	10400	67	304	35	25	28d
$Cd_2(azpy)_3(NO_3)_4$		1.54				66	43	36.5	25	109

chemical formula[a]	common name	ρ_{cryst} (g/cm^3)	V_p (cm^3/g)	surface area (m^2/g)		total CH_4 adsorption[b]				
				BET	Langmuir	cm$^3_{STP}$/cm^3	cm$^3_{STP}$/g	P (bar)	T (°C)	ref
$Co_2(ndc)_2(dabco)$	DUT-8 (Co)	0.67	0.62	1400		52	78	35	25	82
$Zn_2(ndc)_2(dabco)$	DUT-8 (Zn)	0.68	0.3	710		40	59	35	25	82
$Cu_2(PF_6)(NO_3)(4,4'\text{-bpy})_4 \bullet 1.4PF_6 \bullet 0.6NO_3$		1.057		559		33	31	36.5	25	93
$Zn_2(tcpbda)$	SNU-30	0.381	0.28	704	770	27	71	35	25	110
$Co(azpy)_2(NCS)_2$		1.31				19	15	35.5	25	109
$Co_2(azpy)_3(NO_3)_4$		1.32				17	13	36.5	25	109
$Zn_2(tcpbda)(bpta)$	SNU-31	0.459	0.14	308		17	37	35	25	110
$Cu(C_{10}H_6O_4)(ted)_{0.5}$			1.08	3129			214[f]	35	25	111
$Cu(bpdc)(ted)_{0.5}$			1.27	3265			213[f]	35	25	111
$Cu(bdc)(ted)_{0.5}$			0.71	1891			185[f]	35	25	111*b*
VO(bdc)	MIL-47 (V)		0.5	1030			137[f]	35	30	112
$Cu(C_4H_2O_4)(ted)_{0.5}$			0.24	606			103[f]	35	25	111b
$Cu(dhbc)_2(4,4'\text{-bpy})$					320		70[f]	35	25	113
	AX-21 activated carbon	0.49	1.64		4880	154	315	35	25	this work
$C_{25}H_{24}B_4O_8$	COF-102	0.43	1.55	3620	4650	135	313	35	25	114
$C_{99}H_{64}Si_4$	PPN-4	0.284	3.04	6461	10063	109	384	35	25	115
$Na_{86}[(AlO_2)_{86}(SiO_2)_{106}]$	Zeolite NaX	1.43	0.27			106	74	35.5	25	116
$Na_{12}[(AlO_2)_{12}(SiO_2)_{12}]$	Zeolite 5A	1.48	0.2			104	70	35.5	5	116

[a] adip = 5,5′-(9,10-anthracenediyl)di-isophthalate; azpy = 4,4′-azopyridine; bbc = 4,4′,4″-[benzene-1,3,5-triyl-tris(benzene-4,1-diyl)]tribenzoate; bbcdc = 9,9′-([1,1′-biphenyl]-4,4′-diyl)bis(9*H*-carbazole-3,6-dicarboxylate); bdc = 1,4-benzenedicarboxylate; bdcppi = N,N′-bis(3,5-dicarboxyphenyl)pyromellitic diimide; bdi = 5,5′-(buta-1,3-diyne-1,4-diyl)diisophthalate; bdpp = 3,5-bis(3,5-dicarboxylphenyl)-pyridine; BenzTB = N,N,N′,N′-benzidinetetrabenzoate; bhb = 3,3′,3″,5,5′,5″-benzene-1,3,5-triyl-hexabenzoate; bpdc = biphenyldicarboxylate; bpta = 3,6-di(4-pyridyl)-1,2,4,5-tetrazine; bptc = biphenyl-3,3′,5,5′-tetracarboxylate; 4,4′-bpy = 4,4′-bipyridine; bpydb = 4,4′-(4,4′-bipyridine-2,6-diyl)dibenzoate; btb = benzene-1,3,5-tribenzoate; btc = 1,3,5-benzenetricarboxylate; bte = 4,4′,4″-[benzene-1,3,5-triyl-tris (ethyne-2,1-diyl)]tribenzoate; btei = 5,5′,5″-benzene-1,3,5-triyltris(1-ethynyl-2-isophthalate); bttdc = 9,9′,9″,9‴-([1,1′-biphenyl]-3,3′,5,5′-tetrayl)tetrakis(9H-carbazole-3,6-dicarboxylate); cbIM = *b*-chlorobenzoimidazole; ceb = 4-(2-carboxyethyl)benzoate; cvb = 4-(2-carboxyvinyl)benzoate; dabco = 1,4-diazabicyclo[2.2.2]octane; dceni = 6,6′-dichloro-2,2′-diethoxy-1,1′-binaphthyl-4,4′-di(5-isophthalate); dhbc = 2,5-dihydroxybenzoate; dobdc = 2,5-dioxido-1,4-benzenedicarboxylate; ebdc = 5,5′-(1,2-ethynediyl)bis(1,3-benzenedicarboxylate); fddi = tetramethyl 5,5′-(9H-flourene-2,7-diyl)diisophthalate acid; H_2tbcppm = {3,5-bis[(4-carboxyl)phenyl]phenyl}methane; iBu-stpdc = 4,4′,4″-(isobutylsilanetriyl)tris-(triphenyl-3,5-dicarboxylate); Im = imidazole; Me-stpdc = 4,4′,4″-(methylsilanetriyl)tris-(triphenyl-3,5-dicarboxylate); MeIM = 2-methylimidazole; ndc = 2,6-naphthalenedicarboxylate; 2,7-ndc = 2,7-naphthalenedicarboxylate; 1,4-nddi = 5,5′-naphthalene-1,4-diyl-diisophthalate; 2,6-nddi = 5,5′-naphthalene-2,6-diyl-diisophthalate; NH_2-bdc = 2-amino-1,4-benzenedicarboxylate; ntei = 5,5′,5″-(4,4′,4″-nitrilotris(benzene-4,1-diyl)tris(ethyne-2,1-diyl))triisophthalate; OH-stpdc = 4,4′,4″-(hydroxysilanetriyl)tris-(triphenyl-3,5-dicarboxylate); pddi = 5,5′-(pyridine-2,5-diyl)diisophthalate; ptei = 5,5′-((5′-(4-((3,5-dicarboxyphenyl)ethynyl)phenyl)-[1,1′,3′,1″-terphenyl]-4,4″-diyl)-bis(ethyne-2,1-diyl))diisophthalic acid; qptc = quaterphenyl-3,3‴,5,5‴-tetracarboxylate; sbtc = trans-stilbene-3,3′,5,5′-tetracarboxylate; tcbpa = tris(4′-carboxy-biphenyl)amine; tcepbb = 1,3,5-tris[(1,3-carboxylate-5-(4-(ethynyl)phenyl))butadiynyl]-benzene; tcpbda = N,N,N′,N′-tetrakis(4-carboxylphenyl)biphenyl-4,4′-diamine; tdpat = 2,4,6-tris(3,5-dicarboxylphenylamino)-1,3,5-triazine; ted = triethylenediamine; tipb = 1,2,4,5-tetra(5-isophthalate)benzene; tptc = terphenyl-3,3′,5,5′-tetracarboxylate. [b] Values were extrapolated from adsorption isotherms when not explicitly stated in the text or supporting information. Excess adsorption was converted to total using reported pore volumes and the bulk CH_4 density from the NIST REFPROP database. [c] This is the real, measured density of the pellet. Note that the pellet contains 2% Alox C and 3% graphite as additives. [d] Not specified whether uptake is in terms of excess, total or absolute adsorption. Consequently, values are simply reproduced from original publication and not converted. [e] Pore volume was taken from this work to calculate total adsorption. [f] Structure of framework during CH_4 adsorption is uncertain, and volumetric adsorption cannot be reasonably estimated. Also, it is not specified whether uptake is in terms of excess, total or absolute adsorption.

3.6. References and Supplementary Figures

(1) Celzard, A.; Fierro, V. *Energy Fuels* **2005**, *19*, 573.

(2) International Energy Agency, "World Energy Outlook 2011: Are We Entering a Golden Age of Gas", <www.worldenergyoutlook.org>.

(3) (a) Li, H.; Eddaoudi, M.; O'Keeffe, M.; Yaghi, O. M. *J. Am. Chem. Soc.* **1999**, *402*, 276. (*b*) Kitagawa, S.; Kitaura, R.; Noro, S.-I. *Angew. Chem., Int. Ed.* **2004**, *43*, 2334. (c) Matsuda, R.; Kitaura, R.; Kitagawa, S.; Kubota, Y.; Belosludov, R. V.; Kobayashi, T. C.; Sakamoto, H.; Chiba, T.; Takata, M.; Kawazoe, Y.; Mita, Y. *Nature* **2005**, *436*, 238. (d) Millward, A. R.; Yaghi, O. M. *J. Am. Chem. Soc.*, 2005, **127**, 17998. (e) Férey, G. *Chem. Soc. Rev.* **2008**, *37,* 191. (f) Morris, R. E.; Wheatley, P. S. *Angew. Chem., Int. Ed.* **2008**, *47*, 4966. (g) Czaja, A. U.; Trukhan, N.; Müller, U. *Chem. Soc. Rev.* **2009**, *38*, 1284. (h) Chen, B.; Xiang, S.; Qian, G. *Acc. Chem. Res.* **2010**, 1115. (i) Zhou, H.-C.; Long, J. R.; Yaghi, O. M. *Chem. Rev.* **2012**, *112*, 673. (j) Sumida, K.; Rogow, D. L.; Mason, J. A.; McDonald, T. M.; Bloch, E. D.; Herm, Z. R.; Bae, T.-H.; Long, J. R. *Chem. Rev.* **2012**, *112*, 724. (k) Li, J.-R.; Sculley, J.; Zhou, H.-C. C*hem. Rev.* **2012**, *112*, 869.

(4) (a) Furukawa, H.; Miller, M. A.; Yaghi, O. M. *J. Mater. Chem.* **2007**, *17*, 3197. (b) Dincă, M.; Long, J. R. *Angew. Chem. Int. Ed.* **2008**, *47*, 6766. (c) Murray, L. J.; Dincă, M.; Long, J. R. *Chem. Soc. Rev.* **2009**, *38,* 1294. (d) Suh, M. P.; Park, H. J.; Prasad, T. K.; Lim, D.-W. *Chem. Rev.* **2012**, *112*, 782.

(5) Kondo, M.; Yoshitomi, T.; Seki, K.; Matsuzaka, H.; Kitagawa, S. *Angew. Chem. Int. Ed. Engl.* **1997**, *36*, 1725.

(6) (a) Eddaoudi, M.; Kim, J.; Rosi, N.; Vodak, D.; Wachter, J.; O'Keeffe, M.; Yaghi, O. M. *Science* **2002**, *295*, 469. (b) Düren, T.; Sarkisov, L.; Yaghi, O. M.; Snurr, R. Q. *Langmuir* **2004**, *20*, 2683. (c) Zhou, W. *Chem. Rec.* **2010**, *10*, 200. (d) Getman, R. B.; Bae, Y.-S.; Wilmer, C. E.; Snurr, R. Q. *Chem. Rev.* **2012**, *112*, 703. (e) Konstas, K.; Osl, T.; Yang, Y.; Batten, M.; Burke, N.; Hill, A. J.; Hill, M. R. *J. Mater. Chem.* **2012**, *22*, 16698. (f) Makal, T. A.; Li, J.-R.; Lu, W.; Zhou, H.-C. *Chem. Soc. Rev.* **2012**, *41*, 7761. (g) He, Y.; Zhou, W.; Krishna, R.; Chen, B. *Chem. Commun.* **2012**, *48*, 11813. (h) Wilmer, C. E.; Leaf, M.; Yeon Lee, C.; Farha, O. K.; Hauser, B. G.; Hupp, J. T.; Snurr, R. Q. *Nat. Chem.* **2012**, *4*, 83.

(7) Gibbs, J. W. *The Collected Works of J. W. Gibbs*, Longmans and Green, New York, **1928**.

(8) (a) Sircar, S. *Ind. Eng. Chem. Res.* **1999**, *38*, 3670. (b) Sircar, S. *AIChE J.* **2001**, *47*, 1169. (c) Murata, K.; El-Merraoui, M.; Kaneko, K. *J. Chem. Phys.* **2001**, *114*, 4196. (d) Myers, A. L.; Monson, P. A. *Langmuir* **2002**, *18*, 10261. (e) Do, D. D.; Do, H. D. *Carbon*, 2003, **41**, 1777. (f) Gumma, S.; Talu, O. *Langmuir* **2010**, *26*, 17013.

(9) While the total *material* adsorption is defined as the total number of gas molecules inside the pores of an adsorbent, the total *system* adsorption is defined as the total number of gas molecules inside the entire system, which includes interparticle voids and other empty spaces inside the adsorption vessel. Even though the total system adsorption is most important for application in a vehicle, total material adsorption is more meaningful for comparing properties of different adsorbents. In this work, the terms "total material adsorption" and "total adsorption" are used interchangeably.

(10) Gross, K. J.; Carrington, K. R.; Barcelo, S.; Karkamkar, A.; Purewal, J.; Ma, S.; Zhou, H.-C.; Dantzer, P.; Ott, K.; Burrell, T.; Semeslberger, T.; Pivak, Y.; Dam, B.; Chandra, D.

"Recommended Best Practices for the Characterization of Storage Properties of Hydrogen Storage Materials", **2011**, V3-5, U.S. D.O.E. Hydrogen Program document, available online at: www1.eere.energy.gov/hydrogenandfuelcells/ pdfs/best_practices_hydrogen_storage.pdf

(11) (a) Dincă, M.; Dailly, A.; Liu, Y.; Brown, C. M.; Neumann, D. A.; Long, J. R. *J. Am. Chem. Soc.* **2006**, *128*, 16876. (b) Poirier, E.; Dailly, A. *J. Phys. Chem. C* **2008**, *112*, 13047.

(12) For microporous materials, this is a particularly good approximation since most gas molecules inside a micropore should have some degree of interaction with the pore surface. As pores get larger, this may not always be a valid assumption, which can affect the accuracy of using isotherm data to calculate thermodynamic properties.

(13) Sing, K. S. W.; Everett, D. H.; Haul, R. A. W.; Moscou, L.; Pierotti, R. A.; Rouquérol, J.; Siemieniewska, T. *Pure Appl. Chem.* **1985**, *57*, 603.

(14) Gurvich, L. *J. Phys. Chem. Soc. Russ.* **1915**, *47*, 805.

(15) More advanced techniques, such as t-Plots, the Horvath-Kawozoe (H-K) equation, and Density Functional Theory (DFT), can be used to extract detailed pore size distributions, but whether the calculated total pore volume from these methods will differ significantly from the simple single-point calculation using the Gurvich rule is not well studied.

(16) Lowell, S.; Shields, J.; Thomas, M. A.; Thommes, M. *Characterization of Porous Solids and Powders: Surface Area, Pore Size and Density*, Springer, The Netherlands, **2004**, pp. 111-112.

(17) Moellmer, J.; Celer, E. B.; Luebke, R.; Cairns, A. J.; Staudt, R.; Eddaoudi, M.; Thommes, M. *Microporous Mesoporous Mater.* **2010**, *129*, 345.

(18) Krishna, R. *Microporous Mesoporous Mater.* **2012**, *156*, 217.

(19) (a) Keller, J. U.; Robens, E.; du Fresne von Hohenesche, C. *Proc. COPS-VI* **2002**, *144*, 387. (b) Belmabkhout, Y.; Frère, M.; De Weireld, G. *Meas. Sci. Technol.* **2004**, *15*, 848. (c) Broom, D. P. *Int. J. Hydrogen Energy* **2007**, *32*, 4871.

(20) Malbrunot, P.; Vidal, D.; Vermesse, J.; Chahine, R.; Bose, T. K. *Langmuir* **1997**, *13*, 539.

(21) Zhou, W.; Wu, H.; Hartman, M. R.; Yildirim, T. *J. Phys. Chem. C* **2007**, *111*, 16131.

(22) Kunowsky, M.; Suárez-García, F.; Linares-Solano, Á. *Microporous Mesoporous Mater.* **2013**, *173*, 47.

(23) (a) Rosi, N. L.; Kim, J.; Eddaoudi, M.; Chen, B.; O'Keeffe, M.; Yaghi, O. M. *J. Am. Chem. Soc.* **2005**, *127*, 1504. (b) Caskey, S. R.; Wong-Foy, A. G.; Matzger, A. J. *J. Am. Chem. Soc.* **2008**, *130*, 10870. (c) Dietzel, P. D. C.; Blom, R.; Fjellvag, H. *Eur. J. Inorg. Chem.* **2008**, 3624. (d) Liu, Y.; Kabbour, H.; Brown, C. M.; Neumann, A. D.; Ahn, C. C. *Langmuir*, 2008, *24*, 4772. (e) Dietzel, P. D. C.; Johnsen, R. E.; Fjellvag, H.; Bordiga, S.; Groppo, E.; Chavan, S.; Blom, R. *Chem. Commun.* **2008**, 5125. (f) Zhou, W.; Wu, H.; Yildirim, T/ J. Am. Chem. Soc. **2008**, *130*, 15268. (g) Britt, D.; Furukawa, H.; Wang, B.; Glover, T. G.; Yaghi, O. M. *Proc. Nat. Acad. Sci., USA* **2009**, *106*, 20637. (h) Dietzel, P. D. C.; Besikiotis, V.; Blom, R. *J. Mater. Chem.* **2009**, *19*, 7362. (i) Wu, H.; Simmons, J. M.; Srinivas, G.; Zhou, W.; Yildirim, T. *J. Phys. Chem. Lett.* **2010**, *1*, 1946. (j) Valenzano, L.; Civalleri, B.; Chavan, S.; Palomino, G. T.; Areán, C. O.; Bordiga, S. *J. Phys. Chem. C* **2010**, *114*, 11185. (k) Bao, Z.; Yu, L.; Ren, Q.; Lu, X.; Deng, S. *J. Colloid Interface Sci.* **2011**, *353*, 549. (l) Sumida, K.; Brown, C. M.; Herm, Z. R.; Chavan, S.; Bordiga, S.; Long,

J. R. *Chem*. *Commun*. **2011**, *47*, 1157. (m) Queen, W. L.; Brown, C. M.; Britt, D. K.; Hudson, M. R.; Yaghi, O. M. *J. Phys. Chem. C* **2011**, *115*, 24915. (n) Herm, Z. R.; Swisher, J. A.; Smit, B.; Krishna, R.; Long, J. R. *J. Am. Chem. Soc.* **2011**, *133*, 5664. (o) Mason, J. A.; Sumida, K.; Herm, Z. R.; Krishna, R.; Long, J. R. *Energy Environ*. *Sci*. **2011**, *4*, 3030. (p) Queen, W. L.; Bloch, E. D.; Brown, C. M.; Hudson, M. R.; Mason, J. A.; Murray, L. J.; Ramirez-Cuesta, A. J.; Peterson, V. K.; Long, J. R. *Dalton Trans.* **2012**, *41*, 4180. (q) Bloch, E. D.; Queen, W. L.; Krishna, R.; Zadrozny, J. M.; Brown, C. M.; Long, J. R. *Science* **2012**, *335*, 1606. (r) Geier, S. J.; Mason, J. A.; Bloch, E. D.; Queen, W. L.; Hudson, M. R.; Brown, C. M.; Long, J. R. *Chem. Sci.* **2013**, *4*, 2054.

(24) Wu, H.; Zhou, W.; Yildirim, T. *J. Am. Chem. Soc.* **2009**, *131*, 4995.

(25) (a) Chui, S. S. Y.; Lo, S. M. F.; Charmant, J. P. H.; Orpen, A. G.; Williams, I. D. *Science* **1999**, *283*, 1148. (b) Senkovska, I.; Kaskel, S. *Microporous Mesoporous Mater.* **2008**, *112*, 108. (c) Cavenati, S.; Grande, C. A.; Rodrigues, A. E.; Kiener, C.; Müller, U. *Ind. Eng. Chem. Res.* **2008**, *47*, 6333. (d) Moellmer, J.; Moeller, A.; Dreisbach, F.; Glaeser, R.; Staudt, R. *Microporous Mesoporous Mater.* **2011**, *138*, 140. (e) Chowdhury, P.; Mekala, S.; Dreisbach, F.; Gumma, S. *Microporous Mesoporous Mater.* **2012**, *152*, 246. (f) Jeong, N. C.; Samanta, B.; Lee, C. Y.; Farha, O. K.; Hupp, J. T. *J. Am. Chem. Soc.* **2012**, *134*, 51. (g) Wiersum, A. D.; Chang, J.-S.; Serre, C.; Llewellyn, P. L. *Langmuir* **2013**, *29*, 3301.

(26) (a) García-Pérez, E.; Gascón, J.; Morales-Flórez, V.; Castillo, J. M.; Kapteijn, F.; Calero, S. *Langmuir* **2009**, *25*, 1725. (b) Getzschmann, J.; Senkovska, I.; Wallacher, D.; Tovar, M.; Fairen-Jimenez, D.; Düren, T.; van Baten, J. M.; Krishna, R.; Kaskel, S. *Microporous Mesoporous Mater.* **2010**, *136*, 50. (c) Wu, H.; Simmons, J. M.; Liu, Y.; Brown, C. M.; Wang, X.-S.; Ma, S.; Peterson, V. K.; Southon, P. D.; Kepert, C. J.; Zhou, H.-C.; Yildirim, T.; Zhou, W. *Chem. Eur. J.* **2010**, *16*, 5205.

(27) (a) Ma, S.; Sun, D.; Simmons, J. M.; Collier, C. D.; Yuan, D.; Zhou, H.-C. *J. Am. Chem. Soc.* **2008**, *130*, 1012. (b) Lucean, S. M. P.; Mileo, P. G. M.; Silvino, P. F. G.; Cavalcante, Jr., C. L. *J. Am. Chem. Soc.* **2011**, *133*, 19282.

(28) (a) Roswell, J. L. C.; Millward, A. R.; Park, K. S.; Yaghi, O. M. *J. Am. Chem. Soc.* **2004**, *126*, 5666. (b) Wong-Foy, A. G.; Matzger, A. J.; Yaghi, O. M. *J. Am. Chem. Soc.* **2006**, *128*, 3494. (e) Kaye, S. S.; Dailly, A.; Yaghi, O. M.; Long, J. R. *J. Am. Chem. Soc.* **2007**, *129*, 14176. (d) Furukawa, H.; Ko, N.; Go, Y. B.; Aratani, N.; Choi, S. B.; Choi, E.; Yazaydin, A. Ö.; Snurr, R. Q.; O'Keeffe, M.; Kim, J.; Yaghi, O. M. *Science* **2010**, *239*, 424.

(29) (a) Quinn, D. F.; MacDonald, J. A. *Carbon* **1992**, *30*, 1097. (b) MacDonald, J. A. F.; Quinn, D. F. *Fuel* **1998**, *77*, 61. (c) Zhou, L.; Zhou, Y.; Li, M.; Chen, P.; Wang, Y. *Langmuir* **2000**, *16*, 5955.

(30) Stoeck, U.; Krause, S.; Bon, V.; Senkovska, I.; Kaskel, S. *Chem. Commun.* **2012**, *48*, 10841.

(31) Peng, Y.; Srinivas, G.; Wilmer, C. E.; Eryazici,I.; Snurr, R. Q.; Hupp, J. T.; Yildirim, T.; Farha, O. K. *Chem. Commun.* **2013**, *49*, 2992.

(32) Li, B.; Zhang, Z.; Li, Y.; Yao, K.; Zhu, Y.; Deng, Z.; Yang, F.; Zhou, X.; Li, G.; Wu, H.; Nijem, N.; Chabal, Y. J.; Lai, Z.; Han, Y.; Shi, Z.; Feng, S.; Li, J. *Angew. Chem. Int. Ed.* **2012**, *51*, 1412.

(33) Sircar, S. *Ind. Eng. Chem. Res.* **1992**, *31*, 1813.

(34) See for example: Refs 62, 67, 75, 84, 96.
(35) Czepirski, L.; Jagiełło, J. *Chem. Eng. Sci.* **1989**, *44*, 797.
(36) Amankwah, K. A. G.; Schwarz, J. A. *Carbon* **1995**, *33*, 1313.
(37) Langmuir, I. *J. Am. Chem. Soc.* **1918**, *40*, 1361.
(38) See for example: (a) Clarkson, C. R.; Bustin, R. M.; Levy, J. H. *Carbon* **1997**, *35*, 1689. (b) Levy, J. H.; Day, S. J.; Killingley, J. S. *Fuel* **1997**, *76*, 813. (c) Richard, M.-A.; Bénard, P.; Chahine, R. *Adsorption* **2009**, *15*, 43.
(39) Krishna, R.; Long, J. R. *J. Phys. Chem. C* **2011**, *115*, 12941.
(40) See for example: Refs 27a, 28c, 63, 67, 72.
(41) Sillar, K.; Sauer, J. *J. Am. Chem. Soc.* **2012**, *134*, 18354.
(42) He., Y.; Zhou, W.; Yildirim, T.; Chen, B. *Energy Environ. Sci.* **2013**, *6*, 2735.
(43) Saidur, R.; Rezaei, M.; Muzammil, W. K.; Hassan, M. H.; Paria, S.; Hasanuzzaman, M. *Renewable Sustainable Energy Rev.* **2012**, *16*, 5649.
(44) Peng, Y.; Krungleviciute, V.; Eryazici, I.; Hupp, J. T.; Farha, O. K.; Yildirim, T. *J. Am. Chem. Soc.* **2013**, *135*, 11887.
(45) Yilmaz, B.; Trukhan, N.; Müller, U. *Chin. J. Catal.* **2012**, *33*, 3.
(46) Bhatia, S. K.; Myers, A. L. *Langmuir* **2006**, *22*, 1688.
(47) Garrone, E.; Bonelli, B.; Otero Areán, C. *Chem. Phys. Lett.* **2008**, *456*, 68.
(48) NIST Handbook 44 – 2012 Edition, "Specifications, Tolerances, and Other Technical Requirements for Weighing and Measuring Devices", **2012**, D-13.
(49) U.S. Dept. of Energy, **2013**. <www.fueleconomy.gov/feg/ drivehabits.shtml>.
(50) Chang, K. J.; Talu, O. *Appl. Therm. Eng.* **1996**, *16*, 359.
(51) Vasiliev, L. L.; Kanonchik, L. E.; Mishkinis, D. A.; Rabetsky, M. I. *Int. J. Therm. Sci.*, **2000**, *39*, 1047.
(52) Mu, B.; Walton, K. S. *J. Phys. Chem. C* **2011**, *115*, 22748.
(53) (a) Huang, B. L.; Ni, Z.; Millward, A.; McGaughey, A. J. H.; Uher, C.; Kaviany, M.; Yaghi, O. M. *Int. J. Heat Mass Transfer* **2007**, *50*, 405. (b) Liu, D.; Purewal, J. J.; Yang, J.; Sudik, A.; Maurer, S.; Müller, U.; Ni, J.; Siegel, D. J. *Int. J. Hydrogen Energy* **2012**, *37*, 6109.
(54) (a) Aclañiz-Monge, J.; Trautwein, C.; Pérez-Cadenas, M.; Román-Martínez, M. C. *Microporous Mesoporous Mater.* **2006**, *126*, 291. (b) Zacharia, R.; Cossement, D.; Lafi, L.; Chahine, R. *J. Mater. Chem.* **2010**, *20*, 2145. (c) Tagliabue, M.; Rizzo, C.; Milllini, R.; Dietzel, P. D. C.; Blom, R.; Zanardi, S. *J. Porous Mater.* **2011**, *18*, 289. (d) Purewal, J. J.; Liu, D.; Yang, J.; Sudik, A.; Siegel, D. J.; Maurer, S.; Müller, U. *Int. J. Hydrogen Energy* **2012**, *37*, 2723. (e) Peterson, G. W.; DeCoste, J. B.; Glover, T. G.; Huang, Y.; Jasuja, H.; Walton, K. S. *Microporous Mesoporous Mater.* **2013**, *179*, 48.
(55) Tan, J. C.; Cheetham, A. K. *Chem. Soc. Rev.* **2011**, *40*, 1059.
(56) (a) Zhou, W.; Yildirim, T. *Phys. Rev. B* **2006**, *74*, 180301. (b) Wu, H.; Yildirim, T.; Zhou, W. *Phys. Chem. Lett.* **2013**, *4*, 925.
(57) (a) Greenbank, M. **1990**, U.S. Patent 4,972,658. (b) Chang, C. H. **1994**, U.S. Patent 5,308,821.
(58) Arnold, L.; Averlant, G.; Marx, S.; Weickert, M.; Müller, U.; Mertel, J.; Horch, C.; Peksa, M.; Stallmach, F. *Chemie Ingenieur Technik* **2013**, *85*, 1.

(59) (a) Mota, J. P. B. *AIChE J.* **1999**, *45*, 986. (b) Pupier, O.; Goetz, V.; Fiscal, R. *Chem. Eng. Process.* **2005**, *44*, 71.
(60) Lu, Z.; Du, L.; Tang, K.; Bai, J. *Cryst. Growth Des.* **2013**, *13*, 2252.
(61) Lee, J. Y.; Pan, L.; Huang, X.; Emge, T. J.; Li, J. *Adv. Funct. Mater.* **2011**, *21*, 993.
(62) Guo, Z.; Wu, H.; Srinivas, G.; Zhou, Y.; Xiang, S.; Chen, Z.; Yang, Y.; Zhou, W.; O'Keeffe, M.; Chen, B. *Angew. Chem. Int. Ed.* **2011**, *50*, 3178.
(63) Wang, X.-S.; Ma, S.; Rauch, K.; Simmons, J. M.; Yuan, D.; Wang, X.; Yildirim, T.; Cole, W. C.; López, J. J.; de Meijere, A.; Zhou, H.-C. *Chem. Mater.* **2008**, *20*, 3145.
(64) Liu, D.; Wu, H.; Wang, S.; Xie, Z.; Li, J.; Lin, W. *Chem. Sci.* **2012**, *3*, 3032.
(65) Sun, D.; Ma, S.; Simmons, J. M.; Li, J.-R.; Yuan, D.; Zhou, H.-C.*Chem. Commun.* **2010**, *46*, 1329.
(66) Lin, X.; Telepeni, I.; Blake, A. J.; Dailly, A.; Brown, C. M.; Simmons, J. M.; Zoppi, M.; Walker, G. S.; Thomas, K. M.; Mays, T. J.; Hubberstey, P.; Champness, N. R.; Schröder, M. *J. Am. Chem. Soc.* **2009**, *131*, 2159.
(67) Rao, X.; Cai, J.; Yu, J.; He, Y.; Wu, C.; Zhou, W.; Yildirim, T.; Chen, B.; Qian, G. *Chem. Commun.* **2013**, *49*, 6719.
(68) Rallapalli, P.; Patil, D.; Prasanth, K. P.; Somani, R. S.; Jasra, R. V.; Bajaj, H. C. *J. Porous Mater.* **2010**, *17*, 523.
(69) Bourrelly, S.; Llewellyn, P. L.; Serre, C.; Millange, F.; Loiseau, T.; Férey, G. *J. Am. Chem. Soc.* **2005**, *127*, 13519.
(70) Loiseau, T.; Serre, C.; Huguenard, C.; Fink, G.; Taulelle, F.; Henry, M.; Bataille, T.; Férey, G. *Chem. Eur. J.*, 2004, **10**, 1373.
(71) Lyubchyk, A.; Esteves, I. A. A. C.; Cruz, F. J. A. L.; Mota, J. P. B. *J. Phys. Chem. C* **2011**, *115*, 20628.
(72) Duan, X.; Yu, J.; Cai, J.; He, Y.; Wu, C.; Zhou, W.; Yildirim, T.; Zhang, Z.; Xiang, S.; O'Keeffe, M.; Chen, B.; Qian, G. *Chem. Commun.* **2013**, *49*, 2043.
(73) Wilmer, C. E.; Farha, O. K.; Yildirim, T.; Eryazici, I.; Krungleviciute, V.; Sarjeant, A. A.; Snurr, R. Q.; Hupp, J. T. *Energy Envrion. Sci.* **2013**, *6*, 1158.
(74) Eddaoudi, M.; Kim, J.; Rosi, N.; Vodak, D.; Wachter, J.; O'Keeffe, M.; Yaghi, O. M. *Science* **2002**, *296*, 469.
(75) Kim, H.; Samsonenko, D. G.; Das, S.; Kim, G.-H.; Lee, H.-S.; Dybtsev, D. N.; Berdonosova, E. A.; Kim, K. *Chem. Asian J.* **2009**, *4*, 886.
(76) Zhao, X. L.; Sun, D.; Yuan, S.; Feng, S.; Cao, R.; Yuan, D.; Wang, S.; Dou, J.; Sun, D. *Inorg. Chem.* **2012**, *51*, 10350.
(77) Yuan, D.; Zhao, D.; Sun, D.; Zhou, H.-C. *Angew. Chem. Int. Ed.* **2010**, *49*, 5357.
(78) Zhao, D.; Yuan, D.; Yakovenko, A.; Zhou, H.-C. *Chem. Commun.* **2010**, *46*, 4196.
(79) Wang, H.; Getzschmann, J.; Senkovska, I.; Kaskel, S.; *Microporous Mesoporous Mater.* **2008**, *116*, 653.
(80) He, Y.; Zhang, Z.; Xiang, S.; Wu, H.; Fronczek, F. R.; Zhou, W.; Krishna, R.; O'Keeffe, M.; Chen, B. *Chem. Eur. J.* **2012**, *18*, 1901.
(81) He, Y.; Xiang, S.; Zhang, Z.; Xiong, S.; Wu, C.; Zhou, W.; Yildirim, T.; Krishna, R.; Chen, B. *J. Mater. Chem. A* **2013**, *1*, 2543.

(82) Klein, N.; Hoffmann, H. C.; Cadiau, A.; Getzschmann, J.; Lohe, M. R.; Paasch, S.; Heydenreich, T.; Adil, K.; Senkovska, I.; Brunner, E.; Kaskel, S. *J. Mater. Chem.* **2012**, *22*, 10303.
(83) Lu, W.; Yuan, D.; Makal, T. A.; Li, J.-R.; Zhou, H.-C. *Angew. Chem. Int. Ed.* **2012**, *51*, 1580.
(84) Park, H. J.; Lim, D.-W.; Yang, W. S.; Oh, T.-R.; Suh, M. P. *Chem. Eur. J.* **2011**, ***17***, 7251.
(85) Zhao, X. L.; Sun, D.; Yuan, S.; Feng, S.; Cao, R.; Yuan, D.; Wang, S.; Dou, J.; Sun, D. *Inorg. Chem.* **2012**, 51, 10350.
(86) Rowsell, J. L. C.; Yaghi, O. M. *J. Am. Chem. Soc.* **2006**, *128*, 1304.
(87) He, Y.; Furukawa, H.; Wu, C.; O'Keeffe, M.; Krishna, R.; Chen, B. *Chem. Commun.* **2013**, *49*, 6773.
(88) Yuan, D.; Zhao, D.; Sun, D.; Zhou, H.-C. *Angew. Chem. Int. Ed.* **2010**, *49*, 5357.
(89) Klein, N.; Senkovska, I.; Baburin, I. A.; Grünker, R.; Stoeck, U.; Schlichtenmayer, M.; Streppel, B.; Mueller, U.; Leoni, S.; Hirscher, M.; Kaskel, S. *Chem. Eur. J.* **2011**, *17*, 13007.
(90) Pérez-Pellitero, J.; Amrouche, H.; Siperstein, F. R.; Pirngruber, G.; Nieto-Draghi, C.; Chaplais, G.; Simon-Masseron, A.; Bazer-Bachi, D.; Peralta, D.; Bats, N. Chem. Eur. J., **2010**, *16*, 1560.
(91) Prasad, T. K.; Suh, M. P. *Chem. Eur. J.* **2012**, *18*, 8673.
(92) Mendoza-Cortés, J. L.; Han, S. S.; Furukawa, H.; Yaghi, O. M.; Goddard III, W. A. *J. Phys. Chem. A* **2010**, *114*, 10824.
(93) Noro, S.; Kitaura, R.; Kondo, M.; Kitagawa, S.; Ishii, T.; Matsuzaka, H.; Yamashita, M. *J. Am. Chem. Soc.* **2002**, *124*, 2568.
(94) Noro, S.; Kitagawa, S.; Kondo, M.; Seki, K. *Angew. Chem. Int. Ed.* **2000**, *39*, 2082.
(95) Park, M.; Moon, D.; Yoon, J. W.; Chang, J.-S.; Lah, M. S. *Chem. Commun.* **2009**, 2026.
(96) Prasad, T. K.; Hong, D. H.; Suh, M. P. *Chem. Eur. J.* **2010**, *16*, 14043.
(97) Senkovska, I.; Hoffmann, F.; Fröba, M.; Getzschmann, J.; Böhlmann, W.; Kaskel, S. *Microporous Mesoporous Mater.* **2009**, *122*, 93.
(98) Das, M. C.; Xu, H.; Wang, Z.; Srinivas, G.; Zhou, W.; Yue, Y.-F.; Nesterov, V. N.; Qian, G.; Chen, B. *Chem. Commun.* **2011**, *47*, 11715.
(99) Llewellyn, P. L.; Bourrelly, S.; Serre, C.; Vimont, A.; Daturi, M.; Hamon, L.; Weireld, G. D.; Chang, J.-S.; Hong, D.-Y.; Hwang, Y. K.; Jhung, S. H.; Férey, G. *Langmuir* **2008**, *24*, 7245.
(100) Feldblyum, J. I.; Dutta, D.; Wong-Foy, A. G.; Dailly, A.; Imirzian, J.; Gidley, D. W.; Matzger, A. J. *Langmuir* **2013**, *29*, 8146.
(101) Klein, N.; Senkovska, I.; Gedrich, K.; Stoeck, U.; Henschel, A.; Mueller, U.; Kaskel, S. *Angew. Chem. Int. Ed.* **2009**, *48*, 9954.
(102) Prasad, T. K.; Suh, M. P. *Chem. Eur. J.* **2012**, *18*, 8673.
(103) Han, D.; Jian, F.-L.; Wu, M.-Y.; Chen, L.; Chen, Q.-H.; Hong, M.-C. *Chem. Commun.* **2011**, *47*, 9861.
(104) Pérez-Pellitero, J.; Amrouche, H.; Siperstein, F. R.; Pirngruber, G.; Nieto-Draghi, C.; Chaplais, G.; Simon-Masseron, A.; Bazer-Bachi, D.; Peralta, D.; Bats, N. *Chem. Eur. J.* **2010**, *16*, 1560.

(105) Yan, Y.; Yang, S.; Blake, A. J.; Lewis, W.; Poirier, E.; Barnett, S. A.; Champness, N. R.; Schröder, M. *Chem. Commun.* **2011**, *47*, 9995.
(106) Sharma, M. K.; Senkovska, I.; Kaskel, S.; Bharadwaj, P. K. *Inorg. Chem.* **2011**, *50*, 539.
(107) Gedrich, K.; Senkovska, I.; Klein, N.; Stoeck, U.; Henschel, A.; Lohe, M. R.; Baburin, I. A.; Mueller, U.; Kaskel, S. *Angew. Chem. Int. Ed.* **2010**, *49*, 8489.
(108) Grünker, R.; Senkovska, I.; Biedermann, R.; Klein, N.; Lohe, M. R.; Müller, P.; Kaskel, S. *Chem. Commun.* **2011**, *47*, 490.
(109) Konda, M.; Shimamure, M.; Noro, S.; Minakoshi, S.; Asami, A.; Seki, K.; Kitagawa, S. *Chem. Mater.* **2000**, *12*, 1288.
(110) Park, H. J.; Cheon, Y. E.; Suh, M. P. *Chem. Eur. J.* **2010**, *16*, 11662.
(111) (a) Seki, K. *Chem. Commun.*, 2001, 1496. (b) Seki, K.; Mori, W. *J. Phys. Chem. B* **2002**, *106*, 1380.
(112) Llewellyn, P. L.; Bourrelly, S.; Vagner, C.; Heymans, N.; Leclerc, H.; Ghoufi, A.; Bazin, P.; Vimont, A.; Daturi, M.; Devic, T.; Serre, C.; Weireld, G. D.; Maurin, G. *J. Phys. Chem. C.* **2013**, *117*, 962.
(113) Kitaura, R.; Seki, K.; Akiyama, G.; Kitagawa, S. *Angew. Chem. Int. Ed.* **2003**, *42*, 428.
(114) Furukawa, H.; Yaghi, O. M. *J. Am. Chem. Soc.* **2009**, *131*, 8875.
(115) Yuan, D.; Lu, W.; Zhao, D.; Zhou, H.-C. *Adv. Funct. Mater.* **2011**, *23*, 3723.
(116) (a) Rolniak, P. D.; Kobayashi, R. *AIChE J.* **1980**, *26*, 616. (b) Dirar, Q. H.; Loughlin, K. F. *Adsorption* **2013**, *19*, 1149.

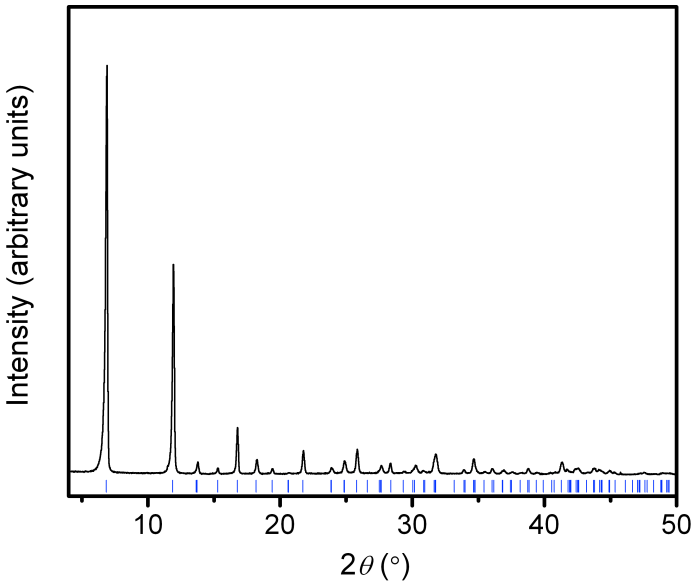

Figure 3.S1. Powder X-ray diffraction pattern of as-synthesized Ni_2(dobdc) (λ = 1.5418 Å). Calculated peak positions from the crystal structure are shown (blue tick marks).

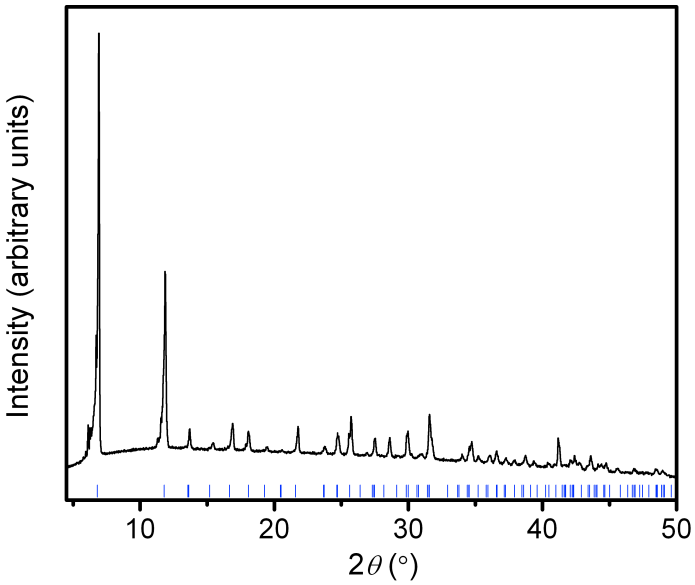

Figure 3.S2. Powder X-ray diffraction pattern of as-synthesized Co_2(dobdc) (λ = 1.5418 Å). Calculated peak positions from the crystal structure are shown (blue tick marks).

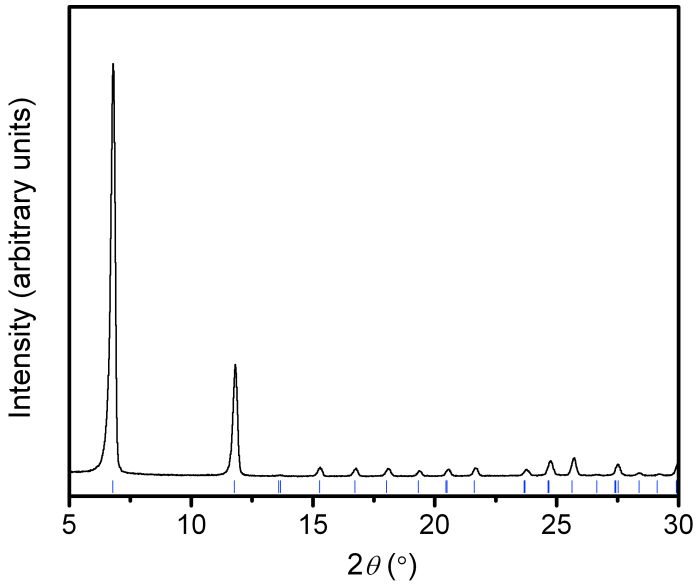

Figure 3.S3. Powder X-ray diffraction pattern of as-synthesized Mg_2(dobdc) (λ = 1.5418 Å). Calculated peak positions from the crystal structure are shown (blue tick marks).

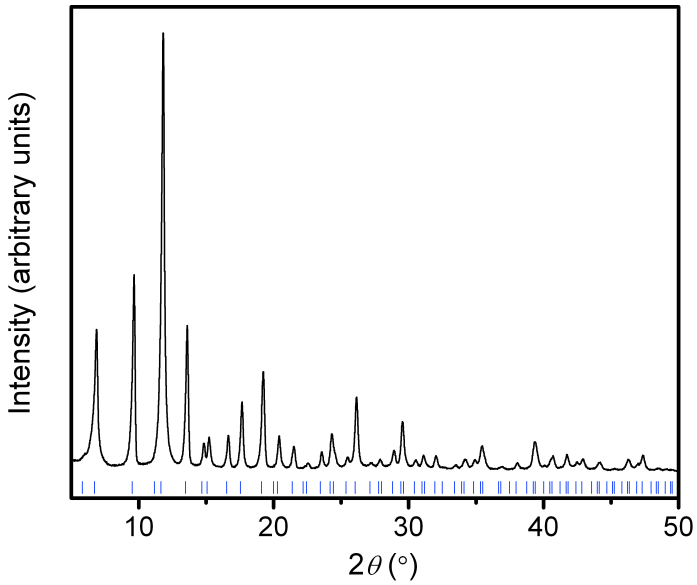

Figure 3.S4. Powder X-ray diffraction pattern of as-synthesized HKUST-1 (λ = 1.5418 Å). Calculated peak positions from the crystal structure are shown (blue tick marks).

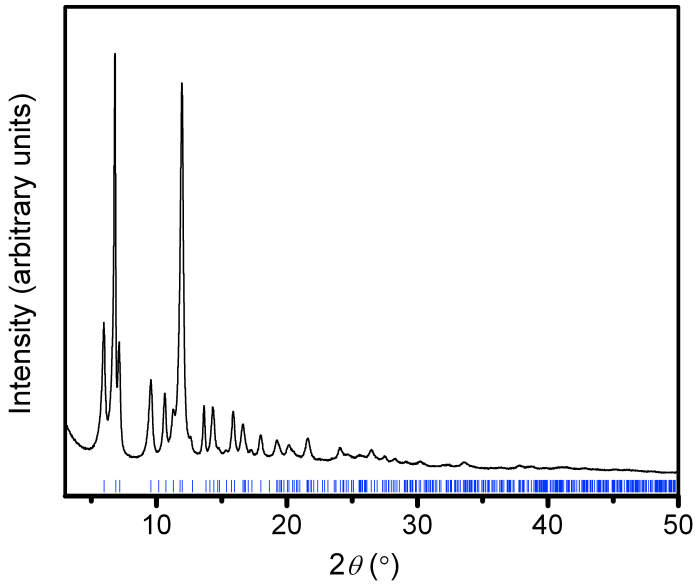

Figure 3.S5. Powder X-ray diffraction pattern of as-synthesized PCN-14 (λ = 1.5418 Å). Calculated peak positions from the crystal structure are shown (blue tick marks).

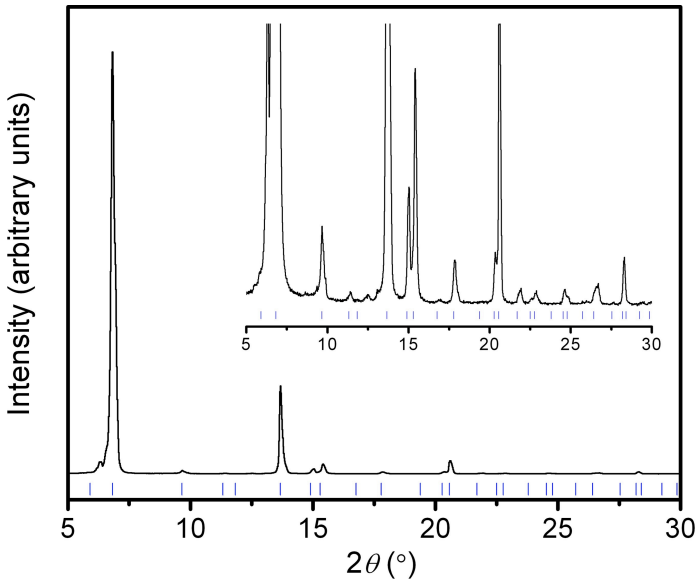

Figure 3.S6. Powder X-ray diffraction pattern of as-synthesized MOF-5 (λ = 1.5418 Å). The baseline is magnified in the inset to make the peak positions more obvious. Calculated peak positions from the crystal structure are shown (blue tick marks).

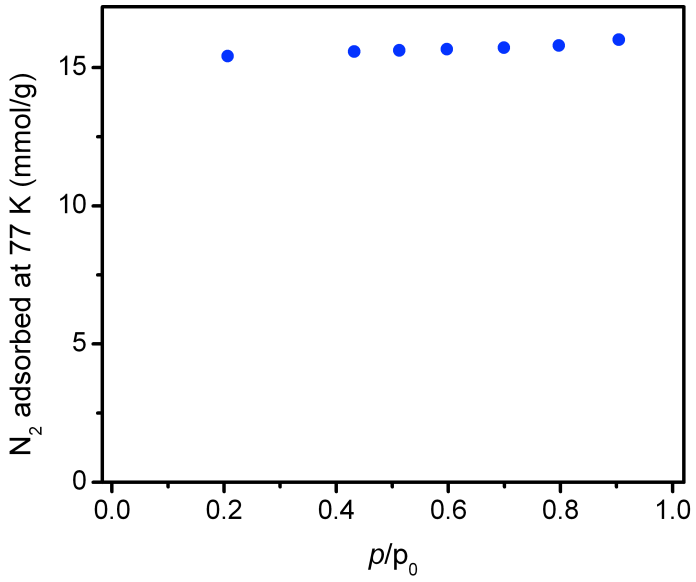

Figure 3.S7. 77 K N_2 adsorption isotherm for Ni_2(dobdc) activated at 180 ºC in the HPVA high-pressure adsorption cell. The calculated Langmuir surface area is 1574 m^2/g (n_{sat} = 16.1 mmol/g), and the total pore volume at p/p_0 = 0.9 is 0.56 cm^3/g. Here, n_{sat} is the amount of N_2 adsorbed at saturation (mmol/g), p is the pressure, and p_0 is the saturation pressure of N_2.

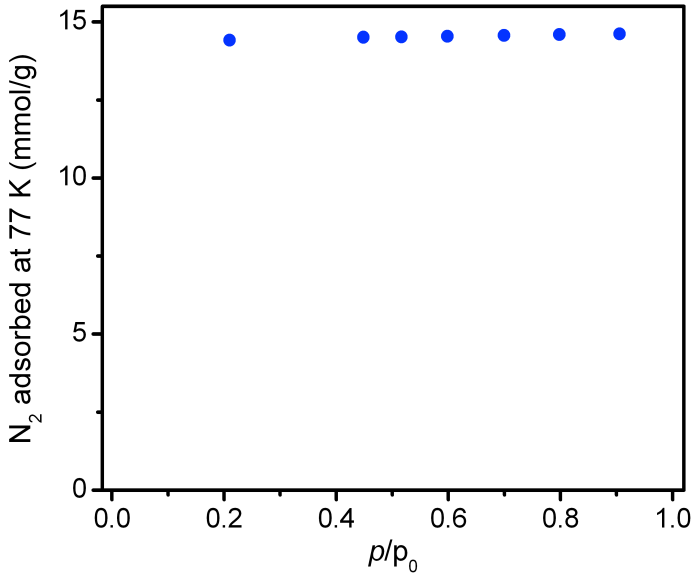

Figure 3.S8. 77 K N_2 adsorption isotherm for Co_2(dobdc) activated at 180 ºC in the HPVA high-pressure adsorption cell. The calculated Langmuir surface area is 1433 m^2/g (n_{sat} = 14.7 mmol/g), and the total pore volume at p/p_0 = 0.9 is 0.51 cm^3/g.

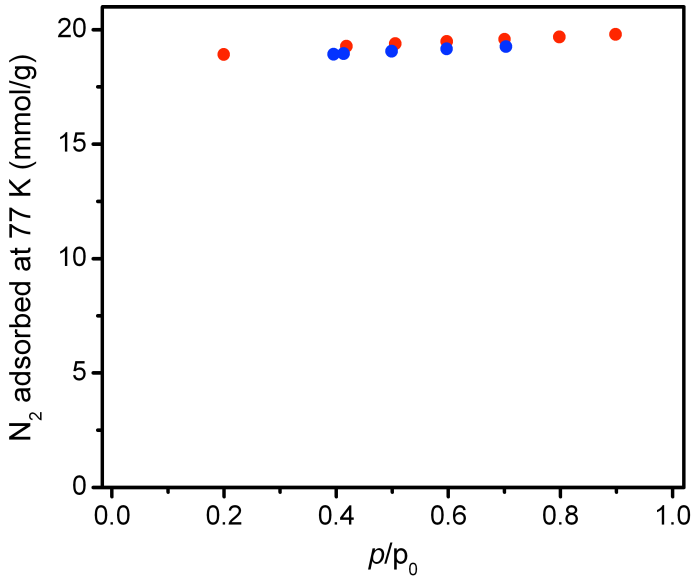

Figure 3.S9. 77 K N_2 adsorption isotherm for Mg_2(dobdc) activated at 180 ºC in an ASAP-2020 low-pressure sample holder (red) and the HPVA high-pressure adsorption cell (blue). The calculated Langmuir surface area is 1957 m^2/g (n_{sat} = 20.1 mmol/g), and the total pore volume at p/p_0 = 0.9 is 0.69 cm^3/g.

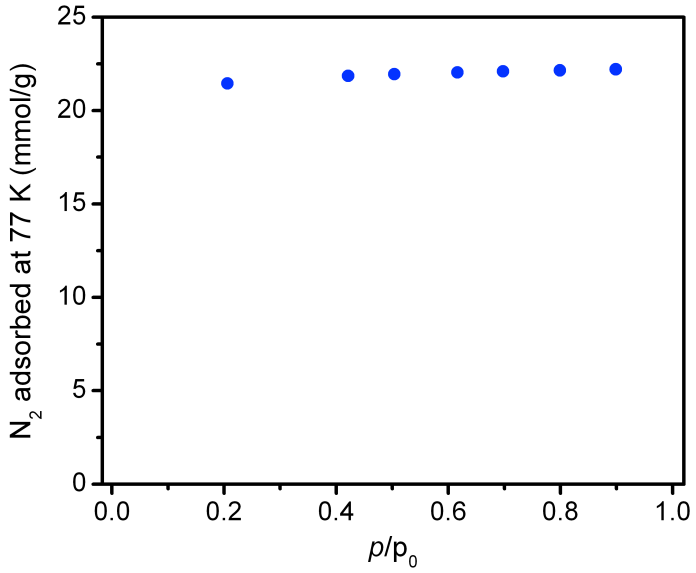

Figure 3.S10. 77 K N_2 adsorption isotherm for HKUST-1 activated at 150 ºC in the HPVA high-pressure adsorption cell. The calculated Langmuir surface area is 2190 m^2/g (n_{sat} = 22.5 mmol/g), and the total pore volume at p/p_0 = 0.9 is 0.77 cm^3/g.

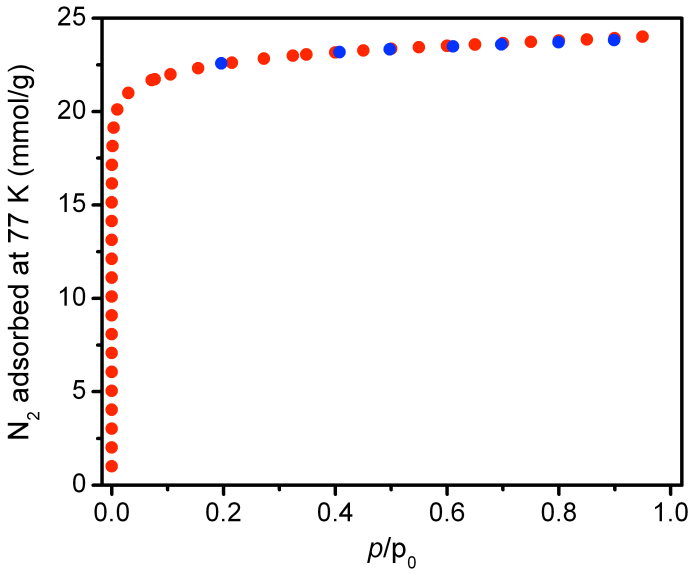

Figure 3.S11. 77 K N_2 adsorption isotherm for PCN-14 activated at 120 ºC in an ASAP-2020 low-pressure sample holder (red) and the HPVA high-pressure adsorption cell (blue). The calculated Langmuir surface area is 2360 m^2/g (n_{sat} = 24.2 mmol/g), and the total pore volume at p/p_0 = 0.9 is 0.83 cm^3/g. The calculated BET surface area is 1984 m^2/g.

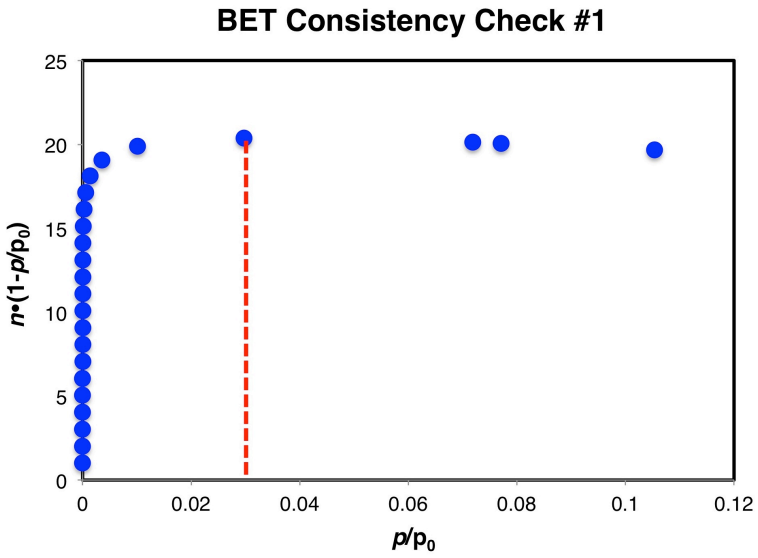

Figure 3.S12. Plot of $n\bullet(1\text{-}p/p_0)$ vs. p/p_0 to determine the maximum p/p_0 used in the BET linear fit according to the first BET consistency criterion.

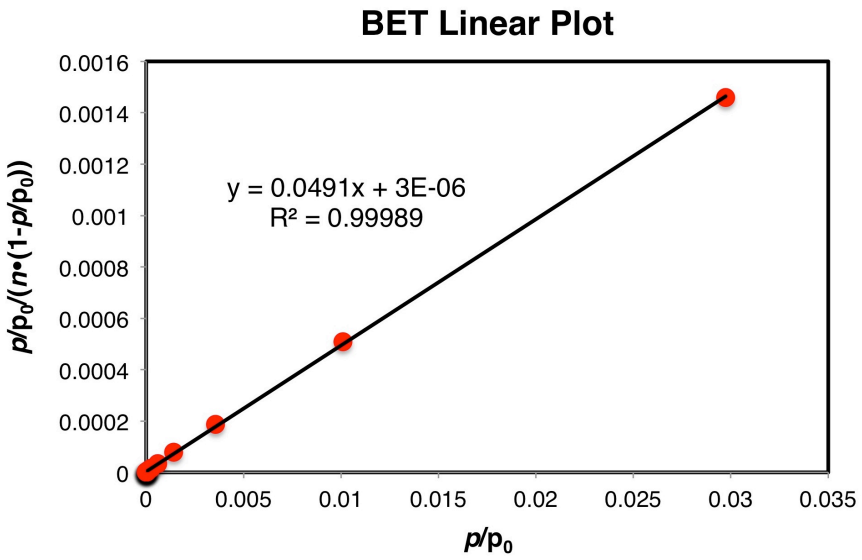

Figure 3.S13. Plot of $p/p_0/(n\bullet(1-p/p_0))$ vs. p/p_0 to determine the BET surface area. The slope of the best fit line for $p/p_0 < 0.03$ is 0.049, and the y-intercept is 2.9 x 10^{-6}, which satisfies the second BET consistency criterion. This results in a saturation capacity of 20.3 mmol/g and a BET surface area of 1984 m^2/g.

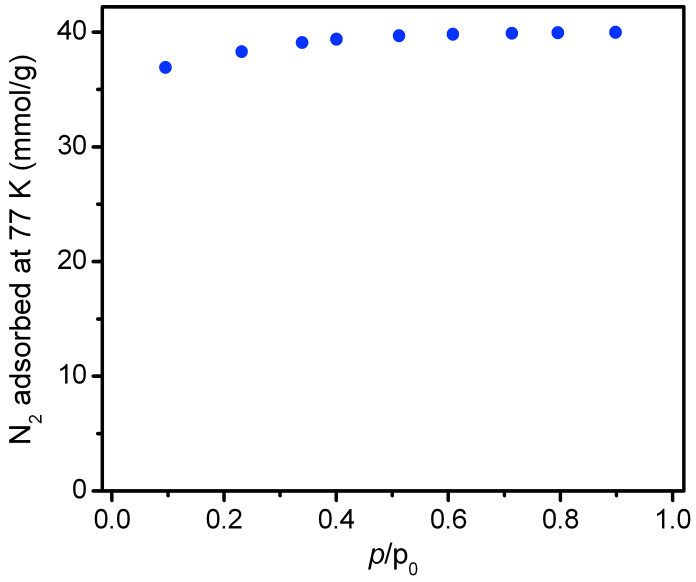

Figure 3.S14. 77 K N_2 adsorption isotherm for MOF-5 activated at 150 ºC in the HPVA high-pressure adsorption cell. The calculated Langmuir surface area is 3961 m^2/g (n_{sat} = 40.6 mmol/g), and the total pore volume at p/p_0 = 0.9 is 1.4 cm^3/g.

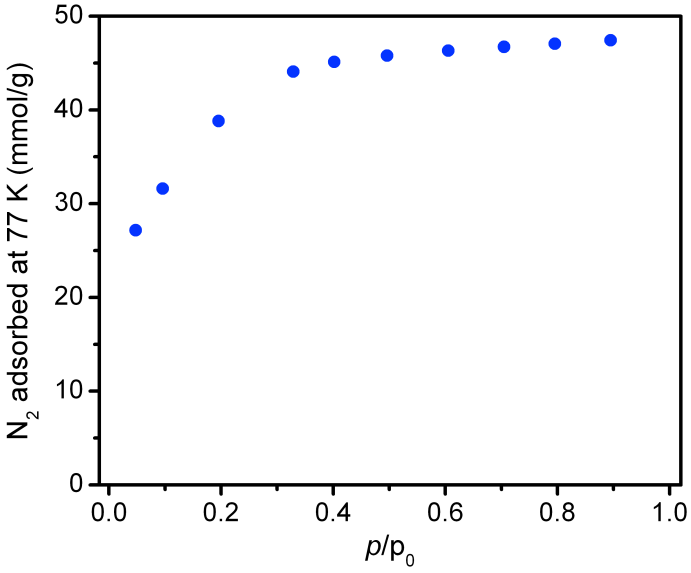

Figure 3.S15. 77 K N_2 adsorption isotherm for AX-21 activated at 200 ºC in the HPVA high-pressure adsorption cell. The calculated Langmuir surface area is 4880 m^2/g (n_{sat} = 50.1 mmol/g), and the total pore volume at p/p_0 = 0.9 is 1.64 cm^3/g.

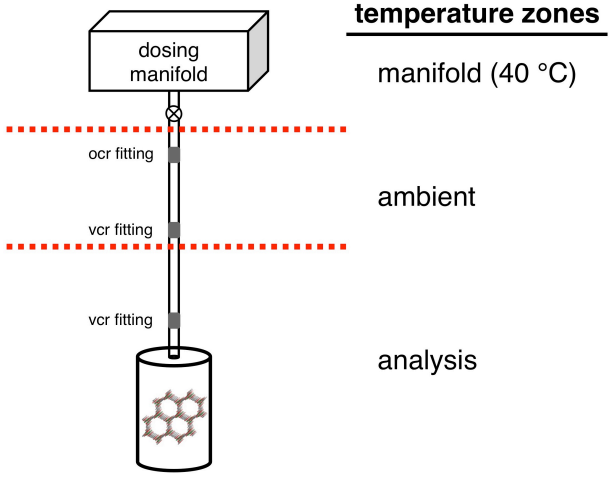

Figure 3.S16. For the HPVA-II-100 high-pressure instrument, there are three distinct temperature zones on the sample holder: 1) manifold zone inside a heated enclosure that contains both the upper part of the sample of the sample holder (3.5 mL) and the calibrated dosing volume, 2) ambient zone that is the upper portion of the sample holder outside of the constant temperature analysis bath (5-6 mL), and 3) analysis temperature zone that is the lower portion of the sample holder inside the constant temperature bath (4-5 mL).

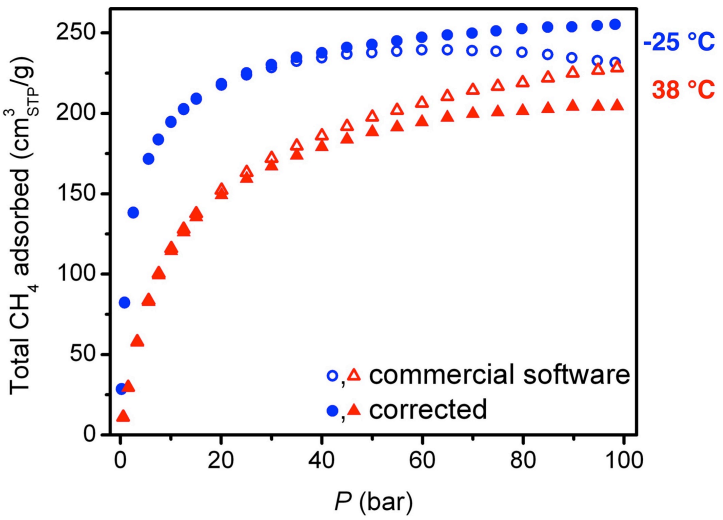

Figure 3.S17. Using the default analysis routine of the HPVA software can lead to large errors in the free space of the sample holder that is in each temperature zone, causing large errors in the resulting adsorption isotherm, especially at the higher pressures where temperature dependent nonideality corrections are most significant.

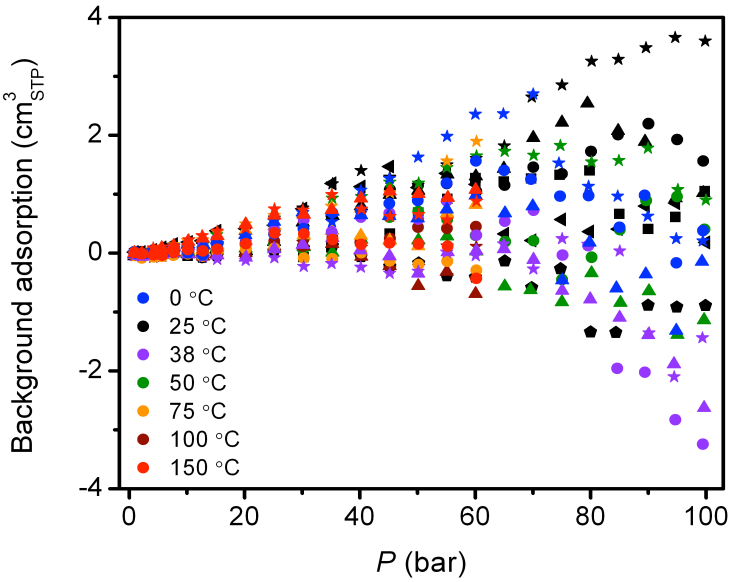

Figure 3.S18. Background CH_4 adsorption isotherms at 0, 25, 38, 50, 75, 100, and 150 °C for the HPVA sample holder containing 0.34 cm^3 of glass beads.

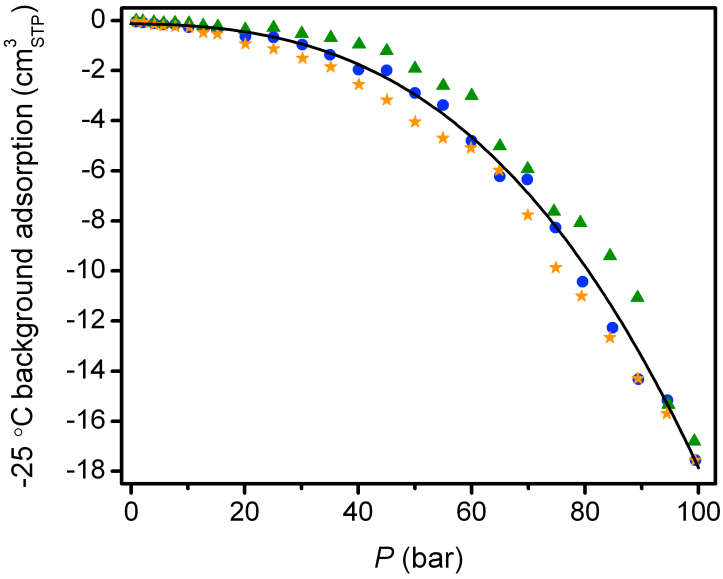

Figure 3.S19. Background CH_4 adsorption isotherms at −25 °C for the HPVA sample holder containing 0.34 cm^3 of glass beads. The black line represents a 3rd order polynomial fit to the background adsorption that was subsequently applied as a correction to all isotherms at −25 °C. The background adsorption is most like the result of a temperature gradient between the ambient and analysis zones on the sample holder.

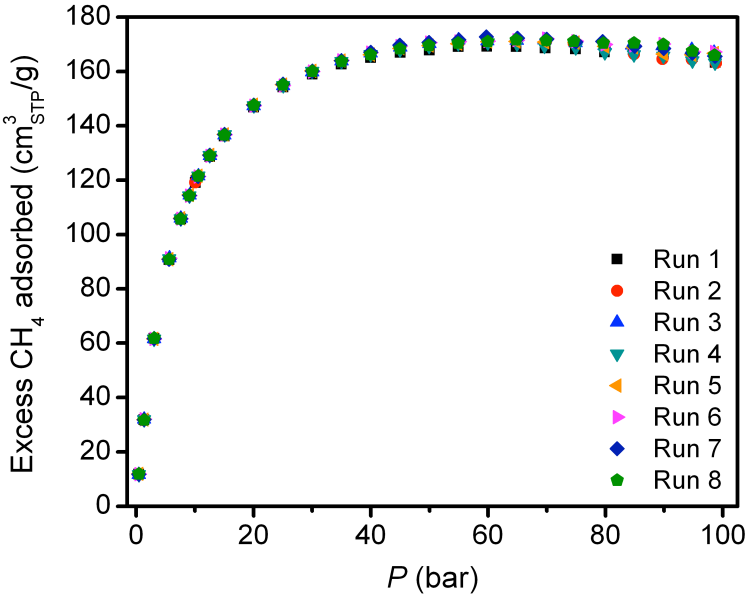

Figure 3.S20. Excess CH_4 adsorption isotherms for Ni_2(dobdc) at 25 °C from 0 to 100 bar repeated eight times.

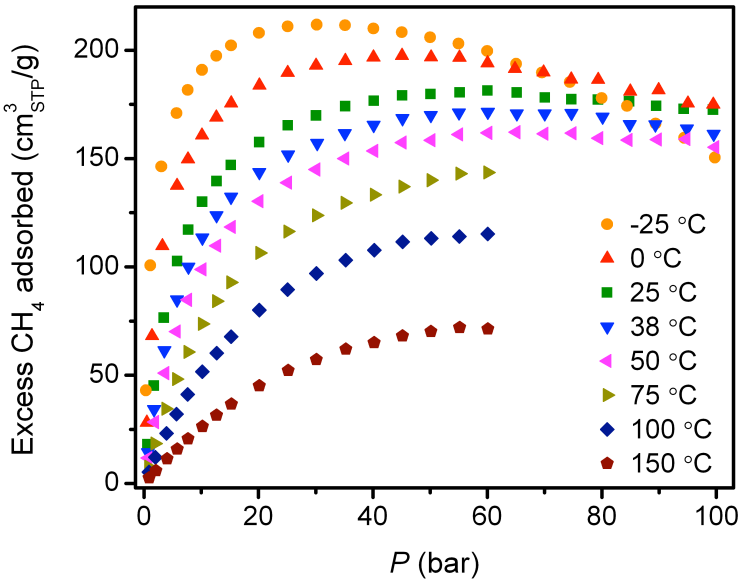

Figure 3.S21. Excess CH_4 adsorption isotherms for Ni_2(dobdc).

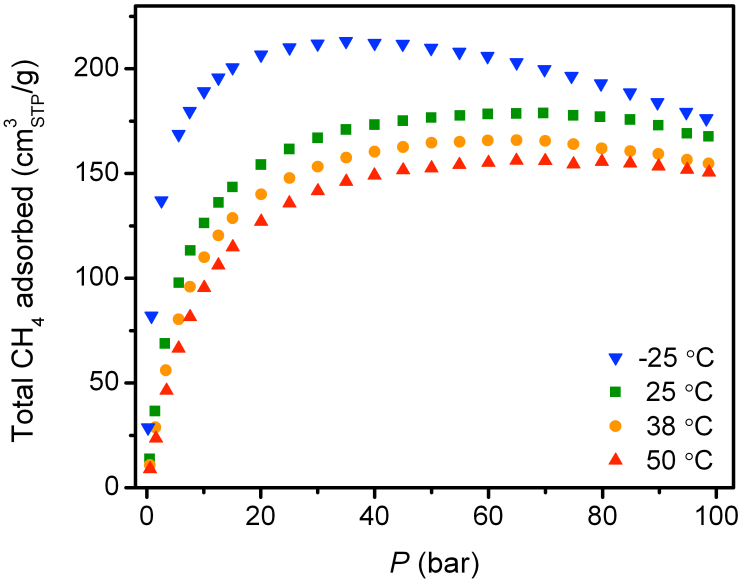

Figure 3.S22. Excess CH_4 adsorption isotherms for Co_2(dobdc).

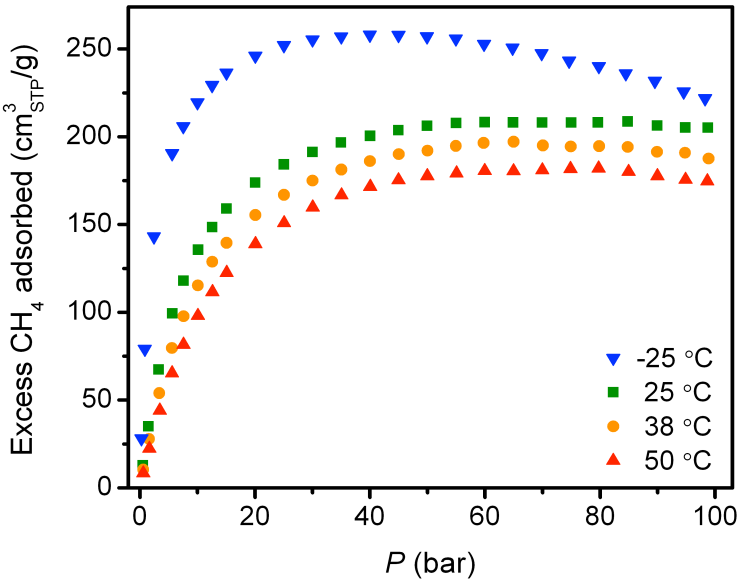

Figure 3.S23. Excess CH_4 adsorption isotherms for Mg_2(dobdc).

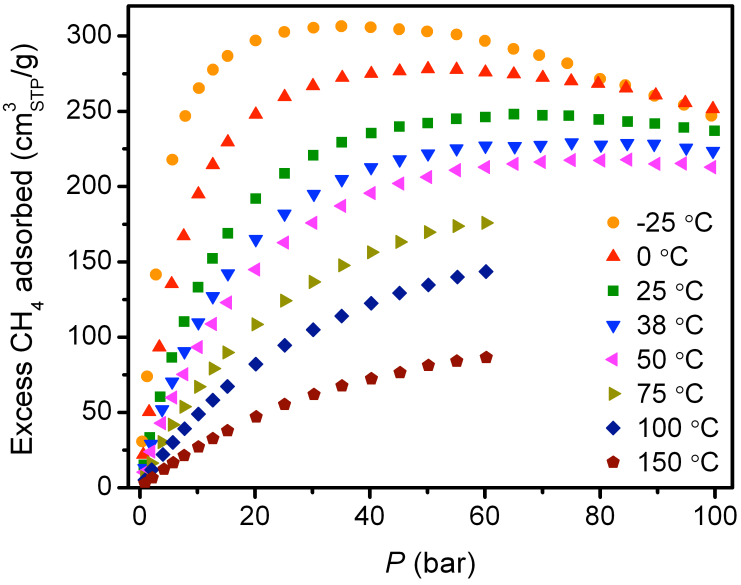

Figure 3.S24. Excess CH_4 adsorption isotherms for HKUST-1.

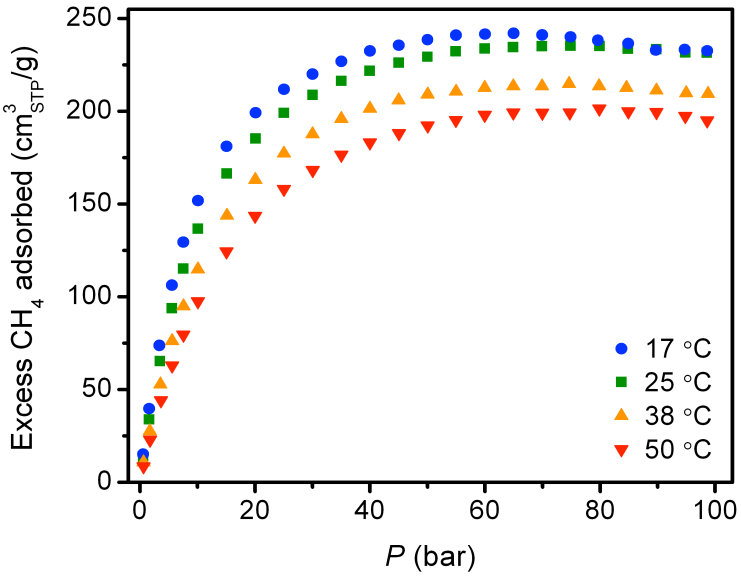

Figure 3.S25. Excess CH_4 adsorption isotherms for PCN-14.

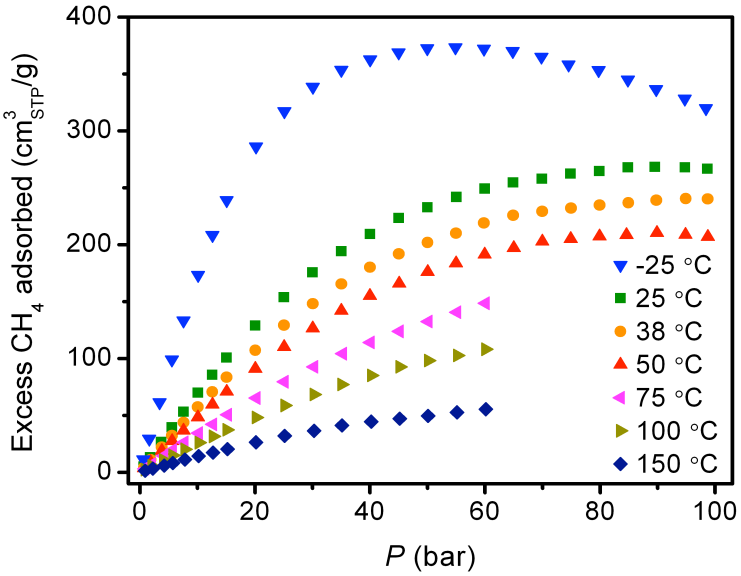

Figure 3.S26. Excess CH_4 adsorption isotherms for MOF-5.

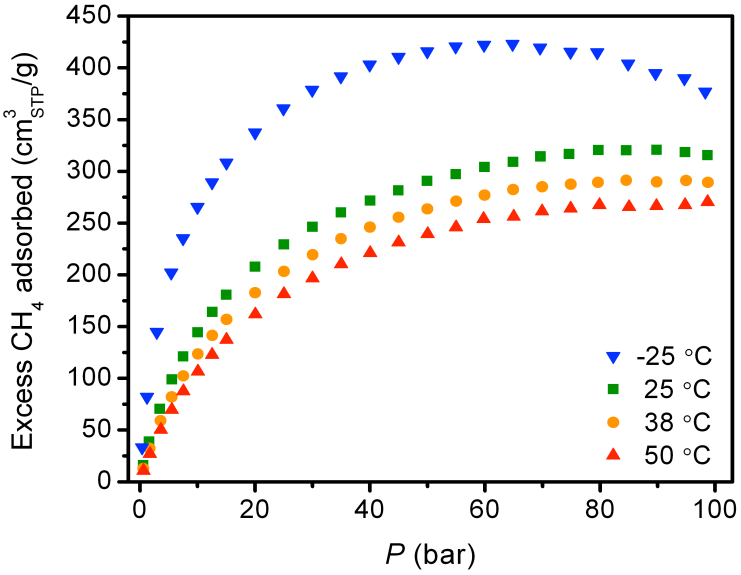

Figure 3.S27. Excess CH_4 adsorption isotherms for AX-21.

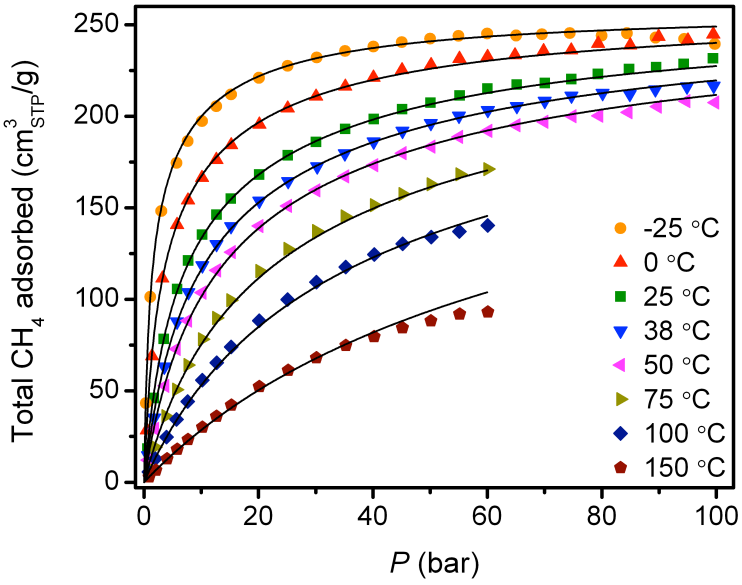

Figure 3.S28. Total CH_4 adsorption isotherms for Ni_2(dobdc) at −25, 0, 25, 38, 50, 75, 100, and 150 °C and the corresponding dual-site Langmuir fits (black lines). See Table 3.S3 for the dual-site Langmuir parameters.

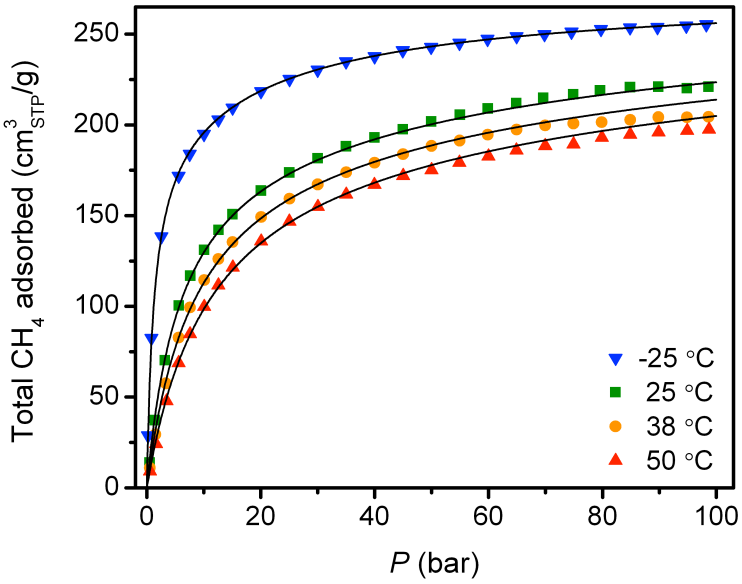

Figure 3.S29. Total CH_4 adsorption isotherms for Co_2(dobdc) at −25, 25, 38, 50 °C and the corresponding dual-site Langmuir fits (black lines). See Table 3.S3 for the dual-site Langmuir parameters.

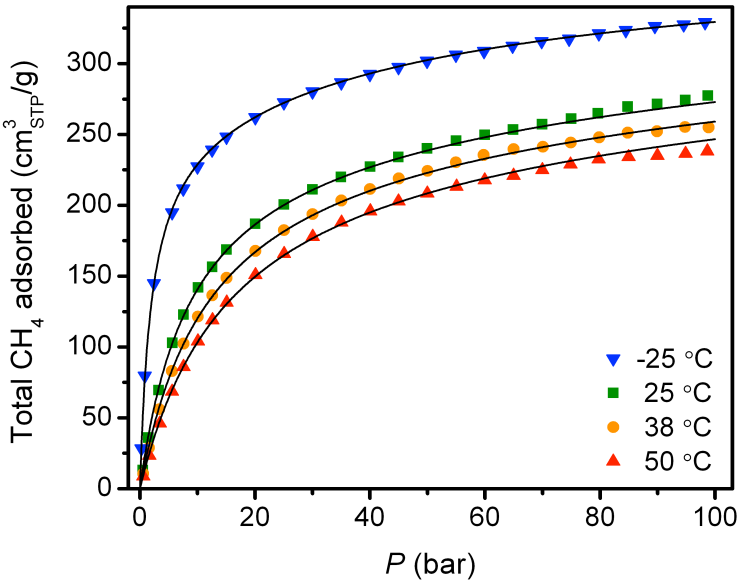

Figure 3.S30. Total CH_4 adsorption isotherms for Mg_2(dobdc) at −25, 25, 38, 50 °C and the corresponding dual-site Langmuir fits (black lines). See Table 3.S3 for the dual-site Langmuir parameters.

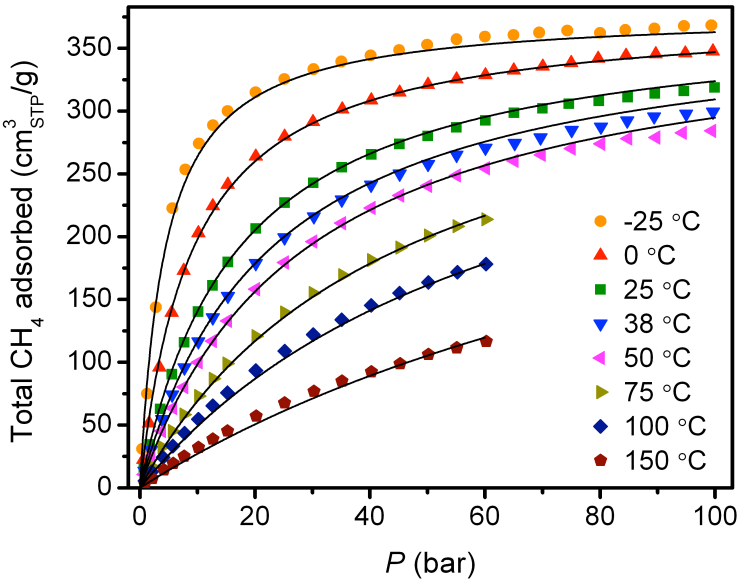

Figure 3.S31. Total CH_4 adsorption isotherms for HKUST- at −25, 0, 25, 38, 50, 75, 100, and 150 °C and the corresponding single-site Langmuir fits (black lines). See Table 3.S3 for the single-site Langmuir parameters.

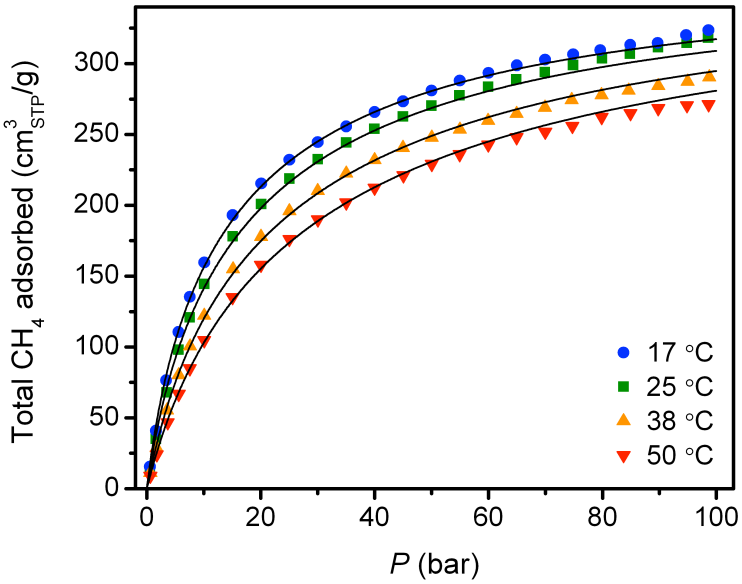

Figure 3.S32. Total CH_4 adsorption isotherms for PCN-14 at 17, 25, 38, 50 °C and the corresponding dual-site Langmuir fits (black lines). See Table 3.S3 for the dual-site Langmuir parameters.

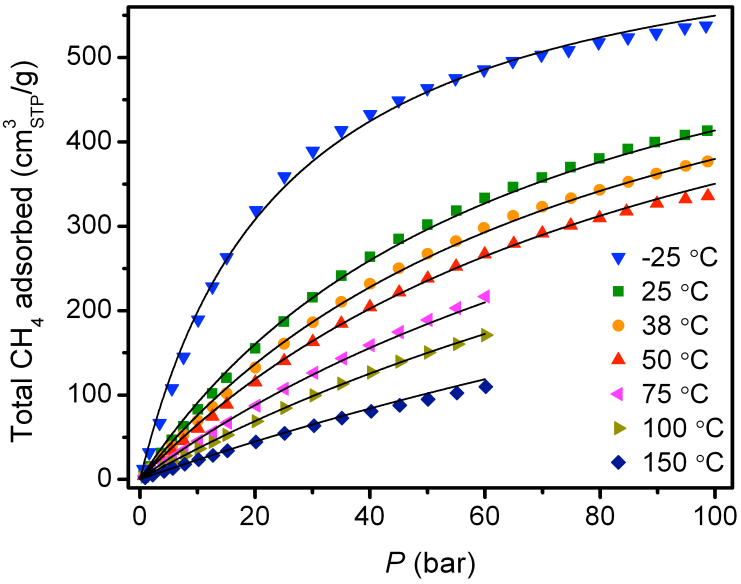

Figure 3.S33. Total CH_4 adsorption isotherms for MOF-5 at −25, 25, 38, 50, 75, 100, and 150 °C and the corresponding single-site Langmuir fits (black lines). See Table 3.S3 for the single-site Langmuir parameters.

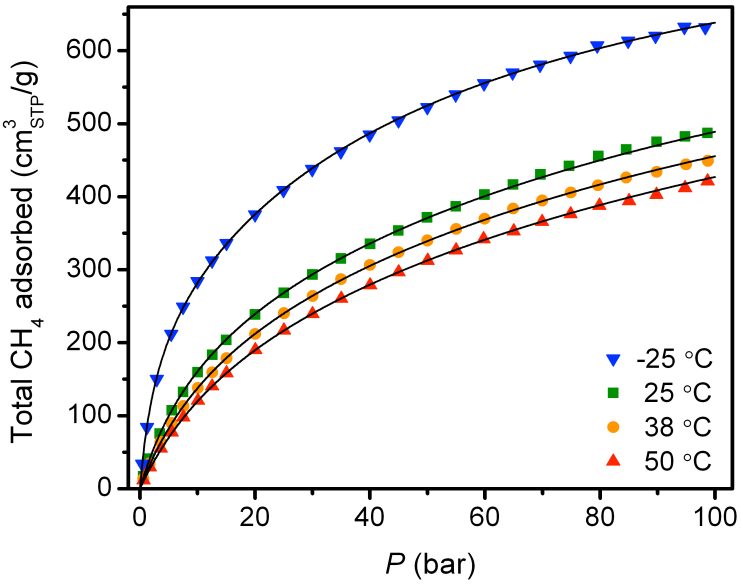

Figure 3.S34. Total CH_4 adsorption isotherms for AX-21 at −25, 25, 38, 50 °C and the corresponding dual-site Langmuir fits (black lines). See Table 3.S3 for the dual-site Langmuir parameters.

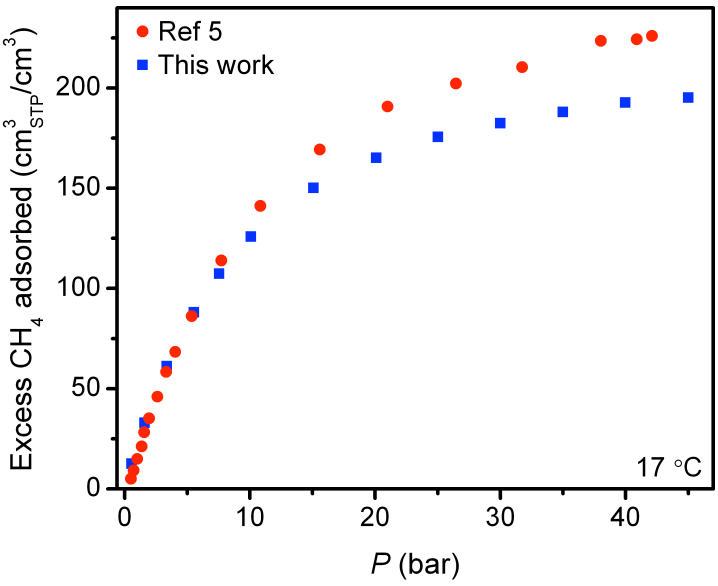

Figure 3.S35. Comparison of the excess CH_4 adsorption isotherms at 17 °C for PCN-14 as originally reported and as measured in this work.

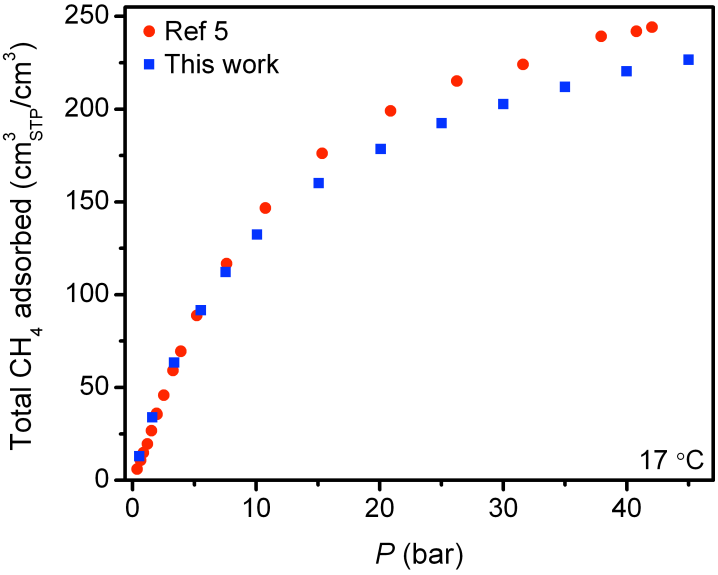

Figure 3.S36. Comparison of the total CH_4 adsorption isotherms at 17 °C for PCN-14 as originally reported and as measured in this work.

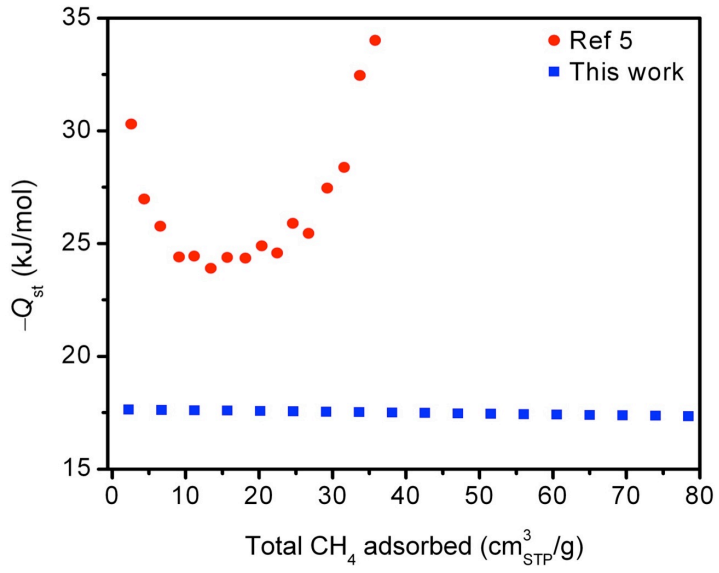

Figure 3.S37. Comparison of the CH_4 isosteric heats of adsorption for PCN-14 as originally reported and as measured in this work.

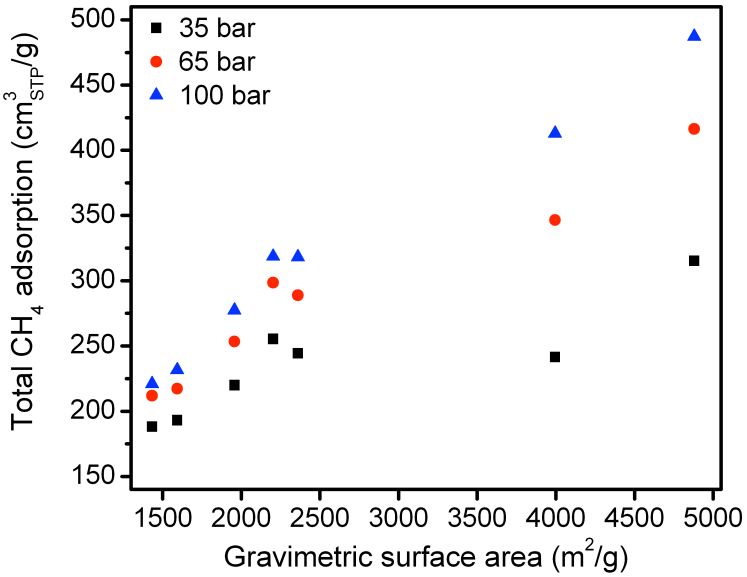

Figure 3.S38. There is a moderate correlation between gravimetric surface area and total gravimetric CH_4 adsorption at 25 °C and 35, 65, and 100 bar for M_2(dobdc) (M = Ni, Co, Mg), PCN-14, HKUST-1, and AX-21.

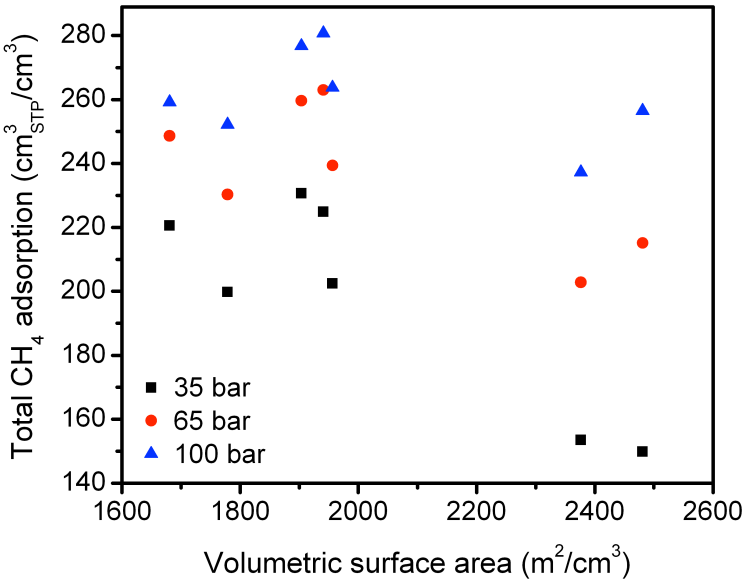

Figure 3.S39. There is little correlation between volumetric surface area and total volumetric CH_4 adsorption at 25 °C and 35, 65, and 100 bar for M_2(dobdc) (M = Ni, Co, Mg), PCN-14, HKUST-1, and AX-21.

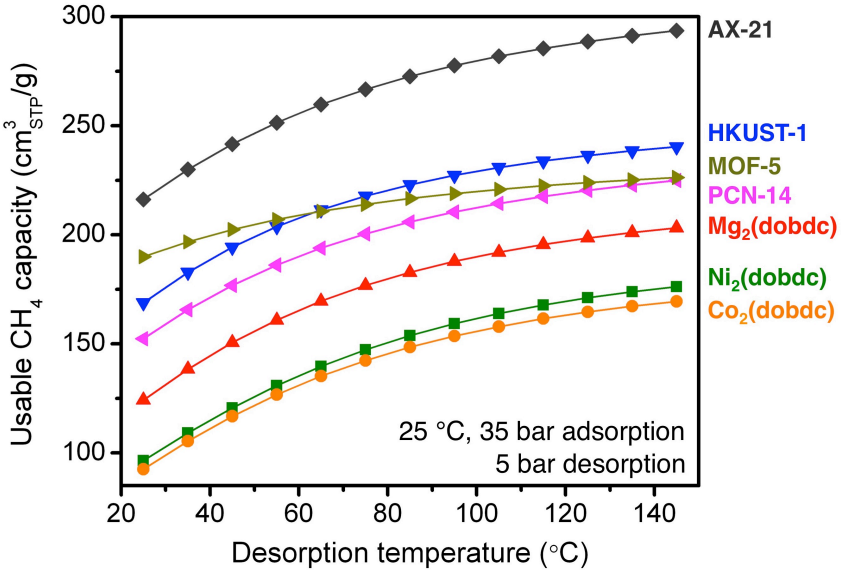

Figure 3.S40. The gravimetric usable CH_4 capacity as a function of desorption temperature for adsorption at 25 °C and 35 bar and desorption at 5 bar.

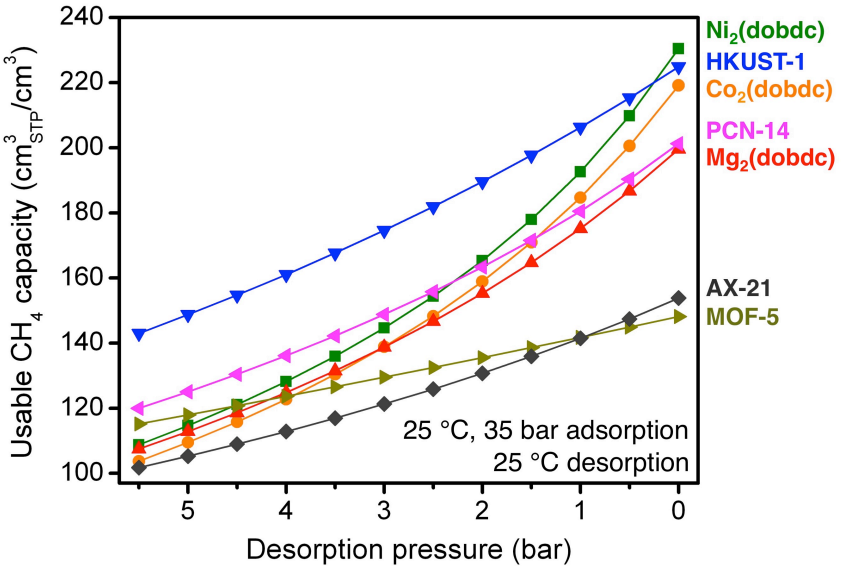

Figure 3.S41. The volumetric usable CH_4 capacity as a function of desorption pressure for adsorption at 25 °C and 35 bar and desorption at 25 °C.

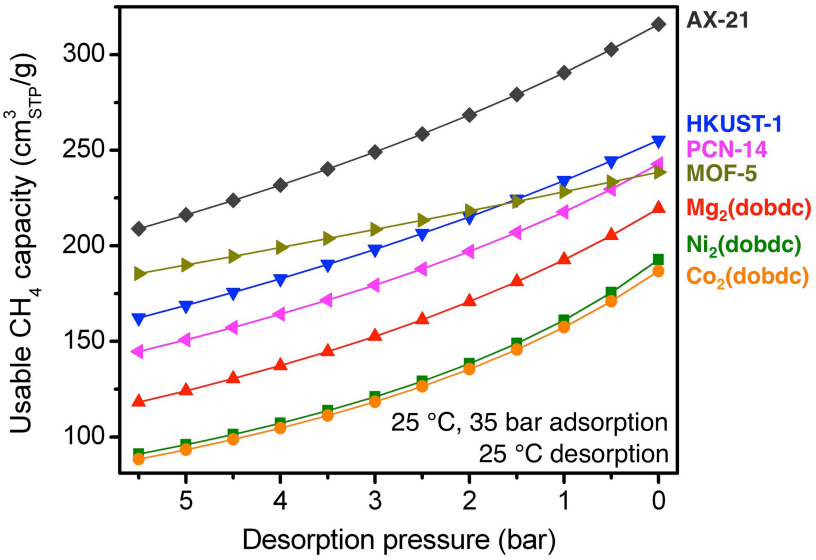

Figure 3.S42. The gravimetric usable CH_4 capacity as a function of desorption pressure for adsorption at 25 °C and 35 bar and desorption at 25 °C.

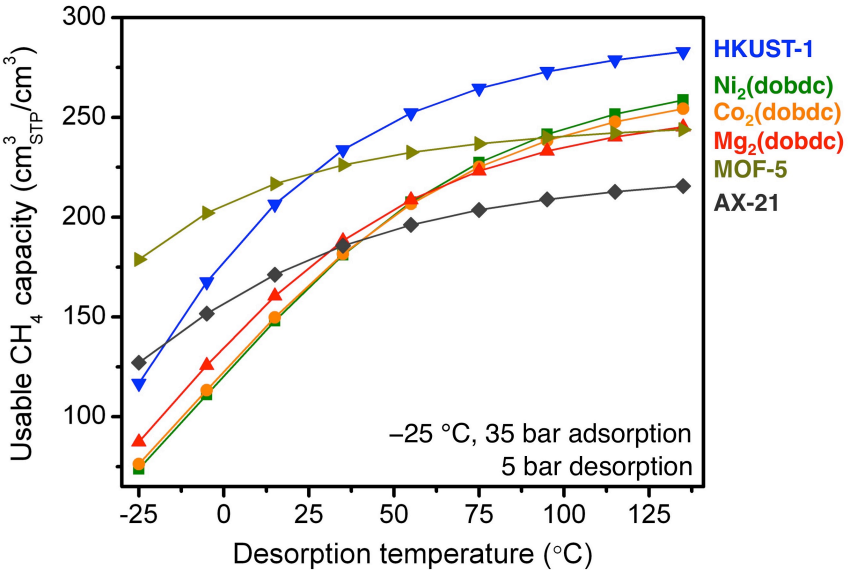

Figure 3.S43. The volumetric usable CH_4 capacity as a function of desorption temperature for adsorption at −25 °C and 35 bar and desorption at 5 bar.

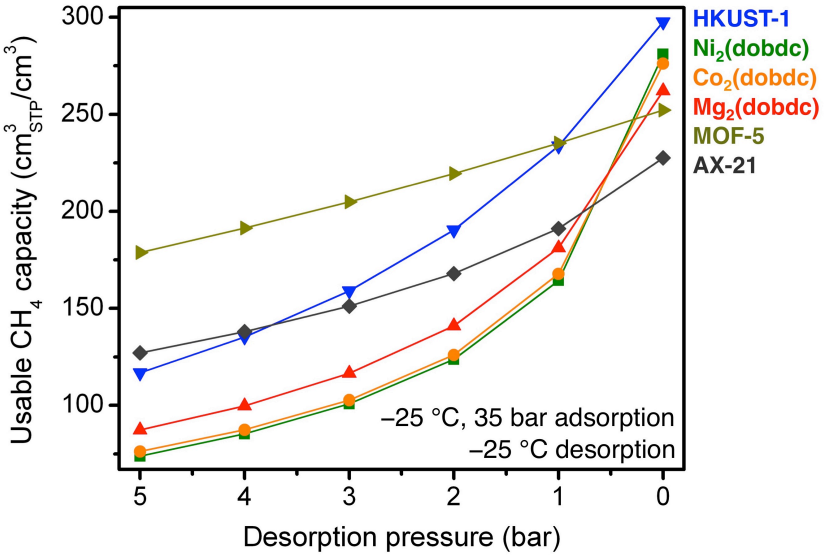

Figure 3.S44. The volumetric usable CH_4 capacity as a function of desorption pressure for adsorption at −25 °C and 35 bar and desorption at −25 °C and pressures from 5 to 0 bar.

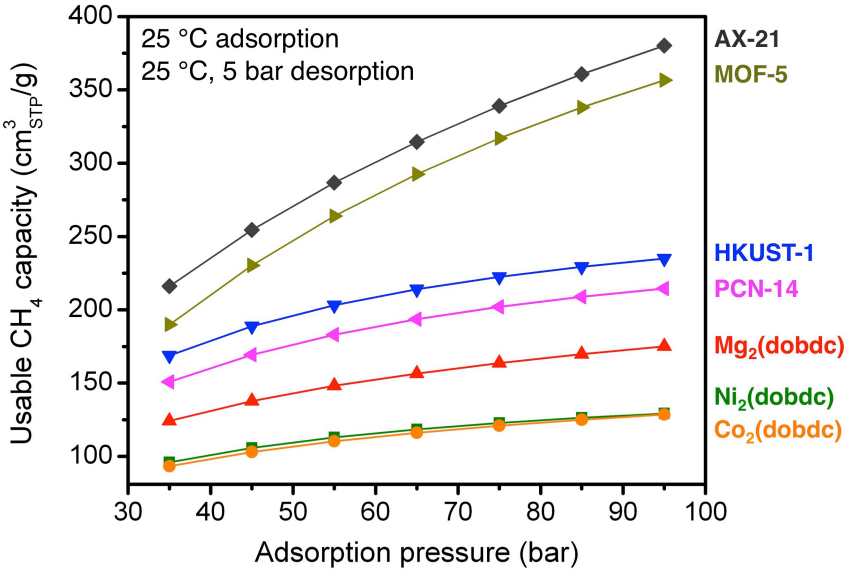

Figure 3.S45. The gravimetric usable CH_4 capacity as a function of adsorption pressure for adsorption at 25 °C and pressures from 35 to 95 bar and desorption at 25 °C and 5 bar.

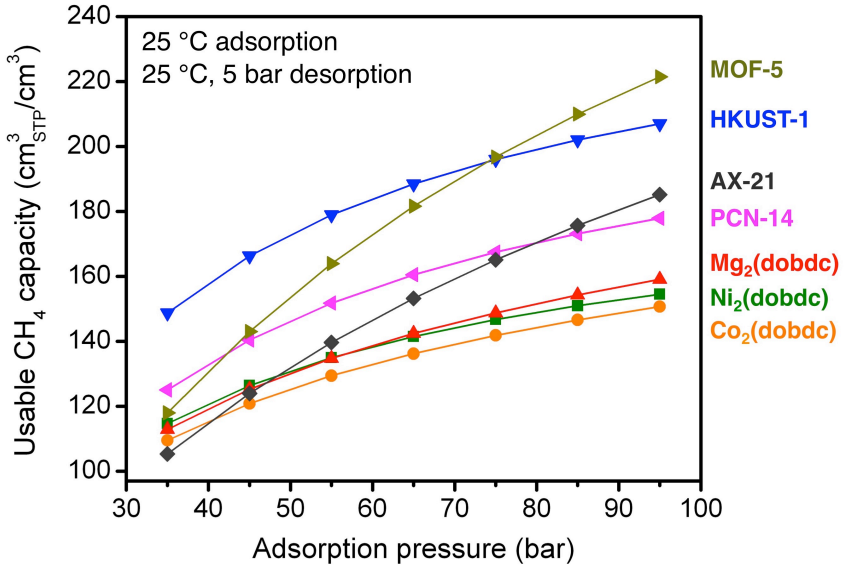

Figure 3.S46. The volumetric usable CH_4 capacity as a function of adsorption pressure for adsorption at 25 °C and pressures from 35 to 95 bar and desorption at 25 °C and 5 bar.

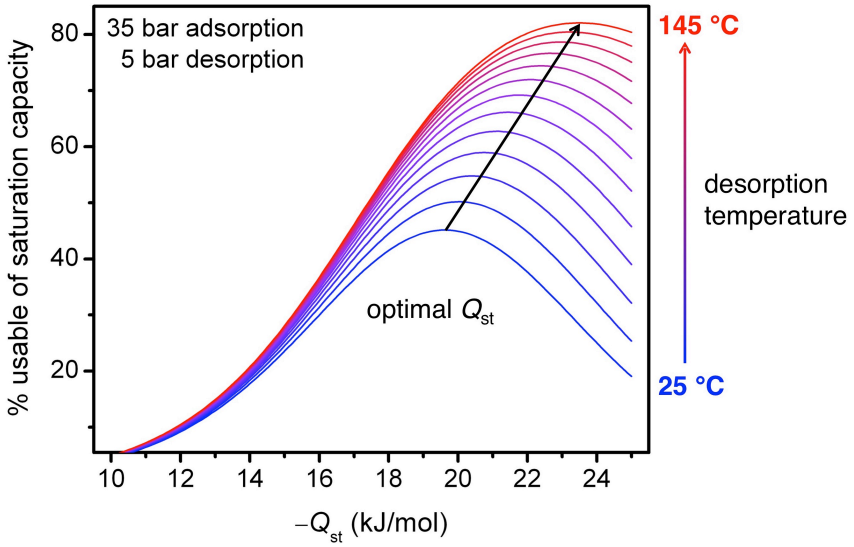

Figure 3.S47 Assuming a single-site Langmuir isotherm, the percentage of the saturation capacity that is usable is plotted for isosteric heats of adsorption, Q_{st}, ranging from 10 to 25 kJ/mol and desorption temperatures from 25 to 145 °C, with adsorption at 35 bar, desorption at 5 bar, and a molar entropy of adsorption of $-10.5R$. As the desorption temperature increases, the optimal Q_{st} and usable capacity also increase. Note that the higher entropy value leads to higher optimal binding enthalpies (see Figure 3.7 for comparison).

Table 3.S1. Summary of gravimetric Langmuir surface area (m^2/g), volumetric Langmuir surface area (m^2/cm^3) pore volume (cm^3/g), and crystallographic density (g/cm^3) for all materials synthesized and evaluated in this work.

	Langmuir surface area (m^2/g)	Langmuir surface area (m^2/cm^3)	Pore volume (cm^3/g)	Crystallographic density (g/cm^3)
Ni_2(dobdc)	1574	1881	0.56	1.195
Co_2(dobdc)	1433	1681	0.51	1.169
Mg_2(dobdc)	1957	1779	0.69	0.909
HKUST-1	2190	1929	0.77	0.881
PCN-14	2360	1956	0.83	0.819
MOF-5	3961	2460	1.4	0.621
AX-21	4880	2377	1.64	0.487

Table 3.S2. Summary of crystallographic density calculations.

	Asymmetric unit	Total mass of asymmetric unit (g)	Z	Unit cell volume ($Å^3$)	Temp (°C)	Density (g/cm^3)
Ni_2(dobdc)	NiC_4HO_3	4.657×10^{-21}	18	3898.3	22	1.195
Co_2(dobdc)	CoC_4HO_3	4.664×10^{-21}	18	3977.3	195	1.173
Mg_2(dobdc)	MgC_4HO_3	3.629×10^{-21}	18	3992.5	27	0.909
HKUST-1	$Cu_3C_{18}H_6O_{12}$	1.608×10^{-20}	16	18247.4	25	0.881
PCN-14	$CuC_{15}H_7O_4$	1.882×10^{-20}	36	22697.7	−183	0.829
MOF-5	$Zn_4C_{24}H_{12}O_{15}$	1.066×10^{-20}	8	17153.6	27	0.621

Table 3.S3. Single- or dual-site Langmuir parameters for all isotherm fits.

	Ni_2(dobdc)	Co_2(dobdc)	Mg_2(dobdc)	HKUST-1	PCN-14	MOF-5	AX-21
$n_{sat,1}$ (mmol/g)	7.2	8.5	11.1	16.9	10.4	30.5	28.3
S_1 (−R)	10.0	9.7	9.6	9.7	9.9	9.2	9.2
E_1 (kJ/mol)	21.0	19.7	18.6	17.1	16.2	12.3	10.7
$n_{sat,2}$ (mmol/g)	4.3	3.7	5.9	-	6.0	-	10.5
S_2 (−R)	10.0	11.6	11.9	-	9.3	-	9.0
E_2 (kJ/mol)	16.1	17.6	16.4	-	18.3	-	16.6

Chapter 4: Application of a High-Throughput Analyzer in Evaluating Solid Adsorbents for Post-Combustion Carbon Capture via Multicomponent Adsorption of CO_2, N_2, and H_2O

4.1. Introduction

In 2012, coal- and natural gas-fired power plants released 11.1 Gt of carbon dioxide—nearly 30% of the total global emissions.[2,3] While there are more than 68,000 power plants currently in operation, approximately 300 of these plants are directly responsible for an astonishing 10% of the world's CO_2 emissions. Capturing and permanently sequestering this CO_2 would have a significant and immediate impact on rising levels of CO_2 in the atmosphere.[4,5] With little financial incentive to reduce CO_2 emissions in most countries, however, existing carbon capture technologies are simply too expensive to be practical at the scales required for large power plants that release upwards of 40 tonnes of CO_2 per minute.[5,6] Since the most expensive component of any carbon capture and sequestration process is the separation of CO_2 from the other gases present in the flue gas of a power plant, a large research effort has focused on developing new materials and processes to remove CO_2 from flue gas using as little energy as possible.[7,8] While the exact composition of a flue gas depends on the design of the power plant and the source of natural gas or coal, a mixture of mostly N_2, CO_2, and H_2O is released at ambient pressure and 40-80 °C (Table 4.1).[9] The effects of potentially more reactive gases that are present in lower concentrations, such as O_2, SO_x, NO_x, and CO, must also be considered, but, at a minimum, materials are needed that can selectively capture a large amount of CO_2 in the presence of N_2 and H_2O.

Table 4.1. Expected Range of Compositions for Flue Gas From a Coal- or Natural Gas-Fired Power Plant.[9]

	Coal	Natural Gas
CO_2 (mbar)	120-150	30-50
N_2 (mbar)	750-800	740-800
H_2O (mbar)[1]	50-140	70-100

Taking advantage of the Lewis acidity of CO_2, Lewis basic aqueous amine solutions have been studied extensively for extracting CO_2 from gas mixtures and are currently used to remove CO_2 from many natural gas streams around the world.[10] Aqueous amine scrubbers can also be used to capture high-purity CO_2 from flue gas, but new materials with lower regeneration energy requirements could lead to a significantly lower overall cost for carbon capture.

To this end, solid adsorbents, including zeolites, activated carbons, silicas, and metal-organic frameworks, have received significant attention as alternatives to amine solutions, demonstrating high CO_2 capacities and high selectivities for CO_2 over N_2, together with reduced regeneration energy penalties.[11] It is now well established that adsorbents must contain strong CO_2 binding sites in order to adsorb a significant amount of CO_2 at 50-150 mbar and to achieve the high CO_2 purities necessary for cost-effective sequestration.[12,13] While many different classes of adsorbents have been studied for CO_2 capture, the most promising materials have typically featured exposed metal cations, exposed anions, or alkylamines, all of which can have strong interactions with CO_2.[11] Despite the large number of adsorbents that have been reported in the

context of CO_2 capture, the majority of studies have relied exclusively on pure CO_2 and N_2 isotherms, which has made it challenging to identify the best materials for capturing CO_2 from an actual flue gas mixture that has a significant amount of H_2O. This is particularly true for metal-organic frameworks and has hindered progress in the field.[14]

There have been some noteworthy computational and experimental efforts to evaluate the stability and CO_2 capture performance of metal-organic frameworks under more realistic conditions,[15,16] but to the best of our knowledge, there are no reports of multicomponent equilibrium adsorption isotherms for mixtures that include CO_2, N_2, and H_2O. In any gas separation application, mixed gas equilibrium adsorption data are critical for comparing the performances of different materials, for designing processes, and for validating theoretical models of mixture adsorption.[17] While models such as ideal adsorbed solution theory (IAST) can be used to predict adsorption for simple gas mixtures such as CO_2 and N_2 with reasonable confidence,[18,19] their accuracy is not well established for more complex mixtures such as CO_2, N_2, and H_2O.[20] More importantly, all models that rely on single-component adsorption isotherms to predict mixed gas adsorption assume that the adsorbent is in the same thermodynamic state in the presence of each gas. For many adsorbents that exhibit structural or chemical changes specific to different gas molecules, this is most certainly not the case, and direct measurement of mixed gas adsorption is the only way to reliably evaluate gas separation performance.

In contrast to single-component adsorption measurements, which are now carried out routinely and with high accuracy using commercial instruments, mixed gas adsorption measurements are often time consuming, requiring carefully designed custom equipment and complex data analysis.[21] As a result, there is a significant lack of mixed gas equilibrium adsorption data reported in the literature.[17] The limited mixed gas adsorption data available is mostly for two-component mixtures in zeolites, and equilibrium adsorption data for mixtures of more than two components is exceedingly rare, even though many industrial gas separations involve multicomponent mixtures.[17a,22]

More routinely, dynamic column breakthrough experiments are used to evaluate the separation performance of an adsorbent by flowing a mixture of gases through a packed bed and measuring the composition of the outlet gas stream as a function of time.[23] It is important to note that a typical breakthrough experiment does not yield equilibrium data, and the relationship between breakthrough results and equilibrium adsorption isotherms is not always clear.[17c] For instance, nearly all adsorbents will show at least some capacity for capturing CO_2 in a standard breakthrough experiment with a mixture of CO_2, N_2, and H_2O, since the front of the bed will desiccate the incoming gas mixture, leaving just CO_2 and N_2 as the gas flows through the bed.[24,25] This can lead to misleading conclusions about the intrinsic ability of a material to adsorb CO_2 at a specific partial pressure of H_2O, particularly when experiments are run on a small amount of sample. Indeed, many factors in addition to multicomponent adsorption capacities can influence experimental breakthrough curves, including column size, column shape, gas flow rates, adsorbent packing density, and extra-column effects.[26] Because breakthrough experiments mimic the dynamic conditions of a large-scale separation, they can be helpful in developing processes for CO_2 capture. However, multicomponent equilibrium experiments are better suited for comparing the properties of different materials under similar conditions, since the amount of each gas adsorbed is determined only by the partial pressure of each gas and the temperature. Moreover, these equilibrium data can be used to model any dynamic process using local equilibrium theory, where an equilibrium is assumed to exist between the gas and adsorbed phases at every cross-section of an adsorbent bed. While this assumption is never entirely true, it

is a reasonable approximation for many processes and relies on accurate multicomponent equilibrium data.[27]

Here, we report the design and validation of a high-throughput instrument for the accurate measurement of multicomponent equilibrium adsorption at conditions relevant to post-combustion carbon capture. These measurements are used to compare the performance of 15 different metal-organic frameworks, activated carbons, zeolites, and amine-appended silicas that are representative of the wide range of adsorbents that have been studied for this application (Figure 4.1).

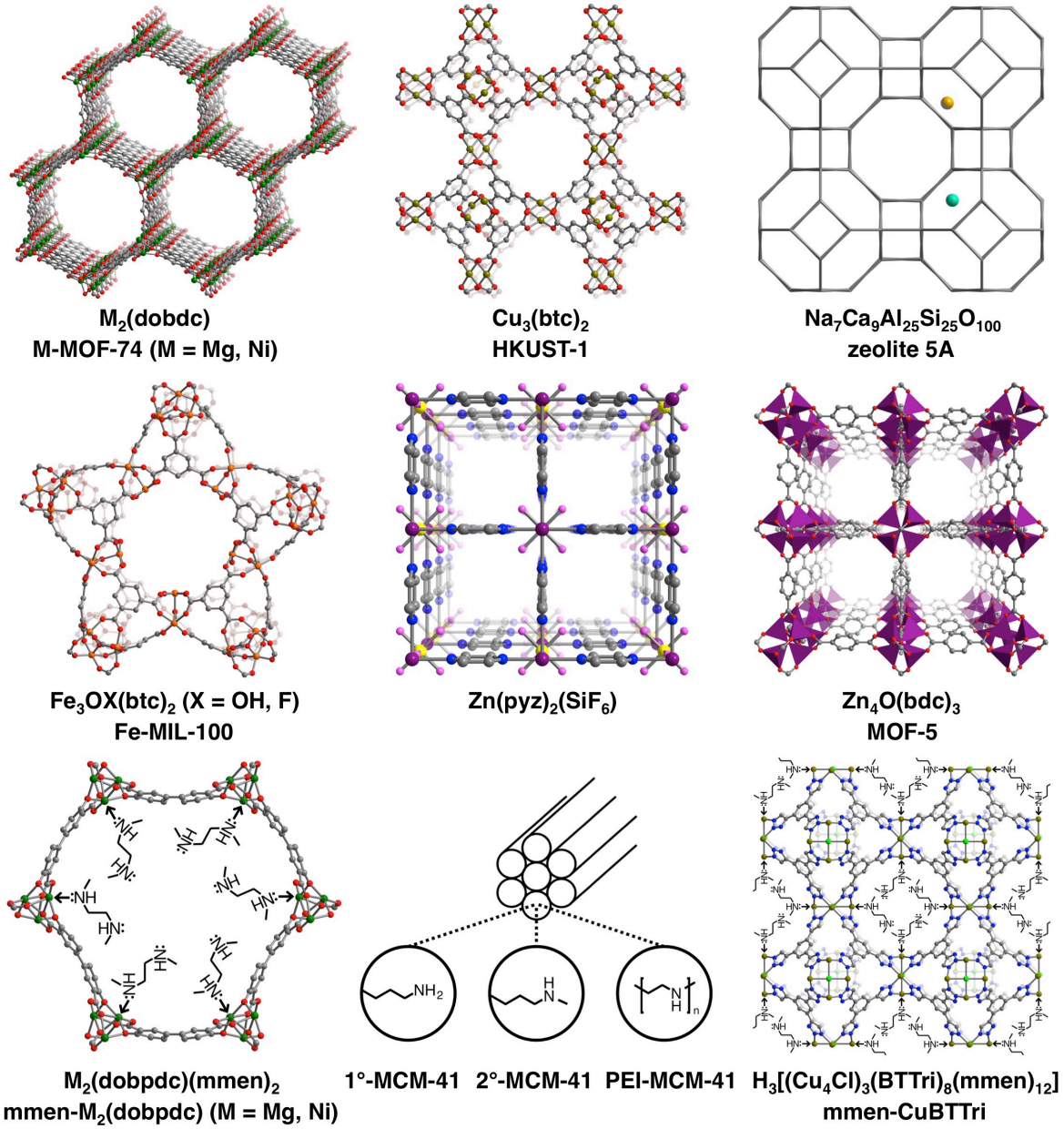

Figure 4.1. Multicomponent adsorption measurements were performed for mixtures of CO_2, N_2, and H_2O in all of the adsorbents shown above, as well as zeolite 13X ($Na_{50}Al_{50}Si_{59}O_{218}$) and an activated carbon (AX-21) that are not pictured. For the metal-organic framework structures, gray, red, blue, dark yellow,

orange, purple, pink, yellow, and bright green spheres represent C, O, N, Cu, Fe, Zn, F, Si, and Cl atoms, respectively; H atoms have been omitted for clarity. Purple tetrahedra represent Zn atoms, and dark green spheres represent Mg or Ni atoms. For the zeolite structure (upper right), each vertex represents a tetrahedral SiO_4 or AlO_4 unit, while teal and dark orange spheres represent typical positions for extra-framework Na and Ca cations, respectively.

4.2. Experimental

4.2.1. General Information. Anhydrous dichloromethane and *N*,*N*-dimethylformamide (DMF) were obtained from a Vac anhydrous solvent system. All other reagents were obtained from commercial vendors and used without further purification. MCM-41 was purchased from Sigma-Aldrich and used as received. Ultra high purity grade (99.999% purity) helium and nitrogen and research grade carbon dioxide (99.998% purity) were used for all adsorption measurements. Mixtures of CO_2 and N_2 were certified standard grade with ±0.01% uncertainty in the gas composition. Distilled H_2O was used for all H_2O vapor dosing and was degassed before use. Single-component H_2O adsorption isotherms were measured on a Micromeritics ASAP 2020 instrument. Infrared spectra were obtained on a Perkin-Elmer Spectrum 100 Optica FTIR spectrometer using either an attenuated total reflectance accessory or in transmission mode between two NaCl plates with the solid sample dispersed in Nujol. Diffraction data were collected with 0.02° steps using a Bruker AXS D8 Advance diffractometer equipped with Cu-Kα radiation (λ = 1.5418 Å), a Göbel mirror, a Lynxeye linear position-sensitive detector, and mounting the following optics: fixed divergence slit (0.6 mm), receiving slit (3 mm), and secondary beam Soller slits (2.5°). The generator was set at 40 kV and 40 mA. Carbon, hydrogen, and nitrogen elemental analyses were obtained from the Microanalytical Laboratory at the University of California, Berkeley.

4.2.2. Surface Area Measurements. Surface area measurements were performed on either a Micromeritics ASAP 2020 or 2420 instrument. For standard measurements, activated samples were transferred under a N_2 atmosphere to preweighed glass analysis tubes, which were capped with a Transeal. The samples were evacuated on the ASAP until the outgas rate was less than 3 μbar/min. The evacuated analysis tubes containing degassed samples were then carefully transferred to an electronic balance and weighed to determine the mass of sample (typically 100-200 mg). The tubes were fitted with an isothermal jacket and transferred back to the analysis port of the gas adsorption instrument. The outgas rate was again confirmed to be less than 3 μbar/min. Langmuir surface areas and pore volumes were determined by measuring N_2 adsorption isotherms in a 77 K liquid N_2 bath and calculated using the Micromeritics software, assuming a value of 16.2 $Å^2$ for the molecular cross-sectional area of N_2.

4.2.3. Synthesis of Adsorbents. The activated carbon AX-21 (Maxsorb) was purchased from a commercial vendor and activated at 200 °C under vacuum prior to adsorption measurements. The compounds $Zn_4O(bdc)_3$ (MOF-5, IRMOF-1; bdc^{2-} = 1,4-benzenedicarboxylate), $Mg_2(dobdc)$ (Mg-MOF-74, CPO-27-Mg; $dobdc^{4-}$ = 2,5-dioxido-1,4-benzenedicarboxylate), and $Ni_2(dobdc)$ (Ni-MOF-74, CPO-27-Ni), $Cu_3(btc)_2$ (HKUST-1; btc^{3-} = 1,3,5-benzenetricarboxylate) were synthesized as described in Chapter 3. The compounds mmen-$Mg_2(dobpdc)$ (mmen = N,N′-dimethylethylenediamine; $dobpdc^{4-}$ = 4,4′-dioxido-3,3′-biphenyldicarboxylate) and mmen-

Ni_2(dobpdc) were synthesized and activated according to literature procedure.[73] The compound $H_3[(Cu_4Cl)_3(BTTri)_8(mmen)_{12}]$ (mmen-CuBTTri; mmen = N,N′-dimethylethylenediamine; H_3BTTri = 1,3,5-tri(1H-1,2,3-triazol-4-yl)benzene) was synthesized and activated according to literature procedure.[72c]

Zeolite Na-A (Ca-A, LTA; $Na_7Ca_9Al_{25}Si_{25}O_{100}$) was purchased as a pure powder from Sigma-Aldrich. Ion-exchange was performed to generate aluminosilicate zeolites containing divalent extra-framework cations.[44c] Zeolite A (1.0 g, hydrated) was dispersed in 20 mL of aqueous $Ca(NO_3)_2$ solutions and stirred for 15 h at 60 °C. After collecting the solid by centrifugation, the ion-exchange procedure was repeated. Then, the solids were washed 5 times with 40-mL aliquots of deionized water and dried at 80 °C. The zeolite was then fully activated by heating at 250 °C under vacuum for 24 h.

Zeolite 13X (Na-X, FAU; $Na_{50}Al_{50}Si_{59}O_{218}$) was purchased as a pure powder from Sigma-Aldrich. The zeolite was activated by heating at 250 °C under vacuum for 24 h.

The compound $Fe_3O(OH)(btc)_3$ (Fe-MIL-100; btc^{3-} = 1,3,5-benzenetricarboxylate) was synthesized and activated using a strategy adopted from a previous report.[58] Specifically, Fe (55.8 mg, 1 mmol), H_3btc (140.8 mg, 0.67 mmol), concentrated HNO_3 (38 μL, 0.6 mmol), 48 wt % HF (73 μL, 2 mmol), and deionized H_2O (5 mL, 278 mmol) were combined in a Teflon autoclave. The autoclave was heated in an oven at 150 °C for 12 h. The as-synthesized compound was recovered by vacuum filtration, then washed 2 times in boiling H_2O, then washed 3 times in ethanol at 60 °C. The compound was collected by filtration and activated by heating at 150 °C under vacuum for 24 h.

The compound $Zn(pyrz)_2(SiF_6)$ (pyrz = pyrazine) was synthesized and activated using a strategy adopted from a previous report.[59a] Specifically, $Zn(SiF_6)$ (6.2 g, 30 mmol) and pyrazine (5.21 g, 65 mmol) were each dissolved in 100 mL methanol. The metal-organic framework $Zn(pyrz)_2(SiF_6)$ was formed by the slow diffusion of pyrazine into $Zn(SiF_6)$ at room temperature for 48 h by a layering technique. The as-synthesized compound was recovered by vacuum filtration, then washed quickly 3 times with room temperature dimethylformamide, then washed quickly 3 times with room temperature methanol. Note that the compound was slightly soluble in MeOH, which necessitated the rapid washes. The compound was collected by filtration and activated by heating at 75 °C under vacuum for 24 h.

3-aminopropyl grafted MCM-41 (1°-MCM-41) was synthesized and activated as previously reported, using regular MCM-41 instead of pore-expanded MCM-41.[69] The amount of amine grafted was determined by elemental analysis (Table 4.S1).

3-methylaminopropyl grafted MCM-41 (2°-MCM-41) was synthesized and activated as previously reported, using regular MCM-41 instead of pore-expanded MCM-41.[69] The amount of amine grafted was determined by elemental analysis (Table 4.S1).

Polyethylenimine impregnated MCM-41 (PEI-MCM-41) was synthesized and activated as previously reported.[70b] The polyethylenimine (PEI) was purchased from Sigma-Aldrich as etylenediamine branched with an average M_w of 800 and used as received. The amount of PEI impregnated was determined from thermogravimetric analysis (TGA) to be 31.9 wt % (7.4 mmol N per g silica) (Figure 4.S1).

4.2.4. Isotherm Fitting. All 40 °C CO_2 isotherms were fit with a single- or dual-site Langmuir-Freundlich model (Eqn 4.1), where p is the pressure in bar and n_{sat} is the saturation capacity in mmol/g, and b is the Langmuir parameter in bar^{-v}, p is the pressure in bar, and v is the Freundlich parameter for up to two sites. The p_0 term is used only for fitting the CO_2 isotherm of

mmen-Mg_2(dobpdc), which has a sharp step at low pressures—p_0 represents the step pressure in bar. These fits were used to calculate the single-component CO_2 loadings at exactly the same equilibrium partial pressure as the multicomponent measurements. The 40 °C N_2 isotherm of AX-21 was also fit with a single-site Langmuir model for the ideal adsorbed solution theory (IAST) calculation. Fits are shown as black lines on all multicomponent isotherm plots, and all fitted parameters can be found in Table 4.S2.

$$n_{\text{ads}} = \frac{n_{\text{sat},1} b_1 (p - p_0)^{v_1}}{b_1 (p - p_0)^{v_1}} + \frac{n_{\text{sat},2} b_2 (p - p_0)^{v_2}}{b_2 (p - p_0)^{v_2}} \tag{4.1}$$

4.2.5. Multicomponent Adsorption Calculations and Error Analysis. The amount of component *i* adsorbed is calculated as the difference between the amount of component *i* that was dosed to a sample and the amount that still remains in the gas phase at equilibrium:

$$n_{\text{ads},i} = n_{\text{dose},i} - n_{\text{free},i} \tag{4.2}$$

$$n_{\text{dose},i} = \left(\frac{P_{\text{dose},i}}{R}\right)\left(\frac{V_{\text{sv}}}{T_{\text{sv}}} + \frac{V_{\text{dv}}}{T_{\text{dv}}}\right)\left(\frac{1}{m}\right) \tag{4.3}$$

$$n_{\text{free},i} = \left(\frac{P_{\text{eq},i}}{R}\right)\left(\frac{V_{\text{sv}}}{T_{\text{sv}}} + \frac{V_{\text{dv}}}{T_{\text{dv}}} + \frac{V_{\text{pv}}}{T_{\text{pv}}}\right)\left(\frac{1}{m}\right) \tag{4.4}$$

For $i = CO_2, N_2$, the amount of gas dosed in a typical multicomponent experiment is given by:

$$n_{\text{dose},CO_2} = \left(\frac{P_{\text{dose}} c_{CO_2}}{R}\right)\left(\frac{V_{\text{sv}}}{T_{\text{sv}}} + \frac{V_{\text{dv}}}{T_{\text{dv}}}\right)\left(\frac{1}{m}\right) \tag{4.5}$$

$$n_{\text{dose},N_2} = \left(\frac{P_{\text{dose}} \left(1 - c_{CO_2}\right)}{R}\right)\left(\frac{V_{\text{sv}}}{T_{\text{sv}}} + \frac{V_{\text{dv}}}{T_{\text{dv}}}\right)\left(\frac{1}{m}\right) \tag{4.6}$$

For $i = CO_2, N_2$, the equilibrium partial pressure of each gas is determined from the total equilibrium pressure, the equilibrium partial pressure of H_2O, and the ratio of CO_2 to N_2 as measured by the residual gas analyzer (rga):

$$P_{\text{eq},CO_2} = \left(P_{\text{eq}} - P_{\text{eq},H_2O}\right)\left(\frac{X}{X+1}\right) \tag{4.7}$$

$$P_{\text{eq},N_2} = \left(P_{\text{eq}} - P_{\text{eq},H_2O}\right)\left(\frac{1}{X+1}\right) \tag{4.8}$$

For $i = H_2O$, the amount of gas dosed in a typical multicomponent experiment is given by:

$$n_{\text{dose},H_2O} = \sum_{j=1}^{J}\left[\left(\frac{P_{\text{dose},H_2O,j} - P_{\text{removed},H_2O,j}}{R}\right)\left(\frac{V_{\text{sv}}}{T_{\text{sv}}} + \frac{V_{\text{dv}}}{T_{\text{dv}}}\right)\right] \tag{4.9}$$

The amount of CO_2 adsorbed at equilibrium is calculated by combining Eqns 4.2, 4.4, 4.5, and 4.7:

$$n_{\text{ads},CO_2} = \left(\frac{P_{\text{dose}} c_{CO_2}}{R}\right)\left(\frac{V_{\text{sv}}}{T_{\text{sv}}} + \frac{V_{\text{dv}}}{T_{\text{dv}}}\right)\left(\frac{1}{m}\right) - \left(P_{\text{eq}} - P_{\text{eq},H_2O}\right)\left(\frac{X}{X+1}\right)\left(\frac{1}{R}\right)\left(\frac{V_{\text{sv}}}{T_{\text{sv}}} + \frac{V_{\text{dv}}}{T_{\text{dv}}} + \frac{V_{\text{pv}}}{T_{\text{pv}}}\right)\left(\frac{1}{m}\right) \tag{4.10}$$

The amount of N_2 adsorbed at equilibrium is calculated by combining Eqns 4.2, 4.4, 4.6, and 4.8:

$$n_{\text{ads},N_2} = \left(\frac{P_{\text{dose}}\left(1 - c_{CO_2}\right)}{R}\right)\left(\frac{V_{\text{sv}}}{T_{\text{sv}}} + \frac{V_{\text{dv}}}{T_{\text{dv}}}\right)\left(\frac{1}{m}\right) - \left(P_{\text{eq}} - P_{\text{eq},H_2O}\right)\left(\frac{1}{X+1}\right)\left(\frac{1}{R}\right)\left(\frac{V_{\text{sv}}}{T_{\text{sv}}} + \frac{V_{\text{dv}}}{T_{\text{dv}}} + \frac{V_{\text{pv}}}{T_{\text{pv}}}\right)\left(\frac{1}{m}\right) \tag{4.11}$$

The amount of H_2O adsorbed at equilibrium is calculated by combining Eqns 4.2, 4.4, and 4.9:

$$n_{\text{ads},H_2O} = \sum_{j=1}^{J}\left(\frac{P_{\text{dose},H_2O,j} - P_{\text{removed},H_2O,j}}{R}\right)\left(\frac{V_{\text{sv}}}{T_{\text{sv}}} + \frac{V_{\text{dv}}}{T_{\text{dv}}}\right) - \left(\frac{P_{\text{eq},H_2O}}{R}\right)\left(\frac{V_{\text{sv}}}{T_{\text{sv}}} + \frac{V_{\text{dv}}}{T_{\text{dv}}} + \frac{V_{\text{pv}}}{T_{\text{pv}}}\right)\left(\frac{1}{m}\right) \tag{4.12}$$

In order to determine the error in the amounts of CO_2, N_2, and H_2O adsorbed for a typical multicomponent experiment, it is assumed that all variables are uncorrelated and have a covariance of 0. The errors in the temperature readings, volume calibrations, and standard gas mixture compositions are assumed to be negligible compared to the errors in the pressure readings, dew point transmitter readings, and rga measurements. The variance in the amount of component *i* adsorbed is given by the difference between the variance in the amount of component *i* dosed to the sample and the variance in the amount of component *i* in the gas phase at equilibrium:

$$\sigma^2\left(n_{\text{ads},i}\right) = \sigma^2\left(n_{\text{dose},i}\right) - \sigma^2\left(n_{\text{free},i}\right) \tag{4.13}$$

The variance in the amount of component *i* in the gas phase at equilibrium is given by:

$$\sigma^2\left(n_{\text{free},i}\right) = \left(\left(\frac{1}{R}\right)\left(\frac{V_{\text{sv}}}{T_{\text{sv}}} + \frac{V_{\text{dv}}}{T_{\text{dv}}} + \frac{V_{\text{pv}}}{T_{\text{pv}}}\right)\left(\frac{1}{m}\right)\right)^2 \sigma^2\left(P_{\text{eq},i}\right) \tag{4.14}$$

The variance in the amount of CO_2 dosed is given by:

$$\sigma^2\left(n_{\text{dose},CO_2}\right) = \left(\left(\frac{c_{CO_2}}{R}\right)\left(\frac{V_{\text{sv}}}{T_{\text{sv}}} + \frac{V_{\text{dv}}}{T_{\text{dv}}}\right)\left(\frac{1}{m}\right)\right)^2 \sigma^2\left(P_{\text{dose}}\right) \tag{4.15}$$

The variance in the amount of N_2 dosed is given by:

$$\sigma^2\left(n_{\text{dose},N_2}\right)=\left(\left(\frac{\left(1-c_{CO_2}\right)}{R}\right)\left(\frac{V_{sv}}{T_{sv}}+\frac{V_{dv}}{T_{dv}}\right)\left(\frac{1}{m}\right)\right)^2\sigma^2\left(P_{\text{dose}}\right) \tag{4.16}$$

The standard error in the pressure transducer was 0.25% of reading as reported by the manufacturer. The standard deviation in the amount of H_2O dosed was estimated based on background H_2O isotherms to be 0.006 μmol for a typical multicomponent experiment.

For the purposes of this error analysis, the following values were used for all volumes and temperatures and for the standard gas mixture composition. These values represent averages across all 28 sample channels during a typical multicomponent experiment.

V_{sv}	21.1 mL
T_{sv}	313 K
V_{dv}	13.7 mL
T_{dv}	300 K
V_{pv}	12.9 mL
T_{pv}	313 K
c_{CO_2}	20.50%

The standard deviations of $P_{eq,i}$ for i = CO_2, N_2, H_2O were determined by dosing known mixtures of CO_2, N_2, and H_2O to empty sample holders, cycling the syringe, and using the pressure transducers, dew point transmitter, and rga to measure the partial pressures of CO_2, N_2, and H_2O in the gas phase, just as would be done in a real multicomponent experiment (Figure 4.4). The standard deviations were calculated for 40 independent experiments by:

$$\sigma\left(P_i\right)=\sqrt{\frac{\sum_{n=1}^{N}\left(P_{n,i,\text{exp}}-P_{n,i,\text{calc}}\right)^2}{N-1}} \tag{4.17}$$

The standard deviations in the measured equilibrium partial pressures of CO_2, N_2, and H_2O were 1.84, 1.76, and 1.74 mbar, respectively. For a confidence interval of 95% (1.96 standard deviations), these errors are 3.6, 3.5, and 3.4 mbar for CO_2, N_2, and H_2O respectively. By inputting these values into Eqns 4.13-4.16, the errors in the amount of CO_2, N_2, and H_2O adsorbed in a typical multicomponent measurement were calculated to be 0.007 μmol, 0.009 μmol, and 0.013 μmol, respectively. These values were divided by the sample mass to calculate the error associated with each multicomponent data point reported in this work.

4.3. Results and Discussion

4.3.1. Multicomponent Adsorption. Although multicomponent adsorption experiments are far less common than single-component experiments in the literature, there has still been significant progress toward developing improved methods for mixed gas measurements. Since it is usually not possible to measure directly the composition of the adsorbed phase, the main challenge in any multicomponent experiment is determining the composition, or relative partial pressures, of the gas phase at equilibrium.[17,21] The composition of the adsorbed phase, as well as the amounts of each gas adsorbed, can then be calculated as the difference between the amount of each component added to the system and the amount that is still present in the gas phase at equilibrium. A variety of techniques have been developed for this purpose in both open and closed systems, but preforming measurements with high enough accuracy to provide meaningful results is not trivial and likely explains the lack of published multicomponent data. Often, the adsorption capacities determined from a multicomponent measurement have such high errors that it is impossible to compare the properties of different materials.[21] If done accurately, however, any open or closed system measurement should generate equivalent multicomponent adsorption data for a given set of equilibrium conditions. Methods for performing multicomponent measurements have been reviewed thoroughly in the literature,[17a,17b,21,22] but will be briefly summarized here in the context of choosing an appropriate technique for high-throughput multicomponent adsorption measurements of CO_2, N_2, and H_2O mixtures at conditions representative of a power plant flue gas.

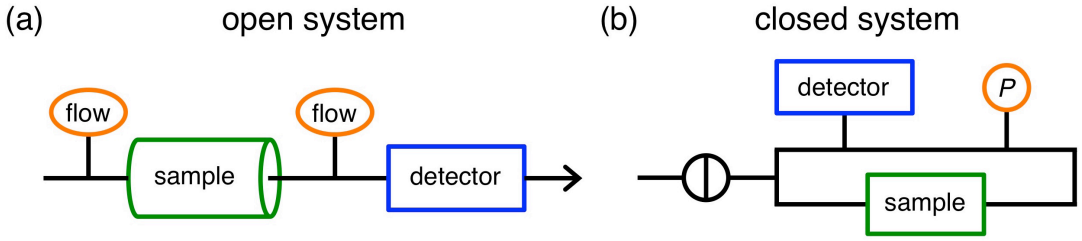

Figure 4.2. (a) In an open system multicomponent adsorption measurement, a mixture of gases is flowed over a packed bed of adsorbent. The flow rate and composition of the inlet and outlet gas streams are recorded until the composition of the outlet gas stream matches the inlet. (b) In a closed system multicomponent adsorption measurement, a mixture of gases is dosed to a sample and allowed to equilibrate. The amount of each component adsorbed is determined from the equilibrium gas phase composition and either the equilibrium pressure in a volumetric measurement or the equilibrium weight in a gravimetric measurement.

In a typical open system experiment, a gas mixture is flowed over a packed bed of adsorbent until the composition of the outlet gas stream is the same as that of the inlet, with a mass spectrometer or gas chromatograph used to record the outlet gas composition (Figure 4.2a).[28] Determining the equilibrium amounts adsorbed of each gas requires the accurate measurement of both the inlet and outlet gas flow rates and compositions, as well as appropriate corrections for extra-column effects and ensuring that the column is isothermal at equilibrium.[21] Because the equilibrium gas phase composition is equivalent to the composition of the inlet gas stream, it is easy to compare the adsorption capacities of different materials under identical equilibrium conditions in an open system multi-component experiment. Correcting for extra-column effects

can, however, be extremely complicated. These corrections are critical to the accuracy of the results, particularly for small sample sizes where the dead volume of the system is not negligible.[26a] Additionally, it can be challenging to measure the outlet flow rate with high accuracy since the calibration of most flow meters is dependent on the composition of the gas that is flowing through them.[26b] As a result of these issues, open system measurements often require a large amount of sample in order to collect accurate data, and consequently are not very amenable to high-throughput screening.[21]

Closed system measurements, on the other hand, are typically more accurate, allowing multicomponent experiments to be performed on smaller quantities of sample.[21] Still, there are significant experimental challenges to using closed systems to measure multicomponent equilibrium adsorption in a high-throughput manner. In a typical closed system experiment, a mixture of gases is dosed to an evacuated sample from a calibrated dosing volume, and the gas phase composition is recorded once the sample has reached equilibrium (Figure 4.2b).[29] Since equilibration times can often be on the order of hours or even days, a circulation pump, or other gas-mixing device that does not alter the amount of gas inside the closed system, is typically needed.[30] Similar to open system measurements, a mass spectrometer or gas chromatograph can be used to measure the composition of the gas phase after equilibrium is reached, but now care must be taken to ensure that the equilibrium conditions are not altered when the gas is analyzed.[21] The total amount adsorbed can be determined using standard volumetric or gravimetric techniques with calibrated volumes and a pressure transducer or with buoyancy corrections and a balance, respectively. Equilibrium amounts adsorbed can then be determined by material balance using the ideal gas law or an appropriate equation of state.

Unlike in open system measurements, it is often challenging to measure multicomponent adsorption consistently at a specific set of equilibrium conditions in a closed system since the composition of the dosed gas mixture required to achieve a specific gas phase composition at equilibrium is difficult to predict.[21] In spite of this, closed systems are more amenable to automation and to comparing multicomponent adsorption for a large number of samples with high accuracy. More advanced versions of the open and closed multicomponent experiments described here have also been developed, including the zero length column technique,[31] total desorption analysis,[32] *in situ* infrared spectroscopy,[33] and the isotope exchange technique.[34] While each of these techniques has certain advantages and disadvantages, none are particularly well suited for high-throughput multicomponent measurements with mixtures of CO_2, N_2, and H_2O.

4.3.2. High-Throughput Multicomponent Adsorption Instrument. In this work, a closed system approach was used to develop a high-throughput adsorption instrument that can measure multicomponent adsorption for up to 28 samples at a time (Figure 4.S13). The instrument, built by Wildcat Discovery Technologies Inc., has 28 independent sample channels that share a common gas-dosing manifold with inputs for up to 8 gases, including H_2O (Figure 4.3). Each sample channel has a calibrated volume ("secondary volume") and a 1000-torr pressure transducer (MKS Seta Model 730 absolute capacitance manometer; accuracy = 0.25% reading), which are contained inside a heated enclosure that is maintained at 40 °C to minimize temperature fluctuation. Each secondary volume is connected via 1/16″ stainless steel tubing to a sample chamber ("primary volume"). The secondary volumes are each approximately 21 mL, while the primary volumes are each approximately 14 mL. The secondary volumes are also connected via 1/16″ stainless steel tubing to two Valco multiposition valves, with the 28 channels

split evenly between the two valves. The multiposition valves allow each of the 28 channels to be independently opened to the shared 14 mL "rga dose volume" (rga = residual gas analyzer), which contains a mass spectrometer (MKS Microvision 2), a dew point transmitter (Vaisala, accuracy = ±3 °C), and a 170-mL gas-tight syringe. All gas lines, dosing volumes, and sample volumes can be heated above 40 °C, allowing H_2O dosing pressures of greater than 70 mbar. Custom software allows multicomponent measurements to be performed in a fully automated manner with complete control over all test parameters. To the best of our knowledge, this is the first instrument reported to be capable of performing high-throughput multicomponent adsorption measurements at equilibrium.

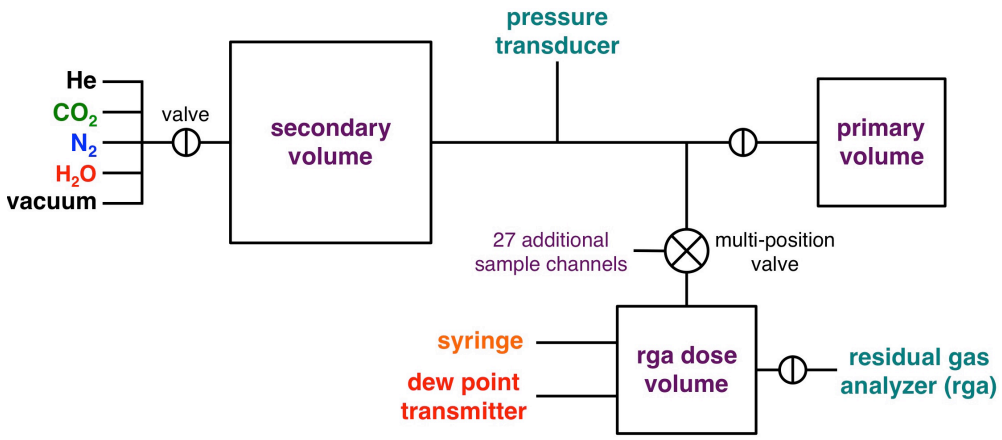

Figure 4.3. Simplified schematic of the high-throughput instrument used in this work to perform multicomponent adsorption measurements. Twenty-eight independent sample channels share a common gas-dosing manifold and are each connected to the residual gas analyzer (rga) dose volume via a multi-position valve. For multicomponent measurements, a mixture of gases is dosed into the secondary volume and rga dose volume, then expanded to the primary volume, which contains the activated adsorbent. The syringe is cycled multiple times, then the equilibrium pressure is recorded. For mixtures of CO_2, N_2, and H_2O, the dew point transmitter is used to record the partial pressure of H_2O, and the rga is used to measure the ratio of the partial pressures of CO_2 and N_2.

In order to accurately measure the sample mass, activated samples are loaded in tared 4-mL vials inside a glovebox under a N_2 atmosphere. The 4-mL vials are then inserted into aluminum sample assemblies that can each hold up to 7 vials and can be fully sealed while inside the glovebox, with a Schrader valve completing the seal above each sample. The sample assemblies are then transferred to the high-throughput adsorption instrument, and the headspace above each sample is fully evacuated. The instrument then actuates each Schrader valve, opening each sample channel to vacuum. Sample temperatures in the range of 25-150 °C are achieved using heating elements under the sample holders, and temperatures throughout the instrument are continuously recorded by eight thermocouples.

Pure-component adsorption isotherms up to a maximum pressure of 1.2 bar are measured using a standard volumetric technique. To ensure that all volume calibrations, pressure transducer calibrations, thermocouple readings, and adsorption calculations are accurate and that any leak rates are negligible, background adsorption isotherms were measured for empty sample

holders on all 28 channels using He, N_2, CO_2, and H_2O (Figure 4.S14). The magnitude of the background adsorption was always found to be less than 5 mmol. For a typical sample size of 50 mg, this corresponds to a maximum error of less than 0.1 mmol/g.

All multicomponent measurements in this work were performed for mixtures of CO_2, N_2, and H_2O at 25 or 40 °C. In a typical experiment, H_2O was first dosed repeatedly to each sample. Since the 40 °C saturation pressure of H_2O is just 73.8 mbar, several H_2O doses were needed to ensure a reasonable partial pressure of H_2O at equilibrium.[35] Once an adequate amount of H_2O was added, a CO_2 and N_2 mixture of known composition was dosed to each sample. Although it is usually difficult to target specific equilibrium conditions in closed system multicomponent measurements, very similar equilibrium partial pressures could be achieved for each sample by selecting appropriate gas dosing pressures and compositions.

After all gases were dosed, the gas-tight syringe was cycled at least 15 times over several hours to force the free gas above the sample to mix, ensuring that the entire system was at equilibrium with a uniform gas-phase composition. At equilibrium, a pressure transducer was used to record the total pressure, and the dew point transmitter was used to record the partial pressure of H_2O (Figure 4.S15). Closing the valves between the secondary and primary volumes then isolated each sample, and the ratio of CO_2 to N_2 in the gas phase was determined by sampling from the secondary volume to the rga (Figures 4.S16, 4.S17). Since the rga operates under high vacuum and requires a low inlet pressure, the gas pressure must be lowered significantly prior to sampling. This was accomplished by expanding the gas into a series of large evacuated volumes in order to ensure that the gas-phase composition remained constant.

Before measuring any multicomponent data, empty sample holders were used to check the accuracy of the instrument by dosing known mixtures of CO_2, N_2, and H_2O, cycling the syringe, and using the pressure transducers, dew point transmitter, and rga to measure the partial pressures of CO_2, N_2, and H_2O in the gas phase, just as would be done in a real multicomponent experiment. The calculated partial pressures were in very good agreement with the expected partial pressures over the full range of conditions targeted for the multicomponent experiments (Figure 4.4). It is worth emphasizing that for just 50 mg of sample, the errors in the amounts of CO_2 and N_2 adsorbed are less than 0.2 mmol/g at a 95% confidence interval, and the error in the amount of H_2O adsorbed is less than 0.3 mmol/g.

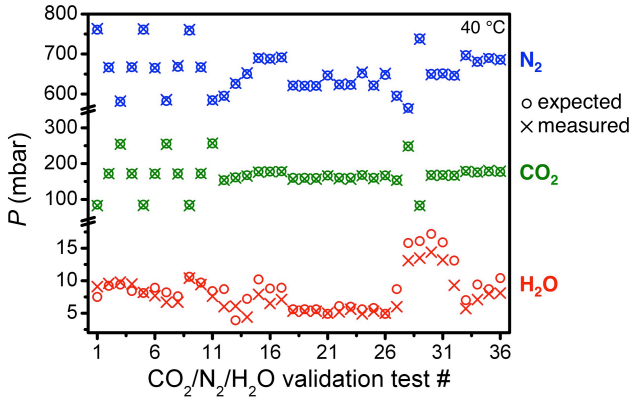

Figure 4.4. To validate the high-throughput multi-component adsorption instrument, the experimentally measured partial pressures (crosses) of N_2 (blue), CO_2 (green), and H_2O (red) are compared to the expected partial pressures (circles) of standard gas mixtures dosed into empty sample holders at 40 °C.

When drawing conclusions from multicomponent adsorption results, particularly with complex gas mixtures, it is always important to ensure that the system is truly at equilibrium when the amounts of each component adsorbed are determined.[17a] In order to ensure that the gas-tight syringe used in this work was cycled enough times to drive the complete system to an equilibrium, multicomponent measurements were performed for two metal-organic frameworks, mmen-Mg_2(dobpdc) (mmen = *N*,*N*′-dimethylethylenediamine, dobpdc^{4-} = 4,4′-dioxido-3,3′-biphenyldicarboxylate) and mmen-Ni_2(dobpdc), with 0, 5, 10, 15, or 20 syringe cycles and with the samples being fully regenerated between each measurement. The multicomponent results are discussed in detail later, but it is important to note here that the measured amounts of CO_2, N_2, and H_2O adsorbed did not vary within the error of the measurement once the syringe was cycled at least 5 times, demonstrating that the system had reached an equilibrium (Figure 4.5). As a result, we are confident that all multicomponent results presented in this work represent equilibrium amounts adsorbed, with the only exception being the amine-appended mesoporous silicas that exhibited exceedingly slow kinetics.

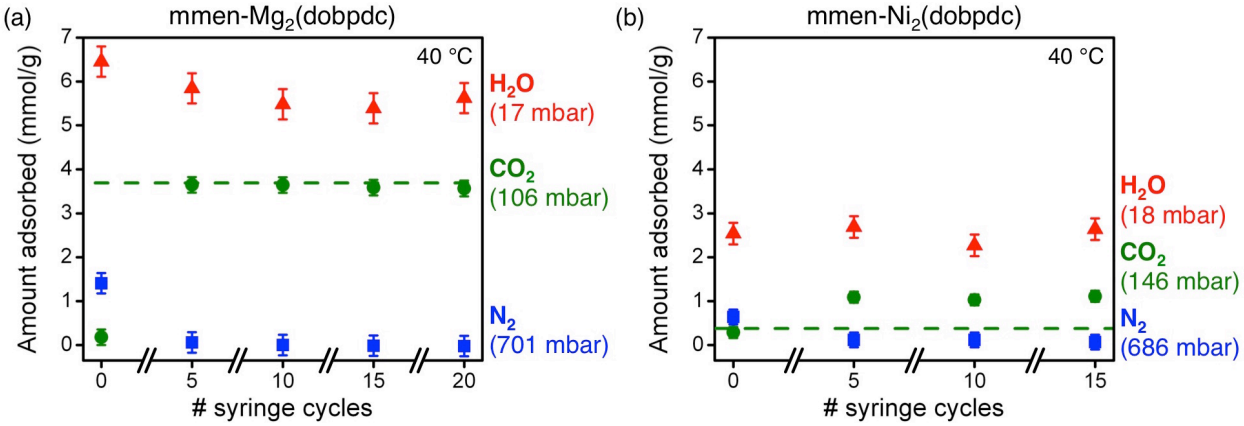

Figure 4.5. The amount of CO_2, N_2, and H_2O adsorbed for (a) mmen-Mg_2(dobpdc) and (b) mmen-Ni_2(dobpdc) is plotted as a function of the number of times the gas-tight syringe was cycled to mix the headspace gas during a multicomponent experiment. For each multicomponent measurement, the samples were fully regenerated by heating to 100 °C under vacuum, and all experimental parameters were identical with the exception of the number of syringe cycles. The dashed green lines represent the amount of pure CO_2 adsorbed from a single-component isotherm at the same CO_2 partial pressure as the multicomponent experiment.

While single-component adsorption isotherms can be conveniently shown on two-dimensional plots since the amount adsorbed is only a function of total pressure, a complete description of the three-component adsorption isotherms measured here would require a four-dimensional plot since the amount adsorbed is a function of three partial pressures.[21] To simplify the presentation of the multicomponent results reported in this work, the amount of CO_2 adsorbed from a mixture of CO_2, N_2, and H_2O is often plotted on the same two-dimensional plot as a single-component CO_2 adsorption isotherm. The single-component isotherm (green circles) effectively represents the amount of CO_2 that would be adsorbed at a given CO_2 partial pressure if N_2 and H_2O had no effect, positive or negative, on CO_2 adsorption. The amount of CO_2

adsorbed from a mixture of CO_2, N_2, and H_2O is then plotted using a square symbol at the appropriate partial pressure of CO_2, and this value can be easily compared to the pure CO_2 isotherm to gauge the effect of N_2 and H_2O on CO_2 adsorption. The partial pressure of H_2O is indicated by the color of the square data points, with the partial pressure of H_2O increasing from blue to purple to red. For nearly all multicomponent experiments reported here, the equilibrium partial pressure of N_2 is very close to 700 mbar. All error bars shown correspond to ±1.96 standard deviations (95% confidence interval).

Note that these two-dimensional plots do not include any information about the amount of N_2 or H_2O adsorbed at equilibrium, but these values are included in Table S3. For carbon capture applications, the amount of N_2 adsorbed is needed to determine the purity of captured CO_2, while the amount of H_2O adsorbed is important for evaluating the energy required to regenerate the adsorbent and to compress the CO_2. Except for a few cases discussed below, the multicomponent N_2 adsorption capacities at equilibrium are within error of zero. Before considering N_2 and H_2O adsorption, however, an adsorbent must at least maintain some capacity for CO_2 in the presence of N_2 and H_2O in order to have any use in CO_2 capture. In the following sections, the multicomponent instrument is used to directly measure the amount of CO_2 adsorbed at flue gas-like conditions for adsorbents with surface chemistries and binding sites representative of the most studied materials for CO_2 capture, including those featuring nonpolar surfaces, exposed metal cations, exposed anions, and alkylamines.

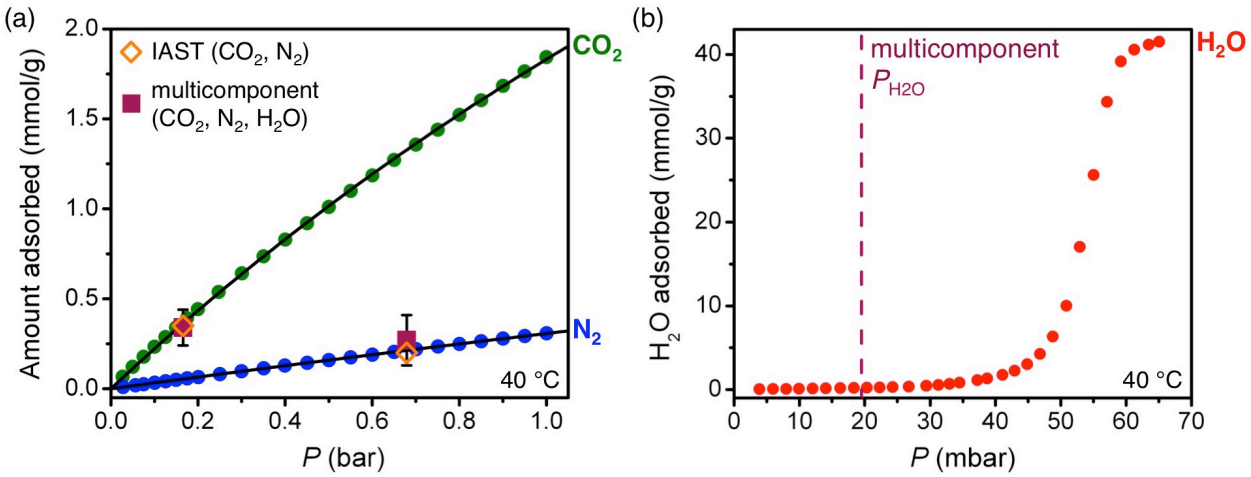

Figure 4.6. (a) Circles represent single-component CO_2 (green) and N_2 (blue) adsorption isotherms at 40 °C for the activated carbon AX-21. Black lines correspond to single-site Langmuir fits. Square data points represent the amount of CO_2 and N_2 adsorbed from a mixture of CO_2 (166 mbar), N_2 (679 mbar), and H_2O (19.5 mbar) at 40 °C. Orange diamonds represent the amount of CO_2 and N_2 predicted to be adsorbed by ideal adsorbed solution theory (IAST) from a mixture of CO_2 (166 mbar) and N_2 (679 mbar). (b) Pure H_2O adsorption isotherm (red circles) for AX-21 at 40 °C. The purple dashed line represents the partial pressure of H_2O in the multicomponent experiment.

4.3.3. Nonpolar Surfaces. Many high surface area metal-organic frameworks and activated carbons have relatively nonpolar pore surfaces that lack any strong CO_2 binding sites, resulting in materials with little affinity for CO_2 at low pressures. For instance, $Zn_4O(bdc)_3$ (bdc^{2-} = 1,4-

benzenedi-carboxylate; MOF-5)[36] and the activated carbon AX-21 (Maxsorb)[37] have Langmuir surface areas of 3995 and 4880 m^2/g but adsorb only 0.1 mmol/g (0.4 wt %) and 0.3 mmol/g (1.3 wt %) of CO_2 at 0.15 bar and 40 °C, respectively. Although many adsorbents have significantly higher 0.15-bar CO_2 capacities, most materials with nonpolar surfaces are relatively hydrophobic, and as a result, they have attracted some interest for post-combustion carbon capture.[11a,38,39]

As is the case for many activated carbons, AX-21 has a classical type V H_2O isotherm at 40 °C—there is negligible H_2O adsorption on its hydrophobic pore surface until pressures above 45 mbar, at which point clustering of H_2O molecules on the surface leads to a sharp increase in the amount of H_2O adsorbed (Figure 4.6b).[40,41] As long as the partial pressure of H_2O is kept below 45 mbar ($p/p_0 = 0.61$), H_2O adsorption should be negligible and would not be expected to interfere with CO_2 adsorption. To confirm this, a multicomponent adsorption experiment was performed for a mixture of CO_2, N_2, and H_2O in AX-21 at 40 °C and equilibrium partial pressures of 166, 679, and 20 mbar, respectively (Figure 4.6a). As expected, no H_2O is adsorbed under these conditions, and the amount of CO_2 adsorbed is 0.3(1) mmol/g, within error of the amount adsorbed from pure CO_2 at the same pressure. Moreover, the experimental amounts of CO_2 and N_2 adsorbed in the presence of H_2O match ideal adsorbed solution theory (IAST) predictions for a binary mixture of just CO_2 and N_2.

While AX-21 has some capacity for CO_2 and negligible H_2O adsorption under these conditions, it has very poor CO_2/N_2 selectivity with nearly the same amount of N_2 adsorbed as CO_2. It is also important to note that the partial pressure of H_2O in 40 °C flue gas is nearly 70 mbar, so the flue gas would likely need to be dried to below 45 mbar for H_2O adsorption to remain negligible. There may, however, be other adsorbents with type V H_2O isotherms at 40 °C that have a step closer to 70 mbar. Regardless, materials with higher selectivities for CO_2 over N_2 and higher CO_2 capacities at 0.15 bar will require stronger adsorption sites than are likely to be found in adsorbents with entirely nonpolar surfaces. Since minimizing H_2O adsorption is important to lowering the regeneration energy in a carbon capture process, designing adsorbents that have both hydrophobic surfaces and strong CO_2 binding sites is a key challenge in developing a next generation of carbon capture materials.

4.3.4. Exposed Metal Cations. Owing to its higher quadrupole moment and greater polarizability (Table 4.2), CO_2 will have a stronger electrostatic interaction than N_2 with an exposed partial charge. By incorporating metal cations with open coordination sites into metal-organic frameworks and zeolites, exposed positive charges can be created that act as strong CO_2 adsorption sites,[42,43] leading to materials with some of the highest reported 0.15-bar capacities for CO_2 and selectivities for CO_2 over N_2. In many zeolites, exposed positive charges result from extra-framework cations that are present in the pores to balance the negative charge generated from replacing a fraction of the Si^{4+} cations in pure silica zeolites with Al^{3+}. Zeolite 13X ($NaAlSi_{1.18}O_{4.36}$; FAU, Na-X) and zeolite 5A ($Na_{0.28}Ca_{0.36}AlSiO_4$; LTA, Ca-A), for instance, feature extra-framework Na^+ and/or Ca^{2+} cations that strongly adsorb CO_2.[44] For certain metal-organic frameworks, exposed metal cations can be generated directly on the framework by post-synthetically removing metal-bound solvent molecules. Exposed Mg^{2+}, Ni^{2+}, Cu^{2+}, and Fe^{3+} cations of this type are present in Mg_2(dobdc) (dobdc^{4-} = 2,5-dioxido-1,4-benzenedicarboxylate; Mg-MOF-74, CPO-27-Mg),[43,45] Ni_2(dobdc) (Ni-MOF-74, CPO-27-Ni),[46] $Cu_3(btc)_2$ (btc^{3-} = 1,3,5-benzenetricarboxylate; HKUST-1),[47] and $Fe_3OX(btc)_2$ (X = OH, F; Fe-MIL-100),[48] respectively.

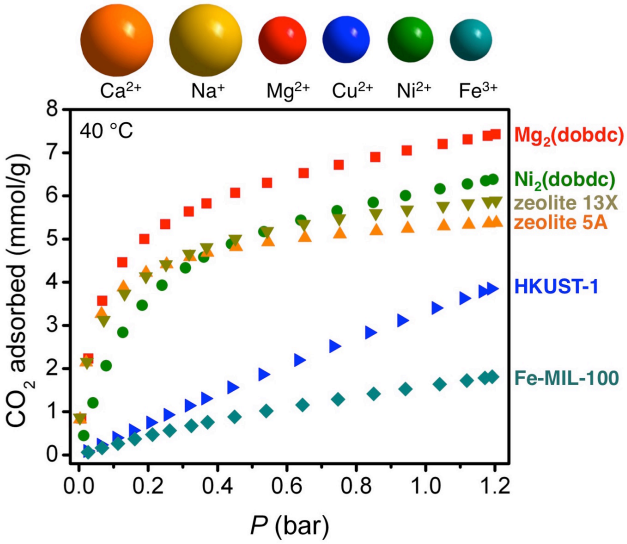

Figure 4.7. Pure CO_2 adsorption isotherms at 40 °C for metal-organic frameworks and zeolites that feature exposed Ca^{2+}, Na^{+}, Mg^{2+}, Cu^{2+}, Ni^{2+}, or Fe^{3+} cations.

4.3.4.1. Zeolites 5A, 13X, and M_2(dobdc). Zeolite 5A adopts the LTA (Linde Type A) structure type, wherein sodalite cages are connected via square faces to form a three-dimensional cubic framework of 4.2 Å diameter pores. Extra-framework Na^{+} and Ca^{2+} cations are located at the 6-ring windows ($Si_nAl_{6-n}O_6$) of the sodalite cages.[49] Zeolite 13X adopts the FAU (faujasite) structure type, wherein sodalite cages are connected via hexagonal faces to form a three-dimensional cubic framework of 7.4 Å diameter pores. Extra-framework Na^{+} cations are located primarily above the plane of the 4-ring and 6-ring windows of the sodalite cages.[50] In contrast to zeolites 5A and 13X, the exposed metal cations in the metal-organic frameworks Mg_2(dobdc) and Ni_2(dobdc) are part of the framework structure, in which helical chains of square pyramidal Mg^{2+} or Ni^{2+} cations, respectively, are bridged by $dobdc^{4-}$ ligands to form 12 Å hexagonal channels (Figure 4.1).

Table 4.2. Physical Properties of CO_2, N_2, and H_2O.[17a]

	CO_2	N_2	H_2O
kinetic diameter (Å)	3.3-3.9	3.64-3.80	2.64
polarizability ($\times 10^{-25}$ cm^3)	26.5	17.6	14.5
dipole moment ($\times 10^{18}$ esu·cm)	0	0	1.87
quadrupole moment ($\times 10^{-26}$ esu·cm^2)	4.30	1.52	-

Because of their high density of exposed metal cations, Mg_2(dobdc), Ni_2(dobdc), zeolite 13X, and zeolite 5A each adsorb over 3.1 mmol/g (12 wt %) of CO_2 at 0.15 bar and 40 °C, and have been extensively studied for carbon capture applications (Figure 4.7).[12a,b,16a,c-e,43,44,51] In fact, the 5.3 mmol/g (18.9 wt %) of CO_2 adsorbed by Mg_2(dobdc) at 0.15 bar and 40 °C is the highest uptake reported for any solid adsorbent under these conditions.[11d] While the majority of studies on the carbon capture potential of metal-organic frameworks and zeolites with exposed metal

cations have relied exclusively on single-component CO_2 and N_2 adsorption isotherms, there has been some work toward understanding the effect of H_2O on CO_2 capacity and selectivity.
Not surprisingly, DFT calculations have shown that H_2O, with its strong dipole moment, is expected to have a much greater affinity than CO_2 for exposed metal cation adsorption sites.[52] Several experimental studies have used binary adsorption measurements for mixtures of CO_2 and H_2O in zeolites 13X and 5A to show that CO_2 adsorption is indeed significantly reduced at low partial pressures of H_2O.[53] While initial breakthrough studies suggested that H_2O did not adversely affect the adsorption properties of Mg_2(dobdc),[51a] this was eventually challenged by two experimental studies that showed a significant decrease in the pure CO_2 adsorption of Mg_2(dobdc) and Ni_2(dobdc) after exposure to mixtures containing CO_2 and H_2O.[16d,e] Additionally, the amount of CO_2 adsorbed at 25 °C was measured for Ni_2(dobdc) at different H_2O loadings, revealing a continuous decrease in CO_2 adsorption with increasing H_2O loading.[16c]

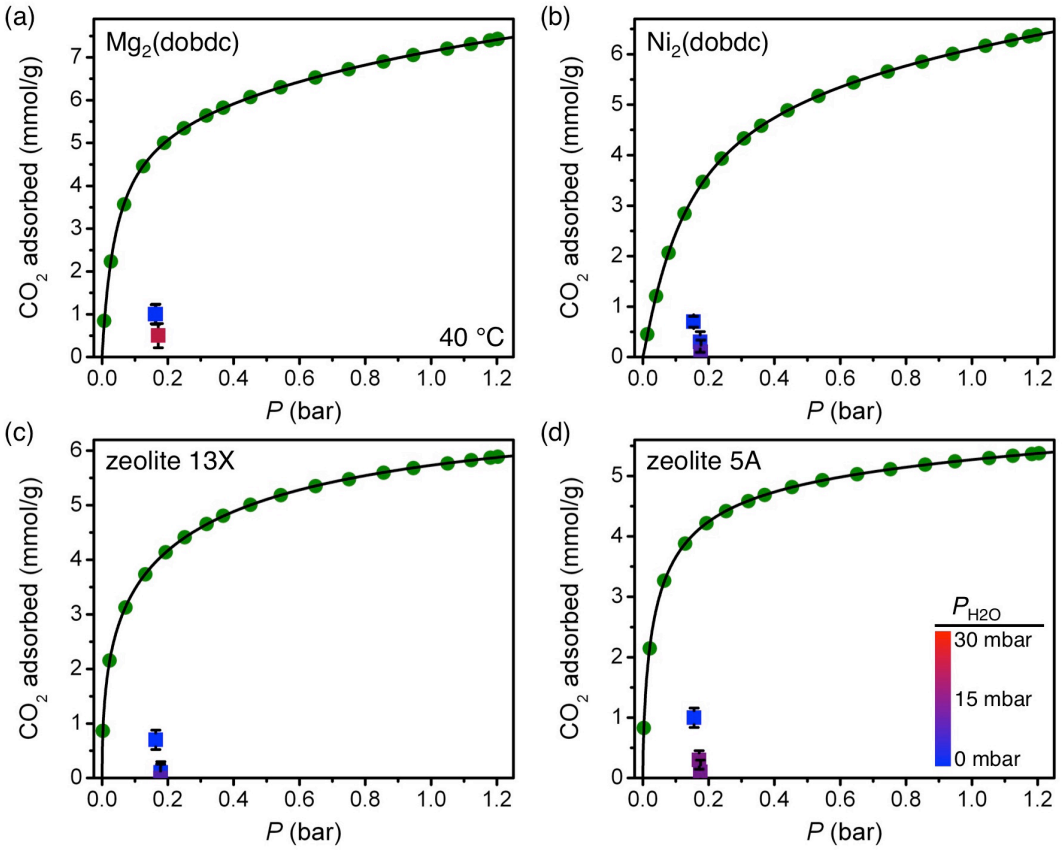

Figure 4.8. A summary of multicomponent equilibrium measurements at 40 °C for (a) Mg_2(dobdc), (b) Ni_2(dobdc), (c) zeolite 13X, and (d) zeolite 5A. Green circles represent pure CO_2 adsorption isotherms for each compound, and black lines are the corresponding single- or dual-site Langmuir fits. Square data points represent the amount of CO_2 adsorbed from a mixture of CO_2, N_2, and H_2O, and the color of the square indicates the equilibrium partial pressure of H_2O, with the partial pressure of H_2O increasing from blue to purple to red. The exact values of P_{H2O} can be found in Table 4.S3. For all multicomponent data points, the partial pressure of N_2 is 680-700 mbar.

Under dynamic breakthrough conditions, a recent study found that Ni_2(dobdc) retained a CO_2 capacity of 2.2 mmol/g (8.8 wt %) in the presence of a 15:85 mixture of CO_2:N_2 with 3% RH (0.95 mbar H_2O) at 25 °C and a total pressure of 1 bar.[54] Based on these results, it was suggested that Ni_2(dobdc) could be used for CO_2 capture from flue gas, provided a desiccant was used to pre-dry the gas to around 1 mbar of H_2O. We note, however, that this measurement was not performed under equilibrium conditions, and that the average partial pressure of H_2O in the bed at the time of CO_2 breakthrough was likely significantly below 1 mbar. Since the column was only cycled 3 times, these experiments may not adequately capture the expected build up of bound H_2O over time, particularly if the H_2O adsorption front remained close to the column inlet in each experiment.[25] Moreover, the CO_2 breakthrough capacity will be highly dependent on the exact set of dynamic conditions used, and the results may not necessarily translate to larger scales. As an alternative, multicomponent experiments can be used to directly evaluate the effects of different partial pressures of H_2O on CO_2 capacity at equilibrium conditions similar to those expected in an actual CO_2 capture process.

In this work, three-component adsorption measurements were performed with mixtures of CO_2, N_2, and H_2O at 40 °C for Mg_2(dobdc), Ni_2(dobdc), zeolite 13X, and zeolite 5A, and all results clearly show a significant decrease in the amount of CO_2 adsorbed in the presence of N_2 and H_2O (Figure 4.8). In fact, the amount of CO_2 adsorbed in all four materials decreases to less than 25% of the pure-component value at H_2O partial pressures of less than 2 mbar. The multicomponent results for zeolites 13X and 5A are in excellent agreement with previously reported binary adsorption equilibria for mixtures of CO_2 and H_2O at similar conditions.[53b] The multicomponent result for Ni_2(dobdc), however, differs significantly from the amount of CO_2 adsorbed in the previously reported breakthrough experiment, where a substantial CO_2 capacity was still observed at a low partial pressure of H_2O.[54] These conflicting results can be attributed to the fact that the breakthrough experiment was performed under dynamic conditions with the adsorbent exposed to a range of H_2O partial pressures below 1 mbar, while the multicomponent experiment was at equilibrium.

At even higher H_2O partial pressures of 10-25 mbar, which are still well short of the greater than 70 mbar expected in a flue gas, all four of these materials have high H_2O adsorption and a negligible CO_2 capacity, directly confirming that H_2O fully outcompetes CO_2 for the exposed metal cations under equilibrium carbon capture conditions (Figure 4.8). In order for any of these materials to be used in a carbon capture process, the flue gas would need to be dried significantly. While part of the adsorbent bed could be sacrificed to dry the incoming flue gas rather than capture CO_2,[24] this would almost certainly be more expensive than processes based on materials that can selectively capture CO_2 in the presence of high partial pressures of H_2O.

On a more fundamental level, it is worth mentioning that pervious *in situ* diffraction studies of CO_2 adsorption in zeolite 5A found that, in addition to exposed Na^+ and Ca^{2+} cations, CO_2 is also strongly adsorbed at the center of 8-ring windows ($Si_nAl_{8-n}O_8$) because of several close interactions between CO_2 and zeolite O atoms.[44c] It had been suggested that these 8-ring sites, which were also shown to strongly adsorb CO_2 in the Chabazite-type zeolite Cu-SSZ-13, may still be able to bind CO_2 in the presence of H_2O,[55] but the multicomponent results do not support this. Additional diffraction studies are needed to probe whether the lack of CO_2 adsorption in the presence of H_2O is due to H_2O binding directly to the 8-ring sites preferentially over CO_2 or due to H_2O adsorption at the exposed metal cations blocking access of CO_2 to the 8-ring sites.

4.3.4.2. HKUST-1. The metal-organic framework HKUST-1 is composed of Cu_2-paddlewheel units bridged by 1,3,5-benzenetricarboxylate to form a cubic structure with three types of microporous cages (Figure 4.1).[47] Although the exposed Cu^{2+} cations in HKUST-1 have a weaker interaction with CO_2 than the exposed Na^+ and Ca^{2+} cations of zeolites 13X and 5A or the exposed Mg^{2+} and Ni^{2+} cations of M_2(dobdc),[56] with just 0.6 mmol/g (2.6 wt %) of CO_2 adsorbed at 0.15 bar and 40 °C, previous experimental and theoretical studies found an increase in the amount of CO_2 adsorbed at low loadings of H_2O.[16b] More specifically, the amount of CO_2 adsorbed at 25 °C was shown to increase by roughly 160%, from 2.2 mmol/g (8.8 wt %) at 0.29 bar to 3.6 mmol/g (13.7 wt %) at 0.24 bar when 2.3 mmol/g of H_2O was pre-adsorbed (0.46 H_2O molecules per Cu^{2+} site). This increase was attributed to a stronger electrostatic interaction between Cu-bound H_2O and CO_2 than between exposed Cu^{2+}cations and CO_2.[16b] A later study on a pelletized sample of HKUST-1 also found an increase in CO_2 adsorption at low H_2O loadings, albeit to a much smaller extent.[16c]

In this work, multicomponent measurements were used to measure the CO_2 capacity of HKUST-1 at conditions more representative of a post-combustion flue gas (Figure 4.S8). Interestingly, we do not observe a significant change in the amount of CO_2 adsorbed by HKUST-1 at 40 °C with 1.9(3) mmol/g of H_2O adsorbed (0.38 H_2O per Cu^{2+}; P_{H2O} = 0.001 bar) and CO_2 and N_2 partial pressures of 0.161 bar and 0.686 bar, respectively. Because of the error in the multicomponent CO_2 adsorption uptake, it is not possible to distinguish between a moderate increase in CO_2 adsorption of up to 0.3 mmol/g and a slight decrease of up to 0.1 mmol/g from the pure-component capacity of 0.6 mmol/g based on this single measurement. Somewhat unexpectedly, we still observe the same amount of CO_2 adsorbed at an even higher equilibrium H_2O loading of 7.7 mmol/g (1.54 H_2O per Cu^{2+}; P_{H2O} = 0.004 bar), which is well past the point at which all Cu^{2+} sites should be saturated with H_2O. This could be explained by the fact that two strong CO_2 adsorption sites exist in HKUST-1: at the exposed Cu^{2+} cations (5.0 mmol/g) and at the center of the windows of the small octahedral cages (3.3 mmol/g).[51c] It is possible that CO_2 has a strong interaction with Cu-bound H_2O as was previously suggested; however, it seems more likely that, provided the CO_2 binding energy at each site is similar, the constant CO_2 capacity at H_2O loadings below 8 mmol/g is due to CO_2 adsorption still occurring at the window sites even as H_2O begins to block the exposed Cu^{2+} cations. Regardless, at higher H_2O partial pressures closer to the 0.075 bar expected in flue gas, all strong CO_2 binding sites are likely occupied or blocked by adsorbed H_2O molecules and HKUST-1 has a negligible CO_2 capacity. This result is in agreement with previous binary measurements performed at 25 °C.[16c,25]

4.3.4.2. Fe-MIL-100. The metal-organic framework Fe-MIL-100 is composed of m_3-O-centered trinuclear iron(III) clusters that are bridged by 1,3,5-benzenetricarboxylate to form a three-dimensional network of supertetrahedra, wherein microporous windows provide entrances to mesoporous cages (Figure 4.1).[48] While 1/3 of the Fe^{3+} cations are ligated by a charge-balancing OH^- or F^- anion, bound solvent can be removed from the remaining Fe^{3+} centers during activation to give five-coordinate exposed metal cations.[57] Intriguingly, it was reported that the amount of CO_2 adsorbed at 25 °C from a mixture of CO_2, N_2, and H_2O at 20% RH (6.3 mbar H_2O) or 40% RH (12.7 mbar H_2O) increased 3-fold or 5-fold, respectively, from the pure CO_2 capacity.[58] This dramatic increase in CO_2 uptake was determined from a breakthrough-type experiment after pre-equilibrating Fe-MIL-100 with H_2O vapor, and was tentatively attributed to the formation of microporous pockets created by partial H_2O filling of the mesoporous cages. Even more surprisingly, the CO_2 adsorption enthalpy at 40% RH was determined using

microcalorimetry to be just –1 kJ/mol, which was believed to be the result of endothermic H_2O desorption offsetting exothermic CO_2 adsorption.

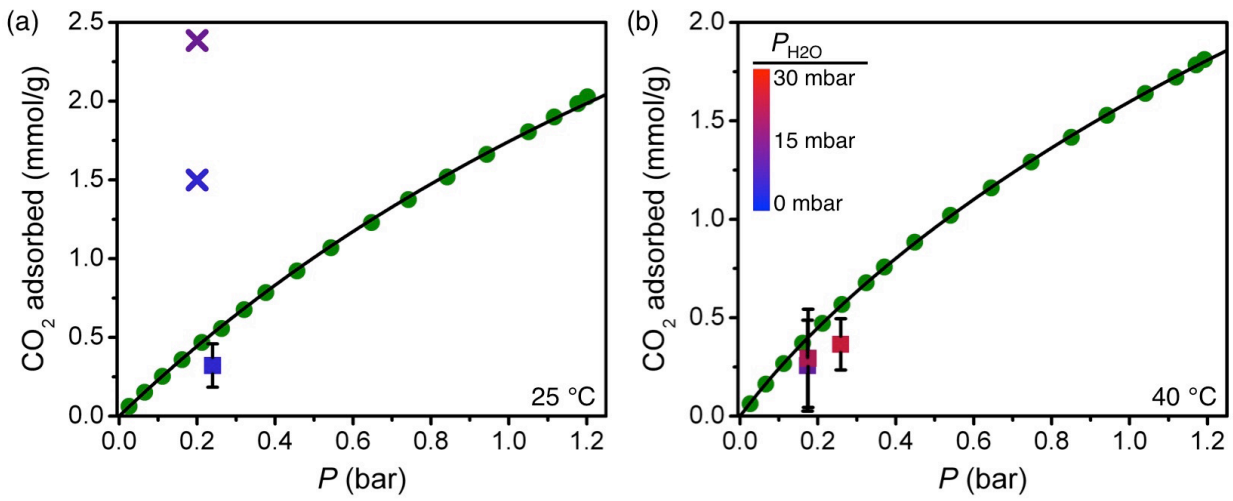

Figure 4.9. A summary of CO_2, N_2, H_2O multicomponent equilibrium measurements for Fe-MIL-100 at (a) 25 °C and (b) 40 °C. Green circles represent pure CO_2 adsorption isotherms at each temperature, and black lines are the corresponding dual-site Langmuir fits. Square data points represent the amount of CO_2 adsorbed from a mixture of CO_2, N_2, and H_2O, and the color of the square indicates the equilibrium partial pressure of H_2O. The exact values of P_{H2O} can be found in Table 4.S3. Crosses represent the amount of CO_2 adsorbed at 25 °C and 6.3 mbar of H_2O (blue) or 12.7 mbar of H_2O (purple), as determined from previous breakthrough experiments.[58]

Because of the significance of these results, we attempted to reproduce this increase in CO_2 adsorption under equilibrium conditions. After synthesizing Fe-MIL-100 and confirming that the surface area and 25 °C CO_2 adsorption isotherm matched those previously reported (Figures 4.S7, 4.S9), multicomponent measurements were performed at both 25 and 40 °C and at different partial pressures of H_2O. Regardless of whether the measurement was at 25 or 40 °C, we consistently observe a slight decrease in the amount of CO_2 adsorbed in the presence of N_2 and H_2O, even at equilibrium partial pressures that are nearly identical to the previously reported breakthrough conditions (Figure 4.9). Note that the crosses in the 25 °C multicomponent plot of Figure 4.9 represent the previously reported CO_2 breakthrough capacities.[58] Further work is necessary to determine the origin of these conflicting results and to establish why a 5-fold increase in CO_2 adsorption might be observed under dynamic conditions, but not at equilibrium.

4.3.5. Exposed Anions. Exposed negative charges are much less common in metal-organic frameworks than exposed positive charges, but just as a positive charge can attract the electronegative O atoms of CO_2, a negative charge can attract its electropositive C atom.[59] The compound $Zn(pyz)_2(SiF_6)$ provides an important example of a three-dimensional framework with exposed anions. Its structure is composed of square grids of Zn^{2+} and pyrazine pillared by hexaflurosilicate (SiF_6^{2-}) anions to form one-dimensional channels that have a 3.8 Å diagonal dimension (Figure 4.1).[60] Although the octahedral Zn cations are coordinatively saturated, the

combination of small pores and exposed F^- anions that protrude from the corners of each channel leads to strong CO_2 adsorption at low pressures, with a low-coverage heat of adsorption of –45 kJ/mol and a capacity of 2.4 mmol/g (9.6 wt %) at 40 °C and 0.15 bar. Even more significantly, breakthrough experiments performed for a mixture of 10% CO_2 in N_2 at 74% RH (23.5 mbar H_2O) at 25 °C suggested that H_2O has a negligible effect on the ability of the material to adsorb CO_2 selectively at high capacity.[59a]

In this work, multicomponent experiments were used to compare the equilibrium capacity and selectivity of $Zn(pyz)_2(SiF)_6$ for CO_2 in the presence of N_2 and H_2O to the earlier breakthrough results. Towards this end, a sample of $Zn(pyz)_2(SiF_6)$ was synthesized, and the resulting CO_2 adsorption isotherms were found to be in close agreement to those previously reported (Figure 4.S11). While previously reported variable temperature powder x-ray diffraction experiments indicated that $Zn(pyz)_2(SiF_6)$ was stable to 250 °C under vacuum,[59a] our thermogravimetric analysis results show rapid thermal decomposition occurring above 115 °C (Figure 4.S12), which is in agreement with the initial report on the thermal stability of $Zn(pyz)_2(SiF_6)$.[60] The reasons for these differences are not clear, but this low thermal stability could be problematic for designing a temperature swing adsorption process with a reasonable CO_2 working capacity.[12b] Regardless, the multicomponent measurements performed here show that at 40 °C and an H_2O equilibrium partial pressure of 13 mbar, the amount of CO_2 adsorbed at a partial pressure of 0.16 bar decreased by 60% to 0.9(2) mmol/g, and the amount of N_2 adsorbed at a partial pressure of 0.7 bar was within error of 0 mmol/g (Figure 4.10a). Under these equilibrium conditions, it thus appears that $Zn(pyz)_2(SiF_6)$ retains at least some capacity for CO_2 and a high selectivity over N_2, but H_2O is clearly affecting the CO_2 capture properties in contrast to the previously reported dynamic breakthrough results.

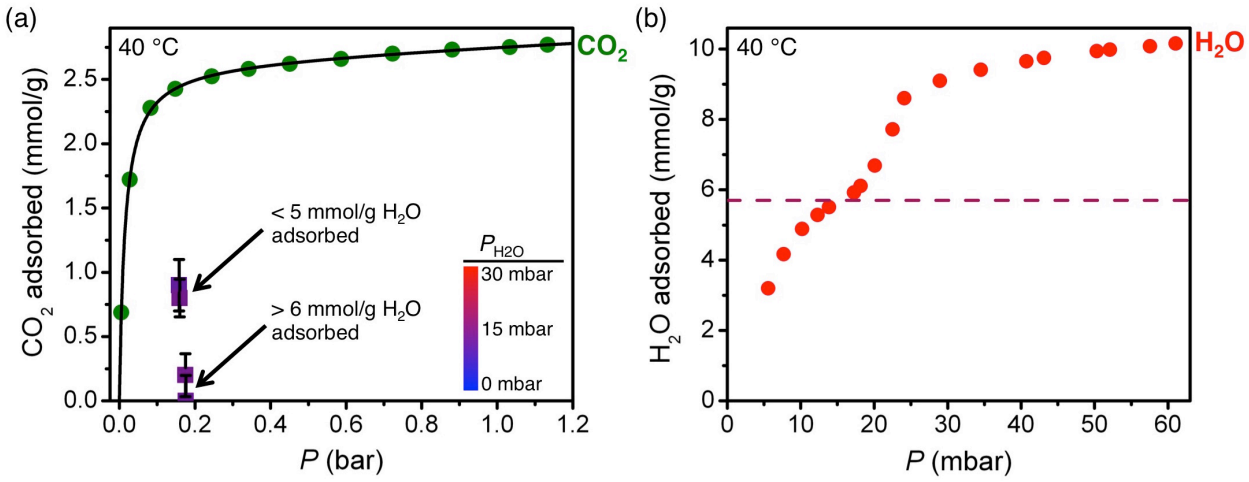

Figure 4.10. (a) A summary of CO_2, N_2, H_2O multicomponent equilibrium measurements for $Zn(pyz)_2(SiF_6)$ at 40 °C. Green circles represent a pure CO_2 adsorption isotherm, and the black line is the corresponding dual-site Langmuir fit. Square data points represent the amount of CO_2 adsorbed from a mixture of CO_2, N_2, and H_2O, and the color of the square indicates the equilibrium partial pressure of H_2O. The exact values of P_{H2O} can be found in Table 4.S3. (b) Pure H_2O adsorption isotherm (red circles) for $Zn(pyz)_2(SiF_6)$ at 40 °C.

Surprisingly, when repeating this multicomponent measurement on a fresh sample, we found that the amount of CO_2 adsorbed at nearly identical equilibrium partial pressures had dropped to within error of 0 mmol/g (Figure 4.10a). While the partial pressure of H_2O was 13 mbar in both measurements, the amount of H_2O adsorbed had increased from 3.8(3) to 6.4(4) mmol/g. Such significant changes in the amount of CO_2 and H_2O adsorbed at nearly constant partial pressures are indicative of a phase transition, something that was previously suggested to occur based on x-ray powder diffraction experiments at increasing partial pressures of H_2O.[59a] To investigate this further, a pure-component H_2O isotherm was measured at 40 °C and found to have an inflection at an H_2O loading of nearly 6 mmol/g (Figure 4.10b). The multicomponent results and pure-component H_2O isotherm are thus consistent with a phase change occurring at H_2O loadings above 6 mmol/g and leading to an unknown material with no capacity or selectivity for CO_2 adsorption in the presence of H_2O. Since this phase change would occur at the over 70 mbar of H_2O that is present in flue gas, it seems unlikely that $Zn(pyz)_2(SiF_6)$ could be used in a post-combustion carbon capture process without significant drying of the flue gas, even if the phase change is fully reversible.

Still, it is interesting that $Zn(pyz)_2(SiF_6)$ has a reasonable capacity for CO_2 and a high selectivity over N_2 before the phase change occurs, and it would be useful to determine exactly where CO_2 and H_2O adsorb in the framework under these conditions. Moreover, it would be informative to measure a similar compound with exposed anions that does not exhibit a phase change to determine the amount of CO_2 adsorbed, if any, at higher partial pressures of H_2O. Additionally, the reasons for the very different CO_2 capacities observed for $Zn(pyz)_2(SiF_6)$ under dynamic breakthrough and equilibrium conditions are not clear and need to be understood. We note, however, that the CO_2 breakthrough capacity appears to have been determined simply by multiplying the CO_2 breakthrough time by the CO_2 flow rate at the inlet of the column, and it is unclear how much H_2O was in the column at the breakthrough time and whether or not any extra-column effects were taken into account.[59a]

4.3.6. Alkylamines. Owing to their ability to capture high purity CO_2 in the presence of N_2 and H_2O, aqueous amine solutions have been the most studied carbon capture technology to date.[10] However, amine solutions suffer from several drawbacks that have prevented major reductions in the cost of captured CO_2, despite nearly 40 years of research and optimization.[6] Most importantly, the concentration of amines in water is limited to 30-40 wt % to minimize corrosion and degradation issues,[61] which in turn limits the CO_2 capacity of the solutions and leads to high regeneration energies, as a significant amount of heat is wasted boiling water rather than desorbing CO_2. Incorporating amines into solid adsorbents represents a promising strategy for increasing CO_2 capacity and reducing regeneration energy while maintaining a high selectivity for CO_2 over other flue gas components.[11a]

In designing amine-based adsorbents, it is important to consider that isolated amine groups do not have a particularly strong affinity for CO_2. Rather, strong CO_2 binding only occurs when the amine binding CO_2 can transfer a proton to another Lewis base. Typically, this proton transfer occurs to another amine to form an ammonium carbamate, resulting in an overall amine:CO_2 stoichiometry of 2:1 (Scheme 1).[62] In humid gas mixtures, H_2O can participate in the reaction of CO_2 with an amine, often leading to the formation of ammonium bicarbonate and an overall amine:CO_2 stoichiometry of 1:1 (Scheme 2).[63]

Scheme 4.1. Under dry conditions, reaction of CO_2 with two equivalents of a 1° or 2° alkylamine amine typically forms ammonium carbamate.

Scheme 4.2. Under humid conditions, reaction of CO_2 with one equivalent of a 1° or 2° alkylamine typically forms ammonium bicarbonate.

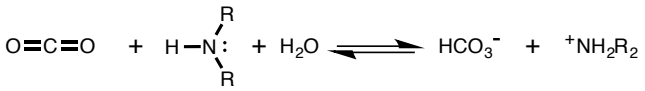

4.3.6.1. Amine-Functionalized Mesoporous Silicas. Early efforts to incorporate amines into porous materials focused primarily on mesoporous silicas. With BET surface areas ranging from 500 to 1500 m^2/g, a high density of amines can be impregnated inside or grafted directly onto the pore surface of a mesoporous silica.[64] While there has been some controversy as to the exact nature of adsorbed CO_2 inside these materials, it is now generally accepted that CO_2 reacts to form an ammonium carbamate under dry conditions (0.5 CO_2 per amine) and ammonium bicarbonate (1 CO_2 per amine) under humid conditions, provided that the silica has a high density of 1° or 2° amines.[62b, 65] It is important to note that although these are the thermodynamically favored products under each set of conditions, ammonium carbamate formation occurs at a much faster rate than bicarbonate formation.[66] As a result, it can take a very long time to reach a full equilibrium capacity of 1 CO_2 per amine in the presence of H_2O, as there is often a mixture of ammonium carbamate and bicarbonate present before equilibrium is reached. This perhaps explains the wide range of CO_2 to amine ratios that have been reported for different amine-appended or -impregnated silicas in the presence of H_2O.[11a] Additionally, the majority of reports on the equilibrium CO_2 capacity of mesoporous silicas in the presence of H_2O involve flowing CO_2 over a sample that has been pre-equilibrated with H_2O and measuring the increase in weight. To calculate the CO_2 uptake, it is assumed that the amount of H_2O adsorbed is unaffected by CO_2 adsorption. Recent binary adsorption measurements, however, have shown that this assumption often leads to incorrect conclusions about the amount of CO_2 adsorbed in the presence of H_2O.[67]

Many of the amine-functionalized silicas investigated for CO_2 capture have been based on MCM-41 (Mobil Composition of Matter No. 41), which consists of cylindrical mesopores that are arranged in a hexagonal lattice.[68] In this work, three amine-functionalized derivatives of MCM-41 were synthesized according to previous reports: 3-aminopropyl grafted MCM-41 (1°-MCM-41), 3-methylaminopropyl grafted MCM-41 (2°-MCM-41), and polyethylenimine impregnated MCM-41 (PEI-MCM-41).[69,70b] Based on elemental analysis, 4.2 mmol of 1° amine per g silica and 3.7 mmol of 2° amine per g silica were grafted in 1°-MCM-41 and 2°-MCM-41, respectively, which is comparable to the average loading for all reported monoamine-appended silicas of just over 3 mmol/g.[11a] At 40 °C and 1 bar, both 1°-MCM-41 and 2°-MCM-41 adsorb nearly 0.5 molecules of CO_2 per amine, as expected for ammonium carbamate formation under dry conditions (Figure 4.11).

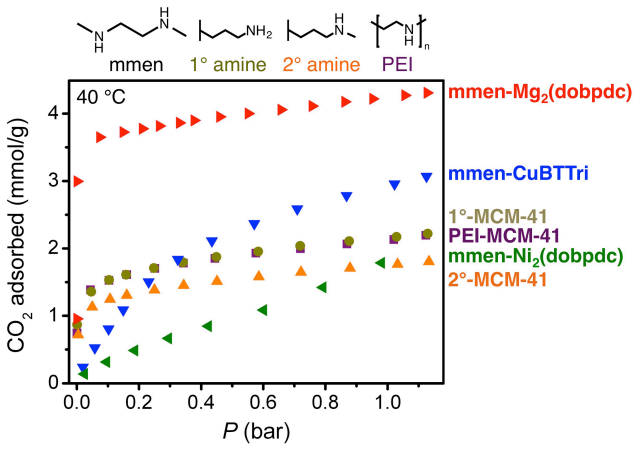

Figure 4.11. Pure CO_2 adsorption isotherms at 40 °C for metal-organic frameworks and mesoporous silicas that feature alkylamine groups.

With 33% of N by mass and a roughly 1:1:1 mixture 1°, 2°, and 3° amines, branched PEI has a high density of amine groups and has been shown to have improved CO_2 capture performance when it is impregnated inside a solid support rather than neat.[70] The PEI-MCM-41 sample synthesized in this work contained 32 wt % of PEI (7.4 mmol N per g silica). At 40 °C and 1 bar, PEI-MCM-41 adsorbs 0.28 molecules of CO_2 per amine (2.1 mmol/g), which is consistent with the amine efficiencies of previously reported amine-impregnated silicas (Figure 4.11).[11]
Here, multicomponent experiments were used to measure directly the amount of CO_2 adsorbed from a mixture of CO_2, N_2, and H_2O at 40 °C and a CO_2 partial pressure near 0.15 bar. Note that since primary amines are prone to deactivate by forming urea linkages under dry conditions,[69] the pure CO_2 and multicomponent isotherms reported here were measured on separate samples. At an equilibrium H_2O partial pressure of 19 mbar (26% RH), the amount of CO_2 adsorbed by 1°-MCM-41 decreased by 25%. This result appears to be in conflict with an earlier report that used a thermogravimetric analyzer coupled to a mass spectrometer to show a 76% increase in CO_2 adsorption for 1°-MCM-41 at 24 mbar of H_2O and 25 °C.[67] The two 1°-MCM-41 samples have nearly identical amine loadings, but the bare MCM-41 silica used in this work has an average pore size of 2.4 nm, while the previously reported material used a pore-enlarged variant of MCM-41 with an average pore size of nearly 11 nm.[71] The different pore sizes of the resulting amine-grafted materials could be responsible for the different CO_2 capacities observed under humid conditions.

The amount of CO_2 adsorbed by 2°-MCM-41 at 17 mbar of H_2O was within error of the dry CO_2 uptake, suggesting that no bicarbonate was formed. Although the sample was equilibrated for over 24 h, it is likely that bicarbonate formation is exceedingly slow in this secondary amine material and equilibrium was not reached over the course of the multicomponent measurement.[66] During the multicomponent measurement, the total pressure of the system was still decreasing at a very slow rate even after 24 h of forced equilibration, which suggests that some CO_2 adsorption was still occurring with very slow kinetics. There are several literature reports of constant CO_2 uptake for amine-appended silicas under both dry and humid conditions, but whether or not kinetics are a factor in these experiments is uncertain.[11a]

In contrast to 1°-MCM-41 and 2°-MCM-41, the amount of CO_2 adsorbed in PEI-MCM-41 increased significantly from 1.5 mmol/g (0.20 CO_2 per N) to 2.5(1) mmol/g (0.34 CO_2 per N) at 17 mbar of H_2O. This 67(7)% increase is slightly higher than the 40% increase observed for 50 wt % PEI-MCM-41 in a dynamic breakthrough experiment at 75 °C.[70c] Although the observed

CO_2 capacity is much less than 1 CO_2 per amine, it is possible that bicarbonate is still forming but the CO_2 partial pressure is not high enough to reach a full capacity of 1 CO_2 per amine or that not all of the amine sites of the PEI are accessible to CO_2.

4.3.6.2. Amine-Appended Metal-Organic Frameworks. While initial efforts to functionalize solid adsorbents with amines involved mostly mesoporous silicas, several amine-appended metal-organic frameworks have recently shown promising CO_2 capture properties.[72] For instance, the amine-appended metal-organic framework $H_3[(Cu_4Cl)_3(BTTri)_8(mmen)_{12}]$ (mmen-CuBTTri; H_3BTTri = 1,3,5-tri(1*H*-1,2,3-triazol-4-yl)benzene) features diamines that are coordinated to the exposed Cu^{2+} cations of its sodalite-type cages (Figure 4.1), resulting in a nearly 250% increase in the amount of CO_2 adsorbed at 0.15 bar and 25 °C as compared to the bare framework.[72c] Similar to 1°-MCM-41, mmen-CuBTTri shows a very slight decrease in CO_2 uptake in the presence of N_2 and H_2O, but still adsorbs 0.9(2) mmol/g of CO_2. This demonstrates that appending amines to exposed metal cation sites in metal-organic frameworks is a viable strategy for adsorbing CO_2 under humid conditions.

In contrast to mesoporous silicas, highly crystalline metal-organic frameworks offer the advantage of well-defined and ordered sites for attaching amines, a feature that was recently shown to lead to unprecedented cooperative CO_2 binding and low CO_2 capture regeneration energies in the diamine-appended metal-organic framework mmen-Mg_2(dobpdc).[73] In this material, which features an expanded version of Mg_2(dobdc), one end of each diamine is attached to an exposed Mg^{2+} cation while the other end is exposed on the surface (Figure 4.1). With all diamines spaced exactly 6.8 Å apart along each hexagonal channel, the density of amine groups in mmen-Mg_2(dobpdc) is 7.3 mmol/mL, exceeding that of a 30 wt % monoethanolamine solution (4.9 mmol/mL).

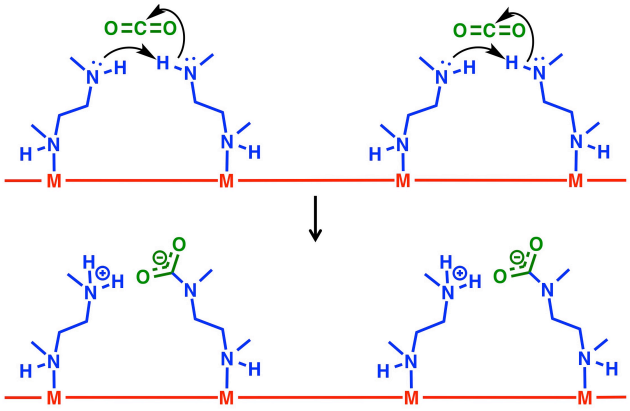

Figure 4.12. The proposed mechanism for CO_2 adsorption in mmen-Ni_2(dobpdc) and pre-step CO_2 adsorption in mmen-Mg_2(dobpdc) is shown at four neighboring M-mmen sites within an infinite one-dimensional chain of such sites running along the crystallographic *c* axis of the compound. Simultaneous proton transfer and nucleophilic attack of an uncoordinated amine on a CO_2 molecule forms an ammonium carbamate species.

At 40 °C and pressures below 0.5 mbar, the mechanism for CO_2 adsorption in mmen-Mg_2(dobpdc) is thought to be similar to that of classical amine-appended silicas—two free amine groups react with a CO_2 molecule to form ammonium carbamate (Figure 4.12). At higher

pressures, however, there is a sharp step in the CO_2 adsorption isotherm of mmen-Mg_2(dobpdc), and both ends of the diamine begin to participate in CO_2 binding. Specifically, a proton is transferred from a metal-bound amine to a neighboring free amine as CO_2 simultaneously inserts into the Mg–N bond, resulting in the formation of one-dimensional chains of ammonium carbamate that run parallel to each chain of Mg^{2+} cations.[73] This insertion-based CO_2 adsorption mechanism leads to strong, cooperative CO_2 binding, and at 0.15 bar and 40 °C, one CO_2 molecule is adsorbed per mmen to give a total capacity of 3.73 mmol/g (14.1 wt %).

Since CO_2, but not N_2 or H_2O, induces a phase transition in mmen-Mg_2(dobpdc), changing both the structure and composition of the adsorbent, it is impossible to use pure-component adsorption isotherms to predict CO_2 selectivity and capacity for a mixture of CO_2, N_2, and H_2O. Instead, the direct measurement of multicomponent adsorption is the only way to investigate the effects of H_2O and N_2 on CO_2 binding in mmen-Mg_2(dobpdc) at equilibrium. Of particular interest is to determine whether the insertion-based CO_2 adsorption mechanism is affected by H_2O and if ammonium carbamate is still the only form of adsorbed CO_2 under humid conditions. Significantly, multicomponent measurements with H_2O partial pressures as high as 19 mbar, CO_2 partial pressures between 100 and 300 mbar, and N_2 partial pressures between 500 and 700 mbar, clearly show that the amount of CO_2 adsorbed from a mixture of CO_2, N_2, and H_2O is the same as, or slightly higher than, from pure CO_2. Thus, H_2O and N_2 do not have a significant effect on CO_2 adsorption in mmen-Mg_2(dobpdc) (Figure 4.13a). To the best of our knowledge, the multicomponent CO_2 uptake of 4.2(2) mmol/g (15.6 wt %) for mmen-Mg_2(dobpdc) represents the highest value ever reported for any metal-organic framework or silica under similar humid conditions. While no N_2 adsorption is observed in mmen-Mg_2(dobpdc) during the multicomponent experiments, between 4.9 and 9.5 mmol/g of H_2O is adsorbed, depending on the exact equilibrium conditions. Since CO_2 and H_2O do not compete for the same binding sites, it should be possible to reduce this H_2O adsorption without affecting the amount of CO_2 adsorbed by, for instance, tuning the alkylamine or bridging organic ligand to increase the hydrophobicity of the pore surface. Note that one of the multicomponent measurements was repeated four further times on the same sample with identical results after regenerating at 100 °C under vacuum for 2 h, demonstrating that CO_2 and H_2O adsorption is fully reversible (Figure 4.5). Longer cycling studies with mixtures of CO_2, N_2, and H_2O and regeneration using a pure temperature swing are currently in progress.

To confirm that CO_2 insertion into the Mg–N bond is still occurring in the presence of H_2O, infrared spectroscopy measurements were performed after equilibrating a sample of mmen-Mg_2(dobpdc) with a mixture of CO_2, N_2, and H_2O (Figure 4.14). Previously, a sharp band was observed at 1334 cm^{-1} in the infrared spectrum of mmen-Mg_2(dobpdc) dosed with pure CO_2. This band was assigned to the C–N stretch of a carbamate, and is only present after insertion of CO_2 into the M–N bond generates an O-bound carbamate species with more double-bond character in the C–N bond.[73] Significantly, there is also a sharp band observed at 1334 cm^{-1} for mmen-Mg_2(dobpdc) in the presence of CO_2, N_2, and H_2O, confirming that CO_2 insertion into the M–N bond is still occurring and that H_2O does not change the mechanism for CO_2 adsorption (Figure 4.13). Although the multicomponent measurements indicate a very slight increase in the amount of CO_2 adsorbed in the presence of H_2O, there is no evidence of any carbonate or bicarbonate species in the infrared spectrum.

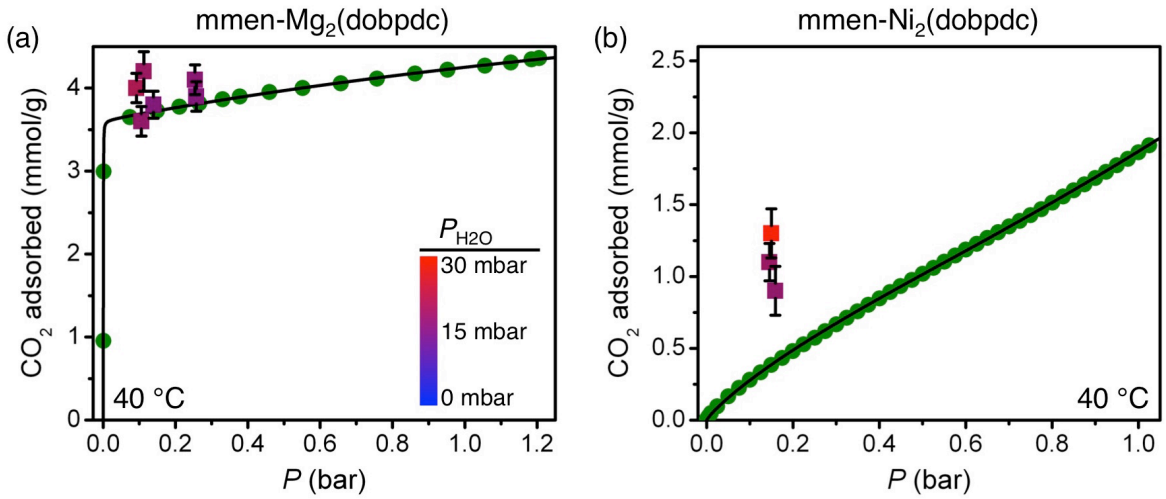

Figure 4.13. A summary of CO_2, N_2, H_2O multicomponent equilibrium measurements at 40 °C for (a) mmen-Mg_2(dobpdc) and (b) mmen-Ni_2(dobdc). Green circles represent pure CO_2 adsorption isotherms for each compound, and black lines are the corresponding dual-site Langmuir fits. Square data points represent the amount of CO_2 adsorbed from a mixture of CO_2, N_2, and H_2O, and the color of the square indicates the equilibrium partial pressure of H_2O. The exact values of P_{H2O} can be found in Table 4.S3.

In the isostructural nickel analogue of this framework, mmen-Ni_2(dobpdc), the increased strength of the Ni–N bond makes the insertion of CO_2 thermodynamically unfavorable, and the CO_2 adsorption isotherms do not contain a step, resulting in just 0.4 mmol/g (1.7 wt %) of CO_2 adsorbed at 40 °C and 0.15 bar.[73] Note that while the pure CO_2 isotherm of mmen-Ni_2(dobpdc) is not nearly as steep as expected for an adsorbent with strong CO_2 binding sites, the isosteric heat of adsorption at low coverage is still –40 to –60 kJ/mol. The isotherm is not as steep as that of most metal-organic frameworks with CO_2 binding energies in this range, such as Mg_2(dobdc), because the entropy of CO_2 adsorption is much more positive in mmen-Ni_2(dobpdc) than in more classical materials.[73] This strong CO_2 binding and large entropy of adsorption can likely be explained by a similar mechanism as for the pre-step adsorption in mmen-Mg_2(dobpdc)—a proton is transferred between the free ends of two neighboring diamines and CO_2 is bound via the formation of ammonium carbamate, resulting in one CO_2 bound per every two mmen (Figure 4.12). In order for this proton transfer to occur, the diamines likely lose some rotational degrees of freedom as ammonium carbamate pairs are formed, which leads to the large entropy penalty associated with CO_2 binding.

To support the proposed mechanism for dry CO_2 adsorption in mmen-Ni_2(dobpdc), infrared spectroscopy measurements were performed on mmen-Ni_2(dobpdc) in the presence of pure N_2 and pure CO_2 (Figure 4.14). Under a pure N_2 atmosphere, two distinct N–H vibrations are observed at 3330 cm^{-1} and 3258 cm^{-1} and can be assigned to the free and Ni-bound ends of the diamines, respectively. The metal-bound N–H stretch is identical to that observed for mmen-Mg_2(dobpdc), while the free N–H stretch is red-shifted by 4 cm^{-1}.[73] Upon exposure to 1 bar of pure CO_2, the free N–H resonance at 3330 cm^{-1} disappears and a new vibration is observed at 3271 cm^{-1}. The disappearance of the free N–H vibration is consistent with the formation of ammonium. If only the free ends of each diamine participate in the reaction with CO_2, then half of all diamines would be expected to have an ammonium on the free end, while the other half of

diamines would have a carbamate (Figure 4.12). Indeed, there are two N–H resonances of roughly equal intensity observed at 3271 and 3258 cm^{-1} in the presence of CO_2 that can be assigned to the N–H on Ni-bound ends of diamines that have either an ammonium or a carbamate on the free end. A broad feature also grows in at roughly 1680 cm^{-1} after CO_2 dosing, which is consistent with the C=O vibration of carbamate. Finally, no new bands are observed between 1275 and 1375 cm^{-1} after CO_2 adsorption, which is consistent with the ammonium carbamate reaction occurring at the free ends of the diamines, with no insertion of CO_2 into the M–Ni bond.

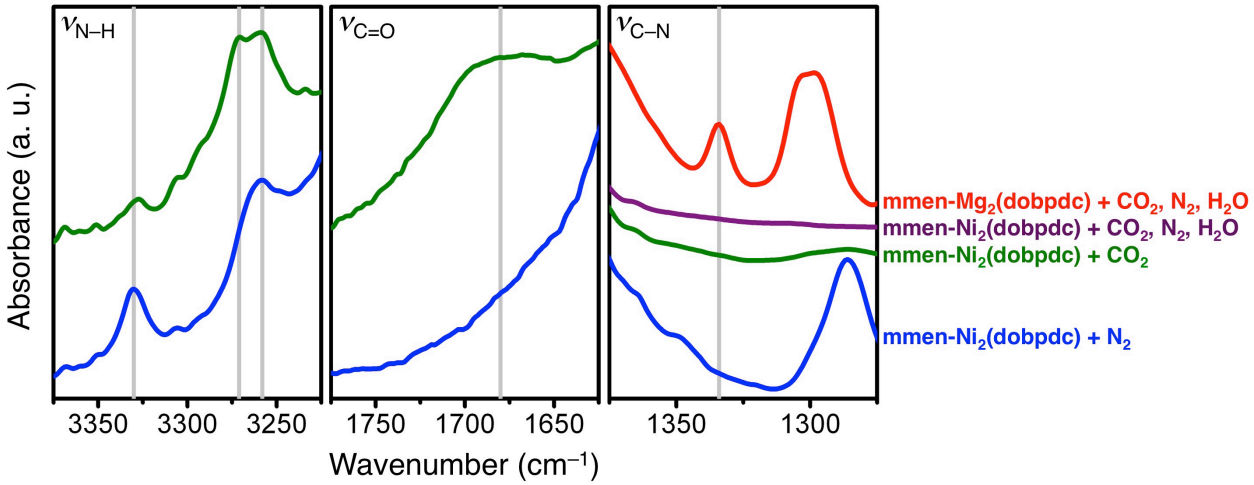

Figure 4.14. Infrared spectra upon dosing activated mmen-Ni_2(dobpdc) with N_2 (blue), CO_2 (green), and a mixture of CO_2, N_2, and H_2O (purple), and dosing activated mmen-Mg_2(dobpdc) with a mixture of CO_2, N_2, and H_2O (red) at 25 °C. The three different regions show bands corresponding to N–H, C=O, and C–N stretching vibrations, from left to right, respectively.

Somewhat unexpectedly, the amount of CO_2 adsorbed in mmen-Ni_2(dobpdc) increases nearly three-fold to 1.3(2) mmol/g (5.4 wt %) in the presence of 29 mbar of H_2O and 691 mbar of N_2 (Figure 4.13b). This substantial increase in CO_2 adsorption is greater than typically observed for amine-appended silicas and suggests that H_2O has a strong effect on the CO_2 binding mechanism. Despite the large increase in CO_2 uptake, only 0.37(7) mmol of CO_2 is adsorbed per mmol of free amine under the multicomponent conditions.

To gain further insight into these multicomponent results, infrared spectroscopy measurements were also performed for mmen-Ni_2(dobpdc) under an atmosphere of N_2, CO_2, and H_2O (Figure 4.14). Unfortunately, a very broad and high intensity band above 3000 cm^{-1}, resulting from the large amount of H_2O in the gas-phase, overwhelms any N–H resonances (4.S18, 4.S19). Still, no new bands are observed between 1275 and 1375 cm^{-1}, demonstrating that CO_2 insertion into the M–Ni bond does not occur in mmen-Ni_2(dobpdc) even in the presence of H_2O. Although CO_2 insertion is ruled out, the infrared spectrum of mmen-Ni_2(dobpdc) does not provide any conclusive evidence that can explain the increased CO_2 uptake in the presence of H_2O. It is possible that bicarbonate is formed, but its infrared bands are masked by H_2O or the organic bridging ligand. Alternatively, H_2O may facilitate the formation of more ammonium carbamate at lower CO_2 partial pressures by, for instance, breaking up hydrogen-bonding

between neighboring diamines to expose more CO_2 binding sites than are present under dry conditions.[65g]

4.4. Outlook and Conclusions

The multicomponent results reported in this work for adsorption of CO_2, N_2, and H_2O in 15 different materials, including metal-organic frameworks, zeolites, mesoporous silicas, and an activated carbon, are summarized in Figure 4.15. Here, a multicomponent data point is plotted for each material at the equilibrium conditions most representative of the composition of a coal-fired power plant flue gas. In the bottom pane of the bar graph, the amount of CO_2 adsorbed from the multicomponent mixture of CO_2, N_2, and H_2O (red) is compared to the amount of CO_2 adsorbed at the same partial pressure in the absence of N_2 and H_2O (green). In the top pane, the amount of H_2O adsorbed in the multicomponent experiment is shown. As has been discussed in detail, all of the adsorbents with exposed metal cations or anions take up a significant amount of H_2O and negligible amount of CO_2 under these simulated flue gas equilibrium conditions, while MOF-5 and the AX-21 activated carbon have mostly nonpolar surfaces that lead to very little H_2O adsorption but also to very little CO_2 uptake at these low pressures. Adsorbents functionalized with alkylamines, however, maintain a significant CO_2 capacity at the multicomponent equilibrium conditions, with mmen-Mg_2(dobpdc) adsorbing a record amount of CO_2 in the presence of H_2O.

In addition to maximizing CO_2 adsorption, minimizing H_2O adsorption is critical to achieving low regeneration energies in any CO_2 capture process that involves a temperature swing since some of the heat supplied to desorb CO_2 will also go toward desorbing H_2O. The direct measurement of equilibrium H_2O adsorption in the presence of N_2 and CO_2 is thus important for identifying adsorbents with the best CO_2 capture performance. This is particularly true for adsorbents that change upon binding CO_2, where H_2O adsorption may be very different before and after CO_2 adsorption. It is worth noting that measuring the amount of H_2O adsorbed in a breakthrough experiment with CO_2 is extremely challenging, if not impossible, when the column is pre-equilibrated with H_2O, as is often necessary when running small-scale breakthrough experiments.

Although the multicomponent results presented in this work targeted equilibrium conditions representative of adsorption from a post-combustion flue gas, evaluating multicomponent equilibria at desorption conditions is also important. Since a pure temperature swing or vacuum-assisted temperature swing process will likely be most effective for CO_2 capture,[9,12c] evaluating the amount of CO_2 and H_2O adsorbed from mixtures as a function of regeneration temperature and pressure is necessary to determine CO_2 and H_2O working capacities and to calculate regeneration energies. Recently, it was shown that the cooperative CO_2 binding in mmen-Mg_2(dobpdc) allows a CO_2 working capacity of nearly 14 wt % (3.7 mmol/g) to be achieved with an unprecedented temperature swing of just 50 °C.[73] The effects of H_2O on this working capacity are currently being investigated under both dynamic and equilibrium conditions. Because of their structural and chemical tunability, metal-organic frameworks functionalized with alkylamines are a particularly promising class of solid adsorbents for achieving high CO_2 working capacities, minimal H_2O adsorption, and low regeneration energies at post-combustion CO_2 capture conditions.

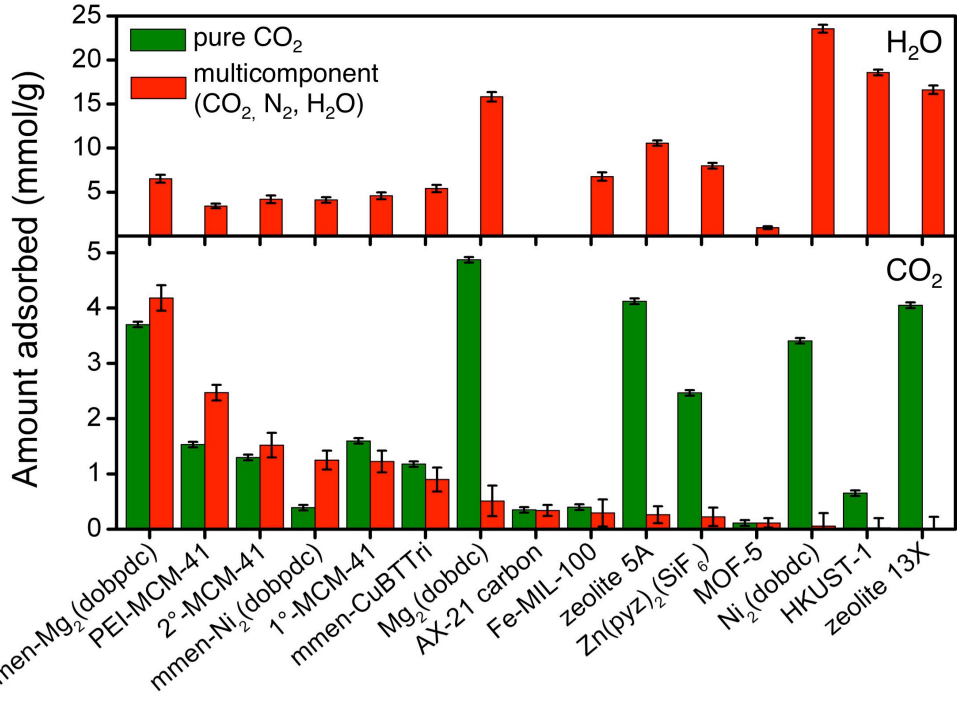

Figure 4.15. A summary of the multicomponent adsorption measurements performed in this work for mixtures of CO_2, N_2, and H_2O at 40 °C and equilibrium conditions representative of a coal-fired power plant flue gas. The green bars represent the amount of CO_2 adsorbed in a single-component isotherm at the same CO_2 partial pressure as the multicomponent experiment. The red bars in the bottom pane represent the amount of CO_2 adsorbed in the multicomponent experiment. The red bars in the upper pane represent the amount of H_2O adsorbed in the multicomponent experiment. For the multicomponent experiments, all partial pressures of N_2 are between 679 and 698 mbar, of CO_2 are between 113 and 178 mbar, and of H_2O are between 10 and 29 mbar. Total pressures are between 821 and 890 mbar. See Table 4.S3 for exact equilibrium partial pressures and amounts adsorbed. Error bars are shown at a 95% confidence interval.

In addition to CO_2, N_2, and H_2O, multicomponent measurements and long-term cycling studies that include other flue gas components, such as O_2, NO_x, and SO_x, will be valuable in assessing adsorbents for CO_2 capture applications. Measuring multicomponent equilibrium kinetics and heats of adsorption, which are particularly challenging experiments, is also important but rarely reported in the literature for gas mixtures.[17b] While no real CO_2 capture process will operate under true equilibrium conditions, equilibrium data is essential for comparing different materials and for simulating the dynamic processes of a large-scale separation.

4.5. Notation

R	gas constant (83.144 mbar mL $mmol^{-1}$ K^{-1})
i	CO_2, N_2, or H_2O
m	mass of sample (g)
$P_{dose,i}$	partial pressure of gas i dosed (mbar)
P_{dose}	total pressure of standard CO_2, N_2 mixture dosed (mbar)
$P_{eq,i}$	partial pressure of gas i at equilibrium (mbar)
P_{eq}	total pressure at equilibrium (mbar)
$n_{ads,i}$	amount adsorbed of gas i (mmol g^{-1})
$n_{dose,i}$	amount dosed of gas i (mmol g^{-1})
$n_{free,i}$	amount of gas i in gas phase at equilibrium (mmol g^{-1})
V_{sv}	secondary volume (mL)
T_{sv}	secondary volume temperature (K)
V_{dv}	residual gas analyzer dose volume (mL)
T_{dv}	residual gas analyzer dose volume temperature (K)
V_{pv}	primary volume (mL)
T_{pv}	primary volume temperature (K)
c_{CO_2}	percentage of CO_2 in standard CO_2/N_2 mixture (%)
X	molar ratio of CO_2 to N_2 in the gas phase at equilibrium
σ	standard deviation
J	total number of H_2O doses
$P_{dose,H_2O,j}$	pressure of H_2O dosed to sample for dose j (mbar)
$P_{removed,H_2O,j}$	pressure of H_2O remaining after expanding to sample for dose j (mbar)
$P_{n,i,exp}$	measured partial pressure of gas i using standard gas mixtures
$P_{n,i,calc}$	calculated partial pressure of gas i in a standard gas mixture
N	total number of CO_2, N_2, H_2O standard mixture measurements

4.6. Acknowledgements

This research was funded by the Advanced Research Projects Agency – Energy (ARPA-E), U.S. Department of Energy. We thank Adam Berger, Dr. Abhoyjit Bhown, Prof. Berend Smit, Prof. Rajamani Krishna, Dr. Zoey Herm, Dr. Eric Bloch, and Dianne Xiao for helpful discussions, and Dr. Tom McDonald, David Gygi, Henry Jiang, Jonathan Bachman for assisting with sample preparation. The multicomponent adsorption instrument was designed, built, and tested in collaboration with Justin Dutton and Dr. Steven Kaye and Wildcat Discovery Technologies Inc.

4.7. References and Supplementary Figures

(1) The H_2O content of a coal-fired power plant's flue gas is highly dependent on whether or not a wet or dry flue gas desulphurization (FGD) process is in use.

(2) International Energy Agency, *CO2 Emissions from Fuel Combustion* **2014**, IEA, Paris. DOI: 10.1787/co2_fuel-2014-en.

(3) IPCC, 2013. Summary for Policymakers, in: *Climate Change 2013: The Physical Science Basis. Contribution of Working Group I to the Fifth Assessment Report of the Intergovernmental Panel on Climate Change*, (eds. Stocker, T. F. *et al.*) (Cambridge Univ. Press, New York, 2013).

(4) (a) Chu, S. *Science* **2009**, *325*, 1599. (b) Haszeldine, R. S. *Science* **2009**, *325*, 1647.

(5) (a) Wheeler, D.; Ummel, K. *Calculating CARMA: Global Estimation of CO2 Emissions from the Power Sector* **2008**, Center for Global Development, Working Paper 145. (b) Ummel, K. *CARMA Revisited: An Updated Database of Carbon Dioxide Emissions from Power Plants Worldwide* **2012**, Center for Global Development, Working Paper 304.

(6) Fout, T.; Murphy, J. T. *DOE/NETL's Carbon Capture R&D Program for Existing Coal-Fired Power Plants;* DOE/NETL 2009/1356; National Energy Technology Laboratory, 2009.

(7) Figueroa, J. D.; Fout, T.; Plasynski, S.; McIlvried, H.; Srivastava, R. D. *Int. J. Greenhouse Gas Control* **2008**, *2*, 9.

(8) (a) Bhown, A. S. *Energy Procedia* **2014**, *63*, 542. (b) Boot-Handford, M. E.; Abanades, J. C.; Anthony, E. J; Blunt, M. J.; Brandani, S.; Mac Dowell, N.; Fernández, J. R.; Ferrari, M.-C.; Gross, R.; Hallet, J. P.; Haszeldine, R. S.; Heptonstall, P.; Lyngfelt, A.; Makuch, Z.; Mangano, E..; Porter, R. T. J.; Pourkashanian, M.; Rochelle, G. T.; Shah, N.; J. G. Yao, Fennell, P. S. *Energy Envrion. Sci.* **2014**, *7*, 130.

(9) Drage, T. C.; Snape, C. E.; Stevens, L. A.; Wood, J.; Wang, J.; Cooper, A. I.; Dawson, R.; Guo, X.; Satterley, C.; Irons, R. *J. Mater. Chem.* **2012**, *22*, 2815.

(10) Rochelle, G. T. *Science* **2009**, *325*, 1652.

(11) (a) Choi, S.; Drese, J. H.; Jones, C. W. *ChemSusChem* **2009**, *2*, 796. (b) D'Alessandro, D. M.; Smit, B.; Long, J. R. *Angew. Chem., Int. Ed.* **2010**, *49*, 6058. (c) Wang, Q.; Luo, J.; Zhong, Z.; Borgna, A. *Energy Environ. Sci.* **2011**, *4*, 42. (d) Sumida, K.; Rogow, D. L.; Mason, J. A.; McDonald, T. M.; Bloch, E. D.; Herm, Z. R.; Bae, T.-H.; Long, J. R. *Chem. Rev.* **2012**, *112*, 724. (e) Liu, Y.; Wang, Z. U.; Zhou, H.-C. *Greenhouse Gasses Sci. Technol.* **2012**, *2*, 239. (f) Liu, J.; Thallapally, P. K.; McGrail, B. P.; Brown, D. R.; Liu, J. *Chem. Soc. Rev.* **2012**, *41*, 2308.9 (g) Zhang, Z.; Yao, Z.-Z.; Xiang, S.; Chen, B. **2014**, *7*, 2868.

(12) (a) Yazaydin, A. Ö.; Snurr, R. Q.; Park, T.-H.; Koh, K.; Liu, J.; LeVan, M. D.; Benin, A. I.; Jakubczak, P.; Lanuza, M.; Galloway, D. B.; Low, J. J.; Willis, R. R. *J. Am. Chem. Soc.* **2009**, *131*, 18198. (b) Mason, J. A.; Sumida, K.; Herm, Z. R.; Krishna, R.; Long, J. R. *Energy Environ. Sci.* **2011**, *4*, 3030. (c) Lin, L.-C.; Berger, A. H.; Martin, R. L.; Kim, J.; Swisher, J. A.; Jariwala, K.; Rycroft, C. H.; Bhown, A. S.; Deem, M. W.; Haranczyk, M.; Smit, B. *Nat. Mater.* **2012**, *11*, 633.

(13) Wang, J.; Ryan, D.; Anthony, E. J.; Wildgust, N.; Aiken, T. *Energy Procedia* **2011**, *4*, 3071.

(14) Keskin, S.; van Heest, T. M.; Sholl, D. S. *ChemSusChem* **2010**, *3*, 879.
(15) (a) Babarao, R.; Jiang, J. *Energy Environ. Sci.* **2009**, *2*, 1088. (b) Ding, L.; Yazaydin, A. Ö. *J. Phys. Chem. C* **2012**, *116*, 22987. (c) Yu, K.; Kiesling, K.; Schmidt, J. R. *J. Phys. Chem. C* **2012**, *116*, 20480. (d) Yu, J.; Ma, Y.; Balbuena, P. B. *Langmuir* **2012**, *28*, 8064. (e) Huang, H.; Zhang, W.; Liu, D.; Zhong, C. *Ind. Eng. Chem. Res.* **2012**, *51*, 10031. (f) Babarao, R.; Jiang, Y.; Medhekar, N. V. *J. Phys. Chem. C* **2013**, *113*, 26976. (g) Yu, J.; Balbuena, P. B. *J. Phys. Chem. C* **2013**, *117*, 3383. (h) Liu, Y.; Liu, J.; Lin, Y. S.; Chang, M. *J. Phys. Chem. C* **2014**, *118*, 6744.
(16) (a) Liang, Z.; Marshall, M.; Chaffee, A. L. *Energy Fuels* **2009**, *23*, 2785. (b) A. Ö. Yazaydin; Benin, A. I.; Faheem, S. A.; Jakubczak, P.; Low, J. J.; Willis. R. R.; Snurr, R. Q. *Chem. Mater.* **2009**, *21*, 1425. (c) Liu, J.; Wang, Y.; Benin, A. I.; Jakubczak, P.; Willis, R. R.; LeVan, M. D. *Langmuir* **2010**, *26*, 14301. (d) Liu, J.; Benin, A. I.; Furtado, A. M. B.; Jakubczak, P.; Willis, R. R.; LeVan, M. D. *Langmuir* **2011**, *27*, 11451. (e) Kizzie, A. C.; Wong-Foy, A. G.; Matzger, A. J. *Langmuir* **2011**, *27*, 6368. (f) Han, S.; Huang, Y.; Watanabe, T.; Dai, Y.; Walton, K.; Nair, S.; Sholl, D. S.; Meredith, J. C. *ACS Comb. Sci.* **2012**, *14*, 263. (g) Han, S.; Huang, Y.; Watanabe, T.; Nair, S.; Walton, K. S.; Sholl, D. S.; Meredith, J. C. *Microporous Mesoporous Mater.* **2013**, *173*, 86. (h) Yang, Q.; Vaesen, S.; Ragon, F.; Wiersum, A. D.; Wu, D.; Lago, A.; Devic, T.; Martineau, C.; Taulelle, F.; Llewellyn, P. L.; Jobic, H.; Zhong, C.; Serre, C.; Weireld, G. D.; Maurin, G. *Angew. Chem. Int. Ed.* **2013**, *51*, 1. (i) Woodward, R. T.; Stevens, L. A.; Dawson, R.; Vijayaraghavan, M.; Hasell, T.; Silverwood, I. P.; Ewing, A. V.; Ratvijivech, T.; Exley, J. D.; Chong, S. Y.; Blanc, F.; Adams, D. J.; Kazarian, S. G.; Snape, C. E.; Drage, T. C.; Cooper, A. I. *J. Am. Chem. Soc.* **2014**, *136*, 9028. (j) Bae, Y.-S.; Liu, J.; Wilmer, C. E.; Sun, H.; Dickey, A. N.; Kim, M. B.; Benin, A. I.; Willis, R. R.; Barpaga, D.; LeVan, M. D.; Snurr, R. Q. *Chem. Commun.* **2014**, *50*, 3296. (k) Burtch, N. C.; Jasuja, H.; Walson, K. S. Chem. Rev. **2014**, *114*, 10575.
(17) (a) Sircar, S. *Ind. Eng. Chem. Res.* **2006**, *45*, 5435. (b) Sircar, S. *Ind. Eng. Chem. Res.* **2007**, *46*, 2917. (c) Broom, D. P.; Thomas, K. M. *MRS Bull.* **2013**, *38*, 412.
(18) Myers, A. L.; Prausnitz, J. M. *AIChE J.* **1965**, *11*, 121.
(19) (a) Krishna, R.; van Baten, J. M. *Chem. Eng. J.* **2007**, *133*, 121. (b) Krishna, R.; van Baten, J. M. *Phys. Chem. Chem. Phys.* **2011**, *13*, 10593.
(20) Siperstein, F. R.; Myers, A. L. *AIChE J.* **2001**, *47*, 1141.
(21) Talu, O. *Chem. Ing. Tech.* **2011**, *83*, 67.
(22) Talu, O. *Adv. Colloid Interface Sci.* **1998**, *76-77*, 227.
(23) Examples for CO2, N2, H2O breakthrough experiments in metal-organic frameworks include: (a) Zhao, Y.; Yao, K. X.; Teng, B.; Zhang, T.; Han, Y. *Energy Environ. Sci.* **2013**, *6*, 3684. (b) Liu, Q.; Ning, L.; Zheng, S.; Tao, M.; Shi, Y.; He, Y. *Sci. Rep.* **2013**, *3*, 2916. (c) Li, D.; Furukawa, H.; Deng, H.; Liu, C.; Yaghi, O. M.; Eisenberg, D. S. *PNAS* **2014**, *111*, 191. (d) Nguyen, N. T. T.; Furukawa, H.; Gándara, F.; Nguyen, H. T.; Cordova, K. E.; Yaghi, O. M. *Angew. Chem. Int. Ed.* **2014**, *53*, 1.
(24) Li, G.; Xiao, P.; Webley, P.; Zhang, J.; Singh, R.; Marshall, M. *Adsorption* **2008**, *14*, 415.
(25) Pirngruber, G. D.; Hamon, L.; Bourrelly, S.; Llewellyn, P. L.; Lenoir, E.; Guillerm, V.; Serre, C.; Devic, T. *ChemSusChem* **2012**, *5*, 762.

(26) (a) Rajendran, A.; Kariwala, V.; Farooq, S. *Chem. Eng. Sci.* **2008**, *63*, 2696. (b) Hofman, P. S.; Rufford, T. E.; Chan, K. I.; May, E. F. *Adsorption* **2012**, *18*, 251.
(27) Pigorini, G.; LeVan, M. D. *Ind. Eng. Chem. Res.* **1998**, *37*, 2516.
(28) Fletcher, A. J.; Benham, M. J.; Thomas, K. M. *J. Phys. Chem. B.* **2002**, *106*, 7474.
(29) (a) Hamon, L.; Frère, M.; Weireld, G. D. *Adsorption* **2008**, *14*, 493. (b) Watson, G. C.; Jensen, N. K.; Rufford, T. E.; Chan, K. I.; May, E. F. *J. Chem. Eng. Data* **2012**, *57*, 93.
(30) Ding, Y.; LeVan, M. D. *Rev. Sci. Instrum.* **2002**, *73*, 230.
(31) Brandani, F.; Ruthven, D. M. *Ind. Eng. Chem. Res.* **2003**, *42*, 1462.
(32) Talu, O.; Zwiebel, I. *AIChE J.* **1986**, *32*, 1263.
(33) (a) Rege, S. U.; Yang, R. T. *Chem. Eng. Sci.* **2001**, *56*, 3781. (b) Cai, B.-C.; Han, Q.-J.; Tang, L.-J.; Zhang, Y.; Yu, R.-Q. *Ind. Eng. Chem. Res.* **2008**, *47*, 6835. (c) Ohlin, L.; Bazin, P.; Thibault-Starzyk, F.; Hedlund, J.; Grahn, M. *J. Phys. Chem. C* **2013**, *117*, 16972.
(34) Rynders, R. M.; Rao, M. B.; Sircar, S. *AIChE J.* **1997**, *43*, 2456.
(35) Note that the multicomponent results reported here should not be dependent on the exact dosing procedure used to achieve a given set of equilibrium conditions, provided H2O adsorption is fully reversible. All H2O gas dosing was preformed in small steps relative to the total amount of H2O adsorbed by a sample so as to minimize any potential effects from hysteresis in H2O adsorption.
(36) (a) Li, H.; Eddaoudi, M.; O'Keeffe, M.; Yaghi, O. M. *Nature* **1999**, *402*, 276. (b) Millward, A. R.; Yaghi, O. M. *J. Am. Chem. Soc.* **2005**, *127*, 17998. (c) Kaye, S. S.; Dailly, A.; Yaghi, O. M.; Long, J. R. *J. Am. Chem. Soc.* **2007**, *129*, 14176. (d) Walton, K. S.; Millward, A. R.; Dubbeldam, D.; Frost, H.; Low, J. J.; Yaghi, O. M.; Snurr, R. Q. *J. Am. Chem. Soc.* **2008**, *130*, 406.
(37) Otowa, T.; Tanibata, R.; Itoh, M. *Gas Sep. Purif.* **1993**, *7*, 241.
(38) Sircar, S.; Golden, T. C.; Rao, M. B. *Carbon* **1996**, *34*, 1.
(39) Hao, G.-P.; Li, W.-C.; Qian, D.; Wang, G.-H.; Zhang, W.-P.; Zhang, T.; Wang, A.-Q.; Schüth, F.; Bongard, H.-J.; Lu, A.-H. *J. Am. Chem. Soc.* **2011**, *133*, 11378.
(40) Barton, S. S.; Evans, M. J. B.; MacDonald, J. A. F. *Carbon* **1991**, *29*, 1099.
(41) Dubinin, M. M.; Zaverina, E. D.; Serpinsky, V. V. *J. Chem. Soc.* **1955**, 1760.
(42) Angell, C. L. *J. Phys. Chem.* **1966**, *70*, 2420.
(43) Caskey, S. R.; Wong-Foy, A. G.; Matzger, A. J. *J. Am. Chem. Soc.* **2008**, *130*, 10870.
(44) (a) Lee, J.-S.; Kim, J.-H.; Kim, J.-T.; Suh, J.-K.; Lee, J.-M.; Lee, C.-H. *J. Chem. Eng. Data* **2002**, *47*, 1237. (b) Wang, Y.; LeVan, M. D. *J. Chem. Eng. Data* **2009**, *54*, 2839. (c) Bae, T.-H.; Hudson, M. R.; Mason, J. A.; Queen, W. L.; Dutton, J. J.; Sumida, K.; Micklash, K. J.; Kaye, S. S.; Brown, C. M.; Long, J. R. *Energy Environ. Sci.* **2013**, *6*, 128.
(45) (a) Rosi, N. L.; Kim, J.; Eddaoudi, M.; Chen, B.; O'Keeffe, M.; Yaghi, O. M. *J. Am. Chem. Soc.* **2005**, *127*, 1504. (b) Dietzel, P. D. C.; Blom, R.; Fjellvåg, H. *Eur. J. Inorg. Chem.* **2008**, 3624.
(46) Dietzel, P. D. C.; Panella, B.; Hirscher, M.; Blom, R.; Fjellvåg, H. *Chem. Commun.* **2006**, 959.
(47) Chui, S. S. Y.; Lo, S. M. F.; Charmant, J. P. H.; Orpen, A. G.; Williams, I. D. *Science* **1999**, *283*, 1148.
(48) Horcajada, P.; Surblé, S.; Serre, C.; Hong, D.-Y.; Seo, Y.-K.; Chang, J.-S.; Grenèche, J.-M.; Margiolaki, I.; Férey, G. *Chem. Commun.* **2007**, 2820.

(49) (a) Adams, J. M.; Haselden, D. A.; Hewat, A. W. *J. Solid State Chem.* **1982**, *44*, 245. (b) Adams, J. M.; Haselden, D. A. *J. Solid State Chem.* **1984**, *51*, 83.
(50) Olson, D. H. *Zeolites* **1995**, *15*, 439.
(51) (a) Britt, D.; Furukawa, H.; Wang, B.; Glover, T. G.; Yaghi, O. M. *PNAS* **2009**, *106*, 20637. (b) Dietzel, P. D. C.; Besikiotis, V.; Blom, R. *J. Mater. Chem.* **2009**, *19*, 7362. (c) Wu, H.; Simmons, J. M.; Srinivas, G.; Zhou, W.; Yildirim, T. *J. Phys. Chem. Lett.* **2010**, *1*, 1946. (d) Valenzano, L.; Civalleri, B.; Chavan, S.; Palomino, G. T.; Areán, C. O.; Bordiga, S. *J. Phys. Chem. C* **2010**, *114*, 11185. (e) Bao, Z.; Yu, L.; Ren, Q.; Lu, X.; Deng, S. *J. Colloid Interface Sci.* **2011**, *353*, 549.
(52) (a) Huang, H.; Zhang, W.; Liu, D.; Zhong, C. *Ind. Eng. Chem. Res.* **2012**, *51*, 10031. (b) Yu, J.; Balbuena, P. B. *J. Phys. Chem. C* **2013**, *113*, 3383. (c) Joos, L.; Swisher, J. A.; Smit, B. *Langmuir* **2013**, *29*, 15936. (d) Lin, L.-C.; Lee, K.; Gagliardi, L.; Neaton, J. B.; Smit, B. *J. Chem. Theory Comput.* **2014**, *10*, 1477.
(53) (a) Brandani, F.; Ruthven, D. M. *Ind. Eng. Chem. Res.* **2004**, *43*, 8339. (b) Wang, Y.; Levan, M. D. *J. Chem. Eng. Data* **2010**, *55*, 3189.
(54) Liu, J.; Tian, J.; Thallapally, P. K.; McGrail, P. B. *J. Phys. Chem. C* **2012**, *116*, 9575.
(55) Hudson, M. R.; Queen, W. L.; Mason, J. A.; Fickel, D. W.; Lobo, R. F.; Brown, C. M. *J. Am. Chem. Soc.* **2012**, *134*, 1970.
(56) Wang, Q. M.; Shen, D.; Bülow, M.; Lau, M. L.; Deng, S.; Fitch, F. R.; Lemcoff, N. O.; Semanscin, J. *Microporous Mesoporous Mater.* **2002**, *55*, 217.
(57) Wuttke, S.; Bazin, P.; Vimont, A.; Serre, C.; Seo, Y.-K.; Hwang, Y. K.; Chang, J.-S.; Férey, G.; Daturi, M. *Chem. Eur. J.* **2012**, *18*, 11959.
(58) Soubeyrand-Lenoir, E.; Vagner, C.; Yoon, J. W.; Bazin, P.; Ragon, F.; Hwang, Y. K.; Serre, C.; Chang, J.-S.; Llewellyn, P. L. *J. Am. Chem. Soc.* **2012**, *134*, 10174.
(59) (a) Nugent, P.; Belmabkhout, Y.; Burd, S. D.; Cairns, A. J.; Luebke, R.; Forrest, K.; Pham, T.; Ma, S.; Space, B.; Wojtas, L.; Eddaoudi, M.; Zaworotko, M. J. *Nature* **2013**, *495*, 80. (b) Noro, S.; Hijikata, Y.; Inukai, M.; Fukushima, T.; Horike, S.; Higuchi, M.; Kitagawa, S.; Akutagawa, T.; Nakamura, T. *Inorg. Chem.* **2013**, *52*, 280. (c) Shekhah, O.; Belmabkhout, Y.; Chen, Z.; Guillerm, V.; Cairns, A.; Adil, K.; Eddaoudi, M. *Nat. Commun.* **2014**, *5*, 4228.
(60) Uemura, K.; Maeda, A.; Maji, T. K.; Kanoo, P.; Kita, H. *Eur. J. Inorg. Chem.* **2009**, *16*, 2329.
(61) (a) Veawab, A.; Tontiwachwuthikul, P.; Chakma, A. *Ind. Eng. Chem. Res.* **1999**, *38*, 3917. (b) Bontemps, D.; Chopin, F.; Le Moullec, Y.; Morand, T.; Zanella, Y.; Pinto, C. *Energy Procedia* **2014**, *63*, 787.
(62) (a) Caplow, M. *J. Am. Chem. Soc.* **1968**, *90*, 6795. (b) Danon, A.; Stair, P. C.; Weitz, E. *J. Phys. Chem. C* **2011**, *115*, 11540.
(63) Leal, O.; Bolívar, C.; Ovalles, C.; García, J. J.; Espidel, Y. *Inorg. Chim. Acta* **1995**, *240*, 183.
(64) Bollini, P.; Didas, S. A.; Jones, C. W. *J. Mater. Chem.* **2011**, *21*, 15100.
(65) (a) Huang, H. Y.; Yang, R. T.; Chinn, D.; Munson, C. L. *Ind. Eng. Chem. Res.* **2003**, *42*, 2427. (b) Chang, A. C. C.; Chuang, S. S. C.; Gray, M.; Soong, Y. *Energy Fuels* **2003**, *17*, 468. (c) Hiyoshi, N.; Yogo, K.; Yashima, T. *Microporous Mesoporous Mater.* **2005**, *84*, 357. (d) Khatri, R. A.; Chuang, S. S. C.; Soong, Y.; Gray, M. *Energy Fuels* **2006**, *20*, 1514.

(e) Harlick, P. J. E.; Sayari, A. *Ind. Eng. Chem. Res.* **2007**, *46*, 446. (f) Brunelli, N. A.; Didas, S. A.; Venkatasubbaiah, K.; Jones, C. W. *J. Am. Chem. Soc.* **2012**, *134*, 13950. (g) Didas, S. A.; Sakwa-Novak, M. A.; Foo, G. S.; Sievers, C.; Jones, C. W. *J. Phys. Chem. Lett.* **2014**, *5*, 4194.

(66) (a) Vaidya, P. D.; Kenig, E. *Chem. Eng. Technol.* **2007**, *30*, 1467. (b) Serna-Guerrero, R.; Belmabkhout, Y.; Sayari, A. *Chem. Eng. J.* **2010**, *158*, 513.

(67) Serna-Guerrero, R.; Da'na, E.; Sayari, A. *Ind. Eng. Chem. Res.* **2008**, *47*, 9406.

(68) Kresge, C. T.; Leonowicz, M. E.; Roth, W. J.; Vartuli, J. C.; Beck. J. S. *Nature* **1992**, *359*, 710.

(69) Sayari, A.; Belmabkhout, Y.; Da'na, E. *Langmuir* **2012**, *28*, 4241.

(70) (a) Satyapal, S.; Filburn, T.; Trela, J.; Strange, J. *Energy Fuels* **2001**, *15*, 250. (b) Xu, X.; Song, C.; Andresen, J. M.; Miller, B. G.; Scaroni, A. W. *Energy Fuels* **2002**, *16*, 1463. (c) Xu, X.; Song, C.; Miller, B. G.; Scaroni, A. W. *Ind. Eng. Chem. Res.* **2005**, *44*, 8113. (d) Xu, X.; Song, C.; Miller, B. G.; Scaroni, A. W. *Fuel Process. Technol.* **2005**, *86*, 1457.

(71) Sayari, A.; Yang, Y.; Kruk, M.; Jaroniec, M. *J. Phys. Chem. B* **1999**, *103*, 3651.

(72) (a) Hwang, Y. K.; Hong, D.-Y.; Chang, J.-S.; Jhung, S. H.; Seo, Y.-K.; Kim, J.; Vimont, A.; Daturi, M.; Serre, C.; Férey, G. *Angew. Chem. Int. Ed.* **2008**, *47*, 4144. (b) Demessence, A.; D'Alessandro, D. M.; Foo, M. L.; Long, J. R. *J. Am. Chem. Soc.* **2009**, *131*, 8784. (c) McDonald, T. M.; D'Alessandro, D. M.; Krishna, R.; Long, J. R. *Chem. Sci.* **2011**, *2*, 2022. (d) Montoro, C.; García, E.; Calero, S.; Pérez-Fernández, M. A.; López, A. L.; Barea, E.; Navarro, J. A. R. *J. Mater. Chem.* **2012**, *22*, 10155. (e) McDonald, T. M.; Lee, W. R.; Mason, J. A.; Wiers, B. M.; Hong, C. S.; Long, J. R. *J. Am. Chem. Soc.* **2012**, *134*, 7056. (f) Choi, S.; Watanabe, T.; Sholl, D. S.; Jones, C. W. *J. Phys. Chem. Lett.* **2012**, *3*, 1136. (g) Lu, W.; Sculley, J. P.; Yuan, D.; Krishna, R.; Zhou, H.-C. *J. Phys. Chem. C* **2013**, *117*, 4057. (h) Lee, W. R.; Hwang, S. Y.; Ryu, D. W.; Lim, K. S.; Han, S. S.; Moon, D.; Choi, J.; Hong, C. S. *Energy Environ. Sci.* **2014**, *7*, 744. (i) Fracaroli, A. M.; Furukawa, H.; Suzuki, M.; Dodd, M.; Okajima, S.; Gándara, F.; Reimer, J. A.; Yaghi, O. M. *J. Am. Chem. Soc.* **2014**, *136*, 8863.

(73) McDonald, T. M.; Mason, J. A.; Kong, X.; Bloch, E. D.; Gygi, D.; Dani, A.; Crocellà, V.; Giordanino, F.; Odoh, S. O.; Drisdell, W.; Vlaisavljevich, B.; Dzubak, A. L.; Poloni, R.; Schnell, S. K.; Planas, N.; Lee, K.; Pascal, T.; Wan, L. F.; Prendergast, D.; Neaton, J. B.; Smit, B.; Kortright, J. B.; Gagliardi, L.; Bordiga, S.; Reimer, J. A.; Long, J. R. *Nature* **2015**, *519*, 303.

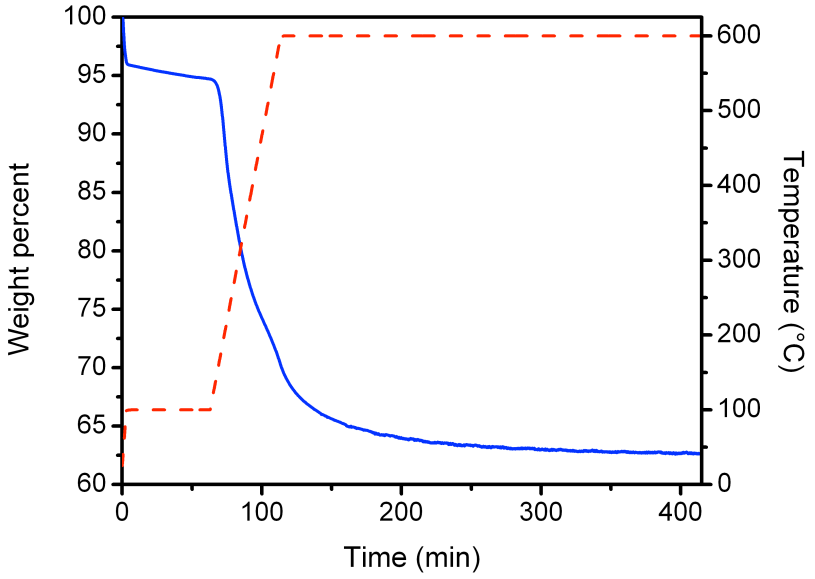

Figure 4.S1. Thermogravimetric analysis (TGA) of PEI-MCM-41 upon heating at 100 °C for 1 h, then heating to 600 °C at 10 °C per min, then holding at 600 °C for 5 h. The blue line corresponds to the weight percent of the original compound that is present, while the dashed red line corresponds to the temperature.

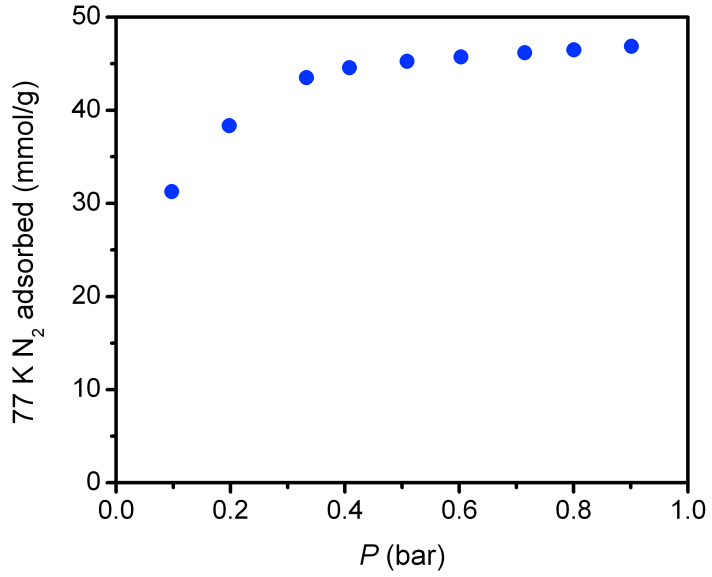

Figure 4.S2. 77 K N_2 adsorption isotherm for AX-21 activated at 200 ºC. The calculated Langmuir surface area is 4830(30) m^2/g (n_{sat} = 49.5 mmol/g).

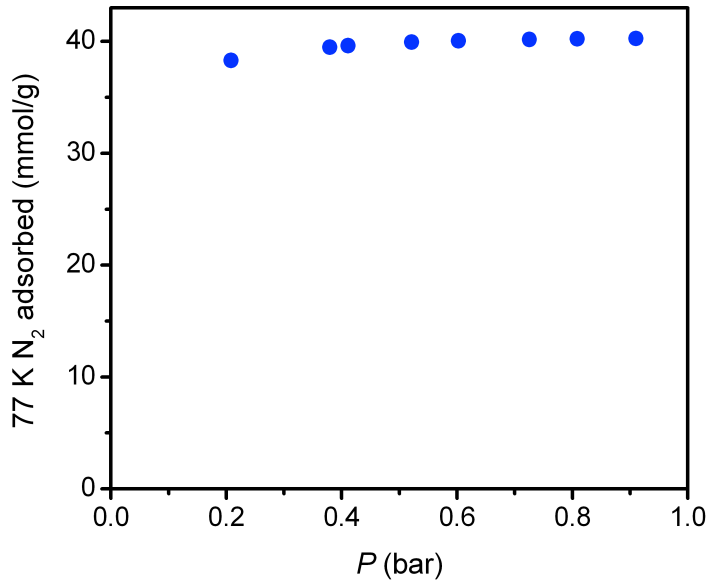

Figure 4.S3. 77 K N_2 adsorption isotherm for MOF-5 activated at 150 ºC. The calculated Langmuir surface area is 3995(4) m^2/g (n_{sat} = 40.9 mmol/g).

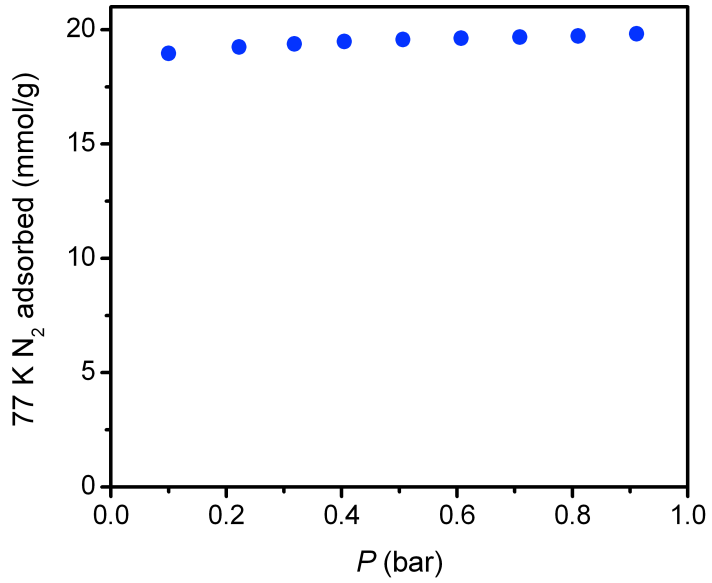

Figure 4.S4. 77 K N_2 adsorption isotherm for Mg_2(dobdc) activated at 180 ºC. The calculated Langmuir surface area is 1940(2) m^2/g (n_{sat} = 19.9 mmol/g).

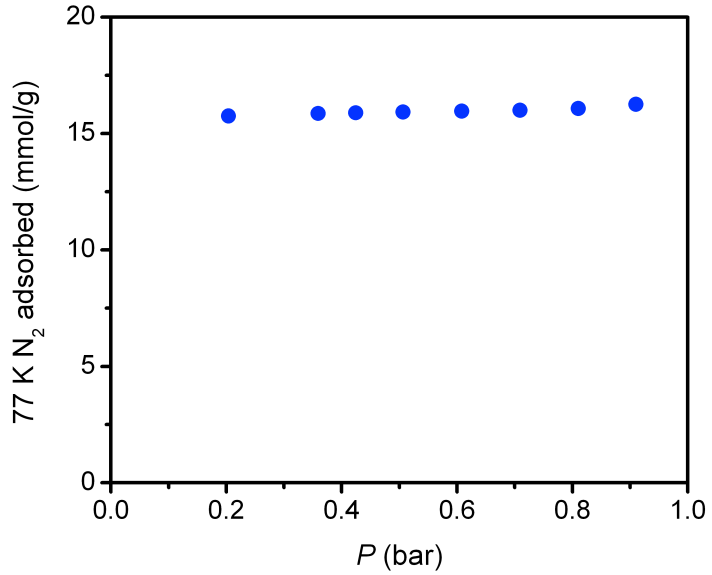

Figure 4.S5. 77 K N_2 adsorption isotherm for Ni_2(dobdc) activated at 180 ºC. The calculated Langmuir surface area is 1593(9) m^2/g (n_{sat} = 16.3 mmol/g).

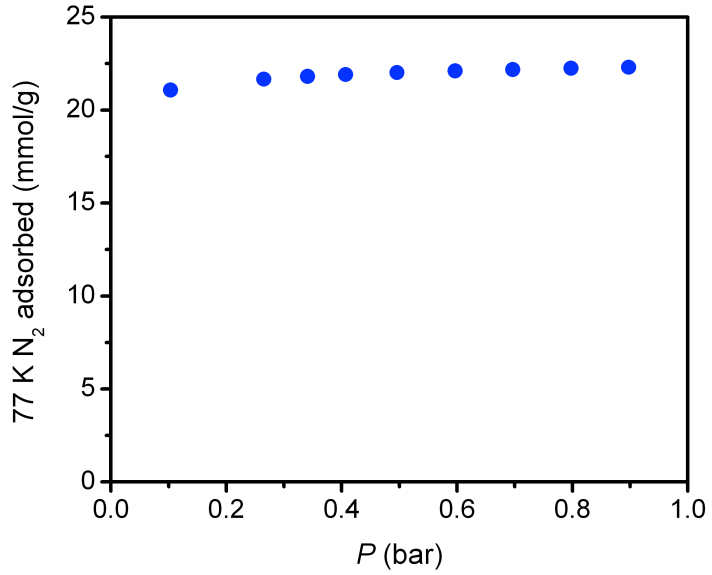

Figure 4.S6. 77 K N_2 adsorption isotherm for HKUST-1 activated at 150 ºC. The calculated Langmuir surface area is 2203(2) m^2/g (n_{sat} = 22.6 mmol/g).

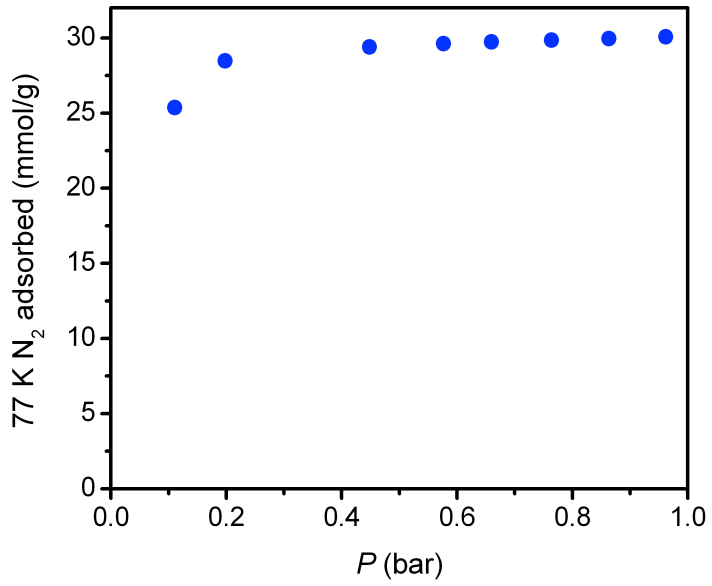

Figure 4.S7. 77 K N_2 adsorption isotherm for Fe-MIL-100 activated at 150 ºC. The calculated Langmuir surface area is 2990(9) m^2/g (n_{sat} = 30.7 mmol/g).

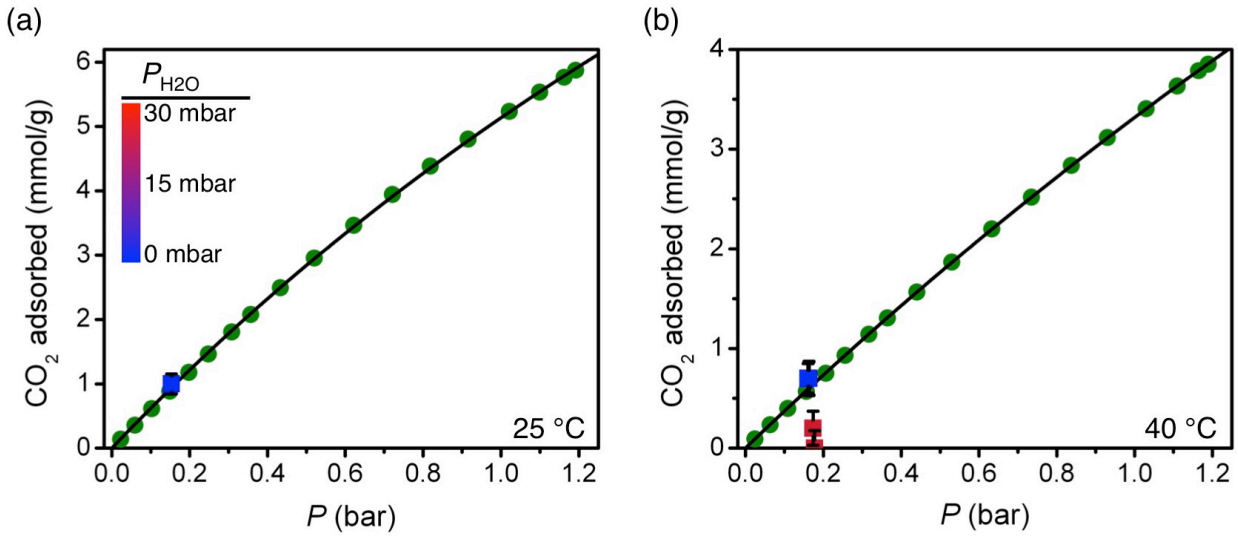

Figure 4.S8. A summary of multicomponent equilibrium measurements at 25 and 40 °C for HKUST-1. Green circles represent pure CO_2 adsorption isotherms for each compound, and black lines are the corresponding single- or dual-site Langmuir fits. Square data points represent the amount of CO_2 adsorbed from a mixture of CO_2, N_2, and H_2O, and the color of the square indicates the equilibrium partial pressure of H_2O, with the partial pressure of H_2O increasing from blue to purple to red. The exact values of P_{H2O} can be found in Table 4.S3.

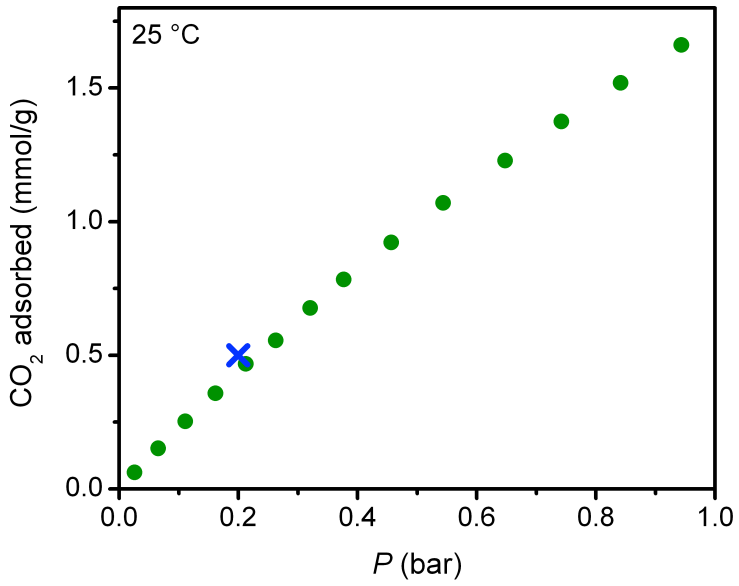

Figure 4.S9. The 25 °C CO_2 for Fe-MIL-100 measured in this work (green circles) is compared to the previously reported uptake for Fe-MIL-100 at 25 °C and 0.2 bar (blue cross).[58]

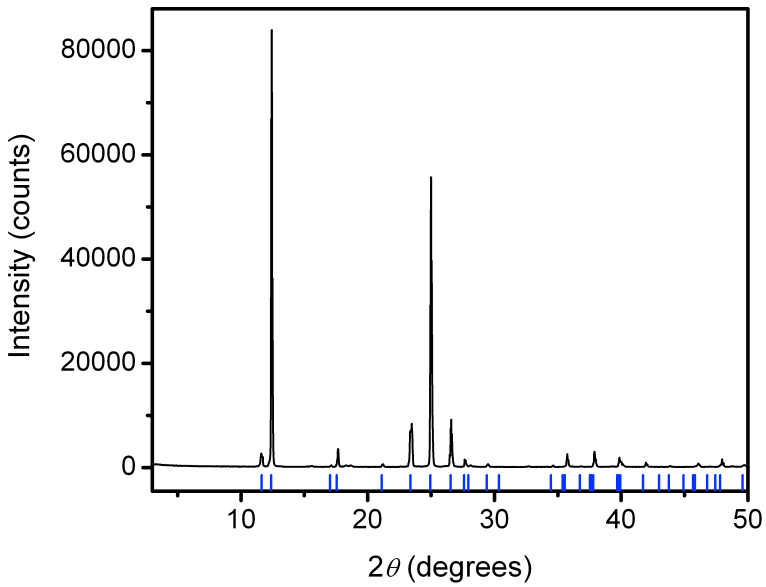

Figure 4.S10. Powder X-ray diffraction pattern for $Zn(SiF_6)(pyrz)_2$ synthesized in this work. Blue tick marks represent expected peak positions based on the reported single crystal structure (λ = 1.5418 Å).[60]

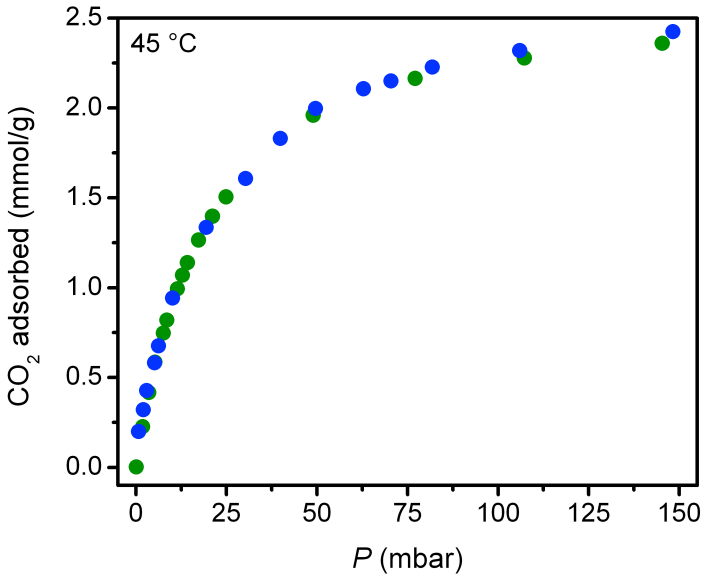

Figure 4.S11. Pure CO_2 adsorption isotherms for $Zn(pyrz)_2(SiF_6)$ at 45 °C measured in this work (green) compared to that previously reported (blue).[59a]

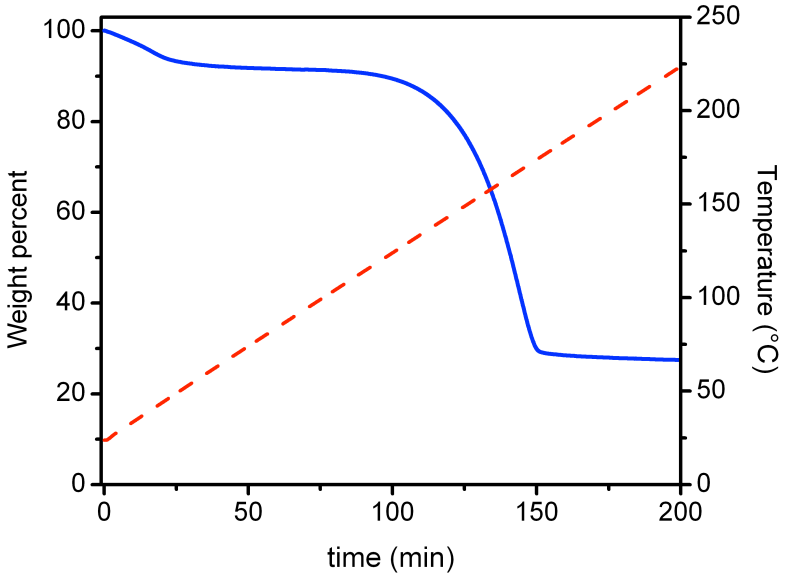

Figure 4.S12. Thermogravimetric analysis (TGA) for $Zn(pyrz)_2(SiF_6)$ heated at 1 °C per minute. The blue line corresponds to the weight percent of the original compound that is present, while the dashed red line corresponds to the temperature.

Figure 4.S13. High-throughput multicomponent adsorption instrument.

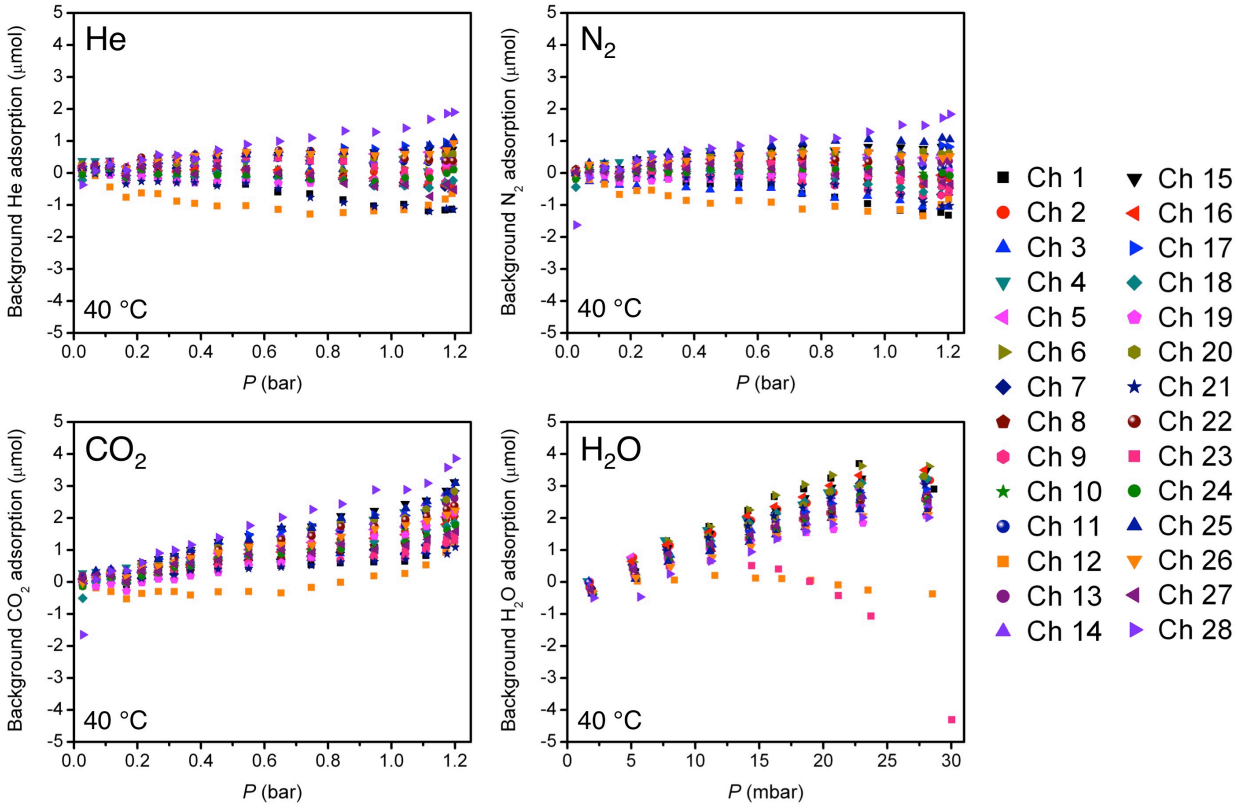

Figure 4.S14. Background adsorption isotherms at 40 °C on all 28 channels of the high-throughput multicomponent adsorption instrument for He, N_2, CO_2, and H_2O.

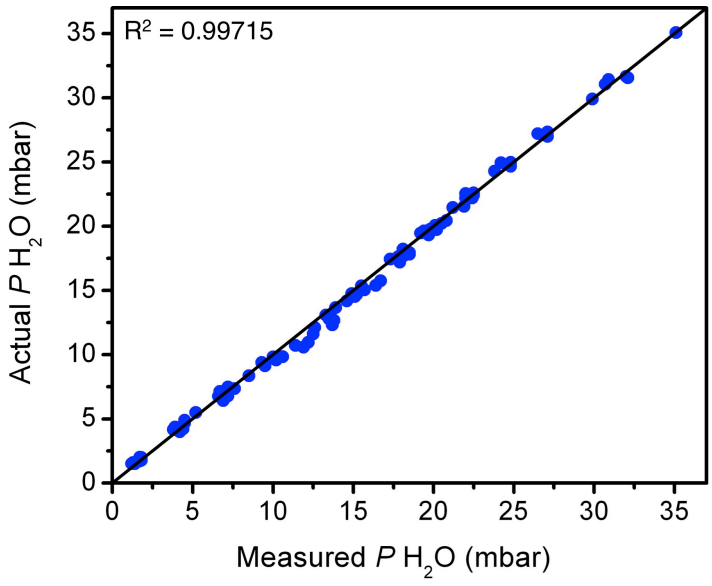

Figure 4.S15. The partial pressure of H_2O measured by the dew point transmitter is compared to the actual partial pressure of H_2O recorded by a calibrated pressure transducer.

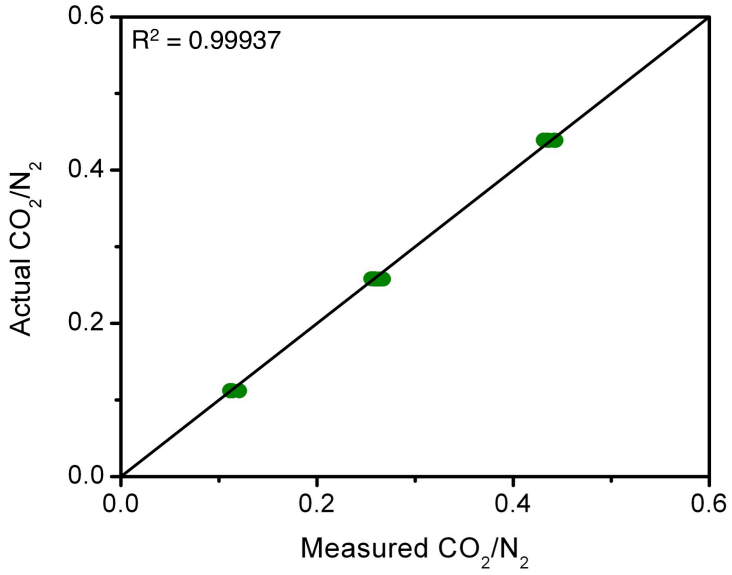

Figure 4.S16. The ratio of CO_2 to N_2 measured by the residual gas analyzer (rga) is compared to the expected ratio of CO_2 to N_2 in standard gas mixtures for 18 independent experiments.

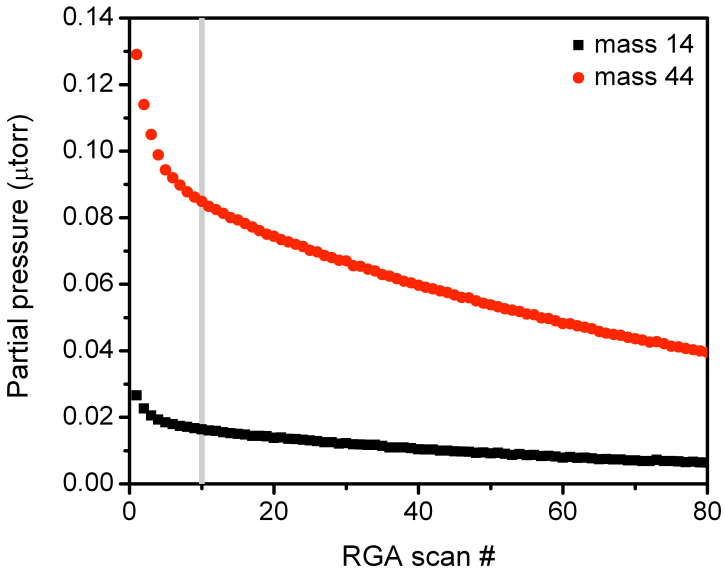

Figure 4.S17. An example of the raw partial pressure traces from the residual gas analyzer (RGA) is show. The red data corresponds to the peak at M/Z = 44, while the black data corresponds to the peak at M/Z = 14. The mass 44 data is proportional to the partial pressure of CO_2, while the mass 14 data is proportional to the partial pressure of N_2. We note that mass 14, rather than mass 28, was used for N_2 in order to avoid complications from CO_2 fractionation to CO, which also has a mass of 28. The ratio of mass 44 to mass 14 at scan number 10 (gray line) was used in each multicomponent experiment to determine the ratio of the partial pressure of CO_2 to the partial pressure of N_2 in the gas-phase at equilibrium. This ratio was calibrated by dosing standard mixtures of CO_2 and N_2 to the RGA.

Table 4.S1. Elemental analysis of amine-appended silicas.

	1°-MCM-41	2°-MCM-41
% C (measured)	15.22	17.54
% H (measured)	3.37	3.94
% N (measured)	5.72	5.24
calculated amine loading (mmol N per g silica)	4.2	3.7
% C (calculated)	15.22	17.69
% H (calculated)	3.41	3.71
% N (calculated)	5.92	5.16

Table 4.S2. Single- or dual-site Langmuir-Freundlich fit parameters for pure-component CO_2 adsorption isotherms.

	$n_{sat,1}$	b_1	v_1	$n_{sat,2}$	b_2	v_2	p_0	T (°C)
zeolite 5A	5.8	8.2	0.7	5.0	0.03	1.4	-	40
zeolite 13X	5.5	4.9	0.6	1.7	2.0	1.0	-	40
Mg_2(dobdc)	5.5	23.9	1.0	5.8	0.46	1.0	-	40
Ni_2(dobdc)	5.4	9.7	1.1	8.0	0.17	1.0	-	40
HKUST-1	27.7	0.1	1.0	-	-	-	-	40
HKUST-1	26.7	0.2	1.0	-	-	-	-	25
Fe-MIL-100	0.4	2.4	1.0	6.0	0.28	1.0	-	40
Fe-MIL-100	0.5	0.44	1.0	6.0	0.37	1.0	-	25
MOF-5	35.0	0.019	1.0	-	-	-	-	40
mmen-Mg_2(dobpdc)	3.6	11925.6	1.0	2.9	0.29	1.0	0.00075	40
mmen-Ni_2(dobpdc)	5.0	0.1	2.8	5.0	0.43	0.9	-	40
$Zn(pyrz)_2(SiF_6)$	2.6	68.2	1.0	5.0	0.03	1.0	-	40
mmen-CuBTTri	3.5	2.9	1.0	5.0	0.07	1.0	-	40
1°-MCM-41	1.0	3073.4	1.0	6.0	0.24	0.4	-	40
2°-MCM-41	1.0	407.4	1.0	6.0	0.10	0.5	-	40
PEI-MCM-41	1.4	2228.5	1.0	1.3	1.4	1.0	-	40
AX-21 carbon	9.3	0.24	1.0	-	-	-	-	40
AX-21 carbon (N_2)	4.5	0.07	1.0	-	-	-	-	40

Table S4.3. **Multicomponent CO_2, N_2, H_2O data**

Adsorbent	*P* CO_2 (mbar)	CO_2 adsorbed (mmol/g)	CO_2 adsorbed error (mmol/g)	Pure CO_2 adsorbed (mmol/g)	*P* N_2 (mbar)	N_2 adsorbed (mmol/g)	N_2 adsorbed error (mmol/g)	*P* H_2O (mbar)	H_2O adsorbed (mmol/g)	H_2O adsorbed error (mmol/g)	*P* total (mbar)	T *(°C)*	
AX-21 carbon	166	0.3	0.1	0.35	679	0.3	0.1	20	0	0.2	865	40	*
MOF-5	173	0.1	0.1	0.11	686	0.1	0.1	11	0.4	0.2	870	40	*
Mg_2(dobdc)	162	1	0.2	4.80	686	0.3	0.3	1	8.1	0.4	849	40	
Mg_2(dobdc)	171	0.5	0.3	4.87	689	0	0.4	23	14.2	0.5	883	40	*
Mg_2(dobdc)	164	1	0.2	4.81	688	0.4	0.3	2	12.4	0.5	854	40	
Ni_2(dobdc)	154	0.7	0.1	3.18	686	0.3	0.1	2	6.3	0.3	842	40	
Ni_2(dobdc)	175	0.3	0.2	3.39	695	0.3	0.3	3	19.4	0.4	873	40	
Ni_2(dobdc)	177	0.1	0.2	3.41	684	0.3	0.3	10	23.0	0.5	871	40	*
zeolite 13X	163	0.7	0.2	3.96	691	0.2	0.2	1	7	0.3	855	40	
zeolite 13X	179	0.1	0.2	4.05	697	0.2	0.3	2	7.1	0.4	878	40	
zeolite 13X	178	0	0.3	4.05	687	0.1	0.3	10	15.2	0.5	875	40	*
zeolite 5A	156	1	0.2	4.04	691	0.2	0.2	1	4.7	0.3	848	40	
zeolite 5A	171	0.3	0.2	4.12	689	0	0.2	15	9.6	0.3	875	40	*
zeolite 5A	175	0.1	0.2	4.14	688	0	0.3	13	6.9	0.4	876	40	
HKUST-1	163	0.7	0.2	0.60	691	0.4	0.2	2	1.5	0.3	856	40	
HKUST-1	154	1	0.2	0.94	685	0.3	0.2	1	1.5	0.3	840	25	
HKUST-1	163	0.7	0.2	0.60	686	0.2	0.2	4	7.7	0.3	853	40	
HKUST-1	161	0.7	0.2	0.59	686	0.4	0.2	1	1.9	0.3	848	40	
HKUST-1	174	0.2	0.2	0.64	695	0	0.2	24	13.5	0.3	893	40	
HKUST-1	177	0	0.2	0.65	689	0	0.2	24	18.2	0.3	890	40	*
Fe-MIL-100	259	0.4	0.1	0.56	608	0.2	0.2	23	8.9	0.3	890	40	
Fe-MIL-100	240	0.3	0.1	0.52	560	0.2	0.2	7	4.2	0.3	807	25	
Fe-MIL-100	174	0.3	0.2	0.40	686	0.3	0.3	12	4.9	4	872	40	
Fe-MIL-100	175	0.3	0.3	0.40	689	0.5	0.3	20	6.8	0.5	884	40	*
$Zn(pyrz)_2(SiF_6)$	158	0.9	0.2	2.44	688	0	0.2	13	3.8	0.3	859	40	

Adsorbent	*P* CO_2 (mbar)	CO_2 adsorbed (mmol/g)	CO_2 adsorbed error (mmol/g)	Pure CO_2 adsorbed (mmol/g)	*P* N_2 (mbar)	N_2 adsorbed (mmol/g)	N_2 adsorbed error (mmol/g)	*P* H_2O (mbar)	H_2O adsorbed (mmol/g)	H_2O adsorbed error (mmol/g)	*P* total (mbar)	T *(°C)*	
$Zn(pyrz)_2(SiF_6)$	176	0	0.2	2.47	683	0.1	0.3	13	6.4	0.4	872	40	
$Zn(pyrz)_2(SiF_6)$	160	0.8	0.2	2.45	700	0	0.2	14	4.2	0.3	874	40	
$Zn(pyrz)_2(SiF_6)$	175	0.2	0.2	2.47	695	0.1	0.2	14	7	0.3	884	40	*
mmen-CuBTTri	162	0.9	0.2	1.18	685	0	0.3	28	5.4	0.4	875	40	*
mmen-CuBTTri	168	0.7	0.2	1.20	695	0	0.3	20	3	0.4	883	40	
mmen-Mg_2(dobpdc)	254	4.1	0.2	3.80	512	0	0.2	16	5.6	0.4	782	40	
mmen-Mg_2(dobpdc)	258	3.9	0.2	3.81	513	0	0.2	16	5.7	0.4	787	40	
mmen-Mg_2(dobpdc)	92	4	0.2	3.68	691	0.1	0.2	20	9.5	0.3	803	40	
mmen-Mg_2(dobpdc)	139	3.8	0.2	3.72	521	0	0.2	16	4.9	0.3	676	40	
mmen-Mg_2(dobpdc)	113	4.2	0.2	3.70	689	0	0.3	19	6.5	0.5	821	40	*
mmen-Mg_2(dobpdc)	106	3.6	0.2	3.69	701	0	0.2	17	5.6	0.4	824	40	
mmen-Ni_2(dobpdc)	159	0.9	0.2	0.41	689	0.3	0.2	17	1.4	0.3	865	40	
mmen-Ni_2(dobpdc)	150	1.3	0.2	0.39	691	0.1	0.2	29	4.1	0.3	870	40	*
mmen-Ni_2(dobpdc)	146	1.1	0.1	0.38	686	0.1	0.2	18	2.6	0.3	850	40	
1°-MCM-41	157	1.2	0.2	1.60	695	0.1	0.3	19	4.6	0.4	871	40	*
1°-MCM-41	154	1.1	0.2	1.59	683	0.2	0.2	17	2.8	0.3	854	40	
2°-MCM-41	149	1.3	0.2	1.29	694	0.2	0.2	17	2.8	0.3	860	40	
2°-MCM-41	155	1.5	0.2	1.30	698	0.2	0.3	17	4.2	0.4	870	40	*
2°-MCM-41	147	1.3	0.2	1.29	696	0.1	0.2	22	2.9	0.3	865	40	
PEI-MCM-41	114	2.5	0.1	1.53	691	0	0.2	17	3.4	0.3	822	40	*

*Indicates data point used in Figure 15.

- All errors are given at a 95% confidence interval
- Error in partial pressure of CO_2 is 3.6 mbar
- Error in partial pressure of N_2 is 3.5 mbar
- Error in partial pressure of H_2O is 3.4 mbar
- Error in pure CO_2 adsorption is less than 0.1 mmol/g

Chapter 5: High-Capacity Methane Storage via Flexible Metal-Organic Frameworks with Intrinsic Thermal Management

5.1. Introduction

As a cleaner, cheaper, and more evenly distributed fuel, natural gas has significant environmental, economic, and political advantages over petroleum as a source of energy for the transportation sector.[1,2] Despite the potential benefits of natural gas, its low volumetric energy density at ambient temperature and pressure presents substantial challenges, particularly for light-duty passenger vehicles that have little extra space available for on-board fuel storage. While many commercial fleets have converted to natural gas, the vast majority of passenger vehicles continue to burn gasoline, because consumers are unwilling to sacrifice driving range, space for passengers and cargo, and convenient access to refueling stations.[3] Adsorbed natural gas (ANG) systems have the potential to eliminate these issues by storing high densities of methane within a porous material at ambient temperature and reduced pressures.[4] Although activated carbons, zeolites, and metal-organic frameworks have been investigated extensively for natural gas storage,[5-8] there are still no commercially available ANG vehicles, owing to the challenges involved in designing a practical storage system with a high capacity of usable CH_4, sufficient thermal management, and a low cost. Here, we introduce a new concept in gas storage, wherein a reversible phase transition is used to maximize the deliverable capacity of a gas while also providing internal heat management during adsorption and desorption. In particular, the flexible metal-organic frameworks Co(bdp) and Fe(bdp) (bdp^{2-} = 1,4-benzenedipyrazolate) are shown to undergo a structural phase transition in response to specific CH_4 pressures, resulting in adsorption and desorption isotherms that feature a sharp step. Such behavior enables storage capacities that push beyond the limits of classical adsorbents,[9] while also reducing the amount of heat released during CH_4 adsorption and the impact of cooling during desorption. Significantly, the pressure and energy associated with the phase transition can be tuned either chemically or by application of mechanical pressure. We anticipate that these results may help facilitate the widespread adoption of ANG vehicles, while further inspiring new strategies and materials for the wide range of industrial gas storage and separation applications that rely on delivering as much gas as possible from an adsorbent with minimal heat management.

The driving range of an ANG vehicle is determined primarily by the volumetric usable CH_4 capacity of the adsorbent, which is defined as the difference between the amount of CH_4 adsorbed at the target storage pressure, generally 35-65 bar, and the amount that is still adsorbed at the lowest desorption pressure, generally 5.8 bar.[8-11] With only a few exceptions,[12] nearly all adsorbents that have been investigated in the context of natural gas storage exhibit classical Langmuir-type adsorption isotherms, where the amount of CH_4 adsorbed increases continuously, and with decreasing steepness, as the pressure is increased (Figure 5.1a). Despite a significant research effort, it has therefore proved difficult to develop adsorbents with the higher usable CH_4 capacities needed for a commercially viable ANG storage system.[9] In pursuit of a new strategy for boosting usable capacity, we endeavored to design an adsorbent with an "S-shaped" or stepped CH_4 adsorption isotherm, where the amount of CH_4 adsorbed would be small at low pressures but rise sharply just before the desired storage pressure (Figure 5.1b). Intriguingly, stepped isotherms have been observed for many flexible metal-organic frameworks that exhibit "gate-opening" behavior, whereby a nonporous structure expands to a porous structure after a

certain threshold gas pressure is reached, but none of these materials have exhibited characteristics beneficial for CH_4 storage applications.[13-17] If, however, a responsive adsorbent could be designed to expand to store a high density of CH_4 at 35-65 bar, and collapse to push out all adsorbed CH_4 at a pressure near 5.8 bar, then it should be possible to reach much higher usable capacities than have been realized for classical adsorbents.

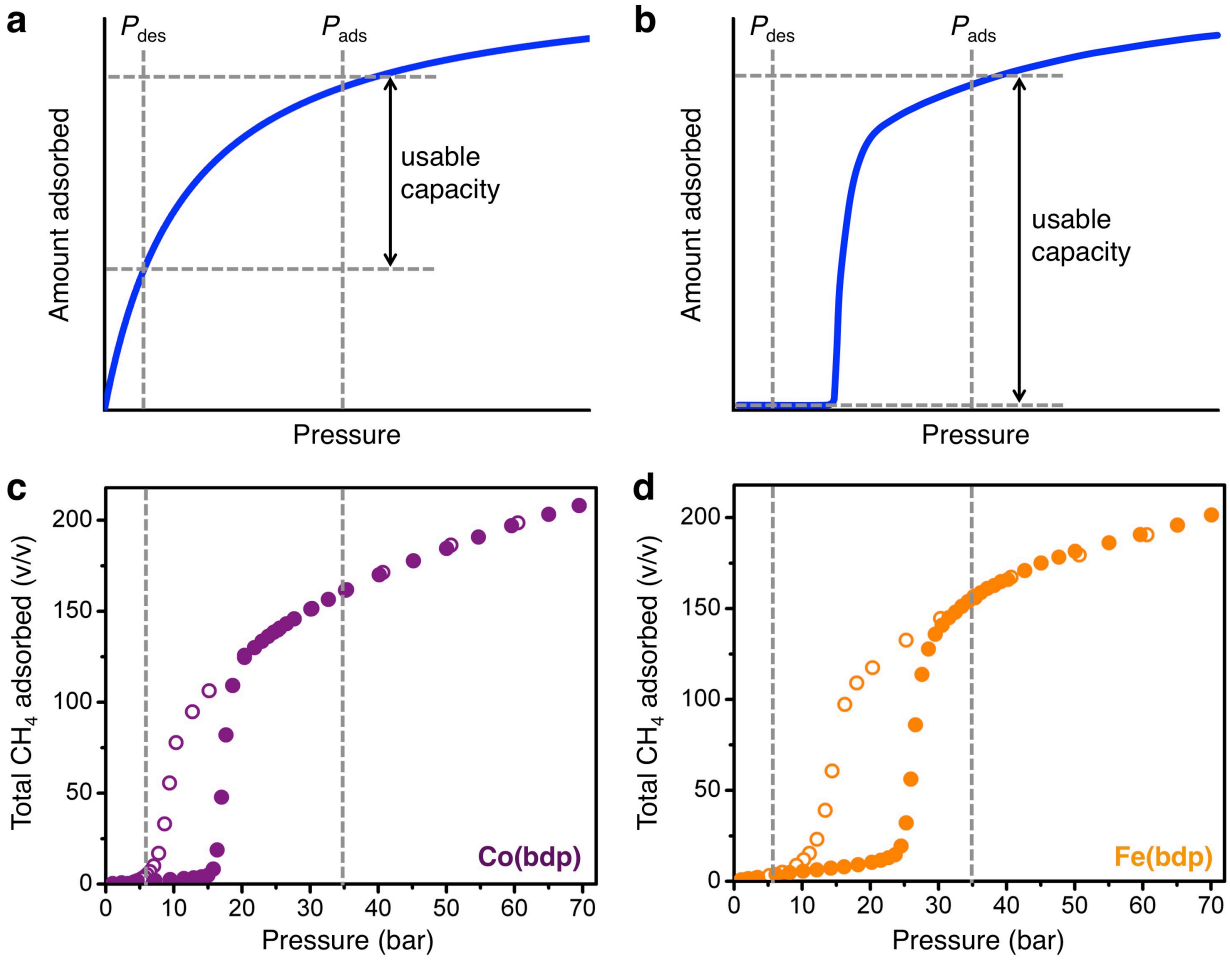

Figure 5.1. The usable capacity is compared for an idealized adsorbent that exhibits a classical Langmuir-type adsorption isotherm (**a**) and an "S-shaped", or stepped, adsorption isotherm (**b**). Total CH_4 adsorption isotherms for Co(bdp) (**c**) and Fe(bdp) (**d**) at 25 °C, where a minimum desorption pressure of 5.8 bar and a maximum adsorption pressure of 35 bar are indicated by dashed gray lines. Filled circles represent adsorption, while empty circles represent desorption.

5.2. Experimental

5.2.1. Materials. Anhydrous *N*,*N*-dimethylformamide (DMF) was obtained from a JC Meyer solvent system. The ligand 1,4-benzenedipyrazole (H_2bdp) was synthesized according to a literature procedure.[19] All other reagents were obtained from commercial vendors and used

without further purification. Ultra-high purity grade (99.999% purity) helium, dinitrogen, and methane were used for all adsorption measurements.

5.2.2. Synthesis of Co(bdp). The compound Co(bdp) was synthesized using a strategy adopted from a previous report.[19] Specifically, a 500 mL solvent bomb was charged with a magnetic stir bar, $Co(CF_3SO_3)_2$ (4.96 g, 0.0139 mol), H_2bdp (2.46 g, 0.0117 mol), and *N*,*N*-diethylformamide (90 mL). The reaction mixture was degassed by the freeze-pump-thaw method for 5 cycles then sealed by closing the stopcock of the solvent bomb while the frozen reaction mixture was still under vacuum. The solvent bomb was then heated at 160 °C for 4.5 days to afford a purple microcrystalline solid. The solvent bomb was backfilled with N_2, and the solid was collected by filtration. Before drying, the wet solid powder was immediately transferred to a 500 mL glass jar, and 400 mL of DMF was added. The jar was heated at 120 °C for 12 h, then cooled to room temperature. The DMF was decanted and replaced with 400 mL of fresh DMF. The jar was reheated at 120 °C, followed by decanting and replacing with fresh DMF. This was repeated four additional times. The DMF was then decanted and replaced with dichloromethane (DCM). The DCM was partially decanted until 50 mL of solution was remaining. The resulting slurry was transferred to a 100 mL Schlenk flask, and the DCM was evaporated by flowing N_2 at room temperature. The resulting solid was dried by flowing N_2 at 160 °C for 12 h, then placed under dynamic vacuum at 160 °C for 24 h. The activated solid was immediately transferred to a glovebox and handled under a N_2 atmosphere for all further experiments.

5.2.3. Synthesis of Fe(bdp). In a glovebox under a N_2 atmosphere, H_2(bdp) (0.200 g, 0.95 mmol) in DMF (9 mL) was heated to 120 °C while stirring for 20 min in a 20 mL glass vial. The resulting yellow suspension was cooled. A solution of $FeCl_2$ (0.197 g, 1.55 mmol) in methanol (1 mL) was added to the cooled suspension of H_2(bdp) in DMF, and the vial was sealed and heated at 120 °C while stirring. The hot, orange-yellow solution yielded a yellow microcrystalline powder after several hours. Samples suitable for gas adsorption studies were prepared using multiple vials of the same reaction scale and by washing the resulting material nine times with hot DMF (9x18 mL), before drying under high vacuum at 170 °C for 24 h. The activated sample was immediately transferred to a glovebox and handled under a N_2 atmosphere for all further experiments. IR (neat) ν/cm^{-1}: 1573 (s), 1336 (w), 1239 (s), 1110 (s), 1041 (s), 952 (s), 859 (s), 849 (s), 832 (s), 824 (s), 644 (s), 534 (s). Anal. Calcd. for $FeC_{12}H_8N_4$: C, 54.58; H, 3.05; N, 21.22. Found: C, 54.18; H, 2.36; N, 20.67. In order to obtain single crystals suitable for X-ray diffraction, a 9:1 mixture of DMF and methanol was used to create solutions of $FeCl_2$ (9.0 mg, 0.07 mmol in 0.1 mL solvent) and H_2(bdp) (4.0 mg, 0.019 mmol in 0.9 mL solvent). The $FeCl_2$ solution and the H_2(bdp) solution were added together in a 4 mL vial. The vial was then sealed, and the clear yellow solution was heated at 120 °C for 24 h. Block-shaped yellow crystals formed on the sides of the vial after several hours.

5.2.4. Low-Pressure Gas Adsorption Measurements. Gas adsorption isotherms for pressures in the range of 0-1.1 bar were measured using a Micromeritics ASAP 2020 or 2420 instrument. Activated samples were transferred under a N_2 atmosphere to preweighed analysis tubes, which were capped with a Transeal. Each sample was evacuated on the ASAP until the outgas rate was less than 3 μbar/min. The evacuated analysis tube containing degassed sample was then carefully transferred to an electronic balance and weighed to determine the mass of

sample (typically 100-200 mg). The tube was then fitted with an isothermal jacked and transferred back to the analysis port of the ASAP. The outgas rate was again confirmed to be less than 3 μbar/min. Langmuir surface areas were determined by measuring N_2 adsorption isotherms in a 77 K liquid N_2 bath and calculated using the Micromeritics software, assuming a value of 16.2 $Å^2$ for the molecular cross-sectional area of N_2. The Langmuir surface areas of Co(bdp) and Fe(bdp) are 2911 and 2780 m^2/g, respectively. Full 77 K N_2 adsorption isotherms for Co(bdp) and Fe(bdp) can be found in Figure 5.S9. Note that BET surface areas cannot be accurately determined for either framework because of the steps in the low-pressure region of the 77 K N_2 adsorption isotherms.

5.2.5. High-Pressure CH_4 Adsorption Measurements. High-pressure CH_4 adsorption isotherms in the range of 0-70 bar were measured on an HPVA-II-100 from Particulate Systems, a Micromeritics company. In a typical measurement, 0.5-1.0 g of activated sample was loaded into a tared stainless steel sample holder inside a glovebox under a N_2 atmosphere. Prior to connecting the sample holder to the VCR fittings of the complete high-pressure assembly inside the glovebox, the sample holder was weighed to determine the sample mass. The sample holder was then transferred to the HPVA-II-100, connected to the instrument's analysis port via an OCR fitting, and evacuated at room temperature for at least 2 h. The sample holder was placed inside an aluminum recirculating dewar connected to a Julabo FP89-HL isothermal bath filled with Julabo Thermal C2 fluid. The temperature stability of the isothermal bath is ± 0.02 °C. Methods for accurately measuring the relevant sample freespace, which involve the expansion of He from a calibrated volume at 0.7 bar and 25 °C to the evacuated sample holder, were described in detail previously.[8] Nonideality corrections were performed using the CH_4 compressibility factors tabulated in the NIST REFPROP database at each measured temperature and pressure.[34]

Note that a sample size of 1.032 g was used for the 25 °C usable capacity calculations, compaction studies, and cycling studies with Co(bdp), while a sample size of 0.584 g was used for the variable-temperature measurements. For Fe(bdp), a sample size of 0.274 g was used for high-pressure adsorption measurements, with the exception for the isotherms measured at –12 and –25 °C for which a sample size of 0.322 g was used.

To determine the usable CH_4 capacity of Co(bdp) and Fe(bdp), experimentally measured excess gravimetric adsorption data (Figure 5.S3) were converted to total volumetric adsorption data using the pore volume and crystallographic density of the CH_4 expanded phases.

5.2.5.1. High-pressure CH_4 adsorption measurements under applied mechanical pressure. For the high-pressure CH_4 adsorption measurements of Co(bdp) at different applied mechanical pressures, a custom aluminum sample holder was designed and used (Figure 5.S5). The sample is loaded in the volume between the fritted and blank gaskets. The free volume between the fritted and blank gaskets in the absence of a sample was determined by expansion of He from a calibrated volume to be 5.242 mL. Initially, 1.032 g of Co(bdp) was loaded into this volume, resulting in a bulk density of 0.197 g/mL for the uncompacted powder. After measuring a high-pressure CH_4 adsorption isotherm, the sample holder was returned to a glovebox under a N_2 atmosphere, and the cell was opened by removing the cap behind the blank gasket. An aluminum rod with an outer diameter slightly less than the inner diameter of the sample holder was then inserted. A mechanical press was used to compact the sample by pushing down on the rod. A fresh blank gasket was then sealed behind the rod so that the rod was left pressed against the sample, with a continuously applied uniaxial mechanical pressure. The sample holder was

returned to the high-pressure instrument and fully evacuated before measuring a high-pressure CH_4 adsorption isotherm. This experiment was repeated after inserting additional metal rods to further compact the Co(bdp), increase the applied mechanical pressure, and reduce the sample volume. Packing densities for each experiment were calculated by subtracting the volume of each rod from the sample volume.

It is important to note that the decrease in the total amount of CH_4 adsorbed at higher mechanical pressures (Figure 5.4) is not due to framework degradation, as is often observed when compacting classical adsorbents,[7] and can instead be explained by insufficient CH_4 pressure to induce a phase transition in some crystallites and by a lack of sufficient free volume for all crystallites to expand into. To confirm this, a CH_4 adsorption isotherm was measured after compacting collapsed Co(bdp) to a packing density of 0.75 g/cm^3, which is just below the crystallographic density of the expanded phase, and releasing the applied mechanical pressure by removing the metal rod. The resulting isotherm was found to be nearly identical to the pre-compaction isotherm, demonstrating that all Co(bdp) crystallites could once again fully expand (Figure 5.S5).

5.2.5.2. Background High-Pressure CH_4 Adsorption Measurements. In order to ensure the high-pressure adsorption experiments were accurate, background CH_4 adsorption and desorption isotherms were measured using sample holders containing glass beads of the same volume as a typical sample and using the same dosing procedure as for the experiments with Co(bdp) and Fe(bdp) (Figure 5.S11). While all background CH_4 adsorption was negligible at 0, 12, 25, 38, and 50 °C (less than ±2 cm$^3_{STP}$ at 35 bar and less than ±4 cm$^3_{STP}$ at 70 bar), there was a small background observed in the desorption isotherms. This is likely due to intrinsic hysteresis in the 100,000 torr GE Sensing UNIK5000 series pressure transducer. Regardless of its exact origins, the desorption backgrounds are very consistent and could be fit with a 4th order polynomial (Figure 5.S11). This polynomial was used to correct all of the desorption data reported in this work. The error in the desorption data is estimated to be less than ±2 cm$^3_{STP}$.

5.2.5.3.Freespace Measurements in Flexible Frameworks. Both Co(bdp) and Fe(bdp) exist in their fully collapsed phases at the conditions of the He freespace measurement—0.7 bar He and 25 °C. Since the expanded phases of Co(bdp) and Fe(bdp) can only be accessed at high CH_4 pressures, it is not possible to measure the freespace (empty volume in the high-pressure sample holder) for when the frameworks are expanded. If the skeletal densities, ρ_{sk}, of the collapsed and expanded phases are the same, however, then the fact that the freespace measurements are performed on the collapsed phase will not affect the accuracy of the adsorption measurements. If, however, the skeletal density of the expanded phase is greater than that of the collapsed phase, then the freespace when the framework is expanded will be higher than when it is collapsed, and the calculated amount adsorbed amount adsorbed will be too high. The narrow pores of collapsed phase of Co(bdp) should not be accessible to He, so the measured skeletal density of the collapsed phase might indeed be expected to be lower than that of the expanded phase since the same mass occupies a larger volume. For Co(bdp), the experimentally determined skeletal density used to calculate the freespace for the 25 °C high-pressure CH_4 adsorption isotherm is 1.43 g/cm^3. The skeletal density of a single crystal of the expanded phase can be estimated to be 1.92 g/cm^3 by using the appropriate crystallographic density (ρ_{cryst}, 0.77 g/cm^3), pore volume (V_p, 0.77 cm^3/g) and Eqn 5.1.

$$\rho_{sk} = \frac{\rho_{cryst}}{1 - \rho_{cryst} V_p} \tag{5.1}$$

The estimated skeletal density of the expanded phase can then be used to recalculate both the freespace in the sample holder and the high-pressure CH_4 adsorption isotherm in order to determine the significance of any errors arising from inaccuracies in our experimental freespace measurement. We note that the CH_4 isotherm calculated using the estimated skeletal density of the expanded phase should represent a maximum error in the experimental isotherm, as we are not accounting for any expansion of the Co(bdp) particles into interparticle voids that may lead to a decrease in the total freespace and partially offset any increase in freespace from errors in the skeletal density after expansion. Regardless, the high-pressure CH_4 adsorption isotherms calculated using the experimental skeletal density and estimated skeletal density of the expanded phase are in very good agreement (Figure 5.S10), and any errors resulting from freespace measurements will not significantly affect the calculated total CH_4 capacities reported in this work. Indeed, the difference between the amounts adsorbed calculated with each skeletal density at 35 bar is less than 0.3 mmol/g.

5.2.6. Conversion to Total Adsorption. The experimentally measured excess amounts adsorbed were converted to total amounts adsorbed using Eqn 5.2, where n_{ex} is the excess amount adsorbed in mmol/g, n_{tot} is the total amount adsorbed in mmol/g, V_p is the pore volume in cm^3/g, and ρ_{bulk} is the bulk density of pure CH_4.

$$n_{tot} = n_{ex} + V_p \cdot \rho_{bulk}(P,T) \tag{5.2}$$

The NIST Refprop database was used to determine ρ_{bulk} at each temperature and pressure[34]. Typically, V_p is determined from an N_2 adsorption isotherm at 77 K by assuming all pores have been completely filled with condensed N_2 at a sufficiently high P/P_0, where P is the pressure and P_0 is the N_2 saturation pressure. The total pore volume can then be calculated using the Gurvich rule by assuming that the molar volume of liquid N_2 is the same regardless of the size or surface chemistry of the pore inside which it is condensed.[38] For microporous materials with negligible external surface areas, which have a well-defined plateau in the N_2 adsorption isotherm at 77 K, the amount of N_2 adsorbed at a P/P_0 of 0.9 to 0.95 is generally used to calculate V_p and will include any pores less than 200-400 Å in the total volume calculation.

In Co(bdp) and Fe(bdp), it is not possible to directly measure V_p of the CH_4 expanded phase using 77 K N_2 adsorption, because this phase can only be accessed at high CH_4 pressures near ambient temperature. Instead, V_p can be calculated directly from the crystal structures of the expanded phases. This can be done by first calculating the accessible surface area using a N_2 sized probe molecule. Surface areas calculated in this manner have been shown in previous studies to be in good agreement with experimentally measured surface areas for a wide range of metal-organic frameworks.[39] Using the cross-sectional area of N_2 (16.2 $Å^2$) and the density of liquid N_2 (0.808 g/mL), the calculated accessible surface area can be converted to a total pore volume that should be analogous to that calculated from a 77 K N_2 adsorption isotherm. To confirm the accuracy of this approach, pore volumes were calculated in this manner for three representative, classical metal-organic frameworks: Ni_2(dobdc) (Ni-MOF-74; $dobdc^{4-}$ = 2,5-dioxido-1,4-benzenedicarboxylate), $Cu_3(btc)_2$ (HKUST-1; btc^{3-} = 1,3,5-benzenetricarboxylate),

and $Zn_4O(bdc)_3$ (MOF-5; bdc^{2-} = 1,4-benzenedicarboxylate). Accessible surface areas were calculated for crystal structures of each activated framework,[40-42] then converted to pore volumes. The calculated and experimental pore volumes are in excellent agreement in all cases: Ni-MOF-74, 0.55 (calculated), 0.56 (experimental); HKUST-1, 0.79 cm^3/g (calculated), 0.77 cm^3/g (experimental); MOF-5, 1.2 (calculated), 1.4 (experimental).

The calculated pore volume of the expanded phase of Co(bdp) is 0.78 cm^3/g, which is well below that of the fully expanded phase at 1 bar of N_2 and 77 K (1.02 cm^3/g). The calculated pore volumes of the 40 bar and 50 bar CH_4 expanded phases of Fe(bdp) are 0.77 cm^3/g and 0.96 cm^3/g, respectively. The collapsed phases of both frameworks do not have any accessible surface area for a N_2 or CH_4 sized probe molecule and thus have pore volumes of 0 cm^3/g.

The conversion of the excess CH_4 adsorption isotherms of Co(bdp) and Fe(bdp) to total adsorption isotherms is complicated by the fact that there is a distribution of crystallites present in the collapsed and expanded phases during the region of the structural transition since smaller crystallites should open at slightly lower pressures than larger crystallites.[32] At pressures above where the hysteresis loop closes, *in situ* powder X-ray diffraction experiments show that only the expanded phase is present (Figure 5.S7), and the excess amounts adsorbed can be converted to total amounts adsorbed using Eqn 5.2 with the calculated pore volume of the expanded phase. At lower pressures, there is a distribution of particles in the collapsed and expanded phases, and thus a distribution of total pore volumes. The total pore volume for each excess amount adsorbed in this region can be calculated by multiplying the pore volume of the expanded phase by the fraction of particles that are in the expanded state at a given pressure. Based on the powder X-ray diffraction results, we assume that 0% of the particles are in the expanded phase for 0 mmol/g adsorption, that 100% of the particles are expanded once the hysteresis loop is closed, and that there is a linear relationship between the amount of CH_4 adsorbed and the percentage of particles in the expanded phase between these values.

5.2.7. Powder X-ray Diffraction Measurements. Powder X-ray diffraction data for Co(bdp) and Fe(bdp) were collected on Beamline 17-BM-B at the Advanced Photon Source (APS) at Argonne National Laboratory and Beamline MS-X04SA at the Swiss Light Source (SLS) at the Paul Scherrer Institut (Figure 5.S7). For variable CH_4 pressure experiments, approximately 10 mg of fully desolvated framework was loaded into 1.5 mm quartz capillaries inside a glovebox under a N_2 atmosphere. Each capillary was attached to a custom designed gas-dosing cell, which is equipped with a gas valve, and was then transferred to the goniometer head. All adsorbed N_2 was removed by evacuating *in situ* using a turbomolecular pump. A cryostat was used to hold the temperature constant at 25 °C, and variable pressures of CH_4 were dosed to the samples. Diffraction data was collected after allowing each dose to equilibrate for several minutes. All X-ray wavelengths were between 0.72 Å and 0.78 Å, and are specified for each experiment in the relevant figures and tables below.

The structure solution and refinement procedure used in this study followed the standard protocol developed by us, and others, in the past, when polycrystalline samples of non-ideal crystallinity, and moderately complex structures, have had to be structurally characterized by *ab initio* powder diffraction methods. Standard peaks search methods, followed by profile fitting analyses were used to determine the accurate peak positions of ca. 20 well separated low-angle peaks, later used in the single-value-decomposition indexing procedure implemented in TOPAS-R (Bruker AXS, v 3.0, 2005, Karlsruhe, Germany). Approximate lattice parameters were found (here, all species showed C-centered monoclinic symmetry) and later refined by the

structureless Le Bail method. Systematic absences, density considerations and previous knowledge of isotypic species coherently allowed the derivation of the correct space group (*C2/c* in all cases), which was later confirmed by successful structure solutions and structure refinements. The structural model was derived by real-space techniques (here, simulating annealing) and the use of the z-matrix formalism, defining (with idealized, literature values) half bdp^{2-} ligand (making the whole bdp^{2-} moiety located about the inversion center at ¼, ¾, 0), and a single freely floating metal ion (eventually found to lie on a twofold axis at 0, y, ¼). Lorentz and absorption factors were applied, and the background was modeled by Chebyshev polynomials. SLS data for the collapsed Co(bdp) phase required a preferred orientation correction in the March-Dollase formulation [g_{100} = 0.898(1)]. A single isotropic B value was attributed to all atoms, and found to act, as expected, as a scavenger for θ-dependent systematic errors, not suitably taken into account in the data-reduction process. The contribution of the (likely tumbling, but not necessarily randomly located) CH_4 molecules to the overall scattering power has been neglected, and, probably, is one of the factors leading to the inaccuracy of the atomic displacement parameter values.

As indicated below, the peak widths of the Co(bdp) phase could not be easily modeled by conventional size and strain (Lorentzian and Gaussian contribution with systematic $\cos^{-1}\theta$ or $\tan\theta$ dependency, respectively) or even hkl (*i.e.* vectorially) dependent, more complex models (here, the spherical harmonics one). The best fit for Co(bdp), thus, required the insertion of a phenomenological description for *hk0* peak width, distinct from the axial reflections of the *h00* and *0k0* type.

A special comment is required for the powder diffraction analysis of Fe(bdp) at 50 bar of CH_4. The paucity of the peaks, their disparate widths (not following an easily interpretable law), and the possibility of the coexistence of coherent crystalline domains of variable sizes made the structure analysis of this species rather troublesome. However, some features could still emerge: the sharpness of a class of peaks with d = 13.41/*n* Å (peaks with *n* = 1-8 are clearly visible); their high-angle tails, which can be explained by the presence of faults, of a contaminant (not fully open) phase, or by both; the occurrence of very broad humps (>0.8° wide) overlapped with sharp(er) peaks (*fwhm* < 0.1°). Altogether, an *average* tetragonal primitive cell with a = 13.41 Å and c = 7.20 Å, space group $P4_2/mmc$, which is isomorphic with the previously reported Zn(bdp) (a = 13.25 Å and c = 7.25 Å), was determined to best describe the experimental diffraction data[35]. Also here, local distortions, likely due to inhomogeneous filling of the pores, induces poor crystallinity. Thus, the proposed coordinates should be taken only as a idealized description of an average structure, good enough, however, to allow the crystallographic density (of utmost importance for calculating the material's volumetric CH_4 capacity at 50-70 bar) to be correctly estimated. We further note that, since this idealized phase represents a fully expanded Fe(bdp) phase, the crystallographic density of this phase is likely underestimated, and thus provides a lower bound on the calculated volumetric usable CH_4 capacity at 65 bar.

5.2.8. Single Crystal X-ray Diffraction Measurements. X-ray diffraction analyses were performed on a single crystal of Fe(bdp) that was coated with Paratone-N oil and mounted on a MiTeGen loop. The crystal of Fe(bdp) was first kept frozen at 100 K by an Oxford Cryosystems Cryostream 800 plus, and after a full data collection, the crystal was warmed to 298 K for a second data collection. Diffraction data for Fe(bdp) was collected at Beamline 11.3.1 at the Advanced Light Source, Lawrence Berkeley National Laboratory using synchrotron radiation (λ = 0.7749 Å) with 1º omega scans for the 100 K structure, and 4º phi and 1º omega scans for

the 298 K structure. A Bruker PHOTON100 CMOS diffractometer was used for data collection, and the corresponding Bruker AXS APEX II software was used for data collection and reduction. Raw data was integrated and corrected for Lorentz and polarization effects using the Bruker AXS SAINT software. Absorption corrections were applied using TWINABS for the 100 K structure and SADABS for the 298 K structure. Space group assignments were determined by examination of systematic absences, E-statistics, and successive refinement of the structures of Fe(bdp) at 100 K and 298 K. The structures were solved using direct methods with SHELXS and refined using SHELXL operated in the OLEX2 interface. Thermal parameters were refined anisotropically for all non-hydrogen atoms. Hydrogen atoms were placed in ideal positions and refined using a riding model for all structures.

The crystal was determined to be twinned at 100 K and a suitable unit cell was determined that is similar to that previously reported for Co(bdp)•3DMF in the space group $P2_1/c$.[36] The program CELL_NOW was used to determine the orientation matrices, and the domains were found to related by a 179.9º rotation around the reciprocal axis [0.5 0 1]. Raw data for both matrices were integrated and corrected for absorption using TWINABS. Solution and refinement of the data in $P2_1/c$ required significantly less restraints in structure refinement and gave much lower values for R1 compared to those solved in other space groups. Solvent molecules could be refined anisotropically in the crystal of Fe(bdp) at 100 K, accounting for all pore void space.

When the crystal was warmed to 298 K, the space group was determined to be $C222_1$ instead of $P2_1/c$ and was refined as an inversion twin (BASF = 0.52(4)). At 298 K, there was extensive solvent disorder that could not be modeled. A solvent mask was applied, as implemented in OLEX2, to account for unassigned electron density within the pores. The loss in intensity of spots upon warming to 298 K, and the large anisotropic displacement parameters that result from linker and solvent disorder, gave rise to A and B level alerts from checkCIF. Responses addressing these alerts have been included in the CIF and can be read in reports generated by checkCIF.

Crystal data for collapsed Co(bdp) at 25 °C: $Co(C_{12}N_4H_8)$; monoclinic, *C2/c*, a = 24.8274(6) Å, b = 6.6747(4) Å, c = 7.1456(3) Å, β = 92.550(2)°, V = 1182.97(9) Å^3; R_{wp} = 0.083, R_p = 0.069, R_{Bragg} = 0.033. Metrical data are available free of charge from the Cambridge Crystallographic Data Centre under reference number CCDC 1058444.

Crystal data for expanded Co(bdp) at 30 bar CH_4 and 25 °C: $Co(C_{12}N_4H_8)$; monoclinic, *C2/c*, a = 21.763(2) Å, b = 15.220(2) Å, c = 6.9827(7) Å, β = 97.37(1)°, V = 2293.8(5) Å^3; R_{wp} = 0.046, R_p = 0.036, R_{Bragg} = 0.018. Metrical data are available free of charge from the Cambridge Crystallographic Data Centre under reference number CCDC 1058445.

Crystal data for collapsed Fe(bdp) at 25 °C: $Fe(C_{12}N_4H_8)$; monoclinic, *C2/c*, a = 25.086(2) Å, b = 6.8878(3) Å, c = 6.9845(5) Å, β = 91.653(6)°, V = 1206.4(1) Å^3; R_{wp} = 0.056, R_p = 0.041, R_{Bragg} = 0.017. Metrical data are available free of charge from the Cambridge Crystallographic Data Centre under reference number CCDC 1058446.

Crystal data for 40-bar expanded Fe(bdp) at 40 bar CH_4 and 25 °C: $Fe(C_{12}N_4H_8)$; monoclinic, *C2/c*, a = 20.15(3) Å, b = 17.91(2) Å, c = 6.953(4) Å, β = 97.34(6)°, V = 2489(5) Å^3; R_{wp} = 0.126, R_p = 0.095, R_{Bragg} = 0.049. Metrical data are available free of charge from the Cambridge Crystallographic Data Centre under reference number CCDC 1058449.

Crystal data for 50-bar expanded Fe(bdp) at 50 bar CH_4 and 25 °C: $Fe(C_{12}N_4H_8)$; tetragonal, $P4_2/mmc$, a = 13.41 Å, c = 7.20 Å, V = 1295 Å^3. Metrical data are available free of charge from the Cambridge Crystallographic Data Centre under reference number CCDC 1058450.

Crystal data for DMF-solvated Fe(bdp) at 100 K: $Fe(C_{21}N_7H_{29}O_3)$; monoclinic, $P2_1/c$, a = 13.4333(4) Å, b = 13.8493(4), c = 26.7477(9) Å, β = 101.5505(18), V = 4875.4(3) Å^3. Metrical data are available free of charge from the Cambridge Crystallographic Data Centre under reference number CCDC 1058447.

Crystal data for DMF-solvated Fe(bdp) at 298 K: $Fe(C_{12}N_4H_8)$; orthorhombic, $C222_1$, a = 17.3648(10), b = 20.4338(11) Å, c = 14.0029(8) Å, V = 4968.6(5) Å^3. Metrical data are available free of charge from the Cambridge Crystallographic Data Centre under reference number CCDC 1058448.

5.2.9. Crystallographic Density Calculations. For Co(bdp), the monoclinic unit cell volumes of the collapsed and expanded phases are 1183.0 and 2293.8 Å^3, respectively. In both cases, the unit cell contains 4 Co atoms and 4 bdp ligands. Each bdp ligand has 12 C, 4 N, and 8 H atoms. The total mass in the unit cell is 1.775 x 10^{-21} g. Therefore, the crystallographic densities of the collapsed and expanded phases are 1.50 and 0.774 g/cm^3, respectively.

For Fe(bdp), the monoclinic unit cell volumes of the collapsed and 40 bar CH_4 expanded phases are 1206.4 and 2488.9 Å^3, respectively. In both cases, the unit cell contains 4 Fe atoms and 4 bdp ligands. Each bdp ligand has 12 C, 4 N, and 8 H atoms. The total mass in the unit cell is 1.755 x 10^{-21} g. Therefore, the crystallographic densities of the collapsed and 40 bar CH_4 expanded phases are 1.45 and 0.705 g/cm^3, respectively.

For Fe(bdp), the orthorhombic unit cell volume of the 50 bar expanded phase is 1295 Å^3. The unit cell contains 2 atoms and 2 bdp ligands. Each bdp ligand has 12 C, 4 N, and 8 H atoms. The total mass in the unit cell is 8.773 x 10^{-22} g. Therefore, the crystallographic density of the 50 bar CH_4 expanded phase is 0.668 g/cm^3.

5.2.10. Scanning Electron Microscopy. Scanning electron microscopy (SEM) samples of Co(bdp) and Fe(bdp) were prepared by dispersing microcrystalline powders into DCM and drop casting onto a silicon chip (Figure 5.S4). In order to dissipate charge, the samples were sputter coated with ~3 nm of Au (Denton Vacuum, LLC). Crystals were imaged at 5keV/12μA by field emission SEM (JEOL FSM6430).

5.2.11. Microcalorimetry Measurements. Approximately 0.2 g of Co(bdp) was used for combined microcalorimetry and high-pressure CH_4 adsorption experiments. Prior to each experiment, samples were outgassed *ex situ* at 423 K for 16 h under a dynamic vacuum of 10^{-3} mbar. The microcalorimetry experiments were performed using a home built manometric adsorption apparatus coupled with a Tian–Calvet type microcalorimeter.[37] This experimental device allows the simultaneous determination of the adsorption isotherm and the adsorption enthalpy using a point by point introduction of gas to the sample. A multi-pneumovalve system allows the introduction of the adsorbate to the sample. An exothermic thermal effect accompanied each introduction, which is due to both the adsorption process and gas compression. This peak in the energy curve with time is thus integrated in order to calculate a

pseudo-differential enthalpy of adsorption for each dose. Errors in this calculation can be estimated at ± 1 kJ mol^{-1}. Experiments were carried out at 303 K and up to 70 bar with CH_4 of a purity of above 99.999%.

5.3. Results and Discussion

The metal-organic framework Co(bdp) was selected as a potential responsive adsorbent for methane storage, owing to its large internal surface area and its previously demonstrated high degree of flexibility.[18] In its solvated form, this framework features one-dimensional chains of tetrahedral Co^{2+} cations bridged by μ^2-pyrazolate units to form 13 Å-wide square channels. Notably, the N_2 adsorption isotherm of the evacuated framework at 77 K exhibits five distinct steps, which have been attributed to four structural transitions as the framework progresses from a collapsed phase with minimal porosity to a maximally expanded phase with a Langmuir surface area of 2911 m^2/g.[19]

5.3.1. High-Pressure Adsorption. To investigate the ANG storage potential of Co(bdp), a high-pressure CH_4 adsorption isotherm was measured at 25 °C (Figure 5.1c). Significantly, there is minimal CH_4 uptake at low pressures and a sharp step in the adsorption isotherm at 16 bar. While there is hysteresis in the desorption isotherm, the hysteresis loop is closed by 7 bar, such that there is less than 0.2 mmol/g of CH_4 adsorbed at pressures below 5.8 bar. The step in the CH_4 isotherm is fully reproducible over at least 100 adsorption-desorption cycles (Figure 5.S1) and can be attributed to a reversible structural phase transition between a collapsed, nonporous framework and an expanded, porous framework at transition pressures that are ideal for ANG storage.

5.3.2. X-Ray Diffraction. To determine the specific structural changes responsible for the stepped CH_4 adsorption isotherm of Co(bdp), *in situ* powder X-ray diffraction experiments were performed under various pressures of CH_4 at 25 °C. Under vacuum, only one crystalline phase is observed in the diffraction pattern, consistent with the complete conversion of Co(bdp) to a collapsed phase upon desolvation. From 17 to 23 bar, there are substantial changes to both the positions and intensities of the diffraction peaks, as peaks corresponding to the collapsed phase decrease in intensity and peaks corresponding to a new expanded phase increase in intensity (Figure 5.2a). During desorption this expanded phase is fully converted back to the collapsed phase between 10 and 5 bar. Owing to the anisotropic peak widths and complex peak shapes that result from paracrystallinity effects (Figure 5.S8),[20] analysis of the powder diffraction data is not trivial, but *ab initio* structure solutions followed by Rietveld refinements (Figure 5.S7) were successfully performed against the diffraction data at 0 and 30 bar to provide crystal structures of the collapsed and expanded phases of Co(bdp) (Figure 5.2d).

Even though the density of the collapsed phase (1.50 g/cm^3) is nearly double that of the expanded phase (0.77 g/cm^3), the Co^{2+} ions adopt a similar pseudotetrahedral geometry in both structures. During the phase transition, the angles between the planes of the pyrazolate rings and the Co–N bonds decrease as the framework expands (Figure 5.S6). In addition, the central benzene ring of the bdp^{2-} ligand twists out of the plane of the two pyrazolates by 25° in the collapsed structure of Co(bdp), resulting in edge-to-face π-π interactions with four neighboring benzene rings that likely provide most of the thermodynamic driving force for the collapse of Co(bdp) at low gas pressures (Figure 5.2e).[21] Additionally, the close contacts between

neighboring bdp^{2-} ligands due to π-π stacking leads to no accessible porosity, and thus no CH_4 adsorption, in the collapsed phase.

5.3.2. Paracrystalline Description of the Collapsed Co(bdp) Structure. Recovering the structural defectiveness of Co(bdp) was possible thanks to the intrinsic ability of the Debye Scattering Equation (DSE)[47] to deal with structural defects in real space and then provide an *exact* modeling, in the reciprocal space, of the whole sample scattering.

The DSE describes the scattering of an ensemble of particles having different and fully random orientations in space (the classical representation of an ideal powder), through the set of interatomic distances, d_{ij}. In its expanded formulation, the DSE reads as:

$$\left\langle \frac{\delta\sigma}{\delta\Omega} \right\rangle_{\text{orient.}} = \sum_{j=1}^{N} f_j(q)^2 o_j^2 + \sum_{j>i=1}^{N} f_j(q) f_i(q) T_j(q) T_i(q) o_j o_i \frac{\sin(2\pi q d_{ij})}{2\pi q d_{ij}} \tag{5.3}$$

with X-ray atomic form factors $f_j(q)$, site occupancy $o_j(q)$ and Debye-Waller $T_j(q)$ factors, and $q = 2\sin\theta/\lambda$, the length of the scattering vector. The added value, compared to standard powder diffraction methods, is that now diffuse scattering enters into the simulation alongside the Bragg intensity, as the entire coherent and elastic scattering over all q-space is modeled.

Following the seminal work by Hosemann, Bachi and Welberry,[21,48] the Debye equation was suitably modified to add anisotropic *paracrystalline* features to the average crystal structure. In a truly periodic (though finite) crystal, the interatomic distance d contributes to the scattered intensity by the interference term $sinc(2\pi dq)$ [$sinc(x) = \sin(x)/x$]. In the presence of paracrystallinity (i.e. atomic correlated displacements), a radial variance V_r (which depends on V_x, V_y for a two-dimensional paracrystalline disorder) can be derived and a Gaussian factor needs to be added to the *sinc* term: $sinc(2\pi dq)\exp(-2\pi^2 q V_r)$.

With specific reference to the case of the collapsed phase of Co(bdp), *damped* correlations in real space between chain axes locations in *ab* were defined with a probabilistic description of the interatomic vectors. For a more detailed description of the model, the interested reader is referred to.[49]

In order to reproduce the experimentally observed features of Co(bdp) in the diffraction pattern simulation, the following model choices were adopted within the DSE approach:

i) a rigid Co(bdp) model taken from the refined structure in *C2/c* symmetry was assumed (eliminating hydrogen atoms to speed up the very long computational times);

ii) the C-centered monoclinic lattice was used to build up nanocrystals of different sizes and to calculate the database of sampled interatomic distances to be used in the DSE according to the Debussy Suite protocol[50]. Driven by the experimental observation of the peak widths of the axial reflections, a fixed base model of 30 x 90 cells in **a** and **b**, respectively, was assumed (the diameter of the circle of equivalent area of the *001* face being *ca.* 75 nm), with an average thickness of 43 nm along **c**;

*iii)*the paracrystalline correlation coefficients (as defined in ref. *51*) were adjusted by an iterative procedure to the final values: $r_a = 1.00$; $s_a = 0.96$; $r_b = 0.96$; $s_b = 1.00$; $\sigma_a = \sigma_b = 2.5$ Å.

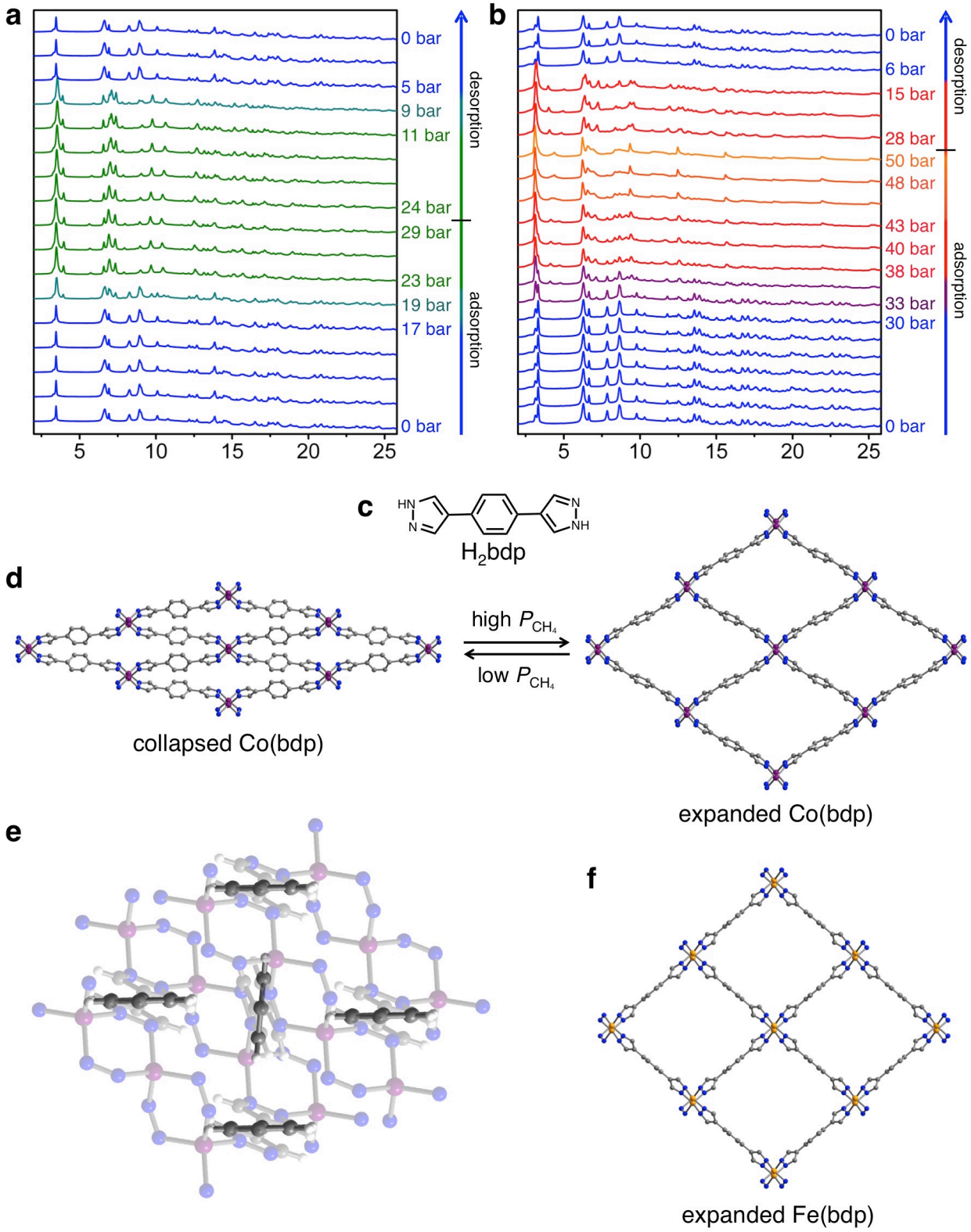

Figure 5.2. X-ray powder diffraction patterns are shown for Co(bdp) (**a**) and Fe(bdp) (**b**) at 25 °C and variable CH_4 pressures, with X-ray wavelengths of 0.75009 Å and 0.72768 Å, respectively. For Co(bdp), the blue and green patterns correspond to the collapsed and expanded phases, respectively. For Fe(bdp), the

blue, red, and orange patterns correspond to the collapsed, 40-bar expanded, and 50-bar expanded phases, respectively. **c,** The bridging ligand precursor H_2bdp is depicted along with (**d**) the crystal structures of the collapsed (0 bar) and CH_4 expanded (30 bar) phases of Co(bdp). **e**, Each benzene ring in the collapsed phase of Co(bdp) has four edge-to-face interactions with neighboring benzene rings. **f,** Crystal structure of the CH_4 expanded (40 bar) phase of Fe(bdp). Purple, orange, gray, blue, and white spheres represent Co, Fe, C, N, and H atoms, respectively; some H atoms are omitted for clarity.

The DSE paracrystalline approach implemented in the Debussy Suite directly provides the simulated pattern shown in Figure 5.S8, where it is compared to the experimental synchrotron trace. Significantly, the DSE paracrystalline model is able to nicely reproduce the peculiar features of observed peak heights and anisotropic peak widths and shapes.

The reasons for the occurrence of such a paracrystallinity are now evident. The rhomboic meshes depend on the length on the bdp spacer, which is rather fixed. If evacuation is not complete (or if an inhomogeneous distribution of pyrazolate-bridged Co chain locations are present, instead of pinned in ideally periodic lattice points), strong correlations among these chains, which cannot manifest *random* displacements, are maintained. Random displacements would afford progressively broadening peaks in reciprocal space (with a well known tanθ dependence, though anisotropic), which is not observed here.

5.3.3. Usable CH_4 Capacity. Significantly, the usable CH_4 capacity of Co(bdp) at 25 °C is 157 v/v for adsorption at 35 bar and 199 v/v for adsorption at 65 bar, which, to the best of our knowledge, are the highest values ever reported under these conditions (Table 5.S1).[22] In fact, a recent computational study of over 650,000 classical adsorbents predicted a theoretical maximum 65-bar usable capacity of 196 v/v.[9] The record Co(bdp) usable capacities, which break through this classical upper bound, are a direct result of the transition from the expanded to collapsed phase leading to near complete CH_4 desorption by 5.8 bar. For comparison, the highest previously reported 35- and 65-bar experimental usable capacities for any adsorbent are 143 v/v and 189 v/v, which were obtained for the metal-organic frameworks HKUST-1 and UTSA-76a, respectively.[7,8,23] Both of these Cu_2 paddlewheel-based frameworks have high densities of CH_4 adsorption sites, with a near optimal binding enthalpy of –15 to –17 kJ/mol, but classical Langmuir-type adsorption isotherms that leave a substantial amount of unusable CH_4 adsorbed at 5.8 bar.

5.3.4. Usable Capacity Comparisons. The usable CH_4 capacities of Co(bdp) and Fe(bdp) were calculated directly from the total CH_4 isotherms using the adsorption uptakes at 35 and 65 bar and the desorption uptake at 5.8 bar. The exact uptakes at 35 and 65 bar were determined by linear interpolation between the two or three experimental adsorption data points closest to each pressure. The exact uptakes at 5.8 bar were determined by linear interpolation between the two or three experimental desorption data points closest to each pressure. Exact values used in the usable capacity calculations can be found in Tables 5.S1-5.S4.

The usable capacities of HKUST-1 and MOF-5 were determined from previously reported total volumetric CH_4 adsorption isotherms at 25 °C.[8] The exact uptakes at 5.8, 35, and 65 bar were determined by linear interpolation between the three experimental data points closest to each pressure, and these values can be found in Tables 5.S1 and 5.S4.

The usable capacity of UTSA-76a (Cu_2(5,5′-(pyrimidine-2,5-diyl)diisophthalate)) was determined from a previously reported total volumetric CH_4 adsorption isotherm at 25 °C.[23] The exact uptakes at 5.8, 35, and 65 bar were determined by linear interpolation between the three experimental data points closest to each pressure, and these values can be found in Tables 5.S1 and 5.S4.

To evaluate the impact of cooling during desorption, which is expected to be a significant problem while driving an ANG vehicle, usable capacities were also calculated for Co(bdp), Fe(bdp), HKUST-1, and MOF-5 for 35 and 65 bar adsorption at 25 °C and 5.8 bar desorption at 0 and –25 °C (Tables S2 and S3). Because the desorption step for Fe(bdp) occurs at pressures above 5.8 bar at 0 and –25 °C, the Fe(bdp) usable CH_4 capacity is not nearly as affected as HKUST-1 and MOF-5 by cooling during desorption. Indeed, Fe(bdp) has a usable capacity of 150 v/v for 0 °C desorption, while HKUST-1 and MOF-5 have usable capacities of just 99 and 97 v/v, respectively. For −25 °C desorption, Fe(bdp) still maintains a usable capacity of 136 v/v, while HKUST-1 and MOF-5 have usable capacities of only 35 and 80 v/v under these conditions.

5.3.5. Usable Capacity of MOF-519. The usable capacity of MOF-519 ($Al_8(OH)_8(BTB)_4(H_2BTB)_4$; BTB^{3-} = 4,4′,4′′-benzene-1,3,-5-tryil-tribenzoate), which was recently reported to have record high volumetric usable capacities at 35 and 80 bar, was determined from a previously reported total volumetric CH_4 adsorption isotherm at 25 °C.[43] The exact uptakes at 5.8, 35, and 65 bar were determined by linear interpolation between the three experimental data points closest to each pressure, and these values can be found in Tables 5.S1 and 5.S4.

We note that there is some uncertainty regarding the value of the crystallographic density of MOF-519 that was used to calculate the reported volumetric usable CH_4 capacity. More specifically, two isostructural analogues of the framework, referred to as MOF-519 and MOF-520, were isolated depending on the exact synthetic conditions used. In MOF-519, which was synthesized using nitric acid, each octameric Al cluster contains 4 terminal H_2BTB^- ligands. In MOF-520, which was synthesized using formic acid, each octameric Al cluster contains 4 terminal formate ($HCOO^-$) molecules. Significantly, single crystals suitable for structure solution were isolated for each framework. Although each framework has a similar unit cell volume, the crystallographic density of MOF-519 (0.953 g/mL) is much higher than that of MOF-520 (0.586 g/mL) because of the greater mass of the terminal H_2BTB ligands compared to the terminal formates. We note, however, that a slightly different synthetic procedure was used to isolate a single crystal of MOF-519 than was used to make the bulk powder employed in the high-pressure CH_4 measurements and that DMF is known to hydrolyze into dimethylammonium and formate under typical MOF synthesis conditions.[46]

Because of the greater mass and steric bulk of the terminal H_2BTB^- ligands, MOF-519 is expected to have a lower surface area than MOF-520. Indeed, the reported BET surface areas for MOF-519 and MOF-520 are 2400 and 3290 m^2/g, respectively. In this work, we simulated the expected surface areas of MOF-519 and MOF-520 from the reported crystal structures. The expected surface area of MOF-520 is 3255 m^2/g, which is nearly identical to the reported value. In contrast, the expected surface area of MOF-519 is only 911 m^2/g, which is significantly lower than the reported value. This suggests that the MOF-519 sample used for the high-pressure CH_4 adsorption measurements may have had a mixture of terminal H_2BTB^- and formate ligands,

resulting in a higher than expected experimental surface area. In addition, this would imply a lower crystallographic density for the material than was originally calculated.

In further support of this, the reported %C determined by elemental analysis for MOF-519 was 59.98%, which is much closer to the value expected for terminal formates (58.81%) than terminal H_2BTB^- ligands (67.51%). The reported %C for MOF-520 was 58.80%, which is close to the expected value. It is also not clear why 22 water molecules were added to the molecular formula for MOF-519 but not MOF-520, as both were supposedly activated prior to the elemental analysis measurement.

Based on the expected surface area and elemental analysis of MOF-519, it seems very likely that the sample used for the high-pressure CH_4 adsorption measurements did not contain the expected stoichiometric amount of terminal H_2BTB^- ligands and that the crystallographic density used to calculate the reported volumetric CH_4 adsorption in MOF-519 was thus far too high. As a result, the usable capacities are likely significantly over-estimated for MOF-519; however, we still include them in Tables 5.S1 and 5.S4 for completeness. We also note that the usable capacities of Co(bdp) and Fe(bdp) at 35 bar are still higher than those originally reported for MOF-519, regardless of whether or not the crystallographic density used was too high. In general, it is extremely important to ensure that the crystallographic density is representative of the bulk samples used in the high-pressure CH_4 adsorption measurements since the volumetric CH_4 uptake, and total volumetric usable capacity, is directly proportional to the crystallographic density.

5.3.6. Intrinsic Thermal Management. One major, and often overlooked, challenge in developing adsorbents for natural gas storage, or indeed for any gas storage application, involves managing the exothermic heat of adsorption and endothermic heat of desorption, both of which always reduce the usable capacity of an adsorbent. These heat effects can be substantial, with temperature changes of as much as 80 °C observed during testing of prototype activated carbon-based ANG systems, and result in large reductions in the usable CH_4 capacity.[24,25] On-board thermal management systems are essential to minimizing the negative impacts of the heats of sorption, but these engineering controls take up already limited space on a vehicle and add significant cost and complexity.[26]

Responsive adsorbents, such as Co(bdp), offer the intriguing possibility of managing heat intrinsically within a material, rather than through an external system, by using the enthalpy change of a phase transition to partially, or perhaps even fully, offset the heats of sorption. For Co(bdp), the expansion of the framework during adsorption is endothermic, since energy is needed to overcome the greater thermodynamic stability of the collapsed phase. As a result, some of the enthalpy of CH_4 adsorption should go toward providing the heat needed for the transition to the expanded phase, lowering the overall amount of heat released compared to adsorption in the absence of a phase transition. Similarly, the transition to the collapsed phase is exothermic, and some of the heat released by the framework as it collapses should offset the endothermic desorption of CH_4.

In classical porous materials, low-coverage differential CH_4 adsorption enthalpies are generally −12 to −15 kJ/mol CH_4 for adsorbents that do not have any strong CH_4 binding sites and are closer to −15 to −25 kJ/mol for adsorbents with the highest volumetric CH_4 capacities.[7,8] For the steepest region of the CH_4 adsorption isotherm of Co(bdp), the differential enthalpy is considerably lower, at just −8.4(3) kJ/mol, since the endothermic framework expansion partially offsets the exothermic heat of adsorption (Figure 5.3c). After the transition to the expanded

Co(bdp) phase is complete, the differential enthalpy approaches –13 kJ/mol, which is consistent with weak CH_4 physisorption in the absence of a phase transition to mitigate heat. To confirm the accuracy of the calculated differential enthalpies, the heat released during CH_4 adsorption was directly measured by performing variable-pressure microcalorimetry experiments. As shown in Figure 5.3c, the differential enthalpies obtained from calorimetry are in excellent agreement with those calculated from the variable-temperature adsorption isotherms.

The total amount of heat released when increasing the pressure of CH_4 adsorbed in Co(bdp) from 5.8 to 35 bar, as would occur during refueling of an ANG vehicle, can be calculated by integrating the differential enthalpy curve. Significantly, the 73.4 kJ of heat released per L of Co(bdp) represents a 33% reduction relative to the 109 kJ/L of heat released by HKUST-1 under the same conditions, even though the amount of CH_4 adsorbed in Co(bdp) is 10% greater. We can further calculate that 93.9 kJ/L of heat would be released for hypothetical CH_4 adsorption in a rigid Co(bdp) framework—28% higher than when adsorption occurs with a phase transition to provide heat mitigation.[27]

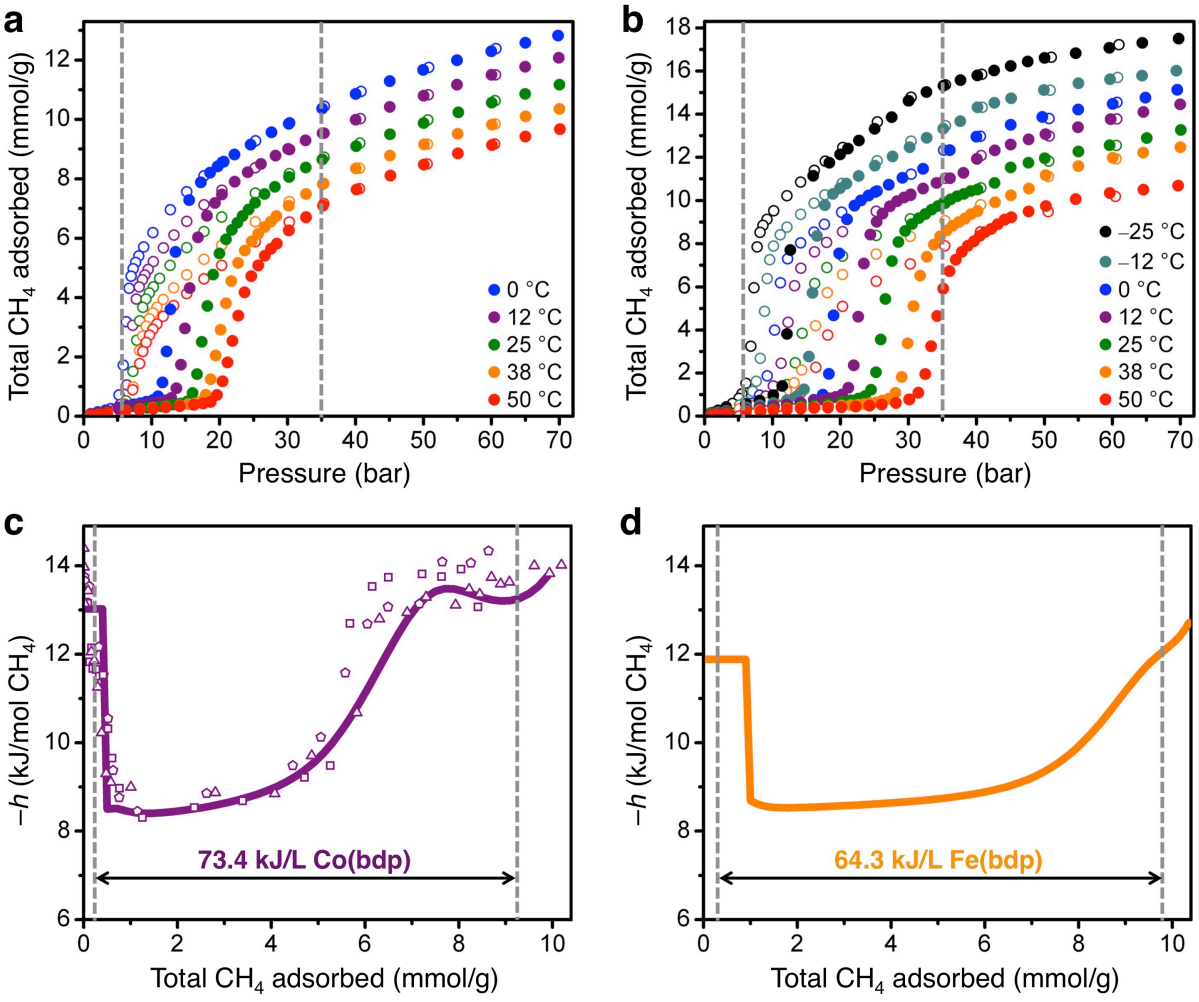

Figure 5.3. Total CH_4 adsorption isotherms at variable temperatures for Co(bdp) (**a**) and Fe(bdp) (**b**), where a minimum desorption pressure of 5.8 bar and a maximum adsorption pressure of 35 bar are indicated by dashed gray lines. Filled

circles represent adsorption, while empty circles represent desorption. **c**, Differential enthalpies of CH_4 adsorption for Co(bdp) as determined from variable temperature adsorption isotherms (purple line) and three separate microcalorimetry experiments (empty symbols). **d,** Differential enthalpies of CH_4 adsorption for Fe(bdp) as determined from variable temperature adsorption isotherms. Dashed gray lines indicate the amount of CH_4 adsorbed at 5.8 and 35 bar.

5.3.7. Tuning the Step Position. By chemically modifying Co(bdp), we hypothesized that it might be possible to obtain a new flexible framework with a similar stepped CH_4 isotherm, but a higher-energy phase transition that could provide even greater intrinsic heat management. Since one-dimensional chains are known to form with tetrahedral Fe^{2+} ions bridged by μ^2-pyrazolate units,[28] we anticipated that it might be possible to synthesize an isostructural iron analogue of Co(bdp). By heating $FeCl_2$ and H_2bdp in a mixture of *N*,*N*-dimethylformamide (DMF) and methanol, we indeed obtained Fe(bdp) as yellow, block-shaped crystals. X-ray analysis of a DMF-solvated crystal (Figure 5.S6) confirmed that Fe(bdp) is isostructural to Co(bdp). Significantly, Fe(bdp) has a stepped high-pressure CH_4 isotherm at 25 °C (Figure 5.1d), suggesting that this new compound also undergoes a reversible phase transition between a collapsed and expanded framework. While the total CH_4 uptake is comparable to Co(bdp), the adsorption and desorption steps occur at the considerably higher pressures of 24 and 10 bar, respectively, suggesting that replacing Co with Fe has in fact increased the energy of the phase transition.

In situ powder X-ray diffraction experiments from 0 to 50 bar of CH_4 (Figure 5.2b) and subsequent Rietveld refinements (Figure 5.S7) afforded the collapsed and CH_4 expanded crystal structures of Fe(bdp). While the collapsed phase is nearly identical to that of Co(bdp) (Figure 5.S6), with edge-to-face π-π interactions and no accessible porosity, the volume of the expanded Fe(bdp) phase at 40 bar is 9% greater than that of Co(bdp) (Figure 5.2f). Interestingly, in contrast to Co(bdp), we observe a second transition for Fe(bdp) at pressures above 40 bar, wherein Fe(bdp) slightly expands to a framework with nearly perfect square channels (Figure 5.S6). In spite of its greater expansion, and lower crystallographic density, the usable CH_4 capacity of Fe(bdp) is still higher than all known adsorbents at 152 and 192 v/v for 35 and 65 bar adsorption, respectively.

Although Fe(bdp) and Co(bdp) have similar 35-bar usable capacities, the Fe(bdp) phase transition offsets more heat, and only 64.3 kJ of heat is released per L of adsorbent during CH_4 adsorption, which is 12% lower than for Co(bdp) and 41% lower than for HKUST-1. This is a direct consequence of the larger increase in the enthalpy of Fe(bdp) (8.1 kJ/mol) than of Co(bdp) (7.0 kJ/mol) during the phase transition, which mitigates more heat of adsorption, thereby providing a greater source of intrinsic thermal management. Importantly, this result demonstrates how a slight variation in the metal-organic framework can be used to improve its intrinsic thermal management, and it is very likely that similar effects will prove possible through alteration of the bdp^{2-} bridging ligand.

Examining the temperature dependence of the CH_4 isotherms of Co(bdp) and Fe(bdp) reveals yet another advantage of these materials, involving a reduction in the impact of cooling during desorption. Consistent with other gate-opening metal-organic frameworks, the CH_4 adsorption and desorption steps in Co(bdp) and Fe(bdp) shift to lower pressures at lower temperatures (Figures 5.3a, 5.3b). As long as the temperature stays above 0 °C in Co(bdp) or –25 °C in

Fe(bdp), however, the transition to the collapsed phase occurs above 5.8 bar, and the usable CH_4 capacity will not be affected by cooling (Tables 5.S2-5.S3). This has practical benefits for driving in cold-weather climates and should further reduce the overall thermal management required in an ANG system.

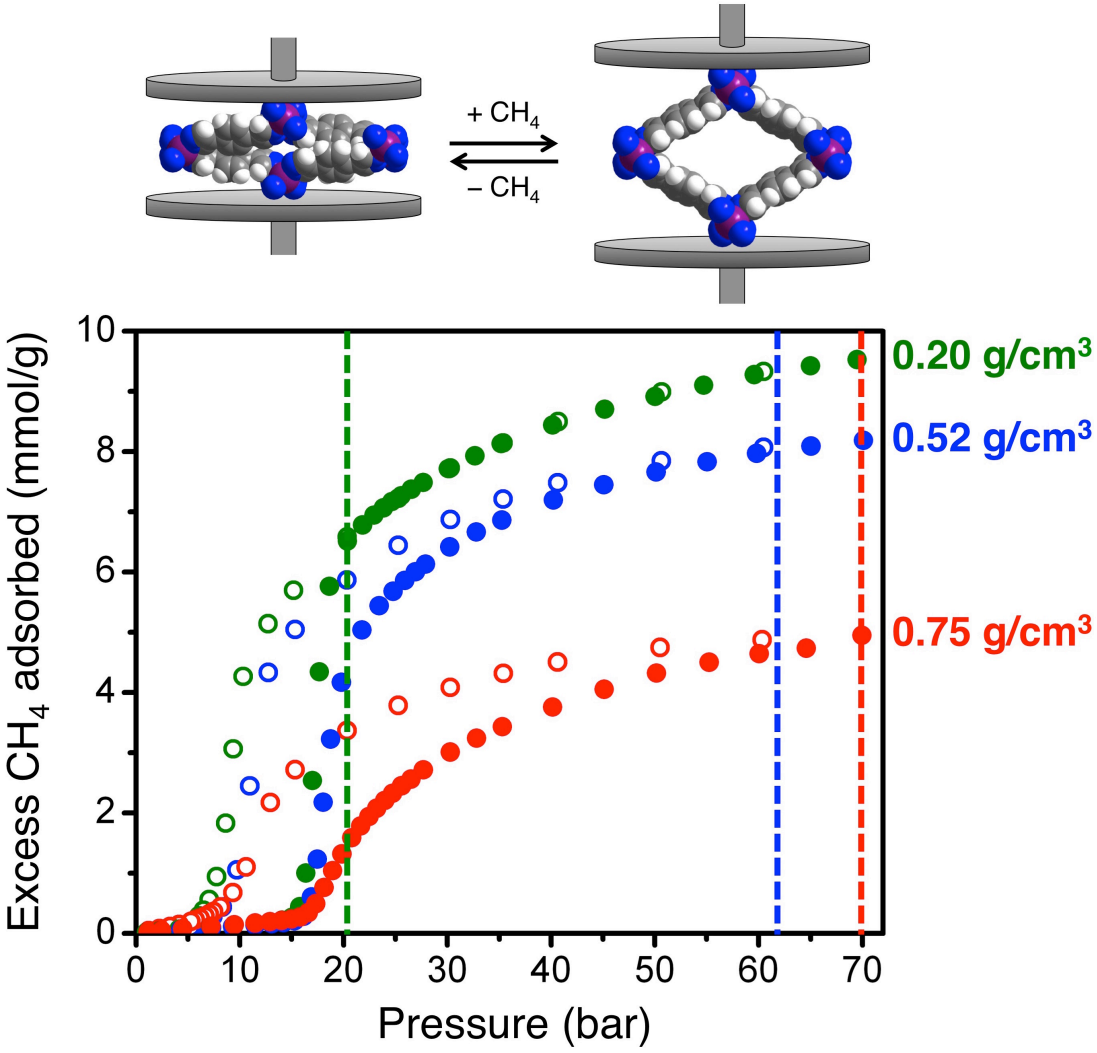

Figure 5.4. Excess CH_4 adsorption isotherms for Co(bdp) at 25 °C with different levels of applied external mechanical pressure are shown along with the corresponding bulk powder densities indicated at the right, wherein higher densities indicate greater applied mechanical pressure. The maximum CH_4 pressure for which hysteresis is still present is indicated by a colored dashed line for each bulk density. Filled circles represent adsorption, while empty circles represent desorption. In the space-filling models of collapsed and CH_4 expanded Co(bdp), purple, gray, blue, and white spheres represent Co, C, N, and H atoms, respectively.

5.3.8. Mechanical Pressure. Recent work has shown that it is possible to induce a phase transition in flexible metal-organic frameworks by applying external mechanical pressure.[29-31] With this in mind, we hypothesized that applying moderate mechanical pressure could provide a means of further tuning the CH_4 adsorption and desorption step pressures in Co(bdp) and Fe(bdp) and of increasing the energy of the phase transition to offset more heat. To investigate this, high-pressure CH_4 adsorption isotherms were measured for Co(bdp) at different levels of applied uniaxial mechanical pressure (Figure 5.S5).

At higher mechanical pressures and higher compaction densities, both the adsorption and desorption isotherm steps shift to higher CH_4 pressures, which is consistent with an increase in the energy of the phase transition (Figure 5.4). In addition, the isotherm hysteresis loop remains opened until higher CH_4 pressures, with hysteresis observed to at least 70 bar for the highest applied mechanical pressure. Since hysteresis at a given pressure implies that a phase transition is still occurring,[32] this result suggests that some Co(bdp) crystallites are expanding at much higher CH_4 pressures when under an applied external mechanical pressure. Because Co(bdp) crystallites in a bulk powder will be at different orientations with respect to the direction of uniaxial compression (Figure 5.S4), there will be a distribution of local mechanical pressures experienced by different crystallites. Crystallites that experience higher external pressures will have a greater free energy change associated with the phase transition and open at higher pressures.[33] Overall, these results present the tantalizing prospect of using mechanical work, such as perhaps provided through an elastic bladder, as a means of thermal management in a gas storage system based upon a flexible adsorbent.

5.3.9. Thermodynamics of CH_4 Adsorption in Co(bdp) and Fe(bdp). We can gain insight into the thermodynamics of high-pressure CH_4 adsorption in Co(bdp) and Fe(bdp) by building on the thermodynamic framework developed by Coudert and coworkers for gas-induced structural transitions in flexible metal-organic frameworks.[27] Note that several equations and results from their work are repeated here for completeness.

At the transition pressure, the thermodynamic potential, Ω, of the collapsed and expanded phases of Co(bdp) or Fe(bdp) are equal:

$$\Omega_{\text{collapsed}} = \Omega_{\text{expanded}} \tag{5.4}$$

$$F_{\text{col}} + P_{\text{trans}}V_{\text{col}} + \Omega_{\text{col}}(P_{\text{trans}}) = F_{\text{exp}} + P_{\text{trans}}V_{\text{exp}} + \Omega_{\text{exp}}(P_{\text{trans}}) \tag{5.5}$$

Here, F is the free energy (Helmholtz) of the collapsed or expanded phase in J per mol metal-organic framework (MOF), P_{trans} is the equilibrium pressure of the phase transition in bar, V is the molar volume of the collapsed or expanded phase, and Ω_{col} and Ω_{exp} are the grand canonical potential for CH_4 adsorption in the collapsed and expanded phases, respectively.

The grand canonical potential for adsorption in the collapsed phase is zero since it is nonporous.

$$\Delta F_{\text{MOF}} + P_{\text{trans}}\Delta V_{\text{MOF}} = -\Omega_{\text{exp}}(P_{\text{trans}}) \tag{5.6}$$

$$\Delta G_{\text{MOF}} = -\Omega_{\text{exp}}(P_{\text{trans}}) \tag{5.7}$$

$$\Delta H_{\mathrm{MOF}} - T\Delta S_{\mathrm{MOF}} = -\Omega_{\mathrm{exp}}(P_{\mathrm{trans}}) \tag{5.8}$$

Here, ΔG_{MOF} is the change in the Gibbs free energy of the MOF during the phase transition (J per mol MOF), ΔH_{MOF} is the enthalpy change of the MOF during the phase transition (J per mol MOF), and ΔS_{MOF} is the entropy change of the MOF during the phase transition (J/K per mol MOF).

Assuming an ideal gas, the grand canonical potential for adsorption in the expanded phase is:

$$\Omega(P) = \int_0^P -n(P)V_{\mathrm{m}}(P)\,dP \tag{5.9}$$

$$\Omega(P) = \int_0^P -n(P)\frac{\mathrm{R}T}{P}\,dP \tag{5.10}$$

where V_{m} is the molar volume of an ideal gas, n is the amount adsorbed in mol CH_4 per mol MOF, T is the temperature in K, and R is the gas constant.

We can assume that adsorption in the expanded phase can be described by a single-site Langmuir model:

$$n(P) = \frac{n_{\mathrm{sat}}bP}{1+bP} = \frac{n_{\mathrm{sat}}e^{S_{\mathrm{ads}}/\mathrm{R}}e^{-h_{\mathrm{ads}}/\mathrm{R}T}P}{1+e^{S_{\mathrm{ads}}/\mathrm{R}}e^{-h_{\mathrm{ads}}/\mathrm{R}T}P} \tag{5.11}$$

where n_{sat} is the saturation amount adsorbed in mol CH_4 per mol MOF, b is the Langmuir parameter in bar^{-1}, S_{ads} is the molar integral entropy of adsorption at saturation in J/K per mol MOF, and h_{ads} is the differential enthalpy of adsorption in J per mol CH_4. Note that the differential enthalpy is constant and independent of CH_4 loading for a single-site Langmuir model.

The experimental high-pressure CH_4 adsorption isotherms in Co(bdp) and Fe(bdp) at 0, 12, 25, 38, and 50 °C were fit with a single-site Langmuir model by fitting only the data for adsorption in the expanded phase, which corresponds to the region of the isotherms after the hysteresis loop has closed. Note that for Fe(bdp), the isotherms were only fit below the 2nd transition pressure so as to describe CH_4 adsorption just in the 40 bar expanded phase. The single-site Langmuir fit parameters are given in Table 5.S5. The variable-temperature single-site Langmuir fits to the experimental data are shown in Figure 5.S2.

Combining Eqns 5.10 and 5.11, we obtain the result originally reported by Coudert and coworkers:[27]

$$\Omega(P) = \int_0^P -n(P)\frac{\mathrm{R}T}{P}\,dP = -\mathrm{R}T\int_0^P \frac{n_{\mathrm{sat}}b}{1+bP}\,dP = -n_{\mathrm{sat}}\mathrm{R}T\ln\left(1+bP\right) \tag{5.12}$$

Combining Eqns 5.8 and 5.12:

$$\Delta H_{\mathrm{MOF}} - T\Delta S_{\mathrm{MOF}} = n_{\mathrm{sat}}\mathrm{R}T\ln(1+bP_{\mathrm{trans}}) \tag{5.13}$$

We can write P_{trans} as a function of T, ΔS_{MOF}, ΔH_{MOF}, and the single-site Langmuir parameters:

$$P_{trans} = \frac{e^{\frac{\Delta H_{MOF} - T\Delta S_{MOF}}{n_{sat} RT}} - 1}{b} \tag{5.14}$$

The total enthalpy change during the phase transition, ΔH_{trans}, is:

$$\Delta H_{trans} = \Delta H_{ads} + \Delta H_{MOF} \tag{5.15}$$

where ΔH_{ads} is the integral enthalpy of CH_4 adsorption in J per mol MOF.

We can write ΔH_{ads} in terms of the differential enthalpy of adsorption:

$$\Delta H_{ads} = h_{ads} n(P_{trans}) \tag{5.16}$$

$$\Delta H_{trans} = h_{ads} n(P_{trans}) + \Delta H_{MOF} \tag{5.17}$$

The total amount of heat released during the phase transition, Q_{trans}, is

$$Q_{trans} = -\Delta H_{trans} \tag{5.18}$$

The differential enthalpy (J per mol CH_4) during the phase transition, h_{trans}, is

$$h_{trans} = h_{ads} + \Delta H_{MOF} / n(P_{trans}) \tag{5.19}$$

The total amount of heat released at any adsorption pressure is

$$Q(P) = -\left(n(P) h_{ads} + \Delta H_{MOF}\right) \tag{5.20}$$

We can mathematically fit the CH_4 adsorption isotherms at each temperature (Figure 5.S2). Note that while no CH_4 adsorption is expected before the phase transition, a very small amount (less than 1 mmol/g) of CH_4 adsorption is observed in both Co(bdp) and Fe(bdp) before the step in the adsorption isotherm. This could be the result of some particles that have not fully collapsed, surface adsorption, or adsorption in small interparticle voids. Regardless, we can fit the pre-step adsorption with a single-site Langmuir model to be sure it is properly accounted for when calculating the total heat released during CH_4 adsorption. The adsorption after the phase transition is fit using a dual-site Langmuir-Freundlich model, where the pressure, P, is offset by the transition pressure, P_{trans}, and n_{sat} is the saturation capacity (mmol/g), b is the Langmuir parameter in $bar^{-\nu}$, and ν is the Freundlich parameter for two sites 1 and 2. All fit parameters are given in Tables 5.S6-5.S8.

$$n(P) = \begin{cases} \dfrac{n_{\text{sat}} bp}{1+bp} & \text{if } P < P_{\text{trans}} \\ \dfrac{n_{\text{sat},1} b_1 \left(P - P_{\text{trans}}\right)^{\nu_1}}{1 + b_1 \left(P - P_{\text{trans}}\right)^{\nu_1}} + \dfrac{n_{\text{sat},2} b_2 \left(P - P_{\text{trans}}\right)^{\nu_2}}{1 + b_2 \left(P - P_{\text{trans}}\right)^{\nu_2}} & \text{if } P \geq P_{\text{trans}} \end{cases} \tag{5.21}$$

We can use the Clausius-Clapeyron equation to calculate the differential enthalpy, or isosteric heat, as a function of the amount adsorbed from these fits.

$$\left(\ln P\right)_n = \left(\frac{h_{\text{ads}}}{R}\right)\left(\frac{1}{T}\right) + C \tag{5.22}$$

where h is the differential enthalpy (J per mol CH_4) at a constant amount of CH_4 adsorbed, n.

Because of the hysteresis in the isotherms, the experimental adsorption amounts in the region of the phase transition do not necessarily represent true thermodynamic equilibria. As a result, the applicability of the Clausius-Clapeyron equation in calculating differential enthalpies is unclear. However, if the extra chemical potential (CH_4 pressure) needed to eliminate the activation barrier to the phase transition is relatively constant at each temperature used, then the results of the Clausius-Clapeyron equation should still be valid. To confirm that the differential enthalpies are indeed representative of the true amount of heat released during CH_4 adsorption, high-pressure calorimetry experiments were used to directly measure the differential CH_4 enthalpy for Co(bdp). Significantly, the calorimetry results are in excellent agreement with the differential enthalpies calculated using the Clausius-Clapeyron equation (Fig. 3C), and the differential enthalpy during the phase transition is within error of –8.4 kJ/mol in both cases.

The experimental differential enthalpy curves of Co(bdp) and Fe(bdp) can be used to calculate ΔH_{MOF} and $T\Delta S_{\text{MOF}}$ for each framework and to determine exactly how much heat of CH_4 adsorption is offset by the phase transition. To illustrate this, consider an idealized differential enthalpy curve, assuming a perfectly vertical phase transition (Fig. S5). In Fig. S5, the area under the differential enthalpy curve before the inflection is equal to the total amount of heat released during the phase transition $-\Delta H_{\text{trans}}$. The area between the isosteric heat curve and the single-site Langmuir differential enthalpy of adsorption is equal to the enthalpy change of the framework during expansion, ΔH_{MOF}.

$$\Delta H_{\text{trans}} = \int_0^{n(P_{\text{trans}})} h \, dn \tag{5.23}$$

$$-\Delta H_{\text{MOF}} = \int_0^{n(P_{\text{trans}})} (h_{\text{ads}} - h) \, dn \tag{5.24}$$

In order to calculate ΔH_{MOF} and ΔS_{MOF} from the experimental differential enthalpy curves, both P_{trans} and the total amount of CH_4 adsorbed during the phase transition, $n(P_{\text{trans}})$, need to be determined. Note that in this work, we do not simply choose P_{trans} to be the observed step pressure in the experimental adsorption isotherm, as has been done previously, since the step pressure does not represent the true equilibrium transitions pressure[33]. Instead, we determine

P_{trans} from the differential enthalpy curve. This is done by assuming that all CH_4 adsorbed during the phase transition has a differential enthalpy of h_{trans}, while all CH_4 adsorbed in the expanded phase has a differential enthalpy of h_{ads} (the single-site Langmuir binding enthalpy). The differential enthalpy during the phase transition, h_{trans}, is simply the lowest magnitude value of the differential enthalpy curve, where CH_4 should only be adsorbing in M(bdp) particles that are undergoing a phase transition. Here, h_{trans} is –8.4 kJ/mol for Co(bdp) and –8.5 kJ/mol for Fe(bdp).

We note that a perfectly vertical phase transition, or adsorption isotherm step, would be expected for a powder containing monodisperse M(bdp) particles, where the extra chemical potential (CH_4 pressure) needed to eliminate the activation barrier to the phase transition would be the same for each particle.[33] Scanning electron microscope (SEM) images show that the Co(bdp) and Fe(bdp) powders contain a wide distribution of particles sizes (Figure 5.S4). Since smaller crystallites should have the activation barrier to the phase transition eliminated at lower pressures than larger crystallites, there is a distribution of step pressures observed, rather than a single transition pressure and a vertical isotherm step. As the pressure is increased, some CH_4 molecules continue to adsorb in particles that are undergoing a phase transition, while other CH_4 molecules adsorb in particles that have already expanded. This causes the differential enthalpy to increase gradually rather than suddenly as expected for an ideal sample. To determine $n(P_{trans})$, the total amount of CH_4 adsorbed (n_{tot}) thus needs to be divided between CH_4 adsorbed with a differential enthalpy of h_{trans}, which we define as n_{trans}, and CH_4 adsorbed with a differential enthalpy of h_{ads}, which we define as n_{exp} (Fig. S5).

$$\Delta H_{tot} = \Delta H_{trans} + \Delta H_{ads} = n_{trans} h_{trans} + n_{ads} h_{ads} \tag{5.25}$$

$$n_{tot} = n_{trans} + n_{ads} \tag{5.26}$$

$$n_{trans} = \frac{\Delta H_{tot} - n_{tot} h_{ads}}{h_{trans} - h_{ads}} \tag{5.27}$$

Here, ΔH_{tot} is the total integral under the differential enthalpy curve from 0 to n_{tot} CH_4 adsorbed.

$$\Delta H_{tot} = \int_0^{n_{tot}} h \, dn \tag{5.28}$$

Once n_{trans} is determined, ΔH_{MOF} can be calculated using Eqn 5.17:

$$\Delta H_{MOF} = n_{trans}(h_{trans} - h_{ads}) \tag{5.29}$$

The equilibrium transition pressure, P_{trans}, can be calculated using Eqn 5.11.

Using Eqn 5.14, ΔS_{MOF} can be calculated:

$$T\Delta S_{MOF} = n_{trans} h_{trans} - h_{ads} n(P_{trans}) - n_{sat} RT \ln(1 + bP_{trans}) \tag{5.30}$$

The calculated thermodynamic parameters for Co(bdp) and Fe(bdp) can be found in Tables 5.S9 and 5.S10. The enthalpy of the phase transition, ΔH_{MOF}, for Co(bdp) and Fe(bdp) is 7.0 and 8.1 kJ/mol, respectively. Note that these values are of similar magnitude to the enthalpy of contraction for Cr(OH)(1,4-benzenedicarboxylate) (Cr-MIL-53) that was previously determined using a combination of differential scanning calorimetry and thermogravimetric analysis.[45] The entropy of the phase transition, ΔS_{MOF}, for Co(bdp) and Fe(bdp) is 9.5 and 6.9 J/mol·K, respectively.

Comparisons between the total amount of heat released in Co(bdp), Fe(bdp), and HKUST-1 when pressurizing from 5.8 bar to 35 or 65 bar of CH_4, as would be the case during refueling of an ANG vehicle, can be found in Table 5.S11. Note that the differential enthalpy of CH_4 adsorption in HKUST-1 is –17.1 kJ/mol CH_4 and is constant over the pressure range of interest for natural gas storage[8]. For the purpose of the 65 bar heat calculation in Fe(bdp), the CH_4 binding enthalpy in the 50 bar expanded phase of Fe(bdp) is assumed to be equal to that of the 40 bar expanded phase, although the true value is likely slightly lower so the total heat released at 65 bar is likely overestimated.

It is interesting to consider what would be needed for zero heat to be released during a similar phase transition as to that reported in this work ($\Delta H_{trans} = 0$). For instance, one could envision tuning the energetics of the π-π stacking interactions[46], in the collapsed phases of Co(bdp) or Fe(bdp), to rationally tune ΔH_{MOF} and ΔS_{MOF}. If the total amount of heat released during the phase transition is zero, then

$$Q_{trans} = -\Delta H_{trans} = 0 = \Delta H_{ads} + \Delta H_{MOF} \tag{5.31}$$

$$\Delta H_{MOF} = -\Delta H_{ads} \tag{5.32}$$

Assuming $\Delta H_{trans} = 0$ and using Eqn 5.30:

$$T\Delta S_{MOF} = -n_{sat} RT \ln\left(1 + bpP\right) - h_{ads} n(P_{trans}) \tag{5.33}$$

Using Eqn 5.11, 5.16, and 5.32, we can write the combination of $T\Delta S_{MOF}$ and ΔH_{MOF} that will lead to zero heat released during the phase transition as a function of P_{trans} and the single-site Langmuir parameters.

$$T\Delta S_{MOF} = -n_{sat}\left(\mathrm{RT}\ln\left(1 + bP_{trans}\right) + \frac{h_{ads} bP_{trans}}{1 + bP_{trans}}\right) \tag{5.34}$$

$$T\Delta S_{MOF} = -n_{sat}\left(\mathrm{RT}\ln\left(1 + e^{S_{ads}/R} e^{-h_{ads}/RT} P_{trans}\right) + \frac{h_{ads} e^{S_{ads}/R} e^{-h_{ads}/RT} P_{trans}}{1 + e^{S_{ads}/R} e^{-h_{ads}/RT} P_{trans}}\right) \tag{5.35}$$

$$\Delta H_{MOF} = -\frac{h_{ads} n_{sat} bP_{trans}}{1 + bP_{trans}} \tag{5.36}$$

$$\Delta H_{MOF} = -\frac{h_{ads} n_{sat} e^{S_{ads}/R} e^{-h_{ads}/RT} P_{trans}}{1 + e^{S_{ads}/R} e^{-h_{ads}/RT} P_{trans}} \tag{5.37}$$

Using the single-site Langmuir parameters for the expanded phase of Co(bdp), we can calculate the combinations of $T\Delta S_{MOF}$ and ΔH_{MOF} that will lead to zero heat released during the phase transition as a function of the transition pressure (Fig. S6).

Note that the transition pressure is determined by ΔG_{MOF} (Eqn 5.7). Since $\Delta G_{MOF} = \Delta H_{MOF} - T\Delta S_{MOF}$, there are many possible combinations of ΔH_{MOF} and $T\Delta S_{MOF}$ that can lead to a given transition pressure. However, there is only one combination at each transition pressure that will lead to zero heat released during the phase transition. These specific combinations of ΔH_{MOF} and $T\Delta S_{MOF}$ are shown as the green and blue lines, respectively, in Fig. S6.

If ΔH_{MOF} and $T\Delta S_{MOF}$ are below these lines, then heat will be released during the phase transition ($\Delta H_{trans} > 0$). If ΔH_{MOF} and $T\Delta S_{MOF}$ are above these lines, then cooling will occur during the phase transition ($\Delta H_{trans} < 0$).

This is a consequence of the 2nd Law of Thermodynamics—any spontaneous process must result in a net increase in entropy. Here, the entropy of adsorption is negative, while the entropy of the phase change or expansion (ΔS_{MOF}) during adsorption is positive. If the total magnitude of the entropy of adsorption is greater than the entropy of the phase change, then the net entropy change of the system will be negative. Therefore, enough heat must be released to the surroundings so that the entropy of the surroundings increases by more than the entropy of the system decreases.

5.4. Outlook and Conclusions

The foregoing results demonstrate the extraordinary potential of the metal-organic frameworks Co(bdp) and Fe(bdp) as adsorbents for methane storage. Designing new flexible adsorbents with stronger gas binding sites and higher-energy phase transitions provides a promising route to achieving even higher usable capacities and greater intrinsic heat management in a next generation of gas storage materials. Moreover, clever compaction and packing strategies should allow further reductions to external thermal management requirements and optimization of the overall storage system performance.

5.5. Acknowledgements

This research was supported by the Advanced Research Projects Agency – Energy (ARPA-E) of the U.S. Department of Energy (DoE). X-ray powder diffraction data were collected at beamline 17-BM-B at the Advanced Photon Source, a DoE Office of Science User Facility operated by Argonne National Laboratory under Contract No. DE-AC02-06CH11357 and at beamline MS-X04SA of the Swiss Light Source (SLS) at the Paul Scherrer Institut. Single crystal X-ray diffraction experiments were performed at beamline 11.3.1 at the Advanced Light Source, a DoE Office of Science User Facility operated by Lawrence Berkeley National Laboratory under Contract No. DE-AC02-05CH11231. In addition, we thank M. Veenstra, D. A. Boysen, T. M. McDonald, D. J. Xiao, M. Nippe, Z. Hulvey, G. J. Halder, K. J. Gagnon, S. J. Teat, and the technical staff of the MS-X04SA beamline at SLS for experimental assistance and helpful discussions. We acknowledge J. Oktawiec and M. K. Taylor for assisting with materials synthesis and characterization, M. R. Hudson, M. I. Gonzalez, C. M. Brown, A. Cervellino, N. Masciocchi, and A. Guagliardi for assisting with diffraction experiments and analysis, J.

Rodriguez and P. L. Llewellyn for performing the calorimetry measurements, and J. E. Bachman for collecting the SEM images.

5.6. References and Supplementary Figures

(1) Service, R. F. Science **2014,** *346*, 538-541.
(2) Yeh, S. *Energy Policy* **2007**, *35*, 5865-5875.
(3) Whyatt, G. A. Issues affecting adoption of natural gas fuel in light- and heavy-duty vehicles. (U.S. Department of Energy, PNNL-19745, **2010**).
(4) Wegrzyn, J.; Gurevich, M. *Appl. Energy* **1996**, *55*, 71-86.
(5) Makal, T. A.; Li, J.-R.; Lu, W.; Zhou, H.-C. *Chem. Soc. Rev.* **2012**, *41*, 7761-7779.
(6) He, Y.; Zhou, W.; Qian, G.; Chen, B. *Chem. Soc. Rev.* **2014**, *43*, 5657-5678.
(7) Peng, Y.; Krungleviciute, V.; Eryazici, I.; Hupp, J. T.; Farha, O. K.; Yildirim, T. *J. Am. Chem. Soc.* **2013**, *135*, 11887-11894.
(8) Mason, J. A.; Veenstra, M.; Long, J. R. Evaluating metal-organic frameworks for natural gas storage. *Chem. Sci.* **2014**, *5*, 32-51.
(9) Simon, C. M.; Kim, J.; Gomez-Gualdron, D. A.; Camp, J. S.; Chung, Y. G.; Martin, R. L.; Mercado, R.; Deem, M. W.; Gunter, D.; Haranczyk, M.; Sholl, D. S.; Snurr, R. Q.; Smit, B. *Energy Environ. Sci.* **2015**, *8*, 1190-1999.
(10) While the minimum desorption pressure required for natural gas to flow from the adsorbent to the combustion engine can vary from 3.5 to 10 bar depending on the specific requirements of fuel injectors, filters, and other engine components, the U.S. DoE recommends a minimum pressure of 5.8 bar for initial materials comparisons. This value has been adopted by other groups studying metal-organic frameworks for CH_4 storage and is therefore also used here for all usable capacity calculations.
(11) Advanced Research Projects Agency – Energy, "Methane opportunities for vehicular energy" (U.S. Department of Energy, Funding Opportunity No. De-FOA-0000672, **2012**).
(12) Noguchi, H.; Kondoh, A.; Hattori, Y.; Kanoh, H.; Kajiro, H.; Kaneko, K. *J. Phys. Chem. B* **2005**, *109*, 13851-13853.
(13) Horike, S.; Shimomura, S.; Kitagawa, S. *Nature Chem.* **2009**, *1*, 695-704.
(14) Férey, G.; Serre, C. *Chem. Soc. Rev.* **2009**, *38*, 1380-1399.
(15) Schneemann, A.; Bon, V.; Schwedler, I.; Senkovska, I.; Kaskel, S.; Fischer, R. A. *Chem. Soc. Rev.* **2014**, *43*, 6062-6096.
(16) Li, D.; Kaneko, K. *Chem. Phys. Lett.* **2001**, *335*, 50-56.
(17) Kitaura, R.; Seki, K.; Akiyama, G.; Kitagawa, S. *Angew. Chem. Int. Ed.* **2003**, *42*, 428-431.
(18) Choi, H. J.; Dincă, M.; Long, J. R. *J. Am. Chem. Soc.* **2008**, *130*, 7848-7850.
(19) Salles, F.; Maurin, G.; Serre, C.; Llewellyn, P. L.; Knöfel, C.; Choi, H. J.; Filinchuk, Y.; Oliviero, L.; Vimont, A.; Long, J. R.; Férey, G. *J. Am. Chem. Soc.* **2010**, *132*, 13782-13788.
(20) Hosemann, R.; Bagchi, S. N. *Direct analysis of diffraction by matter*. (North-Holland Publishing Company, Amsterdam, **1962**).
(21) Sinnokrot, M. O.; Valeev, E. F.; Sherrill, C. D. *J. Am. Chem. Soc.* **2002**, *124*, 10887-10893.

(22) The unit v/v is equivalent to cm^3_{STP} cm^{-3}, where cm^3_{STP} is defined as the volume occupied by an ideal gas at standard temperature and pressure (STP). Here, STP is defined as 273.15 K and 1 atm, resulting in a volume of 22.414 mL for 1 mmol of ideal gas at STP.
(23) Li, B.; Wen, H.-M.; Wang, H.; Wu, H.; Tyagi, M.; Yildirim, T.; Zhou, W.; Chen, B. *J. Am. Chem. Soc.* **2014**, *136*, 6207-6210.
(24) Barbosa Mota, J. P.; Rodrigues, A. E.; Saatdjian, E.; Tondeur, D. *Carbon* **1997**, *35*, 1259-1270.
(25) Walton, K. S.; LeVan, M. D. *Adsorption* **2006**, *12*, 227-235.
(26) Weickert, M.; Marx, S.; Müller, U.; Arnold, L. World Intellectual Property Organization, **2015**, WO 2015/022633 A1.
(27) Coudert, F.-X.; Jeffroy, M.; Fuchs, A. H.; Boutin, A.; Mellot-Draznieks, C. *J. Am. Chem. Soc.* **2008**, *130*, 14294-14302.
(28) Patrick, B. O.; Reif, W. M.; Sánchez, V; Storr, A.; Thompson, R. C. *Polyhedron* **2001**, *20*, 1577-1585.
(29) Beurroies, I.; Boulhout, M.; Llewellyn, P. L.; Kuchta, B.; Férey, G.; Serre, C.; Denoyel, R. *Angew. Chem. Int. Ed.* **2010**, *49*, 7526-7529.
(30) Yot, P. G.; Ma, Q.; Haines, J.; Yang, Q.; Ghoufi, A.; Devic, T.; Serre, C.; Dmitriev, V.; Férey, G.; Zhong, C.; Maurin, G. *Chem. Sci.* **2012**, *3*, 1100-1104.
(31) Coudert, F.-X. *Chem. Mater.* **2015**, *27*, 1905-1916.
(32) Neimark, A. V.; Coudert, F.-X.; Boutin, A.; Fuchs, A. H. *J. Phys. Chem. Lett.* **2010**, *1*, 445-449.
(33) Ghysels, A.; Vanduyfhuys, L.; Vandichel, M.; Waroquier, M.; Van Speybroeck, V.; Smit, B. *J. Phys. Chem. C.* **2013**, *117*, 11540-11554.
(34) Lemmon, E. W., Huber, M. L. & McLinden, M. O. NIST Standard Reference Database 23: Reference Fluid Thermodynamic and Transport Properties-REFPROP, Version 8.0, National Institute of Standards and Technology, Standard Reference Data Program, Gaithersburg, **2007**.
(35) Galli, S.; Masciocchi, N.; Colombo, V.; Maspero, A.; Palmisano, G.; López-Garzón, F. G.; Domingo-García, M.; Fernández-Morales, I.; Barea, E.; Navarro, J. A. R. *Chem. Mater.* **2010**, *22*, 1664-1672.
(36) Lu, Y.; Tonigold, M.; Bredenkötter, Volkmer, D.; Hitzbleck, J.; Langstein, G. *Z. Anorg. Allg. Chem.* **2008**, *634*, 2411-2417.
(37) Llewellyn, P. L.; Maurin, G. *C. R. Chemie* **2005**, *8*, 283-302.
(38) Gurvich, L. *J. Phys. Chem. Soc. Russ.* **1915**, *47*, 805.
(39) Düren, T.; Millange, F.; Férey, G.; Walton, K. S.; Snurr, R. Q. *J. Phys. Chem. C* **2007**, *111*, 15350-15356.
(40) Dietzel, P. D. C.; Panella, B.; Hirscher, M.; Blom, R.; Fjellvåg, H. *Chem. Commun.* **2006**, 959-961.
(41) Wu, Y.; Kobayashi, A.; Halder, G. J.; Peterson, V. K.; Chapman, K. W.; Lock, N.; Southon, P. D.; Kepert, C. J. *Angew. Chem. Int. Ed.* **2008**, *47*, 8929-8932.
(42) Zhou, W.; Wu, H.; Yildirim, T.; Simpson, J. R.; Hight Walker, A. R. *Phys. Rev. B* **2008**, *78*, 054114.
(43) Gándara, F.; Furukawa, H.; Lee, S.; Yaghi, O. M. *J. Am. Chem. Soc.* **2014**, *136*, 5271-5274.

(44) Moh, P. Y.; Brenda, M.; Anderson, M. W.; Attfield, M. P. *CrystEngComm* **2013**, **15**, 9672-9678.
(45) Devautour-Vinot, S.; Maurin, G.; Henn, F.; Serre, C.; Devic, T.; Férey, G. *Chem. Commun.* **2009**, 2733-2735.
(46) Devic, T.; Horcajada, P.; Serre, C.; Salles, F.; Maurin, G.; Moulin, B.; Heurtaux, D.; Clet, G.; Vimont, A.; Grenèche, J.-M.; Le Ouay, B.; Moreau, F.; Magnier, E.; Filinchuk, Y.; Marrot, J.; Lavalley, J.-C.; Daturi, M.; Férey, G. *J. Am. Chem. Soc.* **2010**, *132*, 1127-1136.
(47) Guagliardi, A.; Cervellino, A.; Giannini, C. in *Diffraction at the nanoscale. Nanocrystals, defective & amorphous materials*. Guagliardi, A.; Masciocchi, N. Eds. (Insubria University Press, Varese, Italy, **2010**), pp. 107-126.
(48) Welberry, T. R. *Diffuse X-ray scattering and models of disorder*. **(**OUP, Oxford, UK, **2004**).
(49) Cervellino, A.; Maspero, A.; Masciocchi, N.; Guagliardi, A. *Cryst. Growth. Des.* **2012**, *12*, 3631-3637.
(50) Cervellino, A.; Giannini, C.; Guagliardi, A. *J. Appl. Cryst.* **2010**, *43*, 1543-1547 .

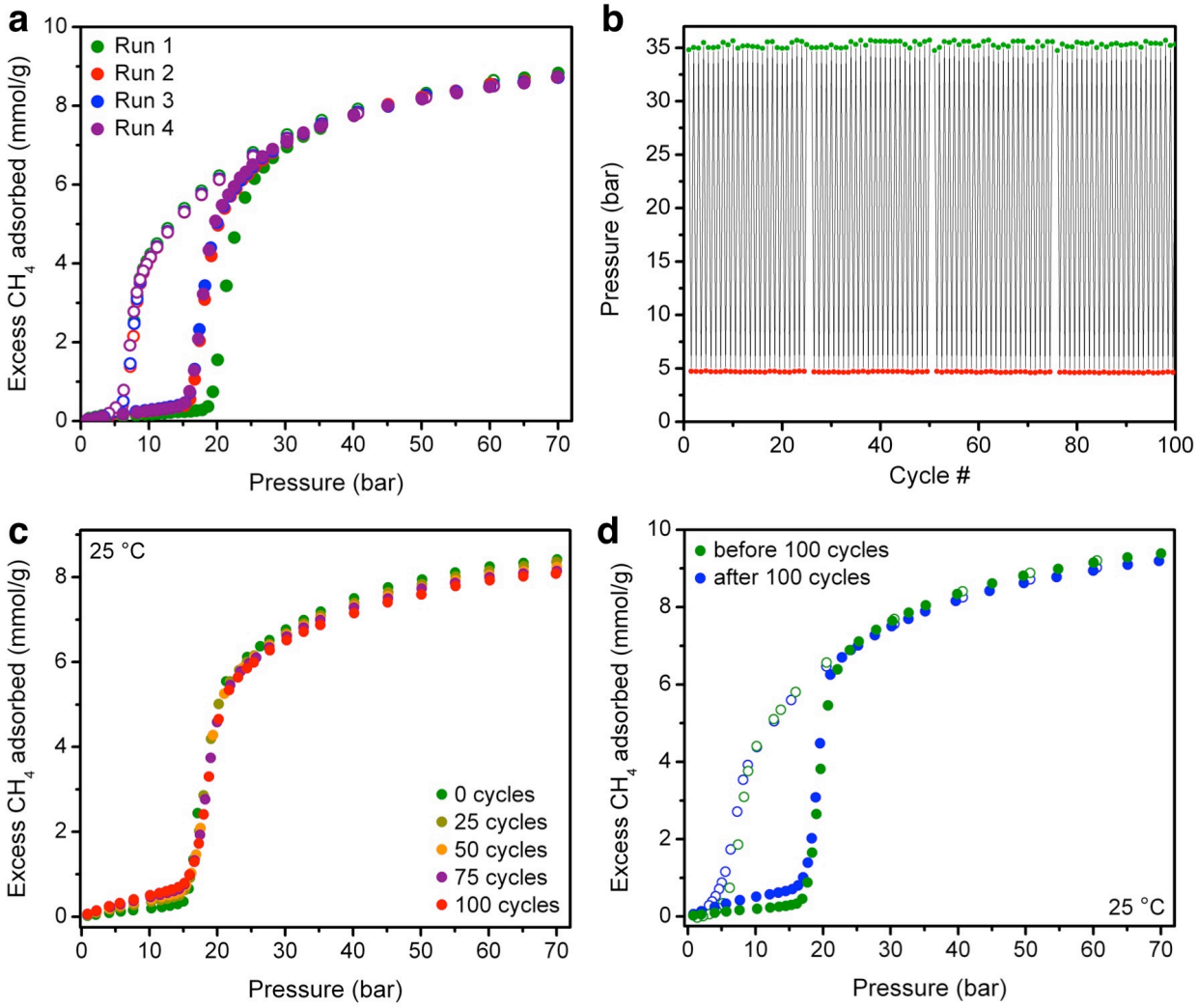

Figure 5.S1. **a,** Excess CH_4 isotherms at 25 °C for Co(bdp) repeated 4 times on the same sample, which was regenerated under vacuum at 25 °C for 2 h between measurements. Note that the adsorption step is at a slightly higher pressure during the first run because there is likely a slightly higher energy barrier to the first expansion of a freshly packed sample; however, the desorption steps occur at identical pressures for all four runs. **b**, The adsorption and desorption pressures are shown as green and red circles, respectively, for 100 CH_4 adsorption-desorption cycles in Co(bdp) at 25 °C. **c,** Excess CH_4 adsorption isotherms at 25 °C for Co(bdp) after 0, 25, 50, 75, and 100 cycles of 35 bar adsorption and 5 bar desorption. **d,** Excess CH_4 isotherms at 25 °C for Co(bdp) before (green) and after (blue) the 100 adsorption-desorption cycles between 35 and 5 bar. Filled and empty circles correspond to adsorption and desorption, respectively.

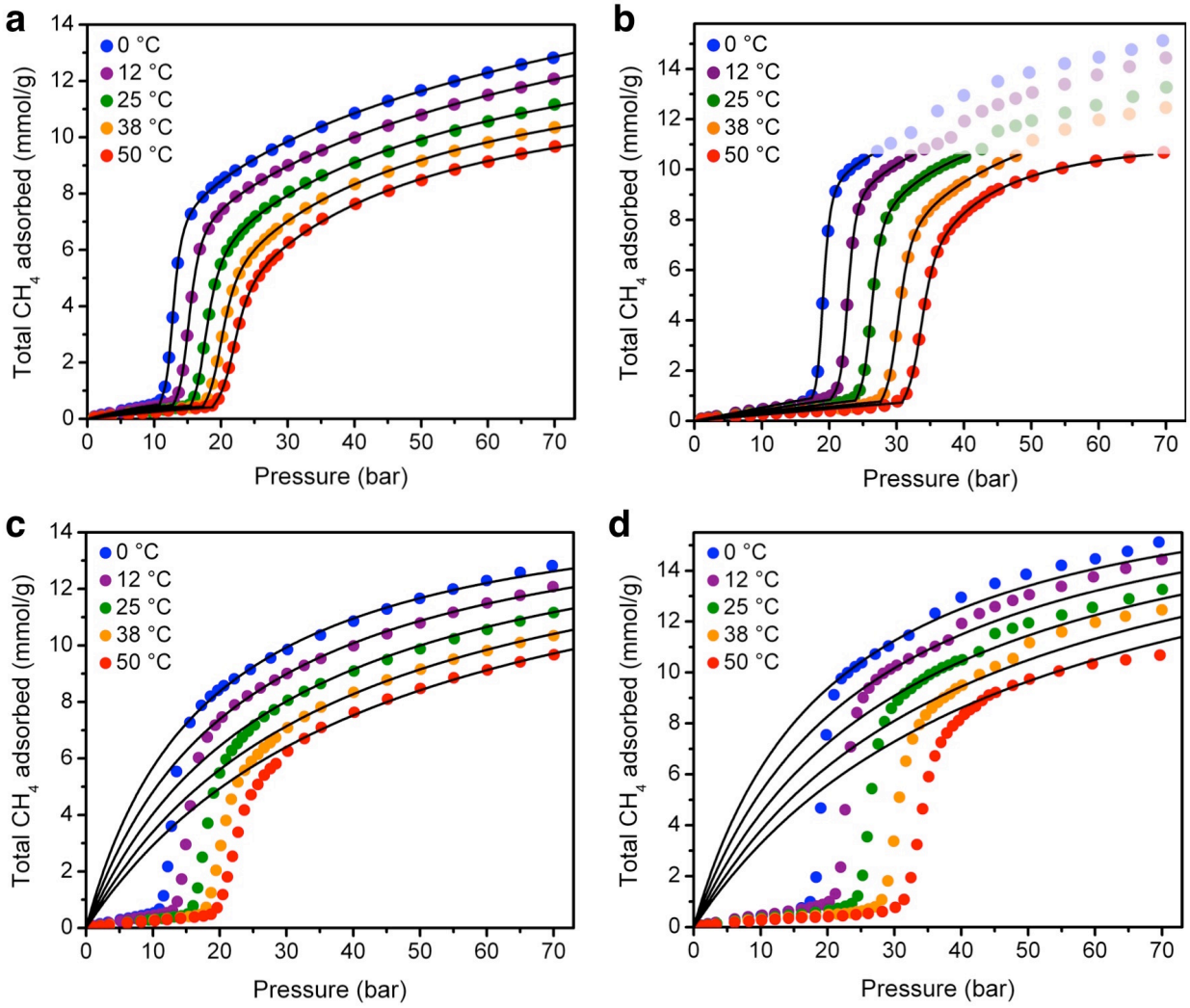

Figure 5.S2. **a,** Total CH_4 adsorption isotherms at 0, 12, 25, 38, and 50 °C for Co(bdp) with adsorption after the step fit independently at each temperature with an offset dual-site Langmuir-Freundlich equation. The small pre-step adsorption was fit with a single-site Langmuir model. **b,** Total CH_4 adsorption isotherms at 0, 12, 25, 38, and 50 °C for Fe(bdp) with adsorption after the phase transition fit independently at each temperature with an offset dual-site Langmuir-Freundlich equation. The pre-step adsorption was fit with a single-site Langmuir model. Additionally, the isotherms were only fit to a maximum loading of 10.6 mmol/g, as indicated by the shading, to avoid complications from the 2nd transition at higher CH_4 loadings. As such, differential enthalpies are only calculated up to a maximum loading of 10.6 mmol/g. **c,** Total CH_4 adsorption isotherms at 0, 12, 25, 38, and 50 °C for Co(bdp) with the corresponding single-site Langmuir fit for CH_4 adsorption in the expanded phase. **d,** Total CH_4 adsorption isotherms at 0, 12, 25, 38, and 50 °C for Fe(bdp) with the corresponding single-site Langmuir fit for CH_4 adsorption in the 40 bar expanded phase. Note that the data were only fit for the region of the isotherms that falls after the initial hysteresis loop closes and

before the 2nd isotherm step. All single- and dual-site Langmuir-Freundlich fits are shown as black lines.

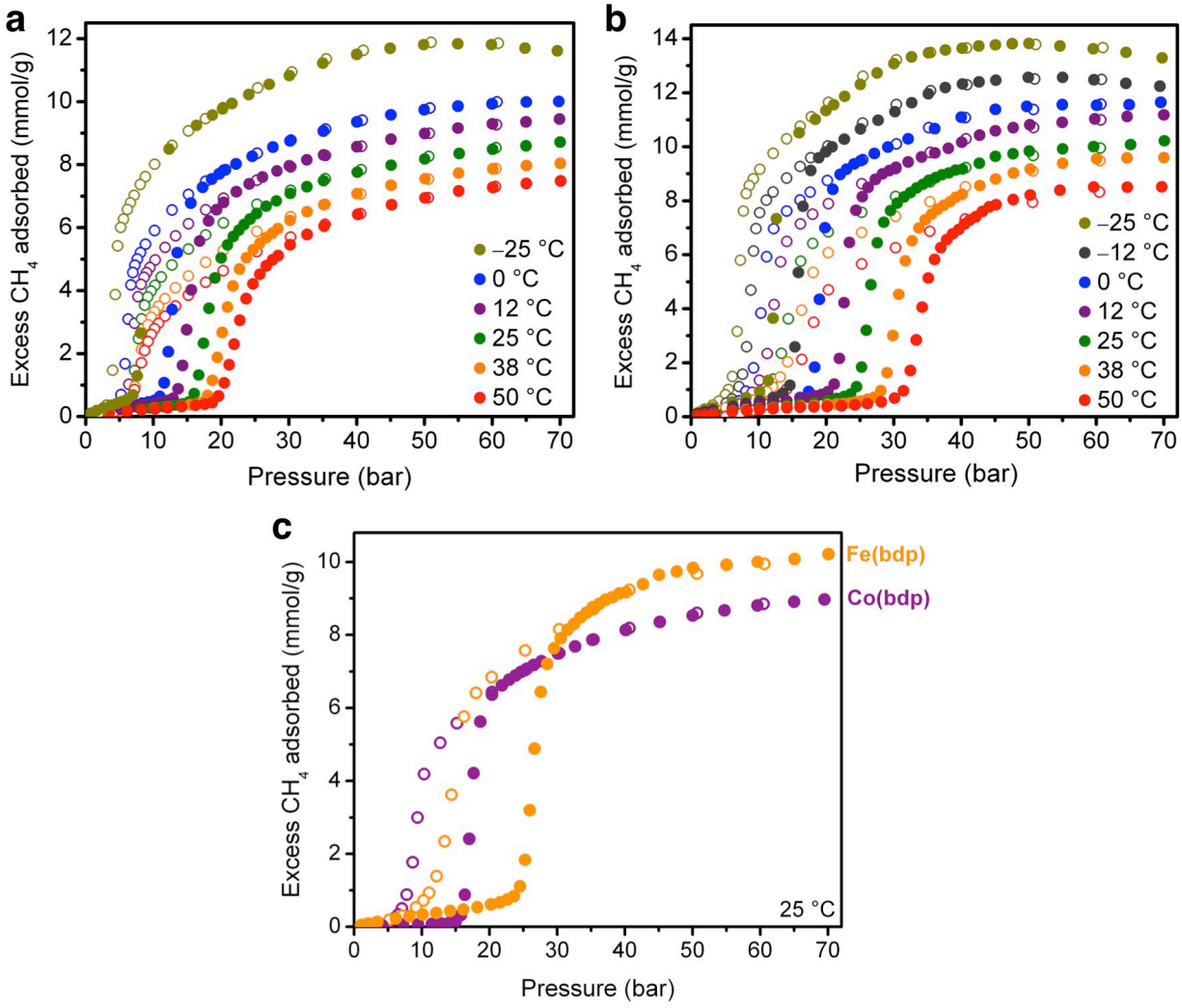

Figure 5.S3. **a,** Excess CH_4 adsorption isotherms at –25, 0, 12, 25, 38, and 50 °C for Co(bdp). **b,** Excess CH_4 adsorption isotherms at –25, –12, 0, 12, 25, 38, and 50 °C for Fe(bdp). **c,** Excess CH_4 adsorption isotherms at 25 °C compared for Co(bdp) (purple) and Fe(bdp) (orange). Filled and empty circles correspond to adsorption and desorption, respectively.

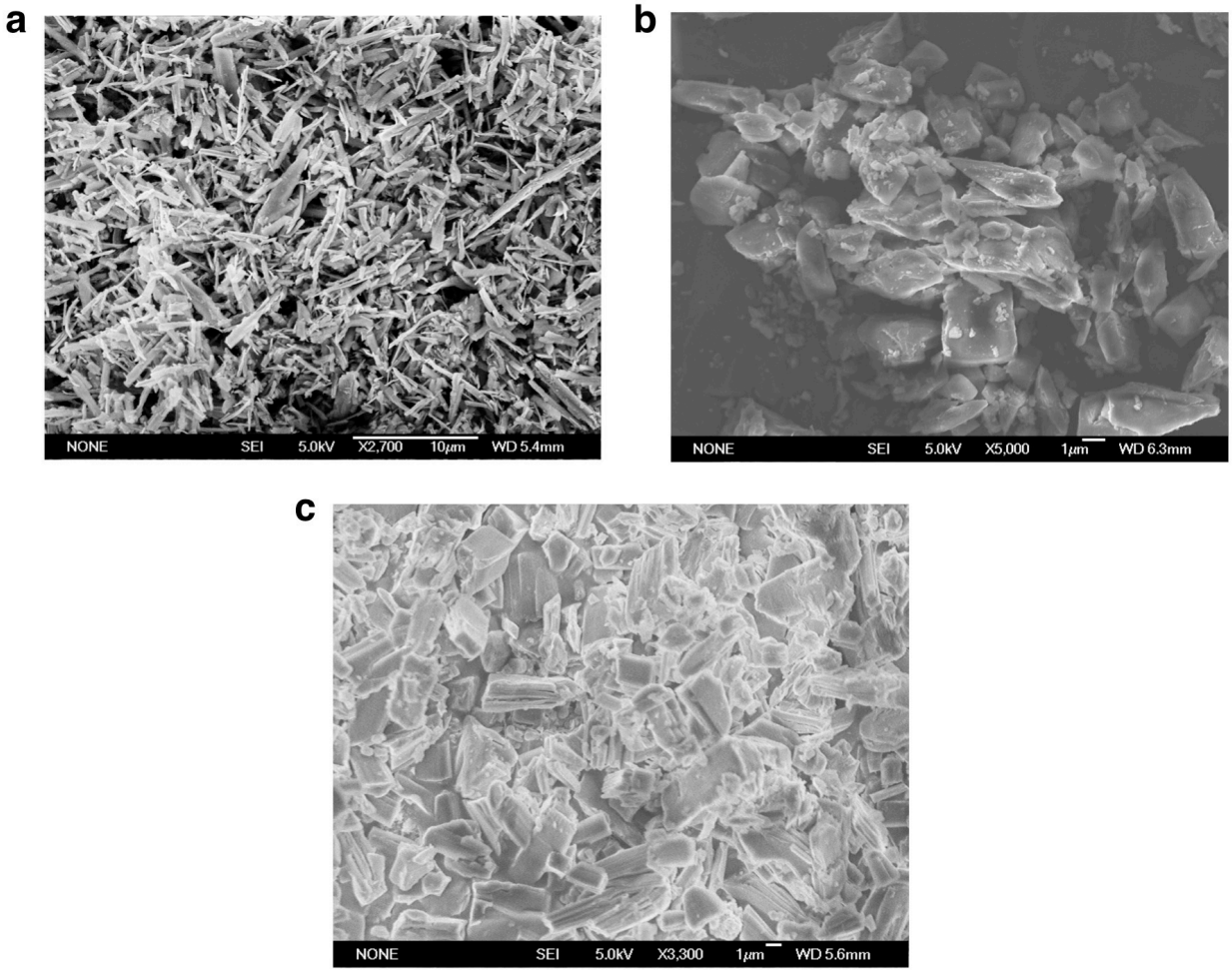

Figure 5.S4. **a,** Scanning electron microscope (SEM) image of DMF-solvated Co(bdp) microcrystalline powder. The scale-bar corresponds to a distance of 10 μm. **b,** SEM image of Co(bdp) microcrystalline powder after more than 100 CH_4 adsorption-desorption cycles. The scale-bar corresponds to a distance of 1 μm. **c,** SEM image of desolvated Fe(bdp) microcrystalline powder. The scale-bar corresponds to a distance of 1 μm.

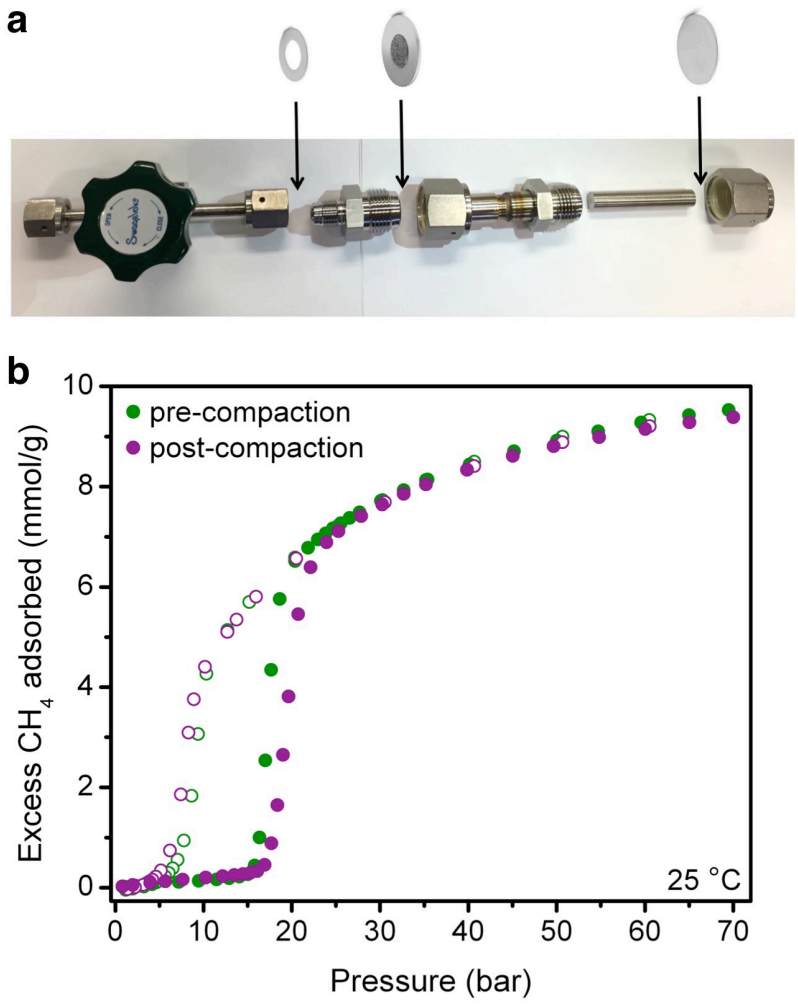

Figure 5.S5. **a,** Sample holder used for combined applied mechanical pressure and high-pressure CH_4 adsorption experiments. The sample is located in the volume to the right of the fritted gasket and to the left of the blank gasket. A press is used to compact metal rods of different lengths against the sample, and the blank gasket is sealed behind the rod so that the uniaxial applied mechanical pressure (and constricted volume) is maintained throughout the high-pressure CH_4 adsorption experiment. **b,** Excess CH_4 isotherms at 25 °C for Co(bdp) before (green) and after (purple) the applied mechanical pressure studies. Filled and empty circles correspond to adsorption and desorption, respectively.

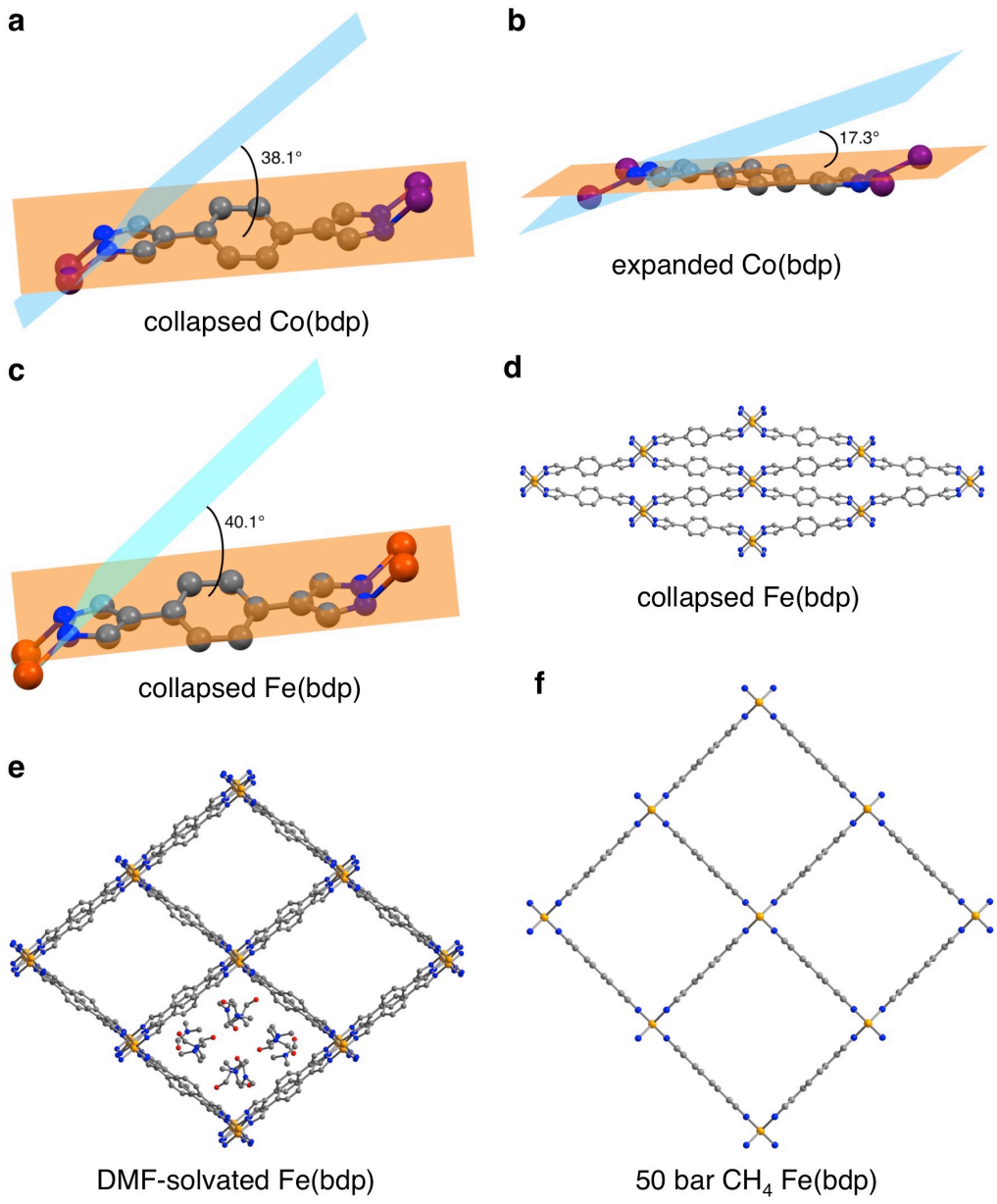

Figure 5.S6. **a,** The angle between the plane of the pyrazolate (light orange) and the Co–N–N–Co plane (light blue) is 38.1° in the collapsed phase of Co(bdp). **b,** The angle between the plane of the pyrazolate (light orange) and the Co–N–N–Co plane (light blue) is 17.3° in the CH_4 expanded phase of Co(bdp). **c,** The angle between the plane of the pyrazolate (light orange) and the Fe–N–N–Fe plane (light blue) is 40.1° in the collapsed phase of Fe(bdp). **d,** Structure of the collapsed phase of Fe(bdp) under vacuum at 25 °C. **e,** Structure of the DMF-solvated phase of Fe(bdp) at 100 K. **f,** Idealized average structure of the 50 bar of CH_4 expanded phase of Fe(bdp) at 25 °C. Gray, blue, red, purple, and orange spheres represent C, N, O, Co, and Fe atoms, respectively; H atoms are omitted for clarity.

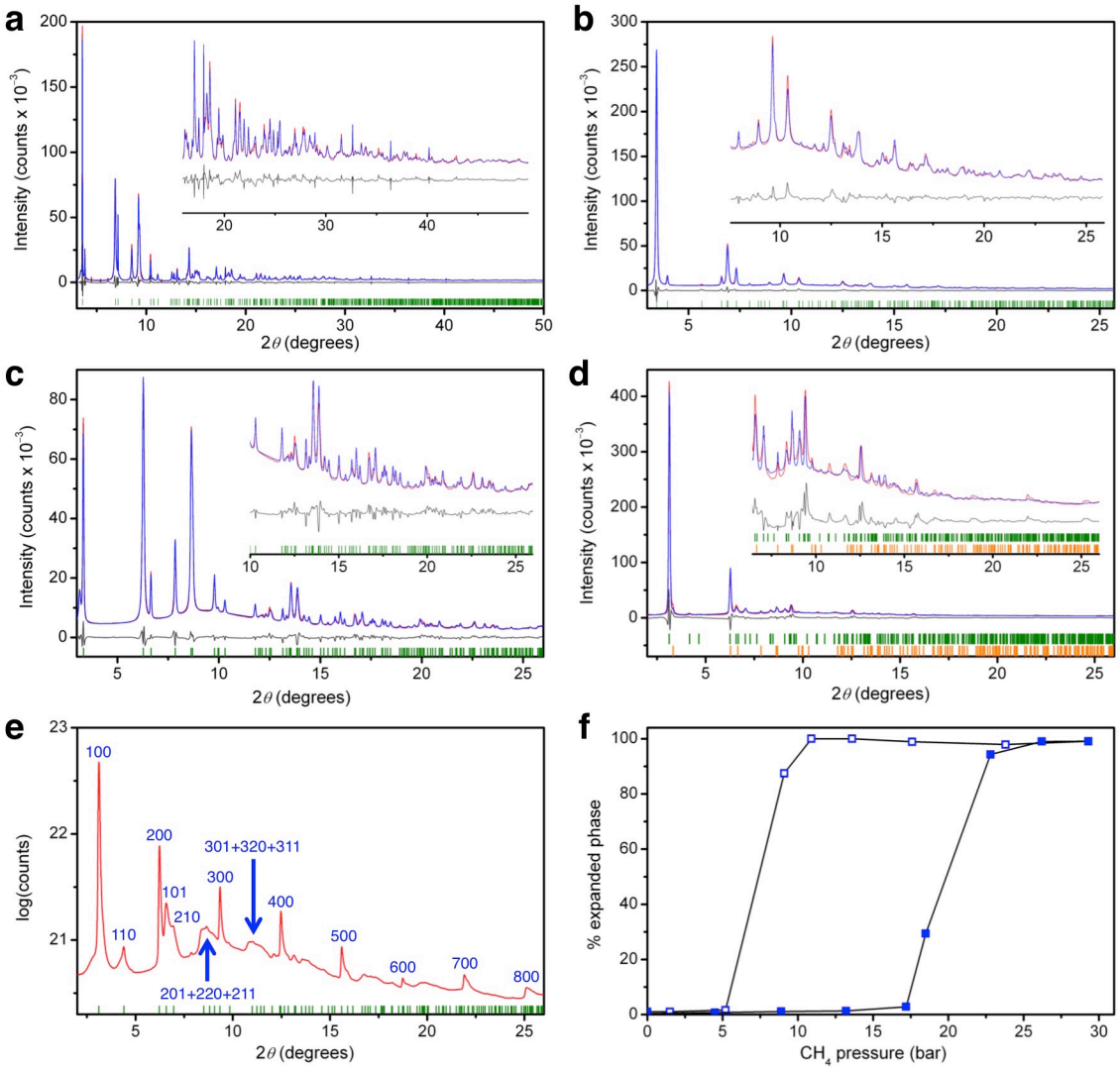

Figure 5.S7. **a-d,** Rietveld refinements for powder X-ray diffraction data for Co(bdp) under vacuum and 25 °C with λ = 0.77475 Å (**a**), for Co(bdp) at 30 bar of CH_4 and 25 °C with λ = 0.75009 Å (**b**), for Fe(bdp) under vacuum at 25 °C with λ = 0.72768 Å (**c**), and for Fe(bdp) at 40 bar of CH_4 and 25 °C with λ = 0.72768 Å (**d**). Red and blue lines represent the observed and calculated diffraction patterns, respectively. Gray lines represent the difference between observed and calculated patterns, and green tick marks indicate calculated Bragg peak positions. **e**, Powder X-ray diffraction data for Fe(bdp) at 50 bar of CH_4 and 25 °C (λ = 0.72768 Å). Green tick marks indicate Bragg angles for space group-permitted reflections, and the corresponding Miller indices are indicated for the most prominent peaks. Blue arrows indicate broad humps where multiple reflections overlap. **f,** The percentage of the expanded phase of Co(bdp) that is present in the variable pressure experimental powder X-ray diffraction patterns is plotted as a function of CH_4 pressure. The filled squares represent data collected during adsorption, while the empty squares represent data collected during desorption.

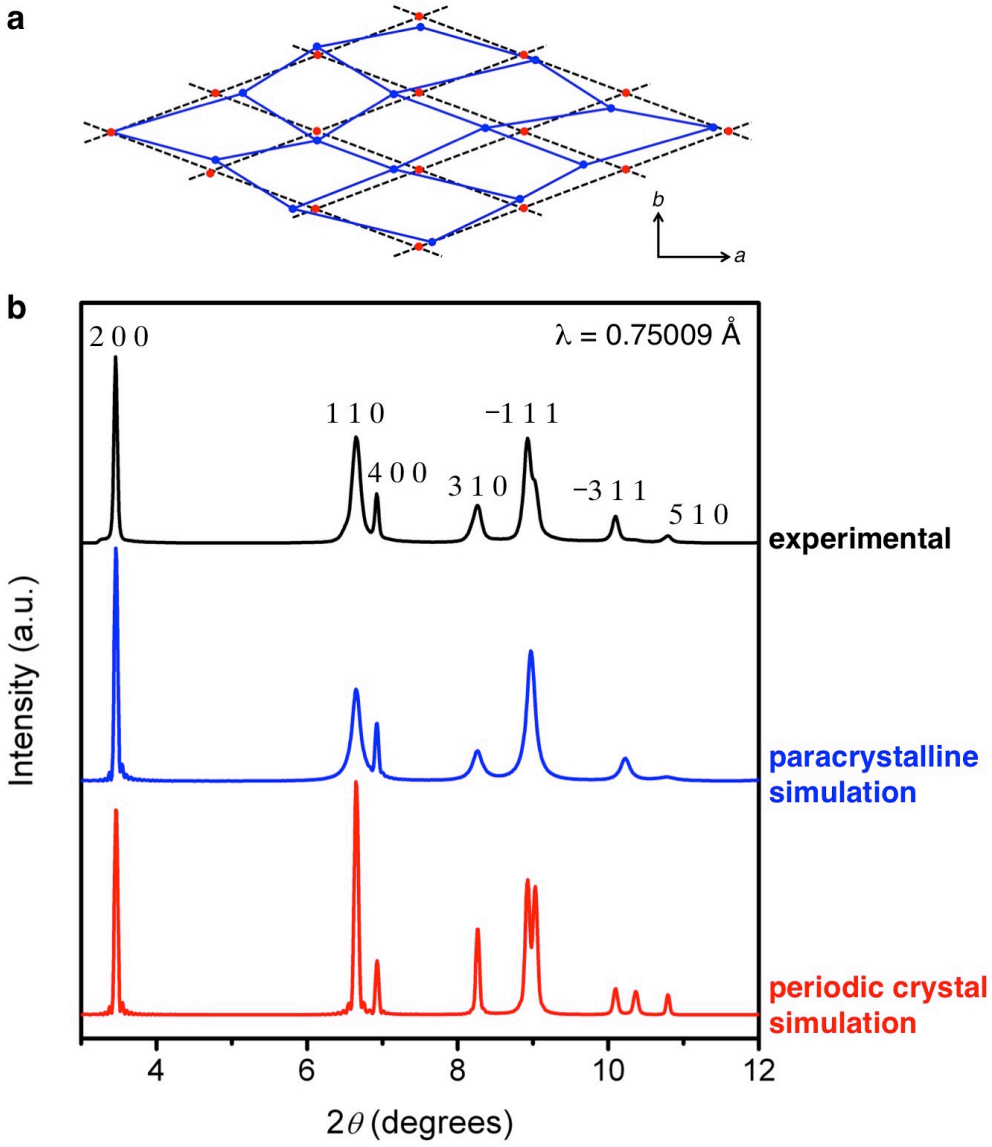

Figure 5.S8. **a,** An illustration of the paracrystalline distortion in the crystallographic *ab* plane of the collapsed phases of Co(bdp) and Fe(bdp) that leads to complex Bragg peak broadening. Black dashed lines represent the periodic crystal lattice, while the blue lines represent the paracrystal. Red circles represent the positions of metal-pyrazolate chains in the periodic lattice, while blue circles represent their positions in a paracrystal. Note that the magnitude of the paracrystalline distortion has been exaggerated for clarity. **b,** Simulated diffraction patterns are shown for a periodic collapsed Co(bdp) nanocrystal (75 nm x 60 nm x 43 nm; red trace) and for a paracrystal of equivalent size (blue trace). The upper trace (black) corresponds to the background-subtracted experimental diffraction pattern of the collapsed phase of Co(bdp) at 25 °C. For clarity, the three patterns have been given an arbitrary *y* offset. Very similar anisotropic peak broadening, which inflates *hk0* peaks (but not *h00* nor *0k0* ones), is clearly visible in the experimental diffraction pattern and the paracrystalline simulation.

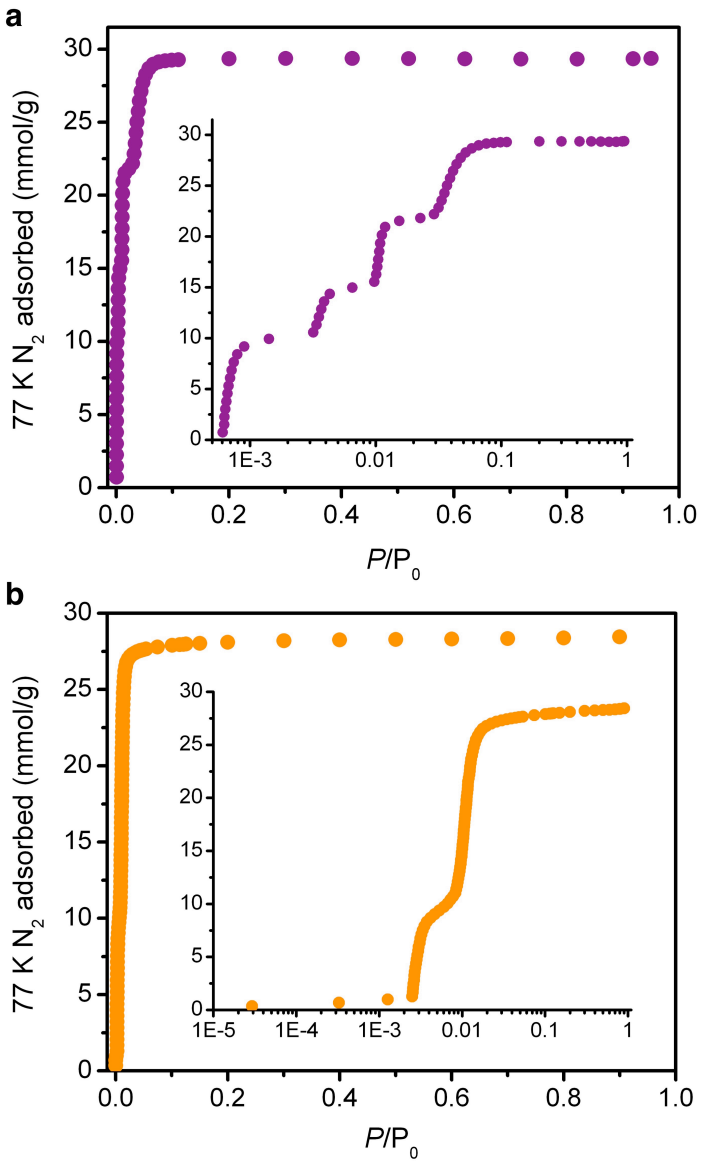

Figure 5.S9. **a,** 77 K N_2 adsorption isotherm for Co(bdp) activated at 160 ºC. The calculated Langmuir surface area is 2911±1 m^2/g (n_{sat} = 29.8 mmol/g), and the total pore volume is 1.02 cm^3/g (P/P_0 = 0.9). **b,** 77 K N_2 adsorption isotherm for Fe(bdp) activated at 170 ºC. The calculated Langmuir surface area is 2780±3 m^2/g (n_{sat} = 28.5 mmol/g), and the total pore volume is 0.987 cm^3/g (P/P_0 = 0.9). The insets show the isotherms with the x-axis (P/P_0, where P_0 is the saturation pressure of N_2) plotted on a logarithmic scale.

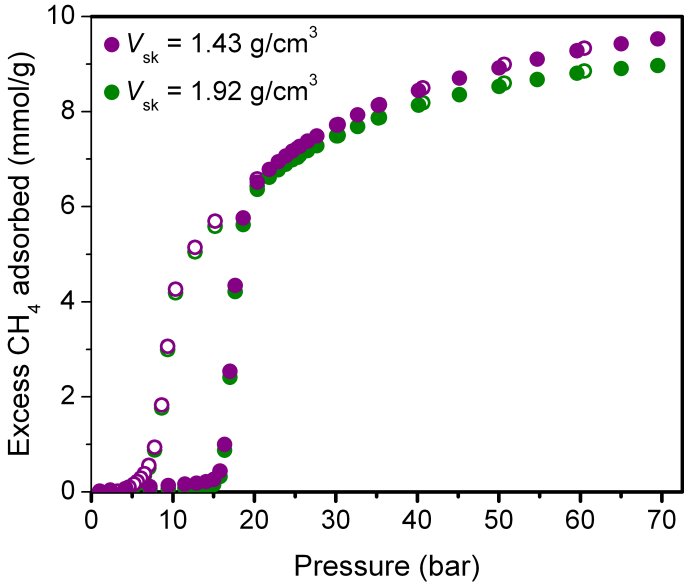

Figure 5.S10. Excess CH_4 isotherms for Co(bdp) at 25 °C where the experimental freespace has been calculated using the experimentally measured skeletal density (purple, 1.43 g/cm^3) and using the expected skeletal density of the pure expanded phase (green, 1.92 g/cm^3). Filled and empty circles correspond to adsorption and desorption, respectively.

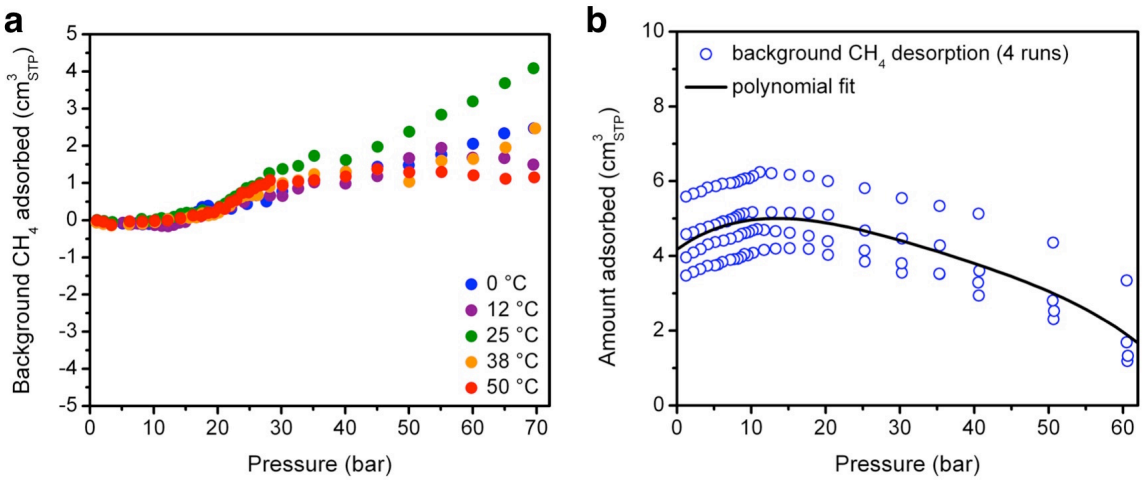

Figure 5.S11. **a,** Background CH_4 adsorption isotherms at 0, 12, 25, 38, and 50 °C for four separate experiments on a sample holder containing glass beads, demonstrating that all background adsorption is less than ±4 cm^3_{STP} (0.2 mmol/g) at 70 bar. At 35 bar and below, the background is less than ±2 cm^3_{STP} (0.1 mmol/g). Here, STP is defined as 273.15 K and 1 atm, resulting in a volume of 22.414 mL for 1 mmol of ideal gas at STP. **b,** Background CH_4 desorption isotherms at 25 °C for four separate experiments on a sample holder containing glass beads. The 4th order polynomial fit used to correct all desorption data in this work reported here is shown as a black line.

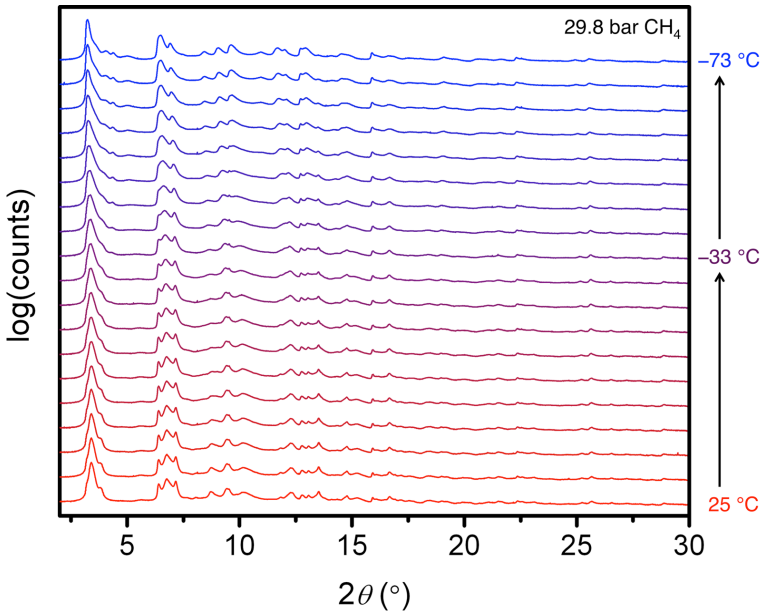

Figure 5.S12. Variable temperature X-ray diffraction patterns collected at APS while cooling Co(bdp) from 25 °C (red) to –73 °C (blue) at a constant CH_4 pressure of 29.8 bar ($\lambda = 0.72959$ Å). Note that there are no changes to the diffraction patterns until below −33 °C, demonstrating that the expanded phase of Co(bdp) does not change as more CH_4 is adsorbed during initial cooling. Below –33 °C, there is likely a 2nd phase transition to a more expanded framework, which is not relevant to the CH_4 storage results presented in this work.

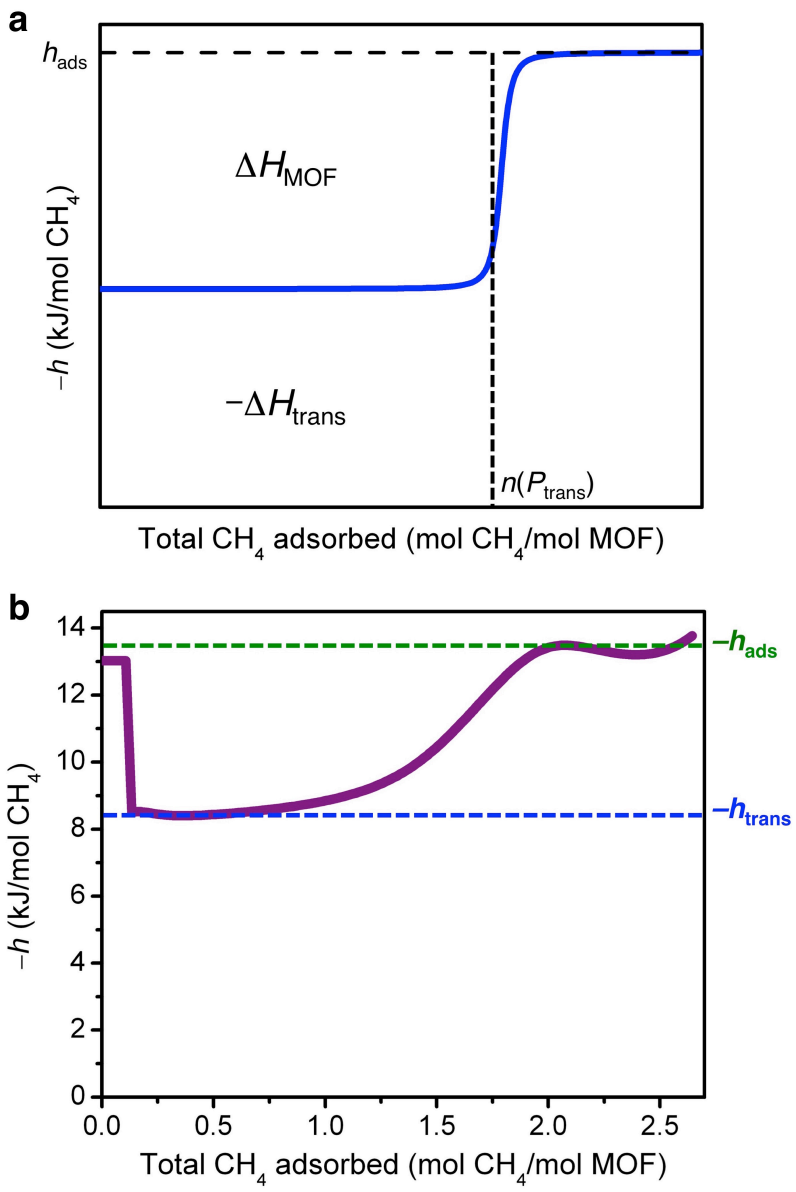

Figure 5.S13. **a,** Idealized differential enthalpy, h, curve that would be expected for CH_4 adsorption in a monodisperse sample of Co(bdp) or Fe(bdp) exhibiting a perfectly vertical phase transition. **b,** Experimental differential enthalpy, h, curve for CH_4 adsorption in Co(bdp) (purple line). The differential enthalpy of CH_4 during the phase transition, $-h_{trans}$, is shown as a dashed blue line. The differential enthalpy of CH_4 adsorption in the expanded phase, $-h_{ads}$, is shown as a green dashed line. Note that h_{ads} is determined from the single-site Langmuir fit.

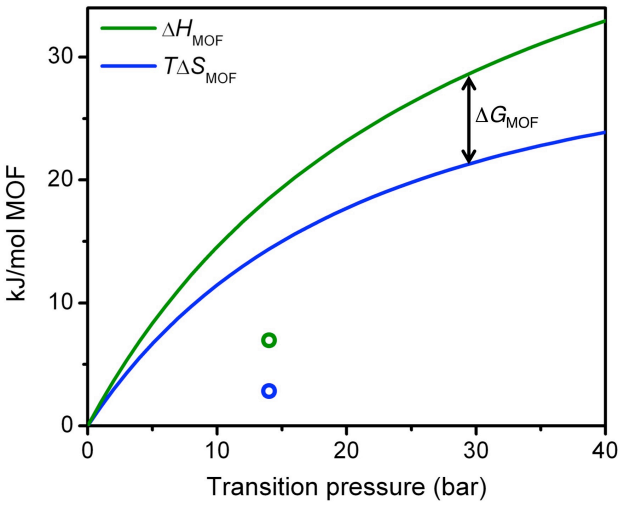

Figure 5.S14. The combinations of ΔH_{MOF} and $T\Delta S_{MOF}$ at different transition pressures that would lead to zero overall enthalpy change during the phase transition at 25 °C are shown as green and blue lines, respectively, while the values of ΔH_{MOF} and $T\Delta S_{MOF}$ for Co(bdp) are shown as empty green and blue circles, respectively. Note that these calculations assume constant single-site Langmuir parameters for adsorption in the expanded Co(bdp) phase.

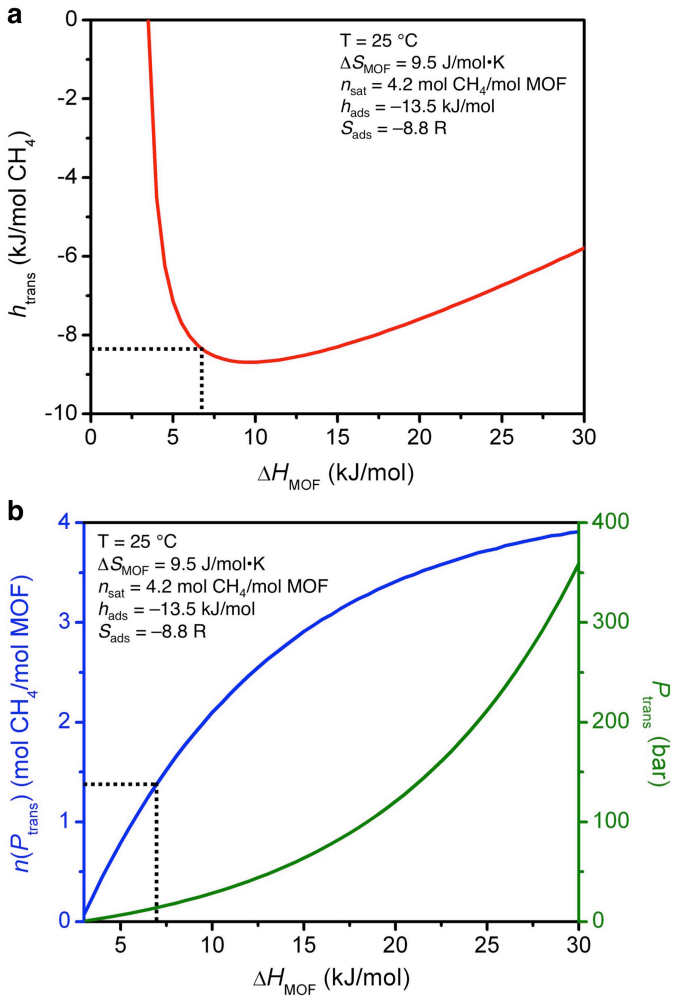

Figure 5.S15. **a,** The expected differential enthalpy for phase transitions, h_{trans}, at 25 °C is plotted for a range of hypothetical enthalpy differences between the collapsed and expanded phases, ΔH_{MOF}, assuming a constant ΔS_{MOF} and constant single-site Langmuir parameters for adsorption in the expanded phase. The experimentally determined combination of h_{trans} and ΔH_{MOF} for Co(bdp) is indicated by the dashed black lines. **b,** The expected transition pressure, P_{trans}, and amount of CH_4 adsorbed during the phase transition, $n(P_{trans})$, is plotted as green and blue lines, respectively, for a range of hypothetical enthalpy differences between the collapsed and expanded phases, ΔH_{MOF}, assuming a constant ΔS_{MOF} and constant single-site Langmuir parameters for adsorption in the expanded phase. In the absence of changes in ΔS_{MOF}, increases in ΔH_{MOF} will lead to significant increases in P_{trans}. The values for Co(bdp) are indicated by the dashed black lines.

Table 5.S1. Summary of the total volumetric usable CH_4 capacity (cm^3_{STP}/cm^3) calculations at 25 °C for Co(bdp), Fe(bdp), and a selection of the best previously reported metal-organic frameworks. The minimum desorption pressure is 5.8 bar.

	5.8 bar total (v/v)	35 bar total (v/v)	65 bar total (v/v)	35 bar usable (v/v)	65 bar usable (v/v)	Ref.
Co(bdp)	4	161	203	157	199	this work
Fe(bdp)	4	156	196	152	192	this work
HKUST-1	81	224	262	143	181	ref. 8
UTSA-76a	68	211	257	143	189	ref. 23
MOF-5	30	149	215	119	185	ref. 8
MOF-519	55*	200*	260*	145*	205*	ref. 43

*The volumetric capacities reported for MOF-519 are expected to be artificially inflated by a significant amount because the crystallographic density used for the framework was likely far too high. The true usable capacities for MOF-519 are thus expected to be much lower than originally reported.

Table 5.S2. Summary of the total volumetric usable CH_4 capacity (cm^3_{STP}/cm^3) calculations for adsorption at 25 °C and desorption at 0 °C for Co(bdp), Fe(bdp), HKUST-1, and MOF-5. The minimum desorption pressure is 5.8 bar.

	5.8 bar total (v/v)	35 bar total (v/v)	65 bar total (v/v)	35 bar usable (v/v)	65 bar usable (v/v)	Ref.
Fe(bdp)	6	156	196	150	190	this work
Co(bdp)	30	161	203	131	173	this work
HKUST-1	125	224	262	99	137	ref. 8
MOF-5	52	149	215	97	163	ref. 8

Table 5.S3. Summary of the total volumetric usable CH_4 capacity (cm^3_{STP}/cm^3) calculations for adsorption at 25 °C and desorption at –25 °C for Co(bdp), Fe(bdp), HKUST-1, and MOF-5. The minimum desorption pressure is 5.8 bar.

	5.8 bar total (v/v)	35 bar total (v/v)	65 bar total (v/v)	35 bar usable (v/v)	65 bar usable (v/v)	Ref.
Fe(bdp)	20	156	196	136	176	this work
Co(bdp)	113	161	203	48	90	this work
HKUST-1	189	224	262	35	73	ref. 8
MOF-5	69	149	215	80	146	ref. 8

Table 5.S4. Summary of the total gravimetric usable CH_4 capacity (mmol/g) calculations at 25 °C for Co(bdp), Fe(bdp), and a selection of the best previously reported metal-organic frameworks. The minimum desorption pressure is 5.8 bar.

	5.8 bar total (mmol/g)	35 bar total (mmol/g)	65 bar total (mmol/g)	35 bar usable (mmol/g)	65 bar usable (mmol/g)	Ref.
Co(bdp)	0.3	9.0	11.2	8.7	10.9	this work
Fe(bdp)	0.2	9.9	12.9	9.7	12.7	this work
HKUST-1	4.1	11.3	13.3	7.2	9.2	ref. 8
UTSA-76a	4.3	13.5	16.4	9.2	12.1	ref. 23
MOF-5	2.2	10.7	15.4	8.5	13.2	ref. 8
MOF-519	2.6	9.4	12.2	6.8	9.6	ref. 43

Table 5.S5. Single-site Langmuir parameters (Eqn 2.8) for CH_4 adsorption in the expanded phases of Co(bdp) and Fe(bdp).

	Co(bdp)	Fe(bdp)
n_{sat} (mol CH_4 per mol MOF)	4.23	4.97
h_{ads} (kJ per mol CH_4)	–13.5	–12.7
S_{ads} (R)	–8.8	–8.6

Table 5.S6. Single-site Langmuir parameters (Eqn 2.18) for CH_4 adsorption in the pre-step region of Co(bdp) and Fe(bdp) isotherms.

	Co(bdp)	Fe(bdp)
n_{sat} (mmol g^{-1})	1.79	25
h_{ads} (kJ per mol CH_4)	–13.0	–11.9
S_{ads} (R)	–9	–11.4

Table 5.S7. Offset dual-site Langmuir-Freundlich parameters (Eqn 2.18) for CH_4 adsorption in Co(bdp).

	0 °C	12 °C	25 °C	38 °C	50 °C
$n_{sat,1}$ (mmol g^{-1})	5.3	5.1	4.3	3.7	3.2
b_1 ($bar^{-\nu_1}$)	0.014	0.0046	0.0067	0.0016	0.00032
ν_1	4.6	4.5	3.9	4.4	4.9
$n_{sat,2}$ (mmol g^{-1})	22.8	17.8	12.2	10.1	9.2
b_2 ($bar^{-\nu_2}$)	0.041	0.036	0.042	0.037	0.030
ν_2	0.61	0.71	0.84	0.99	1.1
P_{trans} (bar)	10.4	12.1	14.5	16.1	17.2

Table 5.S8. Offset dual-site Langmuir-Freundlich parameters (Eqn 2.18) for CH_4 adsorption in Fe(bdp).

	0 °C	12 °C	25 °C	38 °C	50 °C
$n_{sat,1}$ (mmol g^{-1})	7.5	6.9	5.7	5.5	4.2
b_1 ($bar^{-\nu_1}$)	0.0024	$5.3x10^{-5}$	$2.3x10^{-4}$	$2.8x10^{-4}$	$2.8x10^{-5}$
ν_1	5.9	7.2	6.2	5.4	6.3
$n_{sat,2}$ (mmol g^{-1})	22.5	18.7	7.9	9.7	7.2
b_2 ($bar^{-\nu_2}$)	0.040	0.040	0.085	0.052	0.037
ν_2	0.60	0.69	1.0	0.99	1.5
P_{trans} (bar)	16.4	18.9	22.6	26.0	28.7

Table 5.S9. Summary of thermodynamic parameters for the phase transition in Co(bdp).

T	25 °C
n_{tot}	1.9 mol CH_4 per mol MOF
ΔH_{tot}	–18.2 kJ/mol MOF
h_{trans}	–8.4 kJ/mol CH_4
n_{trans}	1.37 mol CH_4 per mol MOF
P_{trans}	14.0 bar
$\Omega(P_{trans})$	–4.1 kJ/mol MOF
ΔH_{MOF}	7.0 kJ/mol MOF
ΔS_{MOF}	9.5 J/mol·K
ΔG_{MOF}	4.1 kJ/mol MOF
$T\Delta S_{MOF}$	2.8 kJ/mol MOF

Table 5.S10. Summary of thermodynamic parameters for the phase transition in Fe(bdp).

T	25 °C
n_{tot}	2.5 mol CH_4 per mol MOF
ΔH_{tot}	–23.3 kJ/mol MOF
h_{trans}	–8.5 kJ/mol CH_4
n_{trans}	1.92 mol CH_4 per mol MOF
P_{trans}	20.2 bar
$\Omega(P_{trans})$	–6.0 kJ/mol MOF
ΔH_{MOF}	8.1 kJ/mol MOF
ΔS_{MOF}	6.9 J/mol·K
ΔG_{MOF}	6.0 kJ/mol MOF
$T\Delta S_{MOF}$	2.0 kJ/mol MOF

Table 5.S11. Summary of the amount of heat released in kJ per L MOF during CH_4 adsorption from 5.8 to 35 or 65 bar in Co(bdp), Fe(bdp), and HKUST-1. The values in parentheses are the average differential enthalpy of CH_4 adsorption in kJ per mol CH_4.

	35 bar adsorption	65 bar adsorption
Co(bdp)	73.4 (10.5)	90.4 (11.0)
Fe(bdp)	64.3 (9.5)	87.1 (10.2)
HKUST-1	109 (17.1)	138 (17.1)

Table 5.S12. Excess and total CH_4 adsorption data for Co(bdp) at 25 °C.

Excess Adsorption		Total Adsorption		
Pressure (bar)	CH_4 adsorbed (mmol/g)	Pressure (bar)	CH_4 adsorbed (mmol/g)	CH_4 adsorbed (cm^3_{STP}/cm^3)
1.0	0.0	1.0	0.0	0
2.3	0.0	2.3	0.0	1
4.2	0.0	4.2	0.1	1
7.2	0.1	7.2	0.1	2
9.5	0.1	9.5	0.1	2
11.5	0.1	11.5	0.2	3
12.9	0.1	12.9	0.2	3
14.1	0.1	14.1	0.2	4
15.0	0.2	15.0	0.3	5
15.8	0.3	15.8	0.5	8
16.4	0.9	16.4	1.1	19
17.0	2.4	17.0	2.8	48
17.7	4.2	17.7	4.7	82
18.6	5.6	18.6	6.3	109
20.4	6.4	20.4	7.2	124
21.8	6.6	21.8	7.5	130
22.9	6.8	22.9	7.7	133
23.8	6.9	23.8	7.8	136
24.7	7.0	24.7	8.0	138
25.6	7.1	25.6	8.1	141
26.5	7.2	26.5	8.2	143
27.7	7.3	27.7	8.4	146
30.2	7.5	30.2	8.7	151
30.1	7.5	30.1	8.7	151
32.7	7.7	32.7	9.0	156
35.2	7.9	35.2	9.3	161
40.1	8.1	40.1	9.8	170
45.2	8.4	45.2	10.2	177
50.0	8.5	50.0	10.6	184
54.7	8.7	54.7	11.0	190
59.6	8.8	59.6	11.3	197
65.0	8.9	65.0	11.7	203

69.5	9.0	69.5	12.0	208
60.5	8.9	60.5	11.4	198
50.7	8.6	50.7	10.7	186
40.7	8.2	40.7	9.9	171
35.4	7.9	35.4	9.3	162
30.3	7.5	30.3	8.7	151
25.3	7.0	25.3	8.0	140
20.4	6.4	20.4	7.2	126
15.2	5.6	15.2	6.1	106
12.7	5.0	12.7	5.5	95
10.3	4.2	10.3	4.5	78
9.4	3.0	9.4	3.2	56
8.6	1.8	8.6	1.9	33
7.8	0.9	7.8	1.0	17
7.1	0.5	7.1	0.6	10
6.5	0.3	6.5	0.4	7
6.1	0.2	6.1	0.3	5
5.7	0.2	5.7	0.2	4
5.3	0.1	5.3	0.2	3
4.6	0.1	4.6	0.1	2
4.2	0.0	4.2	0.1	1
3.2	0.0	3.2	0.0	0
2.0	0.0	2.0	0.0	0

Table 5.S13. Excess and total CH_4 adsorption data for Fe(bdp) at 25 °C.

Excess Adsorption		Total Adsorption		
Pressure (bar)	CH_4 adsorbed (mmol/g)	Pressure (bar)	CH_4 adsorbed (mmol/g)	CH_4 adsorbed (cm^3_{STP}/cm^3)
1.0	0.1	1.0	0.1	1
2.1	0.1	2.1	0.1	1
3.5	0.1	3.5	0.1	2
6.2	0.2	6.2	0.2	4
8.1	0.3	8.1	0.3	5
10.1	0.3	10.1	0.4	6
12.1	0.4	12.1	0.4	6
14.2	0.4	14.2	0.5	7
16.2	0.5	16.2	0.5	8
18.2	0.5	18.2	0.6	9
20.2	0.6	20.2	0.7	11
21.6	0.7	21.6	0.7	12
22.7	0.7	22.7	0.8	13
23.6	0.8	23.6	0.9	15
24.5	1.1	24.5	1.2	19
25.3	1.8	25.3	2.0	32
25.9	3.2	25.9	3.6	56

26.6	4.9	26.6	5.4	86
27.6	6.4	27.6	7.2	114
28.5	7.2	28.5	8.1	128
29.5	7.6	29.5	8.6	136
30.5	7.9	30.5	8.9	141
31.5	8.1	31.5	9.2	145
32.5	8.3	32.5	9.4	148
33.4	8.5	33.4	9.6	151
34.3	8.6	34.3	9.7	154
35.2	8.8	35.2	9.9	157
36.2	8.9	36.2	10.0	159
37.2	9.0	37.2	10.2	161
38.2	9.0	38.2	10.3	163
39.2	9.1	39.2	10.4	165
40.2	9.2	40.2	10.5	166
42.7	9.4	42.7	10.8	171
45.1	9.6	45.1	11.5	175
47.7	9.7	47.7	11.7	178
50.1	9.8	50.1	11.9	181
55.0	9.9	55.0	12.3	186
59.6	10.0	59.6	12.6	191
65.1	10.1	65.1	12.9	196
70.1	10.2	70.1	13.3	202
60.6	9.9	60.6	12.5	191
50.7	9.7	50.7	11.8	179
40.7	9.2	40.7	10.6	167
35.4	8.7	35.4	9.9	156
30.3	8.2	30.3	9.1	145
25.3	7.6	25.3	8.4	133
20.3	6.8	20.3	7.4	117
18.0	6.4	18.0	6.9	109
16.3	5.8	16.3	6.2	97
14.4	3.6	14.4	3.8	61
13.4	2.3	13.4	2.5	39
12.2	1.4	12.2	1.5	23
11.1	0.9	11.1	1.0	15
10.2	0.7	10.2	0.8	12
9.2	0.5	9.2	0.6	9
7.1	0.3	7.1	0.3	5
5.2	0.2	5.2	0.2	3
3.2	0.1	3.2	0.1	2
1.4	0.1	1.4	0.1	1

Table 5.S14. Crystallographic data for X-ray powder diffraction structures.

	Co(bdp)	Co(bdp)	Fe(bdp)	Fe(bdp)	Fe(bdp)
CH_4 pressure (bar)	0	30	0	40	50
Temperature (°C)	25	25	25	25	25
Crystal system	Monoclinic	Monoclinic	Monoclinic	Monoclinic	Tetragonal
Space group	*C* 2/*c*	*C* 2/*c*	*C* 2/*c*	*C* 2/*c*	$P4_2/mmc$
a (Å)	24.8274(6)	21.763(2)	25.086(2)	20.15(3)	13.41
b (Å)	6.6747(4)	15.220(2)	6.8878(3)	17.91(2)	= a
c (Å)	7.1456(3)	6.9827(7)	6.9845(5)	6.953(4)	7.20
β (Å)	92.550(2)	97.37(1)	91.653(6)	97.34(6)	90.0
V (Å^3)	1182.97(9)	2293.8(5)	1206.4(1)	2489(5)	1295
Z	4	4	4	4	2
λ (Å)	0.77475	0.75009	0.72768	0.72768	0.72768

Table 5.S15. Crystallographic data for single crystal X-ray diffraction structures of DMF-solvated Fe(bdp).

	Fe(bdp) 100 K	Fe(bdp) 298 K
Formula	$C_{21}H_{29}FeN_7O_3$	$C_{12}H_8FeN_4$
Crystal System	Monoclinic	Orthorhombic
Space Group	*P2₁/c*	*C222₁*
a, b, c (Å)	13.4333(4), 13.8493(4), 26.7477(9)	17.3648(10), 20.4338(11), 14.0029(8)
α, β, γ (°)	90, 101.5505(18), 90	90
V, (Å^3)	4875.4(3)	4968.6(5)
Z	8	8
Radiation, λ (Å)	Synchrotron, 0.7749	Synchrotron, 0.7749
R1[a], wR2[b] (I>2σ(I))	0.0670, 0.1547	0.0468, 0.1250
R1[a], wR2[b] (all data)	0.0874, 0.1645	0.0558, 0.1308

[a] $R_1 = \sum||F_o| - |F_c||/\sum|F_o|$. [b] $wR_2 = \{\sum[w(F_o^2 - F_c^2)^2]/\sum[w(F_o^2)^2]\}^{1/2}$.

Chapter 6: Synthesis and O_2 Reactivity of a Titanium(III) Metal-Organic Framework

6.1. Introduction

Metal-organic frameworks that feature both high surface areas and high densities of coordinatively unsaturated metal centers have shown promise as a new class of adsorbents for storing and separating gases.[1] When constrained by the framework to an appropriate geometry, low-coordinate metal cations can function as exposed positive charges on the pore surface that strongly polarize specific gas molecules, leading to increased uptake and highly selective adsorption.[2] In the context of hydrogen storage for mobile applications, metal-organic frameworks with exposed divalent metal cations have demonstrated some of the highest H_2 storage densities to date as a direct result of strong M^{2+}–H_2 interactions.[3,4] While the strength of these interactions, which is typically in the range of –10 to –13 kJ/mol, is ideal for low-temperature storage applications, it is too weak for storage at ambient temperature. Frameworks with stronger adsorption sites are therefore required to achieve the higher H_2 capacities at ambient temperature that would allow for a commercially viable H_2 storage system.[5]

The affinity of exposed metal cations for H_2 can be increased by increasing the charge density at the metal center.[3k,m] Synthesizing metal-organic frameworks with exposed trivalent or tetravalent cations thus represents a promising path to reaching the –15 to –20 kJ/mol binding enthalpies that are optimal for ambient temperature H_2 storage.[6,7] While many families of metal-organic frameworks have been synthesized with exposed divalent metal cations, there are comparatively few examples of frameworks with exposed trivalent metal cations.[3k,8,9] In several analogues of the $M_3OX(bdc)_3$ (M-MIL-101; bdc^{2-} = 1,4-benzenedicarboxylate; X = F, Cl, OH; M = Cr,[10] Fe,[11] V,[12] Al[13]) and $M_3OX(btc)_2$ (M-MIL-100; btc^{3-} = 1,3,5-benzenetricarboxylate; M = Cr,[14] Fe,[15] V,[12b] Al,[16] Sc[17]) series of frameworks, however, metal-bound solvent molecules can be partially, or in some cases fully, removed by heating under vacuum to generate five-coordinate metal(III) cations.[8,9] The M-MIL-101 and M-MIL-100 compounds are composed of trimeric $M_3O(COO)_6$ clusters whereby each metal is octahedrally coordinated and bound to bridging carboxylates in the equatorial positions, a μ_3-O in one axial position, and either a solvent molecule or a charge-balancing anion in the other axial position. While exposed Cr^{III} sites in Cr-MIL-100 have led to CO_2 binding enthalpies exceeding –60 kJ/mol,[18] none of these frameworks have displayed the strong H_2 binding that might be expected for a material with a high density of exposed M^{III} centers.[19] We note there is preliminary evidence from infrared spectroscopy for strong M^{III}–H_2 interactions in Sc-MIL-100, but this has not been confirmed by adsorption measurements.[20] Nonetheless, these frameworks represent a promising platform for studying H_2 adsorption on exposed metal(III) cations.

Although there is a significant interest in developing new titanium-based metal-organic frameworks, titanium-analogues of MIL-100 and MIL-101 have not yet been realized. In addition to the potential for characterizing the H_2 adsorption properties of five-coordinate Ti^{III} centers, new titanium-based porous materials are of general interest because titanium has a low toxicity, high abundance, and potentially useful redox and photocatalytic properties. In spite of the over 20,000 metal-organic frameworks that have been reported,[21] there are currently just five examples of Ti-based frameworks that demonstrate permanent porosity: $Ti_8O_8(OH)_4(bdc)_6$ (MIL-125),[22] $Ti_8O_8(OH)_4(NH_2\text{-}bdc)_6$ (MIL-125-NH_2),[23] and $Ti_7O_4(OH)_2$(tetrakis(4-carboxyphenyl)porphyrin)$_3$ (PCN-22),[24] which contain all Ti^{IV} cations, and

$Ti_{3.2}Zr_{2.8}O_4(OH)_4(bdc)_6$ (Ti^{IV}-UiO-66)[25] and $Zn_{3.91}Ti_{0.09}O(bdc)_3$ (Ti^{III}-MOF-5),[26] which are synthesized by partial post-synthetic metal exchange of Zr and Zn, respectively, in the parent frameworks. Noting that Ti^{III}-MOF-5 contains just 2% Ti and 98% Zn, there are, to the best of our knowledge, not any examples of all Ti^{III} porous frameworks. Additionally, despite the extensive literature on carboxylate-bridged Ti-oxo clusters,[27] there are surprisingly no reports of a Ti analogue of the $M_3O(COO)_6$ cluster. Herein, we report the synthesis and characterization of the titanium(III) analogue of MIL-101: $Ti_3O(OEt)(bdc)_3(solv)_2$ (**1**; solv = DMF, THF).

6.2. Experimental

6.2.1. General Information. All reactions and subsequent manipulations were performed under anaerobic and anhydrous conditions in a nitrogen-atmosphere glovebox or on a nitrogen-atmosphere Schlenk line. *N*,*N*-dimethylformamide (DMF) and tetrahydrofuran (THF) were dried by passage over activated molecular sieves using a JC Meyer solvent system. Anhydrous ethanol (EtOH; 99.5%) was purchased from Sigma Aldrich and used as received. All other reagents were obtained from commercial vendors and used without further purification. Ultra-high purity grade (99.999% purity) He, N_2, O_2 and H_2, research grade CO (99.99% purity) and CO_2 (99.998% purity) were used for all adsorption measurements.Infrared spectra were obtained on a Perkin-Elmer Spectrum 100 Optica FTIR spectrometer furnished with an attenuated total reflectance accessory. The instrument was placed inside an N_2-filled glove bag for air-sensitive samples. Elemental analyses for C, H, N, and Cl were performed at Galbraith Laboratories.

6.2.2. Synthesis of $Ti_3O(OEt)(bdc)_3(DMF)_x$ (1). In a glovebox under a dinitrogen atmosphere, a 500 mL Schlenk flask was charged with 1,4-benzenedicarboxylic acid (H_2bdc; 0.675 g, 4.06 mmol), $TiCl_3$ (0.769 g, 4.99 mmol), and a small stir bar, then sealed with a rubber septum. The flask was transferred to a Schlenk line, and 300 mL of anhydrous DMF and 30 mL of anhydrous ethanol (EtOH) were added via cannula transfer. The solution was heated at 120 °C under a positive N_2 pressure with stirring for 18 h. After cooling, the resulting dark purple precipitate (**1**) was recovered by vacuum filtration inside a glovebox under a dinitrogen atmosphere, washed with 450 mL of anhydrous DMF, and dried under vacuum at 75 °C.

Two different methods were investigated for activating **1**. First, the solid powder was directly heated to 150 °C under vacuum for 12 h. Second, 100 mg of the compound and 8 mL of anhydrous THF were loaded in a 10 mL stainless steel reaction vessel that was capped with a ¼" Swagelok fitting. The vessel was heated to 120 °C for 24 h, then the THF was decanted and replaced with fresh THF. This THF exchange was repeated two additional times. The THF was then evaporated under reduced pressure, and the dark purple solid was activated by heating at 150 °C under vacuum for 12 h. As evidenced by the nearly complete disappearance of the infrared band at 1668 cm^{-1} (Figure 6.S19), most titanium-bound DMF molecules were successfully exchanged for THF. Note that attempts to exchange metal-bound DMF for methanol (MeOH) or EtOH instead of THF resulted in framework decomposition after several washes.

6.2.3. NMR Digestion Experiments. To determine the identity and amount of bound solvent and charge-balancing anions, NMR digestion experiments were performed for the DMF-solvated material after activation at 75 and 150 °C and for the THF-exchanged material after activation at 150 °C. Note that two independently synthesized batches of Ti-MIL-101 were used for these experiments. For each digestion, 5-10 mg of metal-organic framework was combined with 1 mL

of DMSO-D6 and 10 mL of 35 wt % DCl in D_2O in a 4 mL glass vial. The vial was lightly capped, and the solution was allowed to slowly oxidize in air overnight. The NMR digestion results are summarized in Tables 6.1-6.3. Note that elemental analysis of **1** showed that there was less than 400 ppm of Cl in the sample, so Cl cannot serve as a charge-balancing anion.

The NMR digestion results for **1** after evacuating at 75 °C are consistent with a composition of $Ti_3O(OEt)_{0.7}(OOC)_{0.3}(bdc)_3(DMF)_2$•0.6DMF. Activation at this temperature was only performed for 6 h, and it is likely that there was a small amount of non-metal-bound DMF left in the framework pores. Also, this sample was synthesized and washed independently from the two samples that were activated at 150 °C, using anhydrous DMF that had been stored in the glovebox for several weeks, and this likely explains why there appears to be both formate (COO) and ethoxide (OEt) as charge-balancing anions as opposed to just OEt as observed for samples synthesized using fresh DMF. Regardless, the NMR digestion of this sample is consistent with solvated **1** containing two Ti^{3+} per cluster with bound solvent and one Ti^{3+} per cluster with a charge-balancing anion.

The NMR digestion results for **1** after evacuating at 150 °C are consistent with a composition of $Ti_3O(OEt)(bdc)_3(DMF)$. We note that it is not possible to determine if the small amount of formic acid observed in the NMR spectrum is derived from charge-balancing formate anions or from DMF decomposition during the digestion process. However, an NMR peak consistent with dimethylamine is observed at δ2.48 ppm (singlet, but overlapped with the DMSO solvent peak), which strongly suggests that the majority of formic acid is from DMF decomposition during digestion. Regardless, the NMR digestion of this sample is consistent with activated **1** containing one six-coordinate Ti^{3+} per cluster with bound solvent, one six-coordinate Ti^{3+} per cluster with a charge-balancing anion, and one five-coordinate Ti^{3+} per cluster.

The NMR digestion results for **1** after THF exchanges and evacuating at 150 °C are consistent with a composition of $Ti_3O(OEt)(bdc)_3(THF)_{0.8}(DMF)_{0.2}$. We note that it is not possible to determine if the small amount of formic acid observed in the NMR spectrum is derived from charge-balancing formate anions or from DMF decomposition during the digestion process. Regardless, the NMR digestion of this sample is consistent with THF replacing 80-90% of metal-bound DMF and with activated **1** containing one six-coordinate Ti^{3+} per cluster with bound solvent, one six-coordinate Ti^{3+} per cluster with a charge-balancing anion, and one five-coordinate Ti^{3+} per cluster.

Table 6.1. NMR digestion results for **1** after evacuating at 75 °C.

	NMR shift (ppm)	H atoms (per mol)	Integral	mol (normalized)
H_2bdc (s)	8.03	4	4.05	3
DMF (s, H)	7.94	1	0.86	2.6
DMF (s, CH_3)	2.87	3	2.52	2.5
DMF (s, CH_3)	2.70	3	2.53	2.5
Formic acid (s)	8.15	1	0.14	0.4
EtOH (q, CH_2)	3.41	2	0.44	0.7
EtOH (t, CH_3)	1.04	3	0.60	0.6

Table 6.2. NMR digestion results for **1** after evacuating at 150 °C.

	NMR shift (ppm)	H atoms (per mol)	Integral	mol (normalized)
H_2bdc (s)	8.03	4	4.00	3
DMF (s, H)	7.94	1	0.26	0.8
DMF (s, CH_3)	2.87	3	0.72	0.7
DMF (s, CH_3)	2.70	3	0.76	0.8
Formic acid (s)	8.15	1	0.10	0.3
EtOH (q, CH_2)	3.41	2	0.73	1.1
EtOH (t, CH_3)	1.04	3	1.03	1.0

Table 6.3. NMR digestion results for **1** after THF exchanges and activating at 150 °C.

	NMR shift (ppm)	H atoms (per mol)	Integral	mol (normalized)
H_2bdc (s)	8.03	4	4.00	3
DMF (s, H)	7.94	1	-	-
DMF (s, CH_3)	2.87	3	0.12	0.1
DMF (s, CH_3)	2.70	3	0.12	0.1
Formic acid (s)	8.15	1	0.06	0.1
EtOH (q, CH_2)	3.41	2	0.77	1.2
EtOH (t, CH_3)	1.04	3	1.08	1.1
THF (m)	3.57	4	0.95	0.7
THF (m)	1.74	4	1.02	0.8

6.2.4. Adsorption Measurements. Gas adsorption isotherms for pressures in the range 0-1.1 bar were measured using a Micromeritics ASAP 2020 instrument. For standard measurements in a glass sample holder, activated samples were transferred under a N_2 atmosphere to a preweighed analysis tube, which was capped with a Transeal. The sample was evacuated on the ASAP until the outgas rate was less than 3 mbar/min. The evacuated analysis tube containing degassed sample was then carefully transferred to an electronic balance and weighed to determine the mass of sample (typically 50-150 mg). The tube was fitted with an isothermal jacket and transferred back to the analysis port of the gas adsorption instrument. The outgas rate was again confirmed to be less than 3 mbar/min.

Langmuir surface areas and pore volumes were determined by measuring N_2 adsorption isotherms in a 77 K liquid N_2 bath and calculated using the Micromeritics software, assuming a value of 16.2 $Å^2$ for the molecular cross-sectional area of N_2. Measurements at –78 °C were performed using a dry ice/isopropanol bath, while measurements at 25 °C were performed using a recirculating dewar connected to an isothermal bath.

6.2.5. Adsorption Isotherm Fitting. The 77 and 87 K H_2 adsorption isotherms were independently fit with a dual-site Langmuir-Freundlich model (Eqn 1), where n is the amount adsorbed in mmol/g, P is the pressure in bar, $n_{sat,i}$ is the saturation capacity in mmol/g, v_i is the Freundlich parameter, and b_i is the Langmuir parameter in bar^{-v} for two sites 1 and 2. The fitted

parameters for each adsorption isotherm can be found in Table 6.4. Plots of the absolute adsorption isotherms with the corresponding dual-site Langmuir-Freundlich fits can be found in Figure 6.2b.

$$n = \frac{n_{\text{sat},1} b_1 P^{\nu_1}}{1 + b_1 P^{\nu_1}} + \frac{n_{\text{sat},2} b_2 P^{\nu_2}}{1 + b_2 P^{\nu_2}} \tag{1}$$

The Clausius-Clapeyron equation (Eqn 2) was used to calculate the isosteric heats of adsorption (differential enthalpy), $-h_{\text{ads}}$, for each compound using the dual-site Langmuir-Freundlich fits at 77 and 87 K.

$$\ln P = \frac{h_{\text{ads}}}{R}\left(\frac{1}{T}\right) + C \tag{2}$$

Here, P is the pressure, n is the amount adsorbed, T is the temperature, R is the universal gas constant, and C is a constant. The isosteric heats of adsorption were obtained from the slope of plots of $(\ln P)_n$ versus $1/T$.

Table 6.4. Dual-site Langmuir-Freundlich fit parameters for H_2 adsorption in **1**.

	77 K	87 K
$n_{\text{sat},1}$	2.6	2.4
b_1	9.3	2.6
ν_1	0.96	0.95
$n_{\text{sat},2}$	14.2	12.9
b_2	0.61	0.26
ν_2	0.88	0.98

6.2.6. Powder X-ray Diffraction. Microcrystalline powder samples of **1** (~5 mg) were loaded into 1.0 mm boron-rich glass capillaries inside a glovebox under an N_2 atmosphere. The capillaries were attached to a gas cell, which was connected to the analysis port of a Micromeritics ASAP 2020 gas adsorption instrument. The capillaries were fully evacuated at room temperature for 15 min then flame-sealed and placed inside a kapton tube that was sealed on both ends with epoxy.

High-resolution synchrotron X-ray powder diffraction data were subsequently collected at beamline 11-BM at the Advanced Photon Source (APS) at Argonne National Laboratory with a wavelength of 0.41397 Å. Diffraction patterns were collected at 100 K. Discrete detectors covering an angular range from −6 to 16º 2θ were scanned over a 34º 2θ range, with data points collected every 0.001° 2θ and a scan speed of 0.01º/s. Note that due to the large number of collected data points, all diffraction patterns were rebinned to a step size of 0.005° 2θ.

A standard peak search, followed by indexing via the Single Value Decomposition approach,[28] as implemented in TOPAS-Academic, allowed the determination of approximate unit cell dimensions. Precise unit cell dimensions were determined by performing a structureless Le Bail refinement in TOPAS-Academic (Figures 6.S13, 6.S14).[29]

Table 6.5. Unit cell parameters from X-ray powder diffraction.

	Temperature	Space Group	a (Å)	V (Å^3)
Cr-MIL-101[10]	90 K	Fd–3m	88.869(1)	701,860.3(1)
1 (activated)	100 K	Fd–3m	89.78(2)	723,600(500)
1 (O_2 dosed)	100 K	Fd–3m	85.35(2)	621,600(400)

6.2.7. UV-Visible-NIR Diffuse Reflectance Spectra. UV-visible-NIR diffuse reflectance spectra were collected using a CARY 5000 spectrophotometer interfaced with Varian Win UV software. The samples were held in a Praying Mantis air-free diffuse reflectance cell. Polyvinylidene fluoride (PVDF) powder was used as a non-adsorbing matrix. The Kubelka-Munk conversion ($F(R)$ vs. wavenumber) of the raw diffuse reflectance spectrum (R vs. wavenumber) was obtained by applying the formula $F(R) = (1 - R)^2/2R$. This transform creates a linear relationship for the spectral intensity relative to sample concentration and assumes that the sample is infinitely diluted in the non-adsorbing matrix, that the sample layer is "infinitely thick", and that the sample has a constant scattering coefficient. Note that data above 12,500 cm^{-1} were offset by a small, constant amount on the y-axis to remove an artifact of the spectrometer after the detector and gradient were changed for the higher-energy region of the scans.

6.2.8. Magnetic Measurements. Magnetic samples were prepared by adding crystalline powder of **1** (65 mg) to a 5 mm inner diameter quartz tube containing a raised quartz platform. Solid eicosane was added to cover the sample to prevent crystallite torqueing and provide good thermal contact between the sample and the cryostat. The tubes were fitted with Teflon sealable adapters, evacuated on a Schlenk line, and flame-sealed under static vacuum. Following flame sealing, the solid eicosane was melted in a water bath held at 40 °C. Magnetic susceptibility measurements were performed using a Quantum Design MPMS2 SQUID magnetometer. Dc magnetic susceptibility measurements were collected in a temperature range of 2-300 K under applied magnetic fields of 1000 Oe and 5000 Oe. Diamagnetic corrections were applied to the data using Pascal's constants to give χ_D = –0.00033324 emu/mol (**1**) and χ_D = –0.00024306 emu/mol (eicosane).

6.2.9. EPR Measurements. Electron paramagnetic resonance (EPR) spectra were obtained at room temperature with a Varian E-12 spectrometer equipped with liquid helium cryostat, an EIP-547 microwave frequency counter, and a Varian E-500 gaussmeter, which was calibrated using 2,2-diphenyl-1-picrylhydrazyl (DPPH, g = 2.0036). The spectrum was fit using a version of the code ABVG[30] modified to fit spectra using the downhill simplex method.[31] The code was modified to use the Pilbrow lineshape.[32] The sample was sealed inside a 4 mm OD quartz tube.

The areas of the EPR signals were determined by double-integration (Figure 6.S24). The first derivative spectrum was integrated using Simpson's rule to give the absorption correction.[31] The baseline was corrected empirically using a second order polynomial, and the absorption spectrum was integrated using by Simpson's rule again.

6.3. Results and Discussion

Heating $TiCl_3$ and H_2bdc in a 10:1 mixture of anhydrous dimethylformamide (DMF) and ethanol (EtOH) at 120 °C for 18 h afforded the solvated form of compound **1** as a dark purple powder. The powder X-ray diffraction pattern of **1** is nearly identical to the simulated diffraction pattern of Cr-MIL-101,[10] demonstrating that the two materials are isostructural (Figure 6.1). A structureless Le Bail refinement further confirmed that **1** has a face-centered cubic unit cell with a = 89.78(2) Å and V = 723,600(500) Å^3, which is slightly larger than that previously determined for Cr-MIL-101 (a = 88.869(1) Å, V = 701,860.3(1) Å^3). Moreover, elemental analysis and NMR digestion experiments confirmed that the molecular formula of **1** is indeed $Ti_3O(OEt)(bdc)_3(DMF)_2$, indicating that the framework contains six-coordinate Ti^{III} centers wherein 1/3 are coordinated to a charge-balancing ethoxide anion and 2/3 are coordinated to a DMF solvent molecule. Efforts to synthesize a Ti^{III} analogue of MIL-100 using a similar procedure with H_3btc were unsuccessful, resulting only in amorphous powders.

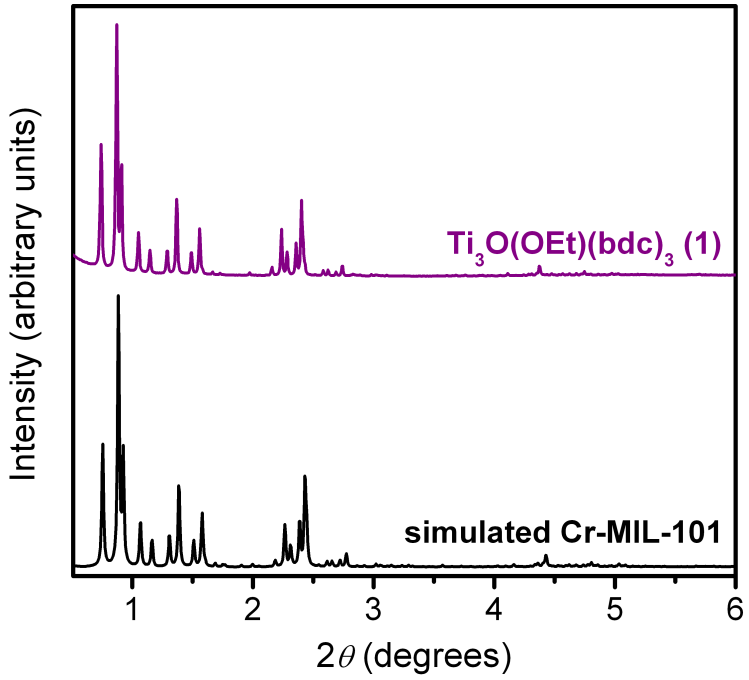

Figure 6.1. X-ray powder diffraction pattern for **1** (purple) is compared with a simulated diffraction pattern of Cr-MIL-101.[10] The wavelength is 0.41397 Å.

A 77 K N_2 adsorption isotherm was measured for **1** after heating to 150 °C under vacuum, and the resulting isotherm shape is characteristic of a material with a combination of micro- and mesopores (Figure 6.S1), as expected for the MIL-101 structure-type. Based on the saturation uptake, the compound has a Langmuir surface area of 3888 m^2/g and a total pore volume of 1.34 cm^3/g, which is consistent with, but slightly lower than, other MIL-101 analogues. In an effort to improve the surface area of **1**, the as-synthesized framework was washed repeatedly with THF at 120 °C in order to exchange all DMF molecules for the more volatile THF and to fully remove any unreacted H_2bdc ligand from the framework pores. As expected, the Langmuir and BET surface areas of **1** were increased substantially after the THF washes to 4440 m^2/g and

2970 m^2/g, respectively, with a total pore volume of 1.50 cm^3/g (Figure 6.2a). To the best of our knowledge, these are by far the highest reported surface areas for any Ti-based porous material.

To probe for exposed Ti^{III} cations in activated **1**, H_2 adsorption isotherms were measured at 77 and 87 K (Figure 6.2b). Many metal-organic frameworks with square pyramidal divalent metal cations exhibit steep 77 K H_2 adsorption isotherm at low pressures,[3] and a similar shaped isotherm might reasonably be expected for a material with a high density of exposed Ti^{III} cations. In **1**, however, the H_2 adsorption isotherms are relatively shallow with a low-coverage H_2 binding enthalpy of just –6.4 kJ/mol, which is characteristic of weak physisorption. In addition, the 25 °C CO_2, N_2, and CO adsorption isotherms of **1** are similar to those of other high surface area materials that have relatively nonpolar pore surfaces (Figures 6.S7-6.S9), further indicating that there are no accessible exposed Ti^{3+} cations in **1**. Speculating that THF might still be bound to most Ti^{III} centers, we attempted to activate the framework at higher temperatures. While activation at 200 °C did not affect the surface area or H_2 adsorption properties of **1**, activation at 225 °C led to a decrease in both surface area and H_2 uptake (Figure 6.S6). These initial adsorption results suggest that either all Ti^{III} centers in the framework remain six-coordinate upon activation or that any five-coordinate centers generated are for some reason unable to interact with and polarize adsorbing gas molecules.

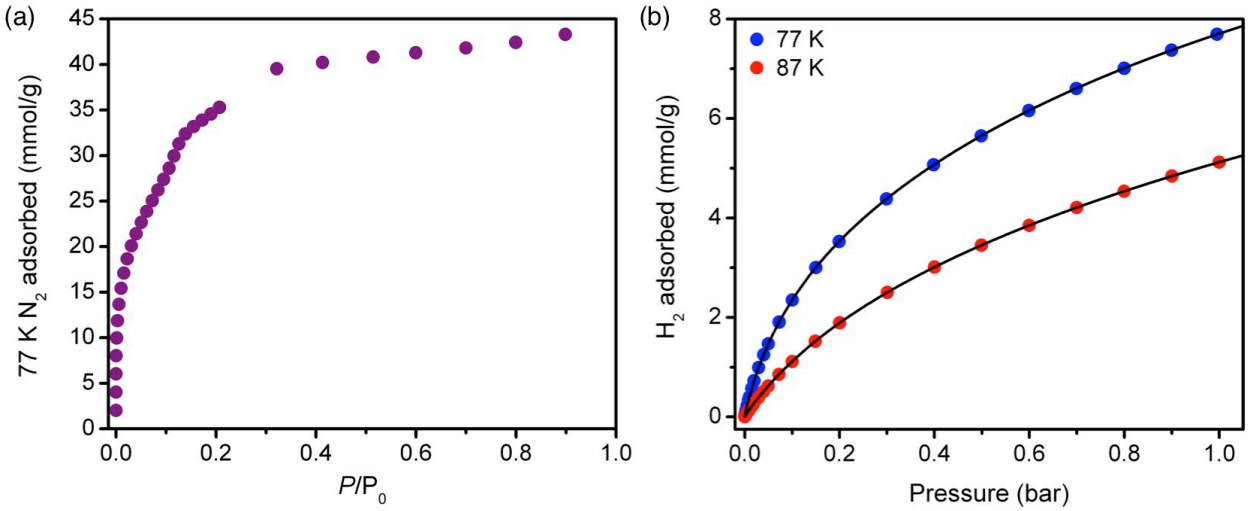

Figure 6.2. (a) N_2 adsorption isotherm at 77 K for **1** after activation at 150 °C. (b) Excess H_2 adsorption isotherms at 77 K (blue) and 87 K (red) for **1** after activation at 150 °C. The black lines correspond to dual-site Langmuir-Freundlich fits to each isotherm.

Since O_2 is well-known to undergo charge transfer reactions with titanium(III) complexes to generate titanium(IV)-superoxo and -peroxo species, we predicted that any coordinatively unsaturated titanium(III) centers would react strongly with O_2, even if these sites were unable to strongly polarize other small gas molecules. In sharp contrast to other gases, the 25 °C O_2 isotherm of **1** is very steep at low pressures, reaching a capacity of 0.85 mmol/g (2.6 wt %) at just 0.9 mbar, and is characteristic of a chemisorption process (Figure 6.3a). The capacity at 0.9 mbar corresponds to an average of 0.65 O_2 molecules bound to each Ti_3O cluster; however, we noticed that the Langmuir surface area of **1** had decreased to just 2635 m^2/g after O_2 adsorption. Because the reaction between Ti^{III} and O_2 is expected to be highly exothermic, we suspected that

some framework decomposition could have occurred due to intense local heating in the sample during the isotherm measurement. To confirm this, we measured low-temperature O_2 adsorption isotherms (Figure 6.3b). At –78 °C, **1** also exhibits a very steep O_2 isotherm, but now, the steep portion of the isotherm reaches a loading of 1.1 mmol/g (3.4 wt %), which is just below that expected for the adsorption of one O_2 per Ti_3O cluster (1.3 mmol/g). Moreover, the Langmuir surface area was only slightly reduced to 3884 m^2/g after the isotherm measurement. To evaluate the reversibility of O_2 adsorption in **1**, a second O_2 isotherm was measured at –78 °C after evacuating at room temperature (Figure 6.3b). The complete disappearance of the steep region of the adsorption isotherm demonstrates that the initial O_2 binding is irreversible under these conditions, and we were unable to find any conditions to regenerate the bare framework, even upon heating to as high as 150 °C.

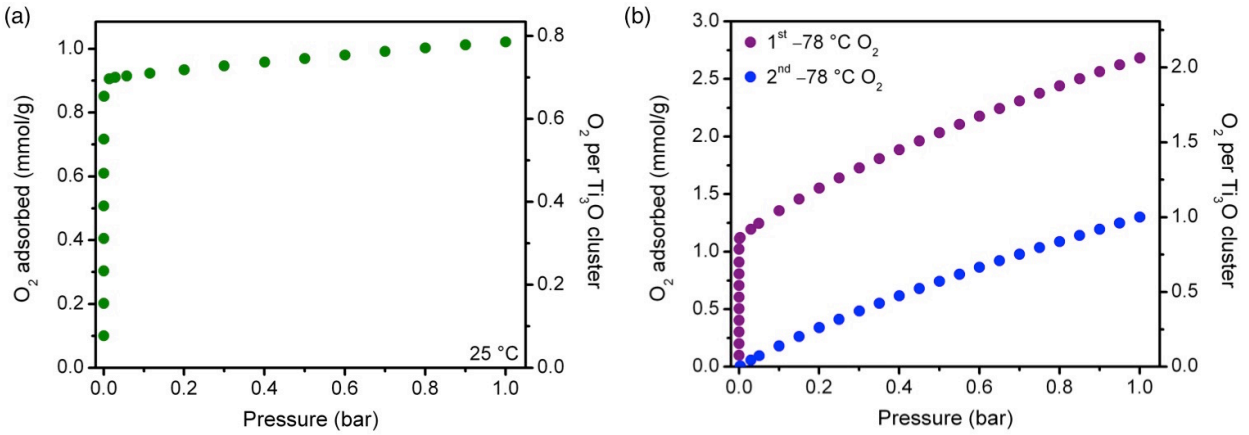

Figure 6.3. (a) Excess O_2 adsorption isotherm for **1** at 25 °C. (b) Excess O_2 adsorption isotherms for **1** at –78 °C on a fresh sample (purple) and after O_2 adsorption followed by reactivation at 25 °C under vacuum (blue).

High-resolution powder X-ray diffraction patterns collected before and after O_2 dosing demonstrate that **1** maintains the same structure after O_2 adsorption, but with a significant volume contraction of 14.1(1)% as the unit cell length decreases from 89.78(2) Å to 85.35(2) Å (Figure 6.S14). This large unit cell contraction, along with the increased molecular weight of the framework, likely accounts for most of the observed decrease in surface area after O_2 binding. Still, the large volume change and stoichiometry of one O_2 reacting per every three Ti^{III} are somewhat surprising, and the exact composition of the oxidized framework is not obvious. While it is possible O_2 reacts with the framework by outer-sphere electron transfer or by displacing a metal-bound solvent molecule, it seems more likely that at least 1/3 of the Ti^{III} cations in the activated framework must be five-coordinate in order for the O_2 adsorption isotherm to be so steep at low pressures. If this were the case, each Ti_3O cluster could bind one O_2 to generate a six-coordinate Ti^{IV}-superoxide with the other two metals remaining as Ti^{III}, or an additional intracluster electron transfer could potentially occur to generate a six-coordinate Ti^{IV}-peroxide with two Ti^{IV} centers and one Ti^{III} center per cluster (Figure 6.4). Owing to the large size of the cubic unit cell and the expected disorder in the location of $Ti^{III/IV}$ species, it was not possible to solve the structure of **1** either before or after O_2 adsorption from the powder diffraction data, and attempts to synthesize single crystals of the framework were unsuccessful. As a result, we turned to spectroscopic techniques in order to determine the mechanism for O_2 adsorption in **1**.

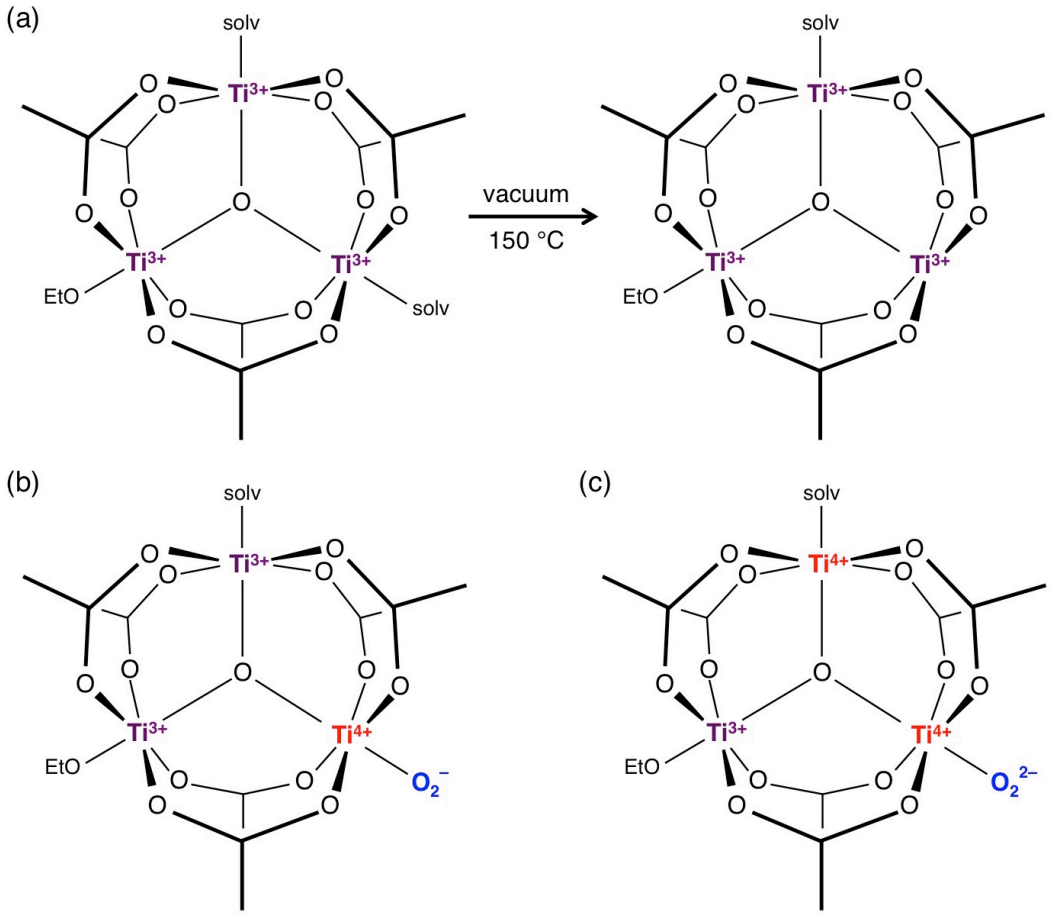

Figure 6.4. Illustration of the proposed composition of the Ti_3O clusters in **1** after (a) heating at 150 °C vacuum, (b) reacting with O_2 to form a titanium(IV)-superoxide, and (c) reacting with O_2 to form a titanium(IV)-peroxide.

While **1** is EPR-silent at room temperature, two clear signals are observed in the EPR spectrum at low and high fields upon O_2 dosing (Figure 6.5). Both segments of the spectrum were simulated separately to determine the relevant g-values for each feature, which are given in Table 6.6. Based on the similarity of the g-values to superoxide adsorbed on TiO_2 and other Ti-oxo clusters,[33,34] the low-field signal is assigned to a superoxide radical anion coordinated to a titanium(IV) center. Likewise, the g-values for the broad signal at higher field are consistent with those reported for octahedral titanium(III) centers in molecular Ti_3O clusters,[27c] and the high field signal is thus assigned to titanium(III).

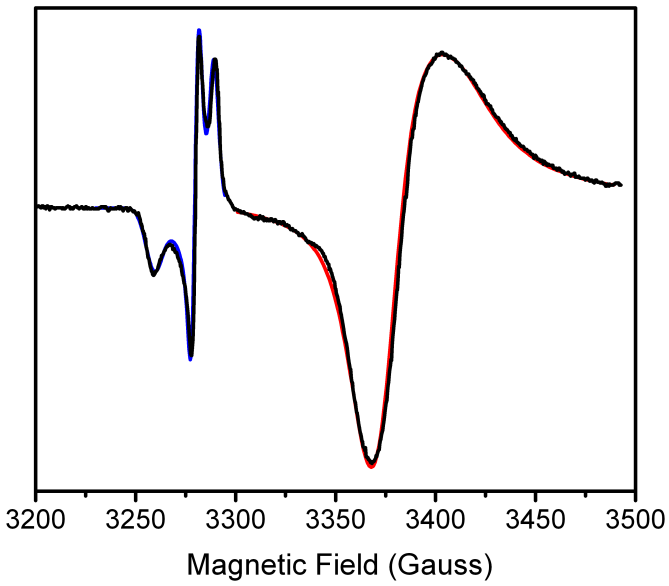

Figure 6.5. EPR spectrum for oxidized **1**. The spectrum is shown in black and the simulations of the low- and high-field signals are shown in blue and red, respectively.

Since both superoxide and titanium(III) are S = 1/2, the areas of the two EPR signals should be directly proportional to their relative concentrations in the oxidized framework. If there are not any titanium(IV)-peroxo species present, then each Ti_3O cluster would contain two titanium(III) centers and one titanium(IV)-superoxide (Figure 4b). As discussed below, the titanium(III) centers should be strongly antiferromagnetically coupled and would therefore not be expected to display an EPR signal. Since the activated framework with all titanium(III) centers is also EPR-silent (Figure 4a), the observed titanium(III) signal can be assigned entirely to clusters containing titanium(IV)-peroxide that have only a single titanium(III) center (Figure 4c).

Table 6.6. EPR g-values for the species in oxidized **1** are compared to those previously reported for a titanium(IV)-superoxide and a titanium(III) center in a carboxylate-bridged oxo cluster.

	Low-field signal	Superoxide on rutile[33a]	High-field signal	Ti^{III} in $Ti_6O_3(bdc)_2(O^iPr)_{14}$ cluster[27c]
g_1	2.021	2.0235	1.952	1.968
g_2	2.008	2.0088	1.939	1.943
g_3	2.002	2.0026	1.923	1.923

By double-integrating the EPR spectrum (Figure S24), we estimate that there is roughly 12 times the amount of titanium(III) as superoxide in the sample. Although integration performed in this manner is not particularly accurate, we can calculate that approximately 8% of the oxidized Ti_3O clusters should have a bound superoxide, while 92% should have a bound peroxide. We note, however, that the sample used for the EPR experiment was stored at ambient temperature

for several days prior to measuring the spectrum. It possible that the 2nd electron transfer to convert the superoxide to a peroxide is much slower than the initial electron transfer, and as a result, the exact distribution of superoxo and peroxo species may depend on both the storage time and temperature. Indeed, the color of the oxidized framework slowly changes from light purple to light pink over several weeks, even when stored under an N_2 atmosphere. Regardless, the presence of titanium(IV)-superoxo and/or -peroxo species should also be observed by infrared spectroscopy.

Infrared spectra were collected for **1** in a solvated state, after activation at 150 °C, after dosing with $^{16}O_2$ at –78 °C, and after dosing with $^{18}O_2$ at –78 °C (Figures 6.S15-6.S21). Typically, the O–O stretching frequencies of superoxo- and peroxo-complexes are observed between 1200 and 800 cm^{-1}.[35,36] In the infrared spectra of both solvated and activated **1**, several overlapping framework vibrations, which are likely associated with the bridging carboxylates and charge balancing ethoxide anions,[37] occur in this region and make the identification of new bands after O_2 adsorption difficult. Nonetheless, a new band is visible in the $^{18}O_2$-dosed sample at 1042 cm^{-1} and can be tentatively assigned to the $\upsilon(^{18}O–^{18}O)$ of a superoxide (Figure 6.S14). Using a simple harmonic oscillator model, the predicted $\upsilon(^{16}O–^{16}O)$ is 1105 cm^{-1}, which is at the same energy as several strong framework vibrations. In addition, a new, weak band is observed at 907 cm^{-1} in the $^{16}O_2$-dosed framework and can be assigned to the O–O stretch of a titanium(IV)-peroxide (Figure 6.S16).[38] Consistent with this assignment, a new shoulder is observed in the $^{18}O_2$-dosed spectrum at the expected frequency of 855 cm^{-1}. In all infrared spectra, a strong band is also present near 740 cm^{-1} and can be assigned to the asymmetric M_3O vibrational mode. As expected for stronger Ti−O bonds, this band occurs at higher frequencies than is observed in the molecular chromium(III) (660 cm^{-1}) and iron(III) (600 cm^{-1}) acetate clusters.[39] After O_2 binding, $\upsilon_{asym}(Ti_3O)$ is blue-shifted from 740 cm^{-1} to 747 cm^{-1} (Figure 6.S17), which is consistent with stronger binding to the μ_3-O after a portion of the titanium(III) sites are oxidized to titanium(IV).

The high fraction of titanium(IV)-peroxo species present in oxidized **1** implies that the barrier to intervalence charge transfer through the oxo-bridge in each Ti_3O unit is relatively low. To further probe the electronic structure of the material, dc magnetic susceptibility measurements were performed for activated 1 under applied magnetic fields of 1000 Oe and 5000 Oe. The $\chi_M T$ value of **1** at 300 K and 1000 Oe is 0.641 emuK/mol, well below the value of 1.125 emuK/mol expected for three noninteracting S = 1/2 spins with g = 2. This low magnetic susceptibility suggests strong intracluster antiferromagnetic coupling in **1**, which is consistent with the lack of an EPR signal for **1** at room temperature. The magnetism of dinuclear oxo-bridged Ti^{3+} molecules has been studied extensively using both experiment and computation, with special emphasis on the type and magnitude of magnetic coupling in relation to the Ti-O-Ti angle.[40] When the Ti-O-Ti angle is close to 120° strong antiferromagnetic coupling is observed, supporting the assignment of strong antiferromagnetic coupling within the Ti_3O clusters in **1**, which is expected to exhibit Ti-O-Ti angles near 120°. The magnetic susceptibility of **1** decreases continuously with lowering temperature until a rough plateau is reached between 50 and 60 K at a $\chi_M T$ value of 0.260 emuK/mol, which is close to the 0.375 emuK/mol expected for a total spin of S = 1/2. This is consistent with antiferromagnetic coupling between two Ti(III) centers in each Ti_3O unit. The strong antiferromagnetic coupling observed between Ti^{III} centers is consistent with the occurrence of intervalence electron transfer to generate Ti-peroxo species upon oxidation. As temperature decreases further, $\chi_M T$ trends towards zero due to antiferromagnetic interactions between Ti_3 clusters through the terephthalate ligands.

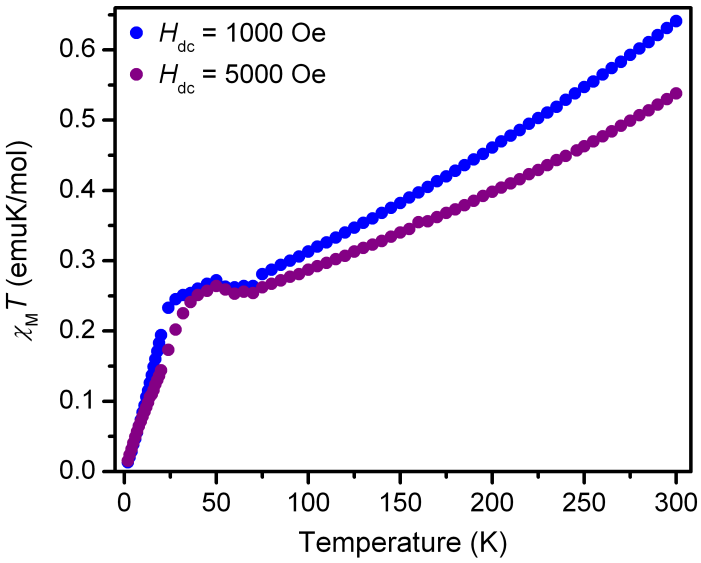

Figure 6.6. Variable-temperature magnetic susceptibility data for **1** activated at 150 °C in an applied field of 1000 Oe (blue) and 5000 Oe (purple).

To gain additional insight into exactly how O_2 reacts with the titanium sites of **1**, electronic absorption spectra were measured for all compounds (Figure 6.7). The solvated framework exhibits three overlapping peaks in the visible region with maxima at approximately 20,370 cm^{-1}, 18,080 cm^{-1}, and 16,260 cm^{-1}. While octahedral Ti^{III} complexes should have a single d-d transition ($t_{2g} \rightarrow e_g$), two transitions are often observed when a distortion of the octahedral ligand field splits the e_g levels.[41] Since the octahedral Ti^{III} centers in solvated **1** likely undergo a tetragonal distortion and exist in two different chemical environments depending on whether there is a bound solvent molecule or anion in the axial position, the three observed peaks are likely the result of four overlapping d-d transitions. The relevant transitions appear to be separated by 1500-2000 cm^{-1}, which is typical for the e_g splitting of Ti^{III} complexes in a distorted octahedral coordination geometry.

After activation, the position of the highest-energy band is relatively unchanged, while the two lower energy bands are shifted to 16,980 cm^{-1} and 15,850 cm^{-1}. More significantly, a new intense feature, which is diagnostic of five-coordinate Ti^{III},[42] is observed in the near-IR region of the spectrum at 6,390 cm^{-1}, along with a small shoulder at 8,830 cm^{-1}. While it is not possible to definitively assign the geometry of the five-coordinate Ti^{III} centers based on this spectrum, trigonal bipyramidal Ti^{III} complexes are known to exhibit two electronic transitions at 7,500-5,000 cm^{-1} ($e'' \rightarrow e'$) and 16,400-14,000 cm^{-1} ($e'' \rightarrow a_1'$).[43] There are also several examples of trimeric Ti clusters with μ_3-O bridges that contain one five-coordinate and two six-coordinate Ti centers; and in all cases, the five-coordinate Ti sites adopt slightly distorted trigonal bipyramidal coordination geometries.[44] The new electronic transition at 6,390 cm^{-1} in activated **1** can thus be assigned to a five-coordinate Ti^{III} center, potentially in a distorted trigonal bipyramidal geometry. Such a coordination geometry would indeed rationalize the lack of strong adsorption of non-redox active gases in **1** as the Ti^{III} charge would be effectively shielded after desolvation.

As discussed in detail in section 6.2.3, NMR digestion experiments also support a molecular formula of $Ti_3O(OEt)(bdc)_3(solv)$ with one metal-bound solvent molecule per Ti_3O cluster after activation at 150 °C. We note that a similar result was observed for Al-MIL-100 by solid state

NMR, where it was hypothesized that H_2O was removed from 1/3 of the Al^{3+} cations in the framework to generate five-coordinate Al^{3+} cations.[9]

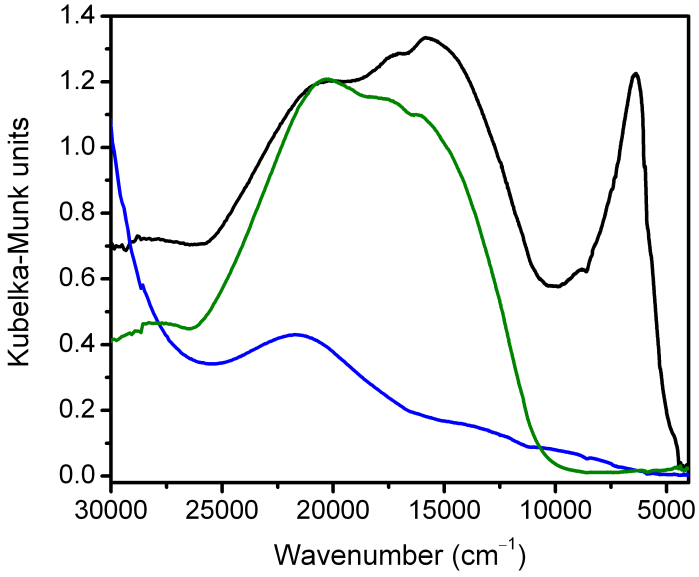

Figure 6.7. Diffuse reflectance UV-vis-NIR spectra of DMF solvated (green), 150 °C activated (black), and O_2-dosed (blue) **1** at ambient temperature. Note that the discontinuities at 12,500 cm^{-1} are artifacts of the spectrometer.

After O_2 adsorption, the near-IR peak associated with five-coordinate Ti^{III} disappears as expected, and there is just one broad peak remaining in the visible region of the spectrum centered at 21,690 cm^{-1}. This band is associated with d-d transitions from the remaining six-coordinate Ti^{III} centers in the framework. The lower relative intensity of this peak could be attributed to the fact that less than half of the Ti centers are in a Ti(III) oxidation state after O_2 adsorption. It is also possible that the Ti^{III} sites adopt a less distorted octahedral geometry, which might explain the absence of any obvious doublet peaks in this region. Additionally, there is significant absorption in the near-UV region after oxidation, which is likely associated with ligand or Ti^{III} to Ti^{IV} charge transfer.

6.5. Outlook and Conclusions

Through a combination of adsorption, diffraction, spectroscopy, and magnetism measurements, the Ti^{III} analogue of MIL-101 was shown to feature five-coordinate Ti^{III} centers that react with O_2 to form both Ti^{IV}-superoxo and -peroxo species. This compound is the highest surface area Ti-based porous material to date and represents the first all Ti^{III} metal-organic framework with permanent porosity. Perhaps more importantly, we have shown that although there are coordinatively unsaturated Ti^{III} in the framework, these sites do not function as exposed metal cations. In order to realize trivalent and tetravalent exposed metal cations capable of polarizing H_2 and other gas molecules, more rigid frameworks are needed to prevent the coordination geometry of the metal from distorting to shield exposed charge after desolvation. While this has been accomplished for divalent metals, it represents an ongoing challenge for the design and synthesis of higher-valent metal-organic frameworks.

6.6. Acknowledgements

This research was supported by the Department of Energy, Office of Energy Efficiency and Renewable Energy (DOE-EERE), Fuel Cell Technologies Office . X-ray powder diffraction data were collected at beamline 11-BM at the Advanced Photon Source, a DoE Office of Science User Facility operated by Argonne National Laboratory under Contract No. DE-AC02-06CH11357. In addition, we thank D. Xiao and D. Zee for helpful discussions, W. Lukens for performing the EPR measurements, and L. Darago for performing the magnetic susceptibility measurements.

6.7. References and Supplementary Figures

(1) (a) Li, H.; Eddaoudi, M.; O'Keefe, M.; Yaghi, O. M. *Nature* **1999**, *402*, 276. (b) Kitagawa, S.; Kitaura, R.; Noro, S.-I. *Angew. Chem., Int. Ed.* **2004**, *43*, 2334. (c) Matsuda, R.; Kitaura, R.; Kitagawa, S.; Kubota, Y.; Belosludov, R. V.; Kobayashi, T. C.; Sakamoto, H.; Chiba, T.; Takata, M.; Kawazoe, Y.; Mita, Y. *Nature* **2005**, *436*, 238. (d) Millward, A. R.; Yaghi, O. M. *J. Am. Chem. Soc.* **2005**, *127*, 17998. (e) Feŕey, G. *Chem. Soc. Rev.* **2008**, *37*, 191. (f) Morris, R. E.; Wheatley, P. S. *Angew. Chem., Int. Ed.* **2008**, *47*, 4966. (g) Czaja, A. U.; Trukhan, N.; Müller, U. *Chem. Soc. Rev.* **2009**, *38*, 1284. (h) Chen, B.; Xiang, S.; Qian, G. *Acc. Chem. Res.* **2010**, *43*, 1115. (i) Zhou, H.-C.; Long, J. R.; Yaghi, O. M. *Chem. Rev.* **2012**, *112*, 673. (j) Sumida, K.; Rogow, D. R.; Mason, J. A.; McDonald, T. M.; Bloch, E. D.; Herm, Z. R.; Bae, T.-H.; Long, J. R. *Chem. Rev.* **2012**, *112*, 724. (k) Chem. Rev. 2012, 112, 869. (l) Herm, Z. R.; Bloch, E. D.; Long, J. R. *Chem. Mater.* **2014**, *26*, 323. (m) Evans, J. D.; Sumby, C. J.; Doonan, C. J. *Chem. Soc. Rev.* **2014**, *43*, 5933.

(2) (a) Caskey, S. R.; Wong-Foy, A. G.; Matzger, A. J. *J. Am. Chem. Soc.* **2008**, *130*, 10870. (b) Dietzel, P. D. C.; Besikotis, V.; Blom, R. *J. Mater. Chem.* **2009**, *19*, 7362. (c) Herm, Z. R.; Swisher, J. A.; Smit, B.; Krishna, R; Long, J. R. *J. Am. Chem. Soc.* **2011**, *133*, 5664. (d) Mason, J. A.; Sumida, K.; Herm, Z. R.; Krishna, R.; Long, J. R. *Energy Environ. Sci.* **2011**, *4*, 3030. (e) Bloch, E. D.; Queen, W. L.; Krishna, R.; Zadrozny, J. M.; Brown, C. M.; Long, J. R. *Science* **2012**, *335*, 1606. (f) Geier, S. J.; Mason, J. A.; Bloch, E.D.; Queen, W. L.; Hudson, M. R.; Brown, C. M.; Long, J. R. *Chem. Sci.* **2013**, *4*, 2054. (g) Peng, Y.; Krungleviciutte, V.; Eryazici, I.; Hupp, J. T.; Farha, O. K.; Yildirim, T. *J. Am. Chem. Soc.* **2013**, *135*, 11887. (h) Mason, J. A.; Veenstra, M.; Long, J. R. *Chem. Sci.* **2014**, *5*, 32. (i) Bloch, E. D.; Hudson, M. R.; Mason, J. A.; Chavan, S.; Crocella, V.; Howe, J. D.; Lee, K.; Dzubak, A. L.; Queen, W. L.; Zadrozny, J. M.; Geier, S. J.; Lion, L. C.; Gagliardi, L.; Smit, B.; Neaton, J. B.; Bordiga, S.; Brown, C. M.; Long, J. R. *J. Am. Chem. Soc.* **2014**, *136*, 10752

(3) (a) Dincă, M.; Dailly, A.; Liu, Y.; Brown, C. M.; Neumann, D. A.; Long, J. R. *J. Am. Chem. Soc.* **2006**, *128*, 16876. (b) Dietzel, P. D. C.; Panella, B.; Hirscher, M.; Blom, R.; Fjellvåg, H. *Chem. Commun.* **2006**, 959. (c) Dincă, M.; Han, W. S.; Liu, Y.; Dailly, A.; Brown, C. M.; Long, J. R. *Angew. Chem. Int. Ed.* **2007**, *46*, 1419. (d) Dietzel, P. D. C.; Johnsen, R. E.; Blom, R.; Fjellvåg, H. *Chem. Eur. J.* **2008**, *14*, 2389. (e) Liu, Y.; Kabbour, H.; Brown, C. M.; Neumann, D. A.; Ahn, C. C. *Langmuir* **2008**, *24*, 4772. (f) Zhou, W.; Wu, H.; Yildirim, T. *J. Am. Chem. Soc.* **2008**, *130*, 15268. (g) Vitillo, J. G.; Regli, L.;

Chavan, S.; Ricciradi, G.; Spoto, G.; Dietzel, P. D. C.; Bordiga, S.; Zecchina, A. *J. Am. Chem. Soc.* **2008**, *130*, 8386. (h) Sumida, K.; Horike, S.; Kaye, S. S.; Herm, Z. R.; Queen, W. L; Brown, C. M.; Grandjean, F.; Long, G. J.; Dailly, A.; Long, J. R. *Chem. Sci.* **2010**, *1*, 184. (i) Sumida, K.; Her, J. H.; Dincă, M.; Murray, L. J.; Schloss, J. M.; Pierce, C. J.; Thompson, B. A.; FitzGerald, S. A.; Brown, C. M.; Long, J. R. *J. Phys. Chem. C* **2011**, *115*, 8414. (j) Sumida, K.; Brown, C. M.; Herm, Z. R.; Chavan, S.; Bordiga, S.; Long, J. R. *Chem. Commun.***2011**, *47*, 1157. (k) Queen, W. L.; Bloch, E. B.; Brown, C. M.; Hudson, M. R.; Mason, J. A.; Murray, L. J.; Ramirez-Cuesta, A. J.; Peterson, V. K.; Long, J. R. *Dalton Trans.* **2012**, *41*, 4180. (l) Sumida, K.; Stuck, D.; Mino, L.; Chai, J.-D.; Bloch, E. D.; Zavorotynska, O.; Murray, L. J.; Dinca, M.; Chavan, S.; Bordiga, S.; Head-Gordon, M.; Long, J. R. *J. Am. Chem. Soc.* **2013**, *135*, 1083. (m) Kapelewski, M. T.; Geier, S. J.; Hudson, M. R.; Stuk, D.; Mason, J. A.; Nelson, J. N.; Xiao, D. J.; Hulvey, Z.; Gilmour, E.; FitzGerald, S. A.; Head-Gordon, M.; Brown, C. M.; Long, J. R. *J. Am. Chem. Soc.* **2014**, *136*, 12119.

(4) (a) Rowsell, J. L. C.; Yaghi, O. M. *Angew. Chem. Int. Ed.* **2005**, *44*, 4670. (b) Dincă, M.; Long, J. R. *Angew. Chem. Int. Ed.* **2008**, *47*, 6766. (c) Murray, L. J.; Dincă, M.; Long, J. R. *Chem. Soc. Rev.* **2009**, *38*, 1294. (d) Suh, M. P.; Park, H. J.; Prasad, T. K.; Lim, D.-W. *Chem. Rev*. **2012**, *112*, 782.

(5) "Target Explanation Document: Onboard Hydrogen Storage for Ligh-Duty Fuel Cell Vehicles", USDRIVE, May 2015, <http://energy.gov/sites/prod/files/2015/05/f22/fcto_targets_onboard_hydro_storage_explanation.pdf>.

(6) Bathia, S. K.; Myers, A. L. *Langmuir* **2006**, *22*, 1688.

(7) Lochan, R. C.; Head-Gordon, M. *Phys. Chem. Chem. Phys.* **2006**, *8*, 1357.

(8) Vimont, A.; Goupil, J.-M.; Lavalley, J.-C.; Daturi, M.; Surblé, S.; Serre, C.; Millange, F.; Férey, G.; Audebrand, N. *J. Am. Chem. Soc.* **2006**, *128*, 3218.

(9) Volkringer, C.; Leclerc, H.; Lavalley, J.-C.; Loiseau, T.; Férey, G.; Daturi, M.; Vimont, A. *J. Phys. Chem. C* **2012**, *116*, 5710.

(10) Férey, G.; Mellot-Draznieks, C.; Serre, C.; Millange, F.; Dutour, J.; Surblé, S.; Margiolaki, I. *Science* **2005**, *309*, 2040.

(11) Bauer, S.; Serre, C.; Devic, T.; Horcajada, P.; Marrot, J.; Férey, G.; Stock, N. *Inorg. Chem.* **2008**, *47*, 7568.

(12) (a) Biswas, S.; Couck, S.; Grzywa, M.; Denayer, J. F. M.; Volkmer, D.; Van Der Voort, P. *Eur. J. Inorg. Chem.* **2012**, 2481. (b) Yang, J.; Wang, Y.; Li, L.; Zhang, Z.; Li, J. *J. Colloid Interface Sci.* **2015**, *456*, 197.

(13) Serra-Crespo, P.; Ramos-Fernandez, E. V.; Gascon, J.; Kapteijn, F. *Chem. Mater.* **2011**, *23*, 2565.

(14) Férey, G.; Serre, C.; Mellot-Draznieks, C.; Millange, F.; Surblé, S.; Dutour, J.; Margiolaki, I. *Angew. Chem. Int. Ed.* **2004**, *43*, 6296.

(15) Horcajada, P.; Surblé, S.; Serre, C.; Hong, D.-Y.; Seo, Y.-K.; Chang, J.-S.; Grenèche, J.-M.; Margiolaki, I.; Férey, G. *Chem. Commun.* **2007**, 2820.

(16) Volkringer, C.; Popov, D.; Loisseau, T.; Férey, G.; Burghammer, M.; Riekel, C.; Haouas, M.; Taulelle, F. *Chem. Mater.* **2009**, *21*, 5695.

(17) (a) Mowat, J. P. S.; Miller, S. R.; Slawin, A. M. Z.; Seymour, V. R.; Ashbrook, S. A.; Wright, P. A. *Mircoporous Mesoporous Mater.* **2011**, *142*, 322. (b) Li, Y. T.; Cui, K. H.; Li, J.; Zhu, J. Q.; Wang, X.; Tian, Y. Q.; *Chin. J. Inorg. Chem.* **2011**, *27*, 951.
(18) Llewellyn, P. L.; Bourrelly, S.; Serre, C.; Vimont, A.; Daturi, M.; Hamon, L.; De Weireld, G.; Chang, J.-S.; Hong, D.-Y.; Hwang, Y. K.; Jhung, S. H.; Férey, G. *Langmuir* **2008**, *24*, 7245.
(19) Latroche, M.; Surblé, S.; Serre, C.; Mellot-Draznieks, C.; Llewellyn, P. L.; Lee, J.-H.; Change, J.-S.; Jhung, S. H.; Férey, G. *Angew. Chem.* **2006**, *118*, 8407.
(20) Areán, C. O.; Cabello, C. P.; Palomino, G. T. *Chem. Phys. Lett.* **2012**, *521*, 104.
(21) Furakawa, H.; Cordova, K. E.; O'Keefe, M.; Yaghi, O. M. *Science* **2013**, *341*, 974.
(22) Dan-Hardi, M.; Serre, C.; Frot, T.; Rozes, L.; Maurin, G.; Sanchez, C.; Férey, G. *J. Am. Chem. Soc.* **2009**, *131* 10857.
(23) (a) Fu, Y.; Sun, D.; Chen, Y.; Huang, R.; Ding, Z.; Fu, X.; Li, Z. *Angew. Chem. Int. Ed.* **2012**, *51*, 3364. (b) Hendon, C. H.; Tiana, D.; Fontecave, M.; Sanchez, C.; D'arras, L.; Sassoye, C.; Rozes, L.; Mellot-Draznieks, C.; Walsh, A. *J. Am. Chem. Soc.* **2013**, *135*, 10942.
(24) Yuan, S.; Liu, T.-F.; Feng, D.; Tian, J.; Wang, K.; Qin, J.; Zhang, Q.; Chen, Y.-P.; Bosch, M.; Zou, L.; Teat, S. J.; Dalgarno, S. J.; Zhou, H.-C. *Chem. Sci.* **2015**, *6*, 3926.
(25) Kim, M.; Cahill, J. F.; Fei, H.; Prather, K. A.; Cohen, S. M. *J. Am. Chem. Soc.* **2012**, *134*, 18082.
(26) Brozek, C. K.; Dincă, M. *J. Am. Chem. Soc.* **2013**, *135*, 12886.
(27) (a) Rozes, L.; Steunou, N.; Fornasieri, G.; Sanchez, C. *Monatshefte für Chemie* **2006**, *137*, 501. (b) Rozes, L.; Sanchez, C. *Chem. Soc. Rev.* **2011**, *40*, 1006. (c) Wu, Y.-Y.; Luo, W.; Wang, Y.-H.; Pu, Y.-Y.; Zhang, X.; You, L.-S.; Zhu, Q.-Y.; Dai, J. *Inorg. Chem.* **2012**, *51*, 8982.
(28) Coelho, A. *Appl. Cryst.* **2003**, *36*, 86.
(29) Coelho, A. *TOPAS-Academic*, Version 4.1, Coelho Software, Brisbane, **2007**.
(30) Daul, C.; Schlapfer, C. W.; Mohos, B.; Ammeter, J.; Gamp, E., *Comp. Phys. Commun.* **1981**, *21*, 385.
(31) Press, W. H.; Teukolsky, S. A.; Vetterling, W. T. *Numerical Recipes in Fortran 77: The Art of Scientific Computing*. Cambridge University Press: Cambridge, 1992.
(32) Pilbrow, J. R. *Transition Ion Electron Paramagnetic Resonance*. Clarendon Press: Oxford, 1990.
(33) (a) Zent, A. P.; Ichimura, A. S.; Quinn, R. C.; Harding, H. K. *J. Geophys. Res.-Planets* **2008**, *113*, 13. (b) Coronado, J. M.; Maira, A. J.; Conesa, J. C.; Yeung, K. L.; Augugliaro, V.; Soria, J. *Langmuir* **2001**, *17*, 5368.
(34) (a) Zhao, Q.; Bao, X.-H.; Wang, Y.; Lin, L.-W.; Li, G.; Guo, X.-W.; Wang, X.-S. *J. Mol. Catal. A: Chem.* **2000**, *157*, 265. (b) Chaudhari, K.; Srinivas, D.; Ratnasamy, P. *J. Catal.* **2001**, *203*, 25. (c) Maurelli, S.; Vishnuvarthan, M.; Berlier, G.; Chiesa, M. *Phys. Chem. Chem. Phys.* **2012**, *14*, 987.
(35) Nakamoto, K. *Infrared and Raman Spectra of Inorganic and Coordination Compounds*, 5th ed.; John Wiley & Sons: New York,

(36) Bloch, E. D.; Murray, L. J.; Queen, W. L.; Chavan, S.; Maximoff, S. N.; Bigi, J. P.; Krishna, R.; Peterson, V. K.; Grandjean, F.; Long, G. J.; Smit, B.; Bordiga, S.; Brown, C. M.; Long, J. R. *J. Am. Chem. Soc.* **2011**, *133*, 14814.
(37) (a) Lynch, C. T.; Mazdiyansi, S.; Smith, J. S. *Anal. Chem.* **1964**, *36*, 2332. (b) Giannetti, E.; Albizzati, E. *Inorg. Chim. Acta* **1983**, *74*, 215.
(38) (a) Mühlebach, J.; Müller, K.; Schwarzenbach, G. *Inorg. Chem.* **1970**, *9*, 2381. (b) Jeske, P.; Haselhorst, G.; Weyhermüller, T.; Wieghardt, K.; Nuber, B. *Inorg. Chem.* **1994**, *33*, 2462. (c) Mattioli, G.; Filippone, F.; Bonapasta, A. A. *J. Am. Chem. Soc.* **2006**, *128*, 13772.
(39) Johnson, M. K.; Powell, D. B.; Cannon, R. D. *Spectrochim. Acta* **1981**, *37A*, 995.
(40) (a) Bodner, A.; Drueke, S.; Wieghardt, K.; Nuber, B.; Weiss, J. *Angew. Chem. Int. Ed.* **1990**, *29*, 1. (b) Weihe, H.; Güdel, H. U. *J. Am. Chem. Soc.* **1998**, *120*, 287.
(41) Clark, R. J. H.; Lewis, J.; Machin, D. J.; Nyholm, R. S. *J. Chem. Soc.* **1963**, 379.
(42) Wood, J. S. *Inorg. Chem.* **1968**, 7, 852.
(43) Crouch, P. C.; Fowles, G. W. A.; Walton, R. A. *J. Chem. Soc. A* **1968**, *2172.*
(44) Boyle, T. J.; Tyner, R. P.; Alam, T. M.; Scott, B. L.; Ziller, J. W.; Potter, B. G. *J. Am. Chem. Soc.* **1999**, *121*, 12104. (b) Mijatovic, I.; Kickelbick, G.; Puchberger, M.; Schubert, U. *New J. Chem.* **2003**, *27*, 3.
(46) Walton, K. S.; Snurr, R. Q. *J. Am. Chem. Soc.* **2007**, *129*, 8552.

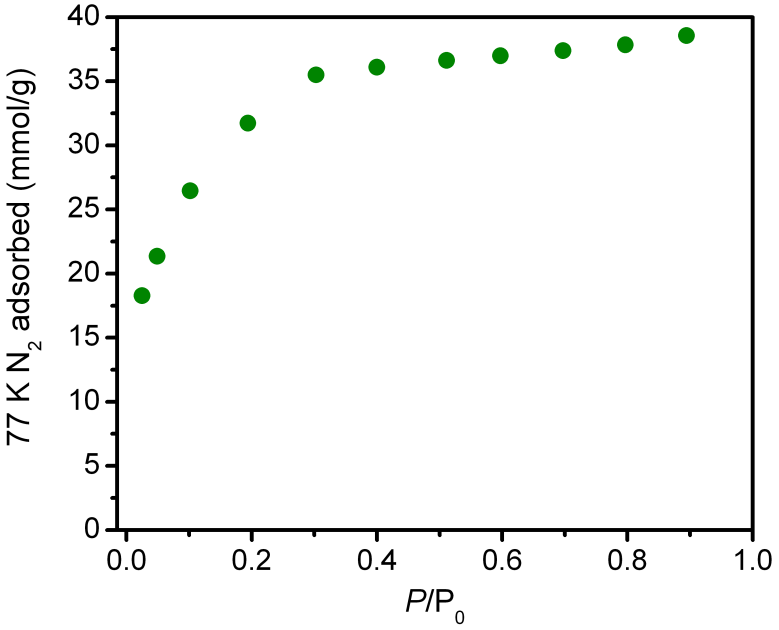

Figure 6.S1. 77 K N_2 adsorption isotherm for **1** after activation at 150 °C without performing THF exchanges. The calculated Langmuir surface area is 3888 m^2/g (n_{sat} = 39.8 mmol/g), and the total pore volume at p/p_0 = 0.9 is 1.34 cm^3/g.

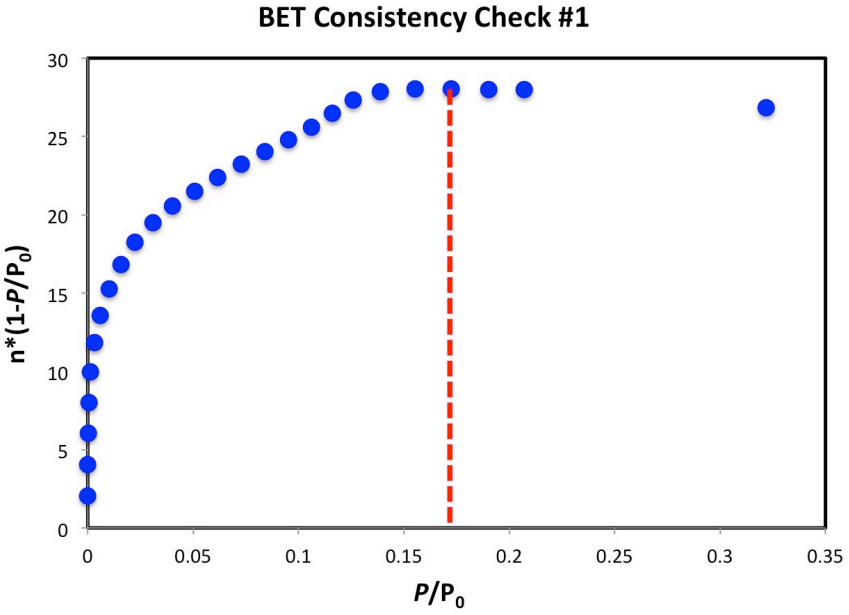

Figure 6.S2. Plot of $n\bullet(1\text{-}p/p_0)$ vs. p/p_0 to determine the maximum p/p_0 used in the BET linear fit of **1** according to the first BET consistency criterion.[46]

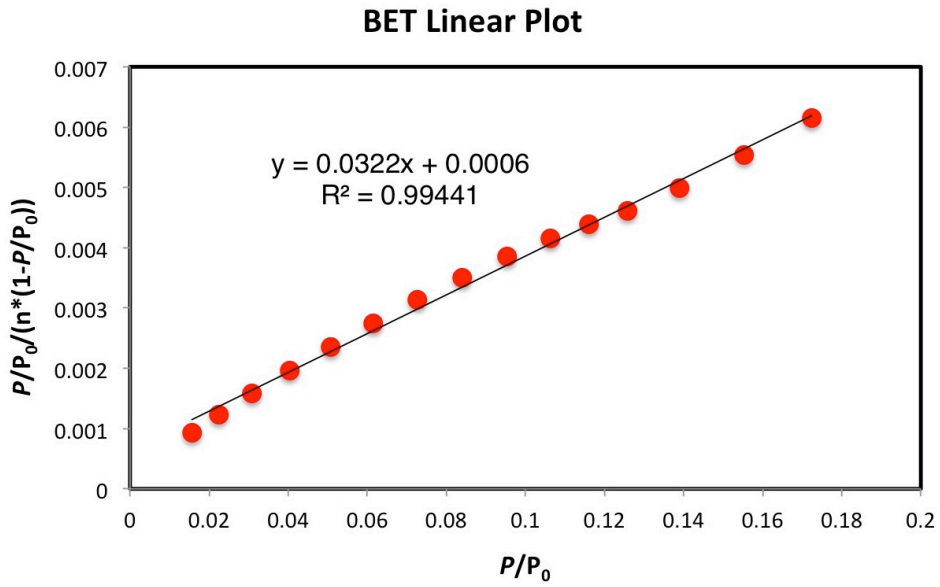

Figure 6.S3. Plot of $p/p_0/(n\bullet(1-p/p_0))$ vs. p/p_0 to determine the BET surface area. The slope of the best fit line for $p/p_0 < 0.17$ is 0.032, and the y-intercept is 6.4 x 10^{-4}, which satisfies the second BET consistency criterion. This results in a saturation capacity of 30.5 mmol/g and a BET surface area of 2970 m^2/g.[46]

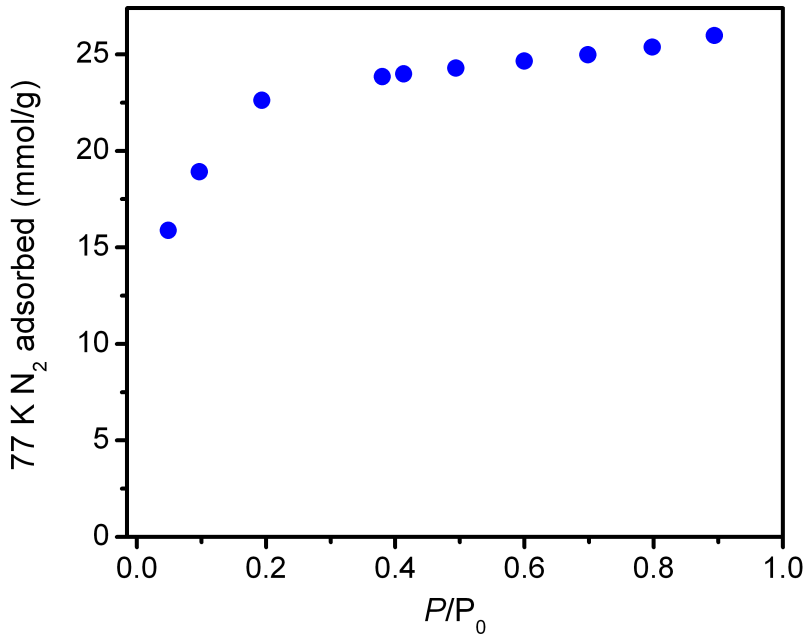

Figure 6.S4. 77 K N_2 adsorption isotherms for **1** after a 25 °C O_2 adsorption isotherm measurement.

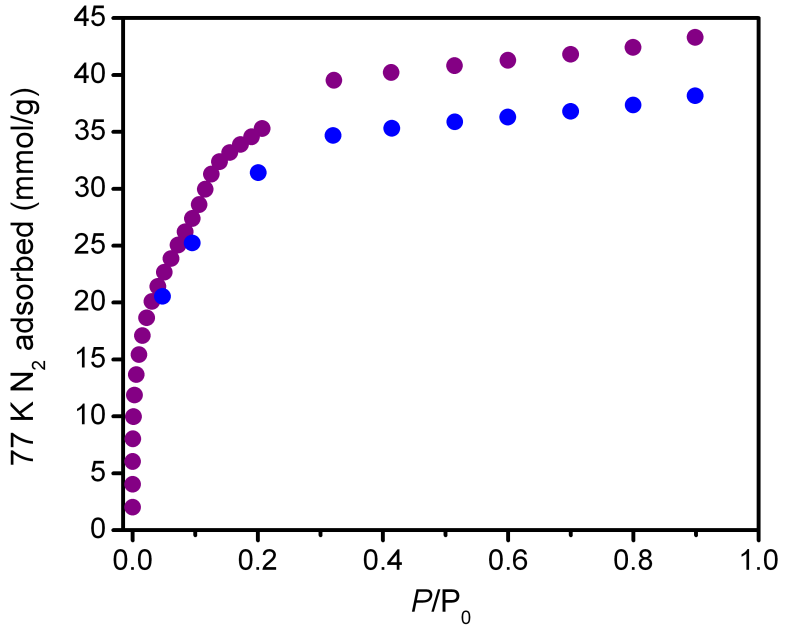

Figure 6.S5. 77 K N_2 adsorption isotherms for **1** before (purple) and after (blue) a –78 °C O_2 adsorption isotherm measurement.

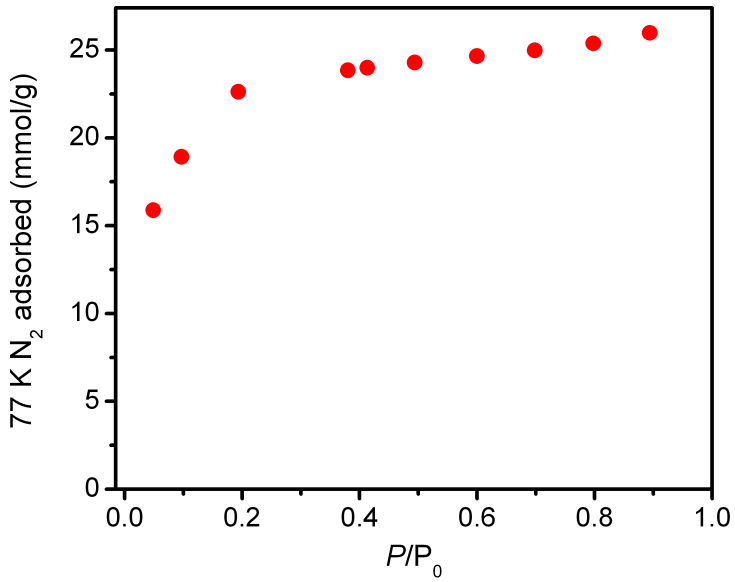

Figure 6.S6. 77 K N_2 adsorption isotherm for **1** after activation at 225 °C.

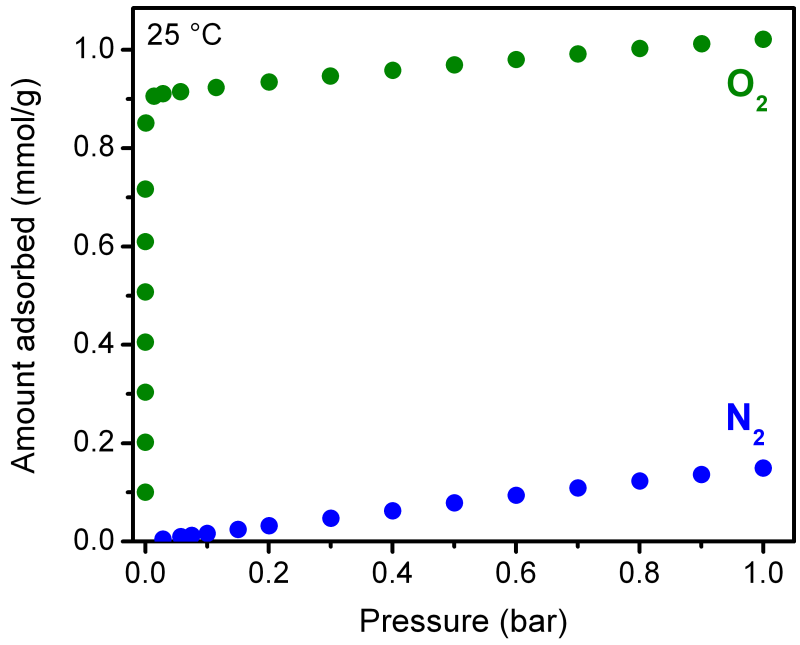

Figure 6.S7. 25 °C O_2 and N_2 isotherms for **1** activated at 150 °C. Note that the N_2 isotherm was measured prior to the O_2 isotherm.

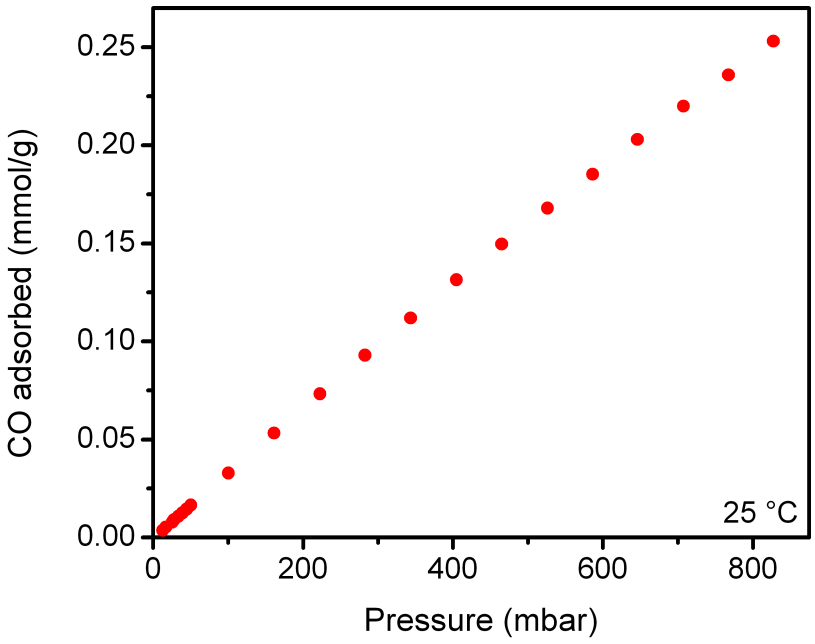

Figure 6.S8. 25 °C CO isotherm for **1** activated at 150 °C.

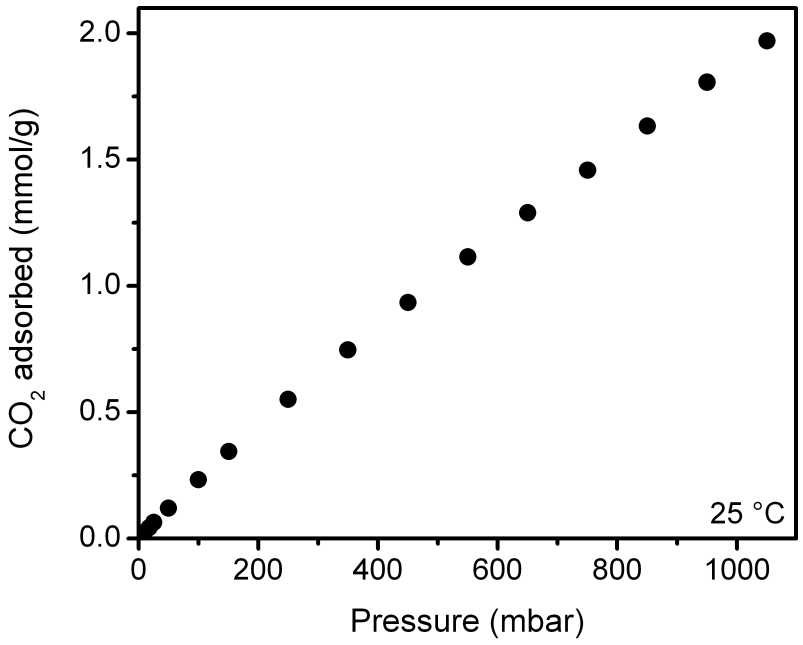

Figure 6.S9. 25 °C CO_2 isotherm for **1** activated at 150 °C.

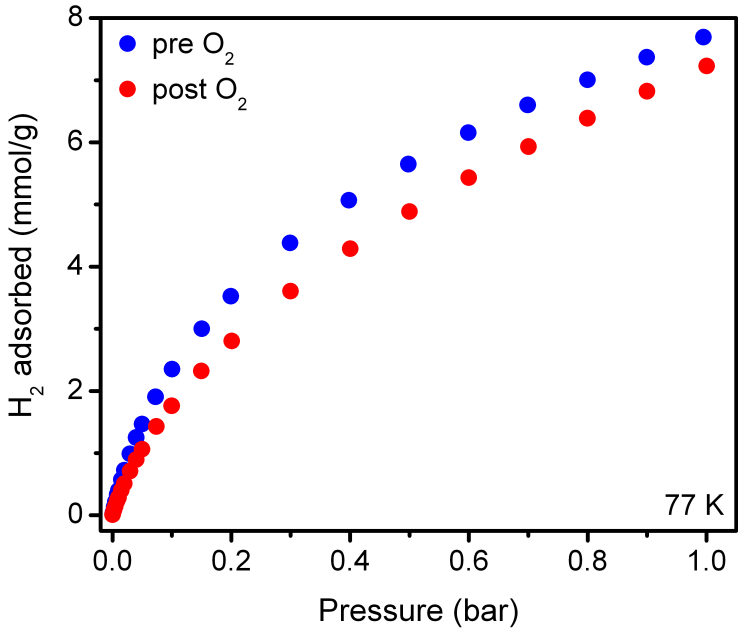

Figure 6.S10. 77 K H_2 adsorption isotherms for **1** before (blue) and after (red) a –78 °C O_2 adsorption isotherm measurement.

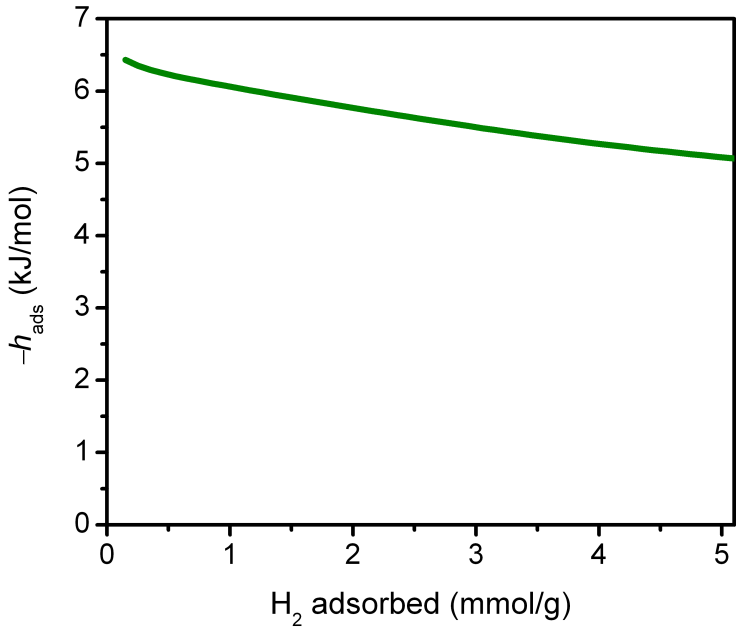

Figure 6.S11. Differential enthalpy of H_2 adsorption, h_{ads}, plotted as a function of the amount of H_2 adsorbed for **1** activated at 150 °C.

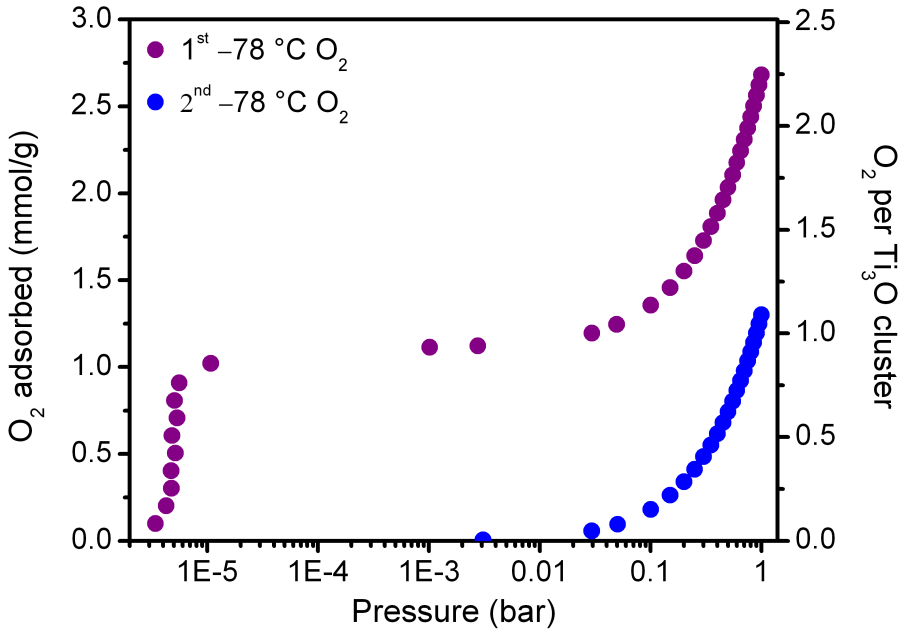

Figure 6.S12. O_2 adsorption isotherms for **1** at –78 °C are shown on a logarithmic scale. The purple isotherm was measured on a freshly activated sample, while the blue isotherm was measured after the initial O_2 isotherm and then evacuating at room temperature.

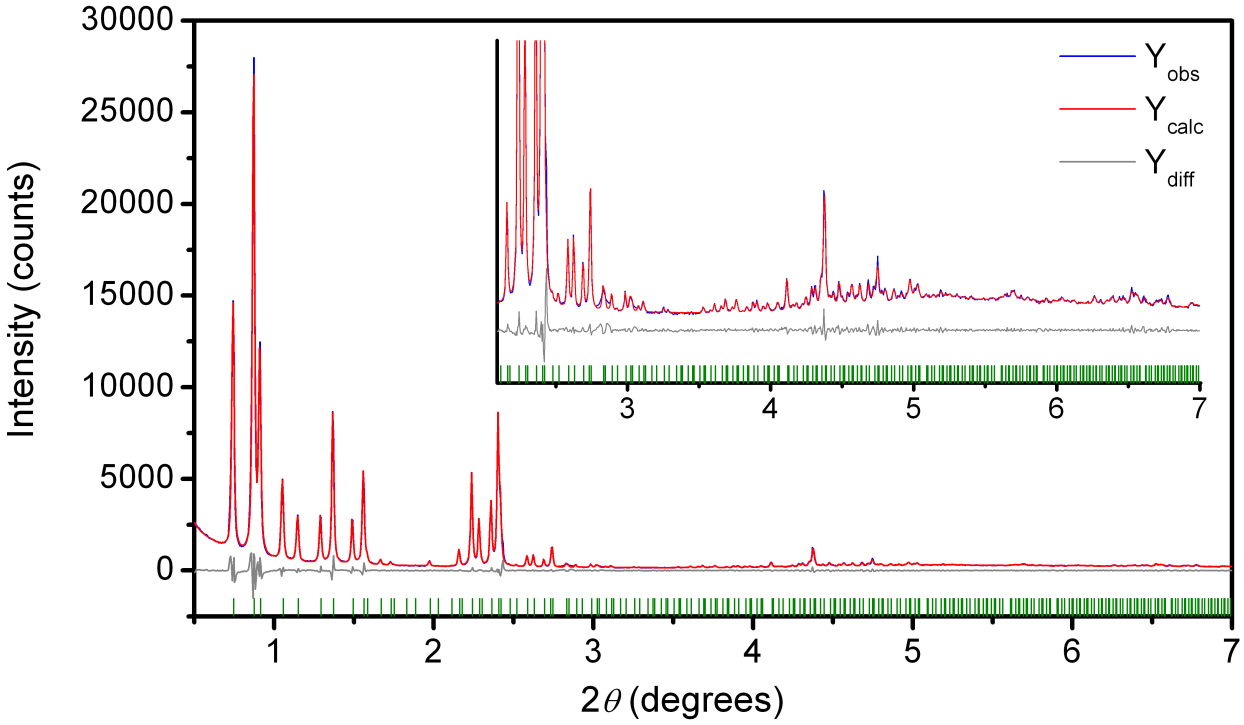

Figure 6.S13. Le Bail refinement of **1** activated at 150 °C. Blue and red lines represent the observed and calculated diffraction patterns, respectively. The gray line represents the difference between observed and calculated patterns, and the green tick marks indicate calculated Bragg peak positions. The inset shows the high angle region at a magnified scale. $R_{wp} = 5.6\%$, $R_p = 4.1\%$. The wavelength was 0.41397 Å.

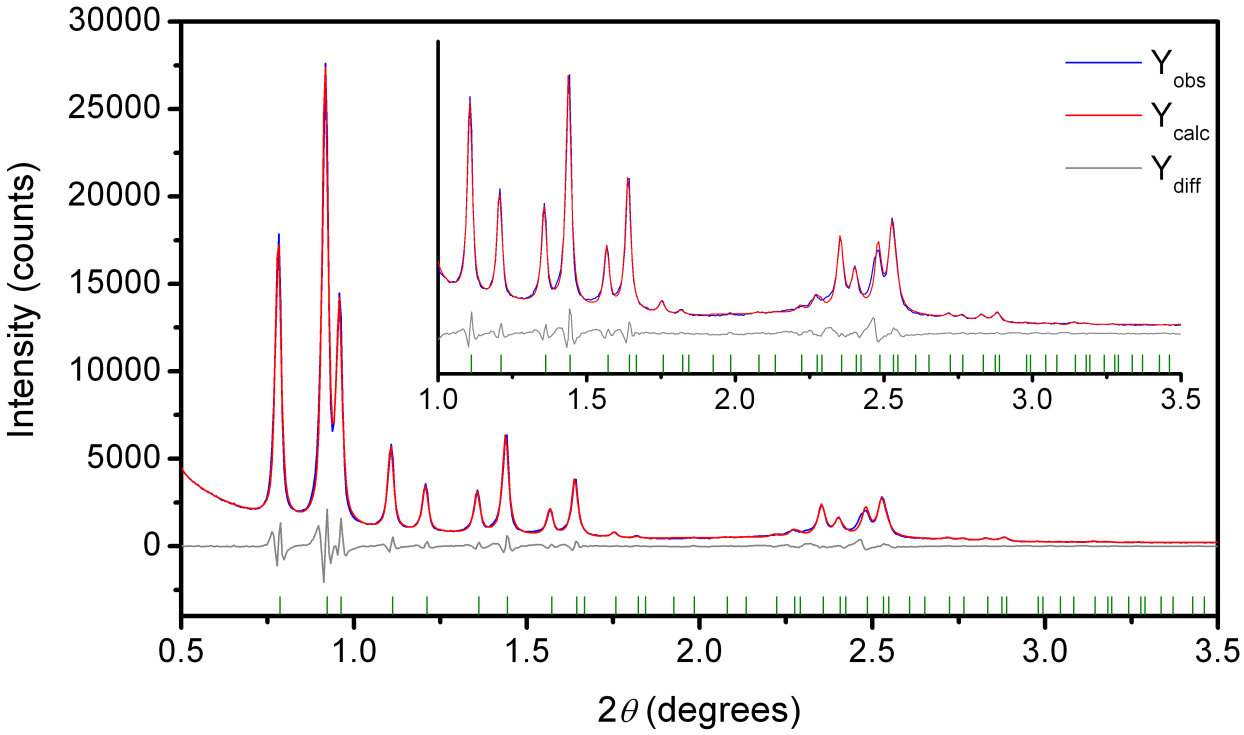

Figure 6.S14. Le Bail refinement of **1** after O_2 adsorption at –78 °C. Blue and red lines represent the observed and calculated diffraction patterns, respectively. The gray line represents the difference between observed and calculated patterns, and the green tick marks indicate calculated Bragg peak positions. The inset shows the high angle region at a magnified scale. R_{wp} = 6.5%, R_p = 5.0%. The wavelength was 0.41397 Å. Note that the O_2-dosed sample exhibited a small loss in crystallinity, with much weaker diffraction peaks observed at higher angles.

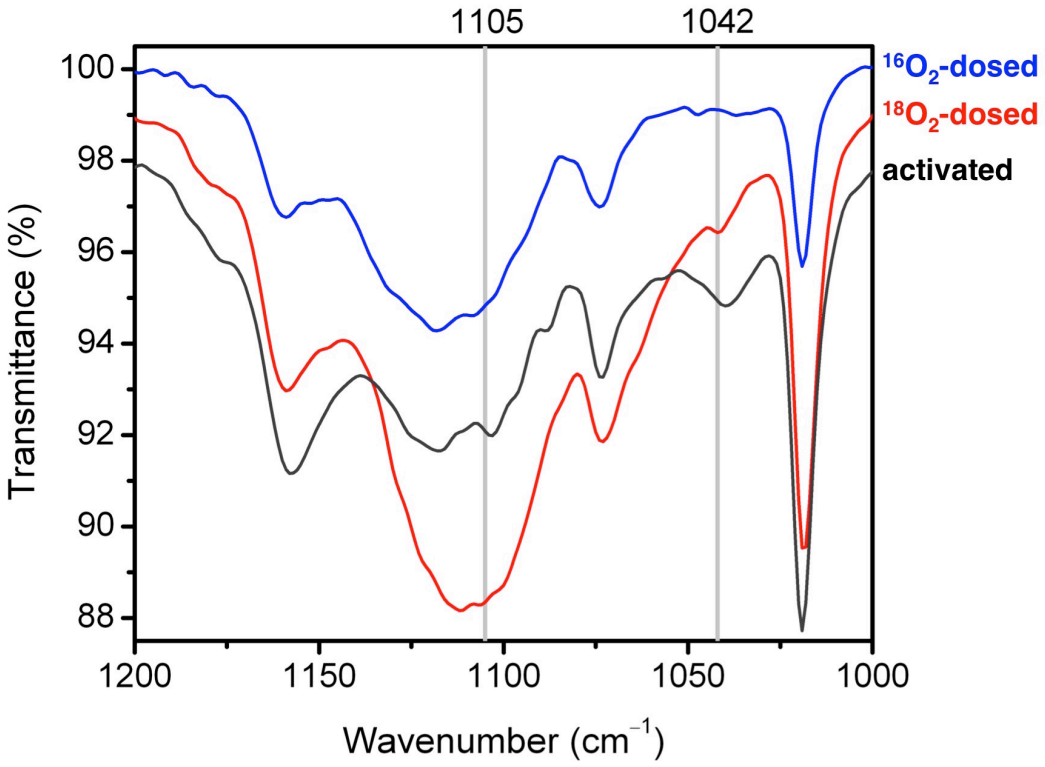

Figure 6.S15. Infrared spectra for **1** activated, dosed with $^{16}O_2$ at –78 °C, and dosed with $^{18}O_2$ at –78 °C. There is a new band observed in the $^{18}O_2$-dosed sample at 1042 cm^{-1}. Based on a simple harmonic oscillator model, a band would be expected in the $^{16}O_2$-dosed spectrum at 1105 cm^{-1}.

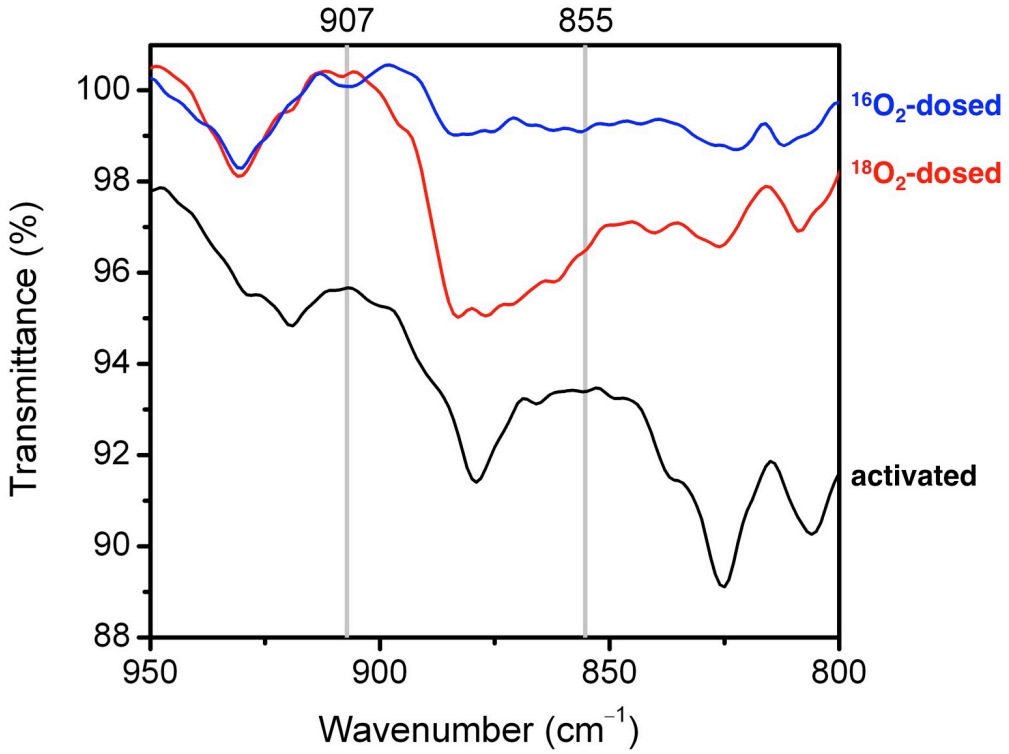

Figure 6.S16. Infrared spectra for **1** activated, dosed with $^{16}O_2$ at –78 °C, and dosed with $^{18}O_2$ at –78 °C. There is a new band observed in the $^{16}O_2$-dosed sample at 907 cm^{-1}. Based on a simple harmonic oscillator model, a band would be expected, and is indeed observed, in the $^{18}O_2$-dosed spectrum at 855 cm^{-1}.

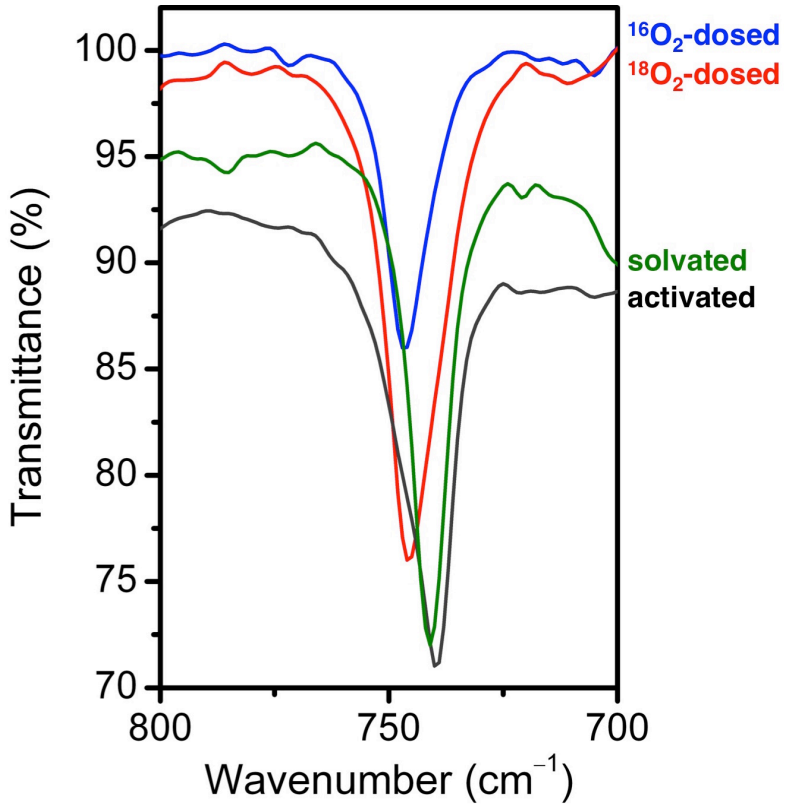

Figure 6.S17. Infrared spectra for **1** solvated, activated, dosed with $^{16}O_2$ at −78 °C, and dosed with $^{18}O_2$ at −78 °C highlighting changes in the $\upsilon_{asym}(Ti_3O)$ vibration.

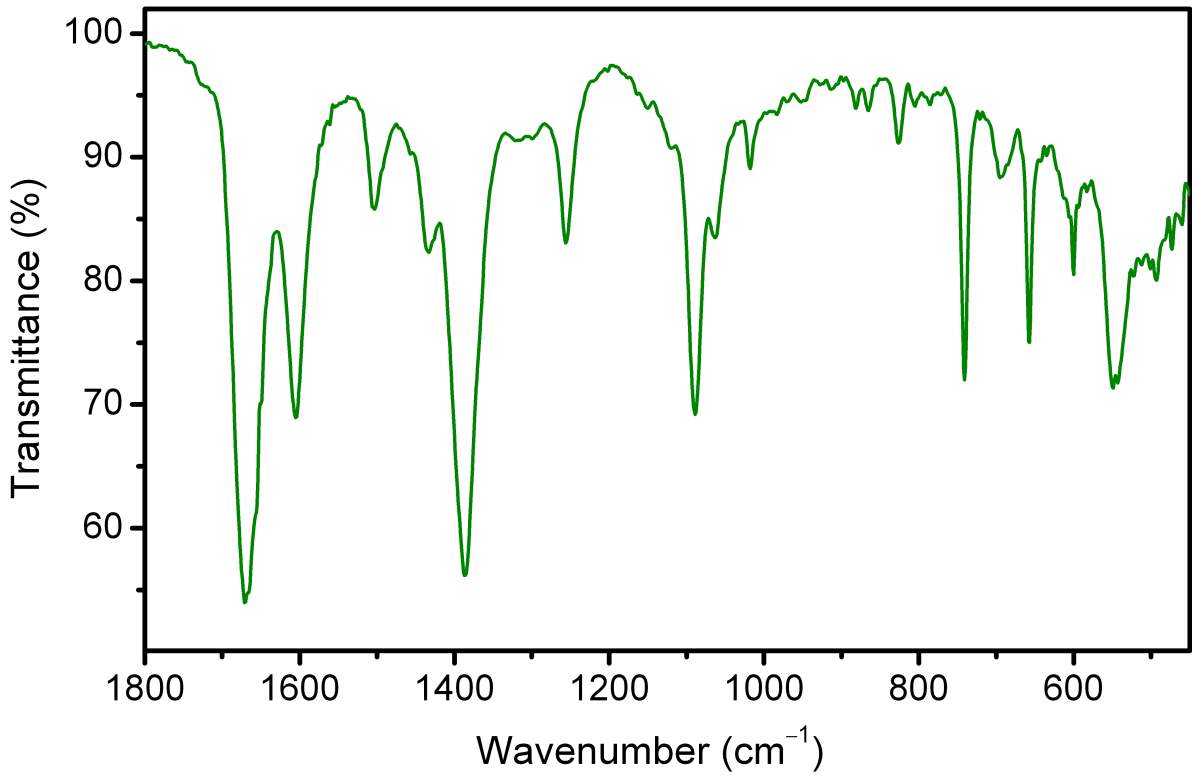

Figure 6.S18. Full infrared spectrum for **1** solvated with DMF.

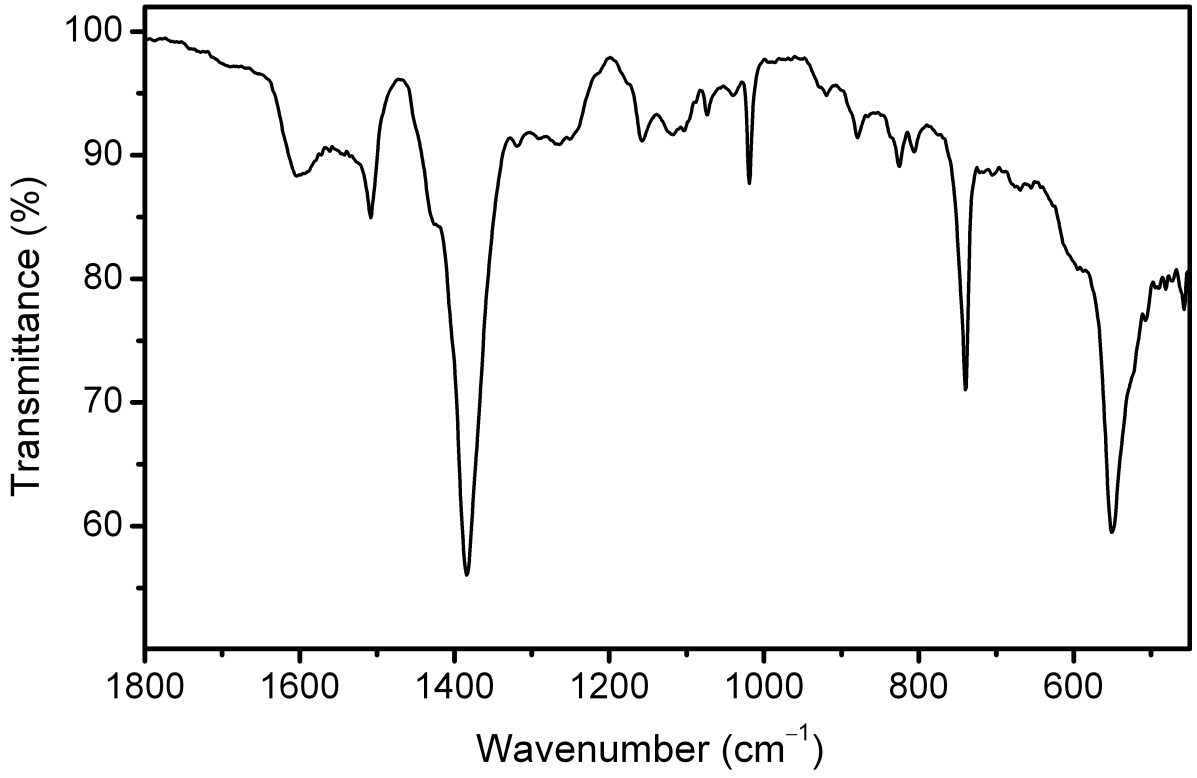

Figure 6.S19. Full infrared spectrum for **1** after activation at 150 °C.

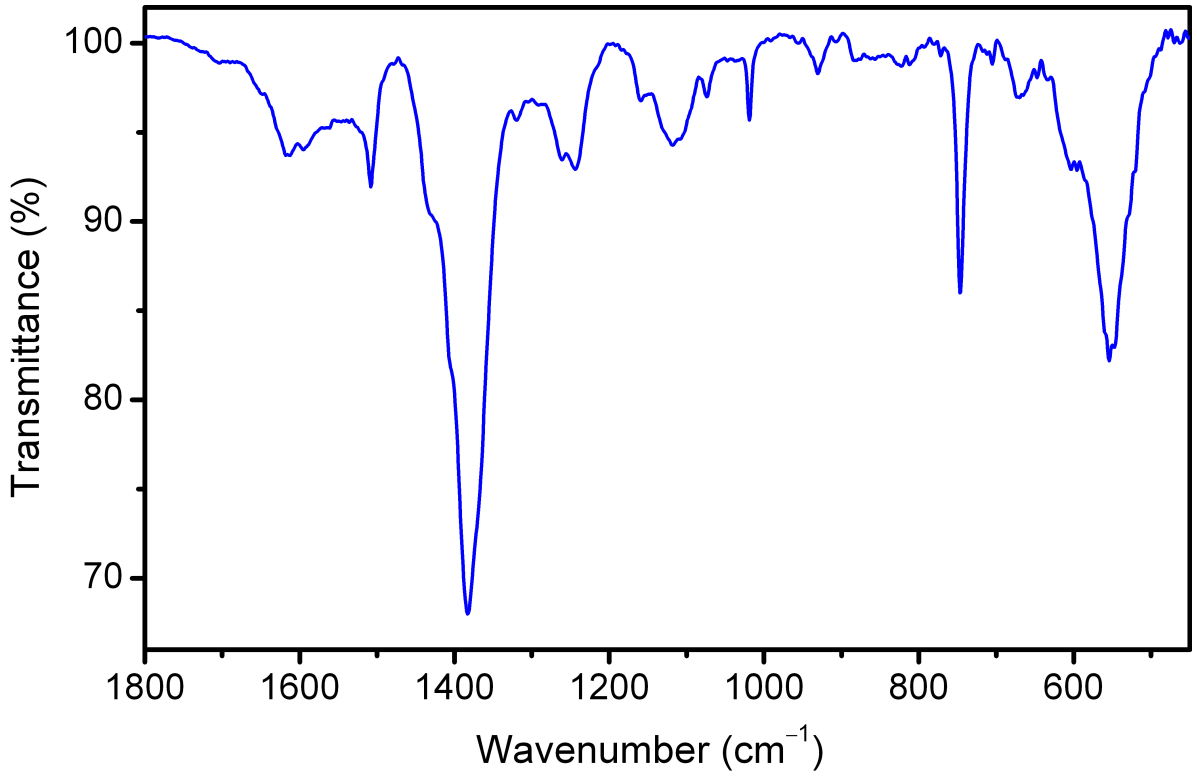

Figure 6.S20. Full infrared spectrum for **1** after dosing with $^{16}O_2$ at −78 °C.

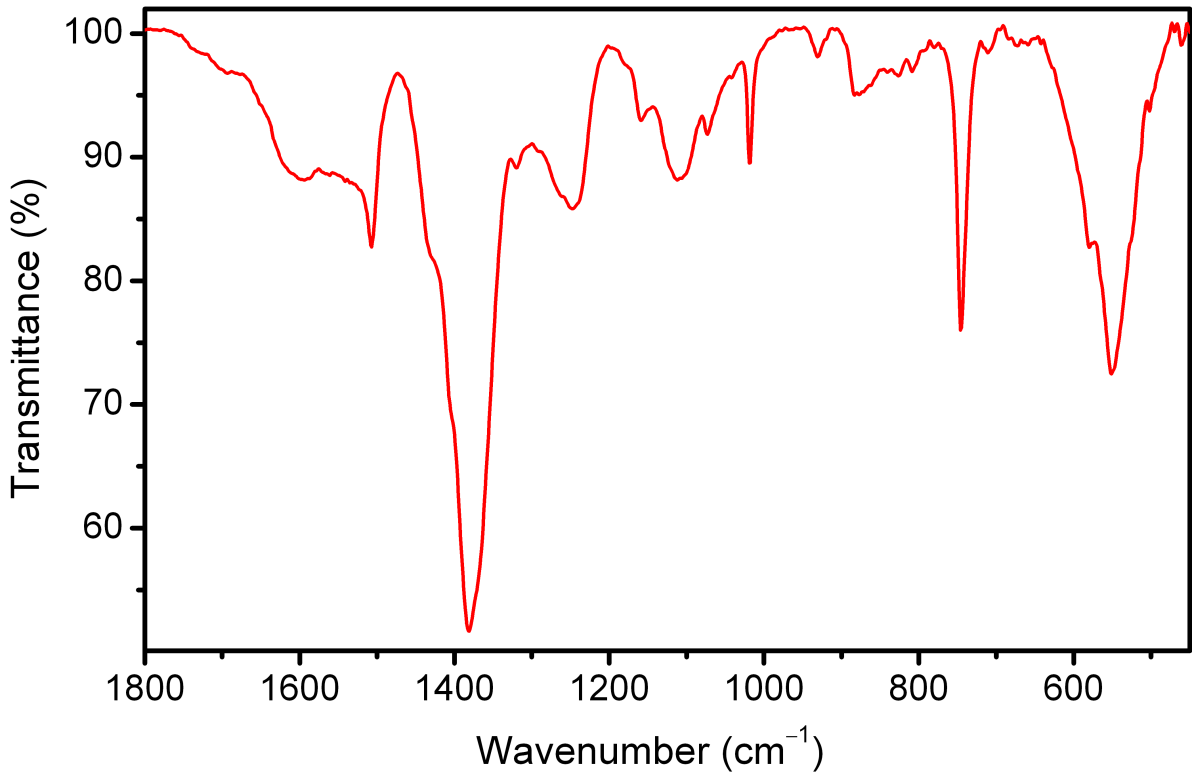

Figure 6.S21. Full infrared spectrum for **1** after dosing with $^{18}O_2$ at −78 °C.

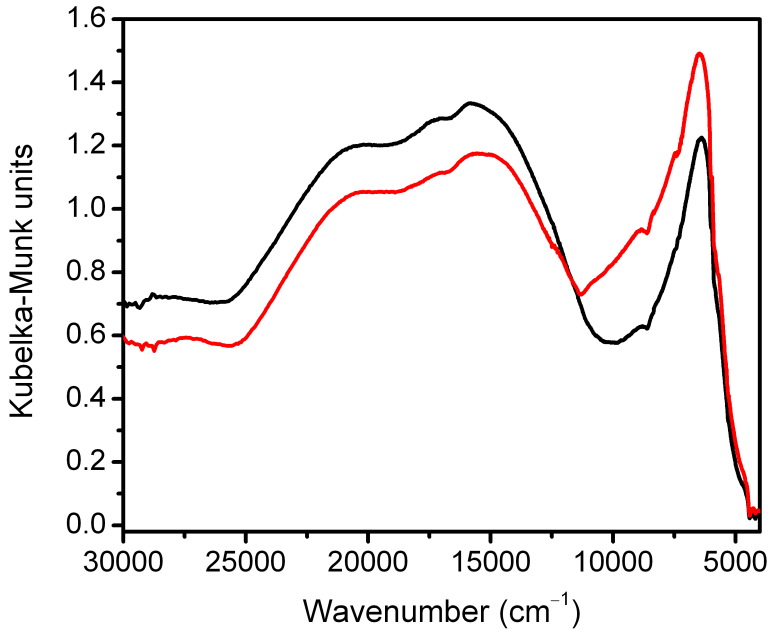

Figure 6.S22. Full diffuse reflectance UV-Vis-NIR for **1** solvated (green), activated at 150 °C (black), and after dosing with O_2 at –78 °C (blue).

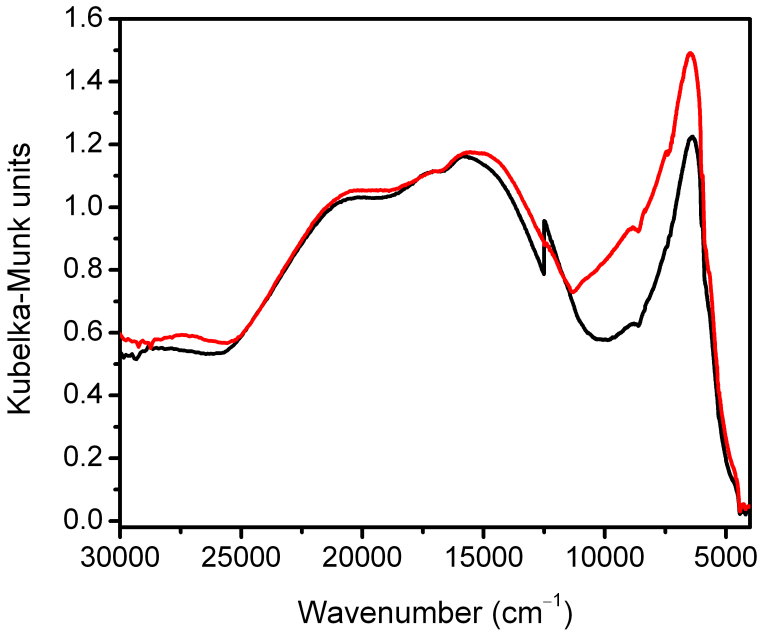

Figure 6.S23. Diffuse reflectance UV-Vis-NIR for **1** activated at 150 °C before (black) and after (red) THF exchanges.

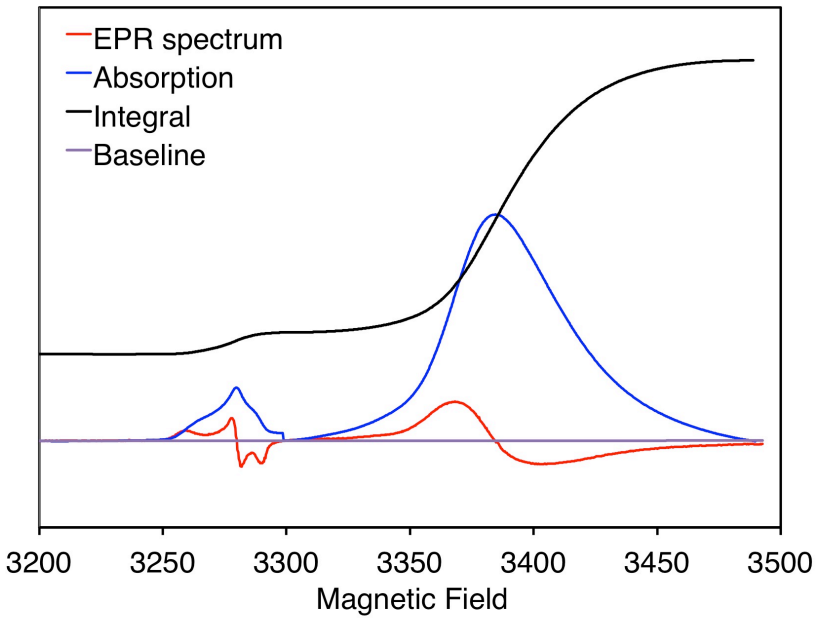

Figure 6.S24. Double integration of the EPR spectrum of **1** dosed with O_2 at −78 °C.

Appendix A: Structure Solution and Thermodynamics of Co-operative CO_2 Insertion in mmen-M_2(dobpdc)

A.1. Introduction

Exceeding 13 gigatons annually,[1] carbon dioxide generated from the combustion of fossil fuels for heat and electricity production is a major contributor to climate change and ocean acidification.[2,3] Implementation of carbon capture and sequestration technologies has been proposed as a means of enabling the continued use of fossil fuels in the near term, while renewable energy sources gradually replace our existing infrastructure.[4] The removal of CO_2 from low-pressure flue gas mixtures is presently effected by aqueous amine solutions that are highly selective for acid gases[5]. As a result of the large energy penalty for desorbing CO_2 from such liquids, solid adsorbents with significantly lower heat capacities are frequently proposed as promising alternatives.[6,7] In particular, owing to their high surface areas and tunable pore chemistry, the separation capabilities of certain metal-organic frameworks have been shown to meet or exceed those achievable by zeolite or carbon adsorbents.[8-10]

Recently, the attachment of alkyldiamines to coordinatively-unsaturated metal sites lining the pores of selected metal-organic frameworks has been demonstrated as a facile methodology for increasing low pressure CO_2 adsorption selectivity and capacity.[11-14] Most notably, functionalization of Mg_2(dobpdc) (dobpdc^{4-} = 4,4′-dioxidobiphenyl-3,3′-dicarboxylate), an expanded variant of the well-studied metal-organic framework Mg_2(dobdc) (dobdc^{4-} = 2,5-dioxidobenzene-1,4-dicarboxylate),[15-18] with *N*,*N*′-dimethylethylenediamine (mmen) generated an adsorbent with exceptional CO_2 capacity under flue gas conditions and unusual, unexplained step-shaped adsorption isotherms.[13] Here, we use *in situ* powder X-ray diffraction experiments to unambiguously determine the unprecedented mechanism giving rise to these step-shaped isotherms and demonstrate that replacing Mg^{2+} with other divalent metal ions enables the position of the CO_2 adsorption step to be manipulated in accord with the metal-amine bond strength. The resulting mmen-M_2(dobpdc) (M = Mg, Mn, Fe, Co, Zn) compounds, hereby denominated "phase-change" adsorbents, can exhibit highly desirable characteristics that make them superior to other solid or liquid sorbents for the efficient capture of CO_2.

A.2. Experimental

Samples of mmen-M_2(dobpdc) were synthesized and activated according to literature procedure.[19]

A.2.1. High-Resolution Powder X-Ray Diffraction. Samples of fully activated mmen-Mn_2(dobpdc) microcrystalline powders (~10 mg) were loaded into 1.0 mm boron-rich glass capillaries inside a glovebox under an N_2 atmosphere. The capillaries were attached to a gas cell, which was connected to the analysis port of a Micromeritics ASAP-2020 gas adsorption instrument. The capillaries were fully evacuated at room temperature for 30 min, dosed with 5 mbar of He [mmen-Mn_2(dobdc)], 5 mbar of CO_2 [100K-CO_2-mmen-Mn_2(dobpdc)], or 100 mbar of CO_2 [295K-CO_2-mmen-Mn_2(dobpdc)] and then equilibrated at room temperature for 15 min, 8 h, or 4 h, respectively. After equilibration, the capillaries were flame-sealed and placed inside a kapton tube that was sealed on both ends with epoxy.

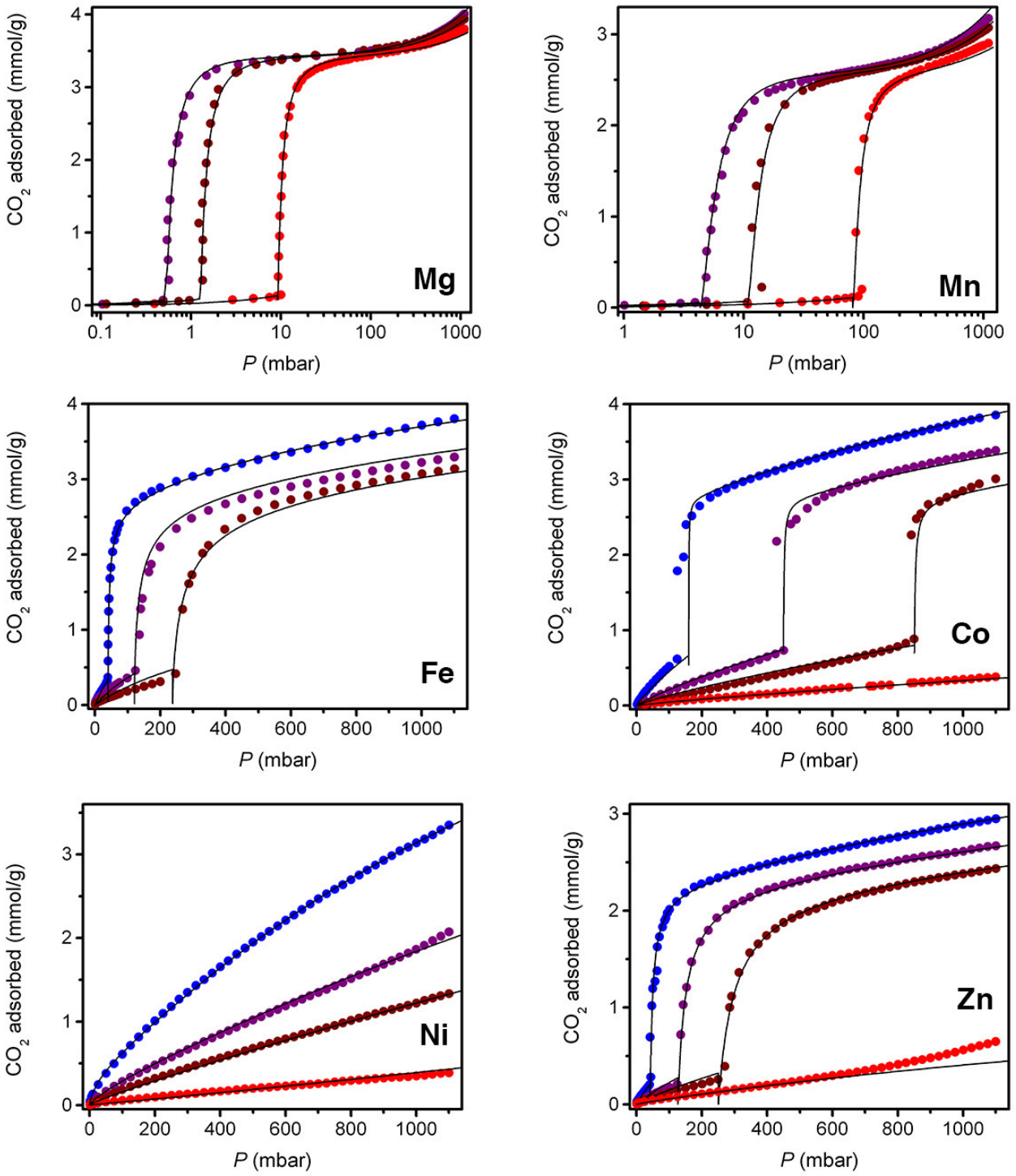

Figure A.1. CO_2 adsorption isotherms for mmen-M_2(dobpdc). Fits to the experimental CO_2 adsorption isotherms series are indicated as black lines (blue: 25 °C; blue-violet: 40 °C; red-violet: 50 °C; red: 75 °C).

High-resolution synchrotron X-ray powder diffraction data were subsequently collected at beamline 11-BM at the Advanced Photon Source (APS), Argonne National Laboratory with an average wavelength of approximately 0.4137 Å. Diffraction patterns were collected at 100 K, 100 K, and 295 K for mmen-Mn_2(dobpdc), 100K-CO_2-mmen-Mn_2(dobpdc), and 295K-CO_2-mmen-Mn_2(dobpdc), respectively. Discrete detectors covering an angular range from −6 to 16º 2θ were scanned over a 34º 2θ range, with data points collected every 0.001° 2θ and a scan speed of 0.01º/s. Note that due to the large number of collected data points, all diffraction patterns were rebinned to a step size of 0.005° 2θ prior to structure solution and Rietveld refinement. Additionally, all diffraction patterns exhibited a high-intensity peak at approximately 1.25° that was roughly 500% more intense than any other diffraction peak. Since this high d-spacing peak does not contribute significant structural information and was heavily biasing all structure solution attempts, all data analysis was performed with a minimum 2θ of 2°.

A standard peak search, followed by indexing through the Single Value Decomposition approach[43], as implemented in TOPAS-Academic,[20] allowed the determination of approximate unit cell parameters. Tentatively, the space groups for both mmen-Mn_2(dobpdc) and CO_2-mmen-Mn_2(dobpdc) were assigned as $P3_221$ since the framework was expected to be isostructural to Zn_2(dobpdc), which was previously characterized by single crystal X-ray diffraction.[13] Precise unit cell dimensions were determined by structureless Le Bail refinements (Table A.S1). Here, the background was modeled by a polynomial function of the Chebyshev type, and anisotropic peak broadening was described using parameters appropriate for a hexagonal crystal system.[21] Successful structure solution and Rietveld refinement confirmed that $P3_221$ was indeed the correct space group for all compounds.

A.2.2. Low-Pressure Gas Adsorption Measurements. For all low-pressure (0-1.1 bar) gas adsorption measurements, 60-130 mg of adsorbent was transferred to a pre-weighed glass sample tube under an atmosphere of nitrogen gas and capped with a Transeal. Samples were then manually transferred to a Micromeritics ASAP 2020 gas adsorption analyzer and heated to the activation temperatures previously specified under vacuum. The sample was considered activated when the outgas rate was less than 2 μbar / min. The evacuated tube containing the activated sample was then transferred to a balance and weighed to determine the mass of the desolvated sample. The tube was then manually placed on the analysis port of the aforementioned instrument where the outgas rate was once again confirmed to be less than 2 μbar / min. Isothermal conditions were maintained at 77 K with liquid N_2, at 25, 40, 50, and 75 °C with a Julabo F32 water circulator, and 100 °C with a heated sand bath controlled by a programmable temperature controller.

A.3. Results and Discussion

A.3.1. Structure Solution and Rietveld Refinement of mmen-Mn_2(dobpdc). Initially, the previously reported crystal structure of the isostructural Zn_2(dobpdc),[13] with the Zn atoms replaced by Mn atoms, was used to calculate a Fourier difference map for mmen-Mn_2(dobpdc). While the Fourier difference maps revealed excess electron density above each Mn site as expected, it was not possible to definitively locate the individual atoms of the appended mmen groups using standard Fourier difference methods. This is a common occurrence when solving crystal structures from powder diffraction data and is primarily due to the significant overlap of intensity from Bragg reflections that occur at nearly, and often exactly, identical diffraction

angles. As a result, direct space methods are often necessary to develop a structural model that can be used for Rietveld refinement. This is particularly true when a large number of atoms need to be found, as is the case for both mmen-Mn_2(dobpdc) and CO_2-mmen-Mn_2(dobpdc).

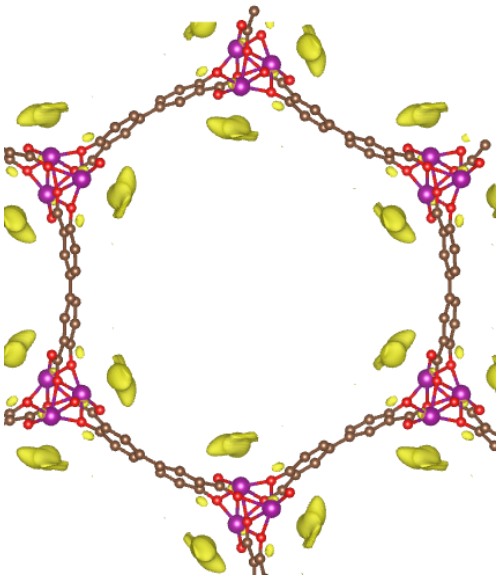

Figure A.2. Fourier difference map for mmen-Mn_2(dobpdc) at 100 K. Purple, brown, and red spheres represent Mn, C, and O atoms, respectively. Yellow blobs represent excess electron density that is not accounted for in the Mn_2(dobpdc) structural model and that is due to the mmen bound to each Mn^{2+} site.

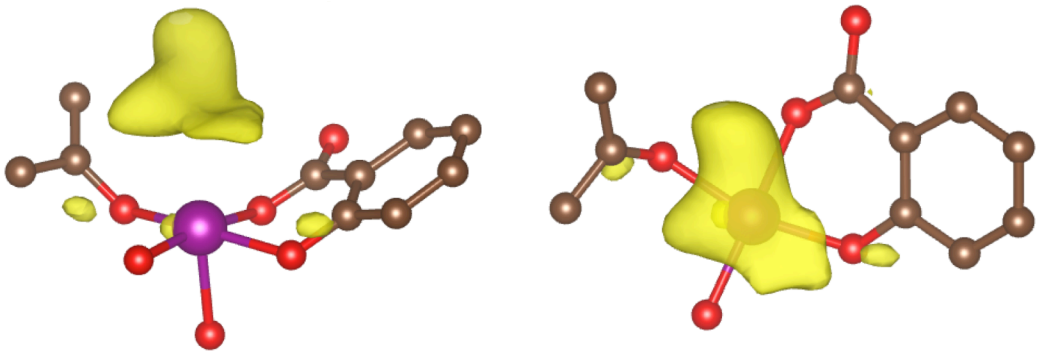

Figure A.3. Additional views of the Fourier difference map for mmen-Mn_2(dobpdc) at 100 K. Purple, brown, and red spheres represent Mn, C, and O atoms, respectively. Yellow blobs represent excess electron density that is not accounted for in the Mn_2(dobpdc) structural model and that is due to the mmen bound to each Mn^{2+} site.

Here, the structure solution of mmen-Mn_2(dobpdc) at 100 K was performed in direct space using the simulated annealing technique, as implemented in TOPAS-Academic. During the simulated annealing process, a rigid, idealized model was employed for the full mmen ligand and for the crystallographically independent portion of the dopbdc^{4-} moiety (one-half ligand). For the mmen rigid body, three dihedral angles were randomized during simulated annealing. In order to

arrive at a chemically reasonable structural model for mmen-Mn_2(dobpdc), additional structural information, including distance restraints and "anti-bump" penalties, were incorporated into the simulated annealing search for a global minimum.

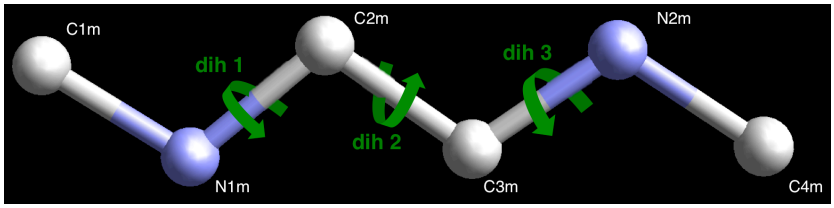

Figure A.4. Rigid body of mmen complex used during the structure solution of mmen-Mn_2(dobpdc). During the simulated annealing process, the three dihedral angles shown above (dih 1-3) were randomized, as was the position (x, y, z) and orientation (α, β, γ) of the entire rigid body. Gray and blue spheres represent C and N atoms, respectively; H atoms are omitted for clarity.

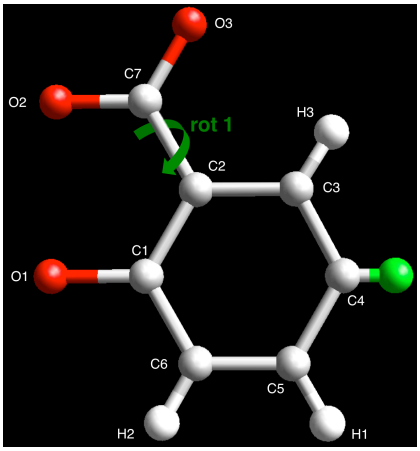

Figure A.5. Rigid body for ½ of the dobpdc ligand, which was used during the structure solution of both mmen-Mn_2(dobpdc) CO_2-mmen-Mn_2(dobpdc). Bond distances and angles were initially fixed to the values that were determined from a single crystal structure of Zn_2(dobpdc) (*13*). During the simulated annealing process, the position (x, y, z) and orientation (α, β, γ) of the rigid body was fixed to that of Zn_2(dobpdc). During the Rietveld refinement, the position and orientation of the rigid body were refined, as were the rotation angle of the carboxylate (Rot 1) and all C−C bond distances. Gray, red, and white spheres represent C, O, and H atoms, respectively. Note that the green sphere is a dummy atom (zero occupancy) used to fix the center of mass of the full dobpdc^{4-} ligand during the simulated annealing process.

Once an initial structural model was developed, a complete refinement was preformed using the Rietveld method, maintaining the rigid bodies for mmen and dobpdc^{4-} during the refinement process. Note that, in contrast to the CO_2-mmen-Mn_2(dobpdc) compound, the diffraction data was not of sufficient quality at high angles to allow for the independent refinement of all atomic positions. Instead, the three dihedral angles of mmen (dih 1-3) were fully refined, as was the position (x, y, z) and orientation (α, β, γ) of the mmen and dobpdc^{4-} rigid bodies. Additionally,

the rotation angle of the carboxylate (rot 1) and all C−C bond distances in the dobpdc^{4-} rigid body were fully refined, as was the Mn atomic position.

A single refined isotropic thermal parameter was assigned to the Mn atom and was free to vary. A single isotropic thermal parameter was assigned to all atoms of the dobpdc^{4-} ligand and was refined with no constraints. With the exception of the metal-bound N atom of mmen (N1m), a single isotropic thermal parameter was assigned to all other mmen atoms, which was refined with no constraints. Note that the fractional occupancies of each mmen atom were constrained to be the same, and the total mmen occupancy was refined. During the initial stages of the Rietveld refinement, excess electron density was observed near the metal-bound N atom of mmen (N1m) and was located at a distance typical of an N−C single bond. This excess electron density was attributed to disorder of the CH_3 bound to N1m since N1m becomes a stereocenter after binding to Mn. This disorder was subsequently modeled with the CH_3 group bound to N1m being disordered over two sites C1ma and C1mb. The total occupancy of the disordered CH_3 groups was constrained to be equal to the total mmen occupancy, but the relative occupancies of each site were free to vary. Finally, all H atoms were constrained to follow the C and N atoms they were bound to, and their atomic positions were not refined independently. The calculated diffraction pattern for the final structural model of mmen-Mn_2(dobpdc) is in excellent agreement with the experimental diffraction pattern.

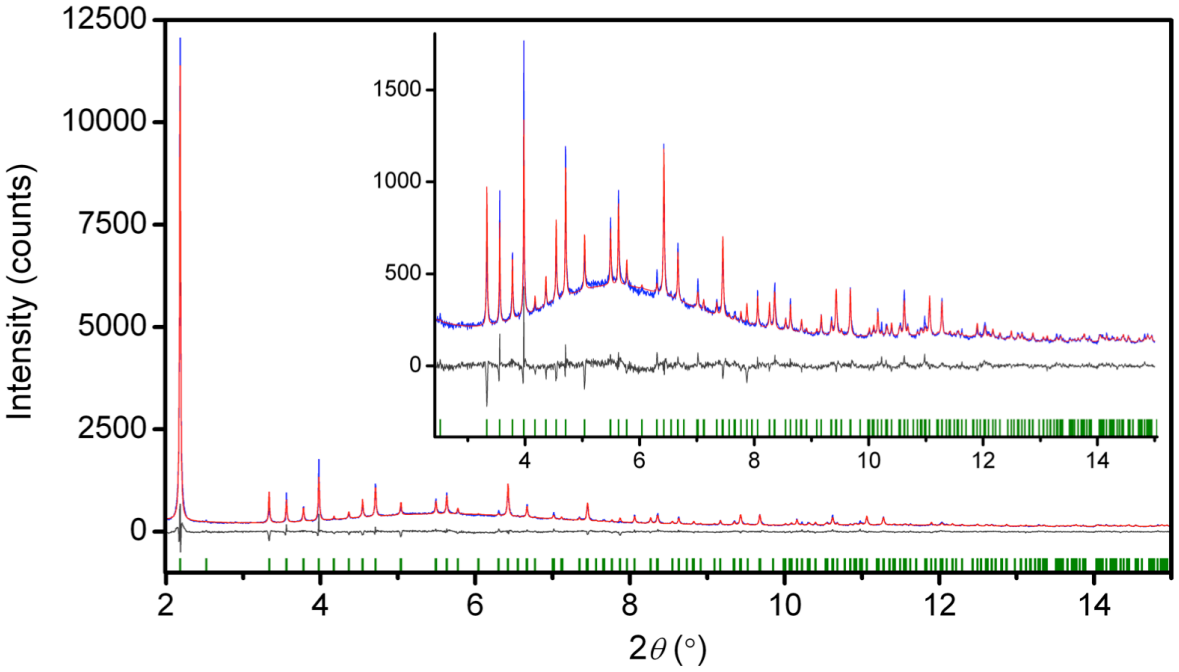

Figure A.6. Rietveld refinement of mmen-Mn_2(dobpdc) at 100 K. This powder diffraction data was obtained from 11-BM at the Advanced Photon Source at Argonne National Laboratory using a wavelength of 0.413735 Å. The blue and red lines represent the experimental and calculated diffraction patterns, respectively. The gray line represents the difference between experimental and calculated patterns. The green tick marks represent the calculated Bragg peak positions.

A.3.2. Structure Solution and Rietveld Refinement of CO_2-mmen-Mn_2(dobpdc). After dosing with CO_2, significant changes in the relative intensities of Bragg diffraction peaks were observed, indicating a structural transition upon CO_2 adsorption (Extended Data Figure 1d). In a manner similar to that described for mmen-Mn_2(dobpdc), the structure solution of CO_2-mmen-Mn_2(dobpdc) at 100 K was performed in direct space using the simulated annealing technique, as implemented in TOPAS-Academic. Based on the IR and solid-state NMR results described earlier, there was strong evidence for the formation of ammonium carbamate upon CO_2 adsorption. As such, a rigid, idealized model was developed for the ammonium carbamate moiety, which was based on the reported single crystal structure of methyl(2-(methylammonio)ethyl)-carbamate.[22] During the simulated annealing process, four dihedral angles of the ammonium carbamate were randomized. In order to arrive at a chemically reasonable structural model for CO_2-mmen-Mn_2(dobpdc), additional structural information, including distance restraints and "anti-bump" penalties, were incorporated into the simulated annealing search for a global minimum.

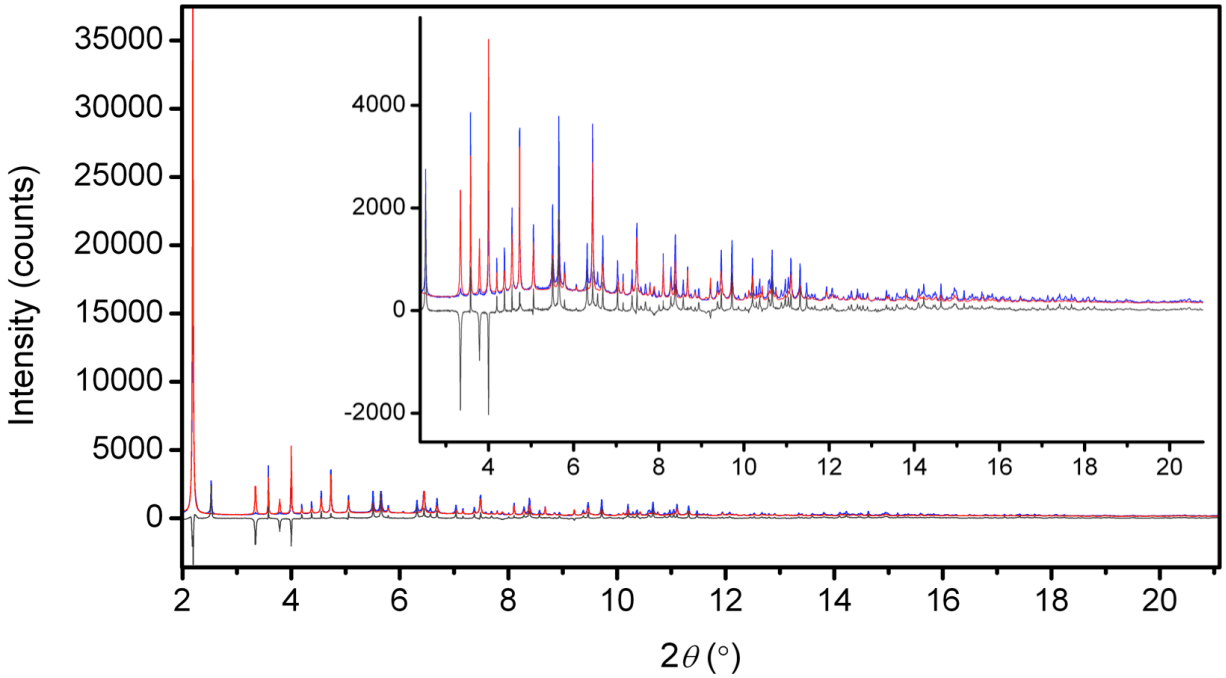

Figure A.7. Plot of the diffraction data for CO_2-mmen-Mn_2(dobpdc) at 100 K (blue), where the calculated pattern (red) is based on the mmen-Mn_2(dobpdc) structural model. The gray line represents the difference between the experimental and calculated patterns. Note that the significant intensity differences indicate a structural transition upon the adsorption of CO_2.

Once an initial structural model was developed, a complete refinement was preformed using the Rietveld method, maintaining the rigid bodies at the initial stages but independently refining all atomic positions in the final cycles of refinement. Note that while the high quality of the diffraction data allowed all atomic positions to be independently refined, a small number of weak C−C and C−N distance restraints were maintained for the purpose of keeping C−C and C−N bond distances within a chemically reasonable range so as to avoid fitting noise in the diffraction

data. With the exception of the dobpdc^{4-} atoms, an independent isotropic thermal parameter was assigned to each C, N, O, and Mn atom, and these parameters were free to vary. A single isotropic thermal parameter was assigned to all atoms of the dobpdc^{4-} ligand and was refined with no constraints. Note that the fractional occupancies of each ammonium carbamate atom were constrained to be the same, and the total occupancy was refined freely. Finally, H atoms were constrained to follow the C and N atoms they were bound to, and their atomic positions were not refined independently.

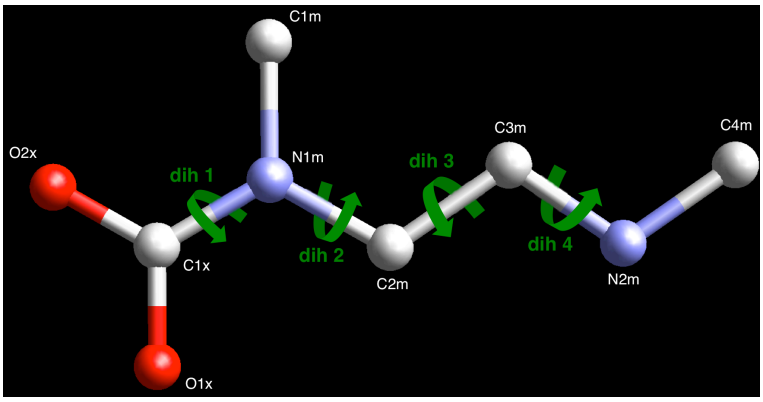

Figure A.8. Rigid body of mmen-CO_2 ammonium carbamate complex used during the structure solution of CO_2-mmen-Mn_2(dobpdc). Bond distances and angles were initially fixed to the values that were determined from a single crystal structure of methyl(2-(methylammonio)ethyl)-carbamate (*21*). During the simulated annealing process, the four dihedral angles shown above (Dih 1-4) were randomized, as was the position (x, y, z) and orientation (α, β, γ) of the entire rigid body. Gray, blue, and red spheres represent C, N, and O atoms, respectively; H atoms are omitted for clarity.

Note that we did not observe any disorder during the refinement process. However, the thermal parameter of the ammonium N atom (N2m) was observed to increase significantly during the refinement. This larger thermal parameter is likely accounting for either thermal motion of the ammonium or a small amount of disorder in the ammonium site position. Since the ammonium has several relatively close interactions with the framework and neighboring carbamate, some disorder or thermal motion might be expected; but regardless, the ESDs of the calculated bond distances are not significantly affected by the large thermal parameter. Additionally, all attempts at modeling any potential disorder with multiple site positions did not improve the overall quality of the refinement, and we opted to capture any disorder by allowing all thermal parameters to vary freely. Most importantly, the calculated diffraction pattern for the final structural model of CO_2-mmen-Mn_2(dobpdc) is in excellent agreement with the experimental diffraction pattern.

A full Rietveld refinement was similarly performed against the diffraction data collected for CO_2-mmen-Mn_2(dobpdc) at 295 K. Initially, the 100 K structural model was used for the refinement, and the calculated diffraction intensities showed excellent agreement with the experimental. Here, a single isotropic thermal parameter was assigned to all atoms of the dobpdc^{4-} ligand and was refined with no constraints. With the exception of the metal-bound O atom of the carbamate (O1m), a single isotropic thermal parameter was assigned to all atoms of the ammonium carbamate and was free to vary. Note that, as expected, all refined thermal

parameters increased moderately compared to the 100 K structure. The refined ammonium carbamate occupancy is slightly higher for the 295 K structure than the 100 K structure due to the higher partial pressure of CO_2 (100 mbar) that was dosed for the 295 K sample (compared to 5 mbar for the 100 K sample). The calculated diffraction pattern for the final structural model of CO_2-mmen-Mn_2(dobpdc) is in excellent agreement with the experimental diffraction pattern, demonstrating that the well-ordered ammonium-carbamate chain structure is maintained at 295 K.

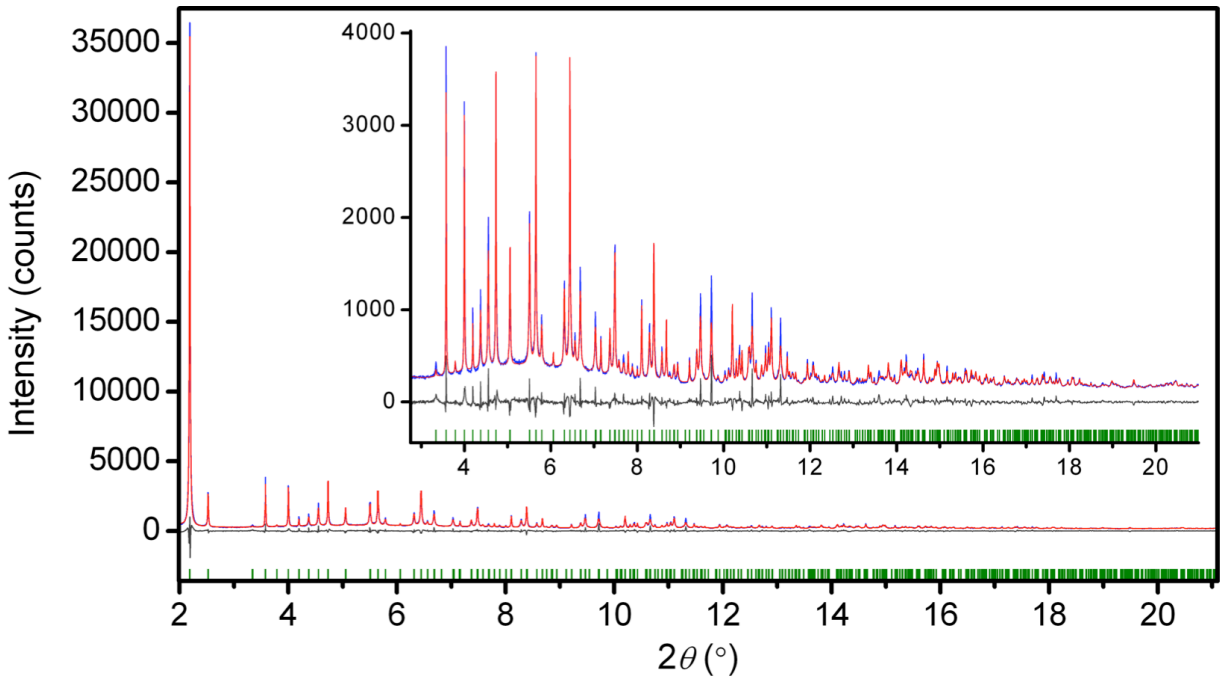

Figure A.9. Rietveld refinement of CO_2-mmen-Mn_2(dobpdc) at 100 K. This powder diffraction data was obtained from 11-BM at the Advanced Photon Source at Argonne National Laboratory using a wavelength of 0.413729 Å. The blue and red lines represent the experimental and calculated diffraction patterns, respectively. The gray line represents the difference between experimental and calculated patterns. The green tick marks represent the calculated Bragg peak positions.

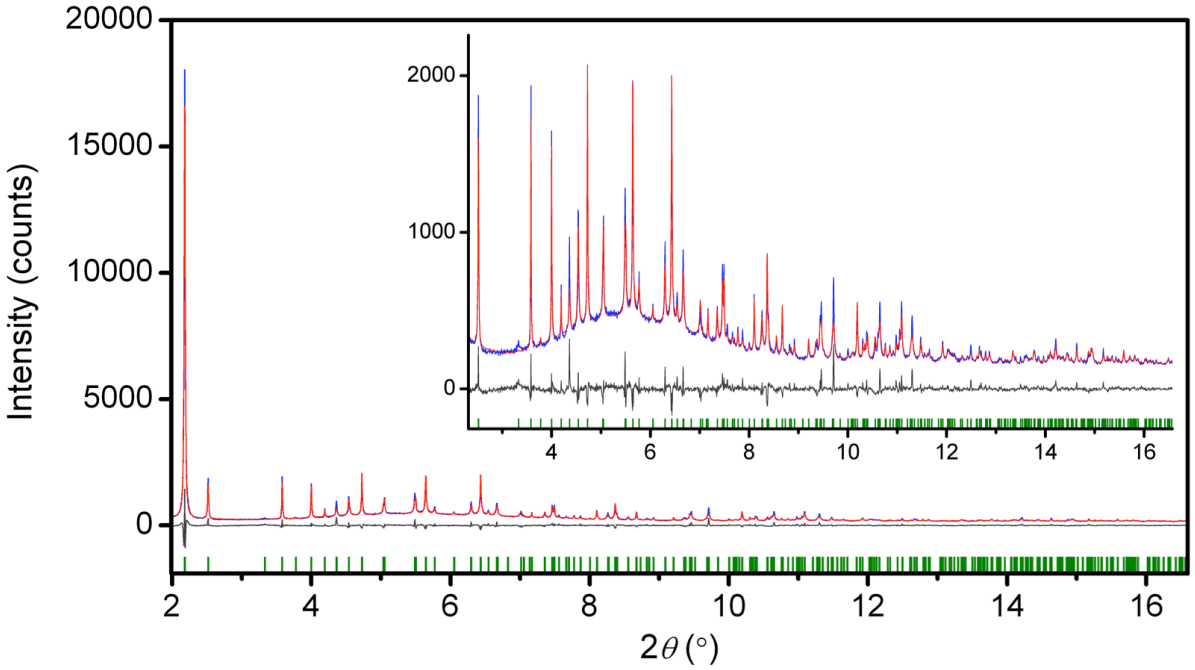

Figure A.10. Rietveld refinement of CO_2-mmen-Mn_2(dobpdc) at 295 K. This powder diffraction data was obtained from 11-BM at the Advanced Photon Source at Argonne National Laboratory using a wavelength of 0.413742 Å. The blue and red lines represent the experimental and calculated diffraction patterns, respectively. The gray line represents the difference between experimental and calculated patterns. The green tick marks represent the calculated Bragg peak positions.

A.3.3. Mechanism of Co-operative CO_2 Insertion. Spectroscopic and diffraction measurements allow the unambiguous determination of the mechanism of CO_2 uptake leading to a steep adsorption step for adsorbents such as mmen-Mg_2(dobpdc). In particular, powder X-ray diffraction studies, which were performed on the isostructural compound mmen-Mn_2(dobpdc) owing to the greater crystallinity of its base framework, provided detailed structural information on how CO_2 binds within the channels of the material. Diffraction data collected at 100 K before and after exposure of a sample to 5 mbar of CO_2 show the unit cell volume to contract by just 1.112(8)%, but revealed significant changes in the relative intensity of selected diffraction peaks. Before CO_2 exposure, the mmen molecules are bound via one amine group to the Mn^{2+} sites with a Mn−N distance of 2.29(6) Å, while the other amine lies exposed on the surface of the framework (Fig. 2c). Counter to our initial assumption that the uncoordinated amine groups would serve to bind CO_2,[13] CO_2 adsorption instead occurs via full insertion into the Mn−N bond, resulting in a carbamate with one O atom bound to Mn at a distance of 2.10(2) Å. Notably, the second O atom of the carbamate has a close interaction of 2.61(9) Å with the N atom of a neighboring mmen, resulting in chains of ammonium carbamate running along the crystallographic *c* axis of the structure. The observed ammonium carbamate N···O distance is similar to the distance of 2.66-2.72 Å in a single crystal of pure mmen-CO_2 (methyl(2-(methylammonio)ethyl)carbamate).[22] Importantly, this well-ordered chain structure is maintained at 295 K, as determined from a full Rietveld refinement against data collected at this temperature. Thus, the adsorption of CO_2 at ambient temperatures is associated with a structural

transition to form an extended chain structure held together by ion-pairing between the metal-bound carbamate units and the outstretched ammonium group of a neighboring mmen molecule.

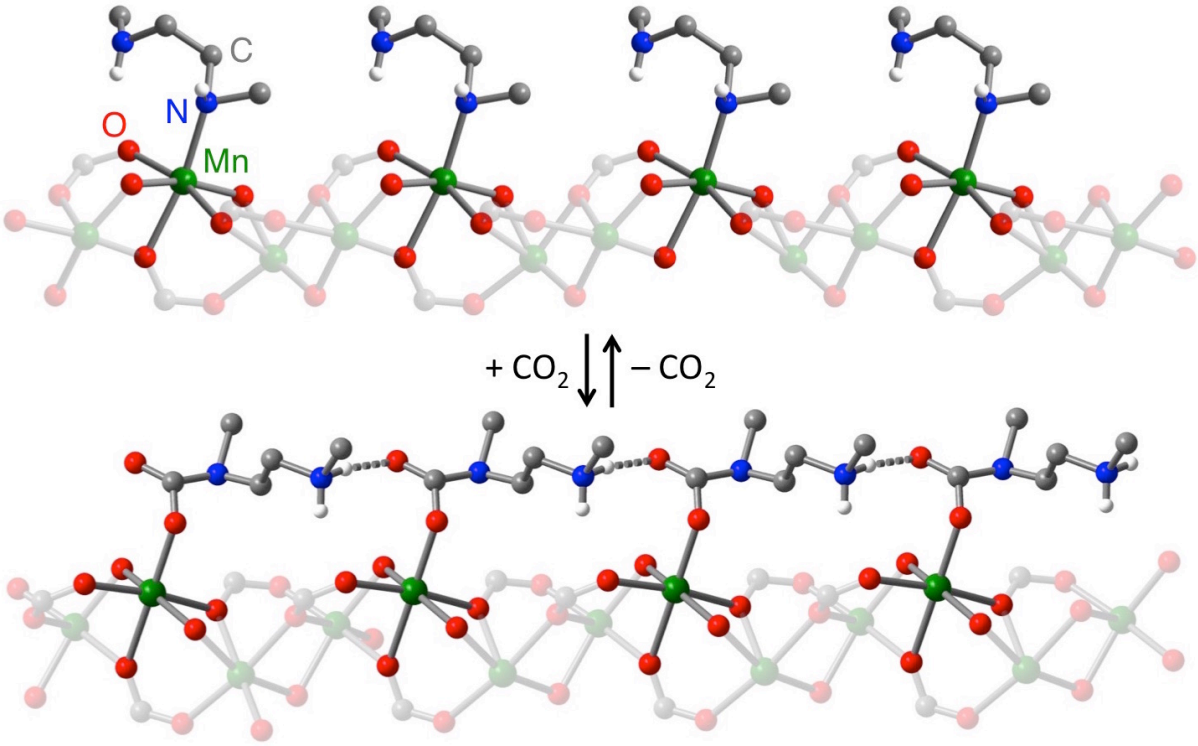

Figure A.11. Structure of mmen-Mn_2(dobpdc) at 100 K. Green, gray, red, blue, and white spheres represent Mn, C, O, N, and H atoms, respectively. This view is along the [100] direction, and the *c* axis runs from left to right.

The foregoing structural information enables formulation of a detailed mechanism for the adsorption of CO_2 in phase change adsorbents of the type mmen-M_2(dobpdc). As shown in Fig. 3, the uncoordinated amine of a mmen molecule acts as a strong base to remove the acidic proton from the metal-bound amine of a neighboring mmen molecule. Deprotonation occurs only in the presence of CO_2, such that simultaneous nucleophilic addition of CO_2 results in the formation of a carbamate with an associated ammonium countercation. At suitable temperatures and pressures, rearrangement of the carbamate is possible such that the M–N bond is broken and a M–O bond is formed. Critically, the ion-pairing interaction causes the mmen molecule to stretch, destabilizing the M–N bond and facilitating insertion at the next metal site. This cooperative effect will propagate until a complete one-dimensional ammonium carbamate chain has formed. Indeed, it is this cooperativity that leads to the sudden uptake of a large amount of CO_2 and a steep vertical step in the adsorption isotherm.

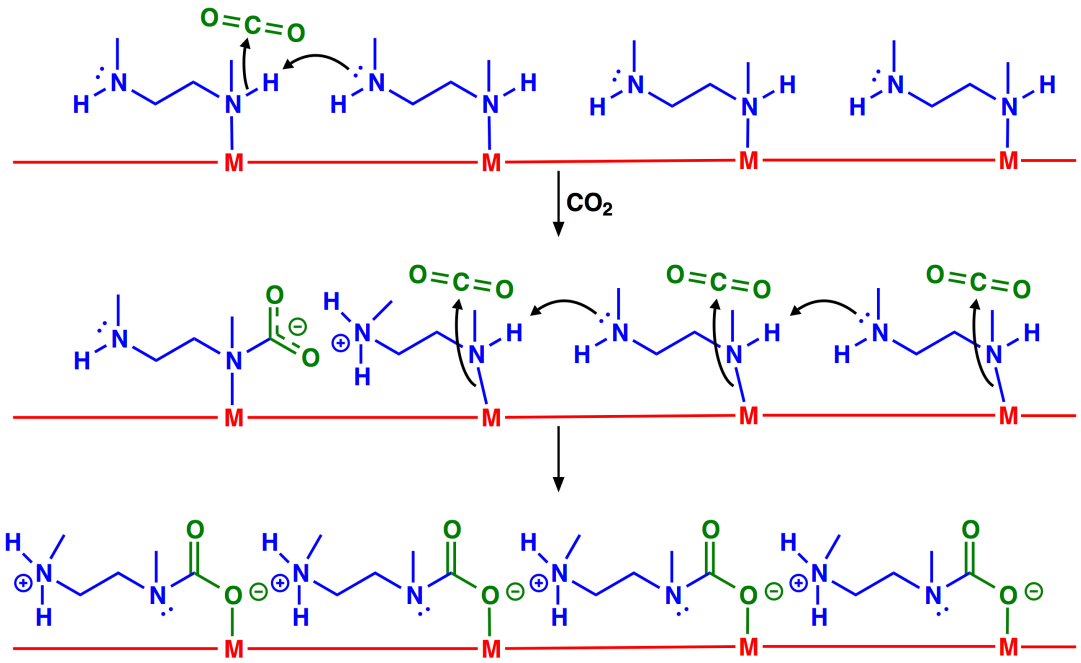

Figure A.12. Depiction of the mechanism for CO_2 adsorption at four neighboring M–mmen sites within an infinite one-dimensional chain of such sites running along the crystallographic *c* axis of a mmen-M_2(dobpdc) compound. Simultaneous proton transfer and nucleophilic attack of N on a CO_2 molecule forms an ammonium carbamate species that destabilizes the amine coordinated at the next metal site, initiating the cooperative adsorption of CO_2 via a chain reaction.

A.3.4. Isotherm Fitting and Isosteric Heats of Adsorption. In order to calculate isosteric heats of adsorption (differential enthalpies), *dH*, as a function of the amount of CO_2 adsorbed, the temperature-dependent adsorption data for each mmen-M_2(dobpdc) compound was fit with a mathematical model. Since mmen-Ni_2(dobpdc) does not have any isotherm steps in the adsorption data measured for this work, the isotherm data was fit with a classical dual-site Langmuir-Freundlich equation. Owing to the sharp step in many of the CO_2 adsorption isotherms, fitting with a continuous function was not possible, and a piecewise function (Eqn A.1) was developed to describe both the pre-step and post-step CO_2 adsorption for all other compounds at each temperature. Specifically, when the pressure, *p*, is less than the step pressure, p_{step}, at a given temperature, *T*, the isotherm is modeled using a classical single-site Langmuir-Freundlich equation where *R* is the ideal gas constant in J mol^{-1} K^{-1}, n_{sat} is the saturation capacity in mmol/g, *S* is the integral entropy of adsorption at saturation in units of R, *H* is the differential enthalpy of adsorption in kJ/mol, and *v* is the Freundlich parameter. When the *p* is greater than p_{step}, the isotherm is modeled using a dual-site Langmuir-Freundlich equation, with two adsorption sites a and b, for which *p* has been offset by p_{step}. The temperature dependence of p_{step} is described using the Clausius-Clapeyron relation (Eqn A.2), as is standard for evaluating the temperature dependence of any phase transition. Here, p_{step} is a function of the step pressure at an initial temperature, $P_{step,T0}$, and the enthalpy of the phase transition that is associated with the step, H_{step}. The stepped CO_2 adsorption isotherms for at least 3 temperatures are fit

simultaneously with one set of parameters for each mmen-M_2(dobpdc) compound. The resulting calculated CO_2 adsorption isotherms agree well with the experimental data. We note that there is a slight discontinuity when p is just above p_{step} and n is less than $n(p_{step})$, but this does not affect the isosteric heat of adsorption calculations.

$$n(P,T) = \begin{cases} \dfrac{n_{sat,1} e^{S_1} e^{-H_1/RT} p^{\nu_1}}{1 + e^{S_1} e^{-H_1/RT} p^{\nu_1}} & \text{if } p \le p_{step} \\ \dfrac{n_{sat,2a} e^{S_{2a}} e^{-H_{step}/RT} \left(p - p_{step}\right)^{\nu_{2a}}}{1 + e^{S_{2a}} e^{-H_{step}/RT} \left(p - p_{step}\right)^{\nu_{2a}}} + \dfrac{n_{sat,2b} e^{S_{2b}} e^{-H_{2b}/RT} \left(p - p_{step}\right)^{\nu_{2b}}}{1 + e^{S_{2b}} e^{-H_{2b}/RT} \left(p - p_{step}\right)^{\nu_{2b}}} & \text{if } p > p_{step} \end{cases} \quad \text{(A.1)}$$

$$p_{step}(T) = p_{step,T_0} e^{\left(\frac{H_{step}}{R}\right)\left(\frac{1}{T_o} - \frac{1}{T}\right)} \quad \text{(A.2)}$$

The isosteric heats of adsorption, or differential enthalpies, can be calculated by solving Eqn A.1 for explicit values of n at a minimum of 3 temperatures. The isosteric heats of adsorption as a function of the amount of CO_2 adsorbed can then be determined using the integrated form of the Clausius-Clapeyron equation (Eqn A.3) by calculating the slope of ln(p) vs 1/T for each loading.

$$(\ln p)_n = \left(\frac{dH}{R}\right)\left(\frac{1}{T}\right) + C \quad \text{(A.3)}$$

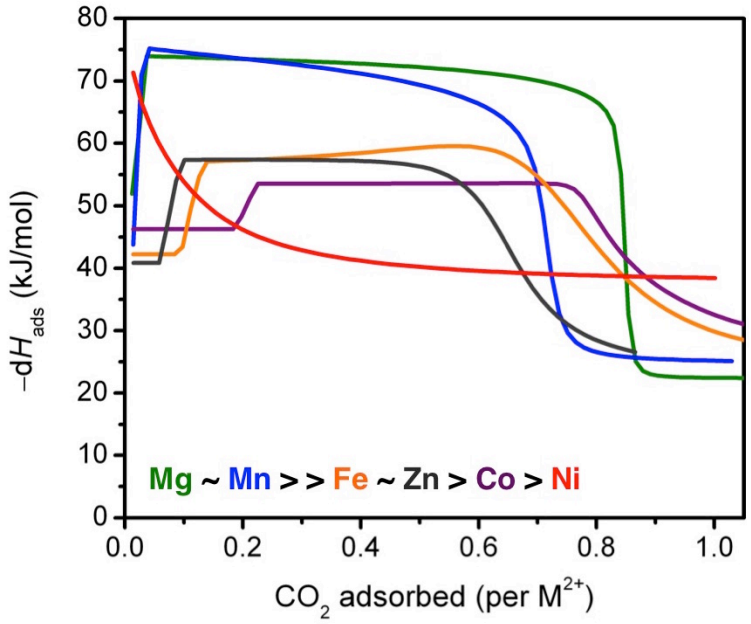

Figure A.13. Differential enthalpies (isosteric heats) of CO_2 adsorption for mmen-M_2(dobpdc).

After calculating the differential enthalpy, *dH*, the differential entropy can be calculated as a function of the amount of CO_2 adsorbed using Eqn A.4.

$$dS = \frac{dH}{T} - \mathrm{R} \ln p \tag{A.4}$$

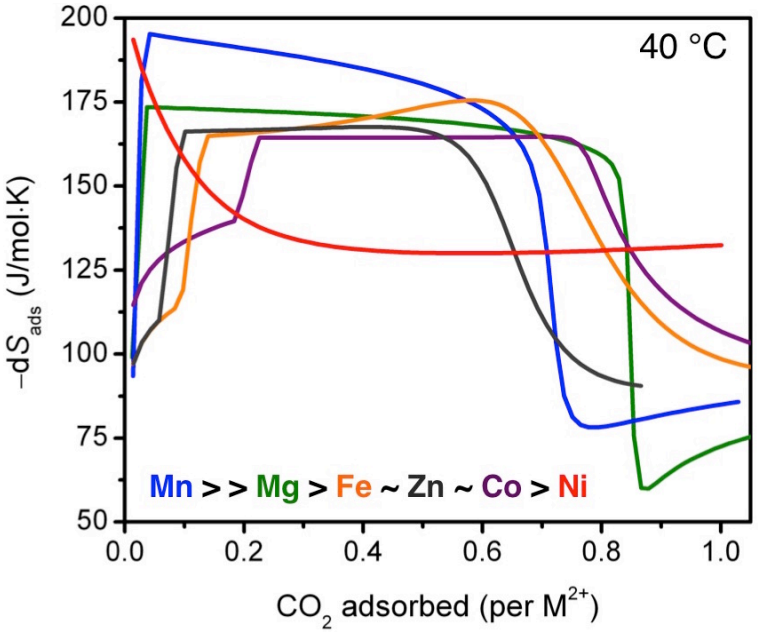

Figure A.14. Differential entropies (isosteric heats) of CO_2 adsorption for mmen-M_2(dobpdc) at 40 °C.

A.4. Outlook and Conclusions

We demonstrate that diamine-appended metal-organic frameworks can behave as "phase-change" adsorbents, exhibiting unusual step-shaped CO_2 adsorption isotherms that shift dramatically with temperature. Based upon spectroscopic, diffraction, and computational studies, the origin of the sharp adsorption step is attributed to an unprecedented cooperative process in which, above a metal-dependent threshold pressure, CO_2 molecules insert into metal-amine bonds, inducing a reorganization of the amines into well-ordered chains of ammonium carbamate. As a consequence, large CO_2 separation capacities can be achieved with small temperature swings, and regeneration energies significantly lower than achievable with state-of-the-art aqueous amine solutions become feasible. The results provide a mechanistic framework for designing highly-efficient adsorbents for removing CO_2 from various gas mixtures.

A.5. Acknowledgments

This research was funded by the Advanced Research Projects Agency-Energy (ARPA-E), U.S. Department of Energy, under Award Numbers DE-AR0000103 and DE-AR0000402. We thank Dr. Lynn Ribaud and the 11-BM staff at the Advanced Photon Source at Argonne National Laboratory for assisting with powder X-ray diffraction experiments. This research used resources of the Advanced Photon Source, a U.S. Department of Energy (DOE) Office of Science User

Facility operated for the DOE Office of Science by Argonne National Laboratory under Contract No. DE-AC02-06CH11357. We thank Dr. Craig Brown for helpful discuss and acknowledge Dr. Thomas McDonald for synthesizing all samples and for contributing to all experiments and data analysis.

A.6. References and Supplementary Figures

(1) International Energy Agency, *CO_2 Emissions from Fuel Combustion: Highlights* (IEA, **2013**; http://www.iea.org/publications/freepublications/publication/CO2EmissionsFromFuelCombustionHighlights2013.pdf).
(2) IPCC, 2013: Summary for Policymakers, in: *Climate Change 2013: The Physical Science Basis. Contribution of Working Group I to the Fifth Assessment Report of the Intergovernmental Panel on Climate Change*, (eds. Stocker, T. F. *et al.*) (Cambridge Univ. Press, New York, **2013**).
(3) Orr, J. C.; Fabry, V. J.; Aumont, O.; Bopp, L.; Doney, S. C.; Feely, R. A.; Gnanadesikan, A.; Gruber, N.; Ishida, A.; Joos, F.; Key, R. M.; Lindsay, K.; Maier-Reimer, E.; Matear, R.; Monfray, P.; Mouchet, A.; Najjar, R. G.; Plattner, G.-K.; Rodger, K. B.; Sabine, C. L.; Sarmiento, J. L.; Schlitzer, R.; Slater, R. D.; Totterdell, I. J.; Weirig, M.-F.; Yamanaka, Y.; Yool, A. *Nature* **2005**, *437*, 681-686.
(4) Haszeldine, R. S. *Science* **2009**, *325*, 1647-1652.
(5) Boot-Handford, M. E. Abanades, J. C.; Anthony, E. J.; Blunt, M. J.; Brandani, S.; Mac Dowell, N.; Fernández, J. R.; Ferrari, M.-C.; Gross, R.; Hallett, J. P.; Haszeldine, R. S.; Heptonstall, P.; Lyngfelt, A.; Makuch, Z.; Mangano, E.; Porter, P. T. J.; Pourkashanian, M.; Rochele, G. T.; Shah, N.; Yago, J. G.; Fennell, P. S. *Energy Environ. Sci.* **2014**, *7*, 130-189.
(6) Choi, S.; Drese, J. H.; Jones, C. W. *Chem. Sus. Chem.* **2009**, *2*, 796-854.
(7) Lin, L. C.; Berger, A. G.; Martin, R. L.; Kim, J.; Swisher, J. A.; Jariwala, K.; Rycroft, C. H.; Bhown, A. S.; Deem, M. W.; Haranczyk, M.; Smit, B. *Nat. Mater.* **2012**, *11*, 633-641.
(8) Sumida, K.; Rogow, D. L.; Mason, J. A.; McDonald, T. M.; Bloch, E. D.; Herm, Z. R.; Bae, T.-H.; Long, J. R. *Chem. Rev.* **2012**, *112*, 724-781.
(9) Zhou, H.C.; Long, J. R.; Yaghi, O. M. *Chem. Rev.* **2012**, *112*, 673-674.
(10) Furukawa, H.; Cordova, K. E.; O'Keeffe, M.; Yaghi, O. M. *Science* **2013**, *341*, 123044.
(11) Demessence, A.; D'Alessandro, D. M.; Foo, M. L.; Long, J. R. *J. Am. Chem. Soc.* **2009**, *131*, 8784-8786.
(12) McDonald, T. M.; D'Alessandro, D. M.; Krishna, R.; Long, J. R. *Chem. Sci.* **2011**, *2*, 2022-2028.
(13) McDonald, T. M.; Lee, W. R.; Mason, J. A.; Wiers, B. M.; Hong, C. S.; Long, J. R. *J. Am. Chem. Soc.* **2012**, *134*, 7056-7065.
(14) Lee, W. R.; Hwang, S. Y.; Ryu, D. W.; Lim, K. S.; Han, S. S.; Moon, D.; Choi, J.; Hong, C. S. *Energy Environ. Sci.* **2014**, *7*, 744-751.
(15) Rosi, N. L.; Kim, J.; Eddaoudi, M.; Chen, B.; O'Keeffe, M.; Yaghi, O. M. *J. Am. Chem. Soc.* **2005**, *127*, 1504-1518.
(16) Dietzel, P. D. C.; Panella, B.; Hirscher, M.; Blom, R.; Fjellvåg, H. *Chem. Commun.* **2006**, 959-961.
(17) Caskey, S. R.; Wong-Foy, A. G.; Matzger, A. J. *J. Am. Chem. Soc.* **2008**, *130*, 10870-10871.

(18) Mason, J. A.; Sumida, K.; Herm, Z. R.; Krishna, R.; Long, J. R. *Energy Environ. Sci.* **2011**, *4*, 3030-3040.
(19) McDonald, T. M.; Mason, J. A.; Kong, X.; Bloch, E. D.; Gygi, D.; Dani, A.; Crocellà, V.; Giordanino, F.; Odoh, S. O; Drisdell, W. S.; Vlaisavljevich, B.; Dzubak, A. L.; Poloni, R.; Schnell, S. K.; Planas, N.; Lee, K.; Pascal, T.; Wan, L. F.; Prendergast, D.; Neaton, J. B.; Smit, B.; Kortright, J. B.; Gagliardi, L.; Bordiga, S.; Reimer, J. A.; Long, J. R. *Nature* **2015**, *519*, 303-308.
(20) Coelho, A. A. TOPAS-Academic, Version 4.1 (Coelho Software, Brisbane **2007**).
(21) Stephens, P. W. *Appl. Cryst.* **1999**, *32*, 281-289.
(22) Tiritiris, I & Kantlehner, W. Orthoamide und Iminiumsalze, LXX [1]. *Z. Naturforsch.* **2011**, *66b*, 164-176.

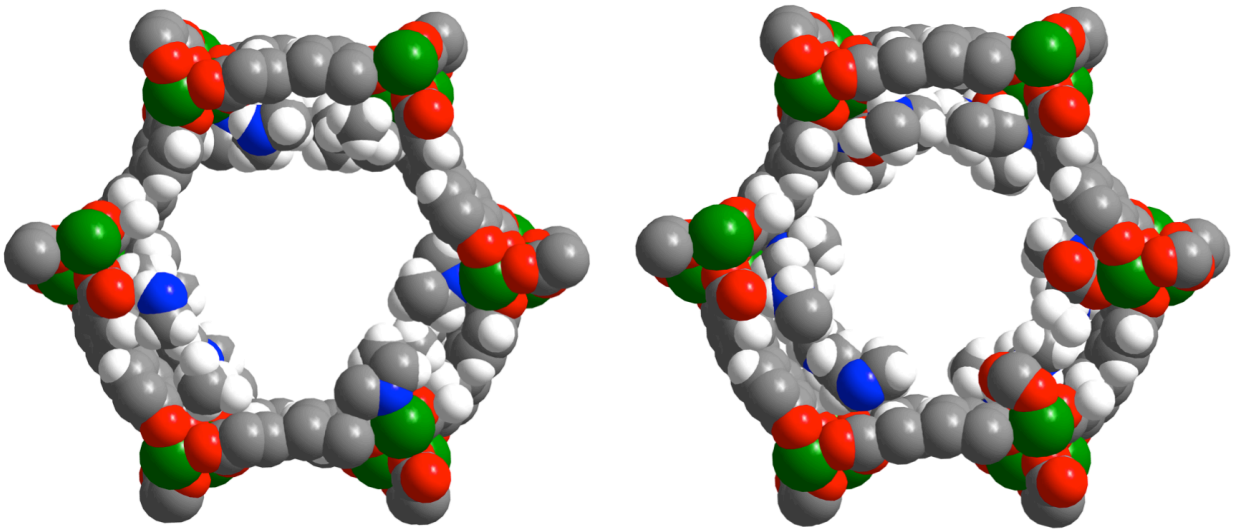

Figure A.S1. Space-filling models of the solid-state structures of mmen-Mn_2(dobpdc) (left) and CO_2-mmen-Mn_2(dobpdc) right at 100 K. Green, gray, red, blue, and white spheres represent Mn, C, O, N, and H atoms, respectively.

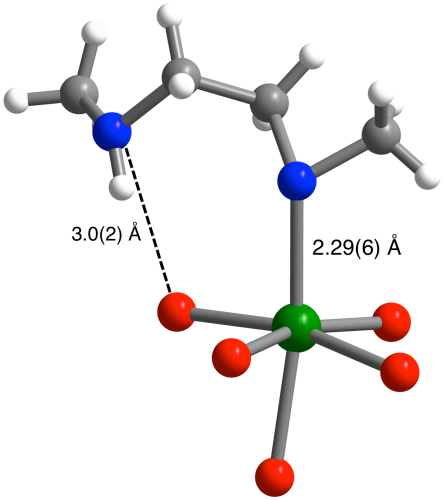

Figure A.S2. The first coordination sphere for the manganese centers in the solid-state structure of mmen-Mn_2(dobpdc) at 100 K. Green, gray, red, blue, and white spheres represent Mn, C, O, N, and H atoms, respectively. Note the Van der Waals contact between the free amine N atom and a non-bridging carboxylate O atom of the dobpdc^{4-} ligand, which is likely responsible for the ordering of the amines at low temperature.

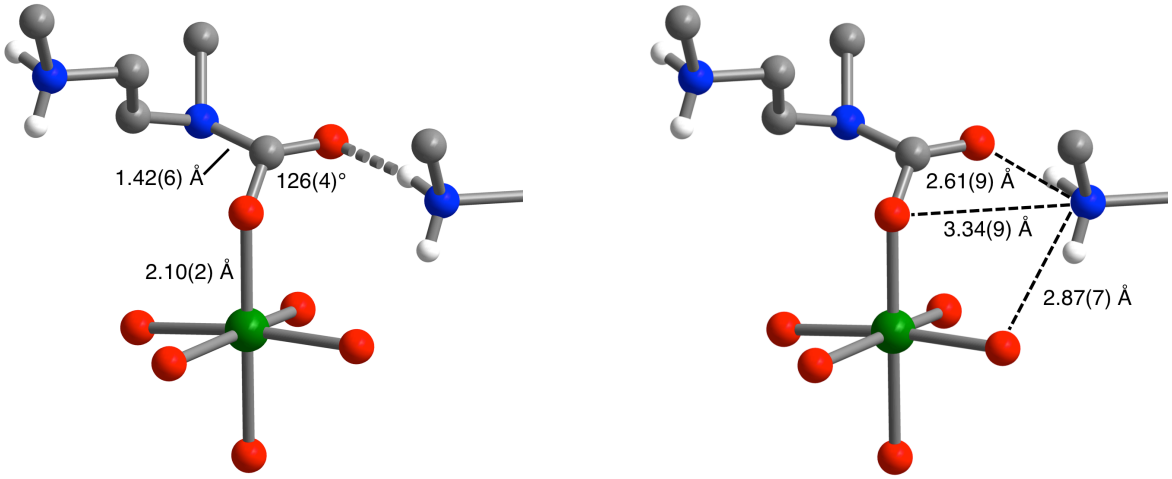

Figure A.S3. The first coordination sphere for the manganese centers in the solid-state structure of CO_2-mmen-Mn_2(dobpdc) at 100 K. Green, gray, red, blue, and white spheres represent Mn, C, O, N, and H atoms, respectively; certain H atoms are omitted for clarity. Note the three Van der Waals contacts between the ammonium N atom and (i) the free O atom of the carbamate, (ii) a non-bridging carboxylate O atom of the dobpdc^{4-} ligand, and (iii) the Mn-bound O atom of the carbamate.

Table A.S1. Unit cell parameters for mmen-Mn_2(dobpdc) and CO_2-mmen-Mn_2(dobpdc).

	a (Å)	*c* (Å)	*V* (Å^3)	*T* (K)	space group
mmen-Mn_2(dobpdc)	21.7291(7)	7.1279(3)	2914.6(2)	100	$P3_221$
CO_2-mmen-Mn_2(dobpdc)	21.6819(4)	7.0794(1)	2882.2(1)	100	$P3_221$
CO_2-mmen-Mn_2(dobpdc)	21.7427(7)	7.0696(2)	2894.4(2)	295	$P3_221$

Table A.S2. Rietveld Refinement of mmen-Mn_2(dobpbdc) dosed with 5 mbar He. Values in parenthesis indicate one standard deviation from the parameter value. Temperature = 100 K, space group $P3_221$, a = 21.7291(7) Å, c = 7.1279(3) Å, V = 2914.6(2) Å^3. Goodness-of-fit parameters: R_{wp} = 5.82%, R_p = 4.52%, χ^2 = 0.907.

atom	*x*	*y*	*z*	*multiplicity*	*occupancy*	U_{iso} (Å^2)
Mn	0.6120(9)	0.2744(9)	1.141(2)	6	1	0.042(5)
O1	0.655(4)	0.241(5)	0.95(1)	6	1	0.075(11)[a]
O2	0.634(3)	0.283(4)	0.62(1)	6	1	0.075(11)[a]
O3	0.586(4)	0.209(3)	0.38(1)	6	1	0.075(11)[a]
C1	0.622(6)	0.175(9)	0.87(2)	6	1	0.075(11)[a]
C2	0.597(6)	0.162(8)	0.67(2)	6	1	0.075(11)[a]
C3	0.565(5)	0.095(7)	0.60(2)	6	1	0.075(11)[a]
C4	0.554(5)	0.035(5)	0.71(2)	6	1	0.075(11)[a]
C5	0.579(5)	0.049(6)	0.90(2)	6	1	0.075(11)[a]
C6	0.613(6)	0.121(7)	0.98(2)	6	1	0.075(11)[a]
C7	0.606(7)	0.221(7)	0.55(2)	6	1	0.075(11)[a]
H1	0.572	0.010	0.98	6	1	0.075(11)[a]
H2	0.629	0.129	1.10	6	1	0.075(11)[a]
H3	0.549	0.088	0.48	6	1	0.075(11)[a]
N1m	0.497(3)	0.208(5)	1.04(1)	6	1.00(5)	0.01(3)
C1ma[b]	0.46(1)	0.25(2)	1.01(6)	6	0.50(15)	0.28(6)[c]
C1mb[b]	0.48(2)	0.20(2)	0.83(7)	6	0.50(15)	0.28(6)[c]
C2m	0.446(96)	0.13(1)	1.04(3)	6	1.00(5)	0.28(6)[c]
C3m	0.396(9)	0.120(8)	1.20(2)	6	1.00(5)	0.28(6)[c]
N2m	0.427(8)	0.118(7)	1.38(2)	6	1.00(5)	0.28(6)[c]
C4m	0.413(9)	0.047(6)	1.43(3)	6	1.00(5)	0.28(6)[c]
H4	0.409	0.216	1.05	6	1.00(5)	0.28(6)[c]
H5	0.479	0.288	1.09	6	1.00(5)	0.28(6)[c]
H6	0.458	0.258	0.88	6	1.00(5)	0.28(6)[c]
H7	0.443	0.200	0.80	6	1.00(5)	0.28(6)[c]
H8	0.525	0.235	0.77	6	1.00(5)	0.28(6)[c]
H9	0.479	0.153	0.80	6	1.00(5)	0.28(6)[c]
H10	0.422	0.116	0.92	6	1.00(5)	0.28(6)[c]
H11	0.472	0.106	1.06	6	1.00(5)	0.28(6)[c]
H12	0.386	0.159	1.20	6	1.00(5)	0.28(6)[c]
H13	0.352	0.076	1.18	6	1.00(5)	0.28(6)[c]
H14	0.467	0.159	1.40	6	1.00(5)	0.28(6)[c]
H15	0.373	0.013	1.35	6	1.00(5)	0.28(6)[c]
H16	0.454	0.043	1.40	6	1.00(5)	0.28(6)[c]
H17	0.401	0.038	1.56	6	1.00(5)	0.28(6)[c]

[a]The thermal parameters for all of atoms of the dobpdc^{4-} ligand were constrained to be equivalent. [b]The CH_3 groups on each Mn-bound N (N1m) are disordered over two positions. [c]With the exception of N1m, the thermal parameters for all atoms of mmen were constrained to be equivalent.

Table A.S3. Rietveld Refinement of 100K-CO_2-mmen-Mn_2(dobpbdc), which was dosed with 5 mbar CO_2 at ambient temperature. Values in parenthesis indicate one standard deviation from the parameter value. Temperature = 100 K, space group $P3_221$, a = 21.6819(4) Å, c = 7.0794(1) Å, V = 2882.2(1) Å^3. Goodness-of-fit parameters: wRp = 6.69%, Rp = 5.14%, χ^2 = 1.31.

atom	*x*	*y*	*z*	*multiplicity*	*occupancy*	U_{iso} (Å^2)
Mn	0.6096(3)	0.2717(3)	1.1455(6)	6	1	0.015(1)
O1	0.6595(9)	0.2387(9)	0.959(3)	6	1	0.011(3)[a]
O2	0.644(1)	0.282(1)	0.595(2)	6	1	0.011(3)[a]
O3	0.594(1)	0.2023(9)	0.379(3)	6	1	0.011(3)[a]
C1	0.632(2)	0.180(2)	0.871(4)	6	1	0.011(3)[a]
C2	0.611(2)	0.165(2)	0.681(5)	6	1	0.011(3)[a]
C3	0.576(2)	0.096(2)	0.617(4)	6	1	0.011(3)[a]
C4	0.563(1)	0.039(2)	0.714(4)	6	1	0.011(3)[a]
C5	0.588(1)	0.050(1)	0.897(4)	6	1	0.011(3)[a]
C6	0.613(2)	0.114(1)	0.987(4)	6	1	0.011(3)[a]
C7	0.618(2)	0.219(2)	0.542(4)	6	1	0.011(3)[a]
H1	0.583	0.010	0.965	6	1	0.011(3)[a]
H2	0.626	0.119	0.117	6	1	0.011(3)[a]
H3	0.562	0.085	0.488	6	1	0.011(3)[a]
O1x	0.509(1)	0.196(1)	1.043(3)	6	0.839(8)	0.005(7)
C1x	0.452(2)	0.191(3)	1.059(5)	6	0.839(8)	0.04(1)
O2x	0.425(2)	0.201(2)	1.212(5)	6	0.839(8)	0.09(1)
N1m	0.443(2)	0.227(2)	0.905(5)	6	0.839(8)	0.05(1)
C1m	0.373(2)	0.227(2)	0.863(5)	6	0.839(8)	0.06(2)
C2m	0.457(2)	0.205(3)	0.729(6)	6	0.839(8)	0.07(2)
C3m	0.418(3)	0.129(3)	0.661(8)	6	0.839(8)	0.09(2)
N2m	0.445(4)	0.125(3)	0.47(1)	6	0.839(8)	0.32(5)
C4m	0.400(2)	0.053(2)	0.370(5)	6	0.839(8)	0.001(11)
H4	0.386	0.259	0.758	6	0.839(8)	0.2
H5	0.338	0.180	0.822	6	0.839(8)	0.2
H6	0.353	0.242	0.962	6	0.839(8)	0.2
H7	0.446	0.231	0.633	6	0.839(8)	0.2
H8	0.507	0.219	0.722	6	0.839(8)	0.2
H9	0.428	0.100	0.748	6	0.839(8)	0.2
H10	0.368	0.112	0.657	6	0.839(8)	0.2
H11	0.433	0.149	0.387	6	0.839(8)	0.2
H12	0.491	0.145	0.470	6	0.839(8)	0.2
H13	0.370	0.057	0.278	6	0.839(8)	0.2
H14	0.432	0.040	0.310	6	0.839(8)	0.2
H15	0.372	0.018	0.463	6	0.839(8)	0.2

[a]The thermal parameters for all of atoms of the dobpdc^{4-} ligand were constrained to be equivalent.

Table A.S4. Rietveld Refinement of 295K-CO2-mmen-Mn_2(dobpdc), which was dosed with 100 mbar CO_2 at ambient temperature. Values in parenthesis indicate one standard deviation from the parameter value. Temperature = 295 K, space group *P*3221, *a* = 21.7427(7) Å, *c* = 7.0696(2) Å, *V* = 2894.4(2) Å3. Goodness-of-fit parameters: wRp = 5.92%, Rp = 4.44%, χ^2 = 1.03.

atom	*x*	*y*	*z*	*multiplicity*	*occupancy*	U_{iso} (Å^2)
Mn	0.6096(8)	0.2717(7)	1.145(2)	6	1	0.036(4)
O1	0.659(3)	0.239(3)	0.959(8)	6	1	0.020(8)[a]
O2	0.644(2)	0.282(3)	0.595(6)	6	1	0.020(8)[a]
O3	0.594(3)	0.202(2)	0.379(7)	6	1	0.020(8)[a]
C1	0.632(4)	0.180(5)	0.87(2)	6	1	0.020(8)[a]
C2	0.611(4)	0.165(6)	0.68(1)	6	1	0.020(8)[a]
C3	0.576(4)	0.096(5)	0.62(1)	6	1	0.020(8)[a]
C4	0.563(4)	0.039(4)	0.71(1)	6	1	0.020(8)[a]
C5	0.588(4)	0.050(4)	0.90(1)	6	1	0.020(8)[a]
C6	0.613(4)	0.114(5)	0.99(1)	6	1	0.020(8)[a]
C7	0.618(5)	0.219(5)	0.54(1)	6	1	0.020(8)[a]
H1	0.583	0.097	0.965	6	1	0.020(8)[a]
H2	0.626	0.119	0.117	6	1	0.020(8)[a]
H3	0.562	0.085	0.488	6	1	0.020(8)[a]
O1x	0.509(4)	0.196(3)	1.04(1)	6	0.90(2)	0.07(4)
C1x	0.452(8)	0.191(9)	1.06(1)	6	0.90(2)	0.15(2)[b]
O2x	0.425(5)	0.201(5)	1.21(2)	6	0.90(2)	0.15(2)[b]
N1m	0.443(6)	0.227(6)	0.91(2)	6	0.90(2)	0.15(2)[b]
C1m	0.373(7)	0.227(6)	0.86(2)	6	0.90(2)	0.15(2)[b]
C2m	0.457(6)	0.205(8)	0.73(2)	6	0.90(2)	0.15(2)[b]
C3m	0.418(8)	0.129(8)	0.66(2)	6	0.90(2)	0.15(2)[b]
N2m	0.445(5)	0.125(6)	0.47(2)	6	0.90(2)	0.15(2)[b]
C4m	0.400(7)	0.053(5)	0.37(2)	6	0.90(2)	0.15(2)[b]
H4	0.386	0.259	0.758	6	0.90(2)	0.19
H5	0.338	0.180	0.822	6	0.90(2)	0.19
H6	0.353	0.242	0.962	6	0.90(2)	0.19
H7	0.446	0.231	0.633	6	0.90(2)	0.19
H8	0.507	0.219	0.722	6	0.90(2)	0.19
H9	0.428	0.100	0.748	6	0.90(2)	0.19
H10	0.368	0.112	0.657	6	0.90(2)	0.19
H11	0.433	0.149	0.387	6	0.90(2)	0.19
H12	0.491	0.145	0.470	6	0.90(2)	0.19
H13	0.370	0.057	0.278	6	0.90(2)	0.19
H14	0.432	0.040	0.310	6	0.90(2)	0.19
H15	0.372	0.018	0.463	6	0.90(2)	0.19

[a]The thermal parameters for all of atoms of the dobpdc^{4-} ligand were constrained to be equivalent. [b]With the exception of O1x, the thermal parameters for all atoms of mmen were constrained to be equivalent.

Table A.S5. Summary of piecewise Lagnmuir-Freundlich fit parameters for stepped CO_2 isotherms of mmen–M_2(dobdc).

	Mg	Mn	Co	Fe	Zn
n_{sat1} (mmol g^{-1})	8.1	1.0	8.2	1.4	2.2
S_1 (R)	–13.9	–9.8	–17.2	–15.0	–14.7
H_1 (kJ/mol)	–38.6	–26.6	–40.7	–42.2	–38.4
v_1	0.7	0.6	0.9	1.0	0.9
n_{sat2a} (mmol g^{-1})	3.4	2.5	2.7	2.5	2.2
S_{2a} (R)	–17.5	–20.0	–14.3	–18.6	–18.3
H_{step} (kJ/mol)	–74.1	–75.9	–53.5	–56.9	–57.3
v_{2a}	1.2	1.4	0.9	0.7	1.0
n_{sat2b} (mmol g^{-1})	12.0	15.0	4.9	9.6	3.5
S_{2b} (R)	10.0	11.7	10.1	7.9	10.1
H_{2b} (kJ/mol)	18.3	22.4	22.2	14.7	21.8
v_3	0.8	0.9	0.9	0.6	0.9
$P_{step,T0}$	0.5	4.3	450.0	120.8	127.0
T_0	313.15	313.15	313.15	313.15	313.15

Table A.S6. Summary of dual-site Langmuir-Freundlich fit parameters for CO_2 isotherms of mmen–Ni_2(dobdc).

	Ni
n_{sat1a} (mmol g^{-1})	6.6
S_{1a} (R)	–18.7
H_{1a} (kJ/mol)	–45.1
v_{1a}	1.2
n_{sat2b} (mmol g^{-1})	0.7
S_{2b} (R)	–25.3
H_{2b} (kJ/mol)	–68.2
v_{2b}	0.8